

AD-A063 163

OFFICE OF NAVAL RESEARCH ARLINGTON VA
PROCEEDINGS OF THE WORKSHOP ON SEISMIC PROPAGATION IN SHALLOW W--ETC(U)
JUL 78

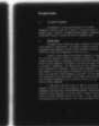
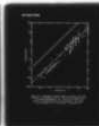
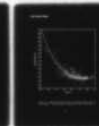
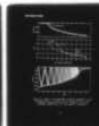
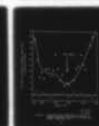
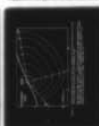
F/G 8/11

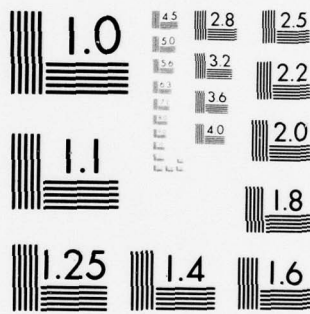
UNCLASSIFIED

NL

1 OF 5

AD
A063163





MICROCOPY RESOLUTION TEST CHART
NATIONAL BUREAU OF STANDARDS-1963-A

LEVEL II



AD A063163

6

PROCEEDINGS

the

WORKSHOP ON SEISMIC PROPAGATION
IN SHALLOW WATER

Held on

6-7 JULY 1978 at

Office of Naval Research,
Arlington,
Virginia.



DDC
RECEIVED
JAN 11 1979
D

11 7 Jul 78

12 434p.

APPROVED FOR PUBLIC RELEASE
DISTRIBUTION UNLIMITED

OFFICE OF NAVAL RESEARCH
800 No. Quincy Street
Arlington, Va.
22217

DISTRIBUTION STATEMENT A
Approved for public release
Distribution Unlimited

79 01 10 017
265 250 LB

TABLE OF CONTENTS

Introduction -----	1
Review and Conclusions -----	2
List of Presentations -----	6
Presented Papers -----	7
Appendix A - List of Attendees -----	A1
Appendix B - Letters -----	B1

ACCESSION FOR	
DTIC	White Section <input checked="" type="checkbox"/>
DDO	Grey Section <input type="checkbox"/>
UNANNOUNCED	<input type="checkbox"/>
JUSTIFICATION	
BY	
DISTRIBUTION/AVAILABILITY CODES	
Dist.	AVAIL. and/or SPECIAL
A	

APPROVED FOR PUBLIC RELEASE
DISTRIBUTION UNLIMITED

DDC
RECEIVED
JAN 11 1979
D

DISTRIBUTION STATEMENT A

Approved for public release;
Distribution Unlimited

79 01 10 017

SEISMIC WORKSHOP

Introduction

This workshop considered

A workshop to consider seismic propagation in the continental margin (e.g., water depths of 200m or less), was sponsored by the Office of Naval Research and the Naval Research Laboratory in Washington, D.C. on 6/7 July 1978.

It has been known for some time that when an acoustic signal is radiated into the water, a certain amount of the energy becomes coupled with the bottom and may be measurable as a seismic signal. Although the mechanism of the coupling, modes of propagation, and signal coherence are poorly understood (if they are at all), there are some indications that a horizontally oriented geophone may provide better signal to noise ratio in shallow water than a hydrophone measuring the same signal. It was the desire to define this improved signal to noise ratio that led to the calling of the workshop.

The workshop was not technology oriented; it was designed to explore some of the physical processes involved with seismic propagation, as described. As time went on, however, it became clear that more specific motivation was required. The following was provided. Under certain circumstances, the conventional acoustic methods for detection of submarines at long range lose their attractiveness, one of these circumstances is shallow water. In shallow water, acoustic energy becomes rapidly attenuated through interactions with the surface and bottom; its coherence likewise is lost through similar interactions. A glance at the globe indicates that a substantial part of the world's oceans can be classified as shallow water, (e.g., less than 200m), and that much of that shallow water lies in important areas (e.g., the North Sea, East Coast of the Americas, etc.). Since acoustic surveillance by conventional means is degraded in these important areas, an alternative is desirable. One possible alternative is seismic surveillance.

The only hard parameter that was mentioned in preparation for the workshop was an upper limit of about 30 Hz; no lower bound was mentioned, nor was any original signal strength postulated. A lower bound of 5 Hz was proposed by Dr. Latham, based on ambient noise considerations.

It may be that seismic surveillance provides an attractive alternative to acoustic surveillance in any oceanic regime. However, in view of the fact that the acoustic problem in deep water is more tractable than in shallow and acoustic surveillance appears to be successful in this area, it is probable that the

greatest contribution of seismic surveillance, if proved to be viable, will be in shallow water. Such comparative tests as have been performed have all been conducted in shallow water.

The objectives of the workshop were to explore the signal to noise ratio as measured by the geophone, the hydrophone, exchange ideas and information, and discuss the following issues related to the subject:

- The Environment: The effect of macro through micro scale geological discontinuities on signals; the anticipated levels of acoustic and seismic noise levels.
- Propagation: Propagation paths; modes; signal coherence; mechanics of acoustic coupling into the bottom; the effect of a shoaling bottom on energy coupling.
- The Signal: Deployment of sensor (surface and/or in bore holes).

Unfortunately, there was so little data to work with, that many questions remain unresolved. The workshop reached a consensus of what further research is desirable. This list is included below.

Review and Conclusions

In his introductory remarks, Dr. Hersey pointed out that we have come a long way in seismology with respect to measuring the geometrical aspects of the earth's structure. However, the question of energetics of wave propagation is largely untouched. The Navy's adroit use of underwater acoustics has resulted from paying a great deal of attention to energetics. Similar efforts must be made with respect to seismic propagation if the Navy is to use this tool. He emphasized that we, as scientists, "Can't quite follow the precept that (we're) going to find out first what is easy to find out - (we're) going to have to find out enough to do (the) job", i.e., satisfy the Navy's purpose.

In the many highly informative presentations and discussions which followed, a number of critical issues and problem areas were addressed. Since the subject matter extends across the disciplines of underwater acoustics and seismology the problem of communication among workers in these two areas was readily apparent. Investigators concerned with the detection of submarines via seismic propagation paths are confronted with a learning process in this respect.

In his presentation, Mr. Urick cited experimental results in which the signatures from passing ships were received by adjacent geophones and a hydrophone with a strong downward refracting profile in the water column. At frequencies below about 70 Hz the horizontal geophones, both radial and transverse, showed higher signal to noise (S/N) ratios than the hydrophone. The surprising features were that the transverse geophone had S/N levels comparable with the radial element and the vertical geophone displayed a markedly lower S/N. In the discussion which followed, Mr. Urick cautioned that the hydrophone and the geophones could possibly be responding to the same signal if the hydrophone was seeing the pressure field resulting from reradiation into the water from ground vibration. He also voiced the opinion that since shear attenuation is very large for frequencies above about 5 Hz, the modes of long-range propagation observed by seismologists are unlikely to be important to long-range propagation.

Data shown by Dr. Latham indicated that the sea floor is very quiet at 15 Hz and that the optimum S/N is at approximately 15 Hz at short ranges and 8 Hz at 1000 Km. The most promising frequency band appears to be in the range of 5 to 25 Hz. In the discussion following his presentation the question of the variation of optimum frequency with depth was brought up. He commented that by going deep you alter the noise background (quieter as you go deeper) and thus this could alter the optimum frequency. In the discussion following Dr. Edsinger's paper, Dr. Edsinger commented that noise increases with decreasing frequency but this is partially compensated by an increasing Q (decreasing attenuation) and that the optimum frequency is a critical issue. He also pointed out the importance of obtaining additional data on seismic noise.

Dr. Sigelmann's paper and also those of Drs. Coppens (presented by Dr. Moose) and Sanders illustrated that in accordance with both experiment and theory, sound propagating toward the apex in a water wedge is rapidly dumped into the bottom when reflection angles reach the critical angle. This results in the formation of a narrow beam (narrower with decreasing slope) which is directed downward at about 15°. The angle of depression of the beam is only weakly dependent on the bottom slope and bottom parameters.

Dr. Walker discussed some unusual data observed on spectrograms of earthquakes having travel paths under the Northwestern Pacific Basin and under the Ontong Plateau. He observed remarkably high energy at frequencies as high as 12 Hz for P_n and 15 Hz for S_n at the Hokkaido Station. This he regards as evidence of some type of ducted or guided propagation the mechanism for which is unknown.

A number of questions involved experimental or operational techniques. Following Dr. Northrup's paper there was a discussion on techniques of coupling geophones to the medium. Questions raised included those concerning burial techniques, resonances in mounting structures, and pipe resonance in bore-holes. Dr. Edsinger commented on the difficulty of array calibration for the frequencies of interest. He thought that deeply buried arrays might be more amenable to calibration.

During the discussion period on the second day interest centered around the types of experiments that might be conducted. Mr. Urick suggested that initial experiments should be kept simple and that details of specific experiments could be readily worked out by a small group of people. Dr. McLeroy pointed out the importance of obtaining a thorough knowledge of the bottom in the experimental site and of the necessity of performing calculations to eliminate consideration of impossible paths. A considerable amount of data may already exist. Several people thought that noise data as a function of depth exists for bore-holes on land. Dr. McLeroy is in possession of a large quantity of relevant data - much of which is unfunded for processing - from the experiments conducted offshore from Panama City. It was suggested by Mr. Ferris that since detection via seismic paths is still in the speculative stage, a need exists for one or more experiments designed to substantiate (or weaken) the possibility of exploiting this technique. Such experiments would not have to be elaborate or optimized but should be designed to show that - at least under good conditions - water-borne targets could be detected via seismic paths. There was some discussion and there appeared to be general agreement that such experiments were needed. It was suggested that, in order to keep the experiments simple, single sets (rather than arrays) of geophones together with a hydrophone should be deployed in several areas where passing ships would provide targets of opportunity. The geophones could be either on the bottom or shallowly buried.

On the afternoon of the second day, those attendees who did not have prior commitments reassembled in a wrap-up session to attempt to summarize the critical issues and to recommend priorities for initial efforts. The results of this effort, which were agreed to by the group, are given below. The critical issues are listed together with a priority ranking and an indication as to whether the emphasis should be on measurements, modeling, or both.

<u>Issue</u>	<u>Priority</u>	<u>Type of Effort</u>
Demonstration experiment for potential	1	Meas.
Ambient Noise	2	Meas.
Attenuation	3	Meas.
Propagation Physics	3	Modeling
Techniques of acquiring bottom characteristics	4	Both
Coherence	5	Meas.

List of Presentations

"Background of the Problems Associated with Seismic Detection of Signal Sources in the Ocean,"

Richard J. Hecht, Underwater Systems, Inc.

(Copy of paper in this Proceedings)

"Seismic Sensing of Sound in the Sea, Signal to Noise Ratios of Hydrophones vs Geophones,"

Robert J. Urick, TRACOR, Inc.

(Copy of published report, "Seismic Sensing of Sounds in the Sea," included in this Proceedings)

"Geoacoustic Parameters of the NOSC Tower Site,"

John Northrup, NOSC

(Copy of paper in this Proceedings)

"The NCSC Shallow Water Seismic Propagation Study,"

Glenn McLeroy, NCSC

(Copy of paper in this Proceedings)

"Shallow Water Acoustic Structure of the Continental Shelf by Continuous Refraction Profiling with a Multichannel Towed Array,"

Mark A. Houston, Jr., U. Texas at Galveston

(Copy of paper in this Proceedings)

"Seismic Properties of Continental Margin Sediments,"

Robert Houtz, LDGO

(Preprint of paper now in press in the Journal of Geophysical Research, "Preliminary Sonobuoy Study of Rapidly Accumulating Shelf Sediments," included in this Proceedings)

"Analysis Techniques for Seismic Signals in an Underwater Acoustic Experimental Range,"

Don Fletcher, Institute for Acoustic Research

(Copy of paper in this Proceedings)

"High Frequency P_n and S_n Phases: Frequency, Efficiency, and Propagation Pathsⁿ in theⁿ Western and North Pacific,"

Dan Walker, U. Hawaii

(Copy of paper in this Proceedings)

"Seismic Measurements on the Sea Floor,"
Gary V. Latham, U. Texas at Galveston
(Copy of paper in this Proceedings)

"The Acoustic Bottom Interaction Problem,"
Ken Hawker, U. Texas at Austin/ARL
(Copy of paper not available)

"Ocean-Earth Acoustic Coupling,"
Rubens A. Sigelmann, U. of Washington
(Copy of report in this Proceedings)

"The Model: Transmission of Sound into a Fast Fluid Bottom
from an Overlying Fluid Wedge,"
Alan Coppens, NPS; Presented by Dr. Paul Moose, NPS
(Copy of paper in this Proceedings)

"The Experiment: Transmission of Acoustic Waves into a Fast
Fluid Bottom from a Converging Fluid Wedge,"
James Sanders, NPS
(Copy of paper in this Proceedings)

"The Inverse Method for Detecting Velocity Variations in the
Bottom,"
Jack Cohen, U. Denver
(Copy of paper not available)

"Buried Seismic Arrays for Shallow Water Surveillance,"
Richard Edsinger, Boeing
(Copy of paper in this Proceedings)

Presented Papers

Where available, authors furnished copies of the presentations and/or published reports from which the presentations were derived. Copies of all furnished material follow in the order given in the preceding list of presentations.

Background of the Problems Associated
With Seismic Detection of Signal Sources in the Ocean

By:
Richard J. Hecht
Underwater Systems, Inc.

The seismic detection of signal sources in the ocean is subject to many interpretations based on one's perception of the problem. In this discussion seismic detection will be limited to the situation for which a significant part of the acoustic signal path is through the bottom. With this definition in mind, six aspects of the background of seismic detection will be presented:

1. the generalized problem which describes the overall situation
2. the shallow water environment which could derive the largest improved capability from seismic detection
3. the background noise against which we detect signals
4. the geophone as a detector, taking advantage of its particular attributes as a detector
5. the design of an array for seismic detection
6. the issues and lack of knowledge in specific areas of seismic detection that are needed for the evaluation of concepts

Generalized Problem

A generalized description of the propagation medium or the communication link together with representative location of acoustic source and receiver is illustrated in Figure 1. The sources of interest are characterized by (1) a spectrum level of 160 to 180//1 μ Pa, (2) a 1 to 30 Hz frequency range, (3) a source depth in water of 0 to 400 meters, and (4) a spectrum comprised of tonals. The typical locations for receivers that may be used to receive seismic energy can be located either in the bottom, in the water, or in boreholes. R_1 and R_4 are located in the water and depend on bottom propagated energy to be refracted into the water for reception. R_2 and R_3 are located at shallow depths in the bottom. Paths to these receivers can be propagated either through a bottom

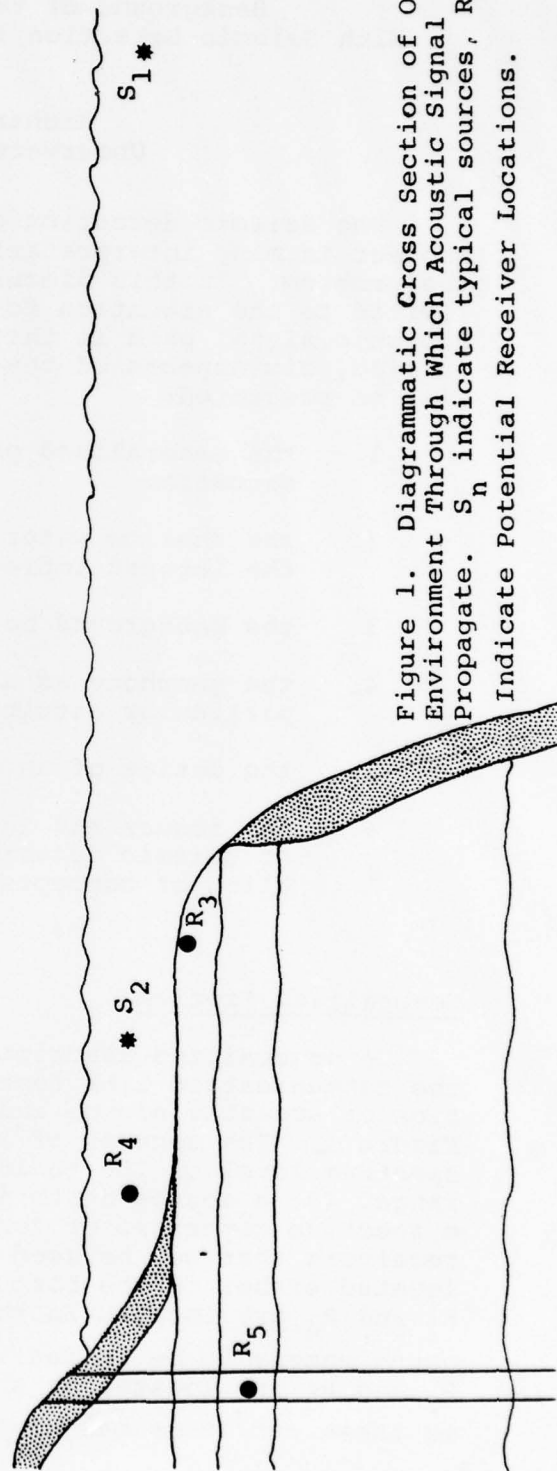


Figure 1. Diagrammatic Cross Section of Oceanic Environment Through Which Acoustic Signal Propagate. S_n indicate typical sources, R_n Indicate Potential Receiver Locations.

layer or from the waterborne energy near the water bottom interface. R_5 and R_6 are located in a borehole. R_5 is located in the sediment and R_6 in the crystalline basement. These two receivers are placed to receive energy propagating in the layer in which they are located. Since the source is always located in the water portion of the communication channel, the total capability of this time-variable heterogeneous channel needs to be considered. The receivers need to be positioned to optimally sample the channel to obtain the best signal to noise ratio.

When favorable velocity profiles exist in the water, transmission through the water is superior to transmission through the bottom. When the velocity profile in the water is unfavorable, then propagation through the bottom, (seismic detection) offers a potential of reliable propagation that is essentially unaffected by propagation conditions in the water. By combining the capabilities of water and bottom propagation, the communication channel can guarantee a minimum range of detection via predominantly seismic paths and yet retain the added capability of the paths that are predominantly waterborne.

The communication channel just discussed exists in both shallow and deep water. However, it is in shallow water that it appears that the largest gain in signal propagation can be achieved by pursuing the total communication channel concept.

Shallow Water Problem

Shallow water investigations that recognized the interaction of the water and bottom were begun previous to World War II. Probably the best known participants in these investigations were Ewing, Pekeris, Press and Worzel of Columbia University. Their work was summarized and interpreted after the War in G.S.A. Memoir 27 (Ref. 1) which even today is the baseline reference for shallow water propagation. Three applicable results from the Memoir are the interpretation of sound transmission using wave theory, i.e. guided transmission; the Ewing effect, which is the dispersion observed in the lower frequency region; and the concept of depth of penetration of acoustic energy into the bottom.

The guided transmission theory for shallow water was adapted from electromagnetic theory. Of particular importance is the description of the pressure and particle velocity as a function of depth. The vertical distribution of pressure in the water

has been confirmed by Ferris (Ref. 2) and others. Figure 2 is a typical amplitude distribution vs. depth for the first mode at a frequency slightly above cut off, for typical low density and low velocity ratios for a liquid bottom. Of particular interest is the pressure amplitude near the bottom. For this particular case the receiver location for the best signal strength is near the sediment-water interface.

The depth of penetration was defined by Pekeris (Ref. 1) as the depth at which no further information on the structure of the bottom at greater depths can be obtained from dispersion data. As a quantitative measure he used the section of the bottom that contained 99% of the total energy in the bottom. Another way to look at depth of penetration is that all useful guided energy will be above that depth. Since we are interested in locating potential seismic energy paths, the depth of penetration tells us how deep we have to consider the sediments or rock. Attenuation in the sediments may also limit depths that need to be considered. The concept of penetration depth was extended by Williams (Ref. 3) in his concept of hidden depths.

The phenomenon of dispersion in the water wave was discovered by Ewing (Ref. 1). Observed dispersion is related to the depth, density, and velocity ratios of the transmission media. Pekeris makes the point that if the dispersion curves from different paths are indistinguishable, so also are the parameters of the media. From this statement one would further conclude that the measurement of dispersion is a pragmatic way of describing the acoustic behavior of the ocean bottom.

In 1955 Kornhauser and Raney (Ref. 4) added the effect of attenuation in the bottom to the wave description of propagation as a function of frequency and mode number, but the attenuation coefficients were not specified.

The next significant step in understanding shallow water propagation as well as propagation through the bottom was made by Tolstoy, Clay, and Blaik (Refs. 5 and 6). In their Fire Island experiment it was concluded that bottom parameters-determined by seismic refraction were inferior to acoustic determined parameters (Ref. 7). The experiment showed the adequacy of the wave model to predict short range shallow water propagation. In Figure 3 relative propagation loss contours for a 10 and 14 Hz source are shown (Ref. 6). The receiver is a vertical geophone located in a borehole on the beach at a depth of 129 meters. The indicated propagation loss exceeds 20 log R. This result will be further discussed in a following section.

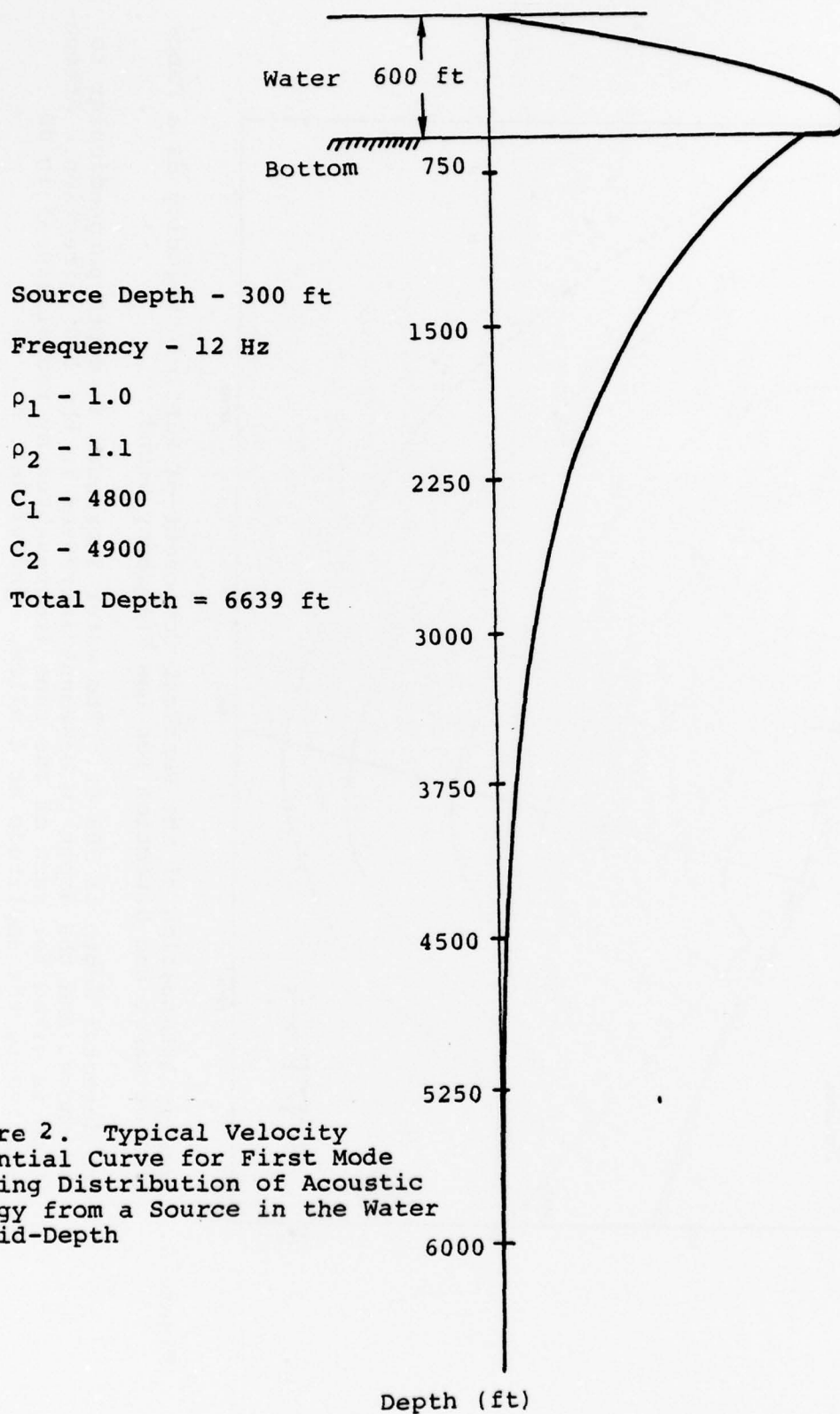


Figure 2. Typical Velocity Potential Curve for First Mode Showing Distribution of Acoustic Energy from a Source in the Water at Mid-Depth

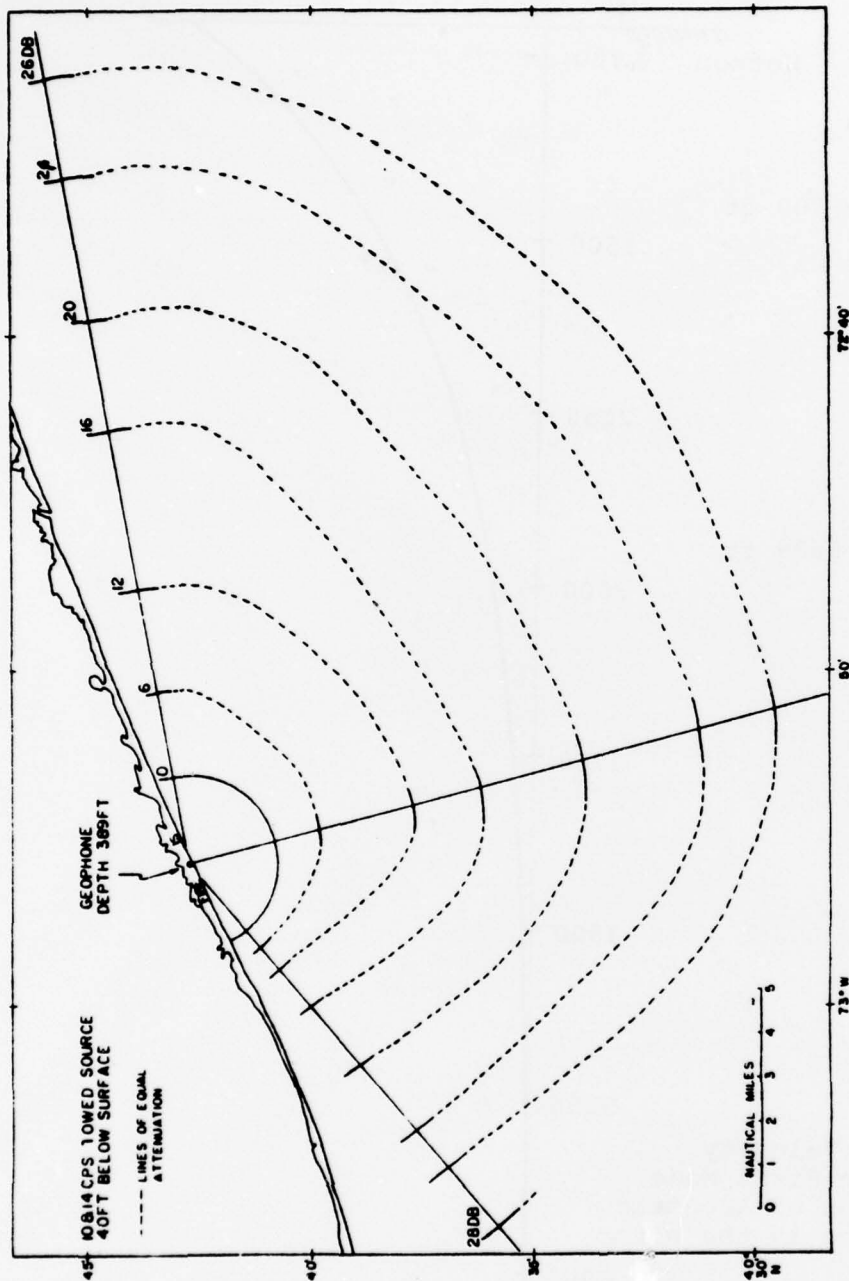


Figure 3. Average Attenuation of the Vertical Component of Particle Velocity as a Function of Range and Direction for Low Frequency Sound.

The detector depth is 389 ft. The water increases in depth perpendicular to the shore, and the depth to basement increases in the 170° direction. Attenuation is given for each of the runs (represented by radial lines) in dB relative to the amplitude at 2 miles. (After Ref. 6).

The effect of a mixture or a loaded liquid has been discussed by Officer (Ref. 8). For the water-bottom interface Figure 4a shows the resulting velocity of the upper region of a structureless bottom to be less than that of the water. Under such a condition the natural question to ask is where is the water-bottom interface for guided transmission? The above results assume an ideal situation. If a water-filled sediment is considered, then the sediment will exhibit some structure, probably very little at the water-bottom interface but the structure increases with depth. Also water has viscosity. With these added real life parameters, consider a high porosity sediment. The viscosity of the water will cause a sediment velocity that is dependent on frequency as illustrated in Figure 4b. A medium that exhibits such behavior will be highly dispersive. The mixture effects are undoubtedly present in the first bottom layer and need to be considered as well as the structure in the sediment.

In an experiment using a Texas Tower as a receiving station, Barakos studied shallow water propagation as a function of season (Ref. 9). Ranges in excess of 100 nautical miles were achieved using bomb shots as sources with favorable sound velocity profiles in the water. By using the dispersion concept of Ewing (Ref. 1) he acoustically categorized a large area of the continental shelf between New Jersey and Nantucket. Bucher added to the dispersion concept by advancing the idea of measuring attenuation by quantitatively measuring the amplitude in small frequency increments for each mode (Ref. 10).

To categorize the shelf Houtz and others (Ref. 11) developed a method for measuring interval velocities of the sediments on the shelf using sonobuoys.

In all the shallow water propagation studies of the past, one theme is highlighted; an adequate acoustic description of the bottom is needed. Tolstoy (Ref. 7), through a sensitivity analysis, showed the importance of accurately knowing the acoustic impedance and layer thickness. An adequate description of the bottom is one of the prerequisites for being able to predict acoustic propagation in the bottom with confidence and accuracy. Another bottom parameter that has a controlling effect on propagation is attenuation.

Attenuation in the sediments has been of concern since the early 1950's. Tolstoy developed empirical attenuation coefficients based on his Fire Island data following the method of Kornhauser and Raney (Ref. 4). Nominal values were $5 \times 10^{-4}/\text{m}$ at 10 and 14 Hz (Ref. 5). Hamilton and others began measuring attenuation and relating it to the porosity of sediments. In

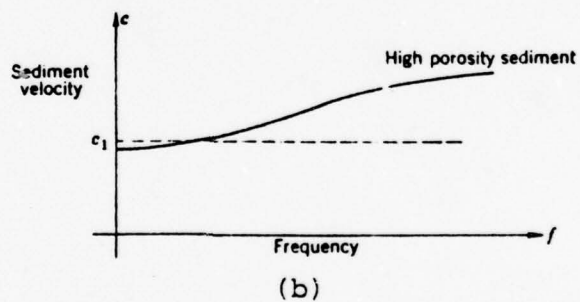
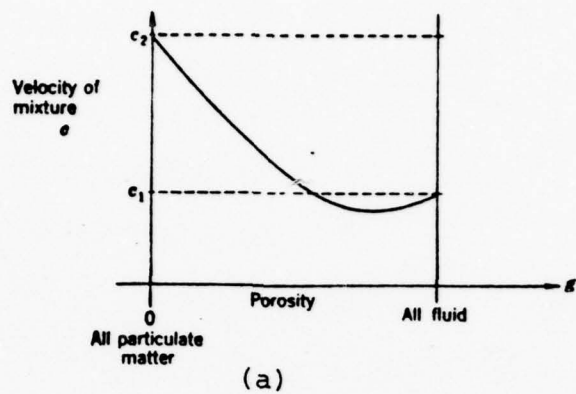


Figure 4. The Effects of Porosity and Frequency on the Sound Velocity in an Unconsolidated Sediment. (After Ref. 8).

a recent study (Ref. 12) he summarized the attenuation of compressional and shear waves; the results are shown in Table 1. Attenuation is in terms of a logarithmic decrement per wavelength, which is the natural log of the ratio of the amplitude of a wave at successive maxima. Therefore attenuation as a function of range can be described as $a(R) = e^{-dR/\lambda}$, where d is the logarithmic decrement, R is range and λ is wavelength. For compressional waves sand and fine sand appear to comprise one attenuation group and the silt clays and clay silts another. The difference in attenuation between these two groupings is a factor of six. Figure 5 shows attenuation vs range for 3 values of logarithmic decrement, 0.1, 0.017 and 0.005 for a frequency of 3 Hz and a wavelength of 600 m. The graph dramatically presents the high attenuation expected for logarithmic decrements (Δ) of 0.1, which is representative of sand. The curve for a decrement of 0.005 is representative of crystalline rocks.

Since there are no known measurements of propagation through these types of sediments some conjectures will be made as to what one might expect from a source in the water. A simple propagation loss (PL) equation will be defined:

$$PL = SLR + \alpha R + P/S$$

where

SLR = spreading loss

αR = attenuation

P/S = the ratio of compressional to shear energy

For spreading loss we will use $10 \log R + 60$ where R is in kilometers. The 60 dB loss for the first kilometer assumes spherical spreading. The compressional to shear energy ratio in the bottom sediments is derived from the amplitude functions of the normal modes (Ref. 13).

$$P/S = \frac{K_n (2 - c^2/\beta^2)}{2 (\sqrt{1 - c^2/\alpha^2})} e^{-K_n (z-H) [\sqrt{1 - c^2/\alpha^2} - \sqrt{1 - c^2/\beta^2}]}$$

Where K_n is the wave number

c = phase velocity

α and β are the compressional and shear velocities in the bottom.

z = depth

H = water depth

Table 1

LOGARITHMIC DECREMENTS OF
ACOUSTIC ENERGY IN SEDIMENTS

	<u>Compressional Waves</u>			<u>Sheer Waves</u>
	<u>Low</u>	<u>High</u>	<u>Average</u>	<u>Average</u>
Sand	0.073	0.130	0.100	0.3
Fine Sand	-	-	0.103	-
Silt Clays	0.007	0.028	0.017	0.1
Clayey Silt	-	-	0.016	-

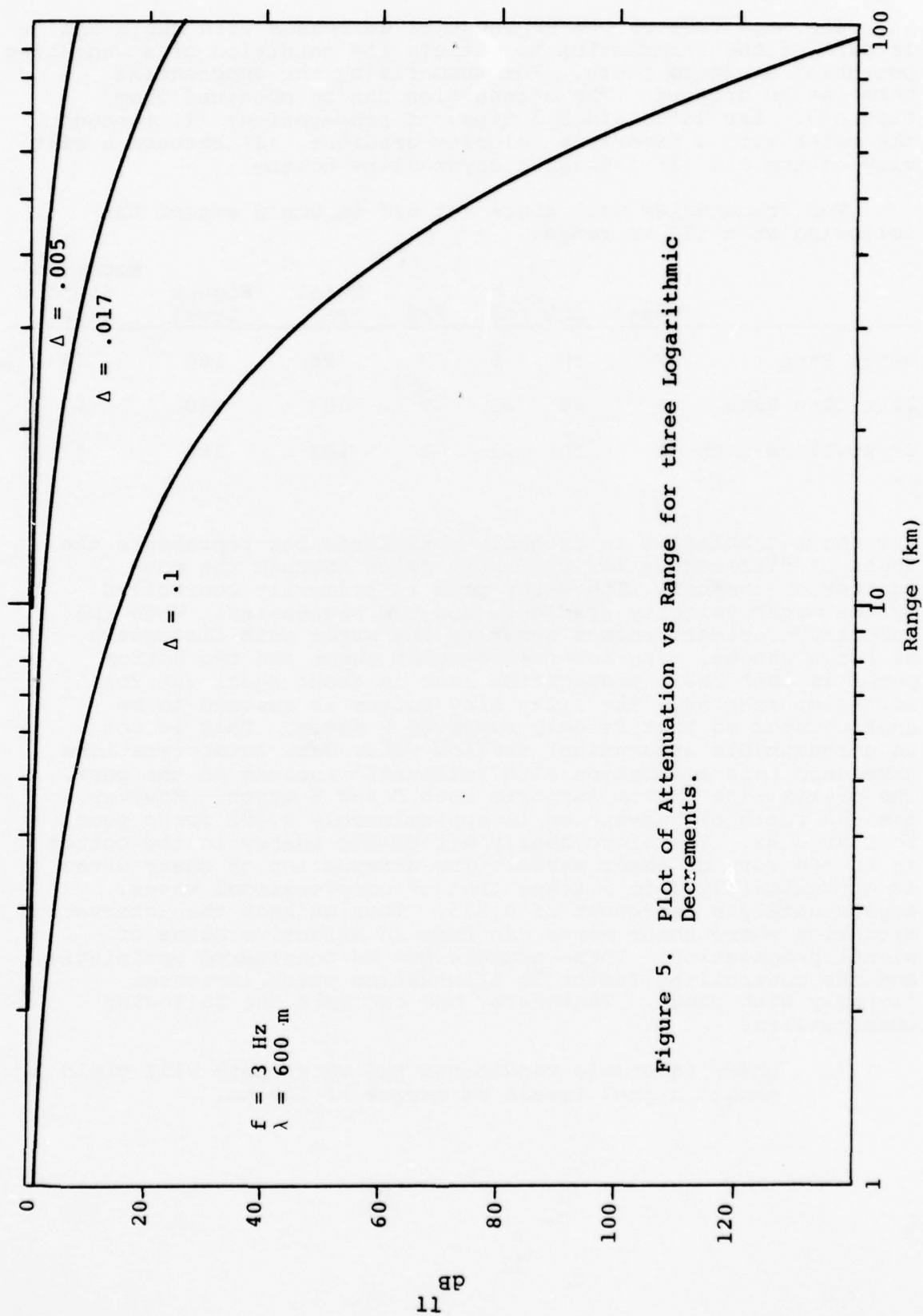


Figure 5. Plot of Attenuation vs Range for three Logarithmic Decrements.

The magnitude of the exponential decreases with depth and is part of the formulation to satisfy the condition of a vanishing potential at large depth. For summarizing the exponential term can be dropped. The attenuation can be obtained from Figure 5. Let us consider 3 types of propagation: (1) through the water with a favorable velocity gradient, (2) through a silt clay bottom and (3) through a crystalline bottom.

For frequencies well above cut off we would expect the following at a 100 km range.

	Type	SLR	αR	P/S	Total PL	Signal Level	Received Signal Level
Water Path	P	80	≈ 6	0	86	160	74
Silt Clay Path	P	80	23	?	103	160	57
Crystalline Path	S	80	22	1	103	160	57

The above tabulation is probably optimistic but represents the types of differences for different paths through the communication channel. The water path is primarily controlled by the water velocity gradient, and the boundaries. When the velocity gradient becomes negative the water path disappears at large ranges. The interesting part about the two bottom paths is that their propagation loss is about equal but for different reasons. The silty clay bottom is assumed to be unstructured so that it only supports P waves. This is not an unreasonable assumption; shallow water data interpretations have used this assumption with reasonable success in the past. The crystalline bottom supports both P and S waves. However, the P/S ratio of conversion is approximately 0.002 for c equal to β at 3 Hz. Therefore nearly all of the energy in the bottom is in the form of shear waves. The attenuation of shear waves is approximately 3 to 5 times that of compressional waves, approximately a decrement of 0.025. Thus we have the interesting situation where shear waves can form an effective means of signal propagation. These numbers can be considered optimistic, and the controlling factor is attenuation which increases linearly with range. Therefore, one can make the following observations:

1. Under favorable conditions the water path will yield useful signal levels at ranges of 100 km.

2. Under unfavorable water conditions the bottom will yield a reliable range estimated to be 10 to 20 km.

Background Noise

There are few measurements of low frequency background noise in shallow water. In spite of lack of information important considerations will be discussed. At present we do not know the directionality of the noise; is it omnidirectional or is it primarily horizontal or vertical? Does the directionality change as a function of frequency? Answers to these questions can strongly affect the type sensor that should be used.

Since geophones are particle velocity devices they are sensitive to all types of media movement. Any water flow around the sensor that causes the slightest movement can increase the background noise level significantly. Wold and Purdy ran an experiment in Buzzards Bay in which they had a sensor mounted on a tripod that was resting on the bottom and another that was on a probe that penetrated the bottom (Ref. 14). Figure 6 shows their results. The sensor on the probe is much quieter and shows no response to the tide. Even at slack tide more than a 6 dB reduction in background noise appears to be achieved by proper sensor implantation.

Geophone as a Transducer

A geophone is an electromechanical sensor based on a non-moving reference point, and a moving earth that causes a voltage to be generated. The mechanical part of the system simulates a point fixed in space by using a relatively large mass. A coil of wire is wound on the mass. Permanent magnets create a magnetic field about the coil; the magnet is attached to the earth. If the earth moves, the magnet moves, the coil remains in place, and an electrical signal is generated in the coil proportional to the rate of relative motion; hence, the often used term velocity geophone. The above ideal system is difficult to achieve. The mass only approximates a fixed point, because it is coupled to the earth both by the suspending spring and the damping dashpot. The result is a mechanical resonance at the low end of the response curve followed by a flat response. The mechanical resonance sets the low frequency cut off for the sensor.

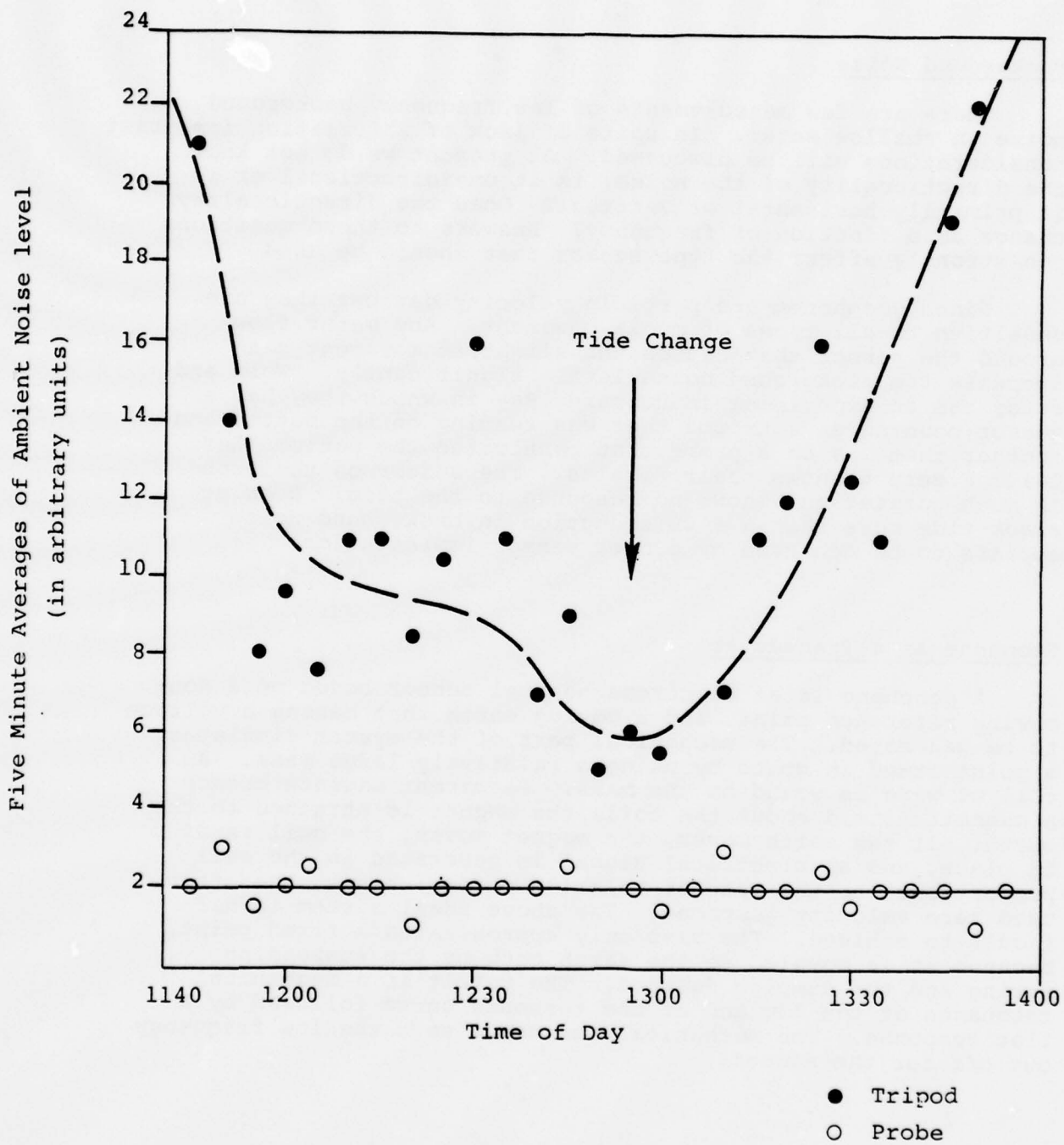


Figure 6. Background Noise Measurement Comparison between geophones mounted on a tripod and a Probe. (After Ref. 14).

A geophone is a unidirectional sensor. An axial guide restricts the motion of the mass; this function is accomplished by the spring. As a result of this restricted motion, only the component of velocity parallel to the axis of the geophone is sensed. As a result, the geophone has a sensitivity pattern that is directly proportional to the cosine of the angle measured from the sensor's axis. Figure 7 shows the pattern of the geophone. The pattern is a dipole with no gain in any direction, only attenuation off-axis. For an omnidirectional ambient noise field and an on-axis signal, the signal to noise ratio for the geophone output has been calculated to be 4.8 dB higher than for an omnidirectional sensor. The improvement in noise performance should be confirmed and studied with experimental data. Because motion restriction is accomplished by the mounting springs, some cross axis coupling can be expected.

Since a geophone is unidirectional, the question arises as to which way it should be oriented for optimum signal reception. Holmer, reanalyzed the basic equations of Pekeris and arrived at the conclusion that for a ratio of phase velocity to layer velocity of $\sqrt{2}$ or less the maximum particle velocity is in the horizontal directional for compressional waves (Ref. 15). McLeroy (Ref. 16) has also demonstrated the same conclusion in one of his experiments.

Since there appears to be a preferred direction for signal arrival and the geophone possesses directionality capabilities in a small package, it is feasible to have maximum response in the signal direction and yet have some noise reduction. To accomplish this triaxial or multi-axial geophones can be used. By phasing the various axial components they can be electrically steered in any desired direction. This capability can be used to increase the SNR at the output of the receiver.

The coupling of a geophone to the medium is an important factor that often may be overlooked. The oil companies often take great pains to match impedances when geophones are implanted in boreholes. A dramatic example of the results of different degrees of coupling is shown in Figure 8 (Ref. 14). The two curves result from the same signal, at the same range but for different mounting and coupling. The upper curve is the result of a probe implanted in the bottom and the lower is the result of the sensor mounted on a tripod sitting on the bottom. The trace from the implanted sensor is sharp and distinct in character, while the other is noisy and indistinct.

In light of the directionality of a geophone, let us re-examine the Fire Island data shown in Figure 3. Vertical geophones were clamped in the well at a depth of 129 meters. At a range of 2 to 20 miles one expects the signal propagation vectors to be mainly horizontal. Therefore, if horizontal geophones had been used it would be expected that the observed propagation loss would have been somewhat less, probably as much as 10 dB.

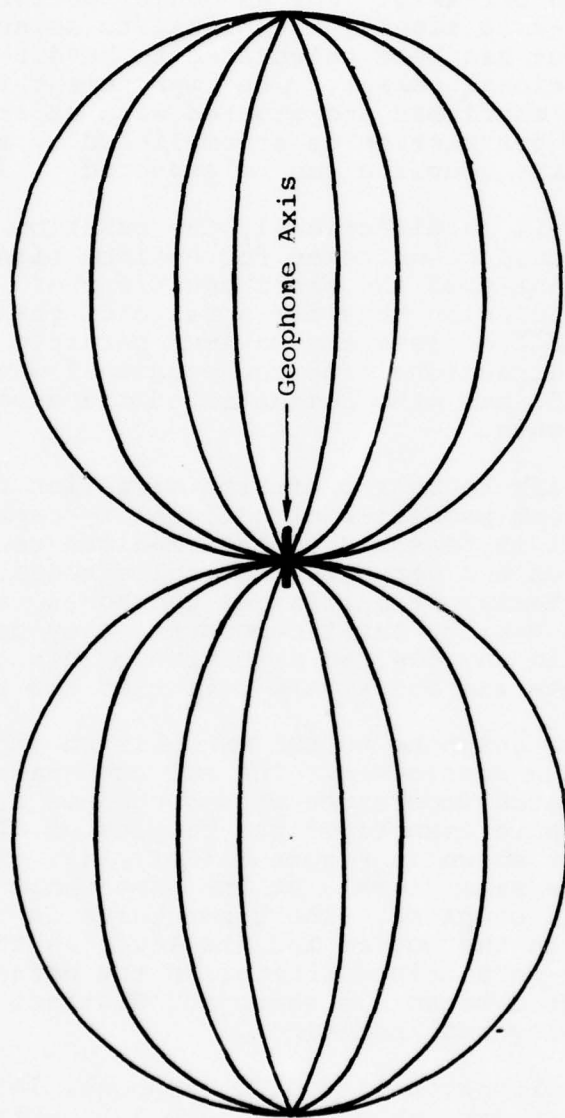


Figure 7. Directivity Pattern of a Geophone

Shot 21: Probe



Shot 21: Tripod



1 sec.

Figure 8. Comparative Responses of Probe- and Tripod-mounted geophones to an explosion (After Ref. 14).

Array Design

The potential for deriving spatial gain is dependent on the spatial and time coherence of a signal. The Large Aperture Seismic Array has demonstrated that beamforming is feasible and results in appreciable gain.

Considering the bottom as the propagation medium, we know from facies changes associated with sedimentation that the propagation medium will be spatially dependent. As a result large deviations from the plane wave assumptions will probably occur, and the wave front curvature problem will need to be effectively dealt with. In addition the inhomogeneities near the sensors may cause serious deviation, whereas the distant ones will blend into a slowly varying simple medium. The inhomogeneity effects near the array can be calibrated in much the same manner that bottom arrays are presently calibrated.

Four potential array designs will be considered, the distributed system, several small aperture arrays, single large aperture array, and borehole receivers. Each of these designs will be considered in turn.

The use of a distributed system is associated with areas of poor acoustic propagation. Although in the signal propagation discussions the propagation loss for the better propagation conditions were investigated, there are other water and bottom conditions in which the propagation is much poorer. For these poorer conditions, the distributed system is probably the ideal system.

If the distributed system is made up of multiaxial geophones, these can be steered and an estimated spatial gain of 3 dB may be realized. Thus each element of the distributed system is in itself a mini-array.

Previously the reliable range for propagation through the bottom was estimated at 10 to 20 km for silt clay type materials. For sand bottoms the range will be considerably shorter. For a distributed system, a sensor separation in the range of 10 to 100 km can be anticipated depending on propagation conditions.

Small aperture arrays have several outstanding attributes for use in the shallow water environment. Small aperture is used here to limit array size to the range of 1 to 10 wavelengths.

With a small aperture the wave front distortion problem should be minimized, thus normal beamforming will yield near theoretical gain; or if special processing is required, it can be less complex than for the large aperture array.

A small aperture array has greater spatial gain per installed sensor, since the increase in array gain is proportional to $\frac{1}{N}$.

The use of geophones as sensors also implies special procedures for coupling each element to the bottom; therefore, the larger part of array installation cost will be the per-element cost. The cost per element will become a much larger factor than with hydrophone arrays.

Another aspect is that two or more small aperture arrays can be used for multiple array processing. This type processing requires coherence between the arrays. The ambiguity plane processing gives high gain for low resolution systems. Also, the multiple array processing yields excellent localization capability.

Even with high attenuation the use of small aperture arrays in a multiple array processing scheme will have greater range capability than a simple large aperture array, will concentrate sensors in few locations as compared to a distributed system, and will provide better localization and classification information than the other concepts.

A large aperture array is useful for good propagation conditions and for wide coherent domain media. In shallow water, propagation loss is in the vicinity of $10 \log R$ for optimal environmental conditions, which are estimated to occur less than 25% of the time and probably over less than 20% of the eastern seaboard continental shelf. Under such conditions the large aperture array would only make a limited contribution to surveillance efforts. For example, a 10 Hz, 50-element array is approximately 8 km in length. With such a large aperture sophisticated calibration and beamforming will be required to begin to realize the potential spatial gain. The large aperture array does not appear to be a viable concept in shallow water.

Locating geophones in boreholes is an interesting concept for two reasons; (1) the receiving location could be located near shore or on shore and (2) the propagation loss through the bottom will be minimized. The minimization of the propagation loss is based on the higher attenuation coefficients of the unconsolidated sediments overlying the crystalline basement. The borehole concept would eliminate the need for the signal to traverse the sediments to the receiver, which is estimated to decrease propagation loss from several dB to as much as 10 to 15 dB. However, there are difficulties with the concept. In the Fire Island experiment the borehole was found to resonate and cause high level artifacts. It may be possible to use these mechanical resonant effects to advantage. Little is known about the interaction of a signal to a borehole and its possibilities.

Since propagation in shallow water is controlled by the size of the attenuation coefficient, the distributed system or small aperture array appear to be the most effective choices. The use of boreholes is a virgin subject and should be investigated.

Needed Measurements

Since data that demonstrates the usefulness of seismic paths for acoustic propagation at long ranges in shallow water is nearly nonexistent, all types of measurements are sorely needed. However, it would appear that concentrating efforts in the more basic areas so that a firm foundation can be established upon which to base surveillance concepts may be a viable basis for selecting needed measurements. Therefore, recommended measurements will be limited to 4 general areas.

1. Background Noise
2. Signal Propagation
3. Comparative SNR
4. Bottom Acoustic Parameters

Background noise measurements should be made at a number of locations to quantify noise directionality and amplitude vs depth in the communication link, i.e., from the water surface to some depth in the bottom. Comparisons of levels between pressure and particle velocity are needed.

Numerous signal propagation measurements have been made in shallow water, but most of these focus on the water path. We need some measurements that quantify propagation in the sediments, to confirm both the wave theory and the attenuation constants, many of which have been determined at relatively high frequency.

Comparative signal to noise ratios (SNR) for hydrophones vs geophones need to be determined. At short ranges there appears to be some benefit from using horizontal geophones. Again these measurements need to be performed as a function of depth. One of the purposes should be to verify the vertical velocity potential predictions of normal mode theory. The lack of bottom acoustic parameter measurements has been recognized as the limiting factor in making propagation predictions in shallow water for a long time. The situation has not changed. However, the issue of how to map the bottom should be resolved before proceeding with any extensive mapping program.

Issues

There are many issues to be resolved before seismic detection is fully understood and its capability completely evaluated. However there appear to be two issues that are rather basic; (1) the acoustic description of the bottom and (2) the sensor to medium coupling.

As mentioned before the lack of bottom information makes acoustic signal predictions risky except in a summarizing sense. The cost of mapping the bottom is expensive. At present 3 methods of determining the parameters are being fostered:

1. Seismic refraction measurements of layer thickness and velocity with density estimates.
2. The dispersion method which determines how the bottom acts as a communication channel as a whole; only inhomogeneities that affect acoustics are determined.
3. The inference method involves the determination of the effect of the fine sedimentation structure on acoustics. Then the sedimentary sequences of the bottom are mapped in detail. From these maps the acoustic properties that one needs to make predictions are inferred.

The first thing that needs to be done is to determine which of the above methods is the most cost effective in conjunction with acoustic signal prediction accuracy.

How to sample the communication link, i.e. the combined water and bottom medium, is another way of stating sensor to medium coupling. Where should the sensors be placed? Is the velocity potential function vs depth a good indication of vertical placement? The use of hydrophones vs geophones as sensors is at present being investigated. Without understanding the effects of medium sampling, the measured results will probably result in contradictory conclusions. For this issue there are more questions than answers. A geophone vs hydrophone receiver competition needs to be based on physical reality rather than a set of measurements that can, at best be related statistically.

If we can gain some insight into these two issues the understanding of seismic detection will make significant step forward and will point out the next issues of importance.

References

1. M. Ewing, J. L. Worzel, C. L. Pekeris, Propagation of Sound in the Ocean, GSA Memoir 27. October 1948.
2. R. H. Ferris, "Comparison of Measured and Calculated Normal-Mode Amplitude Functions for Acoustic Waves in Shallow Water" JASA, Vol. 52 #3, p. 981, February 1972.
3. A. O. Williams, Jr. "Hidden Depths: Acceptable Ignorance About Ocean Bottoms." JASA, Vol. 59 #5, p. 1175, May 1976.
4. E. J. Kornhauser, and W. P. Raney, "Attenuation In Shallow Water Propagation Due to an Absorbing Bottom." JASA, Vol. 27 #4, p. 689, July 1955.
5. I. Tolstoy, "Guided Waves In a Fluid With Continuously Variable Velocity Overlying an Elastic Solid: Theory and Experiment." JASA, Vol. 32 #1, p. 81, 1960.
6. M. Blaik and C. S. Clay, "Detection In the Ground of Sound From a Source In Shallow Water." Hudson Laboratories Technical Report #76. 25 May, 1959.
7. I. Tolstoy, "Shallow Water Test of the Theory of Layered Wave Guides", JASA Vol. 30 #4, p. 348, April, 1958.
8. C. B. Officer, Introduction to the Theory of Sound Transmission. McGraw-Hill Book Co., 1958.
9. P. A. Barakos, "Experimental Determination of Compressional Velocity for the Bottom Layer by the Dispersive Method". JASA, Vol. 34 #12, p. 1919, December 1962.
10. H. P. Bucher, "Normal-Mode Sound Propagation in Shallow Water" JASA, Vol. 36 #2, p. 251 February 1964.
11. R. Houtz, J. Ewing and X. LePichon, "Velocity of Deep-Sea Sediments From Sonobuoy Data." Journal of Geophysical Research, Vol. 73 #8, p. 2615, April, 1968.
12. E. L. Hamilton, "Attenuation of Shear Waves in Marine Sediments", JASA, Vol. 60 #2, p. 334, May, 1976.
13. W. M. Ewing, W. S. Jardetsky, F. Press, Elastic Waves in Layered Media, McGraw-Hill Book Co., 1957.
14. R. Wold, "Private Communication"

15. C. Holmer, "Relation of Particle Velocity and Pressure in a Two-Layer Shallow Water Area", USI Report March 31, 1978.
16. E. G. McLeroy and A. DeLoach, "Measurements of Sea Bottom Elastic Waves from Underwater Explosions", U.S. Navy Mine Defense Laboratory Report #U2727, April 1966.

Tracor Sciences & Systems

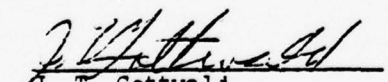
Contract N00173-77-C-0063

FINAL REPORT
SEISMIC SENSING OF SOUNDS IN THE SEA

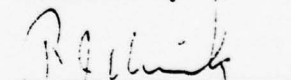
Submitted to:
Receiving Officer
Naval Research Laboratory
4555 Overlook Avenue, S.W.
Washington, D.C. 20375
Attention: Code 8120

31 December 1977

Approved by:


J. T. Gottwald
Director, Applied Systems
Department

Submitted by:


R. J. Urick



H. L. Price

TABLE OF CONTENTS

<u>SECTION</u>	<u>TITLE</u>	<u>PAGE</u>
1.0	INTRODUCTION	1-1
2.0	EXPERIMENTAL DATA	2-1
2.1	Worzel-Ewing Test	2-1
2.2	McLeroy Test	2-2
2.3	Urlick Test	2-4
2.4	Other Tests	2-10
2.5	Propagation From Deep to Shallow Water	2-11
2.6	Discussion	2-13
2.6.1	Seismic Gain of the Horizontal Components	2-13
2.6.2	The Magnitude of the Horizontal Cross-Component	2-13
2.7	Summary	2-15
3.0	ACOUSTIC PROPERTIES OF THE SEA FLOOR	3-1
3.1	Compressional Waves	3-1
3.1.1	Velocity	3-1
3.1.2	Attenuation	3-4
3.2	Shear Waves	3-8
3.2.1	Velocity	3-8
3.2.2	Attenuation	3-10
4.0	TYPES OF SEISMIC WAVES	4-1
5.0	THE AMBIENT BACKGROUND	5-1
5.1	Seismic Noise	5-1
5.2	Water Noise	5-4
6.0	PROPAGATION MODELS	6-1
6.1	Theoretical Introduction	6-1
6.2	Computer Models Studied	6-15
6.3	Acknowledgements	6-20
7.0	SUMMARY AND CONCLUSIONS	7-1
8.0	OUTLINE OF A FOLLOW-ON RESEARCH PROGRAM	8-1
9.0	APPENDIX: LISOL, A COMPUTER MODEL OF A LIQUID LAYER OVER A SOLID HALF-SPACE	9-1
10.0	REFERENCES	10-1

LIST OF TABLES

<u>TABLE</u>	<u>TITLE</u>	<u>PAGE</u>
3-1	Attenuation Coefficients in Hard Rocks	3-10
5-1	Measured Deep-ocean Seismic Noise Levels	5-5
6-1	Typical Values of Acoustical Properties for a Layered Model of the Ocean Floor	6-6

LIST OF ILLUSTRATIONS

<u>FIGURE</u>	<u>TITLE</u>	<u>PAGE</u>
2-1	The "ground wave" recorded in Chesapeake Bay at Solomons, Md, range 4000 yds.	2-3
2-2	Signal-to-noise vs. frequency for the hydrophone H and the 3 geophone components X,Y,Z for a minesweeping CW sound source at 2000 yds.. . . .	2-5
2-3	Seismic gain vs. frequency replotted from Figure 2	2-6
2-4	West-East cross section off Ft. Lauderdale, Fla	2-7
2-5	Signal-to-noise ratio spectra for the four sensors for two vessels at the indicated ranges. . . .	2-8
2-6	Seismic gain for the two ship sources of Figure 2-5	2-9
2-7	Results of an experiment to measure propagation up the continental slope	2-12
2-8	Bottom particle trajectories in the horizontal plane	2-14
3-1	Sound speed vs. porosity from measurements made on core samples	3-3
3-2	Velocity profiles at two East Coast locations	3-5
3-3	Ray diagrams for a linear gradient of 1 sec^{-1}	3-6
3-4	Attenuation vs. frequency in natural, saturated sediments and sedimentary strata	3-7
3-5	Attenuation vs. depth in sediments as compiled by Hamilton	3-9
4-1	Waves generated by a wave in water striking the bottom	4-2
5-1	Seismic noise spectra at three Florida locations	5-2
5-2	Seismic noise spectra, vertical component	5-3
5-3	Shallow-water ambient water noise spectra	5-6
6-1	Physical model of ocean and ocean floor	6-5
6-2	Number scheme used in program to compute sound field in layered media	6-9
9-1	The physical configuration used for computing sound levels in the program LISOL	9-2

Tracor Sciences & Systems

1.0 INTRODUCTION

The purpose of this report is to examine the feasibility of using seismic sensors, responsive to the motion of the bottom, as sensors for underwater sounds. Stated in other words, we will examine the possibility that, under some conditions, a seismometer - alternately called a geophone - may have a higher signal-to-noise ratio, for sounds originating in the water at a distance, than does a conventional hydrophone located nearby.

The essence of our problem, if the effect exists at all, is to identify, however crudely, the conditions of the ocean/bottom transmission medium, as well as the range from source to receiver, under which the effect is likely to take place. Under these conditions, whatever they may be, seismometers become obvious replacements for hydrophones as detectors of distant sounds in the ocean.

It is well recognized that for low frequencies below the cut-off frequency of the first mode in shallow water, the sound from a water-borne source must propagate to a distance via the bottom, perhaps to considerable depths.

Also, in propagation from deep to shallow water over a sloping bottom, it is reasonable to expect the bottom to dominate the transmission, inasmuch as it is encountered repeatedly at ever-greater angles by sound propagating up the slope.

In what follows, we will study the matter via a combination of the existing experimental evidence, the physics of the problem, and the basic theory for computer simulation. Unfortunately, we will find that neither the observational data nor the existing computer models are adequate at the present time for an adequate assessment of the overall-problem. Finally, we will make some recommendations to improve this situation.

Tracor Sciences & Systems

2.0 EXPERIMENTAL DATA

A number of field experiments - here called "tests" - using both geophones and hydrophones have been made in past years. They consist of the recording of shot signals, as well as the output of ships and CW projectors, at a variety of ranges on both a geophone and a nearby hydrophone. In the following sections, these tests and their results will be briefly summarized and identified by the names of the principal investigators.

2.1 Worzel-Ewing Test

In late 1943 and early 1944 Worzel and Ewing conducted a series of field tests in five widely separated areas: in Chesapeake Bay, off Jacksonville, Florida, the Virgin Islands, off the Orinoco River Delta of South America, and Barbados. Water depths ranged from 49 feet (in Chesapeake Bay) to 600 feet (Virgin Islands). At these sites, the outputs of two hydrophones and a geophone were recorded on one ship, while shots were fired from another at various ranges between 1/4 mile and about 12 miles for a typical location, (in one case out to 30 miles). The details are given in one of three papers published in 1948 in a memoir of the Geological Society of America (reference 1); one of the other papers in this volume is the classic paper by C.L. Pekeris on the theory of shallow water sound propagation.

The field trials showed that a low frequency high velocity "ground wave" occurred at all stations on both hydrophones and the geophone. Quoting from the conclusions of this paper, it was stated that "sound waves in the ground from an explosion in shallow water generally precede those in the water to any distant point. The ground waves last a short time after the arrival of the water waves and their rate of travel is governed by the layer depths and physical properties of the geologic column. They are composed mainly of frequencies of 10-30 cycles per second but have also some lower-intensity elements of

Tracor Sciences & Systems

frequencies up to 100 cycles per second". Sample traces of a shot signal received at a range of 4000 yards in Chesapeake Bay are shown in Figure 2-1 which is reproduced from Reference 2.

For our present purposes, this early experiment provides little quantitative information. The work suffered from a number of shortcomings. Only high-speed oscilloscope photographs were recorded (tape had not been invented) so that only crude analyses (by modern standards) could be made; scanty amplitude information was obtained, with most attention being given to travel times; only a vertical component geophone was used; no background noise data was obtained.

However, the program was admirably conceived, and was carried out with the available instrumentation under difficult wartime conditions; it remains a landmark classic piece of work on the propagation of sound in shallow water.

2.2 McLeroy Test

In mine countermeasures an urgent practical problem is to predict the sweep-width for acoustic minesweeping, i.e., to predict how far laterally from a towing craft can a piece of acoustic sweep gear actuate an acoustic mine. Acoustic sweeps are low frequency devices and, in shallow water where most mines are laid, the sea bed must accordingly play an important role in determining the transmission of sound and therefore the sweep width.

In 1960, McLeroy described measurements with a 3-component geophone plus with a nearby hydrophone in the shallow waters of St. Andrews Bay, Panama City, Florida and also at a depth of 60 feet in the nearby Gulf of Mexico. The geophone was buried in the bottom so as to respond to the motion of the bottom, as a velocity detector, in three perpendicular directions: horizontally in the direction of the source ("x"), horizontally in the transverse direction ("y") and vertically ("z"). The hydrophone ("H") responded, of course, to sound

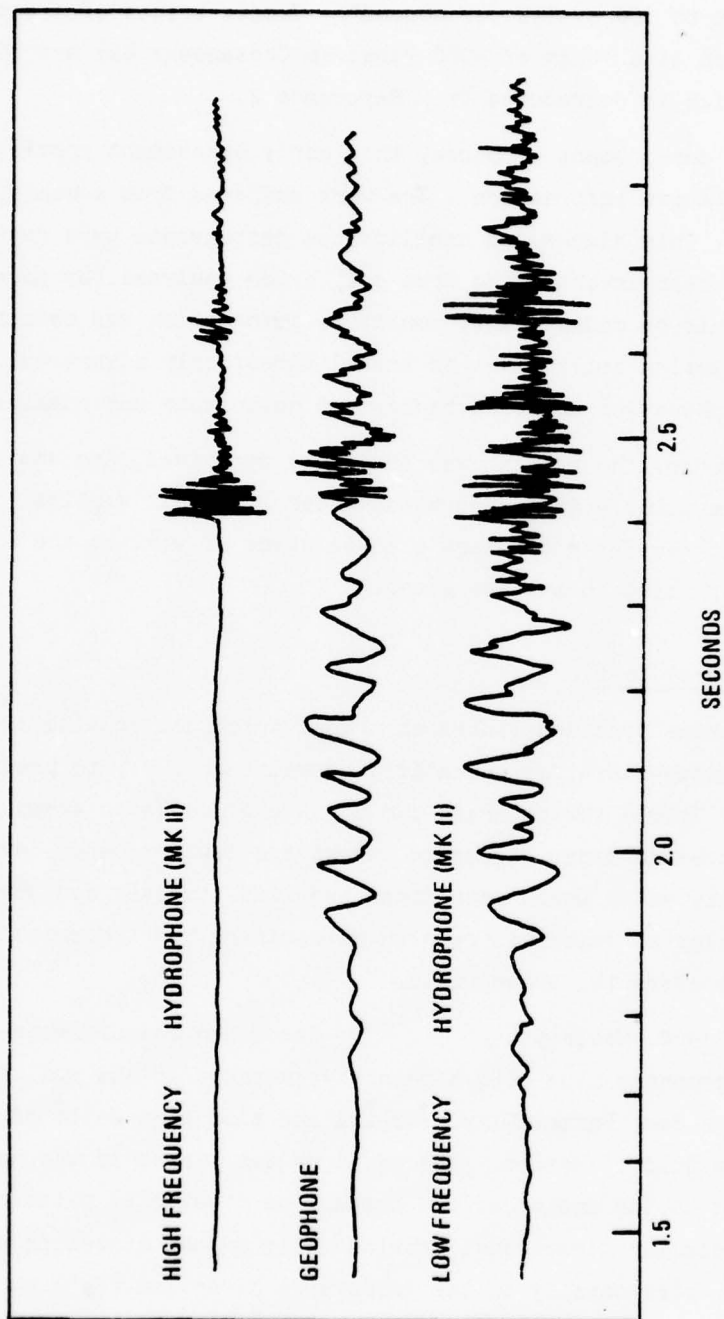


Figure 2-1. The "ground wave" recorded in Chesapeake Bay at Solomons, Md. range 4000 yds. Shot 48, reference 1. Reproduced from reference 2.

Tracor Sciences & Systems

pressure in the water. A high-power broadband CW acoustic minesweeping source was towed at a depth of 27 feet out to a range of a few thousand yards from the units.

It was seen that the "x" and "y" components of the geophone have a higher signal-to-noise ratio, by up to 20 dB relative to the hydrophone, over the entire frequency range. The "z" geophone component shows no essential difference in signal-to-noise ratio.

2.3 Urick Test

The McLeroy test just described was repeated in 1968 by Urick (reference 4) at another location. Again, a three-component geophone was used along with an adjacent hydrophone. The location was off the East Coast of Florida near Ft. Lauderdale in 60 feet of water over a coral sand bottom that sloped rapidly off-shore. A cross-section eastward from this site is shown in Figure 2-4. Southbound freighters and tankers passing at a distance of about a mile at their point of closest approach served as sound sources. As illustrated in the figure, the strong downward refraction prevented direct waterborne transmission from the source to the receivers.

Figure 2-5 shows the signal-to-noise ratio as a function of frequency for the four sensors used in the test, as observed for two freighters at the indicated ranges. Figure 2-6 is also a re-plot of Figure 2-5 showing the comparison of the geophone sensors with the

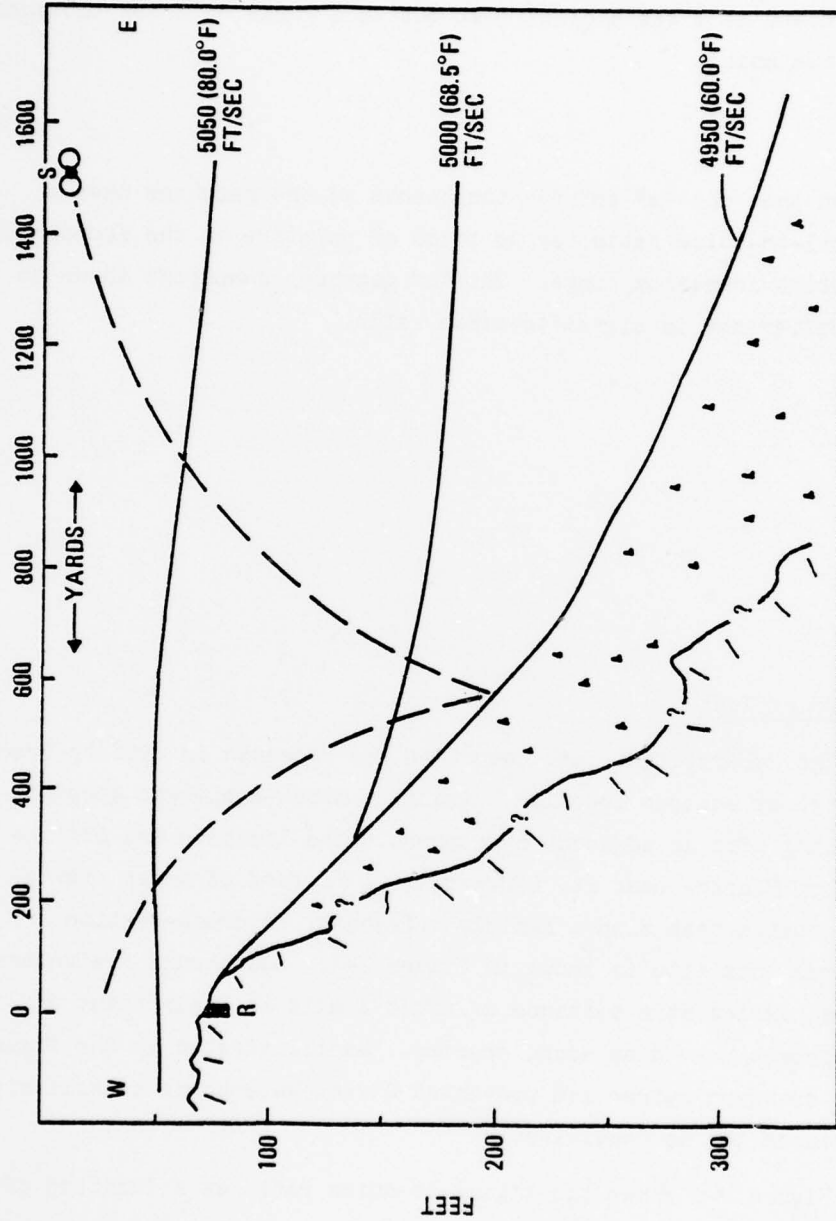


Figure 2-4. West-East cross section off Ft. Lauderdale, Fla. The geophone-hydrophone plant was at R on the reef in 60 ft. of water. The dashed line shows a sound ray leaving the source S horizontally and striking the bottom; other rays would encounter the bottom more often. (Reference 4)

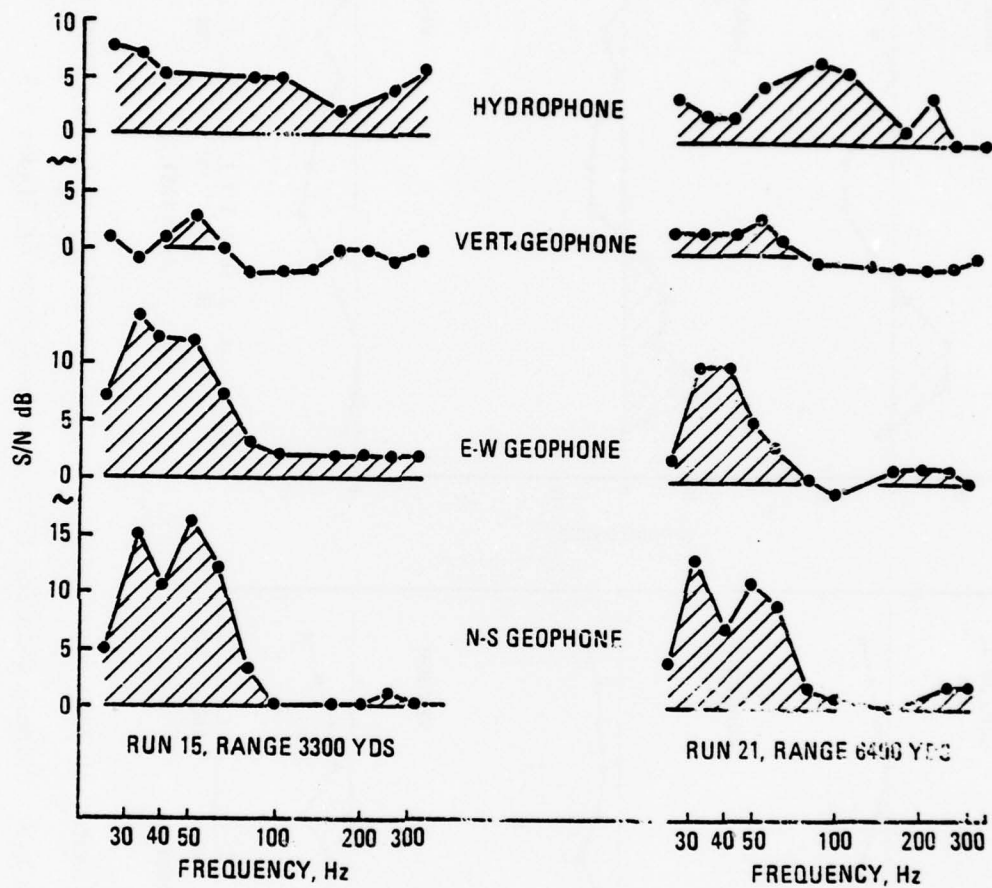
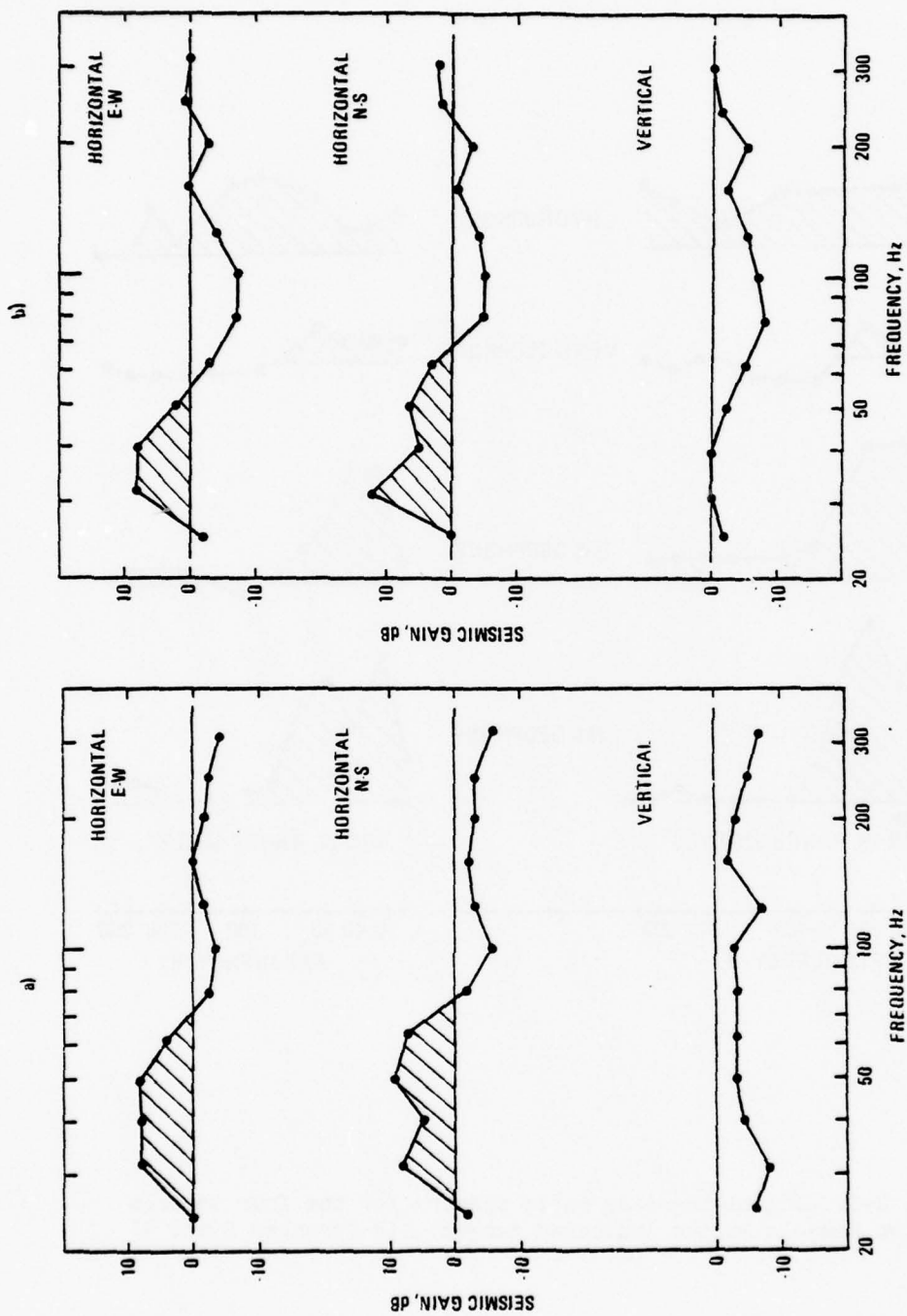


Figure 2-5. Signal-to-noise ratio spectra for the four sensors for two vessels at the indicated ranges. (References 2 and 4)



(a) Freighter, 15 knots, at 3300 yds

(b) Freighter, 19 knots, 6400 yds

Figure 2-6. Seismic gain for the two ship sources of Figure 2-5.

Tracor Sciences & Systems

hydrophone in terms of seismic gain. As in the McLeroy test, the horizontal components were found to have a positive seismic gain, although of lower magnitude (5-10 dB) and occurring only at low frequencies. Again, as in the previous test, the vertical geophone had essentially unity (0 dB) or less seismic gain. Unfortunately, the data were not analyzed at frequencies lower than 25 Hz, nor were shots fired to sort out the prevailing acoustic paths.

2.4 Other Tests

In the late fifties, the Hudson Laboratories of Columbia University carried out a unique experiment (reference 5). A number of vertical-component geophones were placed in a near-shore water well on Fire Island, New York, at depths in the well from 389 and 1956 feet. Recordings of a sound source towed offshore were made, and plots of velocity (the output of the geophone sensor) vs. range of the source out to 10 kyd at frequencies of 10, 24, 88 and 148 Hz were obtained. The resulting loss curves, based on radial runs in four directions, showed some peculiar directional effects, but on the whole tended to indicate a fall-off with range like spherical spreading, or somewhat better. Unfortunately, no comparison with a hydrophone were made. This test was an ingenious and potentially valuable one, but, regretfully, nothing remarkable was found or concluded.

At about this same time vertical and horizontal geophones were used with a hydrophone in measurements by Worley and Walker (reference 6) in the Gulf of Maine in a water depth of 15 fathoms. Unfortunately, no data were obtained with the horizontal geophones. The vertical geophone showed the same fall-off with range as the hydrophone in the band 15-70 Hz; also, a crude detection experiment showed no difference between the vertical geophone and the hydrophone. The results, such as they are, confirm the findings of the McLeroy and Urlick tests in that a vertical geophone fails to give a positive seismic gain.

2.5 Propagation From Deep to Shallow Water

A strangely neglected aspect of underwater sound is propagation from deep to shallow water, and vice versa. An early piece of work was done by C.B. Officer and J.B. Hersey in 1953 (reference 7), but quantitative results were sparse due in part to the analysis limitations existing at that date. A later experiment in 1971 gave some results pertinent to the present study (reference 8). In this test explosive charges detonating at 60 feet were dropped out to 100 miles from a hydrophone located at the edge of the continental shelf off the coast of Delaware in 100 fathoms of water. The signals received at the hydrophone were converted to transmission loss and are summarized in Figure 2-7. Figure 2-7a is a cross-section showing the shot and receiving locations; Figure 2-7b shows the measured transmission loss compared with spherical spreading, while Figure 2-7c is a ray diagram for a shot at a range of 80 miles.

Two features of these results are noteworthy. The first is the excellent transmission, as shown in Figure 2-7b by the comparison with the dashed curve of spherical spreading. The transmission is essentially what it would be in an ideal unbounded lossless medium. The second is the ray diagram, showing an absence of ray paths from source to receiver and predicting a total absence of transmission. In the ray diagram all the rays from the source strike the bottom. They become increasingly steep on successive reflections from the sloping bottom and eventually strike the surface at right angles so as to become, in effect, turned back upon themselves.

The discrepancy between the observations and the ray diagram must lie in the idealizations of the latter. The bottom is not smooth as shown by the ray diagram, but is rough and irregular, sending sound into all other locations. But it is also penetrable; the many encounters of all rays with the bottom must result in the generation of seismic energy that may reach the receiver by some combination of earth and water-borne sound, or by seismic waves alone.

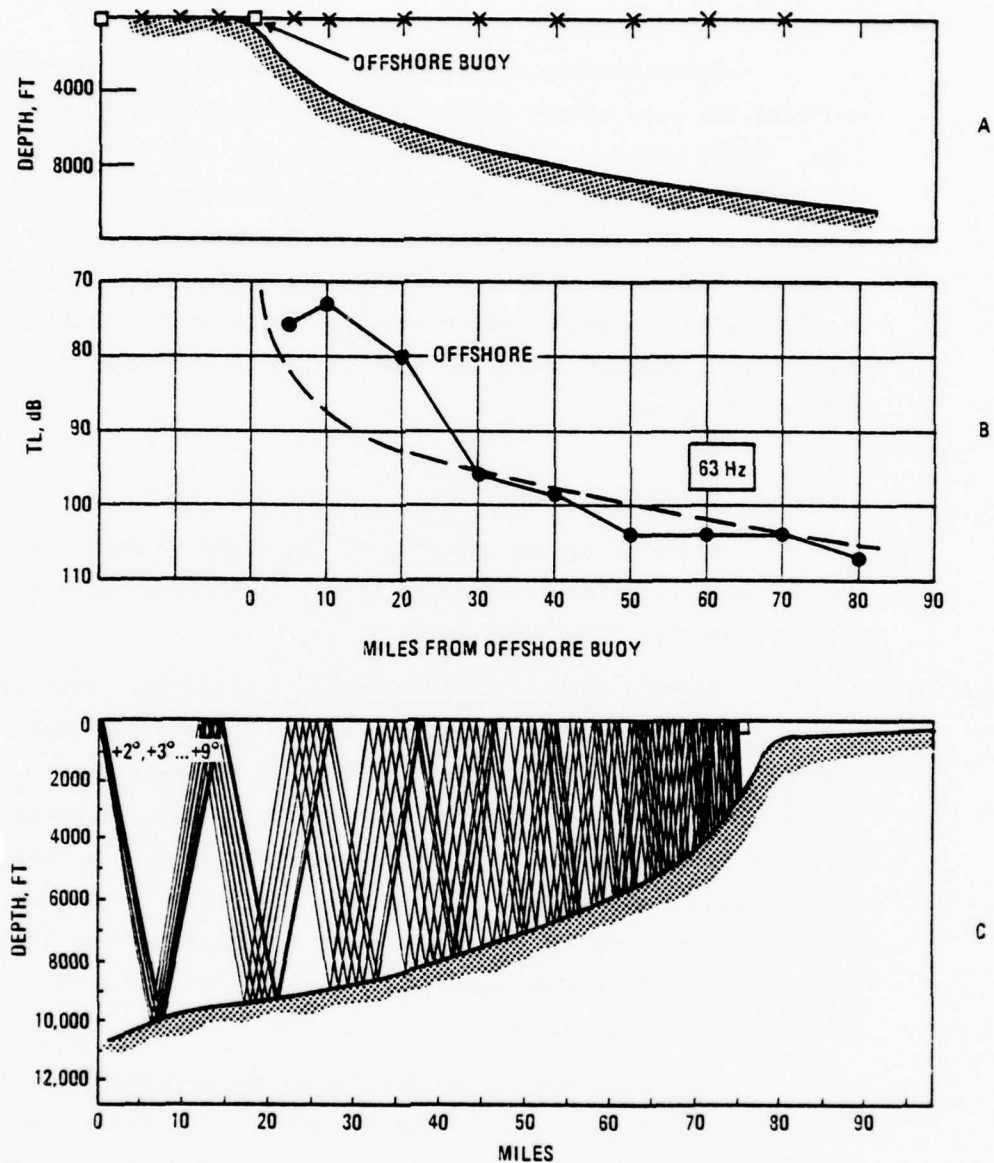


Figure 2-7. Results of an experiment to measure propagation up the continental slope. (a) Shows bottom slope and the 60 ft. shots (b) Measured transmission loss (dots) compared to spherical spreading (dashed curve); (c) ray diagram. (Reference 8)

Tracor Sciences & Systems

Unfortunately, no geophone was used in this test, which provides the only extant published data on deep-to-shallow transmission loss. While it is not possible to assess the role of bottom waves to explain the good transmission, it appears likely that in some way transmission through the bottom must have occurred. In any event, the excellent transmission is noteworthy, suggesting that a hydrophone in shallow water can under some conditions be as good a receptor of the sound from a shallow source as one located at the axial depth of the deep sound channel.

2.6 Discussion

A number of the features of the observed data, as found in the McLeroy and Urick Tests described above, is still unexplained and require further experimental investigation.

2.6.1 Seismic Gain of the Horizontal Components. This is the most striking, and potentially useful, finding of these two field studies. The most reasonable explanation, is that it represents the horizontal flow of energy outward from the source and traveling through the ground as a compressional wave. Such propagation would not be sensed by either the hydrophone or the vertical geophone component. Moreover, propagation through the water alone can be ruled out for frequencies well below shallow-water cutoff, such as the blade-rate frequency of ships and its lower harmonics.

2.6.2 The Magnitude of the Horizontal Cross-Component. Both tests show that the seismic gain of the horizontal transverse component "Y" of bottom-motion is comparable in magnitude, or only somewhat less than that of the longitudinal horizontal component "X". This is illustrated by the particle trajectories of Figure 2-8 as found in the Urick Test (reference 4). Here the ellipses show the bottom motion in the horizontal plane for two different strip sources of sound in the direction X of the large arrow. The two geophone components were

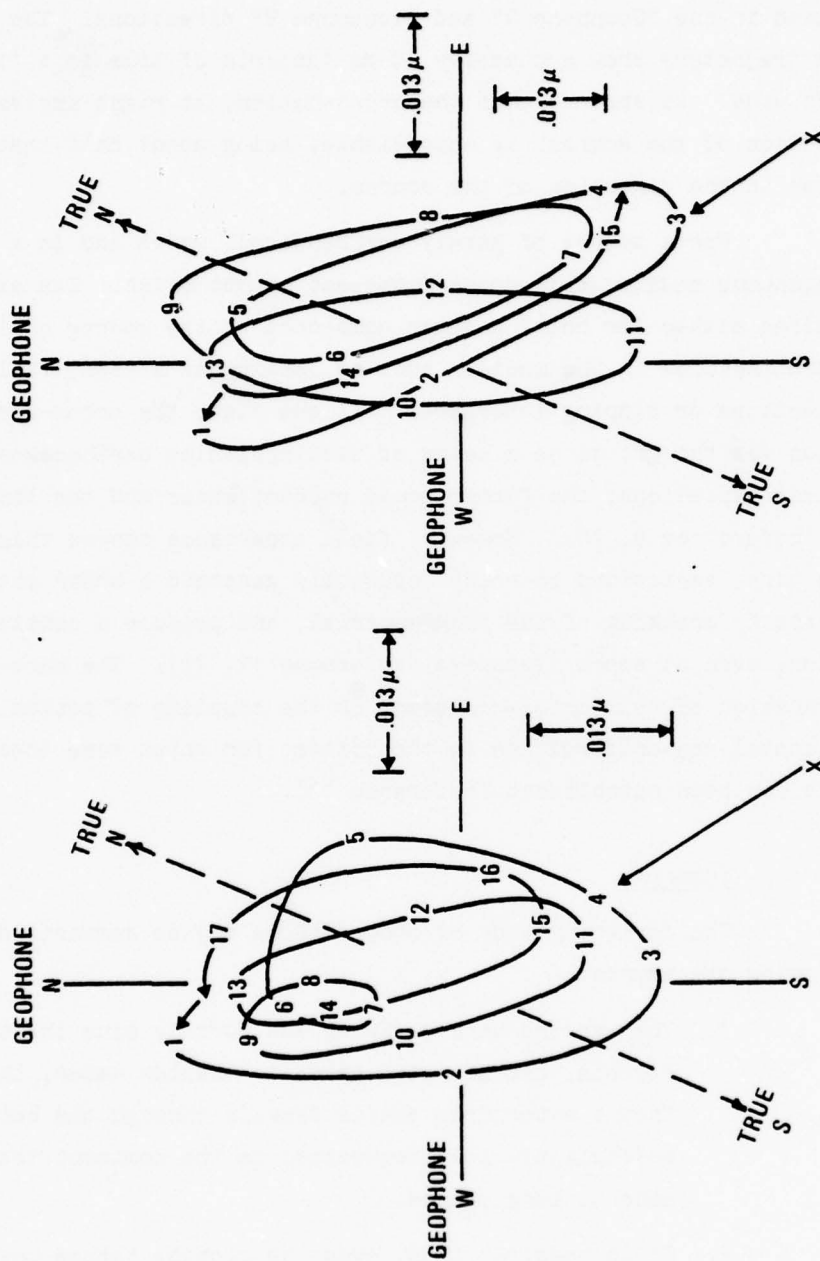


Figure 2-8. Bottom particle trajectories in the horizontal plane. Ship source in direction X, Florida site, frequency 40 Hz. (Reference 4)

Tracor Sciences & Systems

aligned in the "Geophone N" and "Geophone W" directions. The numbers on each trajectory show successive 10 ms instants of time in a filter band 40 Hz wide. We observe that the cross-motion, at right angles to the direction of the source, is appreciable, being about half that of the motion in the direction of the source.

For a source of purely compressional waves and in a laterally homogeneous medium, this cross-component cannot exist. Its existence requires either (or both) a shear component at the source or lateral discontinuities in the medium, such as lensing of strata, faults, side reflections or dipping interfaces. At one time, the cross-component of motion was thought to be a means of distinguishing earthquakes from nuclear explosions; the former would produce shear and the latter would not (references 9, 10). However, field experience showed this to be a vain hope; explosions in rocks apparently generate a shear motion, perhaps by cracking of the rock material, and produce a complex ground motion, even at short distances (reference 11, 12). The more-likely explanation of this cross-component is the coupling of bottom modes by horizontal non-uniformities in the bottom, for which some theoretical basis has been established (reference 13).

2.7 Summary

The foregoing body of observations may be summarized by the following statements:

1. The wartime work of Ewing and Worzel, plus the theory of Pekeris, demonstrated that, in shallow water, the sound from a waterborne source travels through the bottom and at sufficiently low frequencies is the dominant transmission mode to long ranges.
2. It is possible that, over the sloping bottom beyond the continental shelf, sound traveling by repeated bounces off the bottom becomes converted to earthborne sound in proceeding up the slope.

Tracor Sciences & Systems

3. In the two extant comparison tests, both horizontal geophone components showed a substantial improvement in signal-to-noise ratio ("seismic gain") over a nearby hydrophone. The two horizontal geophone components were essentially equal in seismic gain.
4. A vertical geophone in these two tests and in others showed no improvement over the hydrophone.

Tracor Sciences & Systems

3.0 ACCUSTIC PROPERTIES OF THE SEA FLOOR

In order to select realistic parameters to use in a computer model, we consider in this section the salient features of bottom acoustics, as described in the literature. This literature is extensive; many measurements have been made and many papers have appeared on the velocity, attenuation and density of sound in sediments and rocks. Here we will present only a short summary of these subjects, with references to the existing literature.

A number of summary papers on the subject have been published by E.L. Hamilton; particularly noteworthy is a review by Hamilton of the basic elastic and physical properties of marine sediments (reference 14). An older summary paper that may be mentioned is one by Nafe and Drake (reference 15).

3.1 Compressional Waves

3.1.1 Velocity. The speed of compressional waves in sediments has been measured at shallow depths below the bottom by acoustic probes in situ and by core measurements in the laboratory. At deeper depths, a variety of geophysical techniques involving travel time measurements have been employed, including even using conventional sonobuoys and explosive shots for work over deep water (reference 16).

The speed of sound in a sediment is closely related to its porosity and therefore to its density. At the sea bed, high porosity/low density sediments, such as muds, have compressional wave velocities only slightly less (up to 3%) than that of the overlying water; low porosity/high density sediments, such as hard sands, have a velocity 10-20% greater than that of the overlying water. For example, by means of probes placed in the bottom by divers and by measurements on core samples, Hamilton (reference 17) found a coarse sand with a porosity of 39% to have a velocity of 1.836 km/sec, while a silty clay

Tracor Sciences & Systems

of porosity 76% had a velocity of 1.519 km/sec, compared to the water velocity of about 1.56 km/sec. Similarly off San Diego, again using probes inserted into the sediments by divers, Hamilton (reference 18) measured sediment velocities ranging from 1.463 km/sec for a "clayey fine silt" of porosity 65.6% to 1.750 km/sec for a "coarse sand" of porosity 38.3%. The bottom water alone (porosity 100%) had a velocity of 1.478 km/sec.

The many measurements made during the Marine Geophysical Survey are summarized, in terms of porosity, in Figure 3-1.

Since porosity and density are closely related, one would expect the velocity to be closely related to the density of the sediment; that such is indeed the case has been the subject of a soon-to-be published paper by Hamilton (reference 20). Other correlatives between velocity and the physical characteristics of sediments, such as grain size, have been established (reference 21).

In hard rocks, such as those of the basement beneath a sedimentary column, much higher sound speeds occur. In basalts, for example, the velocity ranges from 3.5 to 6.5 km/sec, again depending on the density of the material (reference 20). In the early work of Worzel and Ewing described above (reference 1) refraction shooting established velocities in the range 4.62-6.63 km/sec for the crystalline basement beneath the sediments at the locations where measurements were made.

Below the sea bed, as the porosity is reduced by the increasing pressure of the overburden and, as the sediment particles are forced into closer contact, the velocity increases. This increase with depth is extremely rapid compared to the velocity gradient in the overlying water; it is found (reference 15) to lie in the range 0.5 to 2.0 sec^{-1} (meters per second per meter of depth), with a convenient average value of 1.0 sec^{-1} . (In isothermal water, the corresponding value is .017 sec^{-1} .)

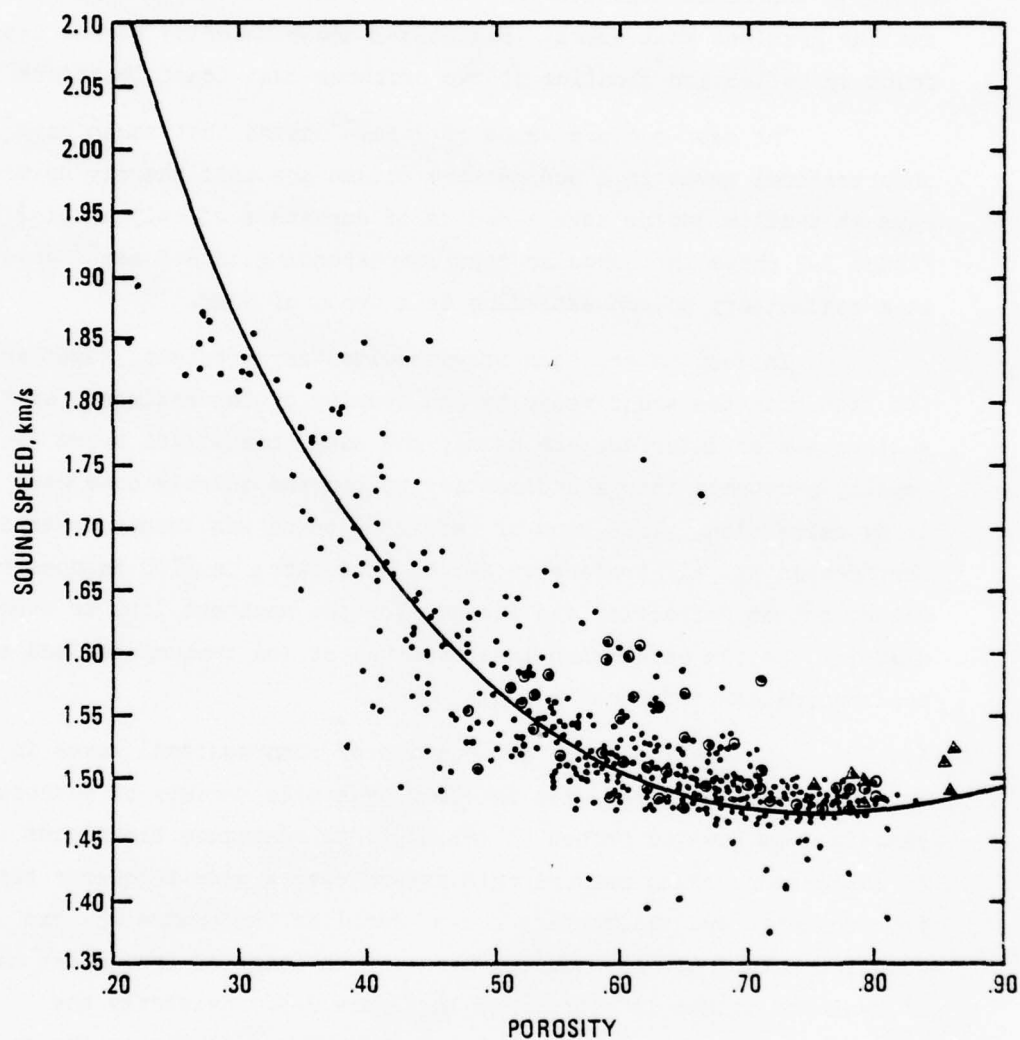


Figure 3-1. Sound speed versus porosity from measurements made on core samples. Data from Marine Geophysical Survey (reference 19).

Tracor Sciences & Systems

This steep gradient cannot continue indefinitely, but applies only for the first kilometer or two of depth. At deeper depths, a smaller gradient must exist. Figure 3-2 shows velocity versus depth as found by reflection shooting at two offshore East Coast locations.

The near-surface value of 1 sec^{-1} means that sound rays for compressional waves in a sedimentary column are bent sharply upward; rays at shallow depths have a radius of curvature of only about 2 km. Figure 3-3 shows the circular rays corresponding to a 1 sec^{-1} gradient in a sedimentary column extending to a depth of 4 km.

In deep water, this steep sedimentary gradient, together with the fact that the sound velocity and density of the sediments at the sediment-water interface are nearly the same, means that sound can readily penetrate into a sedimentary bottom and quickly come back out of it by refraction. This kind of refracted sound was indeed observed by Christensen et. al. (reference 22) in shot tests in 2700 fathoms of water; bottom refraction can account for the apparent low, or even negative, bottom reflection loss observed at low frequencies and small grazing angles (reference 2).

3.1.2 Attenuation. The attenuation of compressional waves in sediments and rocks has been measured by a wide variety of methods, ranging from in-situ probes in sediments to resonance techniques in bars of solid rock. Such measurements extend over a wide frequency range. For sediments and sedimentary rocks, Hamilton (reference 23) has compiled data from many sources over a wide range of frequency; his plot of measured values is reproduced in Figure 3-4. Evidently the attenuation coefficient tends to increase approximately as the first power of the frequency; accordingly, at a frequency of f kHz, the attenuation coefficient α in dB/meter can be written $\alpha(\text{dB/m}) = kf(\text{kHz})$, where k is a constant. k is the attenuation coefficient in dB per kilometer at 1 Hz. In Figure 3-4, the dashed line is drawn for $k = .25 \text{ dB/km/Hz}$, and is seen to give reasonable fit to the measured

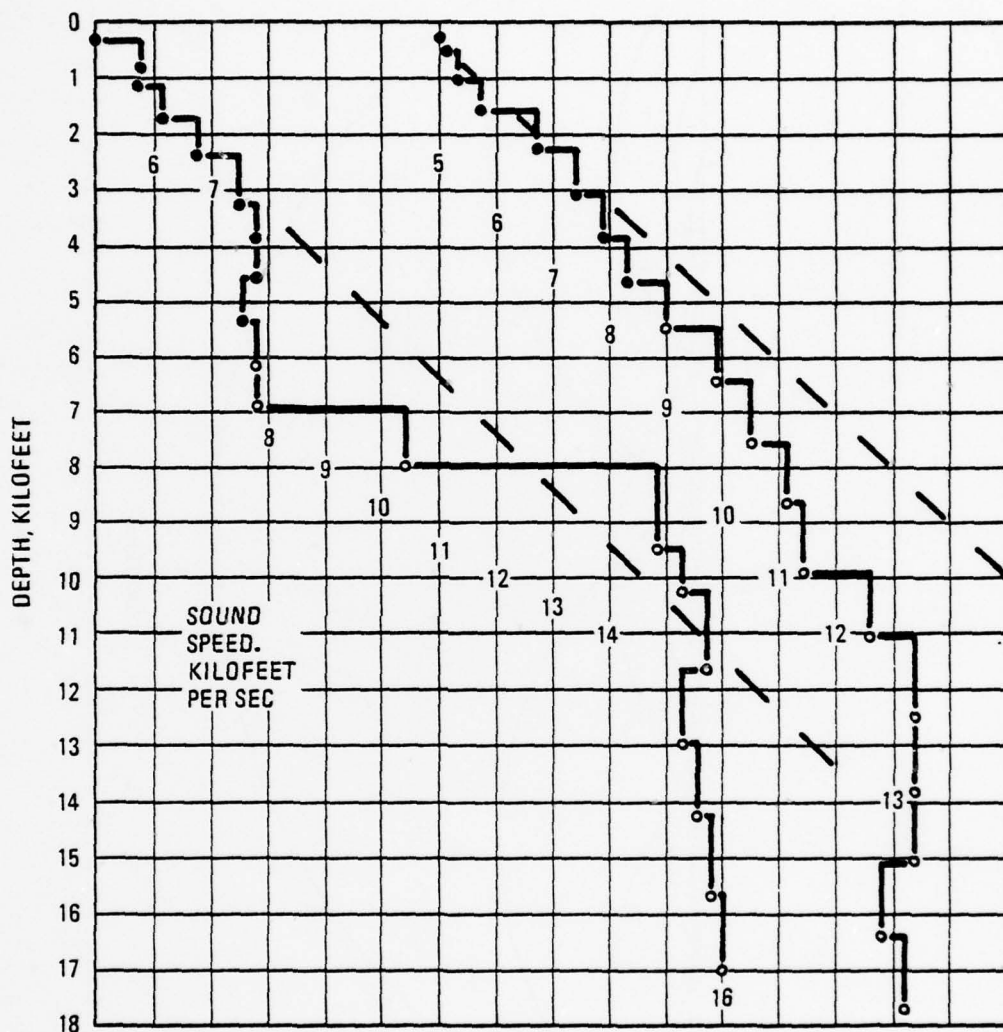


Figure 3-2. Velocity profiles at two East Coast locations.
Data - courtesy Shell Oil Company. Dashed lines show
a velocity gradient of 1 sec^{-1} . (Reference 2)

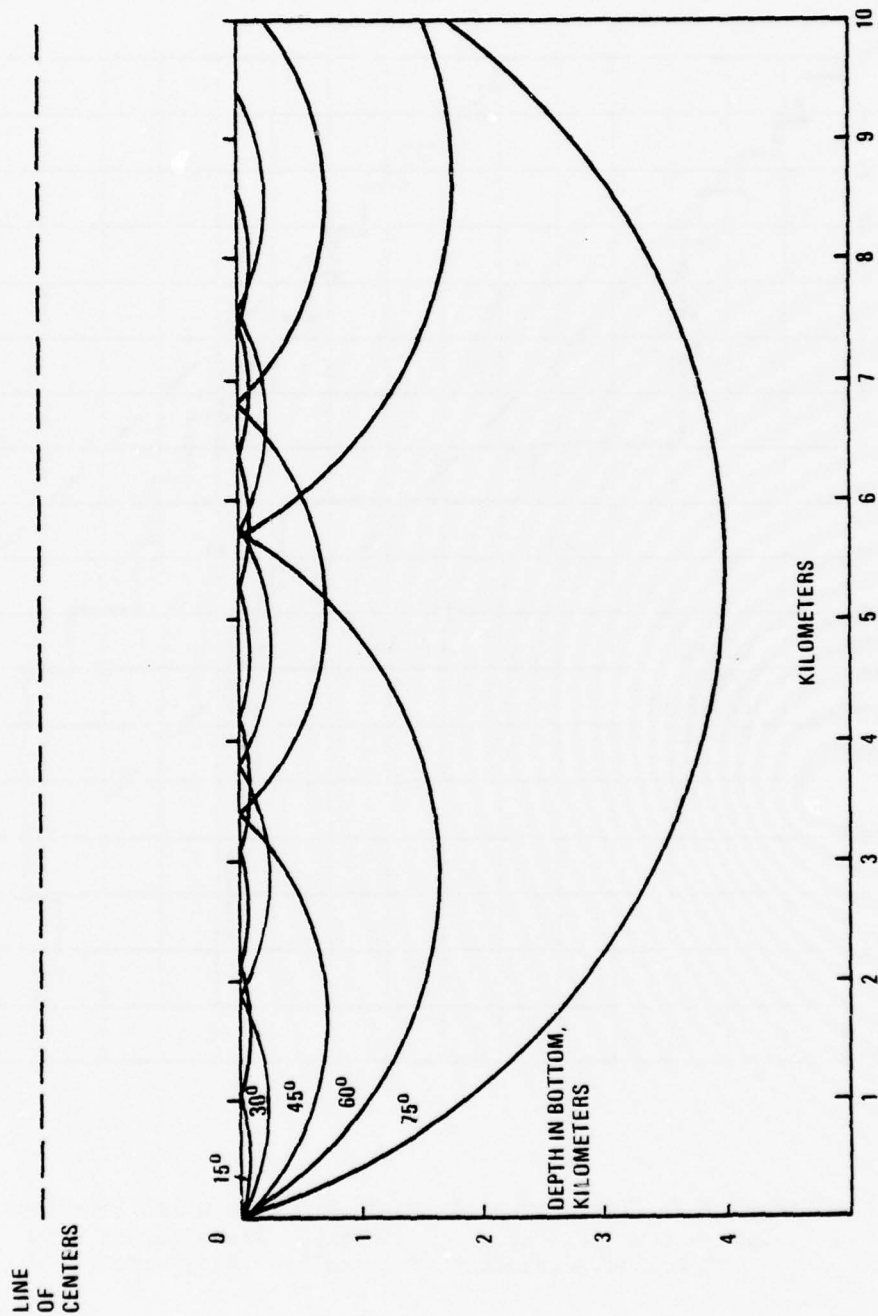


Figure 3-3. Ray diagram for a linear gradient of 1 sec^{-1} . Rays are arcs of circles with centers on a line 1.676 km above zero depth.

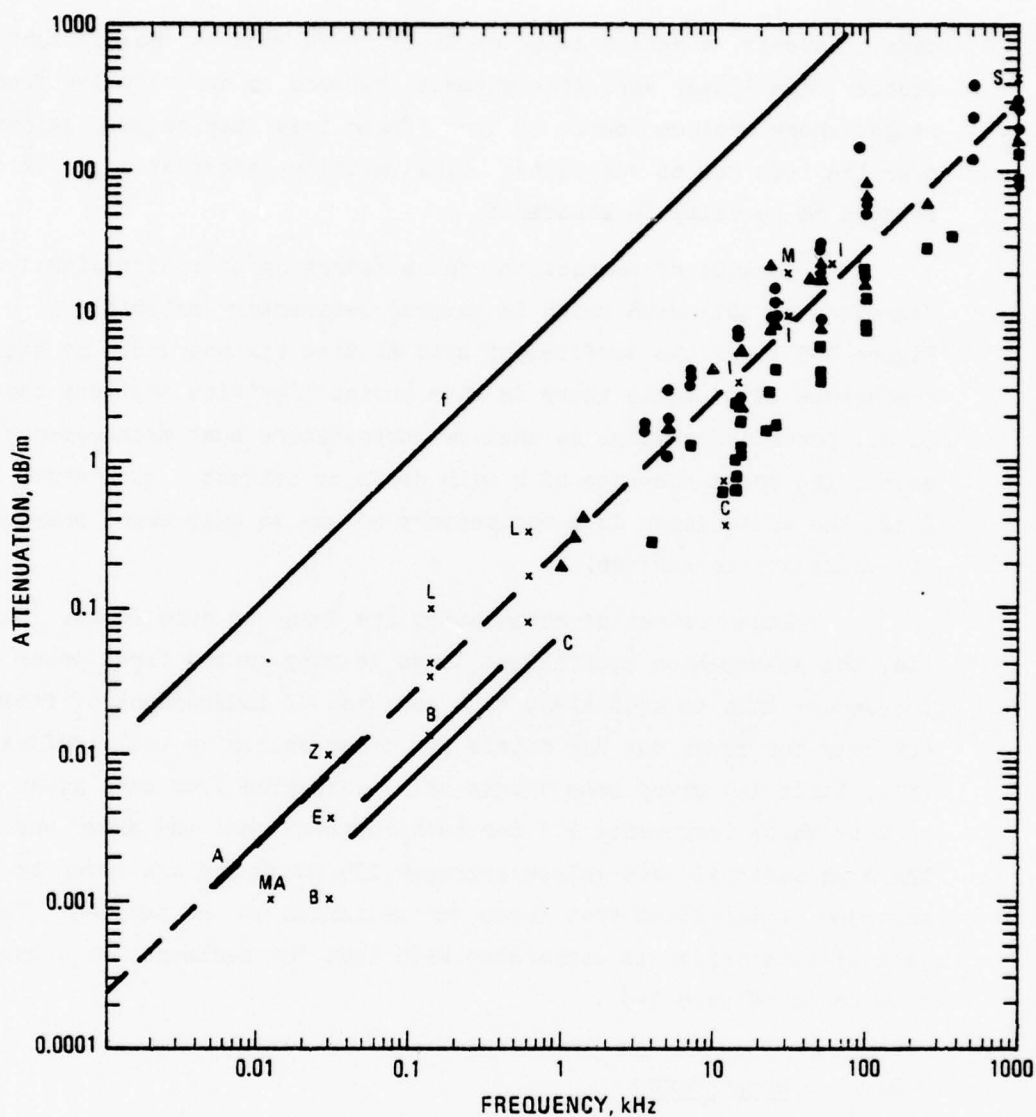


Figure 3-4. Attenuation versus frequency in natural, saturated sediments and sedimentary strata. The different symbols refer to different measurements. The long solid straight line shows a first-power variation with frequency. The dashed line is drawn for $k = .25 \text{ dB/km/Hz}$. (Reference 23)

Tracor Sciences & Systems

data. However, a recent paper by Stoll (reference 24) casts doubt as to whether this linear variation extends downward to our very low frequency range, where another source of loss "frame loss" may become dominant over the loss due to viscosity. Like velocity, attenuation is strongly related to porosity in sediments.

Because of compaction, the attenuation of compressional waves decreases rapidly with depth in natural sedimentary materials. Figure 3-5 shows the coefficient k as plotted against depth by Hamilton (reference 25). While there is wide variability with sediment type (i.e., porosity/density) at shallow depths where most measurements exist, the rapid decrease of k with depth is evident. At a depth of 2 km, the attenuation in a sedimentary column is only about one-tenth of its value at the surface.

Lower values of attenuation are found in hard rocks. Here too, the attenuation coefficient tends to vary as the first power of frequency; this is equivalent to a constant Q , independent of frequency, not only for rocks but for metals and other solids as well (reference 26). Table 3-1 gives some values of k , converted from data given in a book by White (reference 27) for both compressional and shear waves. The compressional wave values average .034 dB/km and are lower by about an order of magnitude than those for sediments at the sea bed. This rate of attenuation is comparable with that for sediments at a depth of 2 km or so (Figure 3-5).

3.2 Shear Waves

In sediments, shear waves have a vastly different velocity and attenuation than do compressional waves, since their propagation is governed by a vastly different elastic constant.

3.2.1 Velocity. At the sea bed, sediments have an extremely low shear wave velocity. A review by Hamilton of this subject (reference 28) shows that at a depth of one meter below the sea bed, marine sands and silt-clays have a shear velocity in the range 50-150 m/sec.

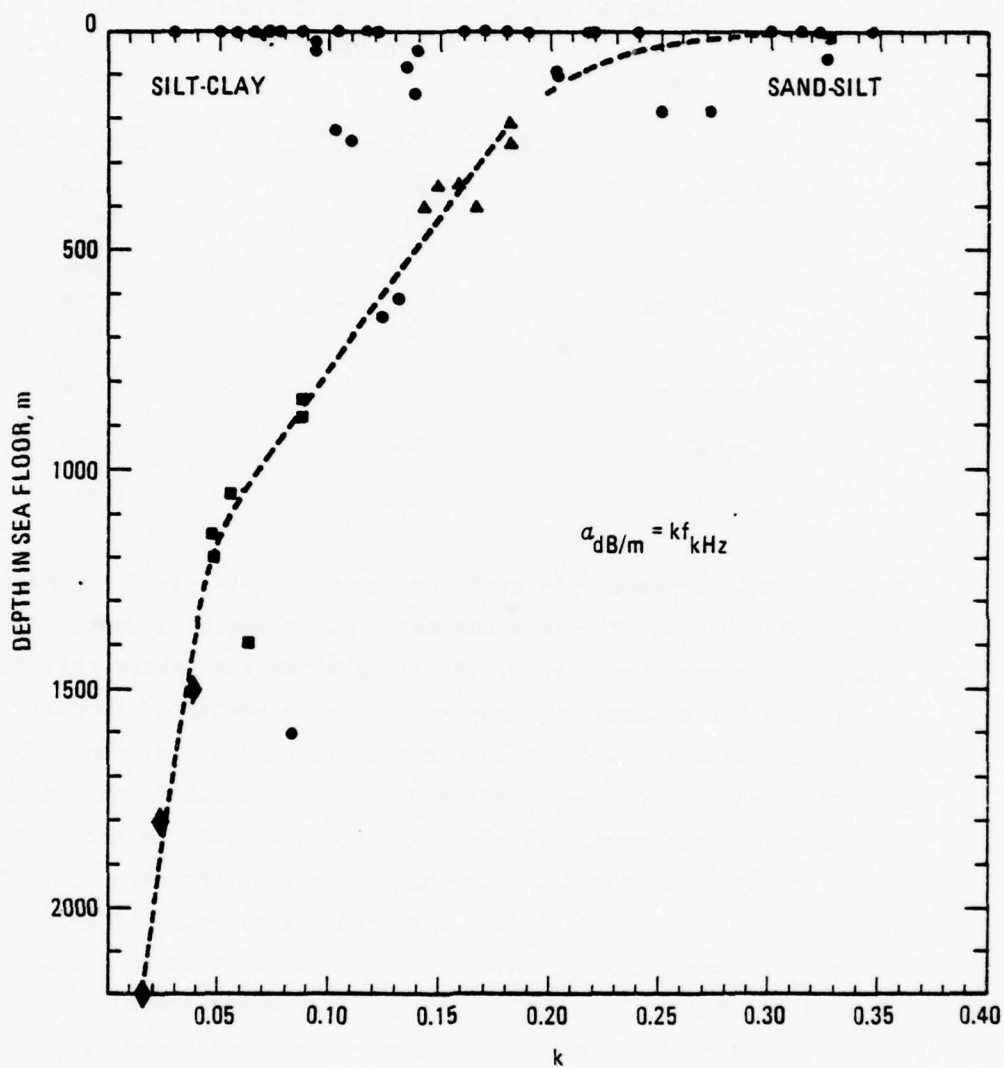


Figure 3-5. Attenuation versus depth in sediments as compiled by Hamilton (reference 25). Symbols refer to different measurements. The coefficient k is the attenuation coefficient in dB per kilometer at 1 Hz.

TABLE 3-1. ATTENUATION COEFFICIENTS IN HARD ROCKS.
VALUES OF k (dB/km/Hz) DERIVED FROM TABLE 3-1
OF REFERENCE 22

	<u>Compressional Waves</u>	<u>Shear Waves</u>
Granite	.019	----
	.017	----
	.119	.146
	.062	.075
Limestone	.023	.025
	.013	.011
Sandstone	.015	----
Chalk	.004	.005
Shale	.200	1.78

However, the increase with depth or compaction is rapid, increasing to about 200 m/sec at 10 meters and about 400 m/sec at a depth of 100 meters. Surface shear waves, traveling along the bottom interface, have comparable velocities; two independent measurements of Stoneley waves gave velocities of 89-123 m/sec in one experiment (reference 29) and 83-110 m/sec in the other (reference 30). In still another measurement, Buckner et al (reference 31) used vertical geophones on the bottom in 60 ft. of water at the NEL tower and, with blasting caps as sources at ranges of 2, 15, 30 and 45 ft., measured the velocity of Stonely waves to be 170 m/sec, with an attenuation of .06 dB/ft at 25 Hz, corresponding to a value of k of 7.9 dB/km at 1 Hz. Such waves travel, in theory, with a speed of 0.9 that of body shear waves (reference 32).

Shear waves are dispersive. For Rayleigh and Love Waves observed in earthquakes, the average shear velocity was found to lie between 200 and 400 m/sec in the upper 0.5 km of sediments for waves of periods shorter than 5-10 seconds (0.1-0.2 Hz); for longer periods, the velocity rapidly rises to about 4000 m/sec (reference 41).

3.2.2 Attenuation. The subject of the attenuation of shear waves in marine sediments has, like many aspects of the subject, been reviewed by

Tracor Sciences & Systems

Hamilton (reference 33). In this summary the following values for a number of materials are listed:

<u>Material</u>	<u>k (dB/km at 1 Hz)</u>
Sand	13.2
Sand and Clay	4.8
Silt	13.4
Mud (silt, clay)	17.3
Water-saturated Clay	15.2
Tertiary Mudstone	10.1
Pierre Shale	3.4

The average of these values is 11 dB/km/Hz; thus, at a frequency of 10 Hz, the shear wave attenuation coefficient would range from 34 to 173 dB/km. An attenuation of this same magnitude would apply for waves of the Rayleigh/Stonley type (Section 4.0) which are surface shear waves traveling near the water-bottom interface. Deeper-going body shear waves would suffer a smaller attenuation, since the shear coefficient, like the compressional wave coefficient, must decrease with depth. However, it appears that the shear wave attenuation is larger by at least an order of magnitude than the attenuation of compressional waves and is so large at sonar frequencies (>5 Hz) as to prohibit long-distance propagation. Although strong Rayleigh waves that have traveled long distances are commonly observed in earthquakes, but they are always of a low frequency (<1 Hz) and have a correspondingly low attenuation.

On the other hand, in rocks such as those of a crystalline basement, the attenuation of shear waves is comparable with, or only slightly greater than, the attenuation of compressional waves. This is indicated by the values listed in Table 3-1.

Tracor Sciences & Systems

4.0 TYPES OF SEISMIC WAVES

When a compressional sound wave in water strikes a sedimentary bottom at P (Figure 4-1), a variety of waves is, in principle, generated.

The most familiar is the bottom-reflected compressional wave (R, Figure 4-1) that remains in the water medium and has been much studied in connection with bottom-bounce sonars. Within the bottom itself, there appears a compressional wave C starting at the water-bottom boundary at nearly the same angle as that of the incident wave (since the bottom velocity there is not greatly different from the water velocity) and propagating outward in range with upward refraction. Another generated wave is the body shear wave, S, originating at a smaller angle. It is similarly upward refracted by the gradient of shear velocity in the bottom and is more highly attenuated than the compressional wave C. The third wave is a surface shear wave ST propagating along the bottom with a still higher attenuation, since the rate of attenuation in a sedimentary column is highest at its top. ST is a guided polarized surface wave; it is called the Stoneley wave when the medium on top of the solid boundary is a fluid, or a Rayleigh wave when the upper medium is a vacuum or air. Its particle motion is in the vertical plane in the retrograde direction if the propagation is to the right. In the literature, this wave is variously called the SV wave, the modified-Rayleigh wave or the Scholte wave.

When a shear wave impinges on a solid boundary, a Love wave or SH wave can be generated; like the Stoneley wave, the Love wave is a polarized surface wave, but its particle motion is in the horizontal plane. Finally, when solid layers exist, flexural waves in the layer can be excited and propagated, and are termed Lamb waves.

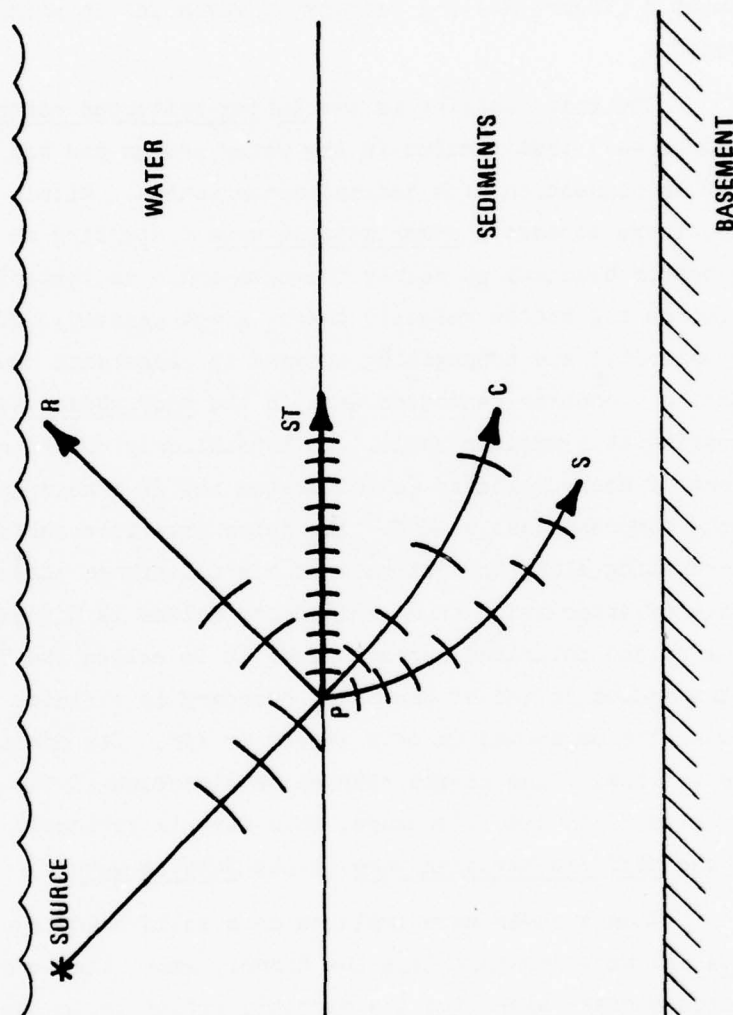


Figure 4-1. Waves generated by a wave in water striking the bottom. The symbolic wave fronts indicate the wavelength of the various waves.

Tracor Sciences & Systems

All of these waves in the bottom, with the exception of the compressional wave, have a shear component and in sediments suffer the high attenuation characteristic of shear waves.

The partition of energy between these various waves is a classic problem in seismology. For two uniform solid media separated by a plane boundary, the problem was solved long ago in a classic paper by Knott (reference 34), who derived the equations that satisfy the boundary conditions in this idealized case. For our simpler problem of an incident compressional wave, the solution was later given by Zoeppritz, and may be found in a seismology text by Macelwane and Sohon (reference 35) as well as in a short readable book by Bullen (reference 36). But for our real world conditions, this idealized model would seem to have little value; the energy partition for a realistic water-bottom model appears to be a yet-unsolved problem.

Tracor Sciences & Systems

5.0 THE AMBIENT BACKGROUND

A hydrophone in the sea operates against a well-known background of acoustic noise that is partly of natural and partly of man-made origin. Similarly, a geophone operates against a background of "earth unrest" partly of natural and partly of man-made origin.

5.1 Seismic Noise

By seismic noise is meant the unrest, or motion, of the sea bed in the absence of a known source. This unrest is caused by distant earthquakes, waves breaking on shores, distant shipping and man-made vibrations of many kinds originating on land and at sea.

Figure 5-1 gives seismic noise spectra as measured at Panama City, Florida (reference 3) and at Ft. Lauderdale (reference 4). The average of these spectra, as measured by the two horizontal components and the vertical component, is indicated by the solid and dashed curves in the figure, respectively. The indicated fall-off with frequency is about 6 dB/octave or 20 dB/decade. These are merely "snapshots", or short samples, of the noise spectra as observed at the various locations; there is no long-time or space averaging in this data. Yet this appears to be essentially all the data extant at the present time on the shallow water near-shore background for the horizontal, as well as for the vertical seismic components.

In deep water, more data exists, at least for the vertical component. This kind of data was collected by various ocean bottom seismographs developed under the VELA-UNIFORM program of nuclear-blast detection of ARPA, beginning in the latter 1950's. Figure 5-2 gives a number of vertical deep-water spectra in the region 1-10 Hz, along with the average spectrum at land stations ("ave") and an average of quiet

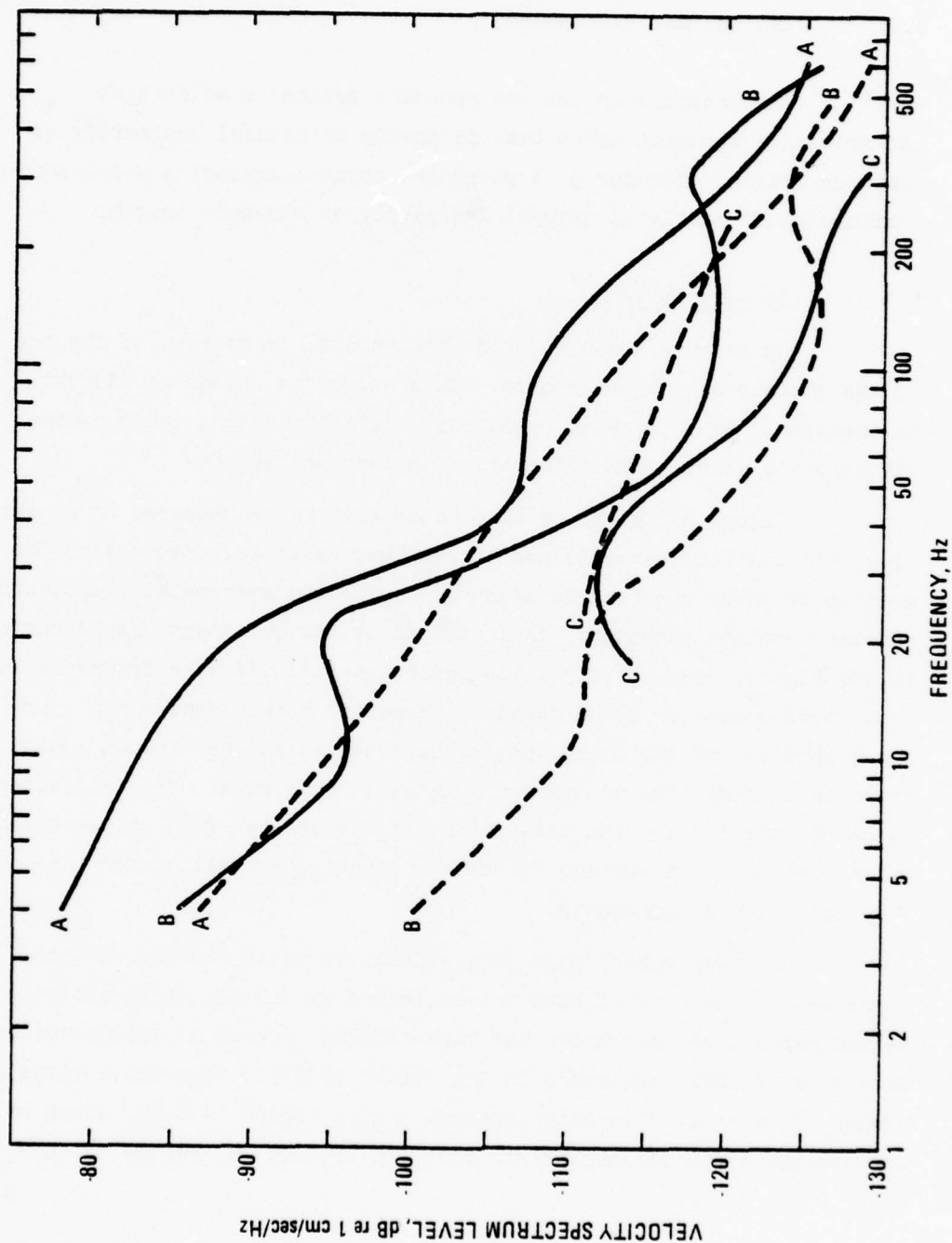


Figure 5-1. Seismic noise spectra at three Florida locations. A: Panama City, Fla in St. Andrews Bay, reference 3. B: Panama City, Fla offshore, reference 3. C: Ft. Lauderdale, Fla offshore, reference 4. Solid curves: average of the two horizontal components. Dashed curve, vertical component.

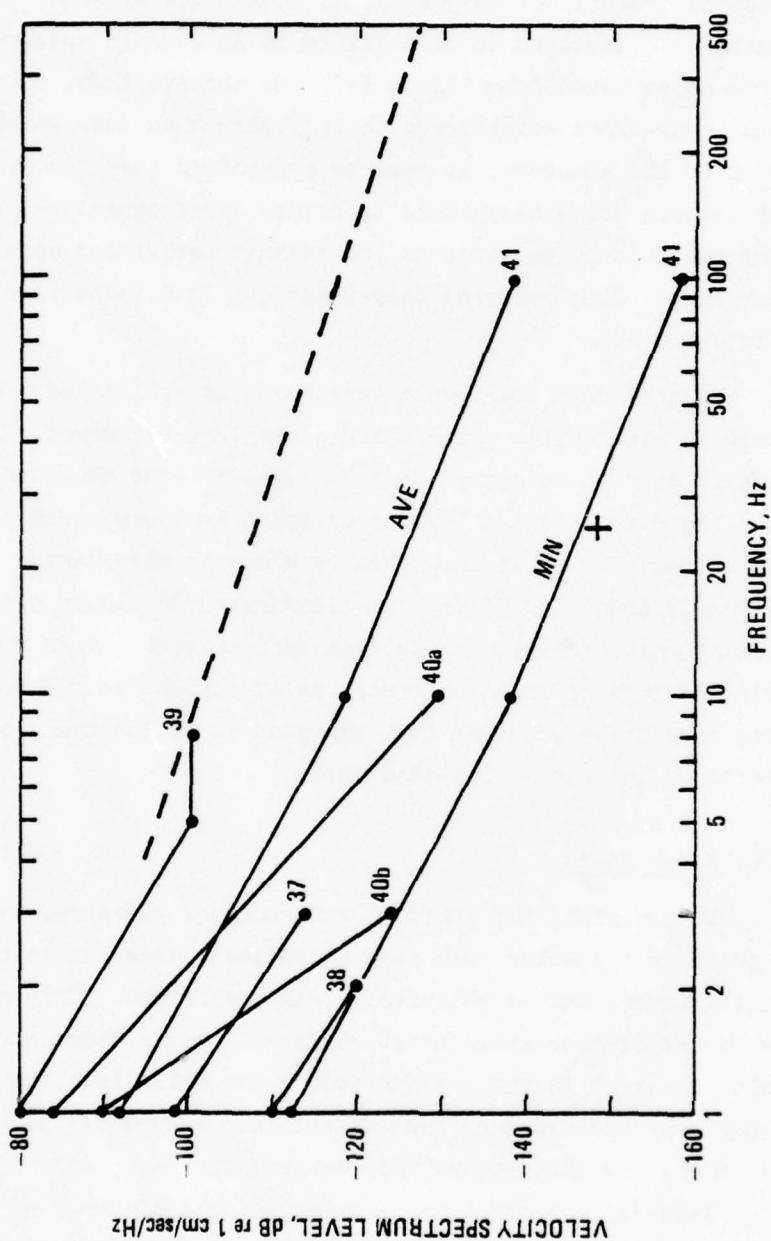


Figure 5-2. Seismic noise spectra, vertical component. Solid lines: deep sea data with average and minimum values on land, as given in Table 6-2. Dashed line, average from Figure 13 plotted for comparison. Cross, quiet value in Narragansett Bay, 25 Hz, reference 42.

Tracor Sciences & Systems

land stations ("min") out to 100 Hz, as summarized by Brune and Oliver (reference 41). Included in this figure is an average spectrum of the near-shore noise taken from Figure 5-1. We observe that, according to this data, near-shore noise tends to be higher than deep-water noise by as much as 20 dB. However, it must be emphasized that the available data for seismic noise background is scanty and fragmentary, and no long-term multi-location study of the seismic background appears yet to have been made. Some reported deep-water and land noise levels are listed in Table 5-1.

Particularly low levels were found by Willis and Dietz (reference 42) in shallow water using a vertical seismometer in Narragansett Bay. A velocity spectrum level of -148 dB is stated to have been the average quiet level recorded over a one-month period at the single frequency of 25 Hz. This is close to the average quiet land value given by Brune and Oliver, as illustrated in Figure 5-2. However, it was found that Narragansett Bay was much noisier, by as much as 40 dB, during periods of tidal currents, as if turbulence due to flow was occurring around the geophone that was said to be "bottomed on", rather than "bottomed in", the silty-sand bottom.

5.2 Water Noise

By contrast, the ambient background of pressure, as sensed by a hydrophone in the water, has been extensively measured in both deep and shallow water, and is relatively well understood. This statement applies to frequencies above about 20 Hz; in the infrasonic range of particular interest in the present study, the noise level sensed by a hydrophone has received much less attention. Figure 5-3 shows noise spectra in shallow water taken from several sources. At frequencies in the range 1-20 Hz, the spectrum is steep, with a slope of -8 to -10 dB, according to Wenz. At higher frequencies, ship or "traffic" noise tends to occur, although in the absence of ship traffic at small and moderate distances, wind-induced noise tends to dominate the spectrum over the

Tracor Sciences & Systems

TABLE 5-1. MEASURED DEEP-OCEAN SEISMIC NOISE LEVELS.
VERTICAL COMPONENT

<u>Reference</u>	<u>Location</u>	<u>Freq. Hz.</u>	<u>Reported Amplitude or Velocity in Bandwidth Stated</u>	<u>Velocity*</u>
37	65 km south of Bermuda	1	3×10^{-4} (microns) ² /Hz	- 99
		3	10^{-6} (microns) ² /Hz	-114
38	Off Catalina Island	1	10^{-3} (microns/sec) ² /Hz	-110
		2	10^{-4} (microns/sec) ² /Hz	-120
39	Off Hawaii and San Diego	1	10^{-2} (micron/sec) ² /Hz	- 80
		5	10^{-2} (micron/sec) ² /Hz	-100
		8	10^{-2} (micron/sec) ² /Hz	-100
40 a.	Southwest of Bermuda	1	10^{-1} micron in 1 octave band	- 84
		10	5×10^{-4} micron in 1 octave band	-130
b.	Gulf of Mexico	1	5×10^{-2} micron in 1 octave band	- 90
		3	10^{-3} micron in 1 octave band	-124
41 ave.	Average of numerous land stations	1	10^{-2} micron in 1/3 octave band	- 92
		10	5×10^{-4} micron in 1/3 octave band	-118
		100	5×10^{-5} micron in 1/3 octave band	-138
min.	Average quiet land stations	1	10^{-3} micron in 1/3 octave band	-112
		10	5×10^{-5} micron in 1/3 octave band	-138
		100	5×10^{-6} micron in 1/3 octave band	-158

* dB re (1 cm/sec²/Hz)

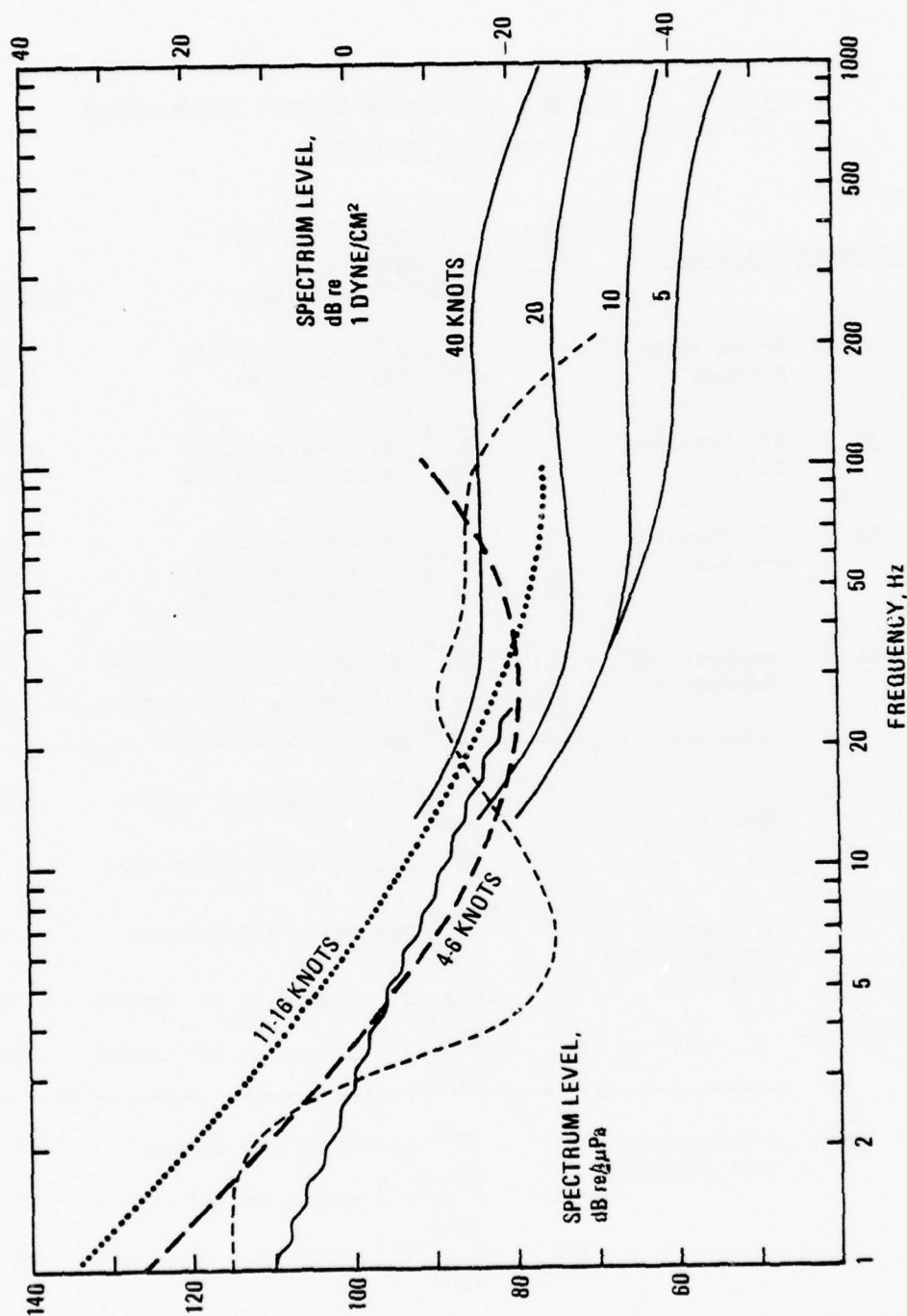


Figure 5-3. Shallow-water ambient water-noise spectra. Dashed curves, unspecified location, depth 25 fathoms, reference 43. Solid curves, location in 28 fathoms off the Scotian Shelf 3 mi. from shore, reference 44. Dotted curve, mean spectrum on the Grand Banks in 614 fm. of water, reference 45. Wavy line, mean of 25 infrasonic measurements in deep and shallow water compiled by Deloach, reference 46.

Tracor Sciences & Systems

entire range. At the low frequency end, this wind noise may well be the pressures of the local turbulence caused by current flow around the hydrophone and its mounting; this form of noise can be reduced by surrounding the hydrophone with a "wind screen" of the kind used to reduce wind noise in microphones. In the measurements of Perrone (reference 45, dotted curve Figure 5-3), a wind dependence was found only over the range 1-4 Hz and was not observed at higher frequencies, where shipping noise tended to dominate the spectrum. This dominance of ship noise, at least for deep water on the Mid-Atlantic Ridge over the frequency range 5-30 Hz, has recently been reported by McGrath (reference 47).

Tracor Sciences & Systems

6.0 PROPAGATION MODELS

Our understanding of physical data stems from our ability to fit this data into the framework of well understood theoretical models. In what follows, we present a summary of the most prevalent theoretical techniques involved in the analysis of acoustic and seismic phenomena. Then a model is presented which corresponds to a class of detection situations, giving levels of seismic vibrations at various ranges from a source. We outline how this model can be computerized to examine the results of the model calculations in the light of the experimental data described in previous sections.

6.1 Theoretical Introduction

It is not our purpose to rederive the equations describing the motions of elastic media, but it would be useful to briefly review the various physical sources of these equations. Our notation follows that of Ewing, Jardetsky, and Press (reference 48), with the exception that our acoustic potentials will be related to particle velocities rather than to particle displacements. We consider only those media which are continuous and isotropic.

By making use of Newton's 2nd Law of Motion, the continuity of the medium, and Hooke's Law, one can arrive at the following equations:

$$\nabla^2 \phi = \frac{1}{\alpha^2} \frac{\partial^2 \phi}{\partial t^2}, \quad \nabla^2 \vec{\psi} = \frac{1}{\beta^2} \frac{\partial^2 \vec{\psi}}{\partial t^2} \quad (1)$$

∇^2 is the well known Laplacian operator, $\frac{\partial^2}{\partial x^2} + \frac{\partial^2}{\partial y^2} + \frac{\partial^2}{\partial z^2}$. The

Cartesian co-ordinates are given by x, y, and z, and the variable t represents time. The variables ϕ and $\vec{\psi}$ are the scalar and vector

Tracor Sciences & Systems

acoustic potentials, giving rise to compressional and sheer waves, respectively. These are related mainly to physically intuitive quantities, such as particle velocity:

$$\vec{v} = \vec{\nabla}\phi + \vec{\nabla} \times \vec{\psi}. \quad (2)$$

Here, \vec{v} is the particle velocity, $\vec{\nabla}$ is the gradient operator, and $\vec{\nabla} \times$ is the curl operator. Lastly, we must identify the quantities α and β in equations (1). These are, respectively, the velocity of the compressional waves and the shear waves in the medium. These velocities are determined by the density of medium and the various proportionality constants in Hooke's Law relating stress and strain, such as Young's modulus.

By definition, liquids have no shear stresses, thus only the first of equations (1) is applicable and only the scalar term appears in equation (2). This illustrates the great simplification of the problem when considering the liquid case only, rather than solids which support shear waves.

The physical quantities in which we are interested are the pressure in liquids and the displacement in solids. Once the solutions (for ϕ and $\vec{\psi}$) to equations (1) are known, the displacement in solids may be found by use of equation (2), and the pressure in liquids may be found by

$$p = -\rho \frac{\partial \phi}{\partial t}. \quad (3)$$

There are many classes of functions which are solutions to equations (1). One commonly used class is the plane wave solution.

$$P(\vec{r}, t) = e^{-i(\vec{k} \cdot \vec{r} - \omega t)}, \quad (4)$$

where \vec{r} is the vector (x,y,z). It can be easily seen that this represents a plane wave traveling with a velocity of $\omega/|\vec{k}|$. The frequency with which these waves pass a given point is $\omega/2\pi$, and the distance between positions of like phase (wavelength) is $2\pi/|\vec{k}|$. These plane waves represent excellent approximations to certain situations; however, we will be considering cases in which these solutions are not sufficient. For continuous wave solutions, the plane wave serves as a useful prototype, and we restrict ourselves to solutions having the same temporal behavior as plane waves, namely, $e^{i\omega t}$. The solutions then take the form

$$\varphi = \varphi(\vec{r})e^{i\omega t} \text{ and } \vec{\psi} = \vec{\psi}(\vec{r})e^{i\omega t}. \quad (5)$$

This allows us to remove the time variable from much of the mathematics, so as to greatly simplify the work. For example, the equation for pressure becomes

$$p = -i\omega\rho\varphi, \quad (6)$$

and the wave equations become

$$\nabla^2\varphi + k_\alpha^2\varphi = 0, \quad \nabla^2\vec{\psi} + k_\beta^2\vec{\psi} = 0, \quad (7)$$

where $k_\alpha = \omega/\alpha$ and $k_\beta = \omega/\beta$.

Equations of this type (known as Helmholtz equations) arise in many areas of physics and have been studied in great detail (reference 49).

The diversity of types of solutions to the Helmholtz equation arises from the variety of boundary conditions imposed upon the solution. In the acoustical application we are considering, the pertinent boundary

Tracor Sciences & Systems

conditions arise from the continuity of the material itself (this is translated into continuity of particle velocity) and the continuity of the stress.

At this point in our development, we make use of the data discussed earlier in order to make some simplifying assumptions. As pointed out earlier, the attenuation of shear waves is considerably larger than that of compressional waves in the ocean floor. Hence, we shall ignore the shear wave potential, $\vec{\psi}$, in equations (2) and (7), due to its small value at large distances from the source. Thus, our continuity conditions become continuity of particle velocity and pressure. If these are known at some surface, then the potential ϕ and its normal gradient are known, and specific solutions to equation (7) can, in principle, be found.

At this point we specify the specific model upon which the calculations are to be based. Consider, from Figure 6-1, a layer of liquid over a semi-infinite floor. The liquid layer contains a source S emitting sound at some frequency $f = \omega/2\pi$. We will assume that the liquid layer is so shallow that we may say it has uniform density ρ_w and speed of sound c_w . In addition, we will note that at our frequencies the attenuation of sound in water is negligible. The sea floor will be specified to have the speed of sound c_s , density ρ_s , and attenuation a_s , that vary only as a function of depth.

The wave equation (7) is still difficult to solve for the situation we have presented. One further physical simplification which we make is that the semi-infinite medium is a series of homogenous layers, rather than one continuously varying layer. If the layers are made thin and numerous enough, they represent a good approximation to the continuously varying case. A typical set of values for these layers is given in Table 6-1. The solution to systems of Helmholtz's equations in layered media has been widely studied (references 50, 51, and 52) and one may draw on these works for much assistance.

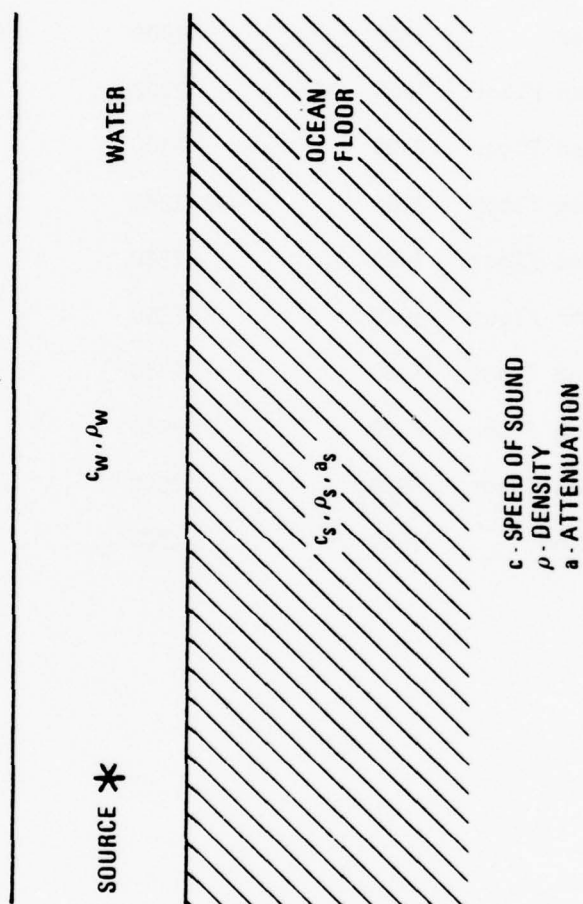


Figure 6-1. Physical model of ocean and ocean floor.
The variables in the ocean floor may vary with depth.

Tracor Sciences & Systems

**TABLE 6-1. TYPICAL VALUES OF ACOUSTICAL PROPERTIES
FOR A LAYERED MODEL OF THE OCEAN FLOOR**

<u>LAYER</u>	<u>SPEED OF SOUND</u> (meter/sec)	<u>DENSITY</u> (kg/m ³)	<u>ATTENUATION</u> (km ⁻¹) (at 1 Hz)	<u>THICKNESS</u> (meters)
1-Water	1500	1000	0	20
2-Ocean Floor	1920	2000	.04	500
3-Ocean Floor	2420	2100	.02	500
4-Ocean Floor	2920	2200	.0097	500
5-Ocean Floor	3420	2300	.0046	500
6-Ocean Floor	3920	2350	.0035	500
7-Ocean Floor	4420	2450	.0035	500
8-Ocean Floor	4920	2500	.0035	500
9-Ocean Floor	5420	2500	.0035	500
10-Bottom	5920	2500	.0035	infinite

Tracor Sciences & Systems

We shall outline here the solutions which have been implemented in a computer program written by Kutschale (references 53, 54) to simply give the propagation loss of the pressure in a multilayered media. This program is particularly useful since it may be modified to give particle velocities, which are of primary interest for our study. This program makes use of the Thomson-Haskell matrix method (references 55, 56) and follows Harkrider (reference 57) for the solution of the wave equation.

Briefly, the solution is as follows. The sound field is represented in each layer by a vector in k -space (wave number space). This vector is a function of depth, but not of the radial distance from the source. The wave equation specifies how the vector is propagated vertically through regions of constant density and speed of sound. Thus, for a homogenous layer, the vector at one surface may be related to that at the other surface by a matrix which is a function of the wave number, the thickness of the layer, the frequency, and the speed of sound. The vector is carried across the joining boundaries by making use of the continuity of particle velocity and pressure. Since these quantities are not continuous when passing through a point source, the boundary passing through the source must be handled in a special way. Thus, the sound vector in the bottom semi-infinite layer, which must represent a sound wave traveling down and not up, may be related to the sound vector at the surface, which must represent a zero pressure condition. This relation may then be solved to give an expression for the sound vector at the surface. One may then propagate this vector down to any desired depth of interest. This vector, in k -space, may then be Fourier transformed back to ordinary space (in the radial direction) to give the sound field as a function of range.

There is no need to reproduce here the complete analysis given in the above references, but we will present some important details so that we may indicate later in this report where the program may be modified to give some theoretical predictions of interest to our problem.

Tracor Sciences & Systems

We refer the reader to Figure 6-2 for the following discussion. The vertical particle velocity, w_m , and the pressure p_m , in the m 'th layer may be decomposed into a z dependent part and an r dependent part (where z and r are the vertical and radial components, respectively) according to:

$$\begin{aligned} w_m(r, z, t) &= \int_0^\infty \hat{w}_m(k, z) J_0(kr) e^{i\omega t} dk \\ p_m(r, z, t) &= \int_0^\infty \hat{p}_m(k, z) J_0(kr) e^{i\omega t} dk. \end{aligned} \quad (8)$$

Due to the similarity of these decompositions, we will find it convenient to use vector notation in referring to the sound field quantities w_m and p_m , and for brevity, we drop the explicit functional dependence on k and z :

$$V_m = \begin{bmatrix} \hat{w}_m \\ \hat{p}_m \end{bmatrix}. \quad (9)$$

The relation between the values of this vector at the top and bottom of a given layer may be written as:

$$V_{mB} = a_m V_{mT}, \quad (10)$$

where a_m is a 2×2 matrix whose elements depend only on the wave number (k), the thickness of the layer, the frequency, and the speed of sound. Due to the continuity of the particle velocity and pressure, we also have:

$$V_{mT} = V_{m-1, B}, \quad (11)$$

where we number the layers from top to bottom.

Tracor Sciences & Systems

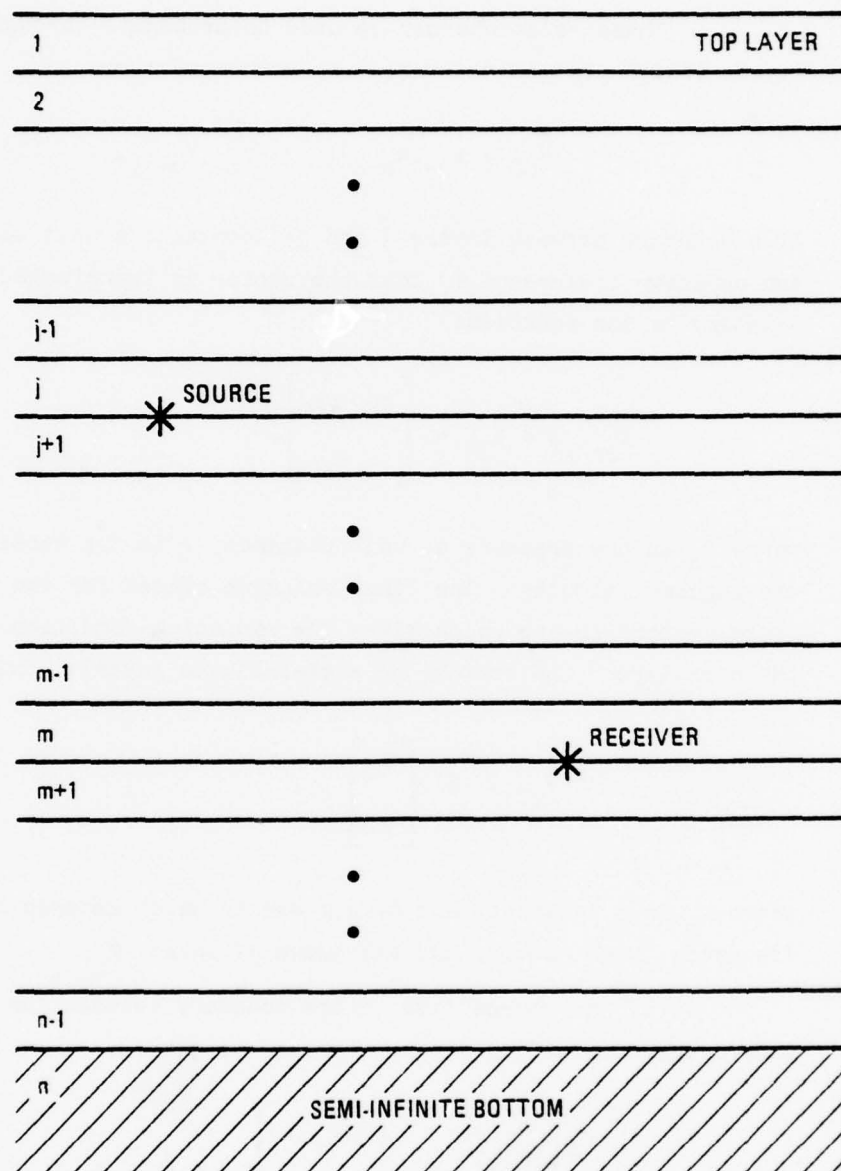


Figure 6-2. Number scheme used in program to compute sound field in layered media.

Tracor Sciences & Systems

These relations may be used to propagate through several layers (which contain no source) by combining them:

$$V_{mT} = a_{m-1} a_{m-2} \cdots a_{m-i} V_{m-i,T} \quad (12)$$

If a boundary between layers j and $j+1$ contains a unit source, then it can be shown (reference 7) that the vector is transformed across the boundary by the equation:

$$V_{j+1,T} = V_{jB} + \begin{bmatrix} 2kP_0/\rho\omega \\ 0 \end{bmatrix}, \quad (13)$$

where P_0 is the pressure at unit distance, ρ is the density, and ω is the angular velocity. The final relation needed for the manipulation of these vectors is one which gives the radiation condition at the top of the n 'th layer (the bottom, or semi-infinite layer). This is given by:

$$V_{nT} = E \begin{bmatrix} -\Delta_n \\ \Delta_n \end{bmatrix}, \quad (14)$$

where Δ_n is a constant, and E is a matrix which depends only on frequency, wave number, and the speed of sound.

If the source lies on the boundary between the j 'th and $j+1$ 'th layer, these relations may be combined to give:

$$\begin{bmatrix} -\Delta_n \\ \Delta_n \end{bmatrix} = E^{-1} A_L \begin{bmatrix} 2kP_0/\rho\omega \\ 0 \end{bmatrix} + E^{-1} A_L A_u V_{1T}, \quad (15)$$

where $A_L = a_{n-1} a_{n-2} \cdots a_{j+2} a_{j+1}$
and $A_u = a_j a_{j-1} \cdots a_2 a_1$.

Tracor Sciences & Systems

The vector at the surface is thus related to the radiation condition at the bottom. If we remember that the pressure at the surface is zero, we may write:

$$V_{1T} = \begin{bmatrix} \hat{w}_1 \\ 0 \end{bmatrix}, \quad (16)$$

and equation (15) becomes

$$\begin{bmatrix} -\Delta_n \\ \Delta_n \end{bmatrix} = E^{-1} A_L \begin{bmatrix} 2kP_o/\rho\omega \\ 0 \end{bmatrix} + E^{-1} A_L A_u \begin{bmatrix} \hat{w}_1 \\ 0 \end{bmatrix}. \quad (17)$$

Δ_n may be eliminated from the 2 equations in (17) to yield an expression for w_1 as a function of k . Now that V_{1T} is known, the sound field vector may be propagated down to any chosen boundary by the same method as was used to propagate upwards. For example, if the vector is wanted at the lower boundary of the m 'th layer, we have:

$$V_{mB} = a_m a_{m-1} \dots a_2 a_1 \begin{bmatrix} \hat{w}_1 \\ 0 \end{bmatrix}, \quad m \leq j \quad (18)$$

if this boundary is above the source. If the boundary is below the source, then we have:

$$V_{mB} = a_m a_{m-1} \dots a_{j+2} a_{j+1} \left(A_u \begin{bmatrix} \hat{w}_1 \\ 0 \end{bmatrix} + \begin{bmatrix} 2kP_o/\rho\omega \\ 0 \end{bmatrix} \right), \quad m > j. \quad (19)$$

Tracor Sciences & Systems

At this point, we now have, in principle, an integral solution which may be evaluated for equation (8), which we rewrite in vector forms:

$$\begin{bmatrix} w_m \\ p_m \end{bmatrix} = \int_0^{\infty} \begin{bmatrix} \hat{w}_m \\ \hat{p}_m \end{bmatrix} J_0(kr) e^{i\omega t} dk. \quad (20)$$

This gives us the vertical particle velocity and the pressure at any point. We also want to be able to compute the horizontal (radial) particle velocity. This may be obtained from the equation for pressure, by the use of equations (6) and (2). The acoustic potential may be written as:

$$\phi_m = \frac{i}{\rho\omega} p_m = \frac{i}{\rho\omega} \int_0^{\infty} \hat{p}_m(k, z) J_0(kr) e^{i\omega t} dk. \quad (21)$$

Then, since $p_m(k, z)$ is not a function of the radial co-ordinate, we get for the horizontal particle velocity u_m :

$$u_m = -\frac{i}{\rho\omega} p_m = \frac{i}{\rho\omega} \int_0^{\infty} \hat{p}_m(k, z) k J_1(kr) e^{i\omega t} dk. \quad (22)$$

The reader is reminded here that these results apply to a layered liquid medium containing no solid layers. However, these results have been generalized to include solid layers as well. Understandably, the solution is more complex. The essential differences are the following. The sound field is described by a 4-vector rather than a 2-vector:

$$V_m = \begin{bmatrix} \hat{u}_m \\ \hat{w}_m \\ \hat{p}_{zzm} \\ \hat{r}_m \end{bmatrix}, \quad (23)$$

Tracor Sciences & Systems

where \hat{u}_m and \hat{w}_m have the same meaning as before. The quantity \hat{p}_{zzm} is the vertical normal stress in the m'th layer, and $\hat{\tau}_m$ is the shear stress on a horizontal plane in the radial direction. These vector representations of the sound field are transformed through layers in a similar manner as in the liquid case. The key difference is that they are transformed by 4x4 matrices whose elements are functions of shear velocity as well as the other variables in the liquid case. Again, the continuities of the stress and material are used to transform the vector across boundaries.

The radiation condition is used in the bottom semi-infinite layer in a similar manner as before to get a solution for the sound field vector at the surface. This is then propagated down to the selected boundary of interest as before, and the solution proceeds in the same fashion as for the liquid case.

One may get an approximation to the integral in (20) numerically simply by evaluating the integrand at closely spaced intervals, multiplying by the interval length and adding up the terms. With the advent of the Fast Fourier Transform (FFT) technique, this method becomes very attractive.

Several precautions must be observed when using this method, however. The region of numerical integration must extend out far enough in k-space to include all the region where the integrand is large enough to contribute significantly to the overall integral. In addition, the integrand must be sampled at intervals spaced closely enough so that any narrow peaks are properly sampled. Lastly, the system must have enough attenuation to move the poles off the real k axis far enough so that the value of the integrand is not so enormous as to be non-representable on the computer.

If one chooses to evaluate the integral (20) in an analytic fashion, the integrand must be investigated in the complex plane of k. Typically, the integrand will have a series of poles on the real axis (or displaced from the real axis some distance depending on the amount

Tracor Sciences & Systems

of absorption in the problem, if present) and a branch line extending from the origin out to some k_B . The integral along the real axis may then be deformed to some contour which may be integrated to yield a sum of residue terms (corresponding to the poles) and a branch line integral. The branch line integral can be shown (reference 1) to diminish rapidly as the distance from the source increases. Thus, the integral (20) reduces to a sum of pole terms. Each of the pole terms corresponds to a specific normal mode of the system, so that this method of solution corresponds to normal mode theory.

In normal mode theory, one expands the solution as a weighted sum of the normal solutions. Initially, one separates the variables in the wave equation. Since we are considering cylindrical symmetric cases, the Laplacian operator in the wave equation may be written as:

$$\nabla^2 = \frac{\partial^2}{\partial r^2} + \frac{1}{r} \frac{\partial}{\partial r} + \frac{\partial^2}{\partial z^2} . \quad (24)$$

This allows us to separate the variables r and z to obtain solutions of the variety:

$$\varphi(r,z) = \sum_n b_n R_n(r) Z_n(z), \quad (25)$$

where R_n and Z_n satisfy the differential equations

$$\frac{d^2 Z_n}{dz^2} + (k^2 - k_{zn}^2) Z_n = 0 \quad (26)$$

$$\text{and } \frac{d^2 R_n}{dr^2} + \frac{1}{r} \frac{dR_n}{dr} + k_{zn}^2 R_n = 0 ,$$

where the eigenvalue k_{zn} is determined by the vertical structure of the system. The last of equations (26) may be recognized as Bessel's equation of order 0. Since outgoing wave solutions are desired, we choose the Hankel solutions of the second kind:

$$R_n(r) = H_0^{(2)}(k_{zn}r) \quad (27)$$

In general, since the speed of sound, α , will be a function of depth, $k = \omega/\alpha$ will be a function of z in the first of equations (26). Hence, an exact analytic solution for $Z(z)$ will be difficult to obtain.

Once the boundary conditions are specified, the differential equation for Z will have solutions only for particular eigenvalues of k_{zn} . The sum over n in equation (25) then is only over these specific eigensolutions. Depending on the relative values of the various speeds of sound in the system, this sum may or may not include an integral over wave number as well as a discrete sum. This integral corresponds to the branch line integral encountered earlier, and its contribution will diminish rapidly as the distance from the source increases.

6.2 Computer Models Studied

The objective of the computer modeling is to study an idealized physical system via theoretical computations made by a computer in order to better understand the experimental data collected heretofore and to be able to indicate which future experiments should be conducted.

Tracor Sciences & Systems

We studied three different computer programs to carry out this part of the study. All three have at least one flaw as far as our problem is concerned. They are all based on a cylindrically symmetric system; thus they do not contain calculations which can give rise to any horizontal transverse motion. This motion was seen to be an important component of the outgoing wave in a previous section. From a point source, this motion can only arise from inhomogeneities in the medium or other properties which are not azimuthally invariant. These properties greatly increase the difficulty of the theory, and no computer models were found which included these important effects. However, two important features of the data may be investigated from a cylindrically symmetric model. The first is the improved signal-to-noise ratio of the longitudinal horizontal motion of the bottom compared to the signal-to-noise ratio of the pressure wave in the water. The second is that the signal-to-noise ratio does not fall off as fast as one would expect from cylindrical spreading for a considerable distance out from the source.

The physical model that is postulated to give rise to these phenomena is the following. If the bottom is composed of layers such that the speed of sound increases with the depth, and the attenuation of the compressional waves decreases with depth, then the following situation would arise. The waves travelling horizontally outward near the surface will undergo a greater attenuation than those which penetrate down at a steeper angle. These deep going and relatively less attenuated waves are refracted back up to the surface by the increasing speed of sound. As they return to the surface at the large distances, they maintain the sound level above that which one would expect from cylindrical spreading.

The first program which we investigated was one which makes use of normal mode theory (reference 58). To find the vertical eigenfunctions and their eigenvalues, this program vertically integrates

Tracor Sciences & Systems

the vertical differential equation through the layers from the bottom layer to the surface, for a given trial eigenvalue. Due to the zero pressure required at the surface for a boundary condition, the eigenfunction must be zero at the surface. If, after the vertical integration, this is not so, a new eigenvalue is chosen, and the integration is carried out again. These iterations are carried out until the value of the eigenfunction at the surface is sufficiently small. The procedure is repeated until the eigenfunction for each mode is found, and then they may be appropriately added and manipulated in order to compute the pressure at a given depth for a series of ranges.

The program allows one to break the physical system up into three layers. The top layer must be fluid and contains the source and the receiving point. The second layer is another fluid layer, and the bottom semi-infinite layer is solid. In the top two layers, the speed of sound may be a function of depth; that is, the speed of sound may be specified at several different depths and the program links these points linearly. Also, one may enter attenuation into the layers, but the attenuation coefficient may not vary with depth within each layer.

After investigation, this program was not chosen to make our computations for the following reasons. The iteration method of integrating the wave equation is a very time consuming process on the computer and hence costly. Also, the FORTRAN code in which the program was written contained many non-standard statements which, though trivial in principle to change, would require an inordinate amount of time to modify to the Tracor computer. In addition, the inability to vary attenuation in the bottom layers would keep us from specifying a key feature of the physics of the problem: that the attenuation in the bottom decreases with depth.

The second program which we considered was one which was written by ourselves. We designed this program to calculate pressures and particle velocities based on a very simple model. This consisted

of a homogenous liquid layer over a homogenous solid semi-infinite layer. For ease and speed of computation, we computed only the wanted quantities at the boundary. The method used was normal mode theory. Due to the simplicity of the model, once the eigenvalues were found by a simple, speedy numerical computation, the eigenfunctions could be expressed in closed form and rapidly evaluated. The details of the program are included in the appendix.

As the study of the acoustic properties of the ocean floor proceeded, it was learned that a realistic model must include variable attenuation as well as speed of sound in the ocean bottom. It was decided that this oversimplified computer model was not sufficient.

A third computer program was considered (reference 54) which, with minor but non-trivial modifications, would have satisfied the requirements of allowing sufficient complexity in the physical model while being fast enough in execution so as not to use unreasonable amounts of computer time. The program allows one to divide a half-space into homogenous layers which can be either solid or liquid. Also, a depth-dependent attenuation may be incorporated in the program. The program makes use of the theory outlined above for propagation from layer to layer, and arrives at the integral (20). Due to the fact that we must have attenuation in the system, the wave number becomes complex and the Bessel functions must be modified to Hankel functions. The program then evaluates the set of integrals.

$$\begin{bmatrix} u_m \\ w_m \\ p_m \end{bmatrix} = \int \begin{bmatrix} -\frac{ik}{\rho\omega} \hat{p}_m H_1^{(2)}(kr) \\ \hat{w}_m H_0^{(2)}(kr) \\ \hat{p}_m H_0^{(2)}(kr) \end{bmatrix} dk, \quad (28)$$

Tracor Sciences & Systems

where we have dropped the time dependent portion of the expression. The program approximates the third of these integrals by the use of an FFT algorithm in the following manner.

The Hankel function $H_0^{(2)}(kr)$ can be approximated by

$$H_0^{(2)}(kr) = \sqrt{\frac{2}{\pi kr}} e^{-i(kr - \pi/4)} \quad (29)$$

for distances large enough that $kr \gg 1$.

The third integral may be rewritten as:

$$p_m = \int_0^\infty \sqrt{\frac{2}{\pi kr}} \hat{p}_m e^{\frac{i\pi}{4}} e^{-ikr} dk \quad (30)$$

If we wish to evaluate this numerically at a series of N range points equally spaced by Δr : such that $r_n = r_0 + n \Delta r$, we may approximate (30) by:

$$p_m(r_n) = \sqrt{\frac{2}{\pi r_n}} \Delta k e^{i(\frac{\pi}{4} - k_0 r_n)} \sum_{l=0}^{N-1} \frac{\hat{p}_m}{\sqrt{k_l}} e^{-ir_0 l \Delta k} e^{\frac{-2\pi i l n}{N}}, \quad (31)$$

where Δk and Δr must be chosen such that

$$\Delta r \Delta k = \frac{2\pi}{N} \quad (32)$$

If N is an integral power of 2, (31) may be seen to be rapidly evaluated by use of an FFT for the quantity in the brackets.

Currently, the program only evaluates the pressure in the above manner. One can see from equation (28) however, that this method can be easily suited to the evaluation of w_m , the vertical particle velocity. Also, since $H_1^{(2)}$ is the same as $H_0^{(2)}$ phase shifted by 90° at large distances, we can make the same statement about u_m , the horizontal particle velocity.

There is another problem with the program in its present configuration as related to our application. Currently, the receiver point must be above the source, since it makes use of equation (18) and not (19) as it propagates the surface sound field vector down to the receiver. Here again, this is not a trivial correction to make, but neither is it a difficult one.

As discussed earlier, precautions must be taken in choosing the interval lengths to make certain that all of the significant portion of the integration region is covered. To aid this determination, the program displays the integrand as a function of wave number in graphical form.

6.3 Acknowledgements

The authors wish to acknowledge valuable assistance in the evaluation of the computer programs used in this study. Useful discussions with J. Miller and F. Ingenito of the Naval Research Laboratory, as well as sample runs of their program are greatly appreciated. In addition, H. Kutschale of the Lamont-Doherty Geological Observatory of Columbia University provided his program along with sample runs and useful guidance for modifications to his program.

Tracor Sciences & Systems

7.0 SUMMARY AND CONCLUSIONS

We may summarize this report by the following statements and conclusions:

1. A number of real-world field tests have been made using seismic sensors placed on the sea bed for observing and recording the signal from a distant sound source in the overlying water. A number of these have used only vertical-component seismic pickings. Only two have employed three-component geophones; both show a higher signal-to-noise ratio on the horizontal geophones than on the vertical geophone or a near-by hydrophone at shallow water locations.
2. The acoustics underlying this phenomenon is unknown. While shear waves of various types in sedimentary bottoms have been identified in theory and by observation, they all have such a high attenuation that they are unlikely to contribute to the received signals. Compressional waves, especially those following deep paths in a sedimentary column, have a relatively low attenuation. Together with the ducting caused by upward refraction, compressional wave propagation may provide the explanation of the gain mentioned in the preceding paragraph.
3. There is no explanation other than horizontal inhomogeneities in the bottom sediments for the horizontal cross-component of the received seismic signals.
4. There is little or no data on the horizontal-component seismic ambient noise background of the sea bed. Vertical-component noise data is relatively abundant, but

Tracor Sciences & Systems

only in deep water, with nothing known about the noise in shallow water or on the continental slopes.

5. Many measurements exist of the physical and acoustical characteristics of sediments, such as sound speed, attenuation, and density. Such bottom characteristics are the input data to a computer model.
6. Any benefit in signal-to-noise provided by a seismic sensor is likely to occur in shallow water and at frequencies, such as the blade-rate frequencies of propeller sources, that are too low to be trapped in the shallow water duct. In deep water, water borne propagation paths are apt to be so excellent that propagation through the bottom will, in all likelihood, be relatively insignificant.
7. While shear waves in sediments are unlikely to be important for long-range propagation in sediments, this may not be the case for hard non-sedimentary bottoms where their attenuation coefficient is comparable to that of compressional waves.
8. None of the computer models examined permit a computation of the particle velocity. Modification to these models, and a search for other computer models that may obtain the desired output under realistic input conditions, is needed.

Tracor Sciences & Systems

8.0 OUTLINE OF A FOLLOW-ON RESEARCH PROGRAM

Initial measurements have indicated that seismic sensors have a signal-to-noise ratio advantage over hydrophones. At present there are no physical models which can explain this phenomena. None of the models which we have examined provide predictions of particle velocity on or in the bottom. In addition, no transmission loss data, as measured by seismic sensors, exists for comparison with a model.

In order to complete the assessment of the feasibility of enhanced detection of waterborne sound sources by geophones, a two phase research program should be conducted as follows:

A. Model Development

1. Develop an adequate computer model to support and extend test data to other conditions. This model would permit computation of the horizontal and vertical bottom velocities, as well as the pressure in the water, at the water-bottom interface for a multi-layered fluid bottom of assignable sound velocities, densities, and attenuation in the various layers. Extensions of the model should be sought for conditions of: (a) rigid, bottom layers supporting shear waves; (b) a sloping bottom; and (c) lateral variability.
2. Exercise the model so developed for the measured or inferred conditions of the field data.

B. Data Collection

1. Collect data using a combined hydrophone - three component geophone package that would enable easy, calibrated comparisons of the four sensors, in an area where the acoustic and geologic characteristics of the

Tracor Sciences & Systems

bottom are already known to some extent, as at Panama City, Florida, or can be determined by coring and geophysical techniques.

2. Extend the tests to a number of areas where the bottom-acoustics can be inferred and are diverse, so as to get a sampling of different locations. An important part of the effort is the collection of seismic and water noise data over a reasonable length of time so as to be able to estimate the mean noise background at the different sites.
3. Collect data using a number of hydrophone-seismic units at one location in order to determine the feasibility of using arrays of seismic sensors to achieve array gain and target bearing.

Tracor Sciences & Systems

9.0 APPENDIX: LISOL, A COMPUTER MODEL OF A LIQUID LAYER OVER A SOLID HALF-SPACE

Ewing, Jardetsky, and Press (EJP) solve the problem of a liquid layer over a solid bottom (reference 48). We follow their solution in what follows. In the body of this report, we have used a velocity potential for the calculations, but here we follow EJP in using a displacement potential. Using the parameters defined in Figure 9-1 we have:

$$\begin{aligned}\varphi_L &= \sum_n A_n \Theta_L(\kappa_n) \sin(\xi_{Ln} h) \sin(\xi_{Ln} z) \\ \varphi_S &= \sum_n A_n \Theta_S(\kappa_n) \sin(\xi_{Ln} h) e^{-\xi_{Sn}(z-H)} \\ \psi_S &= \sum_n A_n \Xi_S(\kappa_n) \sin(\xi_{Ln} h) e^{-\xi_{Sn}(z-H)}\end{aligned}$$

where

$$\begin{aligned}A_n &= \frac{2}{H} \sqrt{\frac{2\pi}{\kappa_n r}} e^{\varphi_n} \\ \varphi_n &= \omega t - \kappa_n r - \pi/4 \\ \xi_{Ln} &= \sqrt{k_{\alpha L}^2 - \kappa_n^2}, \quad k_{\alpha L} = \omega/\alpha_L \\ \xi_{Sn} &= \sqrt{\kappa_n^2 - k_{\alpha S}^2}, \quad k_{\alpha S} = \omega/\alpha_S \\ \xi_{Sn} &= \sqrt{\kappa_n^2 - k_{\beta S}^2}, \quad k_{\beta S} = \omega/\beta_S\end{aligned}$$

AD-A063 163

OFFICE OF NAVAL RESEARCH ARLINGTON VA
PROCEEDINGS OF THE WORKSHOP ON SEISMIC PROPAGATION IN SHALLOW W--ETC(U)
JUL 78

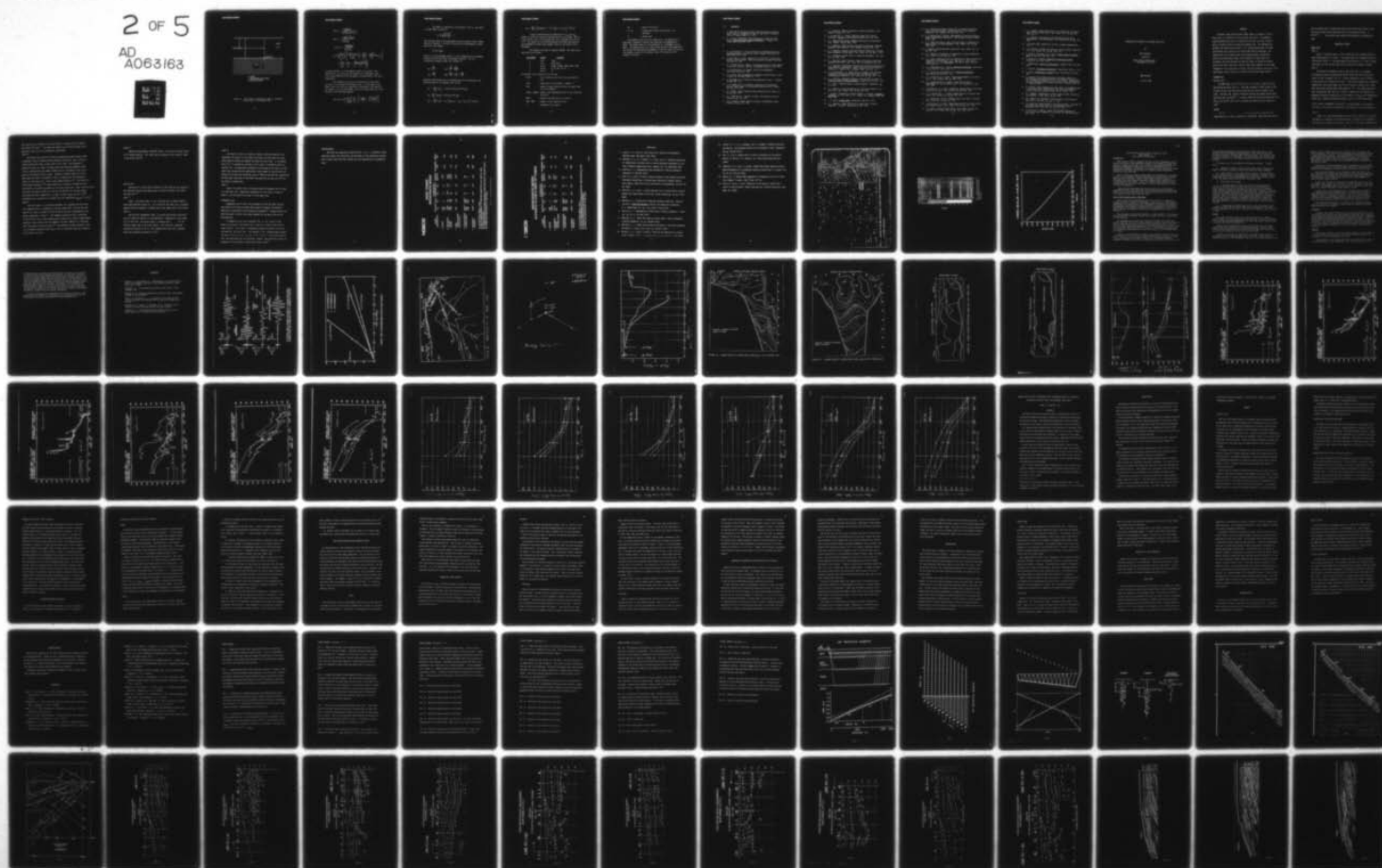
F/G 8/11

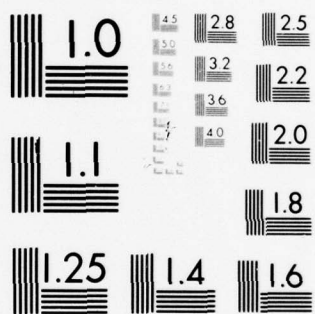
UNCLASSIFIED

NL

2 OF 5

AD
A063163





MICROCOPY RESOLUTION TEST CHART
NATIONAL BUREAU OF STANDARDS-1963-A

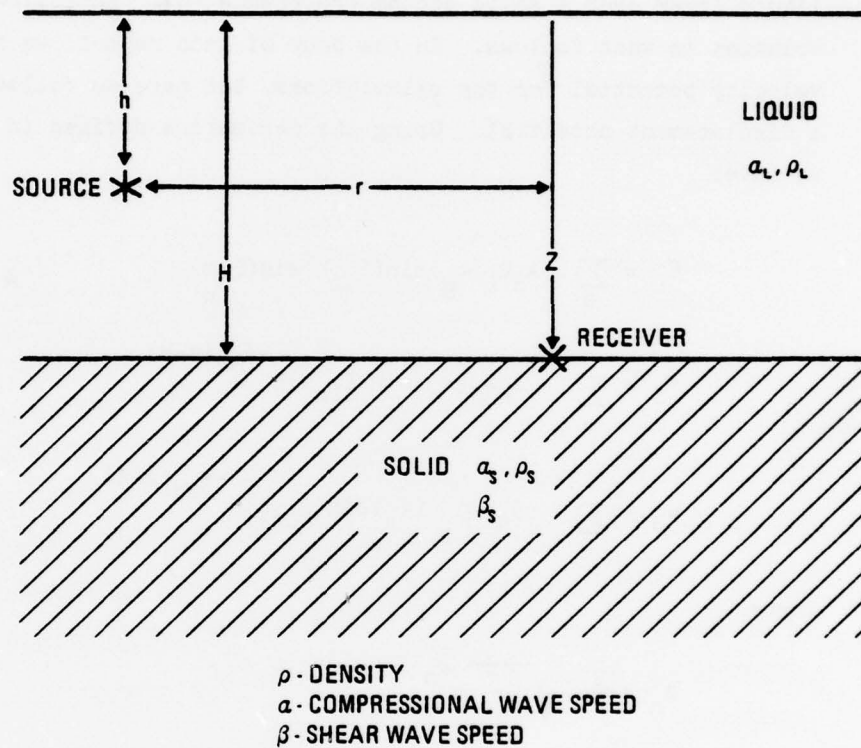


Figure 9-1. The physical configuration used for computing sound levels in the program LISOL.

Tracor Sciences & Systems

$$\Theta_L(\kappa_n) = - \frac{\rho_L k_{\beta S}^4 \xi_{Sn}^H}{\rho_S \kappa_n^2 \xi_{Ln}^2 M_n \cos(\xi_{Ln} H)}$$

$$\Theta_S(\kappa_n) = - \frac{\rho_L k_{\beta S}^2 (\kappa_n^2 + \xi_{Sn}^2) H}{\rho_S \kappa_n^2 \xi_{Ln} M_n}$$

$$\Xi_S(\kappa_n) = - \frac{2 \rho_L k_{\beta S}^2 \xi_{Sn}^H}{\rho_S \kappa_n^2 \xi_{Ln} M_n}$$

$$M_n = \frac{\rho_L}{\rho_S} \left(\frac{k_{\beta S}}{\kappa_n} \right)^4 \left[\frac{\kappa_n^2 \sin(\xi_{Ln} H)}{\xi_{Ln} \xi_{Sn}} \left(1 + \frac{\xi_{Sn}^2}{\xi_{Ln}^2} \right) - \frac{\xi_{Sn} \kappa_n^2 H}{\xi_{Ln}^2} \sec(\xi_{Ln} H) \right] - 4 \left[\frac{\xi_{Sn}}{\xi_{Ln}} + \frac{\xi_{Sn}}{\xi_{Sn}} + 2 \left(\frac{\xi_{Sn} \xi_{Sn} - \kappa_n^2 - \xi_{Sn}^2}{\kappa_n^2} \right) \right]$$

In these equations, ω is the angular velocity of the wave. The quantities α_L , α_S , and β_S are the speeds of the compression waves in the liquid and solid, and the speed of the shear wave in the solid, respectively.

The variables ρ_L and ρ_S are the densities of the liquid and solid, H is the depth of the water layer, L is the depth of the source, and z and r are the cylindrical co-ordinates of the receiver. The quantity κ_n is the wave number of the n 'th normal mode, and is the solution to the following equation:

$$\tan(\xi_{Ln} H) = \frac{\rho_S}{\rho_L} \left(\frac{\kappa_n}{k_{\beta S}} \right)^4 \frac{\xi_{Ln}}{\xi_{Sn}} \left[4 \frac{\xi_{Sn} \xi_{Sn}}{\kappa_n^2} - \left(\frac{\kappa_n^2 + \xi_{Sn}^2}{\kappa_n^2} \right)^2 \right]$$

Tracor Sciences & Systems

The number of solutions to this equation, that is, the number of normal modes is given by:

$$N = \frac{H}{\pi} \sqrt{k_{\alpha L}^2 - k_{\beta S}^2} + 1.$$

Any fractional part of this expression above the greatest lower integer should be truncated. In order to find particle displacements, we must make use of the formula

$$\vec{d} = \vec{\nabla}\varphi + \vec{\nabla}\times\vec{\psi},$$

where d is the displacement vector, φ is the compressional displacement potential and $\vec{\psi}$ is the shear displacement potential. For our cylindrically symmetric case, this reduces to:

$$\begin{aligned} d_{rL} &= \frac{\partial \varphi_L}{\partial r} & d_{rS} &= \frac{\partial \varphi_S}{\partial r} + \frac{\partial^2 \psi_S}{\partial r \partial z} \\ d_{zL} &= \frac{\partial \varphi_L}{\partial z} & d_{zS} &= \frac{\partial \varphi_S}{\partial z} - \frac{1}{r} \frac{\partial}{\partial r} \left(r \frac{\partial \psi_S}{\partial r} \right). \end{aligned}$$

Applying these derivatives to our expressions for the potentials, and evaluating them at the boundary ($z=H$) we get:

$$d_{rL} = - \sum_n A_n \left(\frac{1}{2r} + i\kappa_n \right) \Theta_L(\kappa_n) \sin(\xi_{Ln} h) \sin(\xi_{Ln} H)$$

$$d_{zL} = \sum_n A_n \xi_{Ln} \Theta_L(\kappa_n) \sin(\xi_{Ln} h) \cos(\xi_{Ln} H)$$

$$d_{rS} = - \sum_n A_n \left(\frac{1}{2r} + i\kappa_n \right) \left[\Theta_{Sn}(\kappa_n) - \xi_{Sn} \Xi_{Sn}(\kappa_n) \right] \sin(\xi_{Ln} h)$$

Tracor Sciences & Systems

$$d_{zS} = \sum_n A_n \left[-\xi_{Sn} \Theta_{Sn}(\kappa_n) + (\kappa_n^2 - \frac{1}{4r^2}) \Xi_{Sn}(\kappa_n) \right] \sin(\xi_{Ln} h)$$

It may be observed that the expressions for d_{zL} and d_{zS} appear to differ but continuity requires them to be the same. They do in fact differ, but it can be shown that their difference falls off as $1/r^2$. This should not be surprising because the normal mode solution has discarded the branch line integral, which is the source of this difference.

The program is written in standard FORTRAN. The input cards required are as follows:

<u>CARD NUMBER</u>	<u>FORMAT</u>	<u>VARIABLES</u>
1	79A1	TITLE
2	7I10	IDBG, NPTS
3	5F10.5	ALPHA1, ALPHA2, BETA2, RH01, RH02
4	5F10.5	F, HS, HB, DL, DU
5	5F10.5	SL

The meaning of the variables are as follows:

TITLE	- any 79 character long title the user wishes to use.
IDBG	- debug level of the program - normally 0.
NPTS	- number of radial points at which the sound field is to be evaluated.
ALPHA1, ALPHA2	- speed of the compressional wave in the liquid and the solid.
BETA2	- speed of the shear wave in the solid.
RH01, RH02	- density of the liquid and solid.
F	- frequency of the source.

Tracor Sciences & Systems

HS - depth of the source

DL, DU - closest and furthest radial points to be
 evaluated.

SL - source level

The program is set up to run on MKS units. The speeds are in meters/sec, distances in meters, and densities in kilograms/cubic meter. The source level is in dB referenced to 1 micropascal at one meter. The program prints out a table which gives for each range point, the vertical and horizontal displacement of both the liquid and solid at the boundary, as well as the pressure level of the liquid at the boundary in dB/ μ Pa.

Tracor Sciences & Systems

10.0 REFERENCES

1. J. Lamar Worzel and Maurice Ewing, "Explosion Sounds in Shallow Water, paper in Propagation of Sound in the Ocean", Geological Society of America Memoir 27, 1948.
2. R. J. Urick, "Underwater Sound Transmission Through the Ocean Floor", Physics of Sound in Marine Sediments, L. Hampton, ed., Plenum Press, New York, 1974.
- 3.
4. R. J. Urick and R. J. Urick, "Detection of Underwater Sounds by a Geophone Planted in the Bottom", Naval Ordnance Laboratory Tech Rept NOLTR 68-102, 1968.
5. M. Blaik and C. S. Clay, "Detection in the Ground of Sound from a Source in Shallow Water", Hudson Laboratories, Columbia University Tech Rept 76, 1959.
6. R. D. Worley and R. A. Walker, "Low Frequency Acoustic Measurements in the Gulf of Maine", USN Jour. Underwater Acoust. 9, 435, 1959.
7. C. B. Officer and J. B. Hersey, Woods Hole Oceanographic Institution Ref 53-32, 1953.
8. R. J. Urick, "Sound Transmission from Deep to Shallow Water", Naval Ordnance Lab Tech Rept NOLTR 72-1, 1971.
9. C. Kisslinger et al, SH Motion from Explosions in Soil, J. Geophys. Res 66, 3487, 1961.
10. J. K. Wright and E. W. Carpenter, Generation of Horizontally Polarized Shear Waves from Underground Explosions Jous. Geophys. Res. 67, 1957, 1962.
11. B. F. Howell, Ground Vibrations Near Explosions, Bull Seism. Soc. Am. 39, 285, 1949.
12. R. L. Geyer and S. T. Martner, SH Waver from Explosive Sources, Geophysics 34, 893, 1969.
13. B.L.N. Kennett, Seismic Waves in Laterally Inhomogeneous Media, Geophys. Jous 27, 301, 1972.

Tracor Sciences & Systems

14. E. L. Hamilton, "Elastic Properties of Marine Sediments", Jour. Geophys. Res 76, 579, 1971.
15. J. E. Nafe and C. L. Drake, "Physical Properties of Marine Sediments", The Sea, Interscience Publishers, New York, 1963.
16. E. L. Hamilton and others, "Sediment Velocities from Sonobuoys", Jour. Geophys. Res 79, 2653, 1974.
17. E. L. Hamilton, "Sound Velocity and Related Properties of Marine Sediments, North Pacific", Jour. Geophys. Res 75, 4423, 1970.
18. E. L. Hamilton, "Acoustic and Other Physical Properties of Shallow Water Sediments Off San Diego", Jour. Acous. Soc. Am. 28, 1, 1956.
19. B. C. Schreiber, "Sound Velocity in Deep Sea Sediments", Jour. Mar. Res. 73, 1259, 1968.
20. E. L. Hamilton, "Sound Velocity - Density Relations in Sea-Floor Sediments and Rocks", Jour. Acous. Soc. Am. estimated Feb. 1978.
21. R. S. Anderson, "Statistical Correlation of Physical Properties and Sound Velocity in Sediments", paper in Physics of Sound in Marine Sediments (L. Hampton, ed.), Academic Press, New York, 1974.
22. R. E. Christensen, J. A. Frank, and W. H. Geddes, "Low Frequency Propagation via Shallow Refracted Paths Through Deep Ocean Unconsolidated Sediments", Jour. Acous. Soc. Am. 57, 1421, 1975.
23. E. L. Hamilton, "Geoacoustic Models of the Sea Floor", paper in Physics of Sound in Marine Sediments, Plenum Press, New York, 1974.
24. R. D. Stoll, "Acoustic Waves in Ocean Sediments", Geophysics, 42, 715, 1977.
25. E. L. Hamilton, "Sound Attenuation as a Function of Depth in the Sea Floor", Jour. Acoust. Soc. Am. 59, 528, 1976.
26. L. Knopoff, "Attenuation of Elastic Waves in the Earth", Physical Acoustics, Vol. III, Part B, (W. P. Mason, ed.) Academic Press, New York, 1965.
27. J. E. White, Seismic Waves, McGraw-Hill, New York, 1965.
28. E. L. Hamilton, "Shear Wave Velocity Versus Depth in Marine Sediments: A Review", Geophysics 41, 985, 1976.

Tracor Sciences & Systems

29. E. L. Hamilton and others, "Velocities of Pressional and Shear Waves in Marine Sediments Determined In-Situ from a Research Submarine", Jour. Geophys. Res. 75, 4039, 1970.
30. E. G. McLeroy and A. Deloach, "Measurements of Sea Bottom Elastic Waves from Underwater Explosions", Mine Defense Laboratory Report U2727, 1968.
31. H. P. Buckner and others, "Use of Stoneley Waves to Determine the Shear Velocity in Ocean Sediments", Jour. Acoust. Soc. Am. 36, 1595, 1964.
32. L. Knopoff, "On Rayleigh Wave Velocities", Bull. Seism. Soc. Am. 42, 307, 1952.
33. E. L. Hamilton, "Attenuation of Shear Waves in Marine Sediments", Jour. Acoust. Soc. Am. 60, 334, 1976.
34. C. G. Knott, "Reflection (sic) and Refraction of Elastic Waves with Seismological Applications", Phil. Mag. 48, 64, 1899. See a summary in L. D. Leet Earth Waves, John Wiley & Sons, New York, 1950, Chapt III.
35. J. B. Macelwane and F. W. Schon, Theoretical Seismology, John Siley & Sons, New York, 1936, Sect. 79.
36. K. E. Bullen, An Introduction to the Theory of Seismology, Cambridge University Press, 1953.
37. G. V. Latham and G. H. Sutton, "Seismic Measurements on the Ocean Floor", Jour. Geophys. Res. 71, 2545, 1966.
38. W. A. Schneider and M. M. Backus, "Ocean Bottom Seismic Measurements off the California Coast", Jour. Geophys. Res. 69, 1135, 1964.
39. H. Bradner and J. G. Dobbs, "Comparative Seismic Noise on the Ocean Bottom and on Land", Jour. Geophys. Res. 69, 4339, 1964.
40. D. D. Prentiss and J. I. Ewing, "Seismic Motion of the Deep Ocean Floor", Bull. Seism. Soc. Am. 53, 765, 1963.
41. J. N. Brune and J. Oliver, "Seismic Noise of the Earth's Surface", Bull. Seism. Soc. Am. 49, 349, 1959.
42. J. Willis and F. T. Dietz, "Some Characteristics of 25 cps Shallow Water Ambient Noise", Jour. Acoust. Soc. Am. 37, 125, 1965.
43. G. M. Wenz, "Acoustic Ambient Noise in the Ocean: Spectra and Sources", Jour. Acoust. Soc. Am. 34, 1936, 1962, Fig. 6.

Tracor Sciences & Systems

44. C. L. Piggott, "Ambient Sea Noise at Low Frequencies in Shallow Water Off the Scotian Shelf", Jour. Acoust. Soc. Am. 36, 2152, 1964, Fig. 6.
45. A. J. Perrone, "Infrasonic and Low-Frequency Ambient Noise Measurements on the Grand Banks", Jour. Acoust. Soc. Am. 55, 754, 1974.
46. A. Deloach, NCSL, Panama City, Florida, informal communication, 1977.
47. J. R. McGrath, "Infrasonic Sea Noise at the Mid-Atlantic Ridge near 37°N", Jour. Acoust. Soc. Am. 60, 1290, 1976.
48. W. Ewing, W. Jardetsky, and F. Press, Elastic Waves in Layered Media, McGraw-Hill, New York, 1957.
49. P. Morse and H. Feshbach, Methods of Theoretical Physics, McGraw-Hill, New York, 1953.
50. L. Brekhovskikh, Waves in Layered Media, Academic Press, New York, 1960.
51. I. Viktorov, Rayleigh and Lamb Waves, Plenum Press, New York, 1967.
52. H. Kolsky, Stress Waves in Solids, Dover Publications, New York, 1963.
53. H. Kutschale, "The Integral Solution of the Sound Field in a Multilayered Liquid-Solid Half-Space with Numerical Computations for Low-Frequency Propagation in the Arctic Ocean", Lamont-Doherty Geological Observatory of Columbia University Technical Report No. 1, CU-1-70, 1970.
54. H. Kutschale, "Rapid Computation by Wave Theory of Propagation Loss in the Arctic Ocean", Lamont-Doherty Geological Observatory of Columbia University Technical Report No. 8, CU-8-73, 1973.
55. W.T. Thompson, "Transmission of Elastic Waves Through a Stratified Solid Medium", J. Appl. Phys., 21, 89, 1950.
56. N.A. Hashell, "The Dispersion of Surface Waves on Multilayered Media", Bull. Seis. Soc. Am., 43, 17, 1953.
57. D.G. Harkrider, "Surface Waves in Multilayered Media I. Rayleigh and Love Waves from Buried Sources in a Multilayered Elastic Half-Space", Bull. Seis. Soc. Am., 54, 627, 1964.
58. J. Miller and F. Ingenito, "Normal Mode FORTRAN Programs for Calculating Sound Propagation in the Ocean", NRL Memorandum Report 3071, 1975.

Geoacoustic Parameters of the NOSC Tower Site

by

John Northrop

Code 5311

Naval Ocean Systems Center
San Diego, CA. 92152

ONR Workshop

6-7 July 1978

ABSTRACT

The Naval Ocean Systems Center (NOSC) tower is located in 18 m of water about 2 km offshore of Mission Beach, California. The geologic layering beneath the tower, as revealed by drilling, consists of nearly 200 m of sediment above a crystalline basement rock. The sediments are divided into three distinct layers: (1) unconsolidated sand; (2) semi-consolidated sandy shale and (3) consolidated massive sandstone. The compressional wave (sound) speed, sound speed gradient, attenuation, density and complimentary shear wave parameters of these layers are presented, from both measured and empirical data, as geoacoustic models for both the tower site and a location 1200 m west (seaward) of the tower. Propagation loss predictions at 100 Hz, using environmental predictions from these models, show a slope of 3.7 dB/km in the 5-25 km range interval.

INTRODUCTION

Previous work:

The NOSC tower is at 32° 46' 21" N, 117° 16' 03' W, about 2 km from the Mission Bay jetty (Fig. 1). The tower (erected in 1959) stands in 18 m of water on four legs that slope outward and are securely grouted in the rock¹. Drillers logs, seismic reflection profiles and bottom studies have been made near the tower^{2,3}, a seismic refraction profile has been shot 9 km west of the tower⁴, and a well to basement has been drilled on nearby Pt. Loma⁵.

METHOD

The geoacoustic models presented here are based in part on field measurements and in part on geophysical reasoning⁶. Where possible, data on

buried sediment type, thickness and density were taken from driller's logs. Surficial sediment sound speed were taken from measurements made by divers^{2,3}, while others were deduced from geological and geophysical data.

GEOACOUSTIC MODELS

Tower Site

Layer 1:

Layer 1, the water layer, is 18.3 m thick and has a slightly positive sound speed gradient (in winter). The bottom water has a measured density of 1.025 gm/cm^3 (Table I). The sound speed at the bottom of this layer is about 1500 m/sec, but the surface layer varies slightly from summer to winter¹.

Layer 2:

The surficial sedimentary layer at the tower site is a re-worked Pleistocene-to-recent unconsolidated medium coarse sand 28.5 m thick with layers of shell fragments (Fig. 2). It has a mean grain size of 0.495 mm at the surface and a porosity of 39.2%². The surface sediment has a measured compressional wave sound speed (V_p) 1798 m/s, giving a velocity ratio (sediment sound speed / bottom-water sound speed) of 1.20. This sandy layer has a very low measured shear velocity (197 m/s), a density of 2.01 gm/cm^3 and a measured attenuation constant (k_p) of 0.4 (where $\alpha = kf^1_{\text{kHz}}$) for compressional waves² and a computed attenuation constant (k_s) of 13.2 for shear waves⁷.

Using a method recommended by Hamilton⁸, the sound speed at the bottom of the layer is 1875 m/sec and 1855 m/sec at the middle of the layer (Table I).

Layer 3:

Layer 3 is a semi-consolidated silty-clay with a density of 2.0 gm/cm^2 . The density, as measured in the cored material, increases to 2.14 gm/cm^2 at the mid-point and bottom of the layer. Using this information, together with

the curves for V_p vs density for coarse sands⁶, a velocity (V_p) of 1768 m/s was derived for layer 3. The shear wave speed (V_s) of 452 m/s (Table I) was read from a wave of V_p vs V_s (Hamilton, unpublished).

Layer 4:

The fourth layer consists of massive sandstone and shale strata of the (cretaceous) Rosario formation which outcrops on nearby Pt. Loma. Driller's logs⁵ indicate this layer is 500 m thick on Pt. Loma. This formation is equated to layer "d", found in seismic refraction shooting offshore⁴, where it has a compressional wave speed of 4870 m/s and a thickness of 1411 m at a point 9.3 km offshore from Pt. Loma. Assuming a constant slope (6.1°) between these two points, a thickness of 350 m is deduced for the thickness of layer 4 at the tower site. Using a sound speed gradient of 0.11 (pertinent for consolidated sandstones¹⁰) sound speeds (V_p) of 4889 m/s and 4908 m/s were predicted for the middle and bottom of this layer respectively. Shear wave velocities (V_s) were calculated as 2783 m/s, 2793 m/s and 2804 m/s for the top, middle and bottom sections, respectively, of layer 4 using a V_p/V_s ratio of 1.75¹⁰. The density was calculated as 2.3 gm/cm³ from the relationship $D_{gm/cm^3} = 0.23 V_p$ ¹¹.

Layer 5:

The fifth layer is a crystalline basement rock, probably the Black Mountain formation which is widespread in the San Diego area⁵. The rock has been cored on Pt. Loma at a depth of 1138.4 m⁵ below the basal conglomerate of the Rosario sandstones in layer 4. This basement crystalline rock is described in the driller's log as "hard greenish-grey altered rock, probably metamorphosed rhyolite or some similar form" and deeper in the well (7945 m) as "light grey, hard, fine grained crystalline rock".⁵ The formation has been equated to layer "e" in offshore refraction work⁴ where it has a refraction velocity of 5860 m/s and is about 2 km thick.

Layer 6:

Refraction measurements offshore⁴ reveal a 18 km thick "crustal" layer of 6.7 km/sec material. This layer would correspond to the "oceanic" layer in the Pacific basin¹².

Station D-10

Station D-10 is 1200 m west (offshore) of the tower and was occupied in the 1966-1970 program using SCUBA divers to measure sediment sound speeds and densities^{1,3}.

Layer 1:

Layer 1, the water layer, is 32 m thick and has a slightly negative sound speed gradient (Table II). As is true with the tower site, a stronger negative velocity gradient is present here in the summer than in the winter.

Layer 2:

The surficial sedimentary layer is a coarse sand having a mean grain size of 0.5704 mm, a density of 2.06 gm/cm³ and a compressional sound speed (V_p) of 1817 m/s³. This gives layer 2 a velocity ratio of 1.21, slightly higher than at the tower station. This layer has a measured attenuation constant (k) of 0.5 for compressional waves³ and a computed shear wave attenuation constant of 13.2⁷.

Layer 3:

At site D-10, layer 3 is shown on seismic reflection records¹ to be continuous with layer 4 at the tower site (Layer 3 at the tower site (the delta deposit) pinches out between the tower and site D-10). If a constant dip of 6.1° is assumed for the base of this layer, it thickens to 478 m at station D-10. The geoacoustic parameters are the same as for layer 4 of the tower site, except that the compressional sound speeds at the mid-point and bottom of the layer have predicted values of 4896 m/s and 4922 m/s respectively and the shear velocities at the middle and bottom of the layer are 2797 m/s and 2812 m/s respectively.

Layer 4:

Layer 4 at station D-10 is the same crystalline basement rock as layer 5 at the tower site. Geoacoustic parameters for this layer, as shown in Table II, are the same as for layer 5 of the tower site.

Propagation Loss

Propagation loss at 100 Hz was computed for both the tower location and station D-10 using the normal mode program of Pedersen and Gordon¹³ modified to accept density and attenuation parameters¹⁴. Because results for both sites were similar, only those computed for the tower site will be discussed here.

A propagation loss curve presented (Fig. 3), for a source in the water and receiver on the bottom, has a slope of 3.7 dB/km in the 5-25 km range interval. This slope is intermediate between cylindrical ($10 \log R$) and spherical ($20 \log R$) loss. This program is for a constant depth channel and does not include interface waves or the rigidity of the bottom sediments. Thus, the predictions may be inaccurate. However, the values are similar to propagation loss observed in other shallow water areas¹⁵.

Acknowledgment

This work was supported by ONR Code 463. Dr. E. L. Hamilton of NOSC Code 5311 helped with predicting the parameters in the geoacoustic models, and D. White, NOSC Code 7143, helped with the computations of propagation loss.

NOSC

NOSC TOWER GEOACOUSTIC MODEL

LAYER DESCRIPTION	VELOCITY (m/s)		ATTENUATION CONSTANT (K) ⁽¹⁾		DENSITY (gm/cm ³)	THICKNESS (m)	DEPTH (m)
	V _p	V _s	K _p	K _s			
1. WATER	1499 1501	— —	— —	— —	1.025	18.3	18.3
2. UNCONSOL- IDATED (SAND)	1798 ⁽²⁾	197	0.4 ⁽²⁾	13.2	2.01 ⁽²⁾	8.2	26.5
	1855	331	↓	↓	2.14 ⁽³⁾		
	1875	396	0.3	↓	2.14 ⁽³⁾		
3. SEMI- CONSOLIDATED (SILTY CLAY)	1768	452	0.2	4.8	2.0 ⁽³⁾	11.0	37.5
4. CONSOLIDATED (SANDSTONE)	4870 ⁽⁴⁾	2783 ⁽⁵⁾	0.1	3.4	2.6	350	387
	4889	2794	↓	↓	↓		
	4908	2805	↓	↓	↓		
5. BASEMENT (BASALT)	5860 ⁽⁴⁾	3038	0.03	0.07	2.83	1400	1950

(1) AS IN ATTEN. (dB/m) = K f_{kHz}

(2) IN SITU MEASUREMENT BY DIVERS (HAMILTON, *et al*, JGR 75, 1970)

(3) WELL LOG DATA

(4) SEISMIC REFRACTION MEASUREMENT (SHOR AND RAITT, SIO REF. 58-78)

(5) HAMILTON, GEOPHYSICS, 41, 965 (1976)

8-3699

Table 1. Geo acoustic Model for the tower site.

NOSC

GEOACOUSTIC MODEL **STATION D-10 (1200 m WEST OF TOWER)**

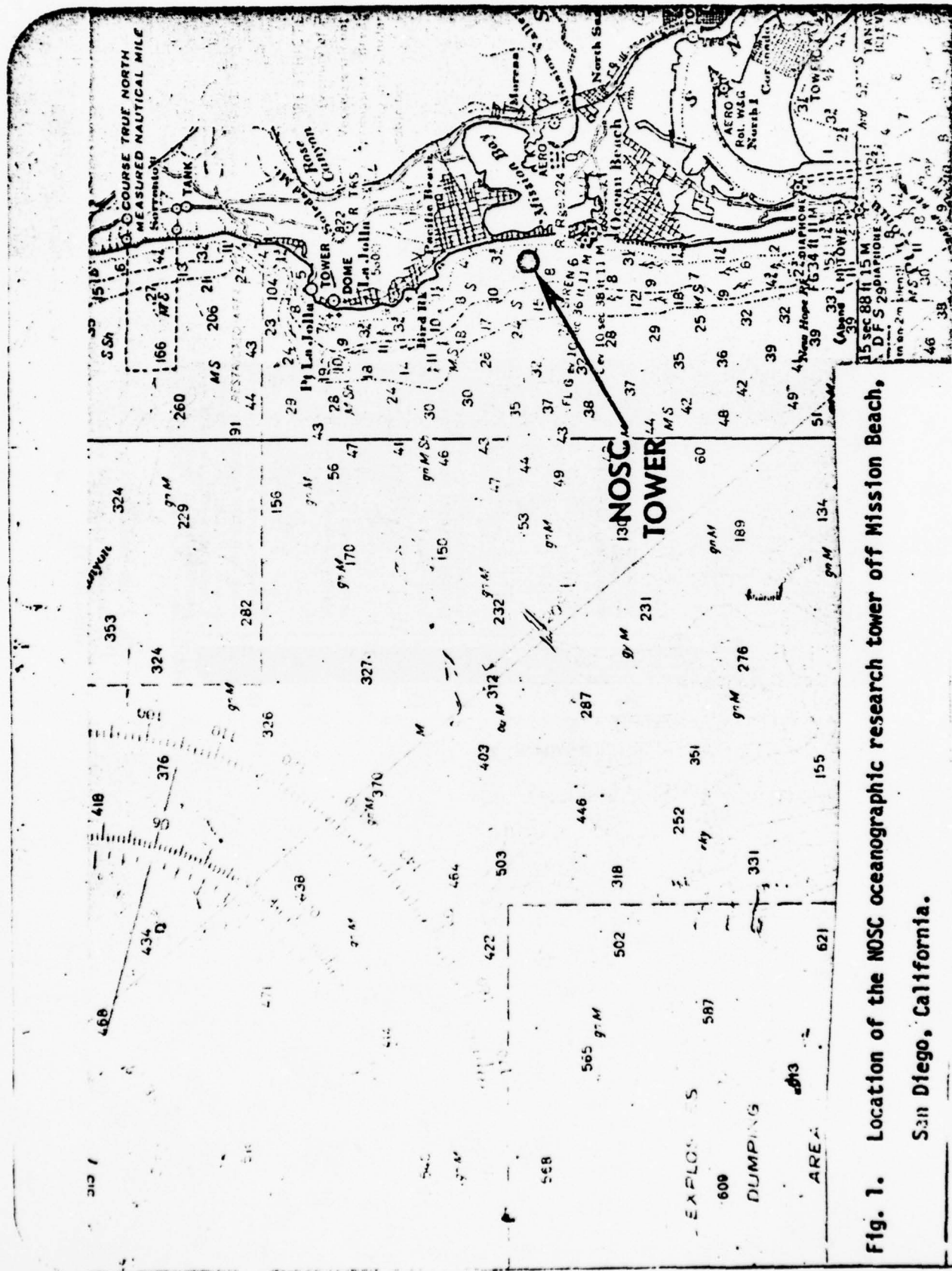
LAYER DESCRIPTION	VELOCITY (m/s)		ATTENUATION CONSTANT (K) ⁽¹⁾		DENSITY (gm/cm ³)	THICKNESS (m)	DEPTH (m)
	V _p	V _s	K _p	K _s			
1. WATER	1499 1498.6	— —	— —	— —	1.025 ↓	32	32
2. UNCONSOL- IDATED (COARSE SAND)	1817 ⁽²⁾ 1917	197 482	0.5 ↓	13.2 ↓	2.06 ⁽²⁾ 2.14	18	50
3. CONSOLIDATED (SANDSTONE)	4870 4896 4922	2783 ⁽⁴⁾ 2797 2812	0.1 ↓	3.4 ↓	2.6 ↓	478	528
4. BASEMENT (BASALT)	5860 ⁽³⁾	3038	0.03	0.07	2.83	1400	1928

- (1) AS IN ATTEN. (dB/m) = Kf_{kHz}
 (2) IN SITU MEASUREMENT BY DIVERS (HAMILTON, GEOPHYSICS 37, 1972)
 (3) SEISMIC REFRACTION MEASUREMENT
 (4) HAMILTON, GEOPHYSICS, 41, 985 (1976)

References

1. LaFond, E. C., The U.S. Navy Electronics Laboratory Oceanographic Research Tower, NEL Report 1342, (1965).
2. Hamilton, E. L., H. P. Bucker, D. L. Keir, and J. A. Whitney, "Velocities of Compressional and Shear Waves in Marine Sediments Determined in situ from a Research Submersible," Jour. Geophys. Res. 75, 4039-4049, 1970.
3. Hamilton, E. L., "Compressional Wave Attenuation in Marine Sediments", Geophysics, 37, 620-646 (1972).
4. Shor, G. G., and R. W. Raitt, "Seismic Studies in the Southern California Continental Borderland, XX International Geological Congress, Mexico City, Mexico, 1956 (also Scripps Institution of Oceanography, SIO Ref. 58-78, 1978).
5. Hertlein, L. G., and U. S. Grant, "Geology and Oil Possibilities of Southwestern San Diego County, Calif.," Jour. Mines and Geology, 35, pp. 37-78, (1939).
6. Hamilton, E. L., "Prediction of Deep-Sea Sediment Properties: State-of-the Art," in Deep-Sea Sediments, Physical and Mechanical Properties, A. L. Inderbitzen, ed., pp. 1-43, Plenum Press, (1974).
7. Hamilton, E. L., "Attenuation of Shear Waves in Marine Sediments", Acoust. Soc. Am. 60, pp. 334-338 (1976).
8. Hamilton, E. L., "Shear Wave Velocity versus Depth in Marine Sediments: A Review," Geophysics, 41, pp. 985-996, (1976).
9. Hamilton, E. L., "Sound Velocity-Density Relations in Sea-Floor Sediments and Rocks", J. Acoust. Soc. Am 63, pp. 366-377, (1978).
10. Gardner, G. H. F. and M. H. Harris, "Velocity and Attenuation of Elastic Waves in Sands", Trans. 9th Annual Logging Symposium, M 1 - M 19, (1968).

11. Gardner, G. H. F., L. W. Gardner, and A. R. Gregory, "Formation Velocity and Density - the Diagnostic Basics for Stratigraphic Traps", *Geophysics* 39, pp. 770-780 (1974).
12. Shor, G. G., H. W. Menard and R. W. Raitt, "Structures of the Pacific Basin", in *The Sea*, A. R. Maxwell, ed., Wiley-Interscience New York (1970).
13. Pedersen, M. A., and D. F. Gordon, "Normal Mode Theory Applied to Short-Range Propagation in an Underwater Acoustic Surface Duct", *J. Acoust. Soc. Am.* 37, pp. 105-118 (1965).
14. Gordon, D. F., "Normal Mode Computation of Propagation Loss for an Arbitrary Number of Layers", NUC TP 236, 1971 (C).
15. Blaik, M., and C. S. Clay, "Detection in the Ground of Sound From A Source in Shallow Water", Hudson Laboratories, Columbia University, Tech. Rept. 76, (1959).



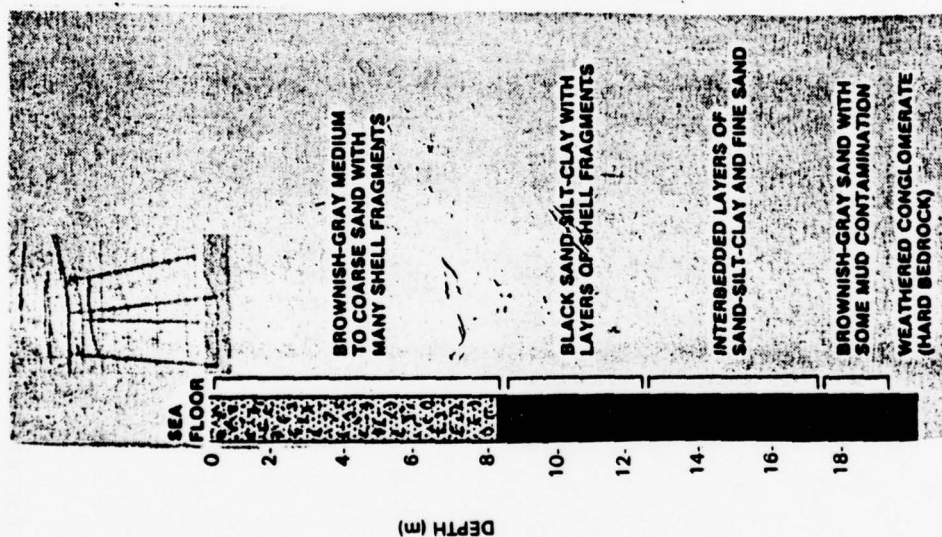


Fig. 2. Sediment layers as determined by the driller's log at the tower site (from Ref. 1).

TOWER, 100 Hz, SD = 10 M, RD = 20 M

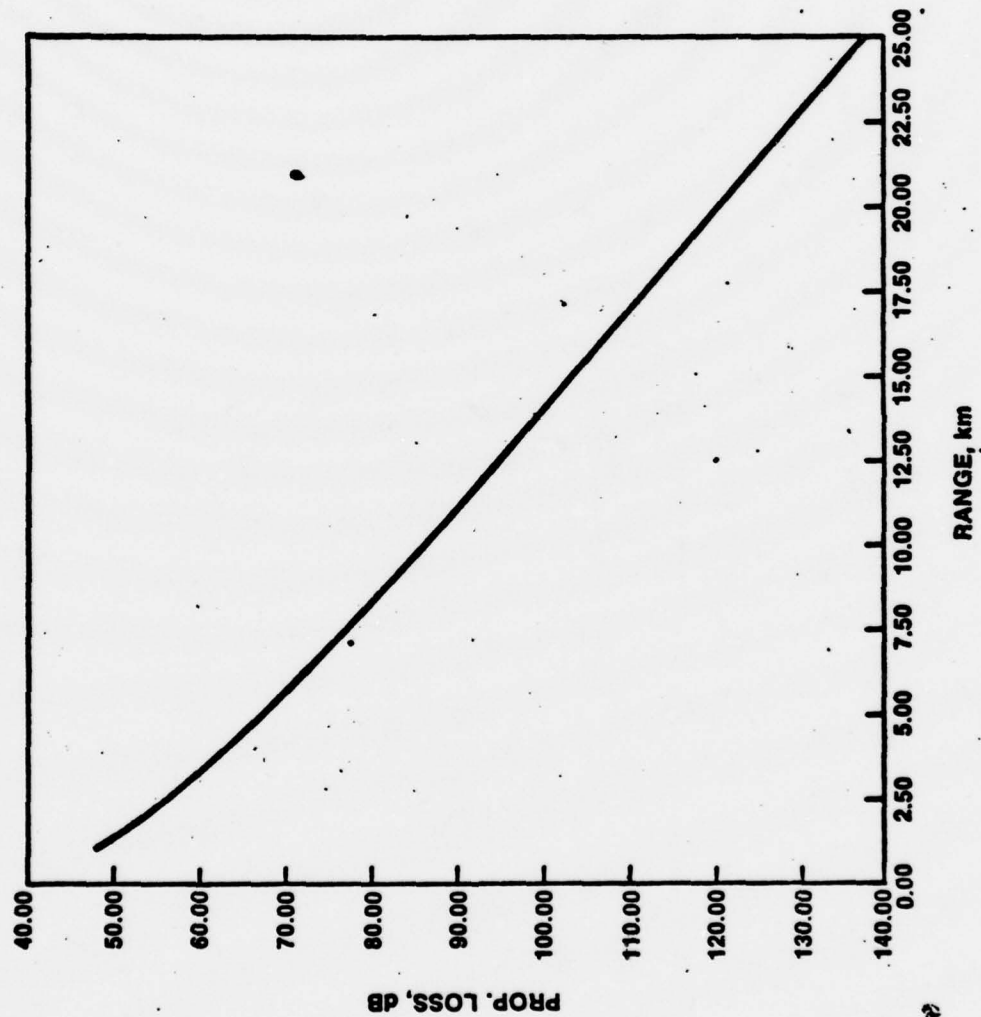


Fig. 3. Propagation loss predictions at the tower site for 100 Hz with the source in the water and receiver on the bottom.

"The NCSC Shallow water Seismic Propagation Study"
Glenn McLeroy
Naval Coastal Systems Center

Introduction

NCSC, under one name or another, has been the Navy minesweeping laboratory for many years, with attendant interests in low frequency shallow water acoustics. About 20 years ago I did a seismic minesweeping experiment that apparently demonstrated seismic waves other than compressional in soft shallow water sediments. [Reference 1] Horizontal bottom variability seemed indicated by these and other shallow water acoustic-seismic experiments carried out about that time.

About 12 years ago we did an experimental study [Reference 2] of ground motion at short distances from explosive sources in shallow water over both sand and soft mud bottoms. Figure 1 shows typical signals received by a hydrophone and a three-component geophone, demonstrating transverse as well as compressional wave motions. These low frequency waves (under 10 hertz) traveled with low velocities (see Figure 2) and with attenuations of from 12 to 25 dB per kilometer.

These and other experiments and the continuing lack of sufficiently quantitative results from speculative shallow water fluid-bottom normal mode theory led me to the firm belief that bottom properties held the key to the low frequency shallow water acoustics issue.

Recent NCSC Seismic-Acoustic Experiment

About 2 years ago an opportunity arose to do the kind of experiment I thought necessary to improve our knowledge of the effect on seismic-acoustic propagation of the many shallow water environmental variables and parameters. The experiment was designed to allow, hopefully, a quantitative statistical determination of the order of dependence of the propagation on those environmental variables and parameters that could be measured either directly or indirectly.

This experiment now has been completed. A small amount of data has been analyzed and some preliminary results will be given here after a description of the experiment.

The experiment was carried out in the Gulf of Mexico off Panama City, Florida, and made use of the two NCSC offshore platforms, Stage I and Stage II. Figure 3 shows the location of the tests and indicates the five courses on which some 200 charges were detonated (at 20 meter depth and/or one meter above the sea bottom) along some 230 miles of track. A CW minesweeping source was also towed along about 80 miles of track in the area, out to a maximum range of 30 miles.

Stage II is approximately 2 nautical miles offshore in about 20 meters of water, while Stage I is 9.5 miles further seaward in about 30 meters of water. At each platform an array (shown in Figure 4) of seven three-component geophones (orthogonal axes) and six hydrophones were placed on the bottom, with

the geophones buried about one foot (X axis oriented along Leg A, Z axis vertical) and the hydrophones suspended about 2 feet above the bottom in mountings intended to decouple them from bottom motion. The frequency band of interest was from 2 to 1000 hertz. All array sensor outputs were simultaneously recorded on two 32-channel analogue tape machines - one on each platform.

An extensive set of environmental measurements was made. Included were:

a) Bathymetry (Figure 5 shows the water depth versus distance from Stage I and Stage II along the various shot legs) and bottom roughness.

b) Sound velocity - about 300 casts were made at the arrays and at the shot location while the recordings were in progress. Figures 6 through 9 show the sound velocity distributions in the water along the shot lines at the time signals were being received along those lines.

c) Wind, waves and currents.

d) A thorough program of bottom and sub-bottom measurements was carried out along the shot lines and cross lines in the test area by Worzel, Houston and other at the Marine Sciences Institute at Galveston (under contract to NCSC) and included deep reflection, continuous refraction using a multi-channel towed array, 3.5 KHz reflection, taking some 80 cores (4-40 feet in length) and doing density and other analyses of the cores obtained. Some of the results of this geophysical program are presented in another paper at this workshop, presented by Mark Houston. Results of previous measurements of surficial sediment properties in the test area were also available, as were the results of some earlier limited refraction shooting.

e) A sing-around velocimeter was placed in the corer barrel to give a measure of sound velocity versus depth in the sediment over the depth interval penetrated by the cover. This was done by Shirley of ARL, University of Texas.

Results

All signal and noise levels to be reported here refer to single sensor values - no array processing has yet been done. Some of the analogue tape recordings have been digitized and the resulting digital tapes analyzed to produce the results presented here.

Ambient noise recordings were made before each shot and over longer periods when source signals were not being transmitted. Figure 10 shows spectral levels derived from octave band levels averaged over several hours on the two days during which the Legs A and B were shot.

Figures 11a, 11b and 11c gives octave band signal levels received by the hydrophone and three-component geophone as a function of range from the explosive source, for the 'groundwave' portion of the received signal arriving

at higher velocity before the arrival of the water wave. At ranges less than 2 kilometers, this portion of the signal was not long enough to obtain a comparable spectral analysis. The average ambient noise detected by the sensors during the time of the shooting of the A leg is also indicated. These signals are those received by a single geophone and an adjacent hydrophone in the Stage I array, and the frequency shown is the geometric mean of the octave.

Figures 12a, 12b and 12c present similar information for the maximum amplitude portion of the 'waterborne' signal arriving at the sensors at the travel time corresponding to the velocity of sound in the water column.

Over the range interval 8 to 16 kilometers, shots were fired at 20 meter depth and at one meter above the bottom, while at shorter ranges they were fired only at one meter off the bottom and at greater ranges only at 20 meter depth. The received signal levels are not much different for shots fired at different depths.

Figures 13a, 13b and 13c consolidate the groundwave data of the last few figures, while Figures 14a, 14b and 14c attempt the same for the water wave data. The parameter chosen here is the r.m.s. signal- to-noise ratio, which is of obvious importance in any detection system.

Looking first at the groundwave data, it appears that the higher S/N ratio demonstrated by the hydrophone output at low frequency and short range actually falls below the S/N ratios of all three of the geophone component sensors, as frequency increases. The X axis sensor (oriented along the line joining the geophone and the sources) and the vertical Z axis sensor have generally higher S/N than does the transverse Y axis.

The same conclusions hold for the portion of the signal here being called the water wave, although at longer ranges the hydrophone performs relatively better as a detector.

Discussion

Although a more careful analysis of this S/N versus sensor type issue is called for and planned, this preliminary look indicates that a substantially higher S/N is available with a geophone sensor than with a hydrophone. This difference becomes more pronounced as frequency increases. Figure 10 suggests that the higher hydrophone noise level above 30 Hz is a cause of this effect, but this has not yet been explained. The directional properties of the noise seen by the geophone sensors are therefore of major interest, as are the propagation parameters of the various elastic waves possibly involved.

Comments

As has been indicated, a rather extensive experiment was performed and a large quantity of data obtained. Only a small amount of analysis has been done. No array processing has been done.

After getting all the analogue shot data in standard format on digital tape and available to those interested, other things I would like to do

include analyses of coherence properties across the arrays as they pertain to possible surveillance systems, determination of directional characteristics of the noise (again important to surveillance systems), and the use of all the acoustic-seismic and environmental data in the development of an empirical propagation model based on statistical analyses that will properly order and quantify the controlling effects of the many environmental parameters that were measured or inferred. Recordings of the hydrophone and geophone signals from about two thousand explosions in the Gulf within a one hundred mile radius of the present array sites were made several years ago and will be analyzed in view of the now much more complete environmental information obtained during the present experiment.

A report presenting the oceanographic data has been published at NCSC [Reference 3] and reports on the geophysical and geological work are just being finished by Houston and others at Galveston [Reference 4].

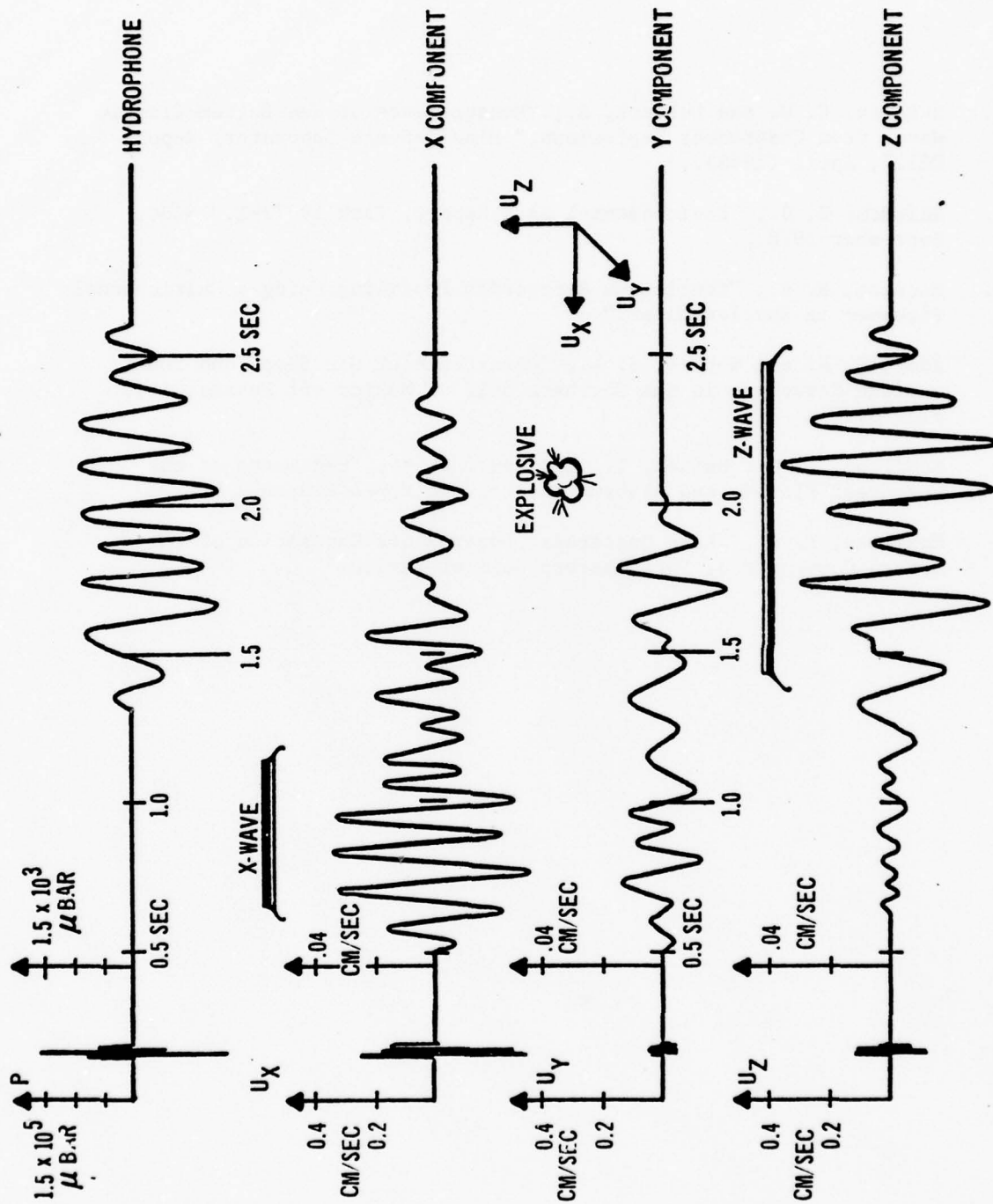
REFERENCES

2. McLeroy, E. G. and DeLoach, A., "Measurements of Sea Bottom Elastic Waves from Underwater Explosions," Mine Defense Laboratory Report U2727, April (1968).
3. Salsman, G. G., "Environmental Data Report, Task 18378-1," NCSC, September 1976.
4. Houston, M. H., "Continuous Refraction Profiling Using a Multichannel Streamer in Shallow Water."

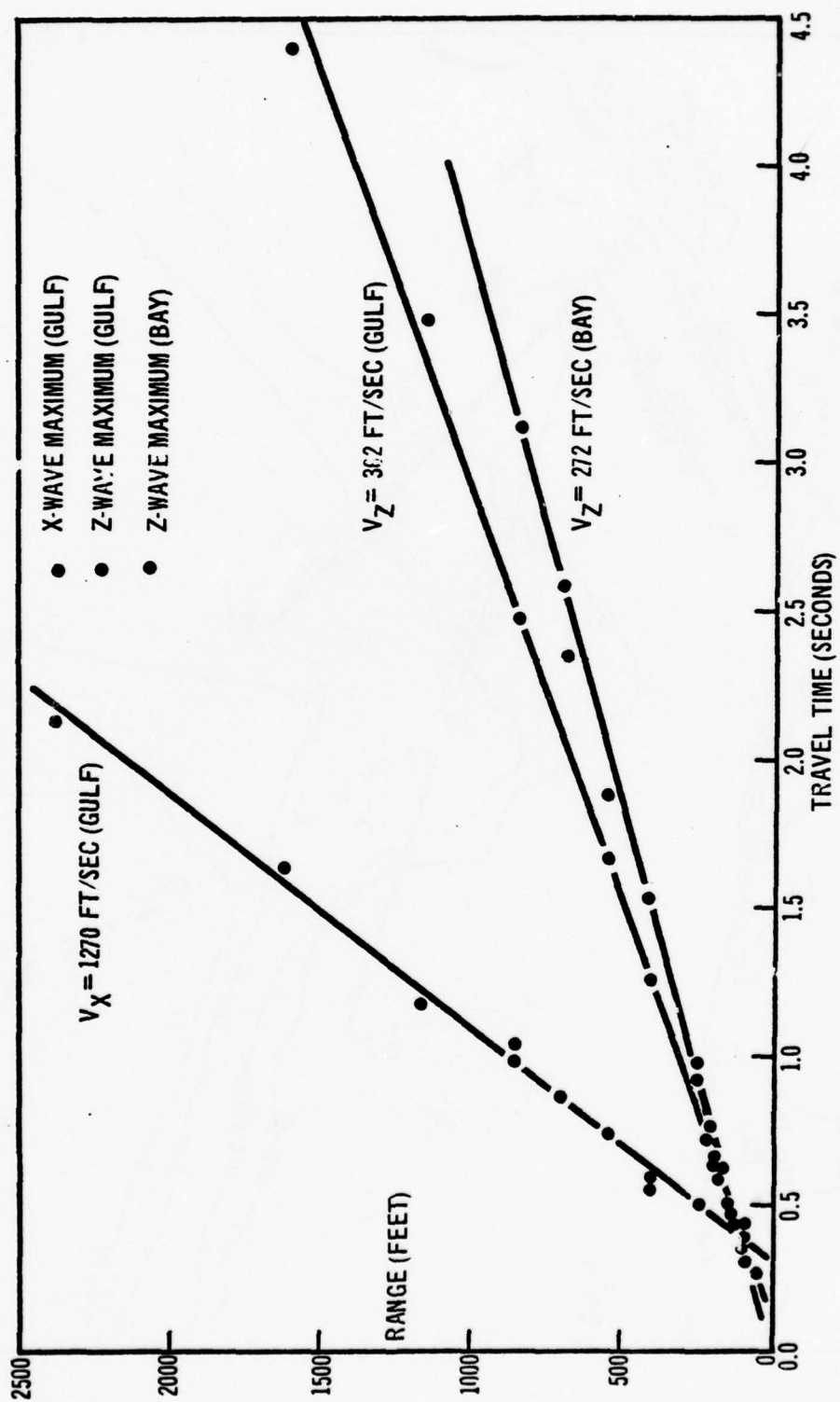
Addy, S. K. and Worzel, J. L., "Occurrence of Gas Seeps and Sub-surface Structure in the Northern Gulf of Mexico off Panama City, Florida."

McMillen, K. J., Haines, T., and Addy, S. K., "Sediments of the Northwest Florida and Alabama Shelves and Upper Slopes."

McMillen, K. J., "Late Quaternary Upper Slope Deposition of the DeSoto Canyon Area, Northeastern Gulf of Mexico."



A TYPICAL OSCILLOGRAPH RECORD OF A 100-GM EXPLOSIVE CHARGE FIRED ON A SAND BOTTOM AT A RANGE OF 700 FEET



TRAVEL TIME TO MAXIMUM AMPLITUDE IN WAVE POCKET

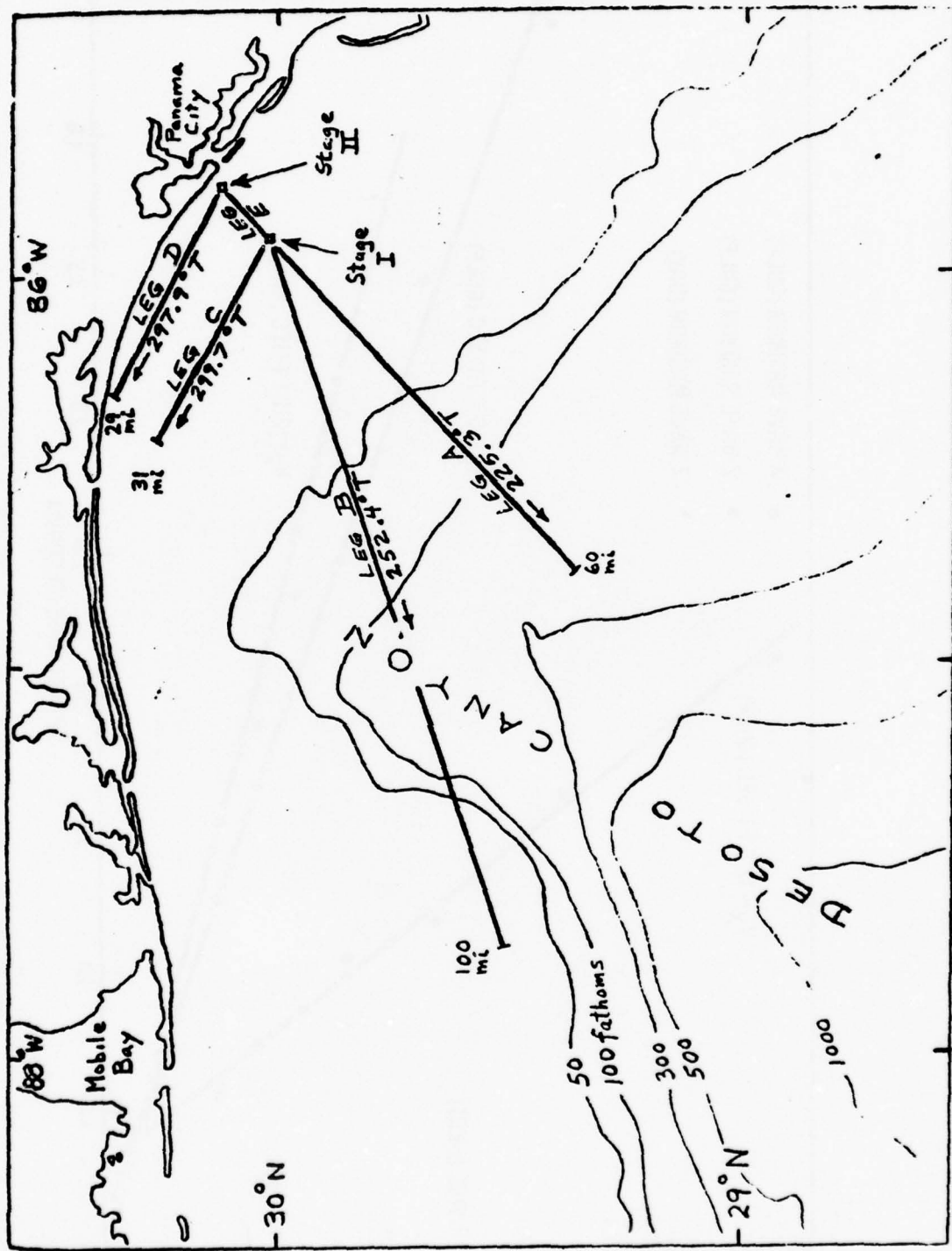
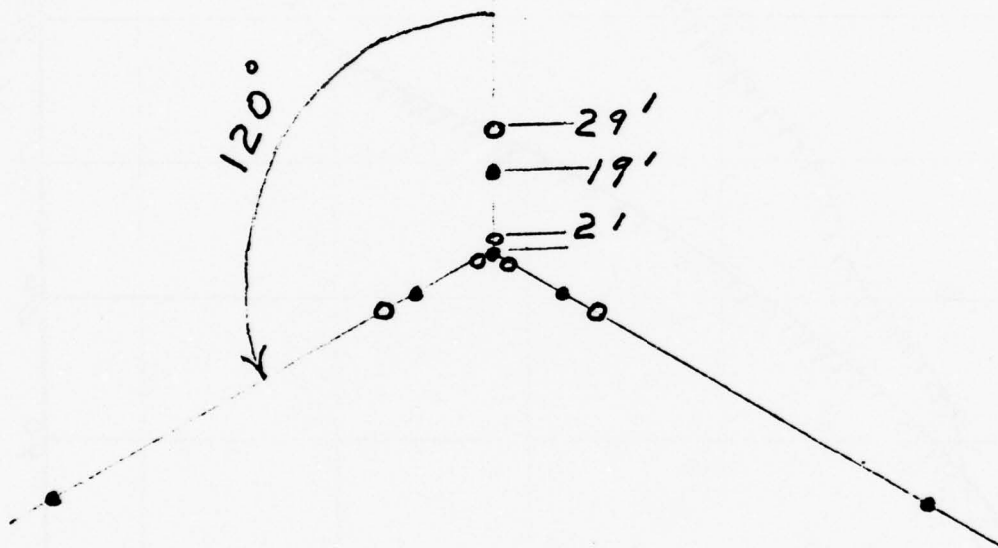


FIGURE 3. CONFIGURATION OF TEST LEGS

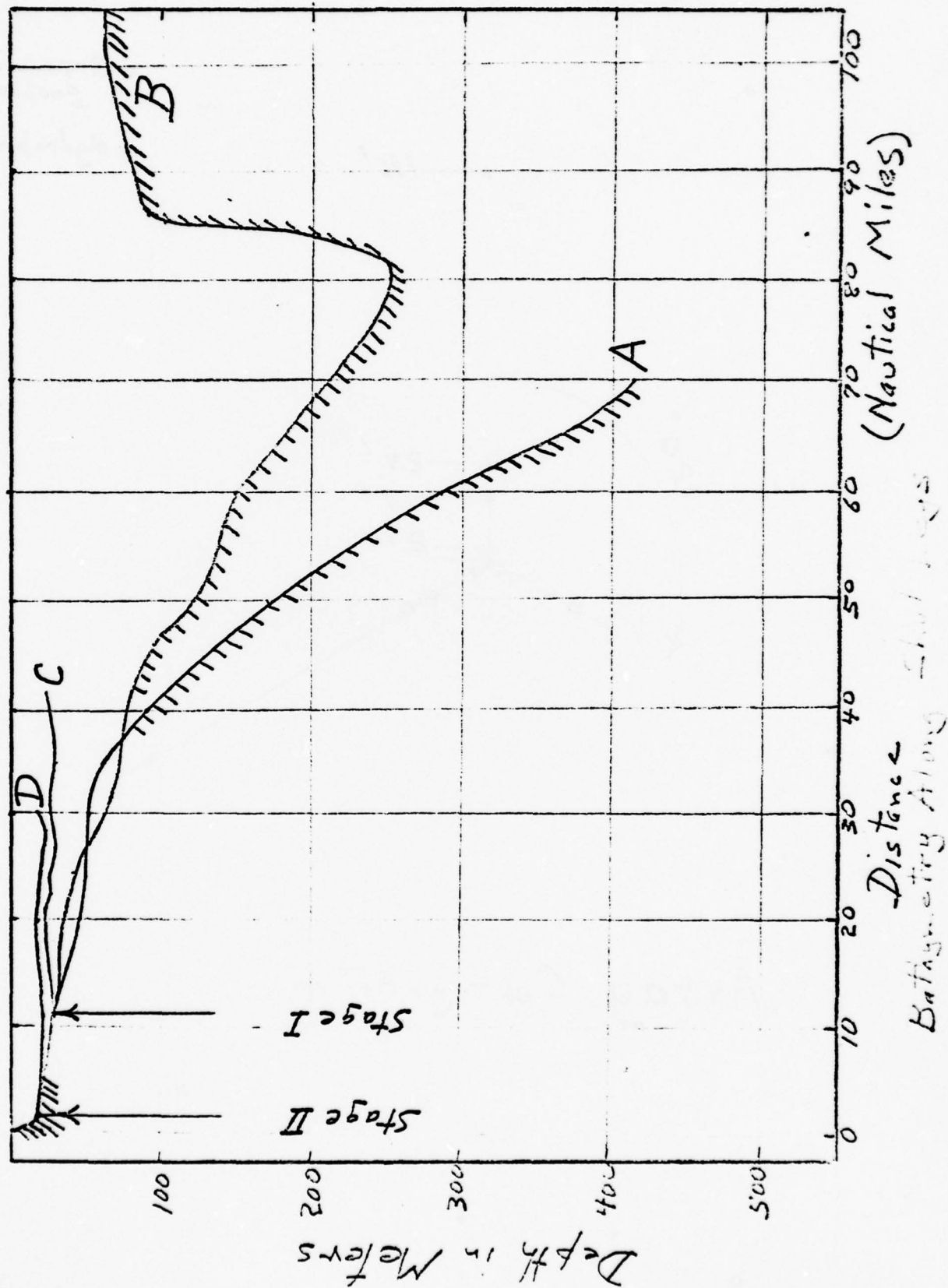
● 3-component
geophone

○ Hydrophone

● — 116'



Array Configuration



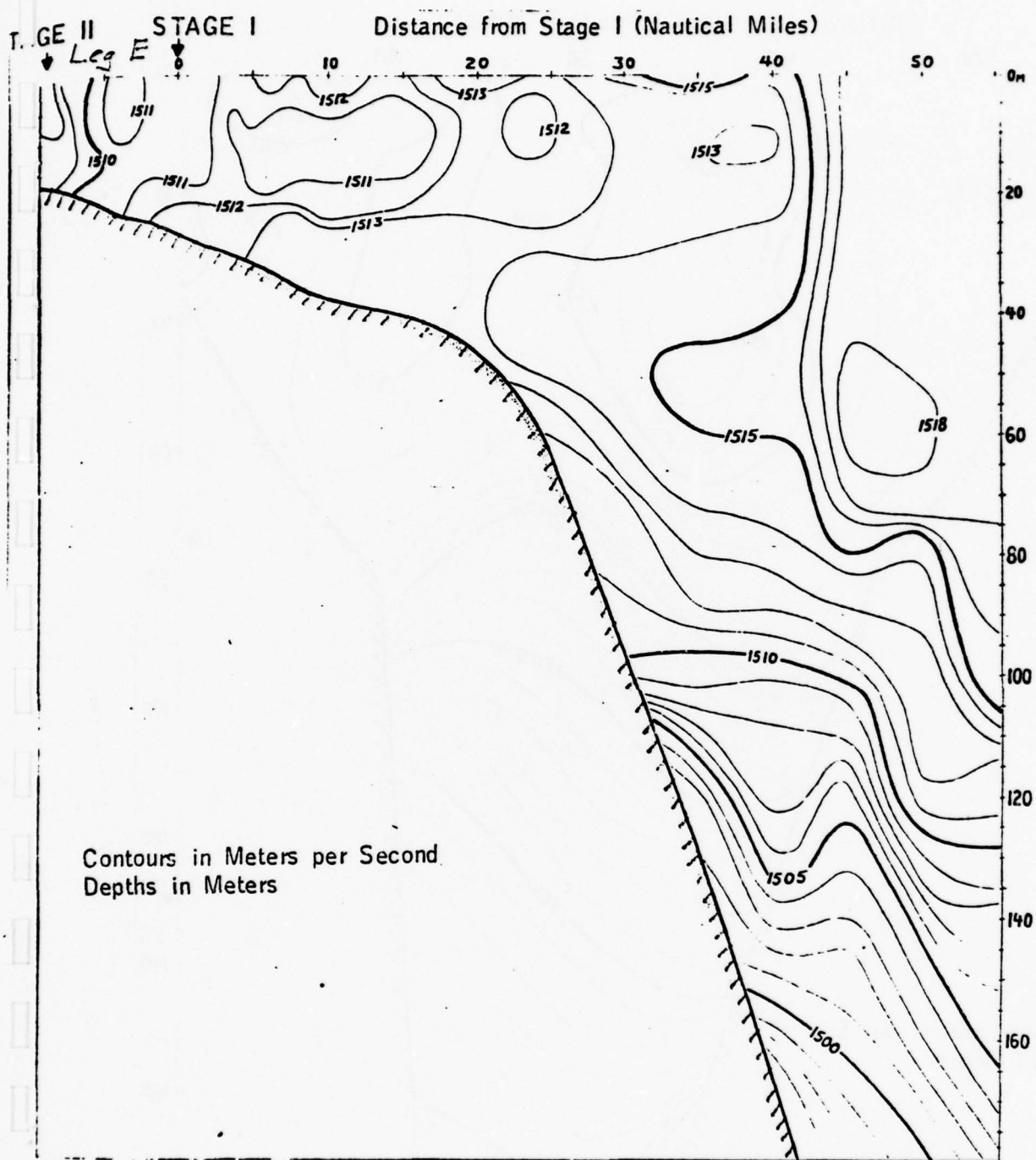


FIGURE 14. SOUND VELOCITY STRUCTURE ALONG LEG A ON 28 MARCH 1976

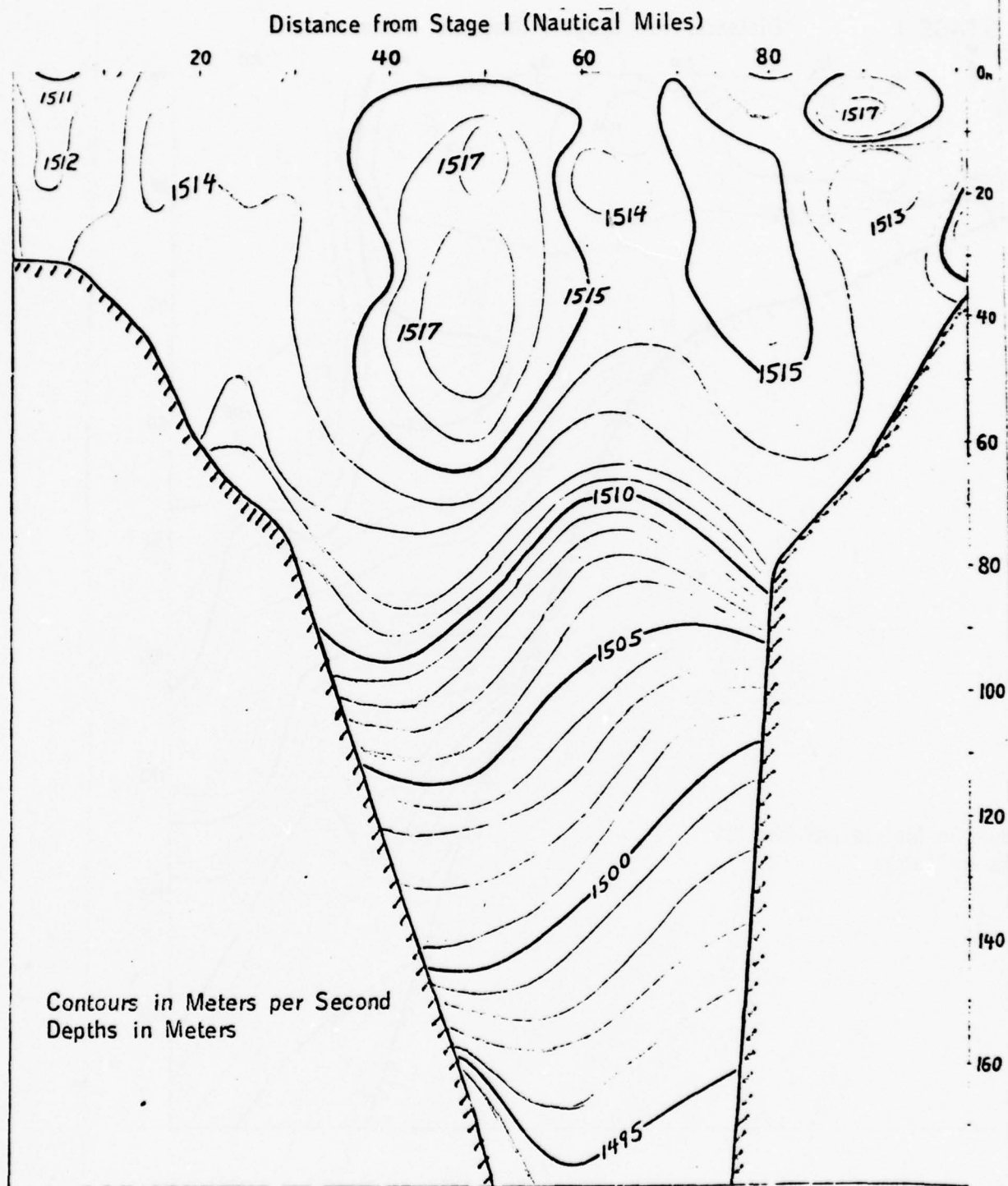


FIGURE 17. SOUND VELOCITY STRUCTURE ALONG LEG B ON 31 MARCH 1976

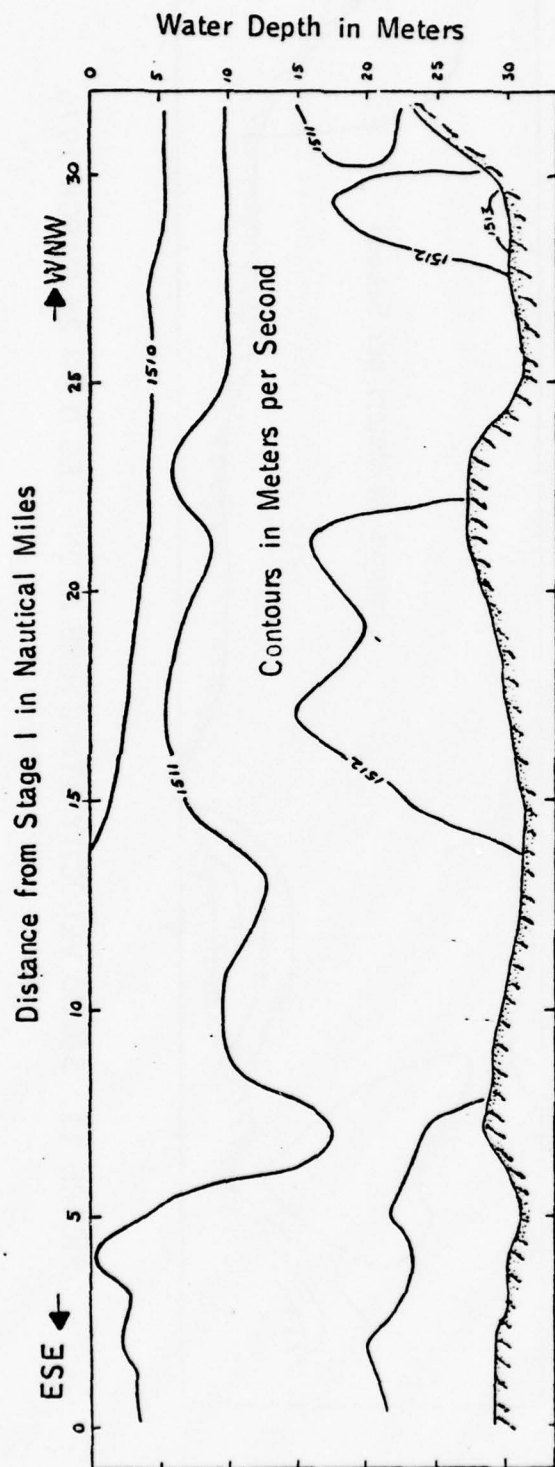


FIGURE 20. SOUND VELOCITY STRUCTURE ALONG LEG C ON 1 APRIL 1976

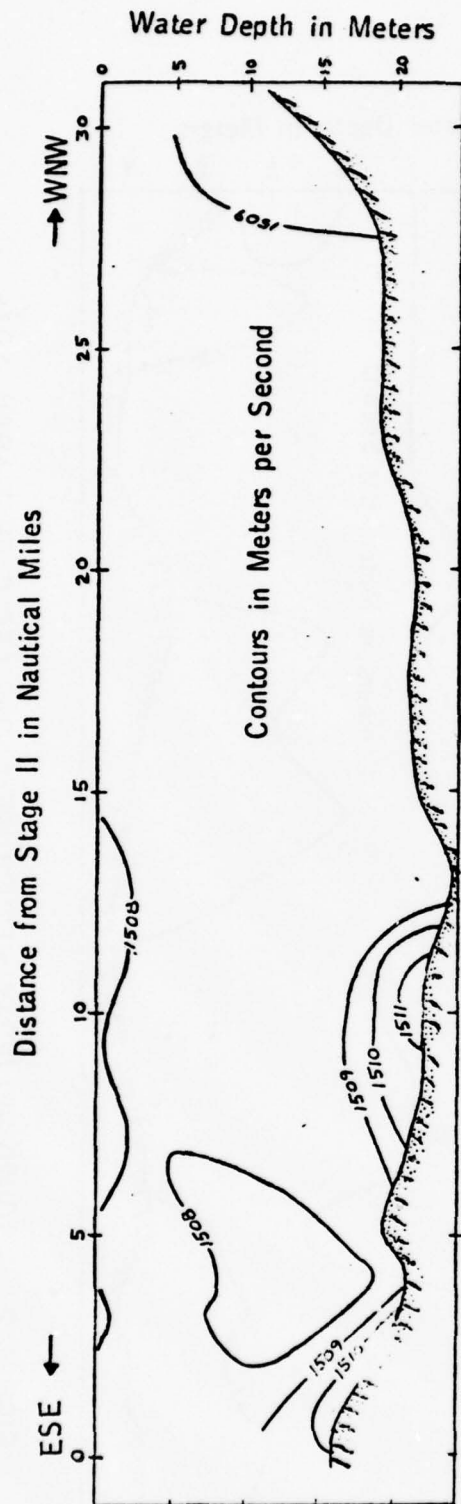
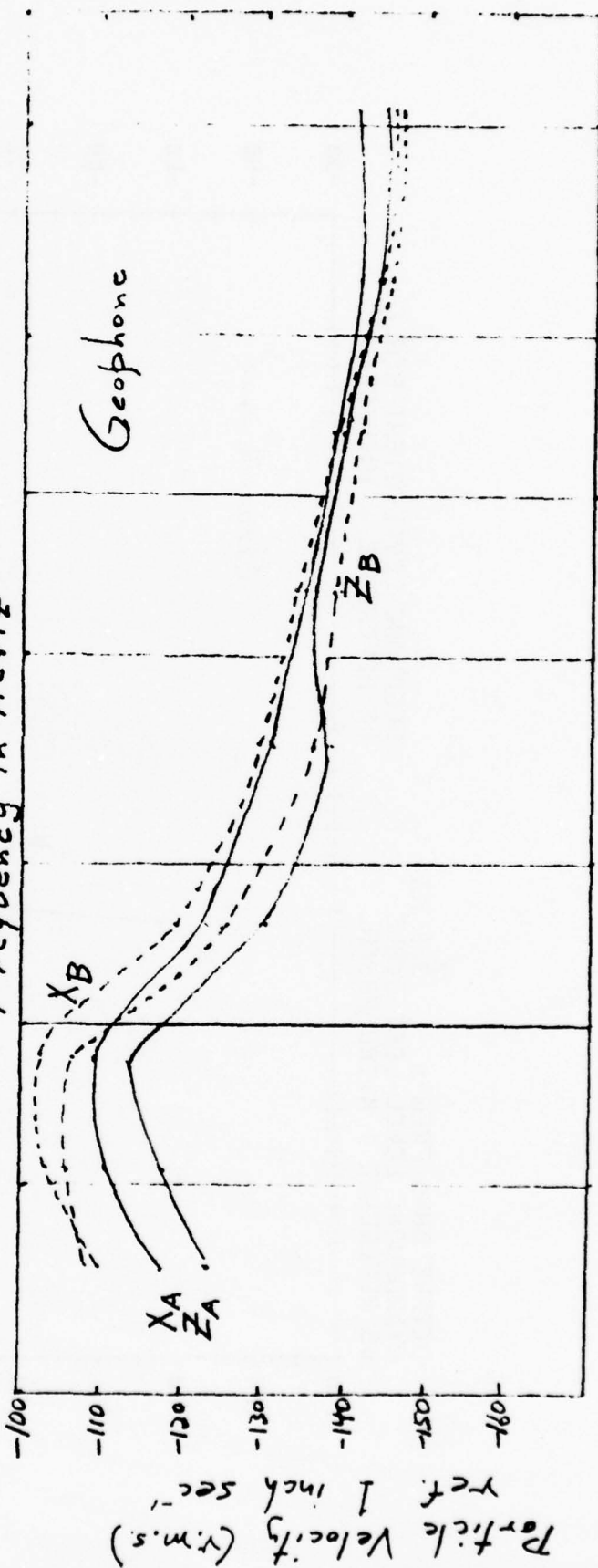
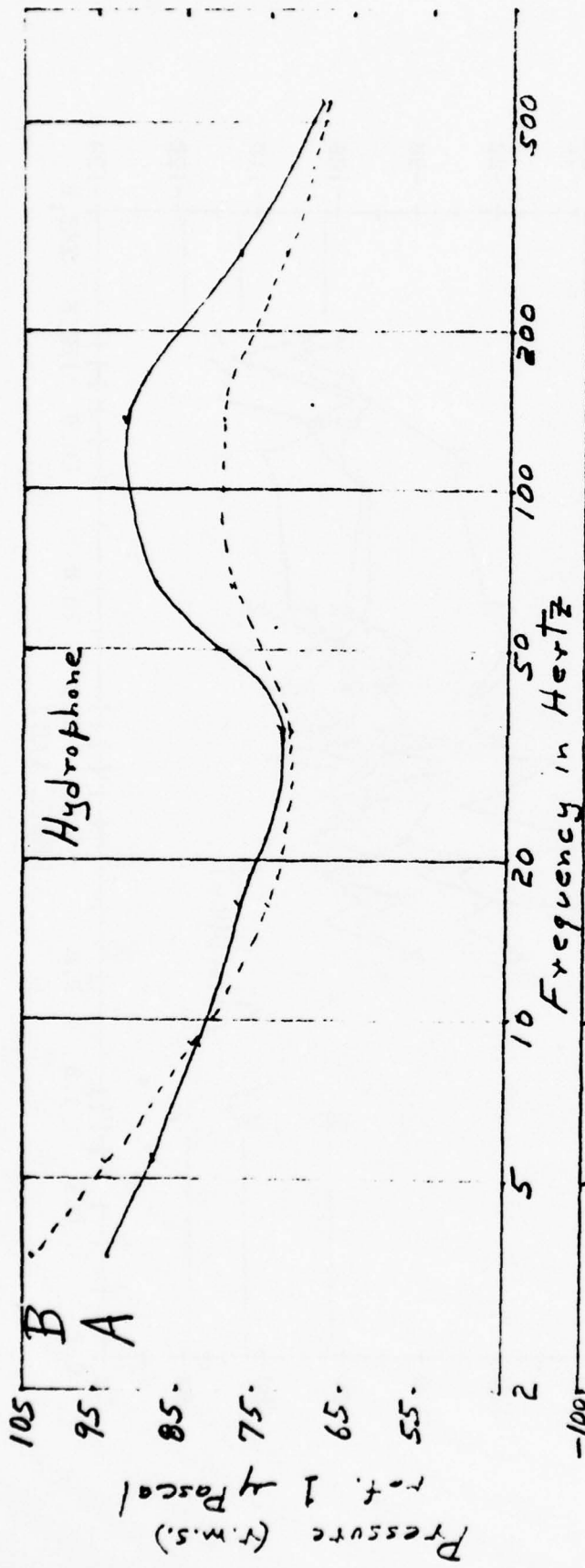


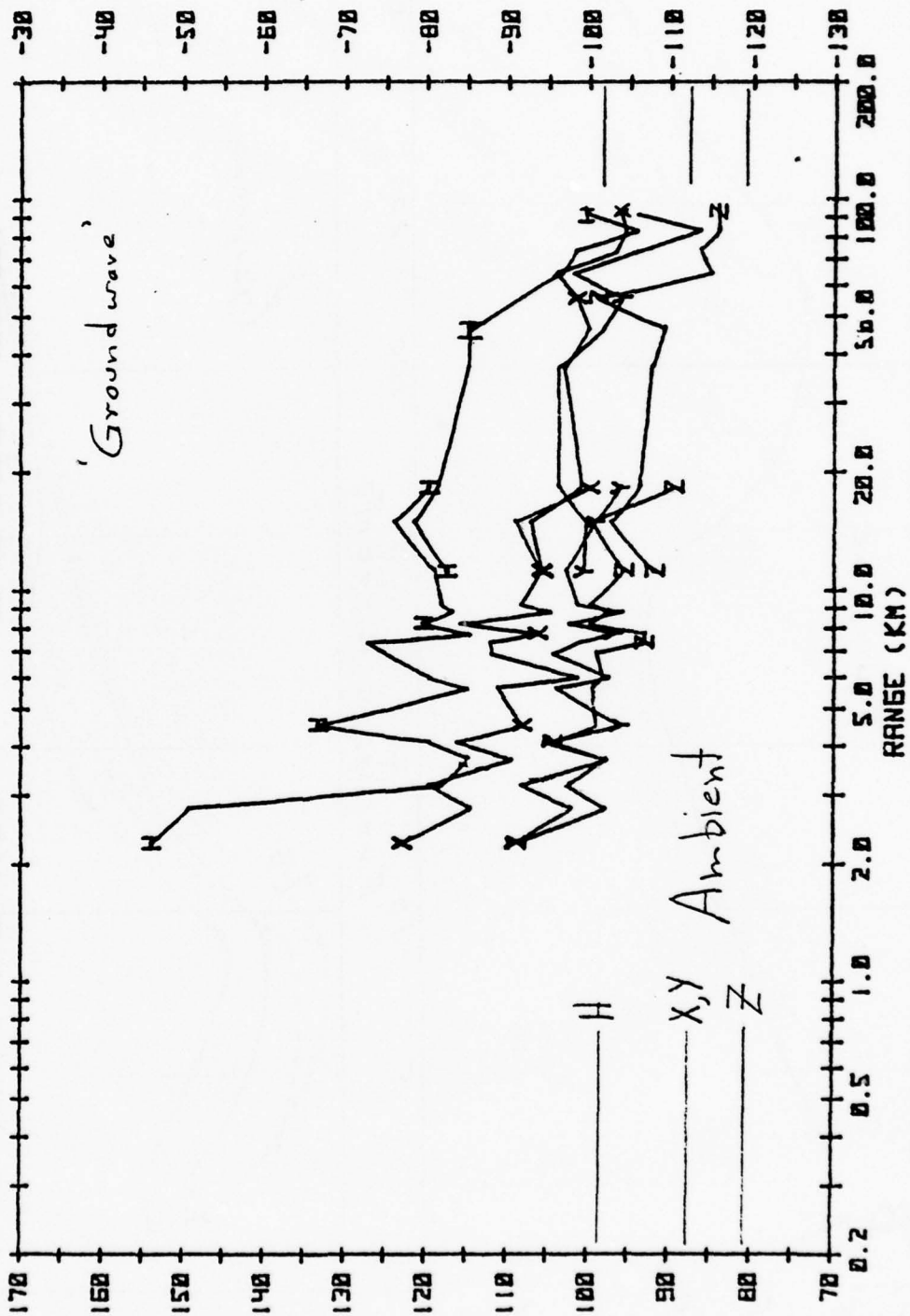
FIGURE 11. SOUND VELOCITY STRUCTURE ALONG LEG D ON 25 MARCH 1976



Ambient Noise at Stage I (Spectral Level)

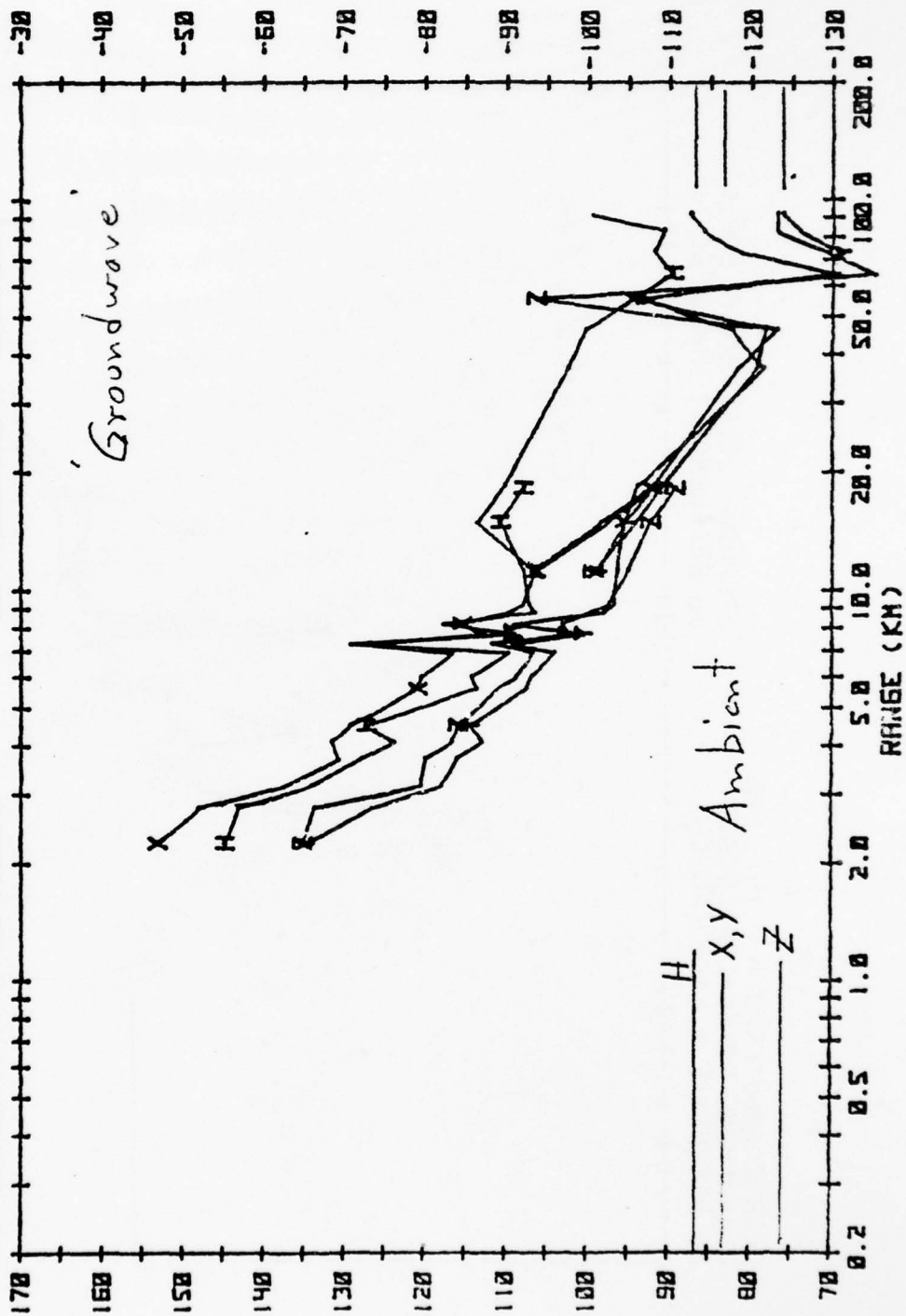
OCTAVE BAND FREQ = 3.5 HZ
 HYDROPHONE LEVEL-LEFT SCALE
 DB REFERENCE 1 MICRO-PASCAL

GEOPHONE LEVEL-RIGHT SCALE
 DB REFERENCE 1 INCH/SEC

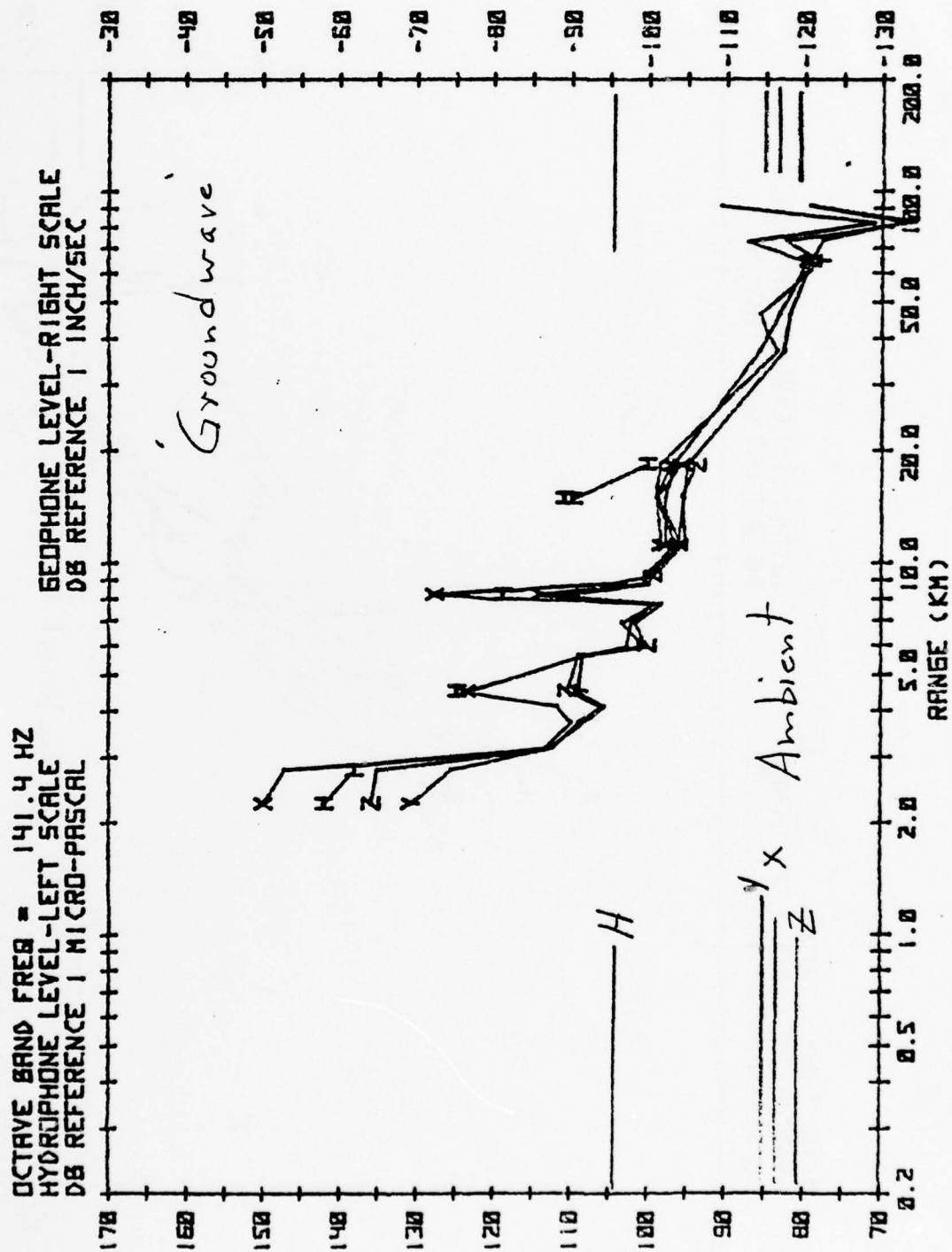


OCTAVE BAND FREQ = 35.4 HZ
HYDROPHONE LEVEL-LEFT SCALE
DB REFERENCE 1 MICRO-PASCAL

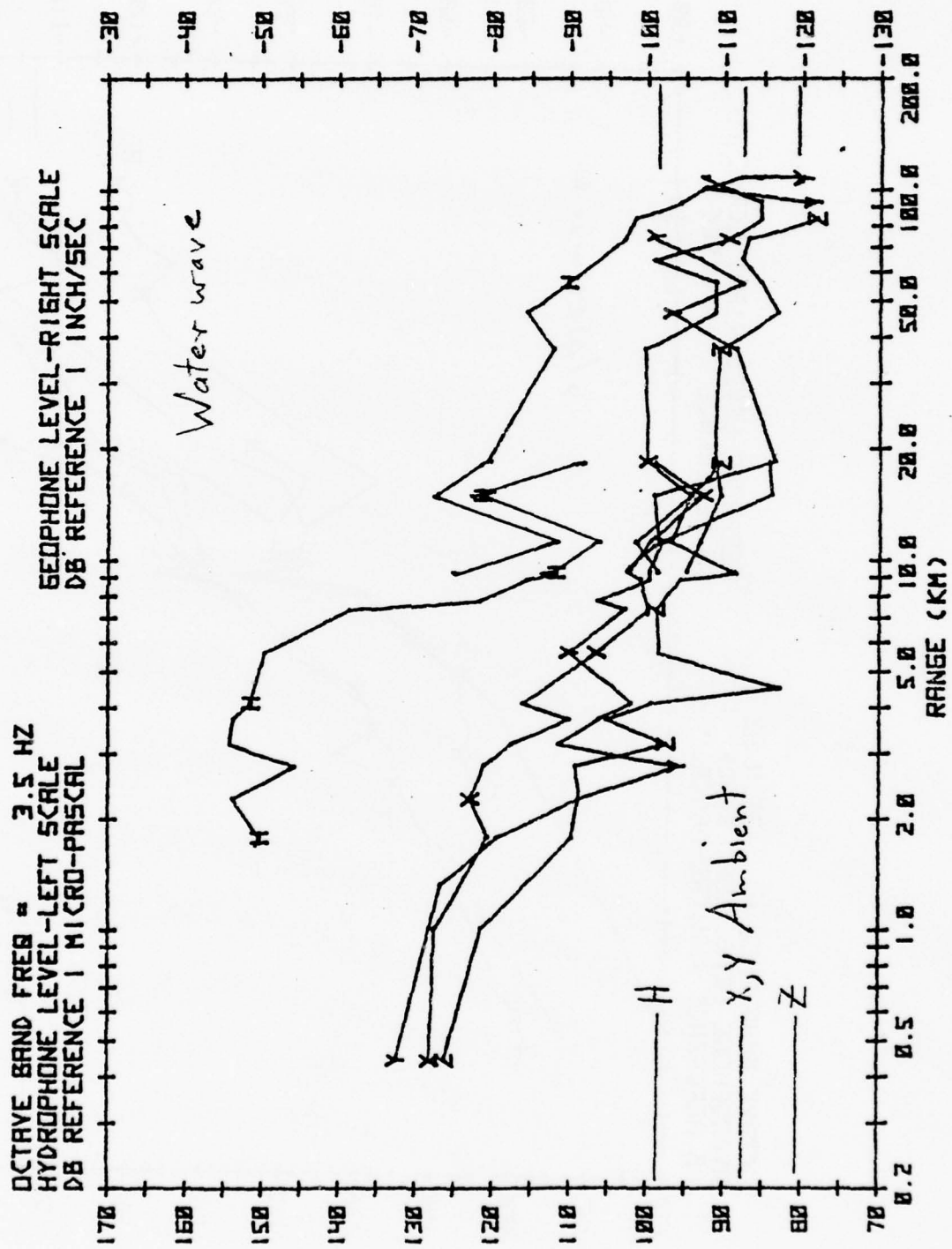
GEOPHONE LEVEL-RIGHT SCALE
DB REFERENCE 1 INCH/SEC



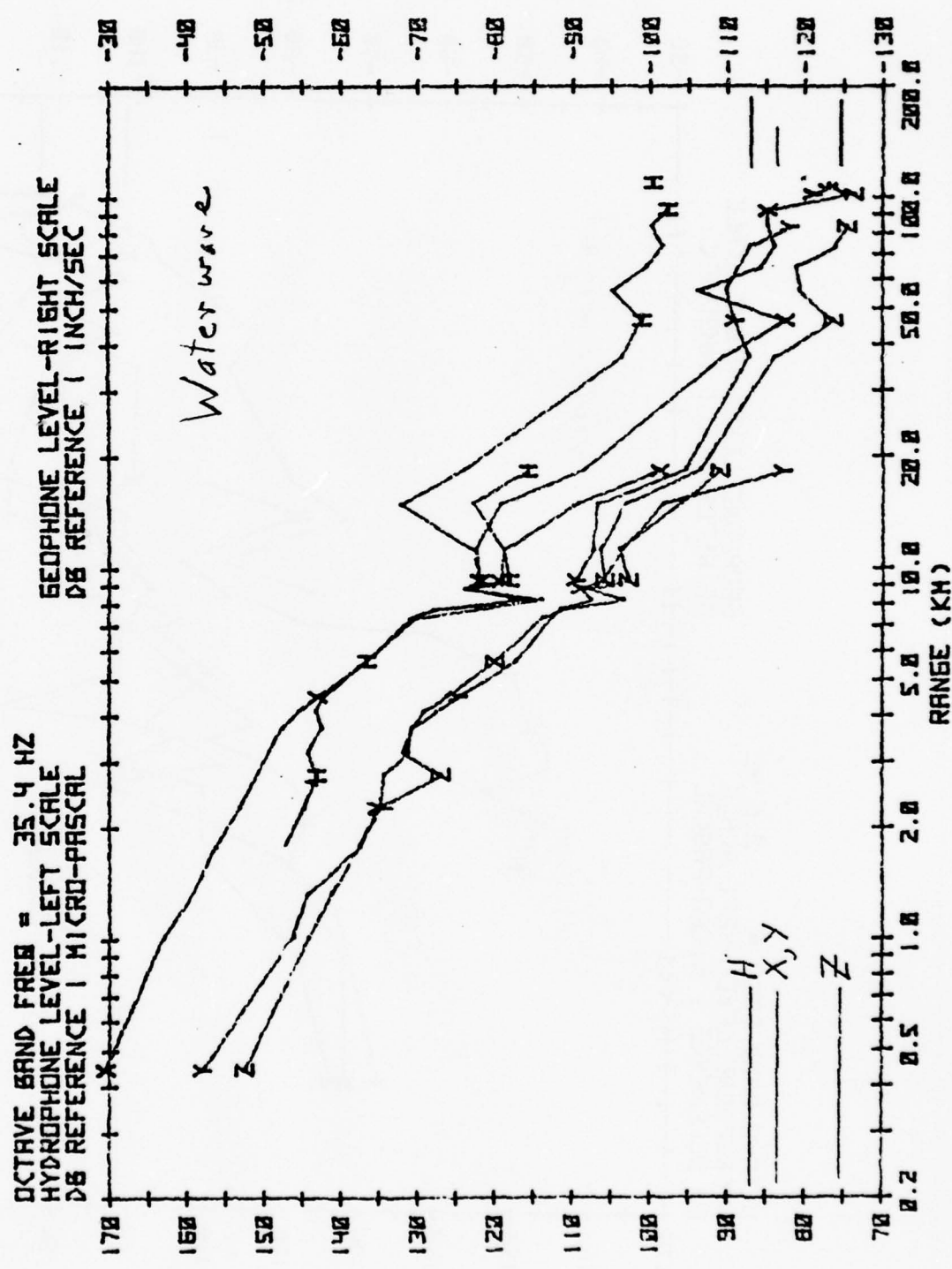
11c



12a

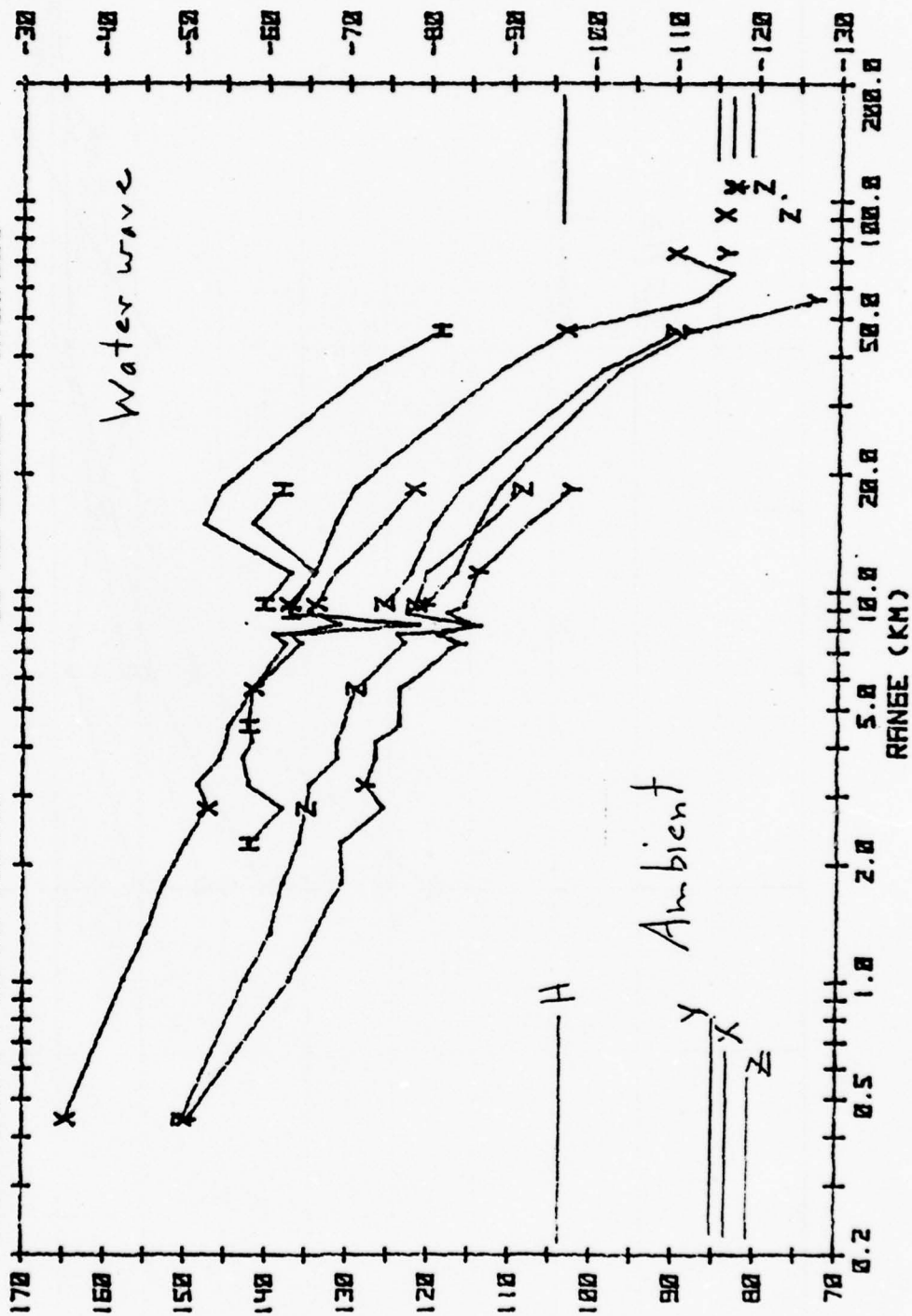


126

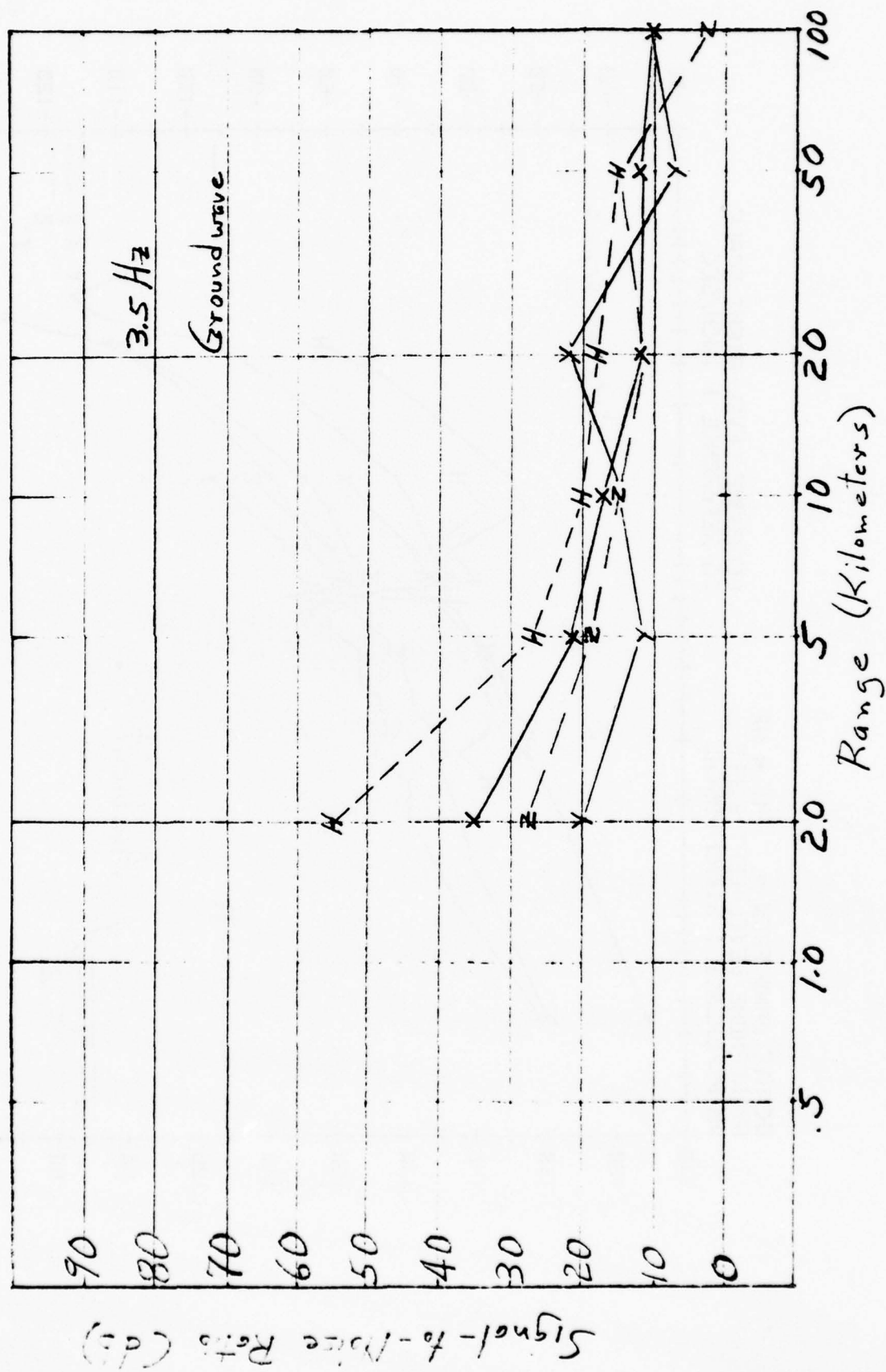


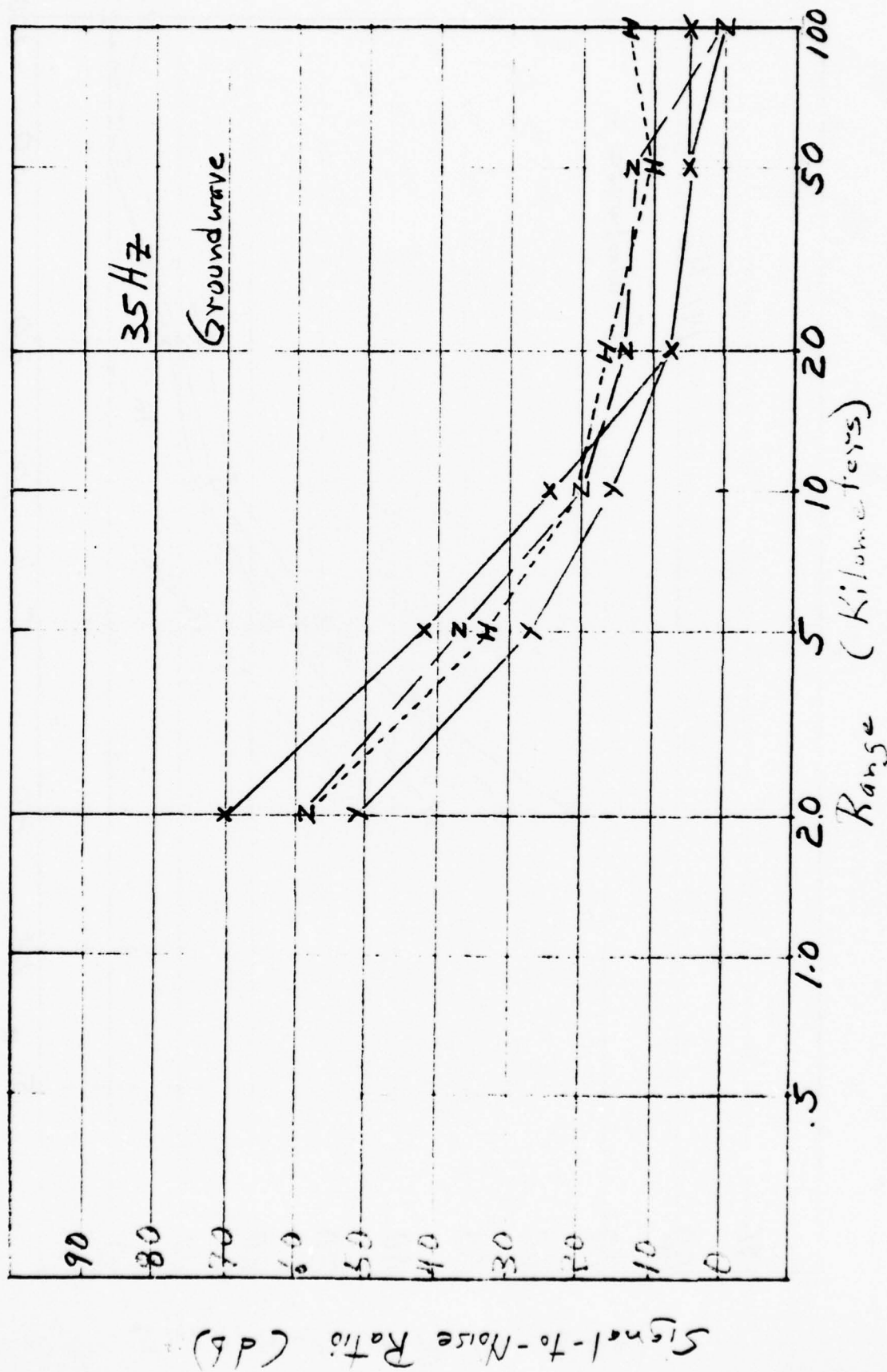
OCTAVE BAND FREQ = 141.4 HZ
 HYDROPHONE LEVEL-LEFT SCALE
 DB REFERENCE 1 MICRO-PASCAL

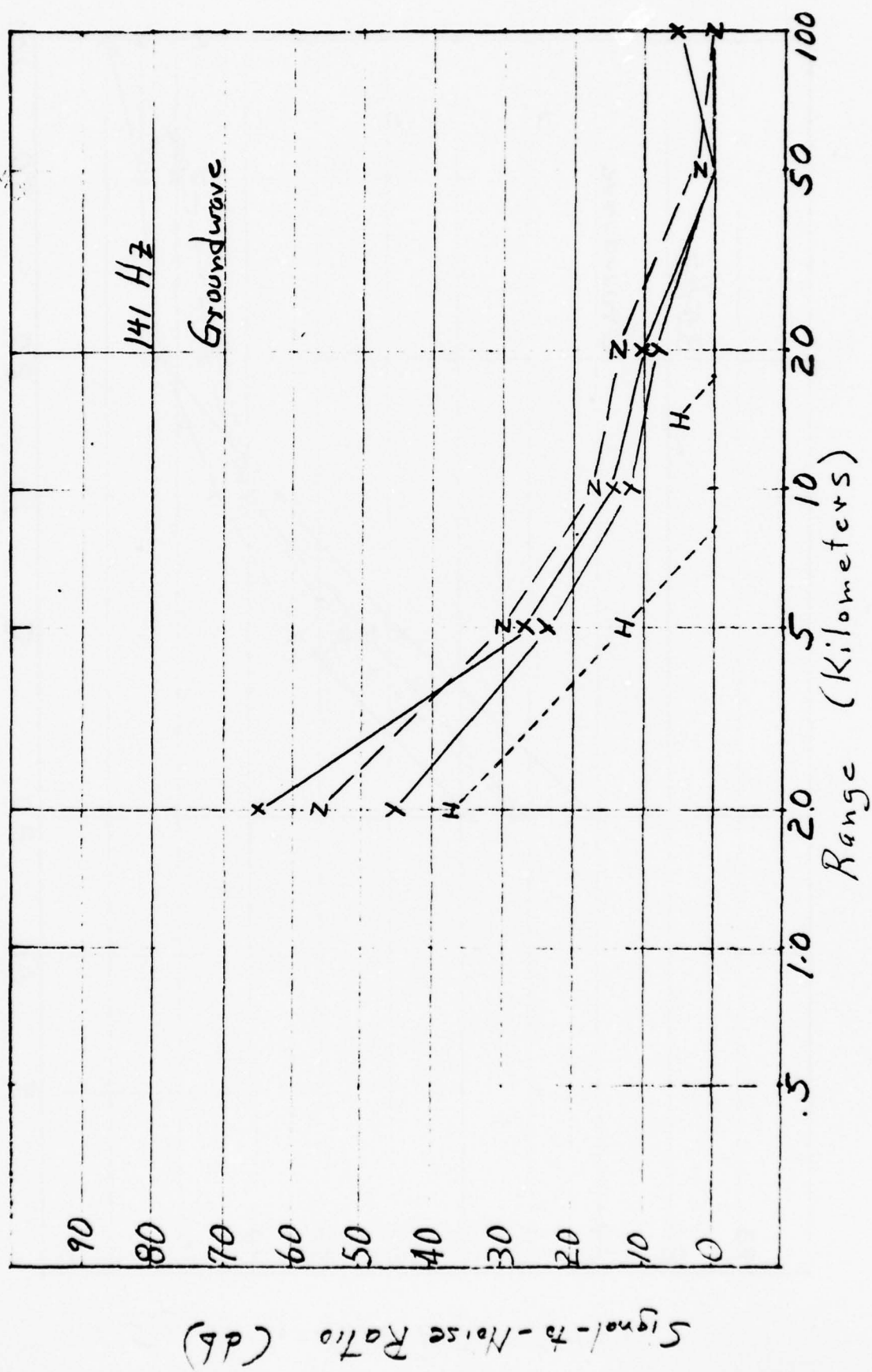
GEOPHONE LEVEL-RIGHT SCALE
 DB REFERENCE 1 INCH/SEC

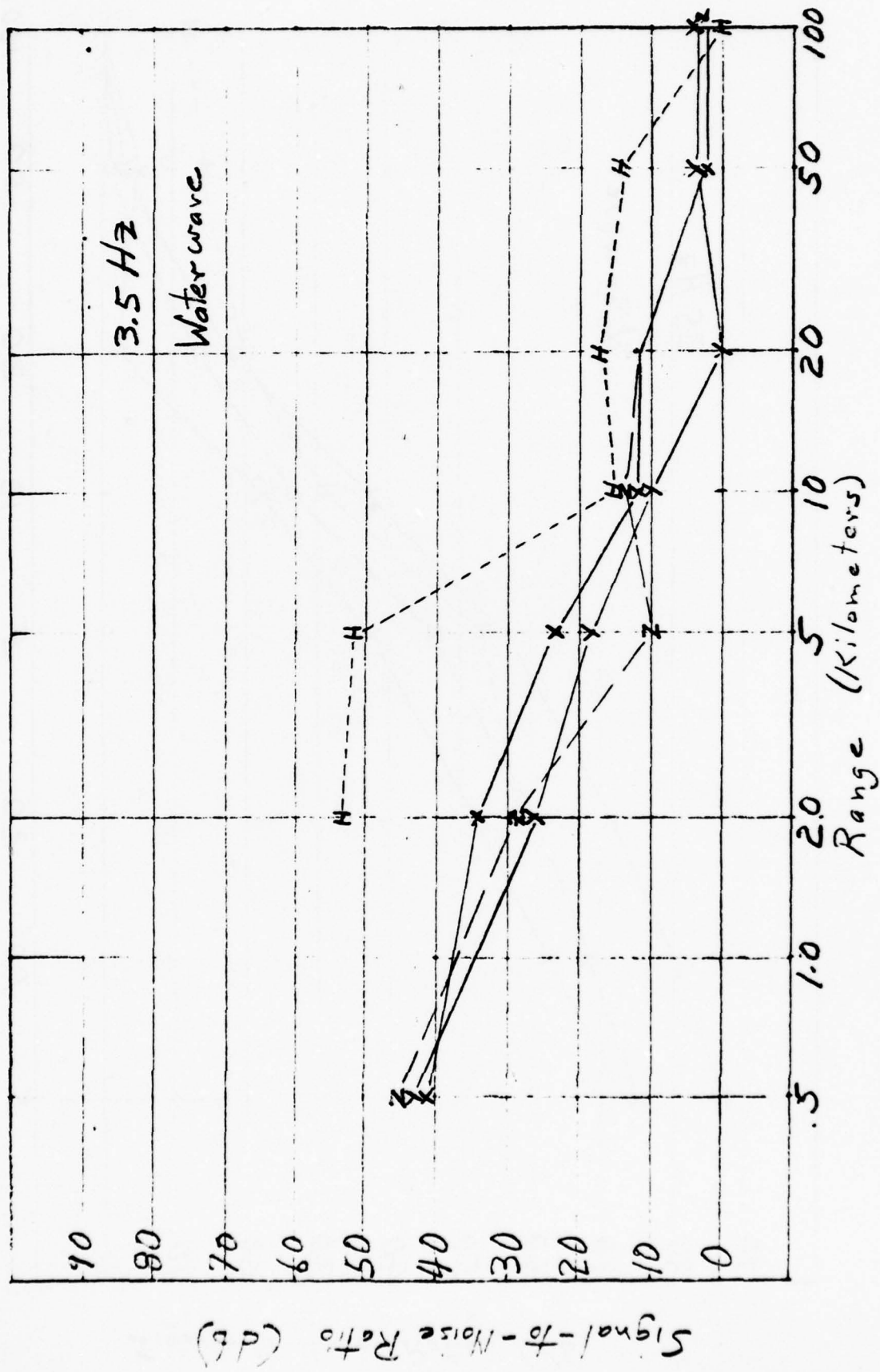


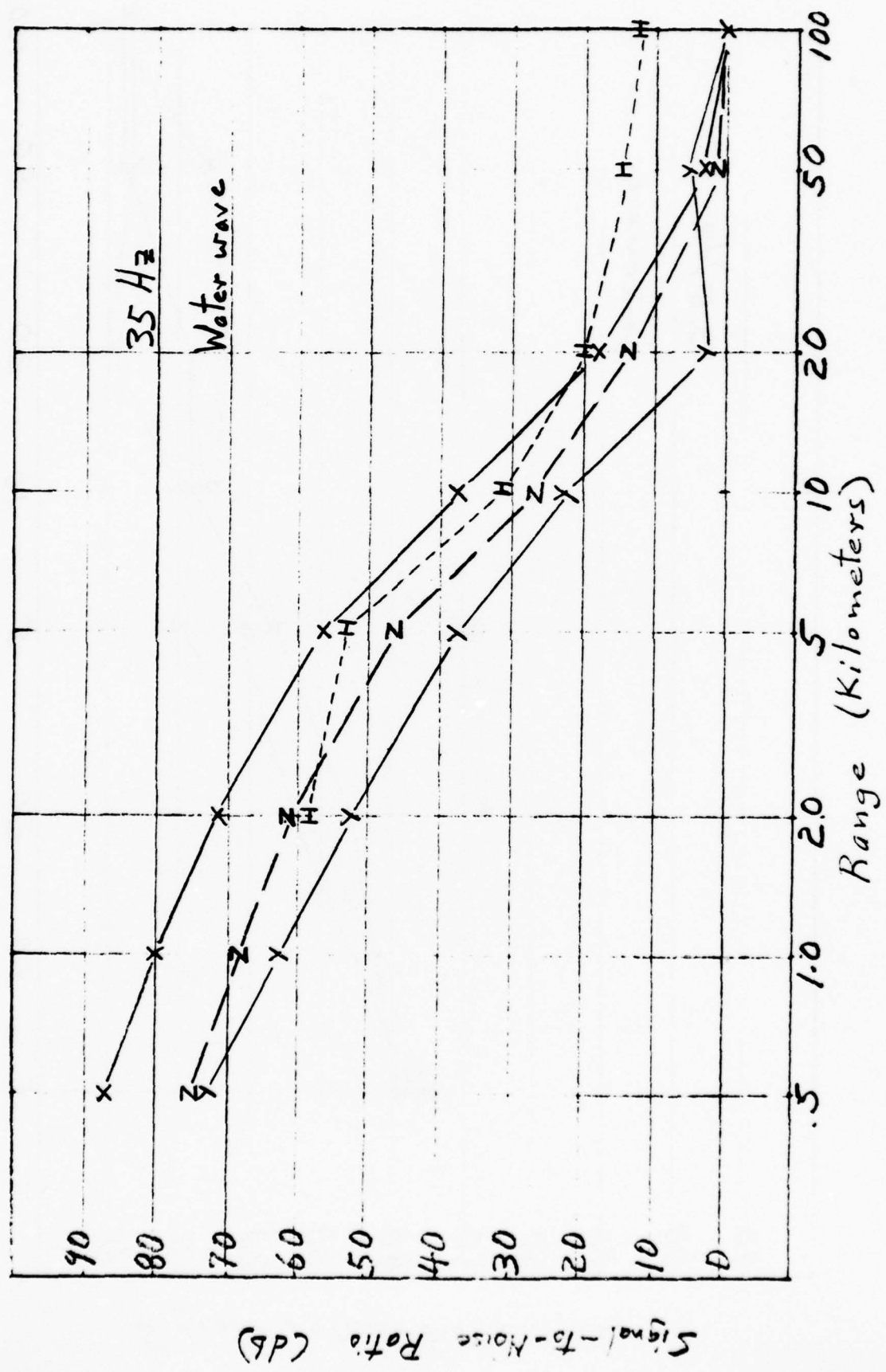
13a



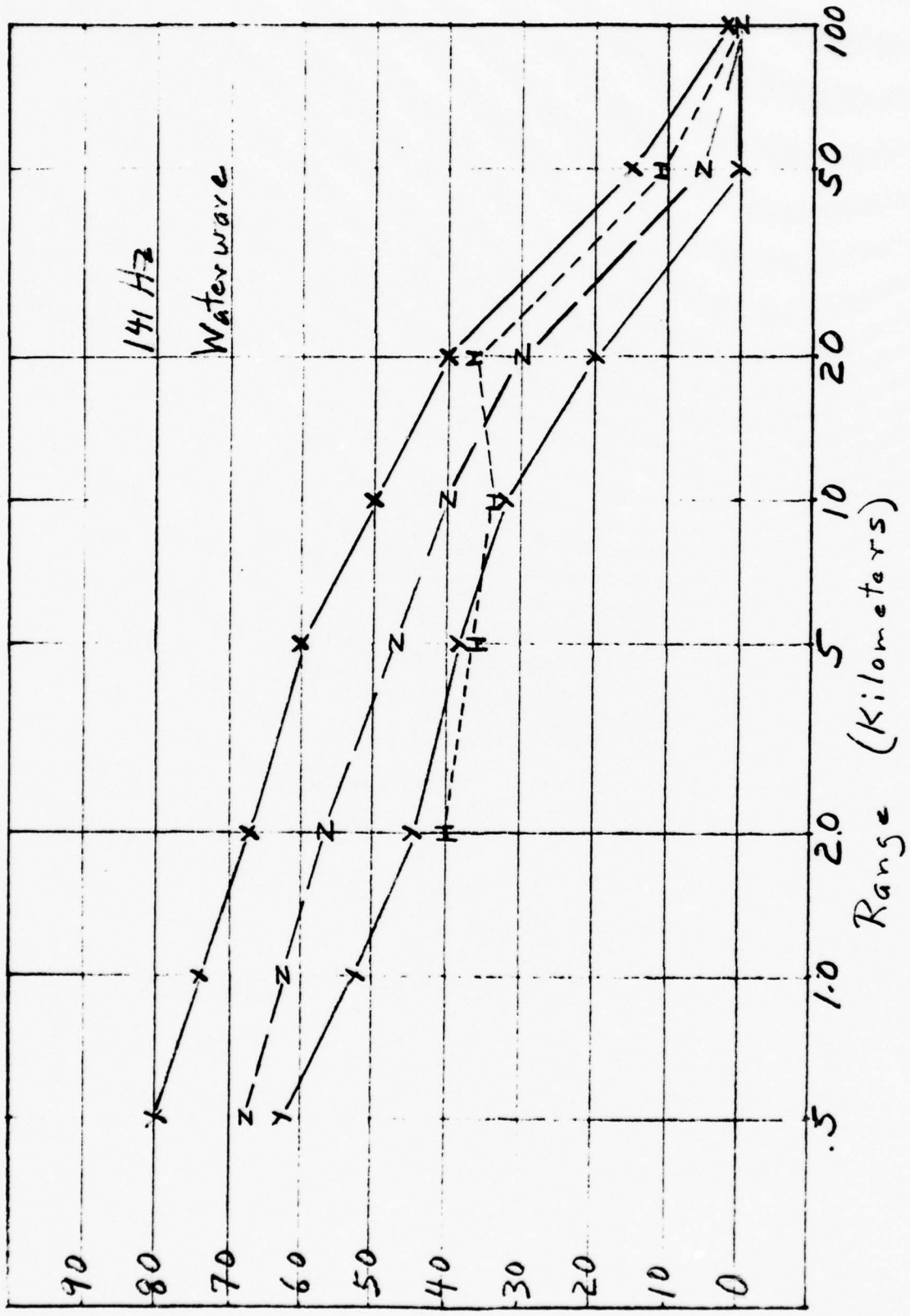








Signal-to-Noise Ratio (dB)



SHALLOW WATER ACOUSTIC STRUCTURE OF THE CONTINENTAL SHELF BY CONTINUOUS
REFRACTION PROFILING WITH A MULTICHANNEL TOWED ARRAY[†]

MARK H. HOUSTON, JR.*

ABSTRACT

Continuous velocity and structural data in shallow water can be extracted from refraction arrivals recorded on a multichannel marine seismic profiling system. Each digitally-recorded shot, which is normally processed for reflections, can also be analyzed for refraction arrivals.

Our algorithm uses adjacent-trace cross correlation to determine first kicks, then fits least-squares straight lines to the arrivals in order to determine layer thicknesses and velocities. A resorting of the single-ended profiles from Common-Source-Point mode to Common-Receiver-Point mode enables extraction of true refraction velocities and dips.

We have used this algorithm to map the near-surface velocities and structure on the Gulf coast continental shelf near Panama City, Florida. Of particular interest was the detection of a low-velocity zone within the upper 100 m of the sedimentary section. This low-velocity zone, which is associated with an area of numerous gas seeps, is most probably caused by gas trapped within the sediment.

With a 4-msec sampling rate and a maximum cable offset of 2300 m, the practical limitations on maximum depth of refraction penetration in the Gulf coast is 500 m; velocities were consistent to 50 m/sec and depths to 10 percent of total depth.

*University of Texas Marine Science Institute, Galveston, Texas 77550.

†University of Texas Marine Science Institute Contribution No. 000, Galveston Geophysics Laboratory.

INTRODUCTION

Multichannel reflection data acquired on land and in shallow water contains refraction energy which arrives ahead of the reflection data. Such refraction arrivals are considered as high-amplitude noise and are removed during reflection processing.

We have developed a computer algorithm to analyze the Common-Source-Point (CSP) refraction arrivals from a marine multichannel survey and to calculate "continuous" (i.e., for every shot) layer velocities and thicknesses. A sorting of the single-ended CSP data into Common-Receiver-Point (CRP) refraction data results in synthetic reversed refraction profiles which can be used to determine true velocities and dips.

We have used the above technique to map near-surface layer velocities and thicknesses on the Gulf coast continental shelf near Panama City, Florida.

A representative cross section extending from 30°N to 86°W in a line nearly perpendicular to the depth contours shows three principal layers, the boundaries of which generally parallel the bathymetry.

The shallowest sedimentary layer thickens offshore, while the deeper layers evidence more subsurface structural variations. The velocity variations in any single layer exceed 200 m/sec with velocities decreasing in an offshore direction. The velocity varies with depth from 1524 m/sec for the water layer to about 2500 m/sec for the deepest refraction layer.

Of particular interest is a low-velocity zone which is most probably caused by gas within layer 1. The low-velocity zone, as characterized by a sudden velocity decrease from 1800 to 1600 m/sec, lies near the seaward margin of a subsurface structural high. The sharp inshore edge of the

low-velocity zone also appears to coincide with a change in the surface sedimentation regime.

METHOD

Previous work

The use of refracted arrivals (to determine shallow velocities) from multichannel data collected primarily for a reflection survey is not new. In the early days of reflection seismology the refraction arrivals were often used for the determination of the thickness of the near-surface weathered layer (Dobrin, 1960; p. 124). But with the advent of higher data densities and computer algorithms for automatic statics, the utility of the refraction arrivals declined. Today the refraction energy has become just high-amplitude noise which must be removed before further analysis and stacking.

The biggest obstacle to the wider use of the refraction arrivals has been our inability to handle large data volumes as routinely as we do for reflection data. The historical modality of refraction analysis has been the painstaking examination of relatively few data points from a limited number of shots. Contrast this with the much higher data density of reflection profiling.

Several previous studies of refractions have been made which take advantage of the high data density of multichannel reflection data. Peraldi (1969) developed a velocity analysis program which examines a field record group of traces (a collection of in-line traces with increasing shot to geophone distances) for linear velocity-time correlation. An equivalent method would be to replace the nonlinear hyperbolic time-distance normal

moveout function commonly employed in stacking power velocity analysis programs (Taner et al, 1970) with a linear NMO-function.

Cunningham (1974) has developed a method to use the refraction arrivals from single-ended reflection data to calculate near-surface statics from velocity anomalies. His method extracts true velocities and dips from successive, overlapping refraction profiles.

Single-ended refraction algorithms

Our method, which is mentioned as an alternative in Cunningham (1974), is to first analyze the data in a Common-Source-Point profile, then sort the trace-shot pairs to synthesize a reversed refraction profile. Combining these two analyses enables the calculation of the refractor velocities and dips from classic refraction techniques. This method is well suited for marine profiling. The "extra" work done in resorting the data is negligible and is amply repaid by the simplicity and reliability of the procedure.

Common-Source-Point (CSP) refraction profiling

The normal configuration for multichannel profiling is equivalent to single-ended refraction profiling. In this CSP mode, as shown in Figure 1, the profiling ship fires an air gun to an array of towed detectors. The time-distance first arrivals are usually interpreted by fits to several straight lines. The slopes of the lines are inverse velocities, and the intercepts are related to the layer thicknesses. In CSP profiling, a refraction analysis is performed for every shot, with considerable overlap between successive shots.

Common-Receiver-Point (CRP) profiling

In normal Common-Depth-Point (CDP) multichannel reflection profiling, the ship's speed and the firing rate are adjusted to achieve a constant distance between shots in a bottom-fixed frame of reference. For a 24-channel system, if the distance between shots is equal to one-half the geophone group spacing in the towed array, then each common reflection point has 24 traces, and the records are 24-fold. CRP refraction profiling selects a sequence of traces from successive shots in such a manner that the receiver point remains fixed in space, while the shot to geophone distance increases in a regular fashion. Figure 2 illustrates the CRP shooting geometry and shot-geophone trace selection for 24-fold CDP shooting. Note that for 24-fold shooting, only alternate shots are used; even- and odd-numbered shots will form overlapping CRP groups. This shot-trace section, which is nothing more than a data reordering, produces a time-distance plot with a single receiver location and multiple source points. By the theorem of reciprocity, any shot-receiver combination may be interchanged without affecting the travel time between them, i.e., point-to-point travel time is unaffected by the direction of propagation. By this means we can construct a "reversed" refraction profile from a reordering of single-ended data. As illustrated in Figure 3, this reversed profile (CRP), together with the forward profile (CSP), can be used to calculate true reflector velocities and dips.

AUTOMATED REFRACTION ANALYSIS

We have developed several computer algorithms to analyze automatically digital, trace sequential, reflection records and to plot "continuous"

refraction structure and velocity sections.

Kicker

In the first phase, time-distance plots are generated by picking first-kick arrivals for each trace as illustrated in Figure 4. A first arrival time for the near-trace is set by the first sample which exceeds a preset amplitude threshold. First arrival times for successive traces are set by trace-to-trace cross-correlation. The difference in first arrival times between adjacent traces is defined as that sample lag, τ , which gives the maximum, normalized, cross-correlation coefficient taken over a short window (on the order of 10 to 20 samples) between adjacent traces.

Figure 4 illustrates the first-kick selection procedure. The first-kick time for trace 24 is at t_{24} . The cross-correlation between trace 24 and trace 23 is calculated over window length w for various lags, τ . For trace 24 the beginning of window w remains fixed at t_{24} , while for trace 23 the beginning of the window time is at time $t_{24} + \tau$. A positive maximum in the plot of normalized, cross-correlation *versus* lag indicates the travel-time difference between the two traces. The first-kick time for trace 23 is $t_{23} = t_{24} - \tau_{ccmax}$. τ_{ccmax} can normally be specified from the peak in the cross-correlation coefficient reliable to one sample. The cross-correlation coefficient for each pick can be regarded as a confidence level for the trace and is used in the subsequent least-squares fit calculations.

Picker -

In the second phase, the time-distance pairs for each shot, together with the cross-correlation coefficients, are used to calculate layer thicknesses and velocities.

A series of straight lines are fitted to the time-distance pairs in the following procedure:

1) Beginning with the near trace, a family of weighted least-square fits, using the cross-correlation coefficients as weights, is calculated for 3 traces, then 4 traces, then N traces, where N = total number of traces.

2) The best refraction line of this family is defined as that linear fit which has a minimum in the geometric mean of the standard deviation of the velocity and the root-mean-square deviation of the time-distance pairs from the linear fit. A minimum in this parameter gives the best overall consistency between "machine" picks and "human" picks.

This best refraction fit defines the number of traces in the fit, n_1 , a slope (the inverse of the velocity), b_1 , and an intercept, a_1 .

3) The linear solution is then tested for consistency with the standard layer-cake refraction assumptions. If the intercept is negative time, the solution is rejected, and the next best fit for the group is tested. If the velocity of the present solution is less than that of the previous layer (water velocity for the first pick), the solution is rejected.

4) With n_1 traces in the first acceptable fit (or eliminated from consideration), the remaining $N - n_1$ traces are repeatedly subjected to the series of tests beginning at item 1 above.

5) When all traces have been either accepted into a consistent linear fit or rejected, adjacent solutions are tested for similarity. If two successive solutions have velocities which differ by less than 50 m/sec (this test limit can be adjusted), then these two solutions are considered to describe the same layer. A new weighted fit is calculated, using all the traces of the original adjacent solutions. This new solution with a

larger number of traces is then subjected to the consistency test of #3 and then tested again for a minimum velocity difference between the next adjacent solution.

6) Finally, when a consistent set of linear fits is found, layer thicknesses and velocities are calculated and output as a section plot.

TRUE LAYER VELOCITIES AND INTERFACE SLOPES

As described above in the discussions of CSP- and CRP-refraction profiling, these two data sets are synthetic reversed refraction profiles when sorted over the same common ground-path. For calculation of true refraction velocities and interface slopes, the refraction analysis is first performed on the CSP-data, then sorted into CRP-time-distance pairs, and finally the refraction analysis repeated on the sorted data. The CSP-velocities and the CRP-velocities can be directly used to calculate true refractor velocities and true interface slopes. This refinement is normally necessary only in areas where the structural slope is greater than several degrees. For example, a slope of $\pm 2^\circ$ in a refractor of velocity 2200 m/sec would show velocity variation of ± 85 m/sec. A 1° slope is about 17 m/km or 162 m/5 nm of vertical elevation change per horizontal distance traveled.

TRACK

Over 500 nautical miles of multichannel reflection data were taken in the summer of 1976 in the vicinity of Panama City, Florida, for the Naval Coastal System Laboratory. This survey, in conjunction with a sediment

sampling program, was designed to examine the structure and acoustic properties of near-surface sediments.

Most of the tracklines, as displayed in Figure 7, run northeast to southwest. The six longest continuous lines are arranged in triplets along two bearings which are drawn through the USN Coastal Observation Platform, "Stage I," located at $30^{\circ}00.8'N$, $85^{\circ}54.2'W$.

The southern A-triplet runs along bearing 225° , and the northern B-triplet extends along bearing 252° . Each triplet of parallel tracks was spaced about 5 nm apart in order to evaluate cross-track variability. Subsequent examination of the data suggests that because of the geologic complexity of the area, a 2-mile spacing with periodic strike-line cross ties would have sampled the lateral variability more effectively.

About 280 nm of the multichannel data taken in water depth less than 200 m were analyzed using automated Common-Source-Point refraction (CSP) profiling. At a shot distance of 20 shots/mile, over 4500 individual refraction analyses were used to produce the structure and velocity maps.

REFRACTION CROSS SECTIONS

The refraction cross sections displayed in Figures 8-15 were derived from the automatic refraction analysis as outlined above. Machine-picked time-distance first arrivals, layer velocities, and thicknesses were calculated automatically for each shot and plotted in a "continuous" display. Layer thicknesses and velocities were then smoothed by eye, so that each "smoothed pick" had consistent velocity and thickness (depth to interface) for at least 25 shots.

Accuracy

Weighted least-square calculations (Parratt, 1961, p. 130) of a fit of the data to a straight line gave standard deviations of the order of 10 m/sec for the velocities and 4 msec (1 sample) for the time intercepts.

Based on the machine plots of velocity, the maximum uncertainty in the refraction velocities is 50 m/sec.

An estimation of the statistical uncertainty in calculated layer depths according to the method of Steinhart and Meyer (1961) was hand calculated for several shots. The results yielded a standard deviation in depth of 10 percent of the cumulative depth. This "calculated" standard deviation was consistent with the standard deviation estimated from the statistics of the machine-plotted depths.

These estimates of refraction depth are valid only if velocities increase downward. The existence of a negative velocity gradient (Northwood, 1967) or the presence of near-surface sediments with velocity less than water (Press and Ewing, 1948) would bias the results. Since we do have evidence (Figure 6) for a hidden layer, the absolute layer depths may not be as reliable as the statistics indicate.

A-Bearing

Figure 16 shows the interpreted CSP refraction cross-section derived from line PC1A1. Because of the low structural relief of the upper layers and their gentle dips, it was not necessary to employ the reversed refraction method. The sections were constructed from CSP refraction analyses with occasional CRP-refraction analyses to check consistency. The scale along the bottom shows distance from Stage I. Also shown at the right edge of the section are sonobuoy refraction results which were recorded a

short distance inshore of Stage I.

Figure 16 shows six distinct layers: the water layer (1524 m/sec), a low-velocity layer ("LV-layer") (1640 m/sec) near the left-hand side of the section, and four additional refraction layers with typical velocities of 1780, 2100, 2280, and 2680 m/sec.

In our nomenclature layer 1 refers to the uppermost sedimentary layer with a consistent refraction velocity (1780 m/sec) exclusive of the water layer and the low-velocity "zone" or "layer." Layer 2 is the next deeper sedimentary layer with a consistent refraction velocity of about 2100 m/sec, etc. In general the layers are subparallel to the water bottom, and they tend to thicken seaward. The LV zone appears as a wedge-shaped refractor in which the velocities are lower than layer 1 by at least 100 m/sec. The horizontal width of the transition zone between the LV layer and layer 1 is less than 2 km (20 shots). The projection of the sloping boundary of the low-velocity layer to the ocean bottom surface lies near a surficial sediment boundary observed in a companion coring program (McMillen, Haines, and Addy, 1977).

The velocities in layer 1 smoothly decrease in the seaward direction, while the velocities in the deeper layers irregularly increase seaward. Because of its limited detection within the survey, the deepest layer with velocity 2680 m/sec has not been included in the following contour maps.

B-Bearing

Figure 17 shows the interpreted CSP cross section derived for the B-bearing from data of lines PC2B3 and PC1B3. Here, too, the refraction boundaries tend to parallel the bathymetric profile, but there are indications of a more complex subsurface structure. The velocity of layer 2

remains nearly constant across the section until it reaches the vicinity of the edge of the LV layer. Near this boundary, which is also a boundary of subsurface structural faulting, layer 1 begins to thicken. The LV zone is characterized by a sudden decrease of refraction velocity of 300 m/sec. The thicknesses of the other layers are variable and reflect the geologic complexity of the area. The velocity of layer 1 is almost constant across the section with a slight increase in velocity over the position of the subsurface structural high as defined by a strong reflector in the CDP reflection sections at 1.5 to 2.0 sec. Despite some variation, the general trend within the deeper layers seems to be one of decreasing velocities seaward.

COMPARISON OF REFRACTION AND REFLECTION CROSS SECTIONS

Figures 18-25 are the Common-Depth-Point reflection cross sections derived from the multichannel data. An expanded time-scale playout of the first half-second of data is presented. Also drawn on the time-sections are the equivalent refraction interfaces, where the conversion from depth to time has been accomplished using the refraction velocities.

In those situations where the sedimentary layering is simple and planar, refraction interfaces and reflection horizons are parallel. For the shallow sections there does not seem to be a neat correspondence between refractors and the relative strength of a reflector; i.e., we do not see any obvious relationships between a refractor and a strong reflector. In areas of complex geologic structure and in areas of rapidly changing sedimentary conditions, we find that the refractors may jump to a different reflector or may have a low-angle cross-cutting relationship with the reflection

seismic stratigraphy. Despite this, the overall structural features are outlined within the "continuous" CSP profiles. High-angle, cross-cutting relationships between refractors and reflectors are associated principally with the low-velocity zone.

The precise cause of the LV zone is unknown, although the close association of the zone with a well-defined area of gas seeps, Figure 26a (from Addy and Worzel, 1977) suggests that the velocity decrease may be attributed to gas distributed within the shallow sediments (Tinkle, Antoine, and Kuzeia, 1973; Watkins and Worzel, 1977). For example, sandstone compressional wave velocities can be lowered as much as 10 percent with 10 percent gas saturation at 1 bar hydrostatic pressure (Toksöz, Cheng, and Timur, 1976). The other possible explanation is that the LV zone is due to an abrupt sediment transition with a corresponding P-wave velocity change (exclusive of gas content). However, surface cores (McMillen, Haines, and Addy, 1977) do not support the latter interpretation. As shown in Figure 26a, the gas seep area and the low-velocity region blanket the zone of sediment transition from coarser shelf quartz sand and algal sand to finer slope foraminiferal sandy mud.

The area of gas seeps seems to be closely tied to a subsurface structural high as defined by a strong regional reflector at a two-way time of about 18 sec at its shallowest. Figure 26b (from Addy and Worzel, 1977) illustrates the structure and shows a crestal shear zone in which numerous small faults cut the section at depth. Most of these small faults fail to penetrate to the surface.

The region of the low-velocity zone seems to roughly coincide with the closure of the structure at depth. Therefore, we conclude that the low-velocity zone is caused by gas within the sediments and that the

source of the gas is probably derived from the subsurface structure. The gas percolates up through the section, which is cut by numerous small faults concentrated in the crestal region. The bulk of the gas likely escapes as seeps, but part of the gas is trapped within the unconsolidated surficial sediments. The abrupt northeastern edge of the LV zone may be structurally controlled.

CONTOUR MAPS

The contour maps of Figures 27-33 were obtained by smoothing of the data from the CSP refraction profiles. A comparison of the refraction depth-cross section with the expanded scale reflection time-cross sections was used to define smoothed layer boundaries, then layer depths and velocities for these smoothed layers were picked for every 100th shot point. These values were plotted at the corresponding position in the shot-point map, and the values for each layer contoured to produce the isopach and iso-velocity maps.

The practical water depth limit for the refraction analysis is 200 m; however, at this water depth the deeper layers are beyond reach. The most reliable data for the deeper layers was obtained inshore of the 100-m contour. We must caution that beyond the 100-m contour, isopleths for the deeper layers have been extrapolated in a manner which we feel is consistent with the overall geological structure obtained from the deeper penetrating multichannel reflection data. We feel justified in this procedure because where we do have reliable refraction data, the structure interpreted from the refraction data is consistent with the deeper geologic structure as revealed by the reflection sections.

Isopach maps

Figure 27 shows the isopachs for the low-velocity zone. Within this zone the refraction velocities range from 1600 to 1660 m/sec as compared to a layer 1 velocity of from 1750 to 1850 m/sec. The boundary of the low-velocity zone, the inshore boundary of which can be fixed by the CSP refraction data to within 2 nm, outlines a triangular-shaped region lying directly within the survey area. The seaward boundary of the zone is not defined, as it is exterior to the refraction data. However, we have positioned the seaward boundary consistent with the area of gas seeps as detected from the 3.5-kHz records.

The isopach maps for layers 1 and 2 (Figures 28, 29) illustrate several structural features. First is the general trend of a thickening of both layers from inshore to offshore. The second major feature is thinning of the beds over a slight structural high. The area of thinning coincides with the general position of the low-velocity zone. The reflection sections show evidence of numerous small faults within this same area.

Figure 30 shows the depth to the top of layer 3. A comparison between this figure and the isopach maps for layers 1 and 2 indicates that the variation in the thicknesses of layers 1 and 2 is probably caused by differential sedimentation or compaction on preexisting topography.

Isovel maps

Figures 31-33 show the refraction velocities for layers 1, 2, and 3, respectively. The velocities in layer 1 range from nearly 1900 to 1750 m/sec. Were it not for a tongue of lower velocity material intruding into the northern part of the section, the velocities in layer 1 could be described as decreasing seaward. A ridge of higher velocity (>1850 m/sec)

which runs along the B-bearing is paralleled by a trough of lower velocities running along the A-bearing.

Layer 2 and layer 3 velocities show a more regular trend with refraction velocity decreasing seaward. In layer 2 the isovels trend nearly parallel to the bathymetric contours. In layer 3 the velocity maximum appears to have shifted to the northern part of the survey area. Velocities in layer 2 range from >2200 to 1800 m/sec; in layer 3 the velocities range from 2300 to >2500 m/sec.

MODELS FOR A- AND B-BEARINGS

Figures 34-37 present the models of refraction structure and velocity variations along the A- and B-bearings. These profiles have been synthesized from all the data and are derived from the contour maps. In both tracks the presence of the low-velocity zone should have the greatest effect on variations of acoustic transmission along the track.

CONCLUSIONS

The most significant discovery of the survey is the presence of a near-surface, low-velocity zone, which is most probably caused by petrogenic gas within the sediments of the uppermost layer. The presence of this low-velocity zone and its boundaries could not have been positively established without the CSP-refraction profiling. Standard multichannel reflection velocity analyses are not very effective for vertical incident reflection times of $< \frac{1}{2}$ sec. The presence of gas "plumes" in the 3.5-kHz profiles is an indirect clue, but the source of the gas and its distribution within the

subsurface, and therefore its effects on acoustic velocities, would still remain uncertain. The refraction surveying is a direct measure of horizontal acoustic propagation conditions.

The general structure of the surficial layers and their velocity variations tends to mirror the deeper geologic structure as revealed from the multichannel reflection records. For the deeper layers there seems to be a coincidence between refractors and reflectors. A precise correspondence could not be established because of depth uncertainties attributable to inherent measurement uncertainties. Within these limits we did see an apparent "jumping" of refractors to reflectors of differing seismic stratigraphic horizons, though this point requires further verification. We can say that discordances between reflection and refraction horizons have been found in the near-surface layer, in this case caused principally by the presence of gas. I would postulate that these same discordances would occur in circumstances in which differential dewatering of sediments was favored, i.e., along the edges of the continental shelves in areas of rapid sedimentation, and in areas of rapidly changing sediment types. The present example makes it clear that it is not always a correct assumption that acoustic propagation horizons parallel sedimentation horizons or reflection horizons.

RECOMMENDATIONS

The use of a multichannel towed array is a cost-effective tool to examine the shallow acoustic structure on the continental shelf. Common-Shot-Point refraction analysis and the standard multichannel reflection sections provide complementary information.

Future surveys

For future surveys I recommend the use of a 48-channel streamer with 50-m spacing of line sections and a 2-ms sampling rate. These changes should lead to better resolution in both velocity and depth determinations. From hindsight, in geologically complex areas like Panama City, I would also favor more close-spaced lines together with several cross-tie lines. One additional piece of gear, a high-resolution profiler (200 to 1000 Hz), might be very useful in looking at the shallow structure. Shallow "pods" of gas should be detectable with the high-resolution profiler.

Future improvements

I believe that we may be able to extract additional acoustic information from our multichannel data. As an example, one admittedly speculative idea is to use the multichannel data to determine bottom sediment shearing strength and density. With further refinement of processing techniques, we might be able to detect converted shear-wave arrivals (P-S-P waves) (Whitcomb, 1966; Hall, 1964). These arrivals could give us sediment shear-wave velocities, and with some simple assumptions we could estimate bulk sediment properties such as shearing strength and density (Tatham and Stoffa, 1976). By tying the underway seismic measurements to a sparse grid of bottom sample stations, it would be possible to construct maps of gross bottom sediment properties from underway acoustic measurements.

ACKNOWLEDGMENTS

This work was supported by U.S. Naval Coastal Systems Laboratory Contract No. N-61339-76-D-0014. Thanks are due to Teledyne Exploration Company who donated computer time during the development of the algorithm. Credit is due also to J. L. Worzel who pointed out that the CRP-mode by the reciprocity theorem is an exact reversed profile of the CSP-mode.

My thanks in particular to numerous coworkers for help in typing, drafting, proofing, and discussion.

REFERENCES

- Addy, S. K., and Worzel, J. L., 1977, Occurrence of gas seeps and subsurface structure in the northern Gulf of Mexico, off Panama City, Florida: in prep.
- Cunningham, A. B., 1974, Refraction data from single ended refraction profiles: *Geophysics*, v. 39, p. 292-301.
- Dobrin, M. B., 1960, *Introduction to Geophysical Prospecting*: New York, McGraw-Hill, 2nd Ed., 446 p.
- Hall, D. H., 1964, Converted waves in refraction surveys over markers with variable depth: *Geophysics*, v. 29, p. 733-744.
- Northwood, E. J., 1967, Notes on errors in refraction interpretation, in *Seismic refraction prospecting*: A. W. Musgrave, editor, Soc. Exploration Geophysicists, p. 459-465.

- McMillen, K. J., Haines, T., and Addy, S. K., 1977, Sediments of the north-west Florida and Alabama shelves and upper slope: in prep.
- Parratt, L. G., 1961, Probability and Experimental Errors in Science: New York, John Wiley & Sons, 255 p.
- Peraldi, R., 1969, Contribution du traitement numerique a l'analyse et a l'interpretation des enregistrements refraction: Geophysical Prospecting, v. 17, p. 126-164.
- Press, F., and Ewing, M., 1948, Low-speed layer in water-covered areas: Geophysics, v. 12, p. 404-420.
- Taner, M. T., Cook, E. E., and Neidell, N. S., 1970, Limitations of the reflection seismic method; lessons from computer simulations: Geophysics, v. 35, p. 551-573.
- Tatham, R. H., and Stoffa, P. L., 1976, V_p/V_s — A potential hydrocarbon indicator: Geophysics, 4, 41, p. 837-849.
- Tinkle, A. R., Antoine, J. W., and Kuzeia, R., 1973, Detecting natural gas seeps at sea: Ocean Industry, v. 8, p. 139-142.
- Toksöz, M. N., Chang, C. H., and Timur, A., 1976, Velocities of seismic waves in porous rocks: Geophysics, v. 41, p. 621-645.
- Watkins, J. S., and Worzel, J. L., 1978, The serendipity gas seep areas, South Texas offshore: AAPG Bull., v. 62/6, p. 1067-1074.
- Whitcomb, J. H., 1966, Shear-wave detection in near-surface seismic refraction studies: Geophysics, v. 31, p. 981-983.

FIGURE LEGENDS

FIG. 1. Common-Source-Point (CSP) single-ended refraction profiling using a multichannel streamer in shallow water. A plot of time-distance first arrival times shows refraction energy arriving ahead of the reflection energy. Layer depths and velocities can be calculated from straight line fits to the refracted first arrivals.

FIG. 2. Common-Receiver-Point (CRP) refraction profiling. Geometry illustrated is for 24-CDP reflection profiling with a 24-trace cable. Horizontal distance between shots equals one-half the group separation distance. Odd-numbered shots have been selected to show the grouping of successive shot-geophone combinations which make up the Common-Receiver-Point refraction profile.

FIG. 3. Illustration of Common-Source-Point and Common-Receiver-Point refraction profiles which make up classic reversed refraction profiles. CSP profile has single shot and multiple receiver locations; time-distance plot is from A to B. CRP profile has multiple shot locations and a single receiver location; time-distance plot is from B to A.

FIG. 4. Illustration of first-kick picking procedure. For trace 24, t_{24} is the first-kick time. W is the window over which a normalized, cross-correlation coefficient between traces 24 and 23 is calculated for lag τ . τ_{ccmax} is the lag at which the coefficient is a maximum. First-kick time for trace 23 is $t_{23} = t_{24} + \tau_{ccmax}$.

FIGURE LEGENDS, Continued - p. 2

FIG. 5. Sample multichannel record showing refraction arrivals as a function of time and trace number. Horizontal distance between traces is approximately 92 m. Distance to the far trace is 2331 m. Vertical scale is in units of 100 ms with 0-sec and 1-sec indicated. Machine first kicks are located with large dots. Machine-picked refraction layers are indicated by heavy lines and labeled with the velocity in m/sec.

FIG. 6. Sample multichannel record showing refraction arrivals as a function of time and trace number. Time shift between machine-picked refraction solutions with 1926 m/sec and 2077 m/sec is due either to refractor structure or to the presence of a low-velocity zone or a "hidden layer." Since a pronounced low-velocity zone has been detected along this same line and the reflection section shows smooth layering near this shot point, we feel that this refraction time-shift is due to a "hidden layer" of low-velocity material.

FIG. 7. Shot point map showing multichannel track lines. Solid lines indicate processed reflection data with locations shown for every 500 shots. Refraction analyses were limited to data inside the 200-m bathymetric contour. Small circle near 30°N, -86°W indicates the position of the USN Coastal Observation Platform, "Stage I." Bathymetry in meters has been derived from NOAA chart no. NOS NH 16-8, 1975.

FIG. 8. Refraction depth section for line PC1A1. Line positions are identified in Figure 1. Large numerals at top of section above vertical

FIGURE LEGENDS, Continued - p. 3

lines indicate positions of even-hundred shot points. Arrow at top of sections shows direction of profiling; Stage I is always at right. Smaller numbers along top of section indicate beginning and ending shot points for individual field reels. Small underlined numbers show ship's position for GMT time at hour intervals. Horizontal distance between 100 shots is approximately 5 nm. Depth scale is in 100-m increments. Vertical exaggeration is about 45. Numbers within the cross section show measured refraction velocities in m/sec. A velocity of 1524 m/sec was measured for the water layer. Interface depths are indicated by solid lines within the shot-point-depth grid.

FIG. 9. Refraction depth section for line PC2A2.

FIG. 10. Refraction depth section for line PC3A1.

FIG. 11. Refraction depth section for line PC2B2.

FIG. 12. Refraction depth section for line PC1B3.

FIG. 13. Refraction depth section for line PC3B1.

FIG. 14. Refraction depth section for line PC1C.

FIG. 15. Refraction depth section for line PC1F. This line runs nearly perpendicular to the other lines. North lies to the right of the section.

FIG. 16. Refraction depth section for A-Bearing (PC1A1). Scale along the bottom measures distance from USN Observation Platform, Stage I.

FIGURE LEGENDS, Continued, p. 4

FIG. 17. Refraction depth section for B-Bearing (PC1B3 and PC2B2). This cross section is a composite of two lines. Scale along the bottom measures distance from USN Observation Platform, Stage I.

FIG. 18. Reflection time section for line PC1A1. The horizontal scale is approximately the same as Figure 8. The vertical scale is two-way reflection time in milliseconds. The heavier horizontal grid lines indicate intervals of 100 ms, the lighter lines 50 ms. Maximum plotted time is 500 ms. Full-scale vertical exaggeration for a water velocity of 1524 m/sec would be approximately 25.

The heavy lines plotted on the time section are refraction interfaces taken from the corresponding refraction depth sections. Refractor depths have been converted to two-way reflector times by using depth-weighted average velocities calculated from the refraction section.

FIG. 19. Reflection time section to line PC2A2.

FIG. 20. Reflection time section for line PC3A1.

FIG. 21. Reflection time section for line PC2B2.

FIG. 22. Reflection time section for line PC1B3.

FIG. 23. Reflection time section for line PC3B1.

FIG. 24. Reflection time section for line PC1C.

FIG. 25. Reflection time section for line PC1F.

FIGURE LEGENDS, Continued, p. 5

FIG. 26a. Map showing the distribution of gas seeps and the areas of wipe outs, fuzziness, and smearing. Taken from Addy and Worzel, 1977. Each solid circle shown here represents one identifiable gas seep. The main gas seep area is shown by a dashed line. The locations of the piston cores in the main gas seep area are marked with asterisks. The surface sediments in the western part of the main gas seep area are fine-grained foraminiferal sandy mud, whereas in the eastern part coarse algal sand and shelf sand are found.

FIG. 26b. Map showing structure of strong, regional, dual reflector. Contour interval is 0.2-sec of two-way time. Dashed line outlines area of gas seeps. Stippled area denotes a "shear" region of numerous small subsurface faults. Taken from Addy and Worzel, 1977.

FIG. 27. Isopach map of low-velocity layer. Contour interval is 50 m. All Isopach maps and velocity maps are smoothed contours of data taken from the CSP refraction cross sections. In this map, the dashed contour beyond 200-m isobath is drawn consistent with an area of distributed gas seeps detected by the 3.5-kHz profiler.

FIG. 28. Layer 1 Isopach map. Contour interval is 20 m.

FIG. 29. Layer 2 Isopach map.

FIG. 30. Map showing depth to top of layer 3.

FIG. 31. Map of layer 1 velocities. Contour interval 50 m/sec.

FIGURE LEGENDS, Continued, p. 6.

FIG. 32. Map of layer 2 velocities. Contour interval is 100 m/sec.

FIG. 33. Map of layer 3 velocities.

FIG. 34. Refraction structure along A-bearing. Horizontal distances are measured in nm from USN Observation Platform, Stage I. Vertical scale is measured in meters. Vertical exaggeration is about 92. Contours of the smoothed areal maps have been used to draw the structure projected along the bearing from Stage I.

FIG. 35. Velocity variations along A-bearing. Horizontal distances are measured in nm from USN Observation Platform, Stage I. Vertical scale is velocity in m/sec. Contours of the smoothed areal maps have been used to draw the velocity variations projected along the bearing from Stage I.

FIG. 36. Refraction structure along B-bearing.

FIG. 37. Velocity variations along B-bearing.

CSP REFRACTION GEOMETRY

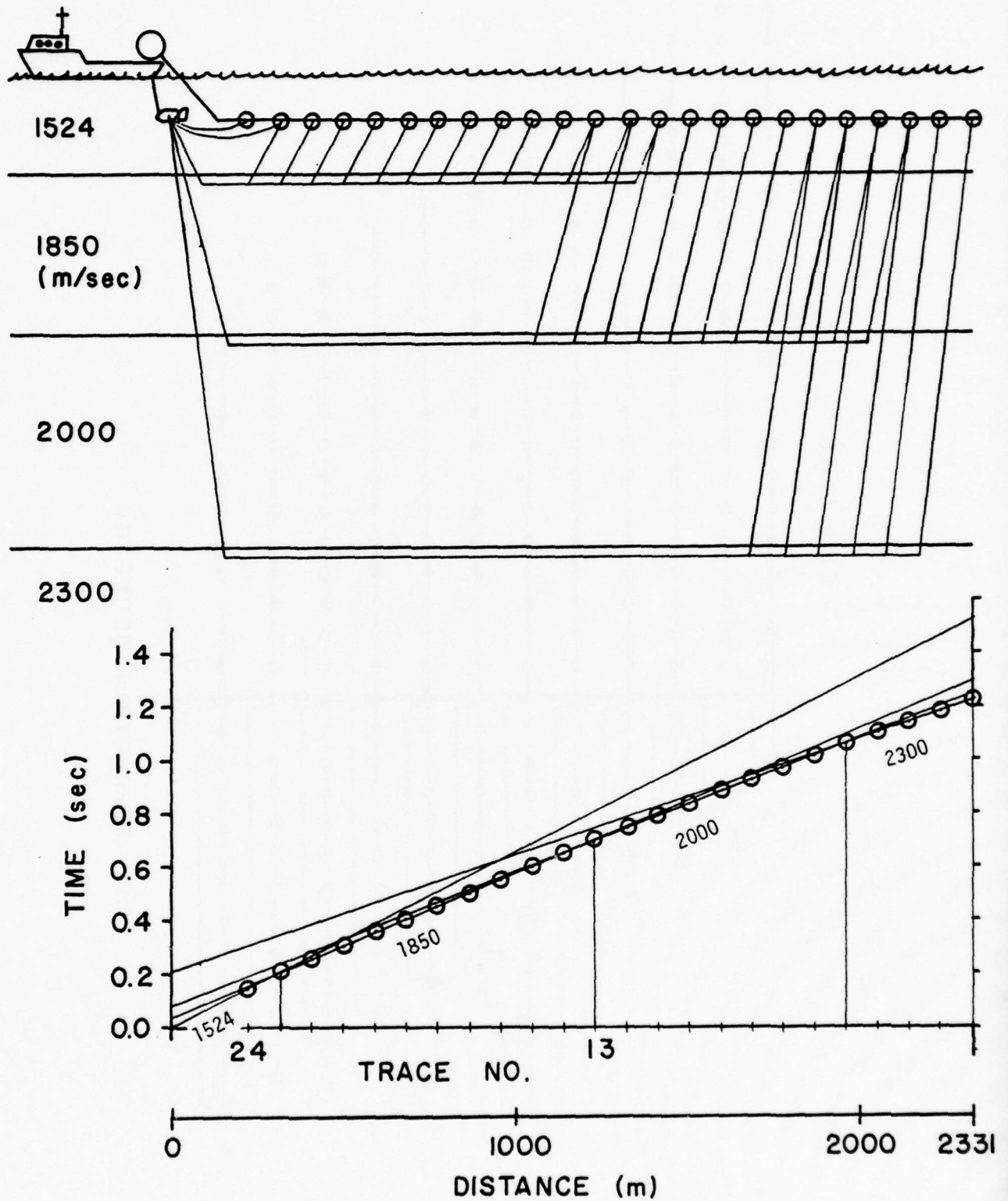
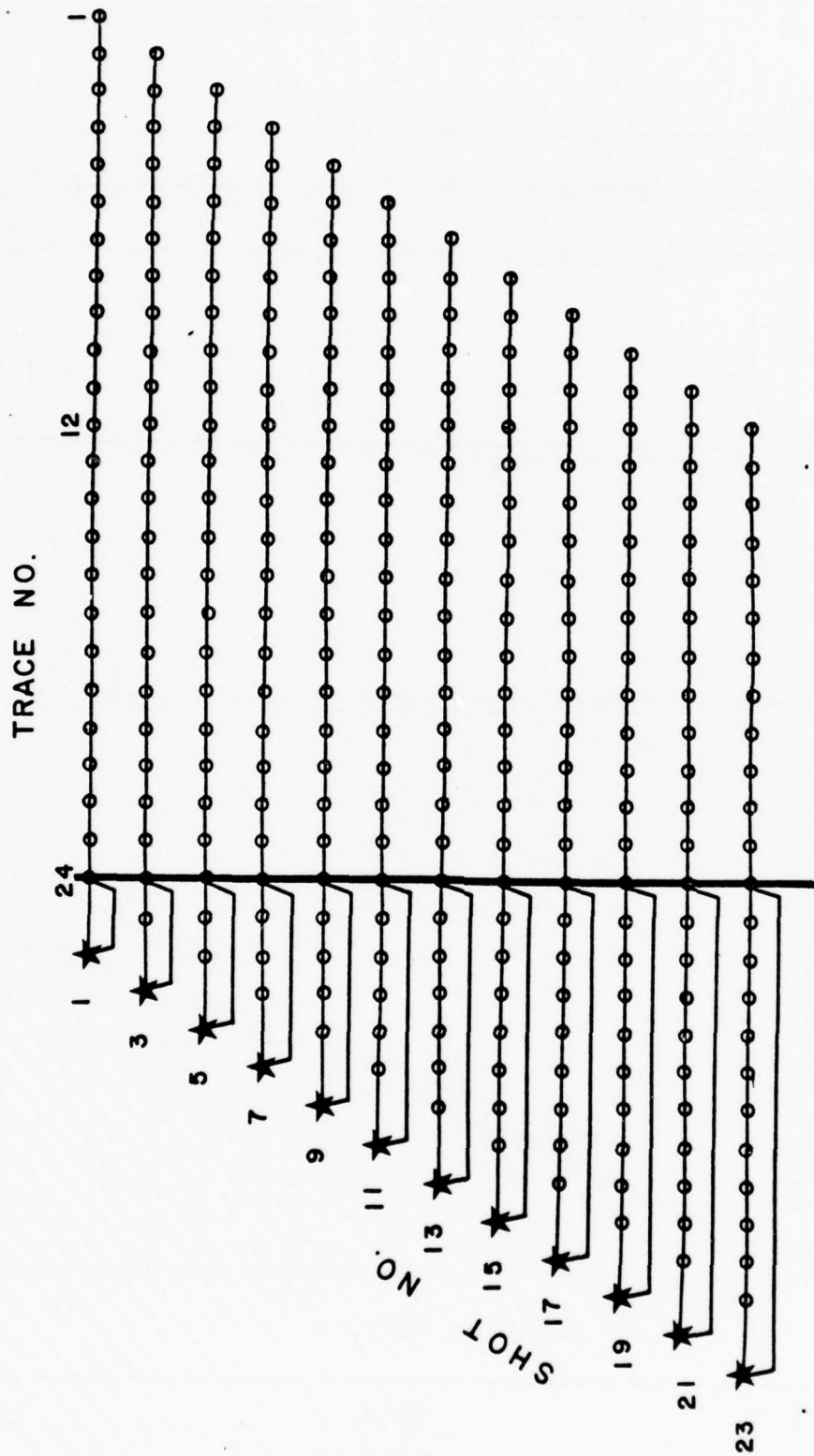


FIG. 1



CRP REFRACTION GEOMETRY

FIG. 2

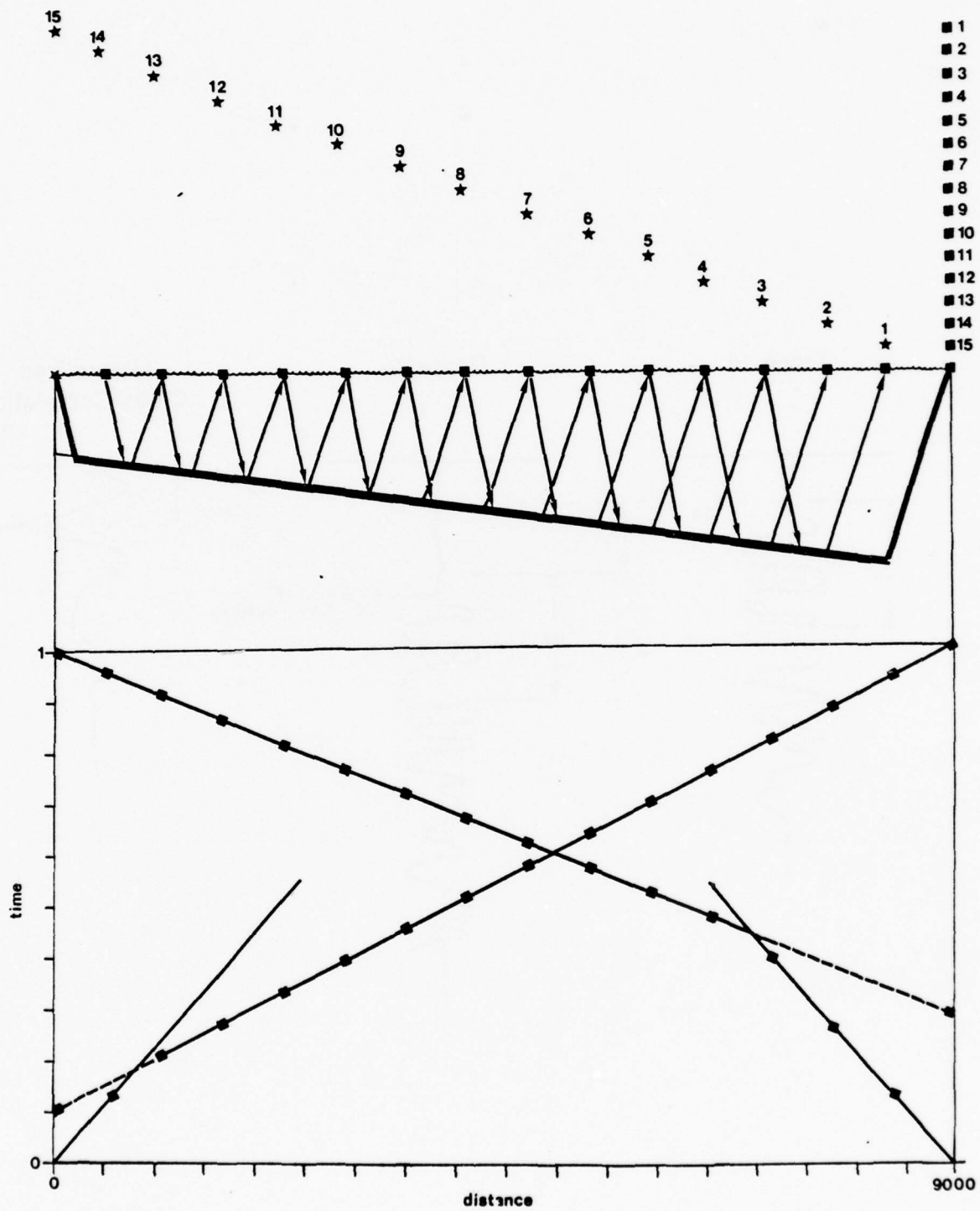


FIG. 3

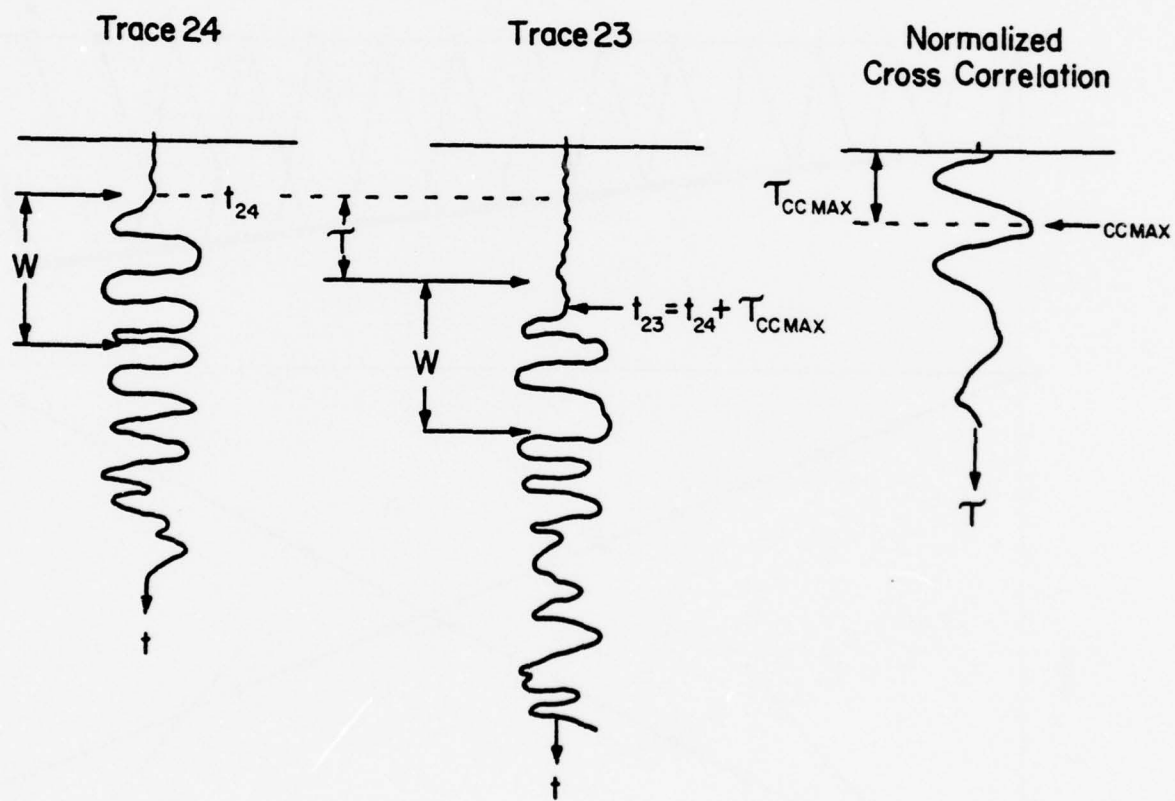
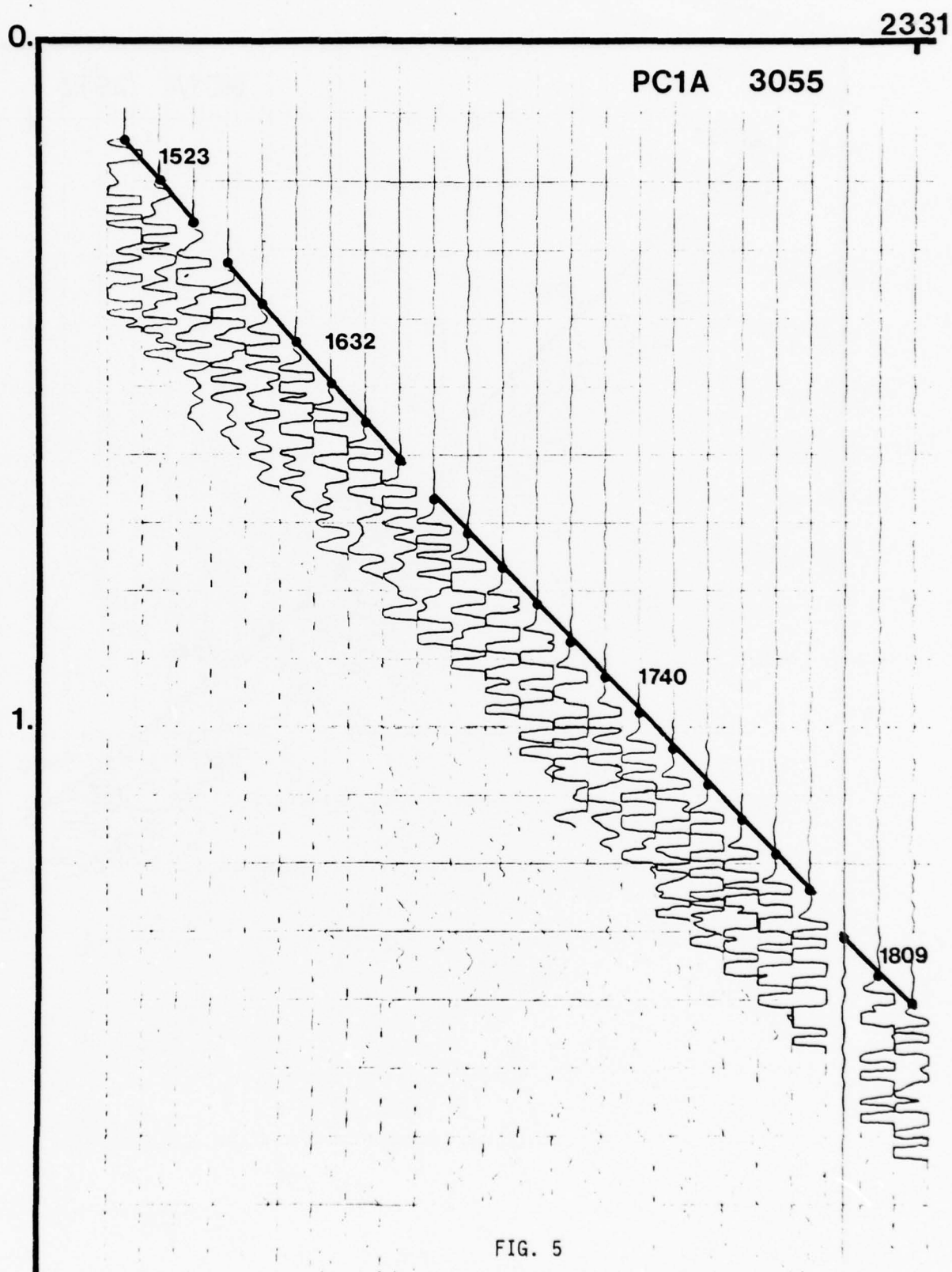
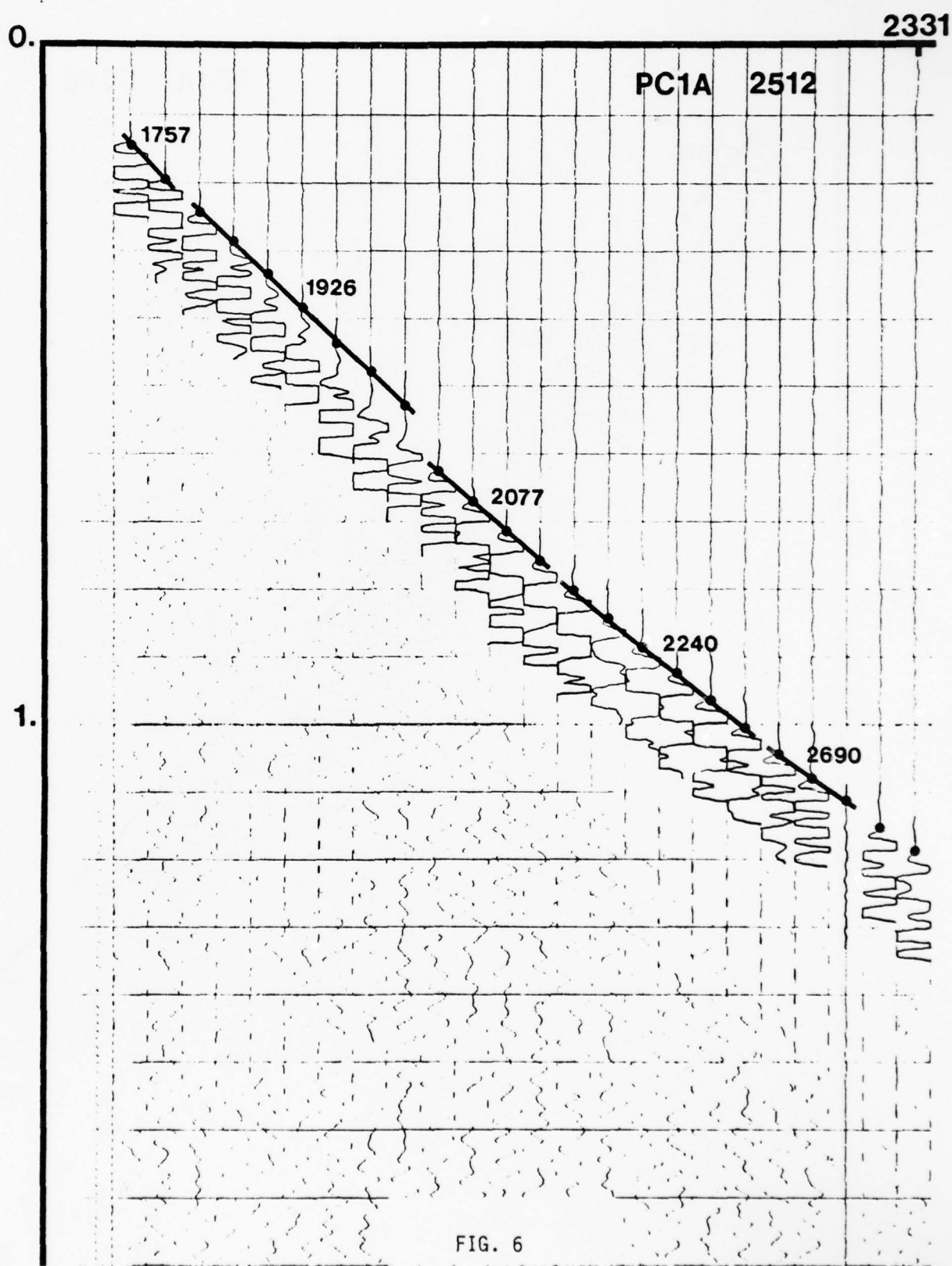


FIG. 4





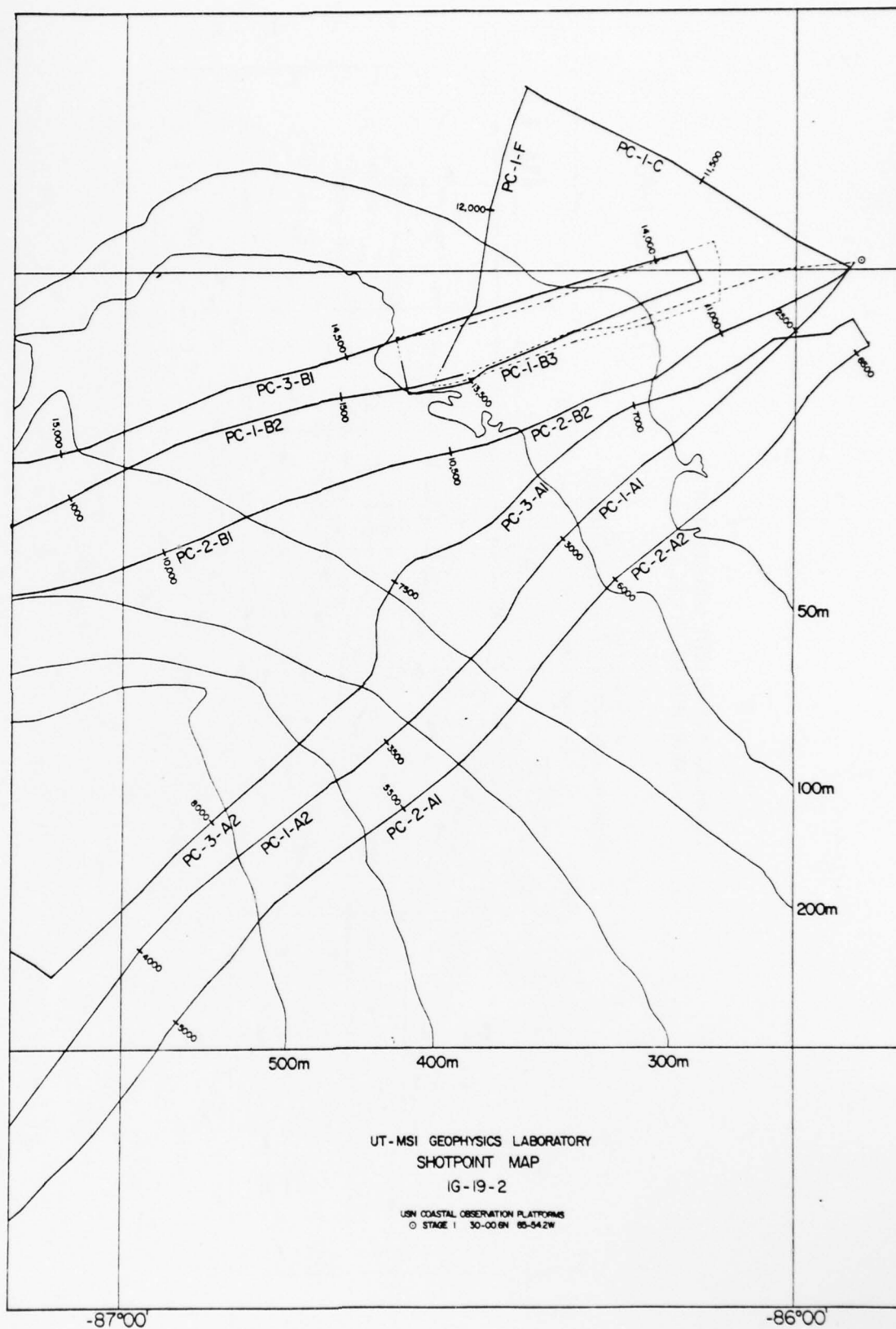


FIG. 7

OCEAN BOTTOM VELOCITY MEASUREMENT
NEAR PANAMA CITY, FLA

LINE PC-1-A1

SHALLOW
BY REFRACTION FROM MULTI-CHANNEL STREAMER

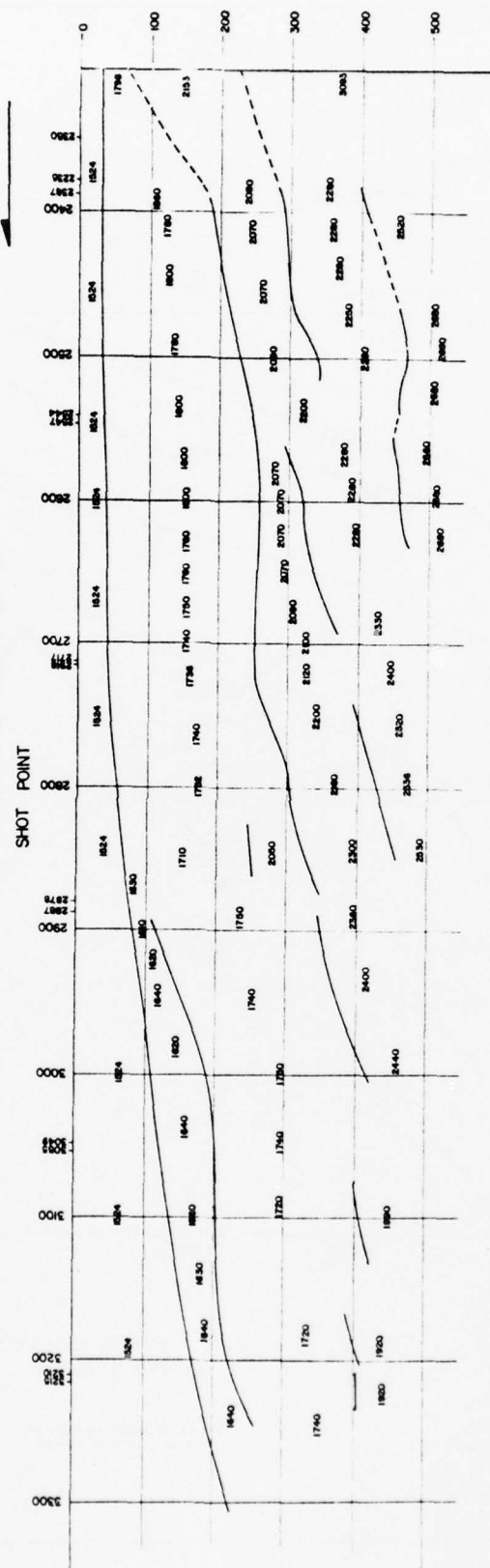


FIG. 8

OCEAN BOTTOM VELOCITY MEASUREMENTS
NEAR PANAMA CITY, FLA

LINE PC-2-A2

SHALLOW
BY REFRACTION FROM MULTI-CHANNEL STREAMER

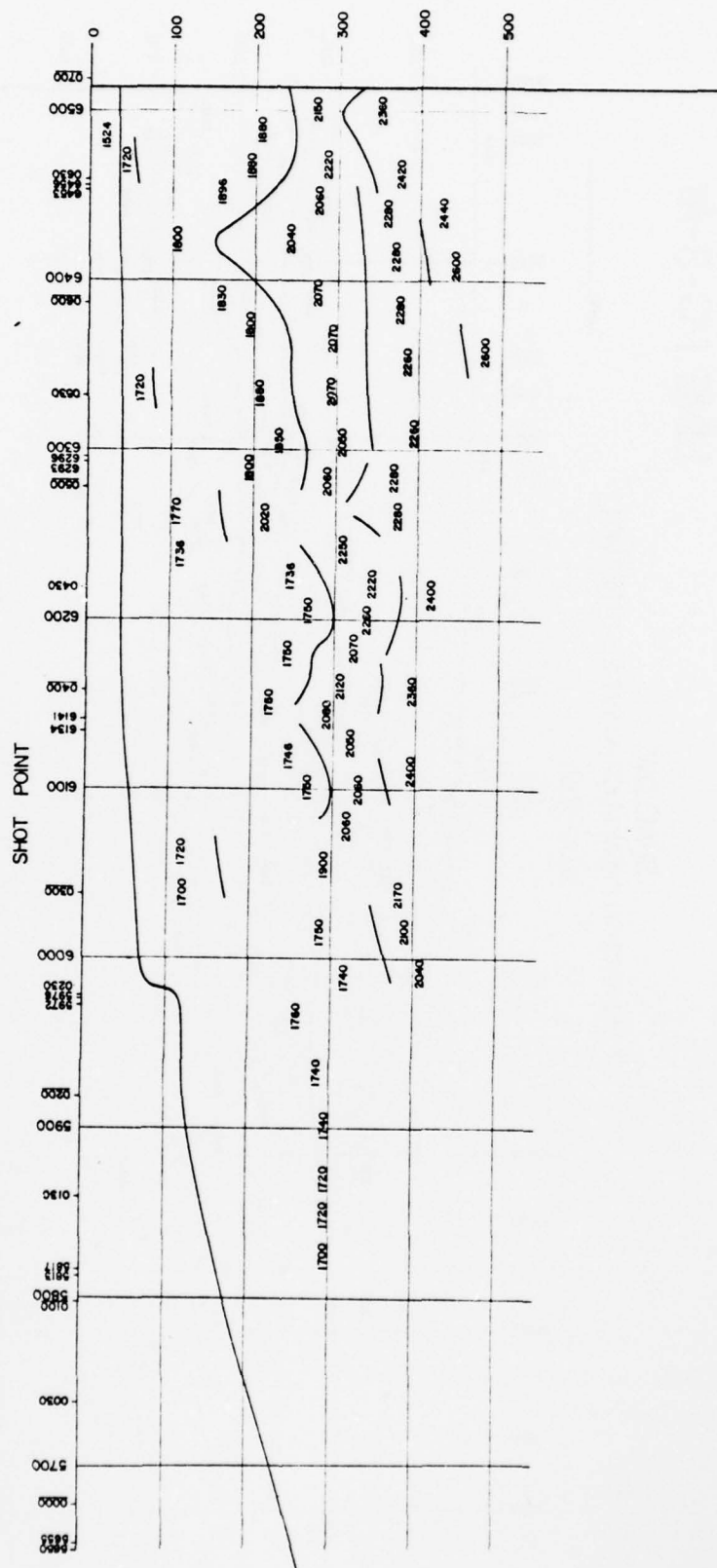


FIG. 9

OCEAN BOTTOM VELOCITY MEASUREMENTS
NEAR PANAMA CITY, FLA

LINE PC-3-A1

SHALLOW
BY REFRACTION FROM MULTI-CHANNEL STREAMER

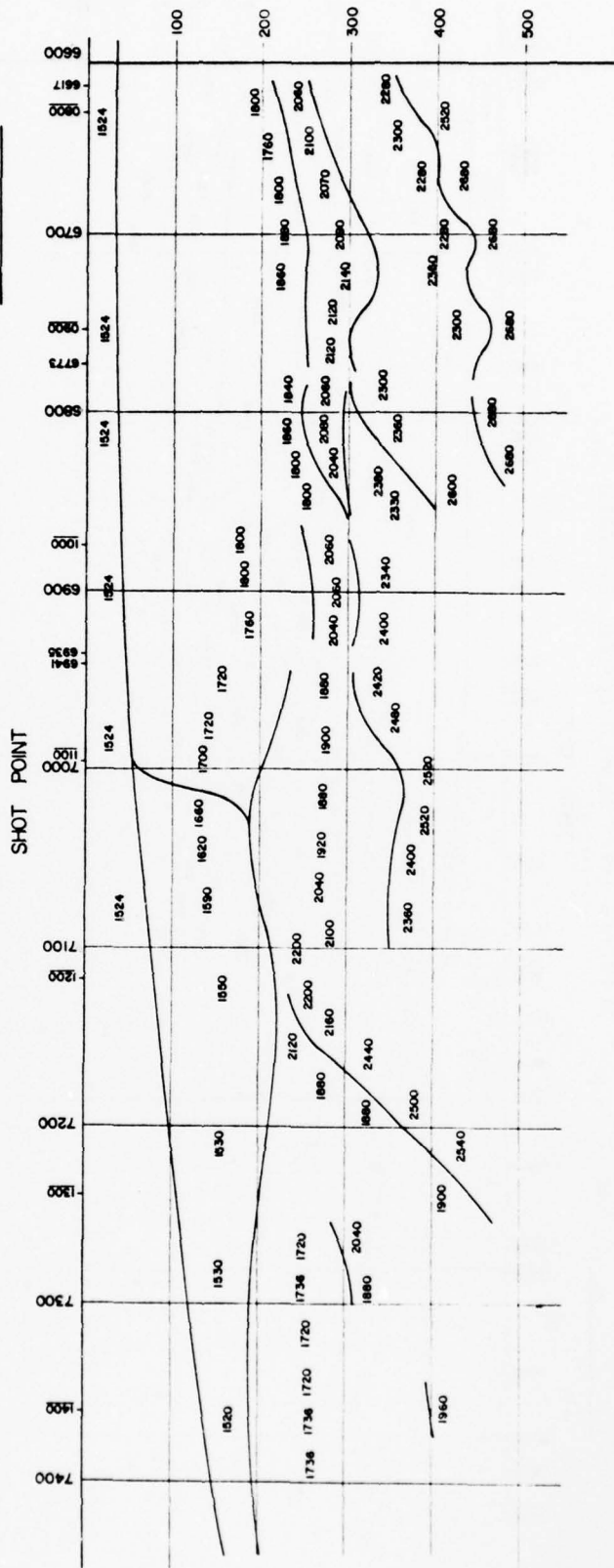


FIG. 10

OCEAN BOTTOM VELOCITY MEASUREMENTS
NEAR PANAMA CITY, FLA.

LINE PC-2-B2

SHALLOW
BY REFRACTION FROM MULTI-CHANNEL STREAMER

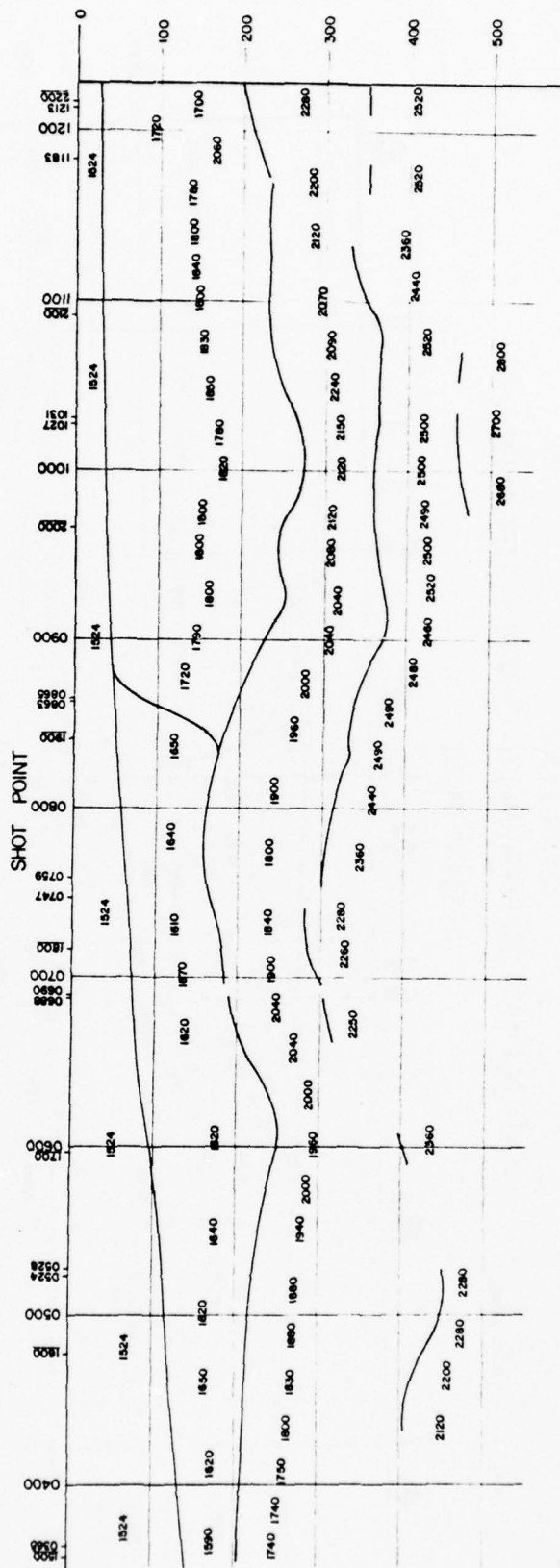


FIG. 11

LINE PC-1-B3

SHALLOW BY REFRACTION FROM MULTI-CHANNEL STREAMER

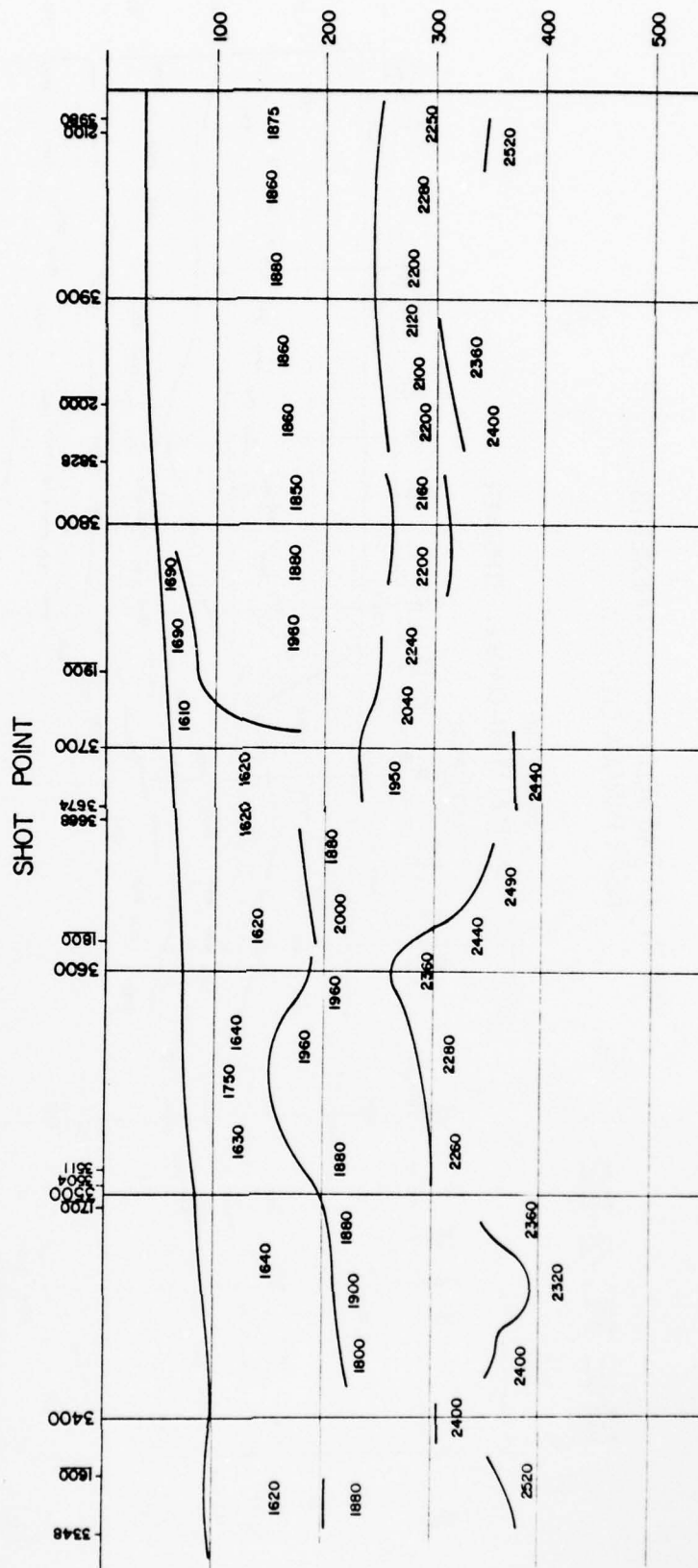


FIG. 12

LINE PC-3-BI

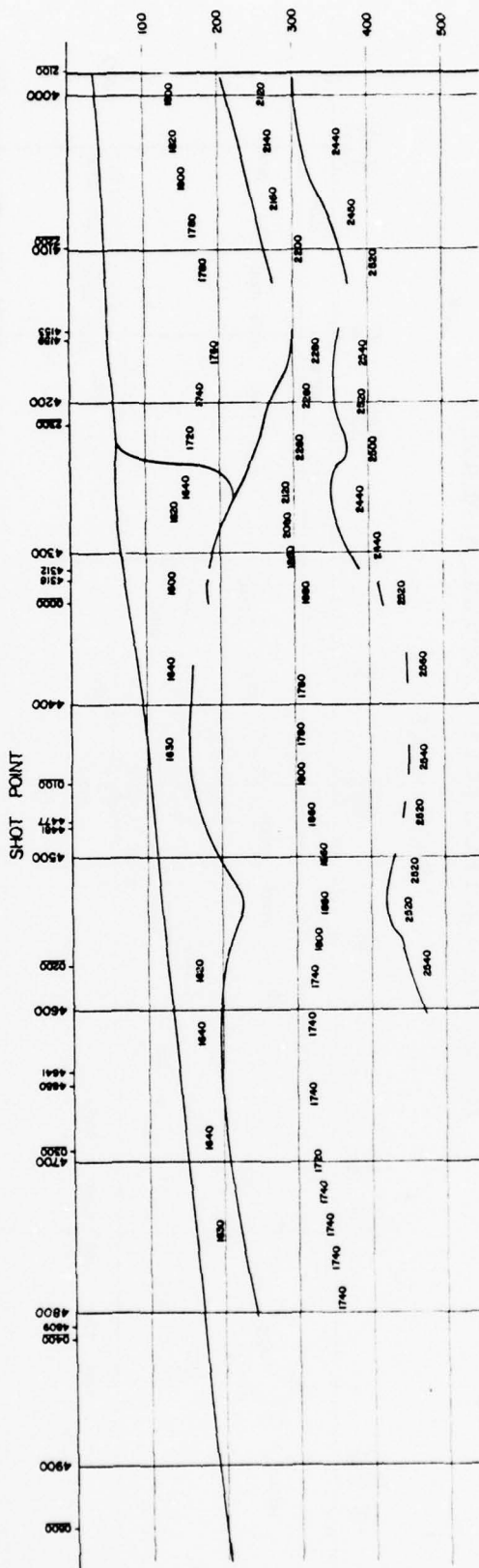
SHALLOW
BY REFRACTION FROM MULTI-CHANNEL STREAMER

FIG. 13

OCEAN BOTTOM VELOCITY MEASUREMENTS
NEAR PANAMA CITY, FLA.

LINE PC-1-C

SHALLOW

BY REFRACTION FROM MULTI-CHANNEL STREAMER

SHOT POINT

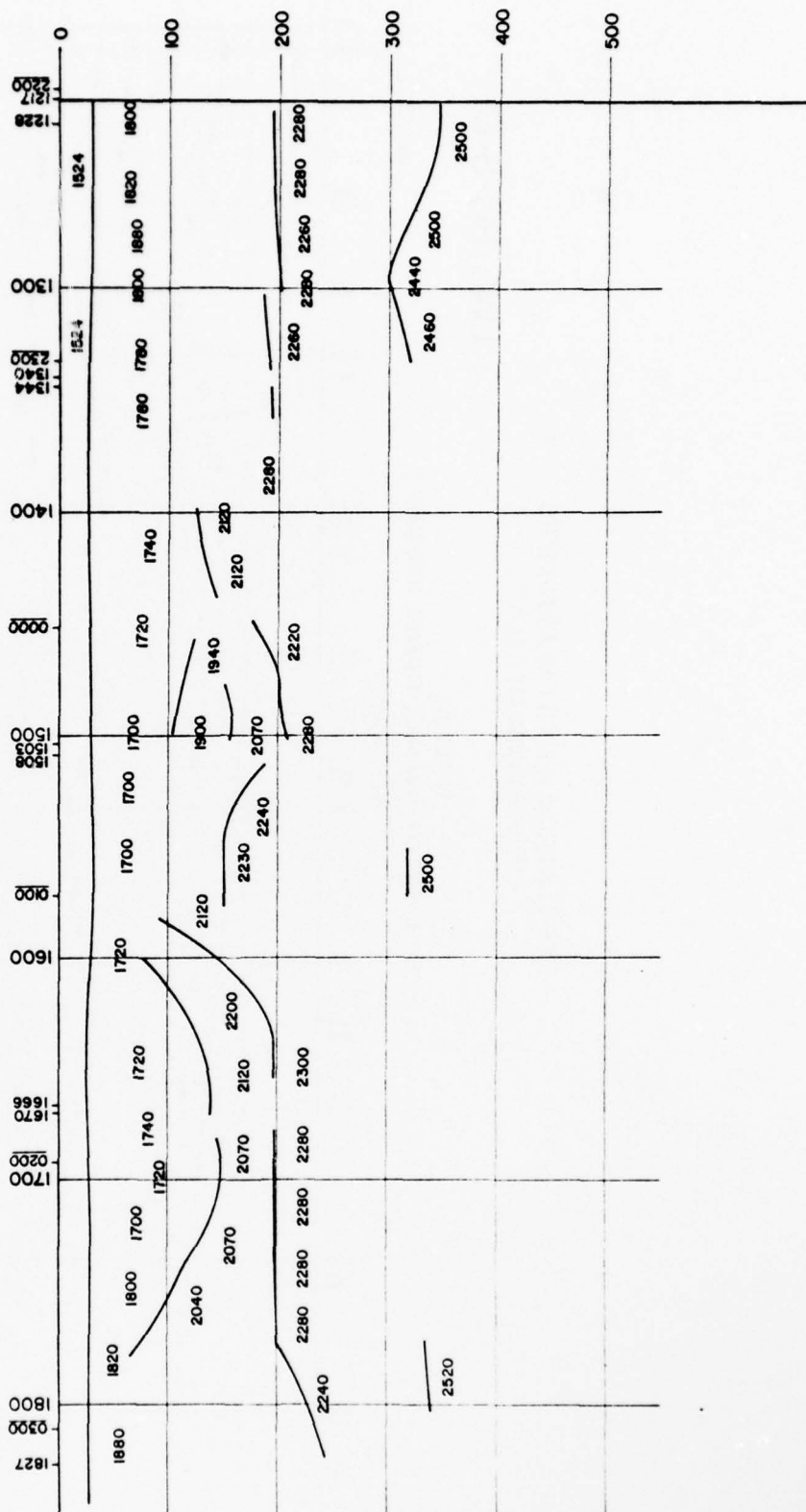


FIG. 14

OCEAN BOTTOM VELOCITY MEASUREMENTS
NEAR PANAMA CITY, FLA.

LINE PC-1-F

SHALLOW
BY REFRACTION FROM MULTI-CHANNEL STREAMER

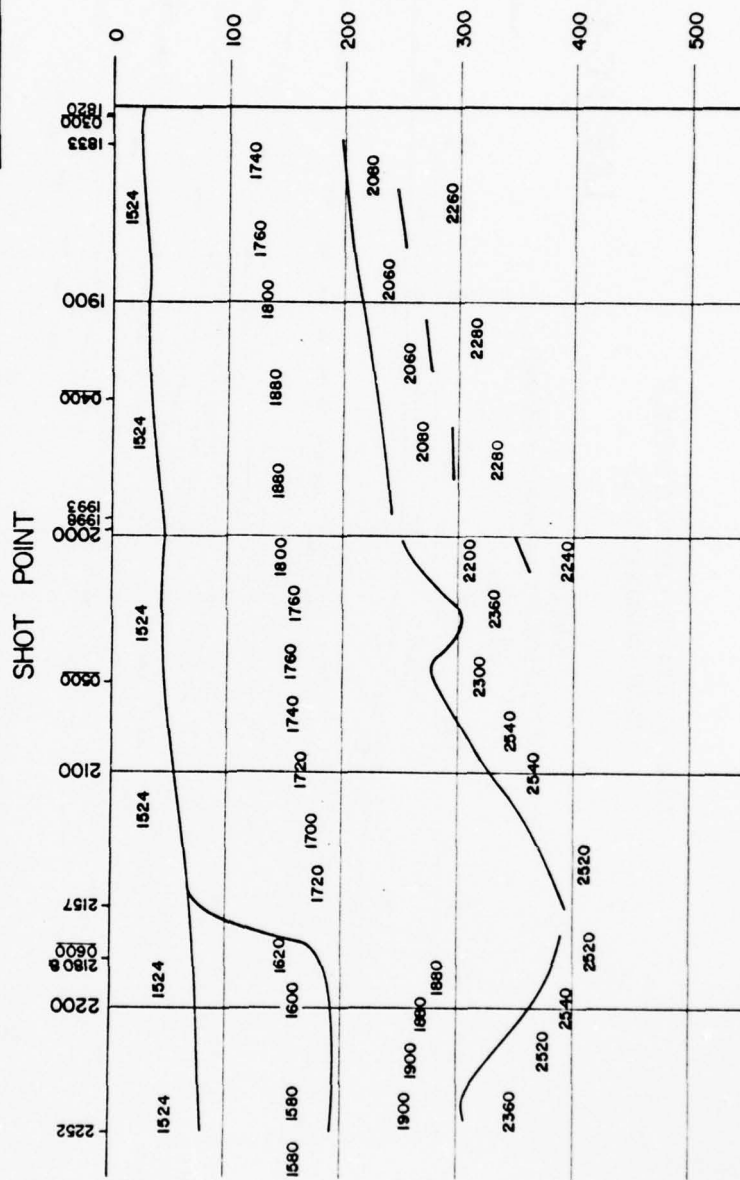
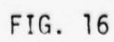


FIG. 15

LINE PC-1-A1

SHALLOW
BY REFRACTION FROM MULTI-CHANNEL STREAMER

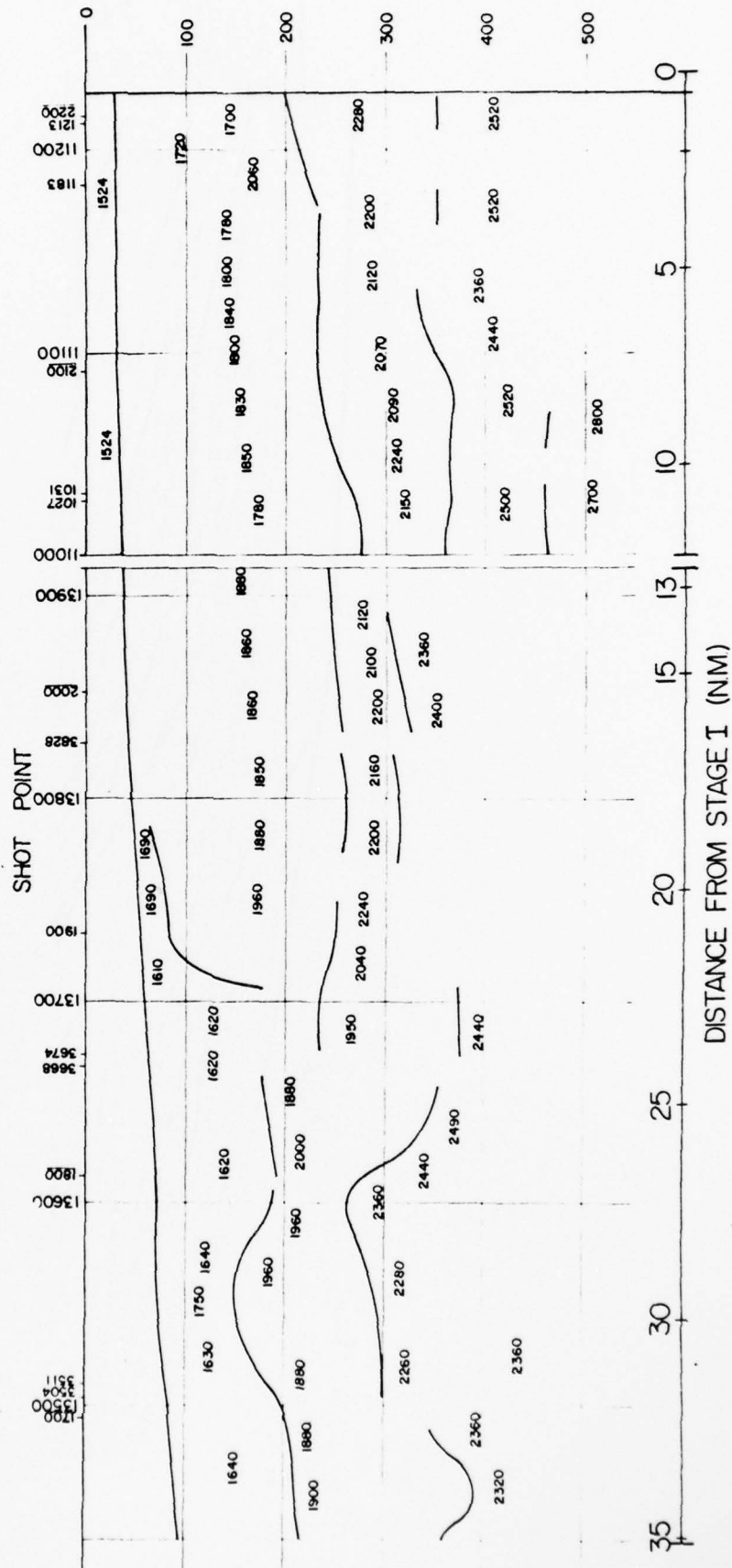


OCEAN BOTTOM VELOCITY MEASUREMENTS NEAR PANAMA CITY, FLA.

LINE PC-1 B3

LINE PC-2-B2

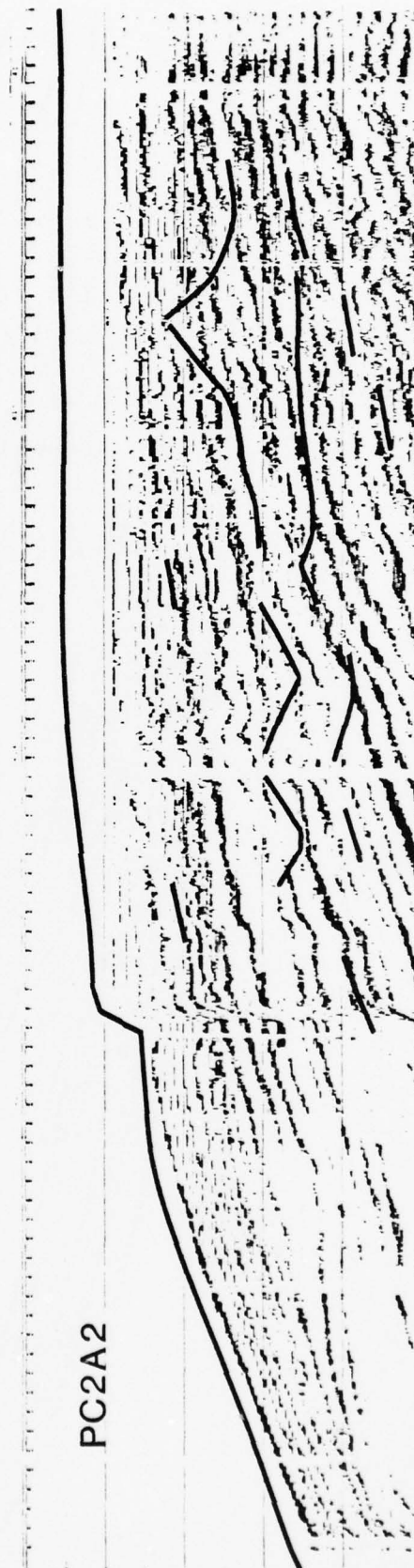
SHALLOW
BY REFRACTION FROM MULTI-CHANNEL STREAMER



PC1A1



FIG. 18



PC2A2

FIG. 19

PC3A1

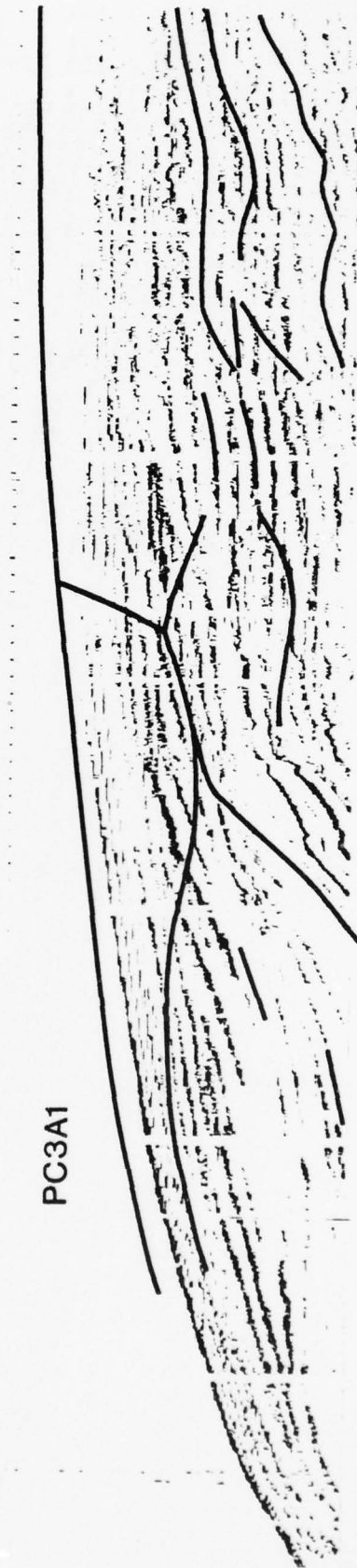


FIG. 20

AD-A063 163

OFFICE OF NAVAL RESEARCH ARLINGTON VA
PROCEEDINGS OF THE WORKSHOP ON SEISMIC PROPAGATION IN SHALLOW W--ETC(U)
JUL 78

F/G 8/11

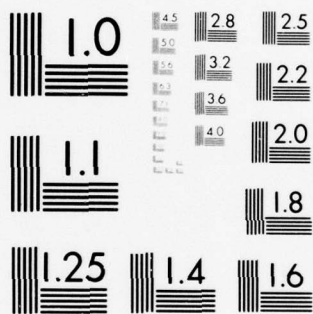
UNCLASSIFIED

NL

3 OF 5

AD
A063163





MICROCOPY RESOLUTION TEST CHART
NATIONAL BUREAU OF STANDARDS-1963-A

PC2B2



FIG. 21

PC1B3

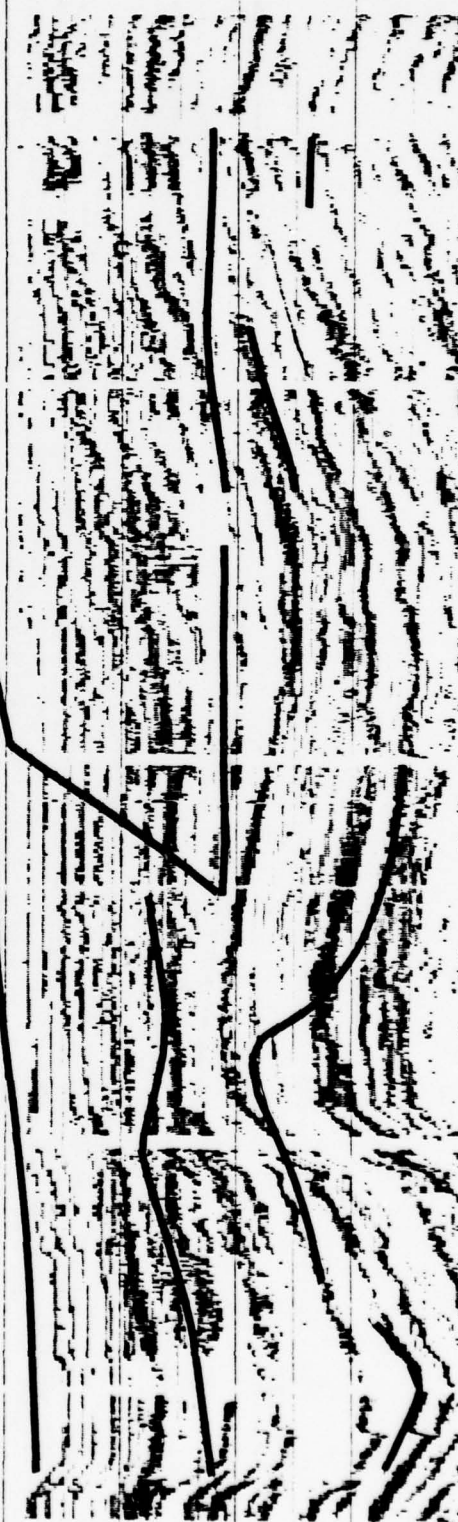


FIG. 22

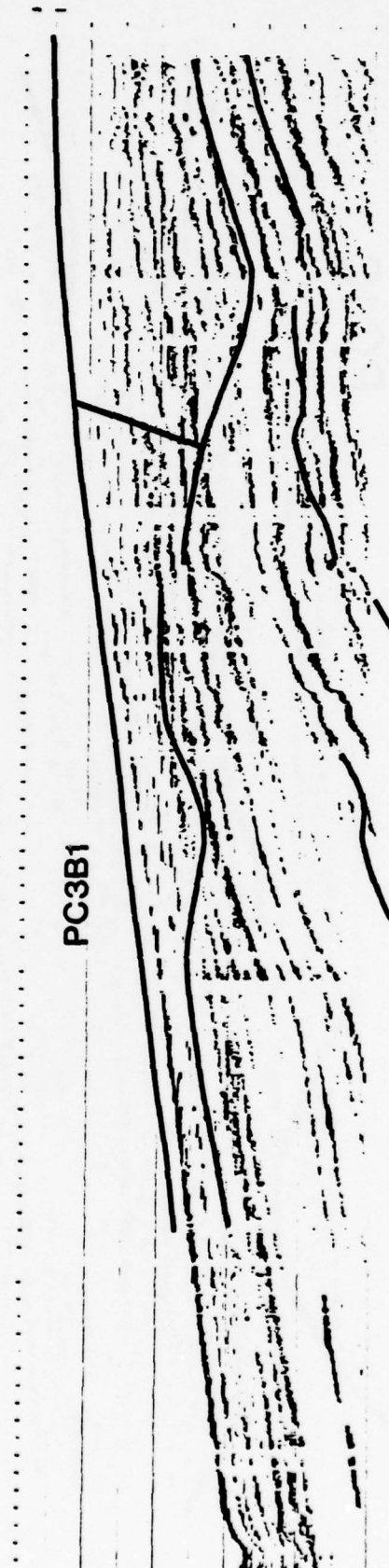


FIG. 23

PC1C

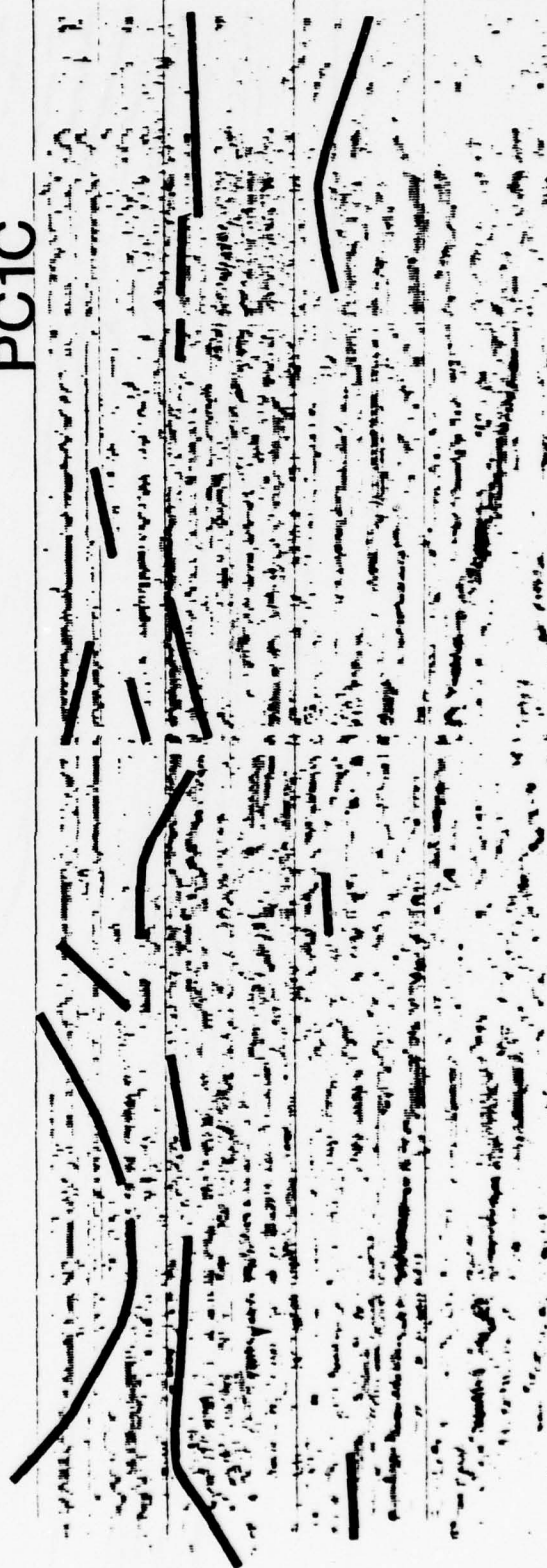
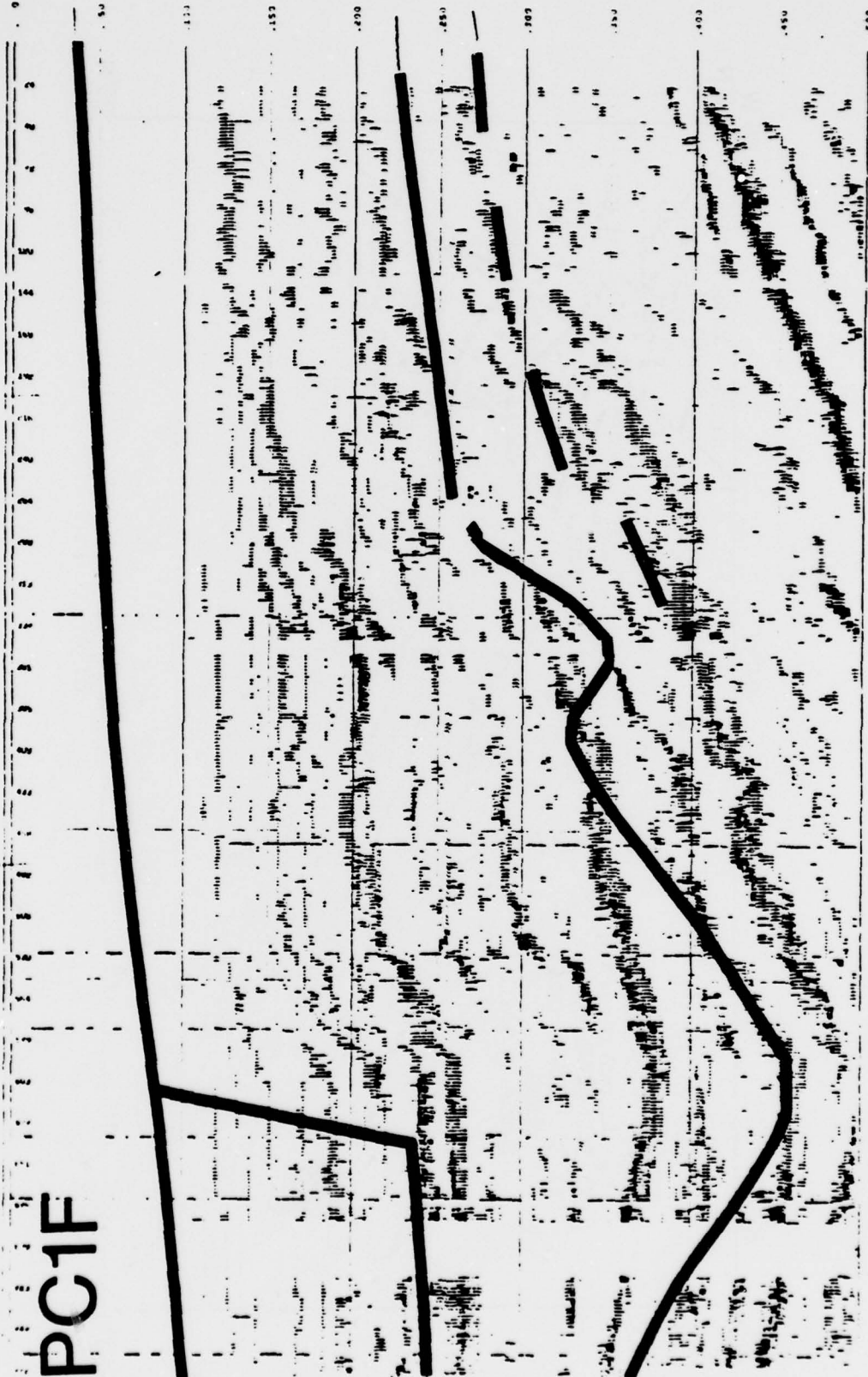


FIG. 24



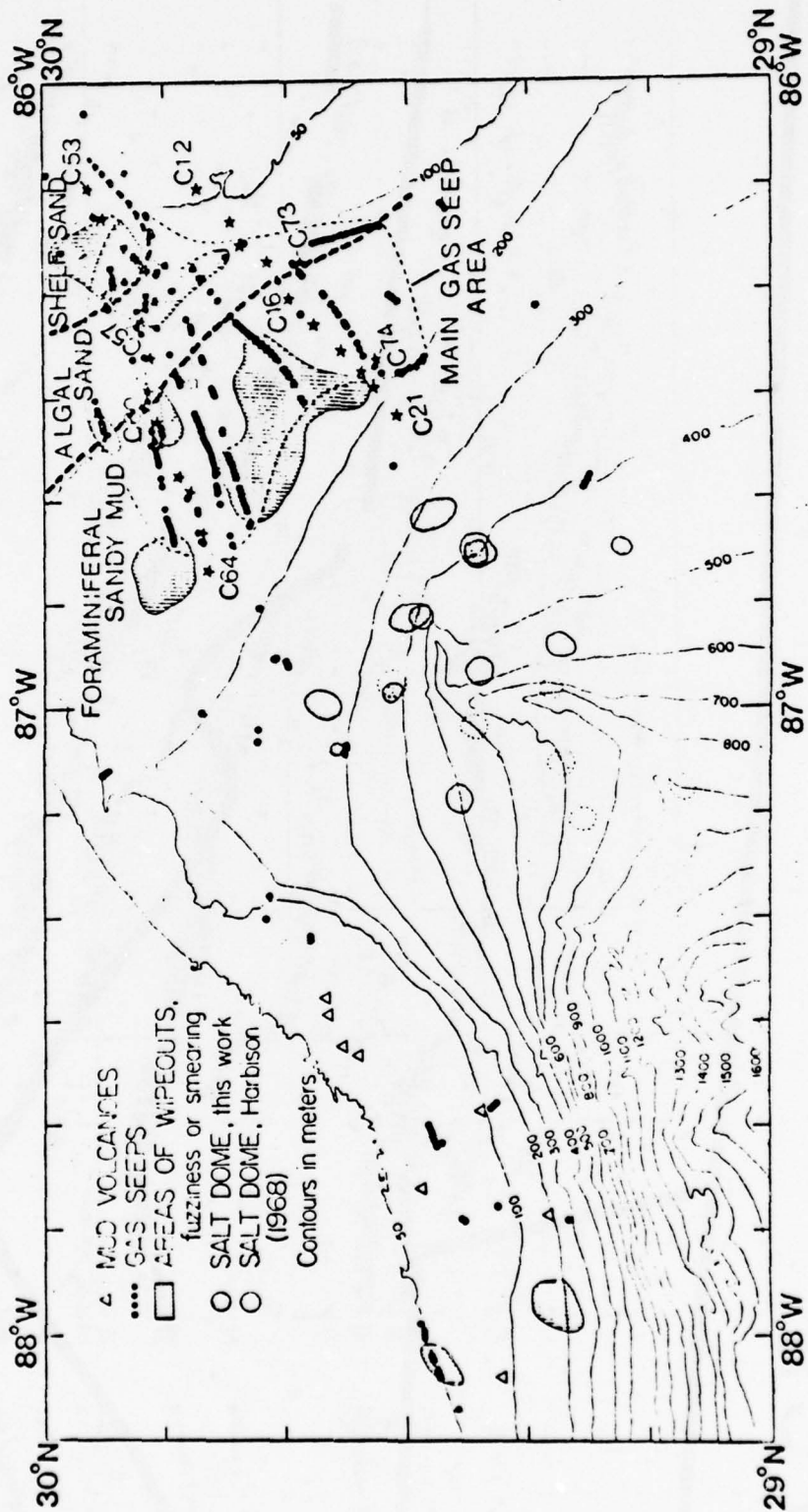


FIG. 26a

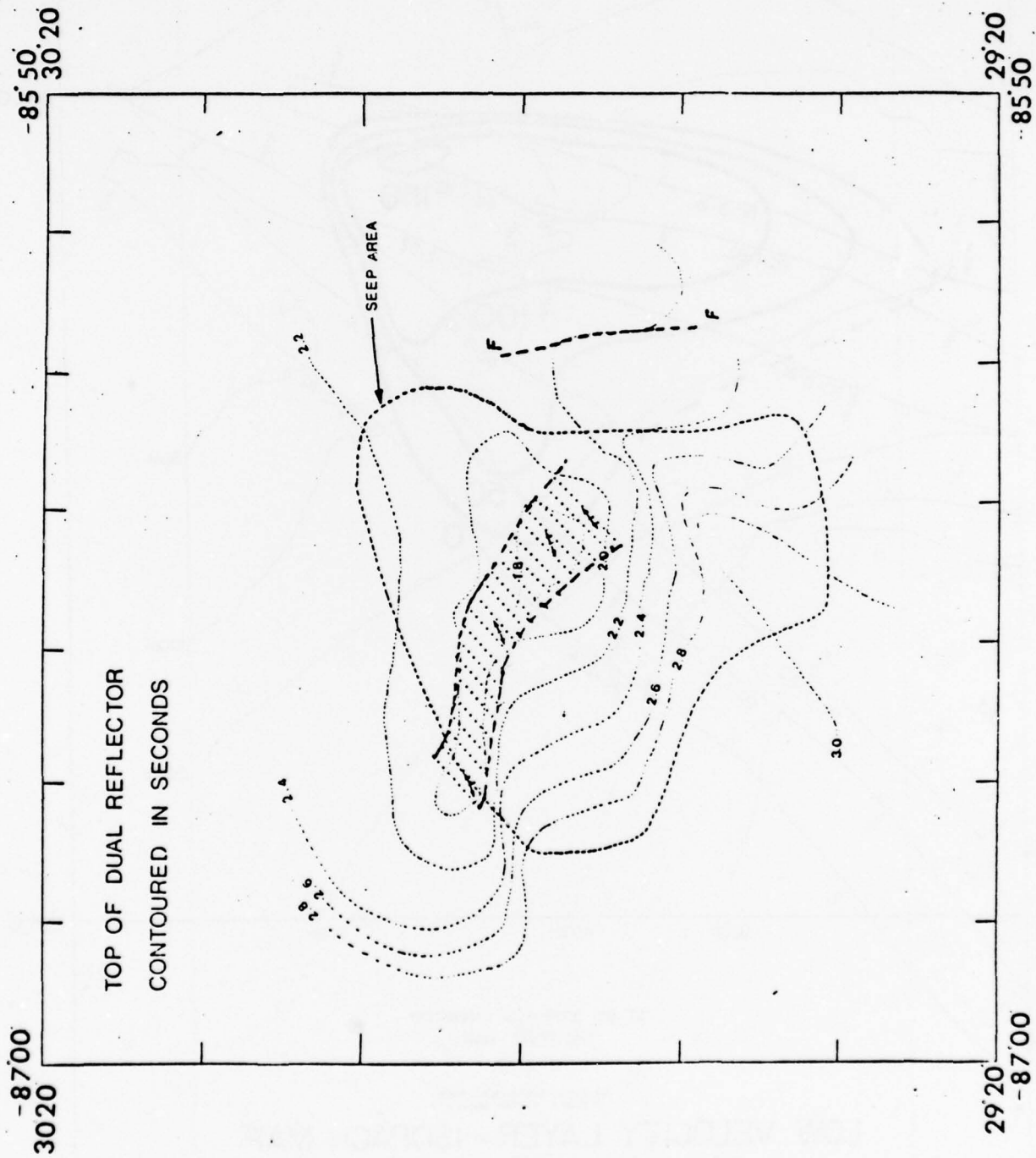


FIG. 26b

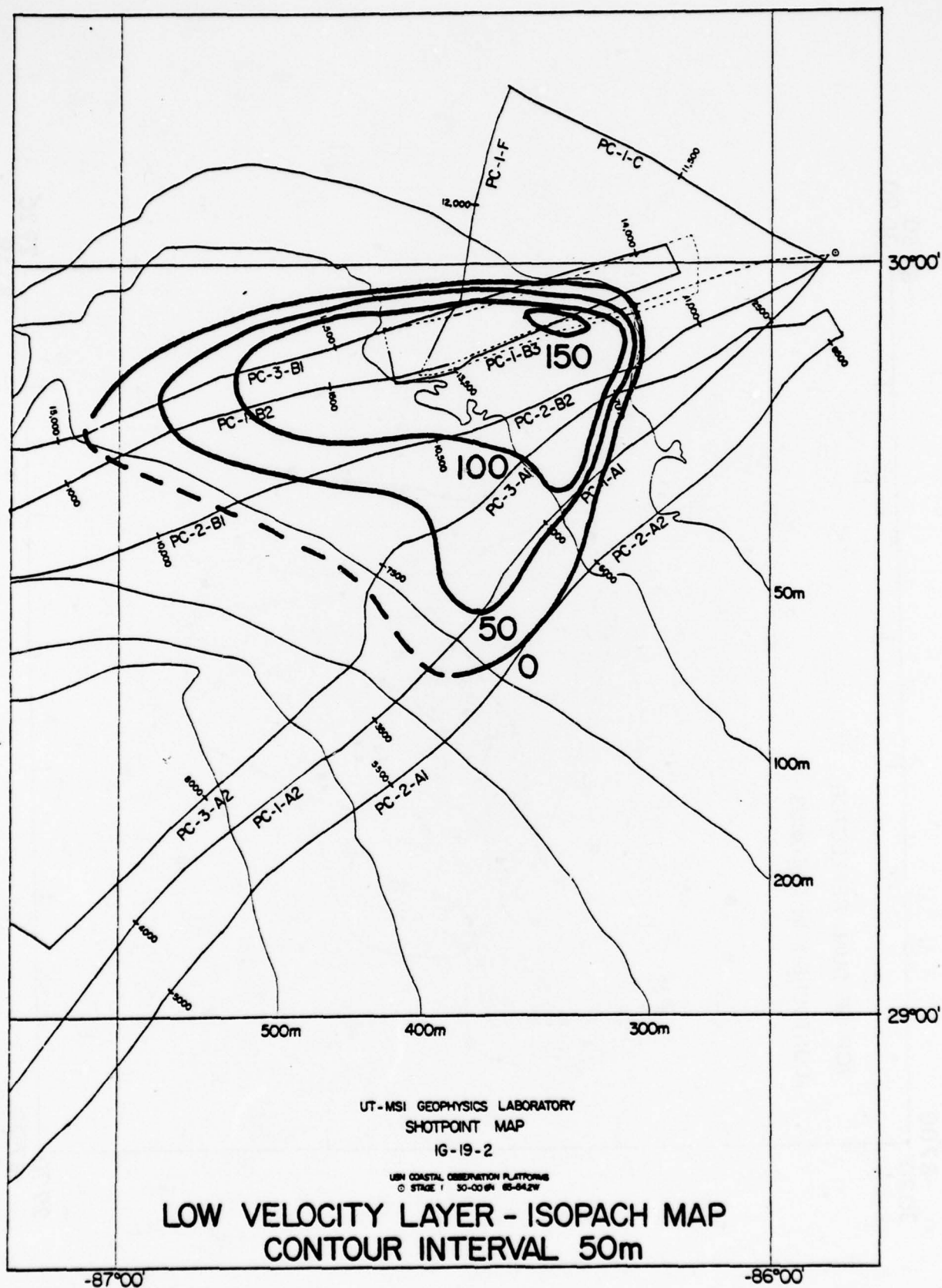


FIG. 27

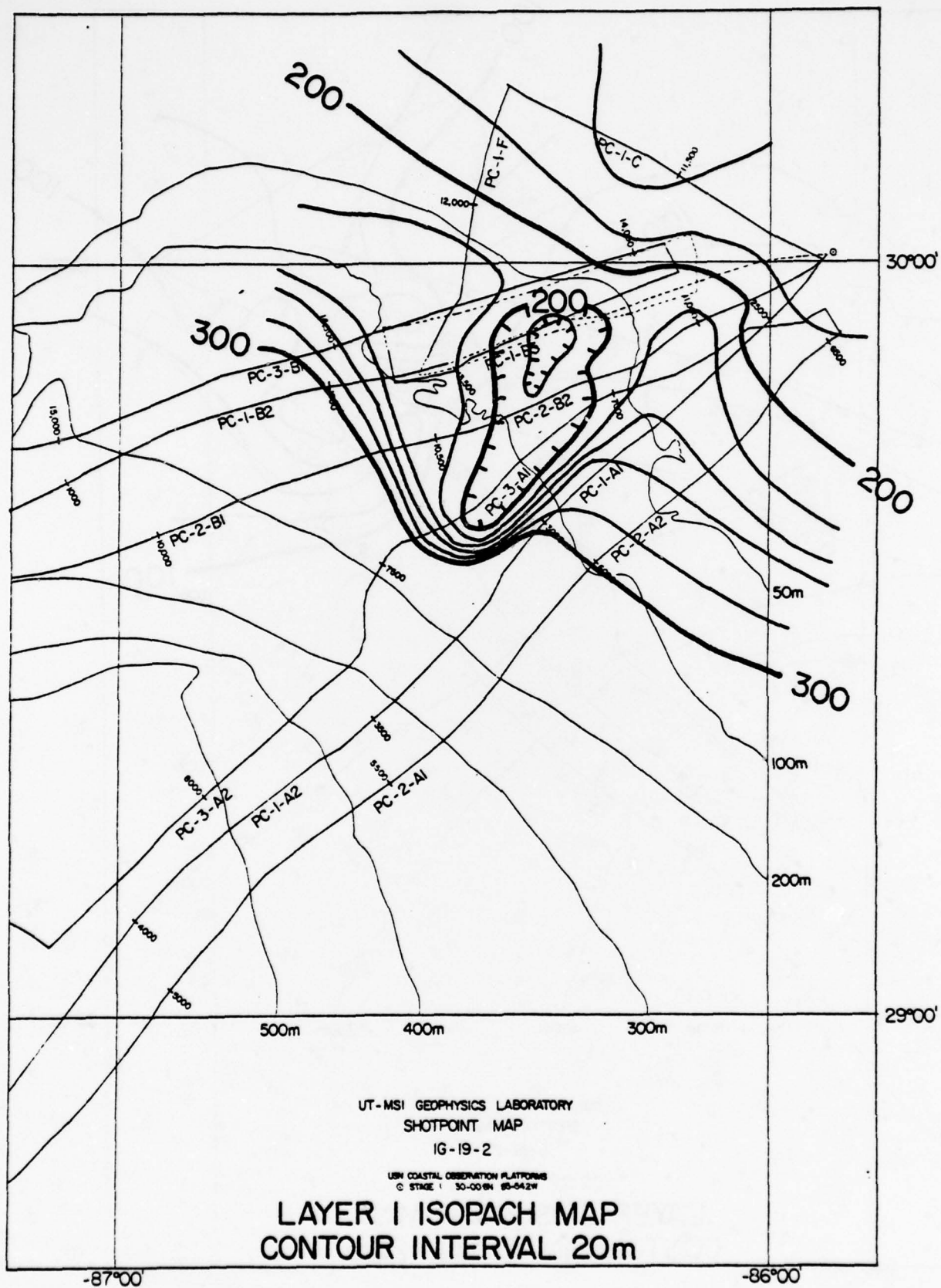


FIG. 28

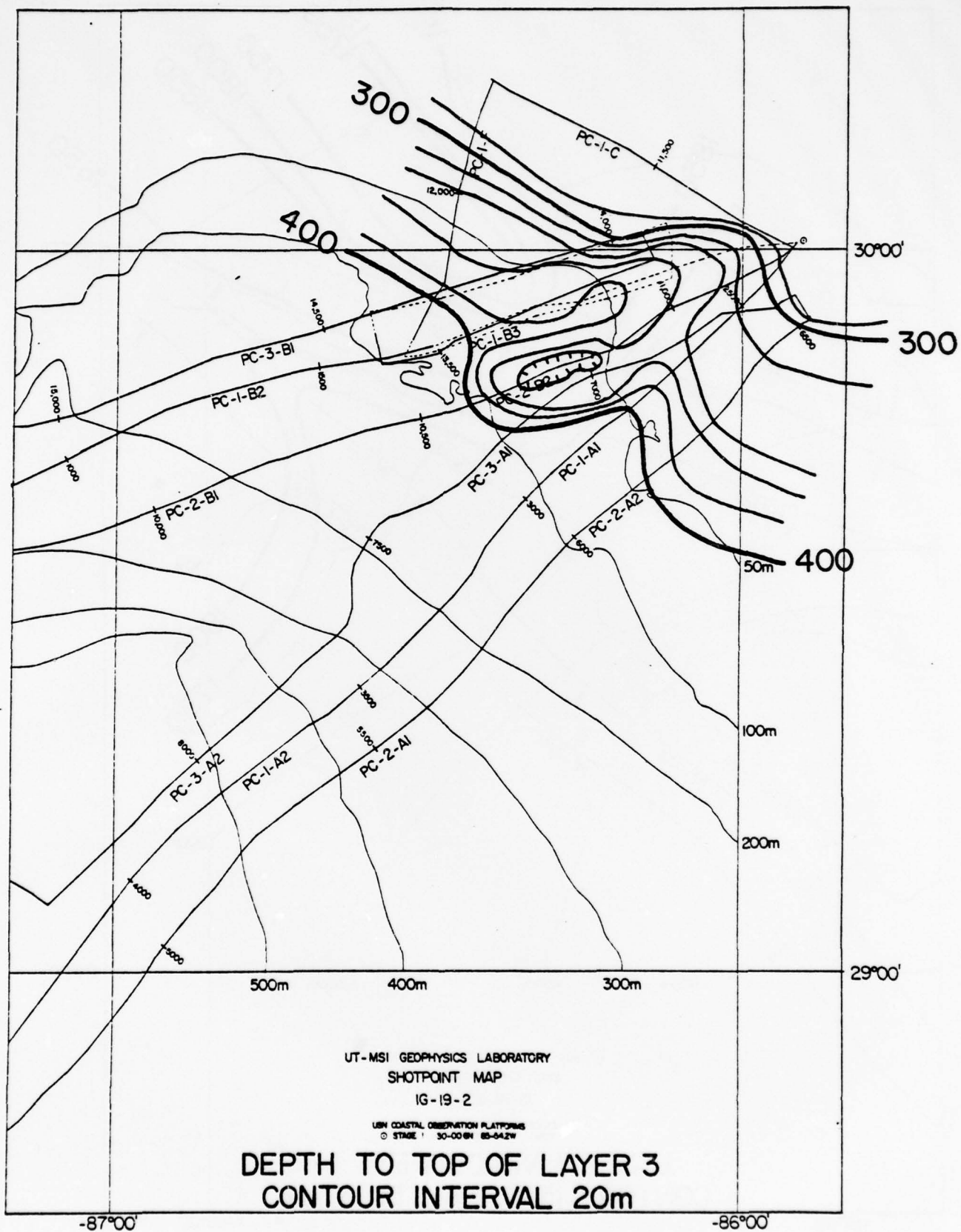


FIG. 30

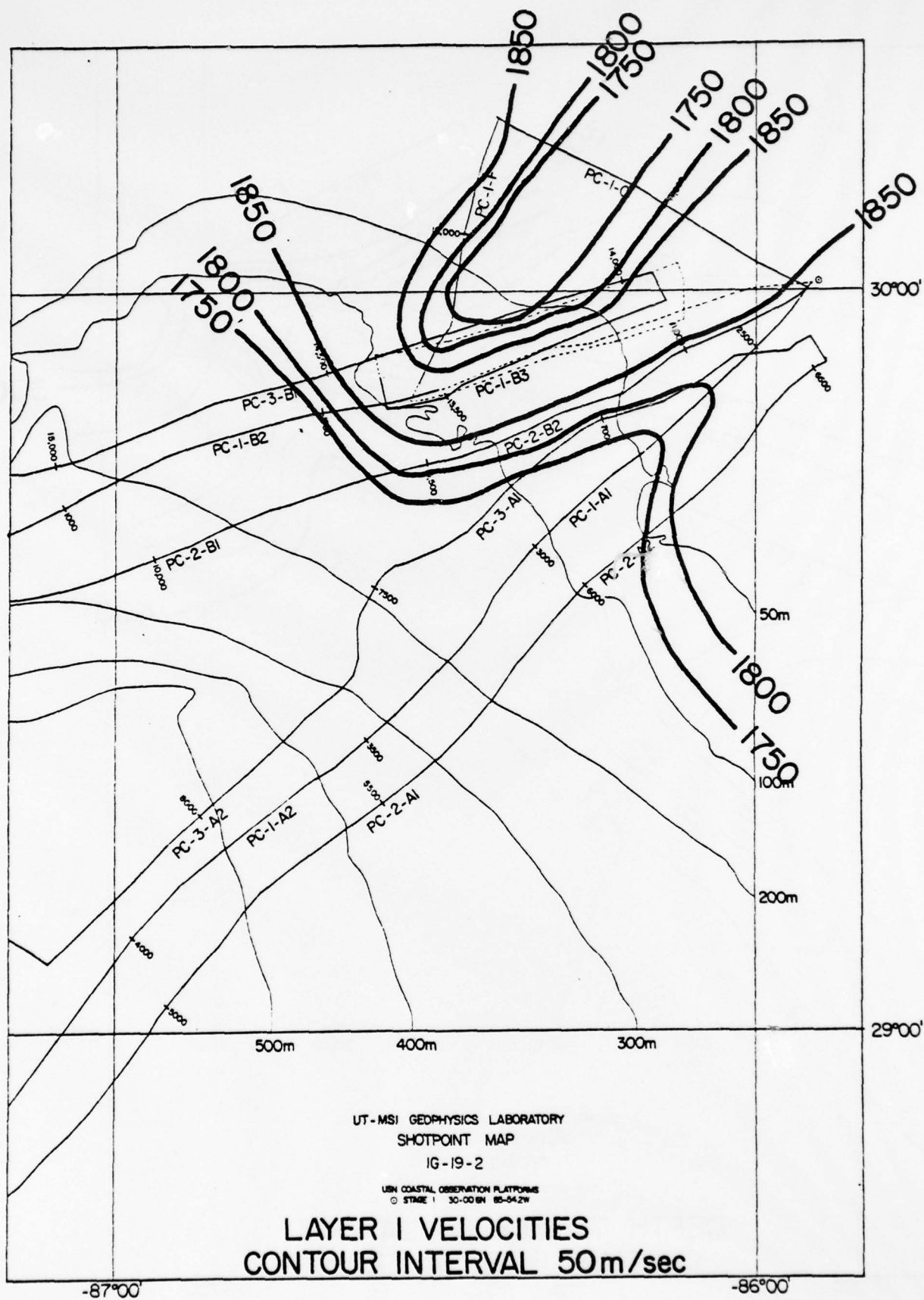


FIG. 31

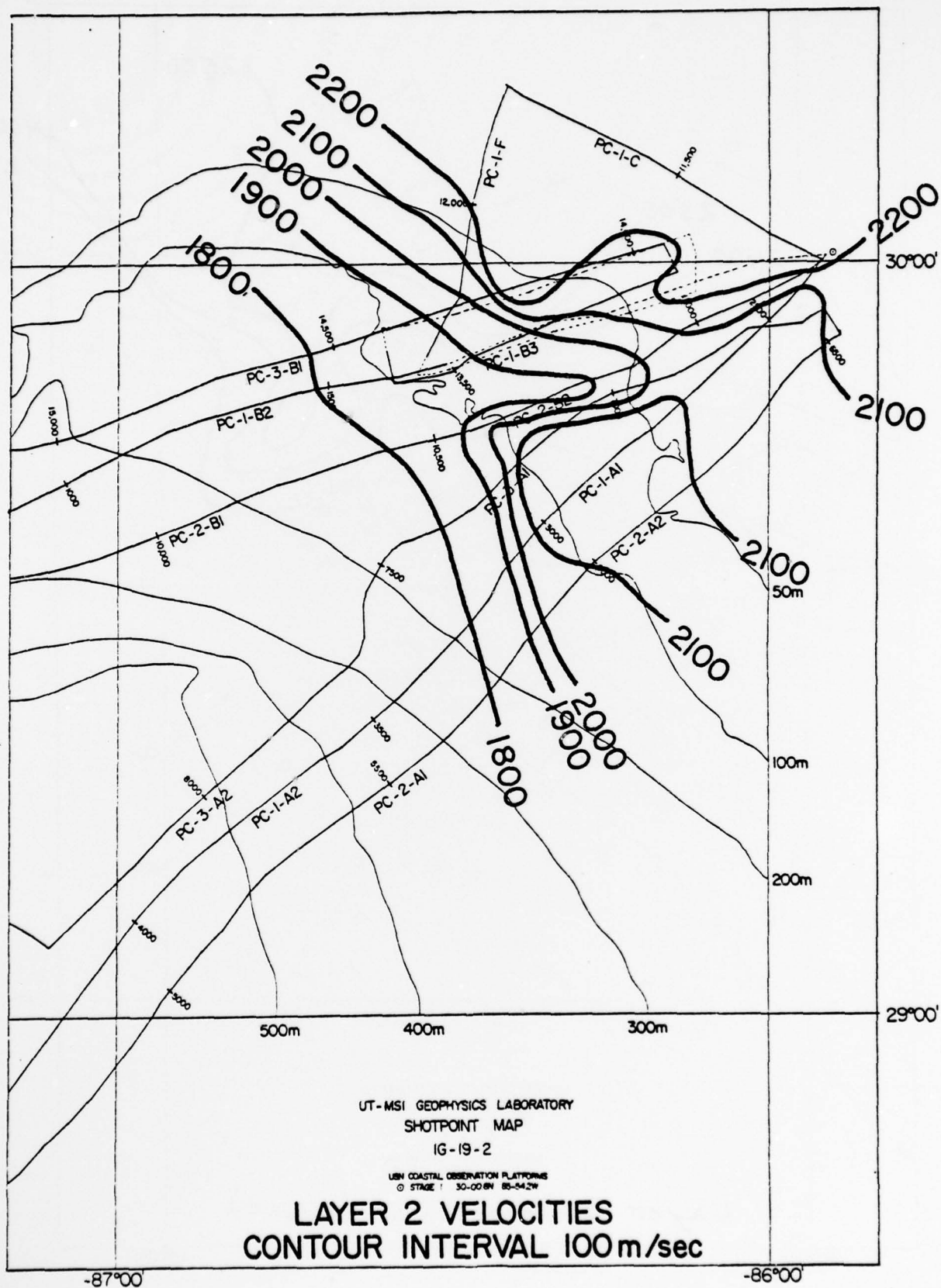


FIG. 32

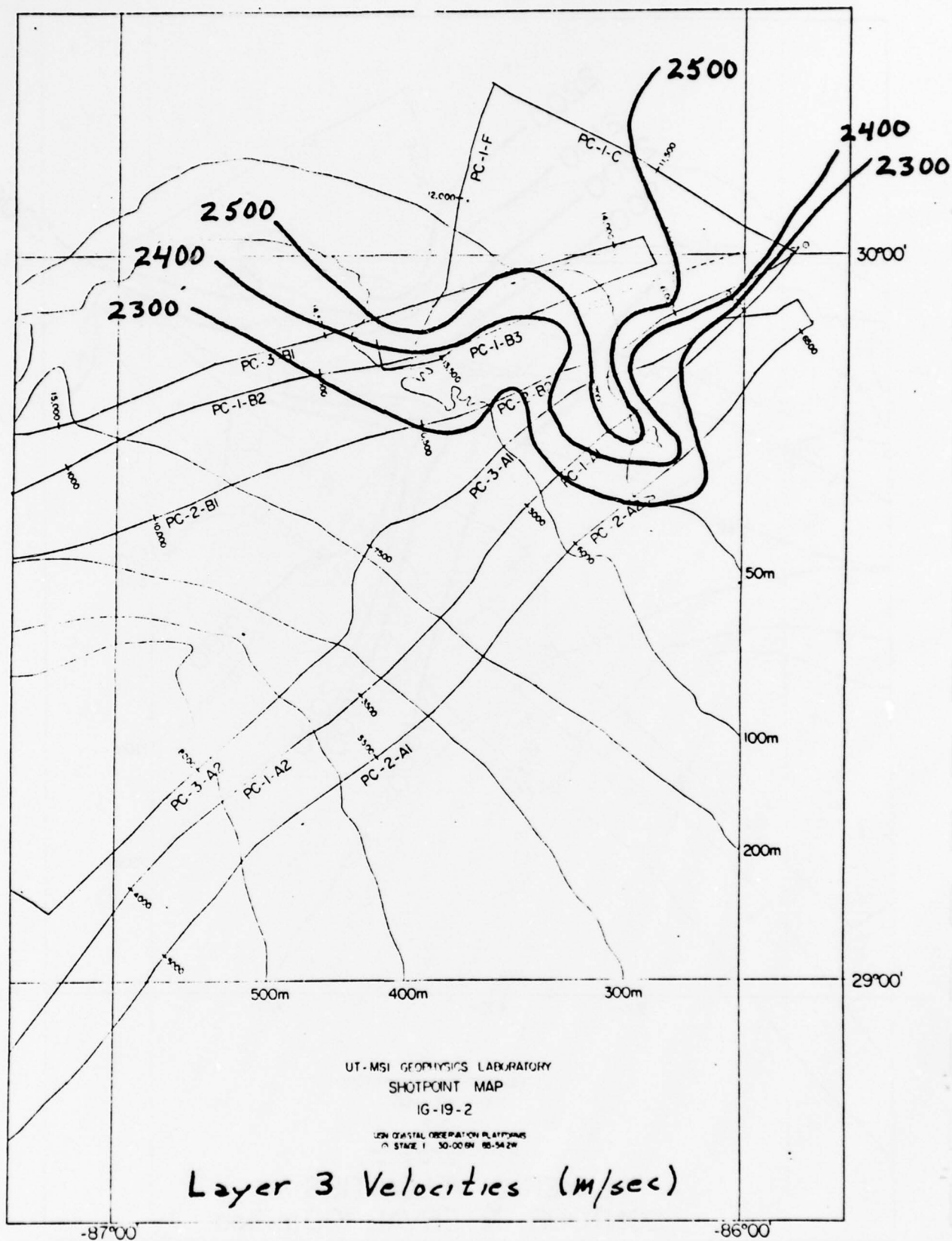
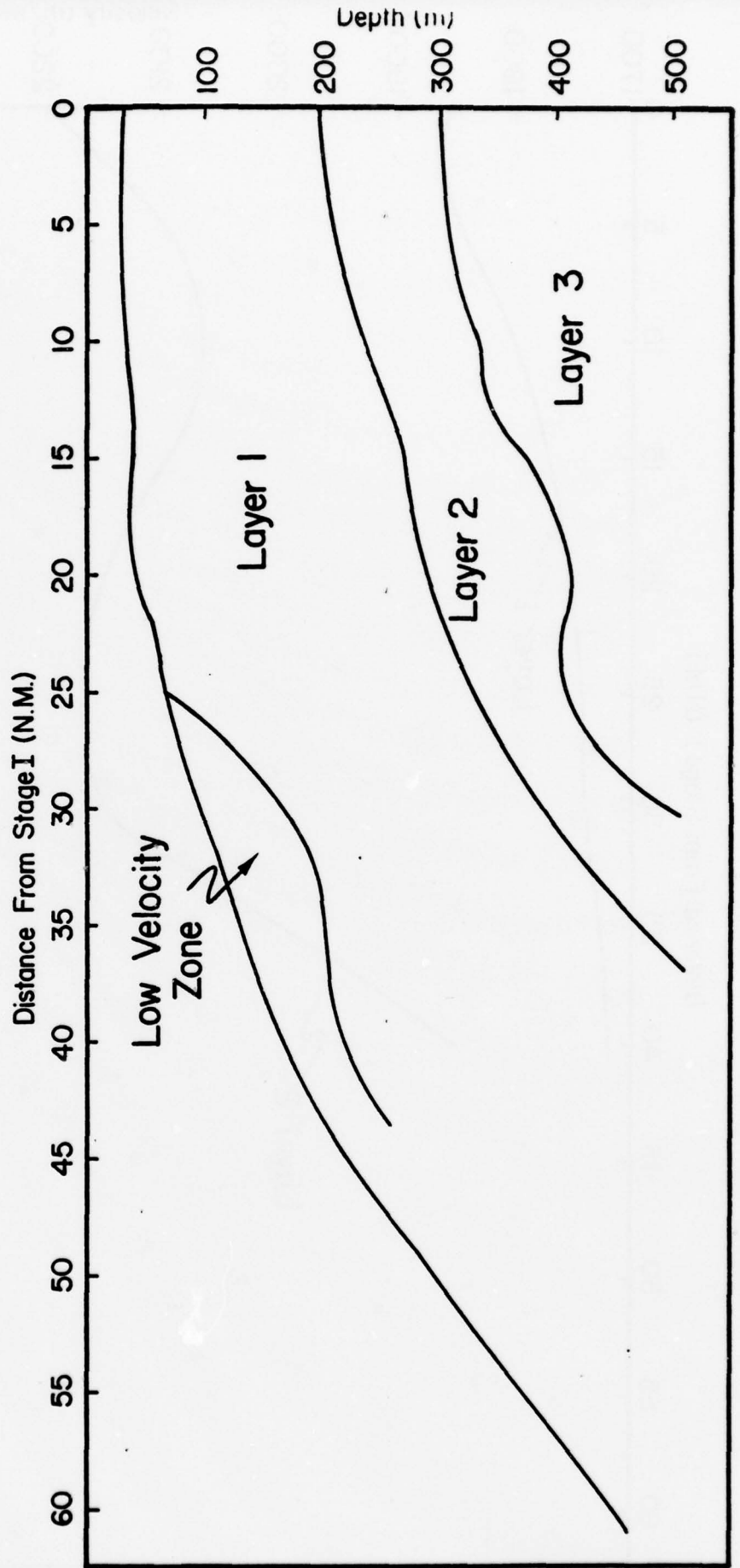
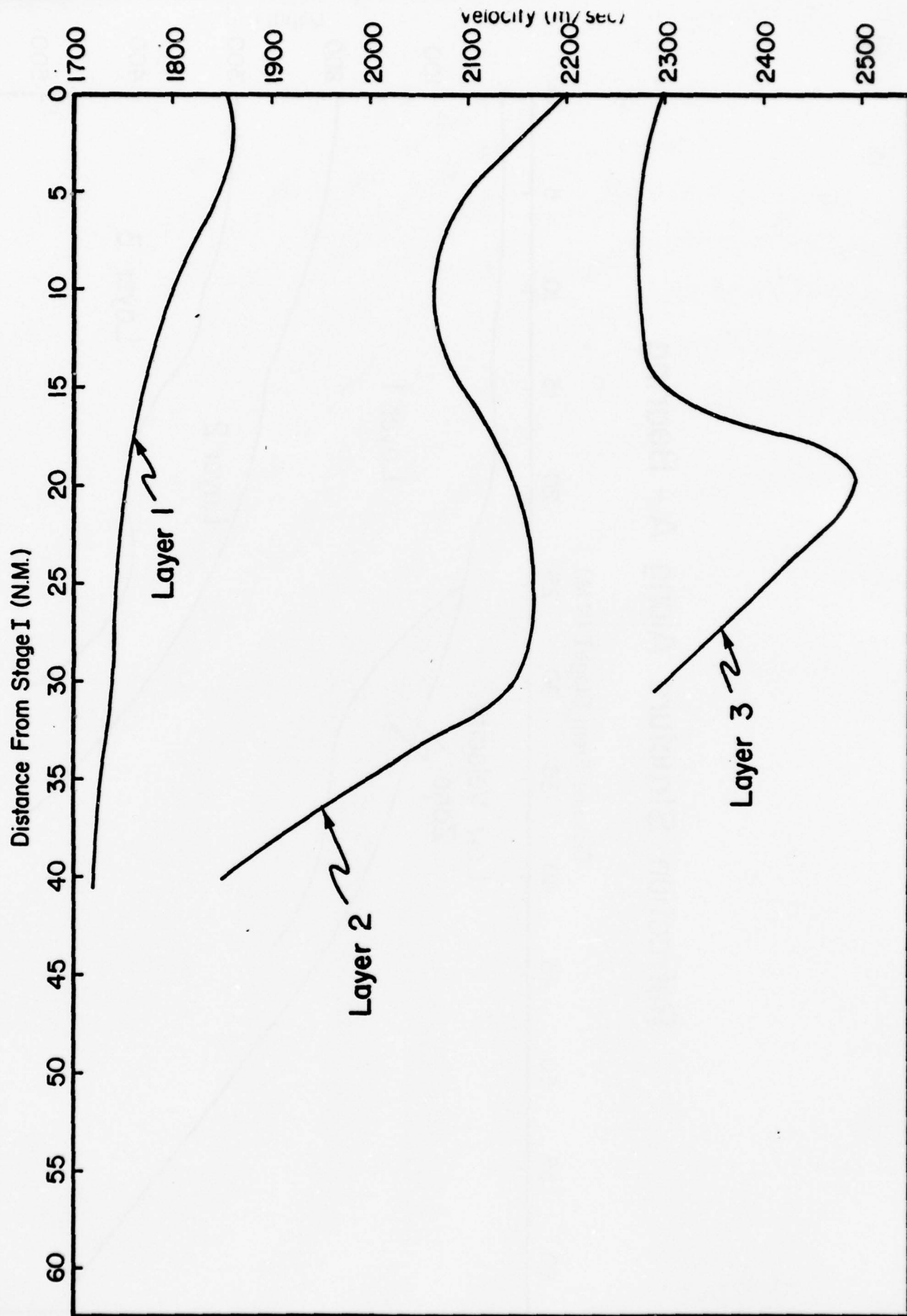


FIG. 33

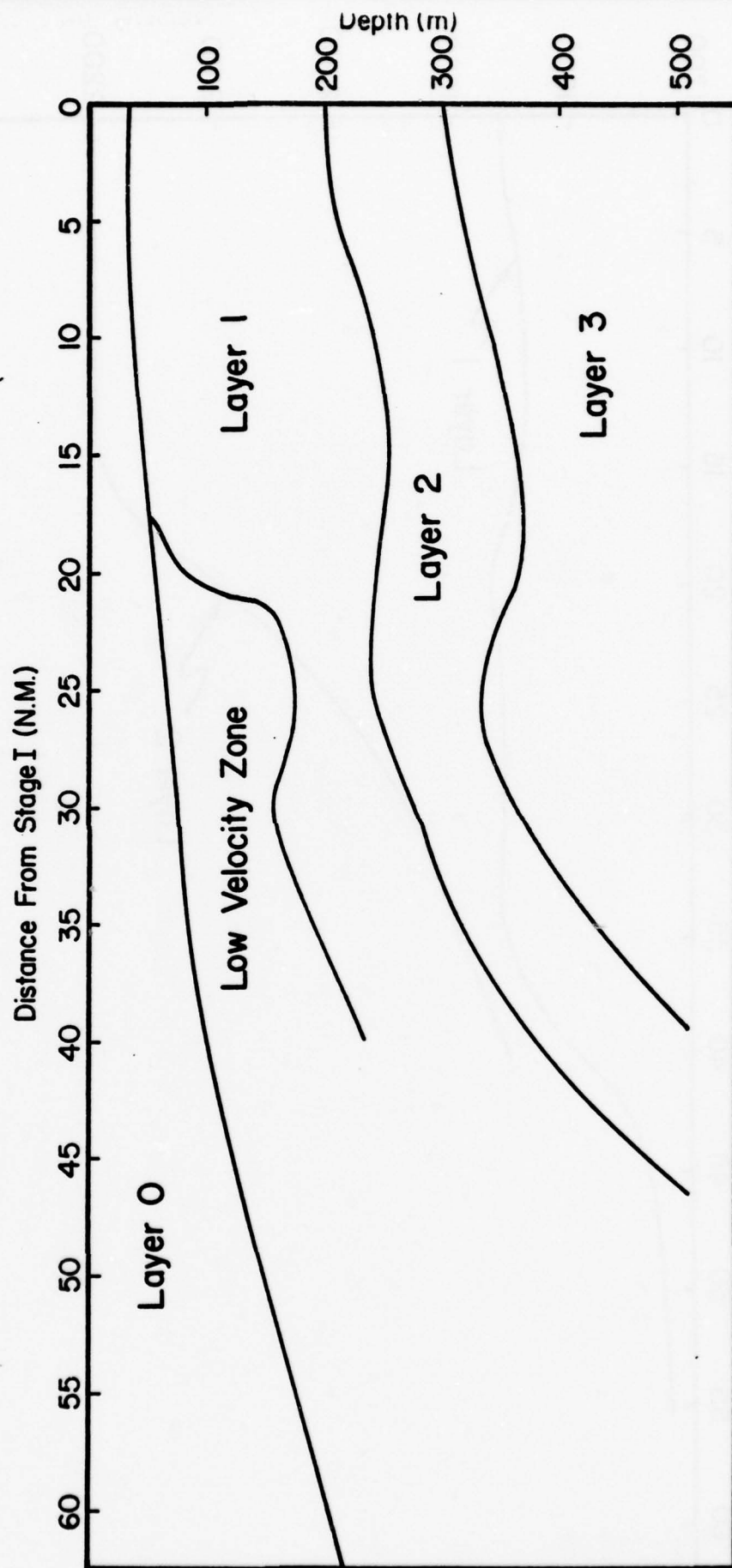
Refraction Structure Along A - Bearing



Velocity Variation Along A - Bearing

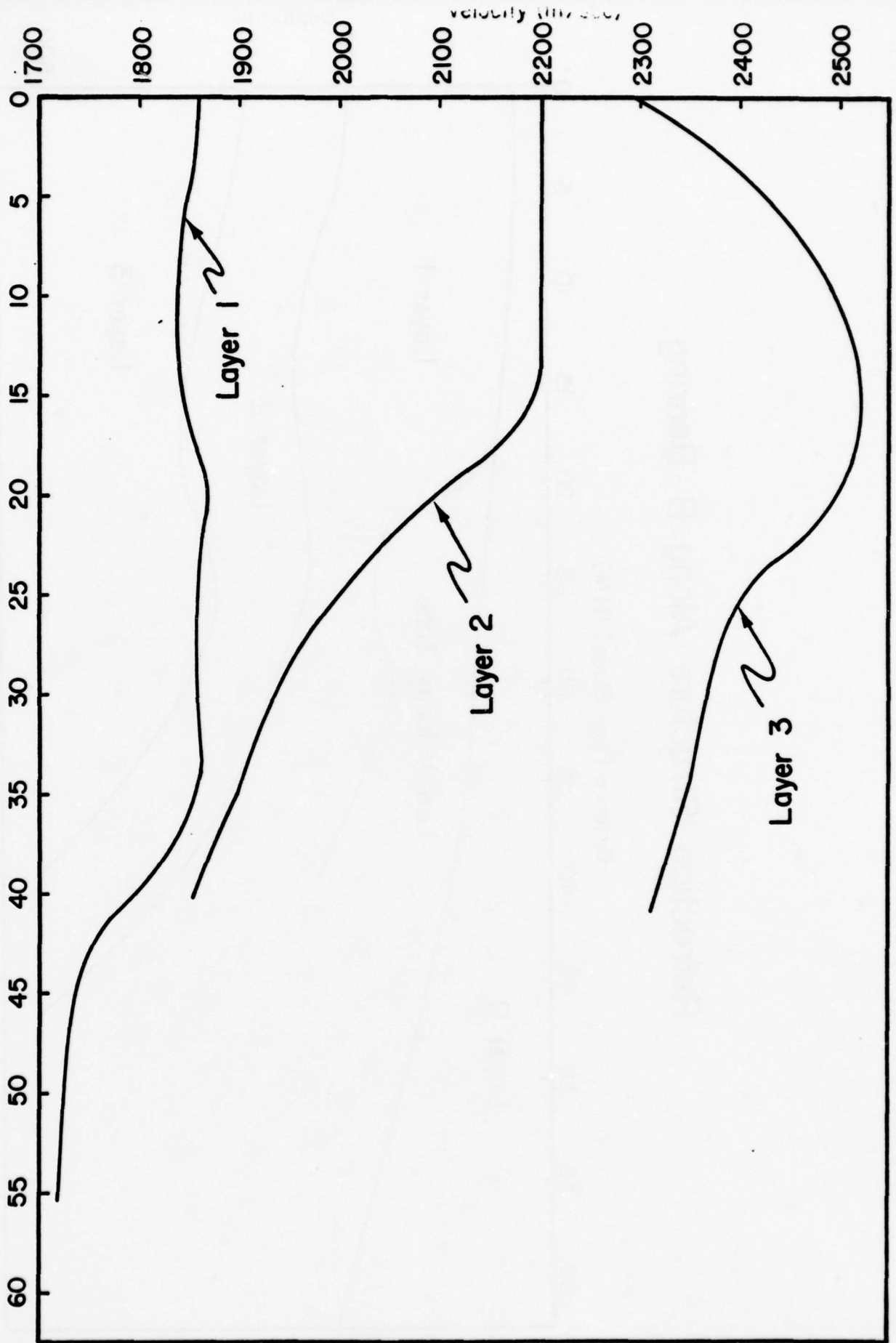


Refraction Structure Along B-Bearing



Velocity Variation Along B-Bearing

Distance From Stage I (N.M.)



PRELIMINARY SONOBUOY STUDY OF RAPIDLY
ACCUMULATING SHELF SEDIMENTS¹

R. E. Houtz

ABSTRACT

Sonobuoy records with smoothly curved travel-time data are found most commonly near rapidly out-building shelves and near the mouths of major rivers. It is judged that the smooth increase of velocity with depth is most likely where sediments are young and have accumulated rapidly.

These sonobuoy records are amenable to analytical techniques for determining velocity gradients in shelf sediments. These methods / are simpler and more accurate than is possible in deep water (if the source and receiver are at the surface). Also, seafloor sound velocity can be determined by measuring the critical angle of reflection from seafloor multiples, which form an energetic and clearly defined wedge of closely spaced multiples slightly later than the simple seafloor reflection. Velocity inversion techniques applied to the travel-time data provide accurate velocity-depth information. These techniques show that shelf areas with thick sections of rapidly accumulating sediments are ideal for the measurement of detailed velocity characters.

A method is proposed for measuring in situ attenuation on shelves where the velocity increases smoothly with depth. The method takes advantage of the

¹Lamont-Doherty Geological Observatory of Columbia University, Palisades,
New York, 10964, Contribution # 0000.

apparent lack of prominent reflectors in rapidly accumulating sediment bodies, and uses the decay in amplitude observed between first-arrival refractions and their simple multiples. In this proposed technique, the first-arrival refractions are considered to be the 'source'.

Simple ray theory shows that maximum focussing occurs in the shallow curved path arrivals at a velocity cusp. The velocity cusps can form in shallow water (less than about 100m) only when the velocity contrast at the seafloor is non-existent or slightly positive.

INTRODUCTION

The present work was originally undertaken to examine velocity gradients in the shelf environment, where the elimination of the deep water layer simplifies the analytical techniques and increases the accuracy. A search of our sonobuoy data from water depths less than 100m revealed that a substantial portion show curved travel-time data, which indicates a smooth increase of velocity with depth. Shortly it became apparent that sonobuoy records with smooth travel-time data are clustered in remarkably clear-cut geographical zones. This paper has therefore been enlarged from its original scope to include the locations of these zones and to discuss their distribution.

Simple ray theory has been applied to a few of our sonobuoys to measure velocity gradients and seafloor sound velocities in shallow water. Ray theory has also been used to determine the conditions for maximum intensity of curved path arrivals. A method for measuring low-frequency in situ attenuation has also been proposed. Since the regions where these measurements can be made are geographically restricted, no field tapes are presently available. The present study is based entirely on variable-density analogue recordings. However, field tapes are now being collected to follow through with the attenuation measurements, and will form the basis of a future paper.

SONOBUOYS WITH CURVED TRAVEL-TIME DATA

Velocity gradients are relatively difficult to measure in deep sea sediments (if source and receiver are at the surface), because the refractions most affected by ray curvature arrive only slightly later than the seafloor reflections.

These curved path refractions were discussed by Ewing and Nafe (1963) who called them ' R_g arrivals'. A deeper curved path also exists in a half-space with a velocity gradient, and was called R_D by Ewing and Nafe. This arrival is not normally observed in deep-sea data because of excessive path length, as discussed by Ewing and Nafe. However, in very shallow water the R_D refractions are observed as strong first arrivals, whereas R_g is masked in the seafloor reflections, even at short ranges. The two branches are illustrated for deep and shallow water environments in Figure 1(a).

Analogue sonobuoy recordings of R_D (first-arrival, curved-path refractions) are easily handled to produce accurate velocity-depth data by any of several 'velocity inversion' techniques. This can be done with excellent resolution because none of the refractions are masked and the continuous travel-time curves are easily differentiated.

Examples of sonobuoy records with well-defined R_D arrivals are shown in Figure 2. The phase labelled M1 in the figure can be generated by doubling the travel-time and the range of R_D . This property identifies M1 as a simple multiple, as shown schematically in Figure 1(b). The phase labelled V_g (Sonobuoy 176C12 in Fig. 2) is made up of separate critical reflection events from the water layer multiples. Since water depth here is only 90m, the seafloor multiples arrive about .2 sec apart. This is so close that the bubble-pulse ringing blurs the individual returns and produces a wedge of noise whose leading edge represents the onsets of unattenuated reflections at and beyond the critical range. This effect is illustrated schematically in Figure 1(c) where

the bubble-pulse coda has been eliminated (compare V_g in Fig. 5). The ray diagram in Figure 1(c) shows how the combined path lengths at any distance from the source can be used to find the critical reflection angle (J. Ewing, personal communication; cf. Katz and Ewing, 1956).

Sonobuoy records with curved travel-time data were plotted on a world-wide basis from shelves where we had sufficient data to provide a meaningful sample. The results are shown in Figure 3. The distinction between a convincingly smooth travel-time curve, and a segmented curve is not precise. In an effort to limit ambiguity, all doubtful or transitional-type data were ignored, including records with velocity cusps (indicating a change in the velocity gradient). By selecting only those sonobuoy records with uninterrupted travel-time curves, the study has been limited to thick sediment sections. This can be seen in Figure 3, where the stippled regions, indicating smoothly increasing sound velocities, are confined primarily to the thick sediment sections at the mouths of major rivers and on the edges of out-building shelves. Since these properties are conspicuously localized, B. Naini (personal communication) has suggested that the crust is depressed by the rapid accumulation of sediment, which would tend to confine the accumulations to specific zones.

However, not all thick accumulations of shelf sediments share this characteristic. An additional requirement for a smooth velocity-depth function seems to be the rapid accumulation of the sediment. Since sedimentation conditions on the shelves are unlikely to remain constant over long periods of time (in the

geological sense), a section that has accumulated over a relatively short time is more likely to have a uniform composition. Even if the above conditions have been met, complications may arise if the sediments have had time to become decidedly cemented, a process that may not produce a uniform variation of properties with depth. Accordingly, rapid sedimentation from a uniform source that is currently active, which implies a fairly young sediment body, may be a further requirement for smoothly increasing sound velocities. These seem to be the prevalent conditions of the sediment bodies mapped in the figures. The existence of these sediment bodies does not seem to be mentioned in the literature, at least not from the standpoint of velocity-depth relations.

The refraction velocity of sediments at the seafloor is very rarely observed. Typically, velocities of about 1.8 km/sec are observed several hundred meters subbottom, and the uppermost sediment velocities are unmeasured. This has led some investigators to fit velocity/depth curves to the observed range of velocities down to depths of 3 km or more. These curves, when projected to the surface, yield velocities of 1.5 to 1.7 km/sec at the seafloor (Houtz, 1977; Bryan and Simpson, 1971). Velocity gradients (the value a , in $v=v_0+ah$, where v_0 =seafloor sound velocity and h =depth) obtained by these investigators in thick shelf sediments normally range from 1.0 to 2.0 sec^{-1} .

Sonobuoy 176C12 in the right side of Figure 2 was taken from the Orange River delta, where Bryan and Simpson have determined an accurate velocity function. Although they have very few seafloor velocity measurements, a least-squares solution fitted to many velocity points at depth projects to the seafloor

to give $v_0 = 1.65$ km/sec. In Figure 2 the direct water wave (D) and the line formed by the critical seafloor reflections (V_g) are labelled on Sonobuoy 176C12. The critical angle can be obtained immediately from the time and distance pairs observed anywhere along V_g as shown in Fig. 1(c). In this particular case, $\sin \theta = .85$ (where θ is the critical angle), and therefore the seafloor sound velocity ($1.5/\sin \theta$) is 1.76 km/sec. In the case of sonobuoy 297C12 (left side Fig. 2), there is no obvious line of critical reflection points, which indicates a very slight or no velocity contrast at the seafloor.

VELOCITY INVERSION DATA

The Herglotz-Bateman-Weichert (Bullen, 1959) velocity inversion technique was applied to sonobuoys 176 and 297C12 to yield the velocity depth solutions shown in Figure 4. Although not essential to the present discussion, the velocity depth solutions are shown down to depths of several kilometers to illustrate how the velocity varies with depth over the entire section. Velocity gradients can be estimated by measuring the slope between the first two velocity-depth points of each plot. This yields $a = 1.5 \text{ sec}^{-1}$ for 297C12, and $a = 1.2 \text{ sec}^{-1}$ for 176C12; in both instances the measured gradients are not reliable at sub-bottom depths less than about 200m. However, by combining the surface velocity measurements (based on V_g) with the velocity-depth data, the near-surface velocity gradient for 297C12 ($v_0 = 1.5$) becomes 1.9 sec^{-1} , whereas 176C12 yields a seafloor sound velocity (from critical reflection data) of 1.76 km/sec that is practically equal to the shallowest solution in Figure 4. The data therefore indicate a thin, constant-velocity layer at 176C12. This is borne out

convincingly by the short refracting segment in Figure 1 that has been labelled with a refraction velocity of 1.75 km/sec. It should be noted in Figure 4 that the distribution of velocity is not linear with depth, but that the assumption of a linear increase of velocity with depth near the surface is probably adequate down to several hundred meters.

The velocity-depth distribution from sonobuoy 55V27 appears in Fig. 5, along with a photocopy of the original sonobuoy record. Houtz and Windisch (1977) obtained an estimated seafloor sound velocity of 2.5 km/sec from the region of the Barents Sea where this sonobuoy was launched. The phase labelled W_m is parallel to R_D and delayed by slightly more than the seafloor reflection time, identifying it as a refracted arrival that has experienced a doubled path in the water layer. The high-speed sound velocity of the seafloor sediments can be confirmed in Figure 5 where V_g is considerably delayed. Note that the increased water depth permits the resolution of individual reflection events (6 separate arrivals can be seen forming the leading edge of V_g). In this case $\sin \theta = .63$ and the seafloor sound velocity computes to about 2.34 km/sec.

The velocity structure can therefore be modelled as shown in the upper part of Figure 6, where the upper 300m of sediment is shown as a constant-velocity section, which reconciles the similarity of the seafloor velocity (2.34 km/sec) to the shallowest velocity measurement (2.50 km/sec at 300m) in Figure 5. The lower half-space is shown with a velocity gradient of 1.3 sec^{-1} , as required by the velocity-depth data in Figure 5.

These examples serve to show that rapidly accumulating sediments in shallow water can be analyzed to provide detailed velocity structure solutions and seafloor sound velocities. Velocity gradients can be measured very near the seafloor by combining the techniques.

The existence of shelf environments with continuous velocity-depth characteristics probably results in the improvement of signal coherence. The continuity also indicates that more precise ranging is possible. In these conditions, lateral variations in sound velocity can also be easily detected by comparing the primary and multiple travel-time data.

ESTIMATION OF ACOUSTIC ATTENUATION

The study of sound loss is facilitated by the conditions that exist in the stippled areas shown in Figure 3. This comes about because the velocity-depth profiles can be determined with considerable accuracy, and the existence of smooth first-arrival curves indicates a lack of prominent reflectors. Furthermore, the multiples can be used to measure amplitude decay without a knowledge of the source level. This is to say, the amplitude of a primary arrival is the measured source for the first multiple.

With well-determined velocity-depth data, a set of amplitude measurements (at various ranges) can be corrected for spreading losses along a well-estimated path length. The remaining losses are due to reflections and attenuation. If there are no prominent reflectors other than the seafloor interface, the corrected amplitudes therefore provide a measure of the attenuation. The velocity characteristics of the seafloor are well-determined, and reasonable assumptions

can be made for the impedance mis-match. This can be done with Hamilton's (1978) density curves for terrigenous silts and clays, the type of material that is most likely to be in near-shore conditions of very rapid sedimentation. The existence of reflections within the sediment can be tested by plotting corrected amplitudes as a function of depth or range. Serious dislocations in the amplitude-depth (or range) plots would indicate the presence of important reflectors. If the plot appears to be smooth, it could be assumed that the residual decay in amplitude results from attenuation losses. The method has the potential for determining attenuation as a function of depth, although it is not yet possible to know if the data can be corrected to such a high level of precision. Field tapes, now being gathered at sea, will form the basis of a future attempt to measure in situ attenuation.

LONG RANGE PROPAGATION

At large distances from the source, the dominant arrivals in shallow water will be those shown as A and B in the lower part of Figure 6. The strength of path B is primarily dependent on the acoustic impedance mismatch at the sea-floor, whereas A, which is identical to the R_s path shown in Figure 1(a), is dependent as well on the subbottom velocity structure. The range, X , of each of the path A segments can be expressed as

$$X = 2 h \tan \theta_0 + \frac{2 v_0}{a} \cot \theta_1 \quad (1)$$

where it is assumed that the velocity of sound in the sediments increases linearly with depth. Here h represents water depth, v_w =water velocity, v_0

and \underline{a} are taken from the linear relation $v=v_0+ah$, and $\sin \theta_1=(v_0/v_w) \sin \theta_0$.

In typical shelf conditions the curved rays at the minimum range (path A) rarely penetrate more than 100 m below the seafloor. Accordingly, the assumption of a linear increase of velocity with depth is justified, even though the velocity inversions reveal non-linear increases (Figs. 4 and 5). The curved path arrivals (type A) will be the only important source of energy if there is little or no impedance mis-match at the seafloor. Since this condition occurs widely in the marine environment, it is necessary to investigate under what conditions the curved paths are most intensely focussed. Because long-range propagation involves multiple bounce paths, any conditions that increase the strength of path A will have a large effect when summed with path B on distant, incoming signals.

If there is no velocity contrast at the seafloor ($\theta_1=\theta_0$ in Equation 1), the minimum range at which rays can return to the surface is also the point at which the rays are most intensely focussed. This comes about because the prograde and retrograde travel-time branches combine to form a cusp (Bullen, 1959), resulting in reinforcement. Hence strong arrivals via path A (R_g) at long ranges from the source will be more likely if a velocity cusp can develop. It is therefore important to consider whether velocity cusps can form when $v_0 \neq v_w$, and what effect the water depth will have on their development.

In the general case where $v_0 \neq v_w$, the degree of focussing is not so straight-forward. This can be shown by differentiating Equation 1 with respect to θ_0 and setting the derivative equal to zero, which establishes the conditions of

a curved ray path at a minimum range from the source:

$$\frac{dX}{d\theta_0} = \tan^2 \theta_0 - \frac{v_w \cos \theta_0}{ah \cos \theta_1} = 0 \quad (2)$$

where $d\theta_1$ has been expressed in terms of $d\theta_0$ by use of Snell's Law. Equation 2 can be re-arranged to facilitate the graphical solutions shown in Figure 7, by writing

$$\frac{v_w}{ah} = \frac{\tan^2 \theta_0 \cos \theta_1}{\cos \theta_0} \quad (3)$$

These expressions relate only to R_s paths, which penetrate only about 100m into the sediment, although they do form an important contribution to the 'bottom-bounce' return.

The right side of Equation 3 has been plotted in Figure 7 for three different values of seafloor sound velocity (1.6, 1.7, and 2.0 km/s, where $v_w=1.5$ in each case), as identified in the figure. The left side of (3.) appears as horizontal lines, which show that v_w/ah must be equal to or less than 2.8, 1.35, and .5 respectively for each of the examples to provide the necessary conditions for a solution. Since v_w is normally about 1.5 km/sec, typical shelf depths of about .2 km will not be sufficiently deep to provide curved path focussing at the minimum range unless the seafloor sound velocity is equal to or only slightly greater than water velocity.

Note that the singular solutions, where v_w/ah passes through the apex of the curves in Figure 7, will provide a greater degree of focussing than lower

lines that develop two solutions. This is shown in Figure 8 where the velocity model, $v=1.7 + 1.2h$ has been used to plot range (X) as a function of incident angle at the source. The three cases where water depth, $h=.5, .9$, and 2.0 km represent (cf. Fig. 7) respectively those conditions where v_w/a is greater than, equal to, and less than 1.35 . The degree of focussing ($d\theta_o/dX$) can be estimated in Figure 8 by noting that when $h=2$, a subtended angle of 8 degrees near the minimum represents a change in range of about $.1$ km, or $\Delta\theta_o/\Delta X=80$ deg/km. However, when $h=.9$, $\Delta\theta_o/\Delta X=140$ deg/km, or nearly double the focussing. At $h=.5$ (no minimum curved path range can exist) only 30 deg/km is available. Focussing defined in this way, ignores the effect of travel-time differences between various paths; hence the amplitudes at the 'focussed' points are only greater if the incoming signal is summed over an interval of time. These R_g arrivals closely follow the seafloor reflections and their multiples, and are not distinguishable on the records, even though they may contribute significantly to the noise in the vicinity of "D" in the figures.

DISCUSSION

In the earlier sections it was shown that rapidly accumulating shelf sediments frequently provide smoothly curved travel-time plots. The smoothness is convenient because the lack of discontinuities provides the best conditions for velocity inversion techniques, i. e., there are no masked refraction events.

Seafloor reflections at critical incidence in shallow water also provide accurate measurements of seafloor sound velocities. These techniques can be combined to yield accurate velocity structures in rapidly accumulating shelf sediments.

In the previous section simple ray theory considerations reveal that multiple curved ray paths may be better focussed in rapidly accumulated sediments, since they most frequently lead to small velocity contrasts at the seafloor. It was also implied that if a velocity-depth relation is known with accuracy, these parameters can be used to predict which shelf environments are favorable for incoming signals that have traversed multiple curved paths.

Owing to the lack of prominent discontinuities in rapidly accumulated sediments, they also provide ideal conditions for estimating attenuation losses. The development of strong curved path multiples provides a means for measuring amplitude decay independently of source level, and can be used to detect relatively small horizontal variations in sound velocity.

ACKNOWLEDGEMENTS

This research was supported by the Earth Physics Program of the Office of Naval Research under Contract number N00014-75-C-1126. The sonobuoys used in this study were provided by the Office of Naval Research. Their worldwide distribution results from numerous grants for ship support and science that were awarded during the past 10 years.

This paper was kindly reviewed by Prof. R. Stoll and Dr. P. Pomeroy. Notable contributions to this paper were provided by the reviewers and by Dr. G. Bryan, and Mr. John Ewing.

REFERENCES

- Bryan, G., and E. Simpson, Seismic refraction measurements on the continental shelf between the Orange River and Cape Town, Institute of Geological Sciences Report No. 70/16, 187-198, Cambridge, 1971.
- Bullen, K., An Introduction to the Theory of Seismology, 2nd Edition, Cambridge Univ. Press, 296 pgs., 1959.
- Ewing, J., and J. Nafe, The unconsolidated sediments, in The Sea, vol. 3, 73-84, John Wiley and Sons, New York, 1963.
- Hamilton, E., Sound velocity-density relations in the sea-floor sediments and rocks, J. Acoust. Soc. Am., 63(2), 366-377, 1978.
- Houtz, R., Sound-velocity characteristics of sediment from the eastern South American margin, Geol. Soc. Am. Bull., 88, 720-722, 1977.
- Houtz, R., and C. Windisch, Barents sea continental margin sonobuoy data, Geol. Soc. Am. Bull., v. 88, p. 1030-1036, 1977.
- Katz, S., and M. Ewing, Seismic refraction measurements in the Atlantic Ocean, Part VII, Bull. Geol. Soc. Amer., 67, p. 475-510, 1956.

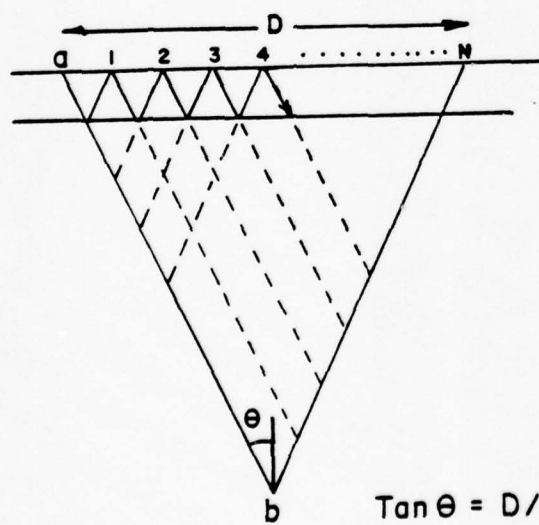
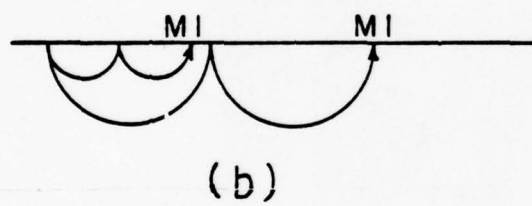
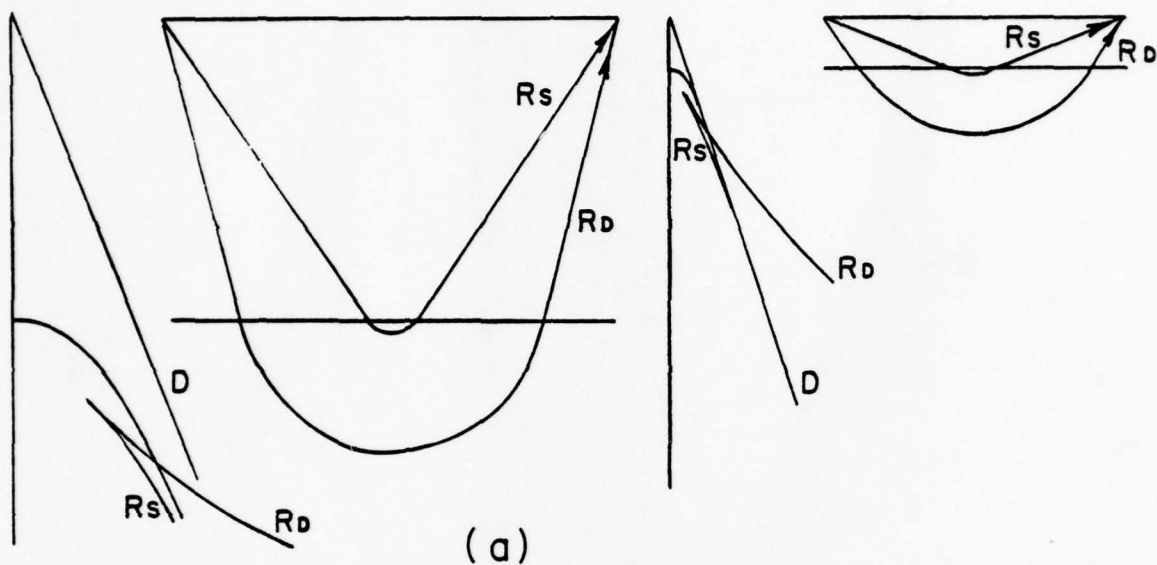
FIGURE CAPTIONS

- Fig. 1→ (a) Schematic diagram of curved path arrivals (R_s, R_D) and their appearance in travel-time data. (b) Diagram showing several ray paths of the multiple M1. (c) Diagram showing water layer multiples whose leading edge define V_g . Ray diagram shows how combined paths can yield the critical angle, θ .
- Fig. 2→ Sonobuoys showing well-developed curvature in the travel-time data. Sonobuoy on the left is from the Malaysian shelf; that on the right from the Orange River delta, South Africa. V_g formed by critical reflections from the seafloor yields a velocity of 1.76 km/sec, which is identical to that observed as a near-surface critical refraction (1.75 km/sec).
- Fig. 3→ Stippling indicates shelf areas where the velocity increases smoothly with depth. Small solid circles represent sonobuoy stations. Where the stations are closely spaced, a single circle may represent two or three stations.
- Fig. 4→ Velocity-depth plots after inversion by means of the Herglotz-Bateman-Weichert method.
- Fig. 5→ Photocopy of sonobuoy 55V27. Group velocity formed by critical reflection points from high-speed seafloor labelled V_g . Simple water layer multiple labelled W_m . Direct water wave is labelled D. Curved-path multiple labelled M1. Velocity depth plot appears on the right. Note that the intensity of the arrivals diminishes markedly (just left of W_m) when the velocity gradient diminishes abruptly at a depth of about 3 km.

Fig. 6→ Upper diagram shows velocity model based on data from sonobuoy 55V27. Lower diagram shows curved ray multiple path labelled A. Source shown as S. Multiple bottom-bounce path labelled B. The dominant component of path A will be at the minimum range that curved rays can return to the surface.

Fig. 7→ The intersections of the lines $(v_w/a h)$ with the apex of the curves $(\tan^2 \theta_0 \cos \theta_1 / \cos \theta_0)$ are single-valued solutions of Equation 3 for the minimum range of curved ray paths in shelf sediments. Three examples with seafloor sound velocities of 1.6, 1.7, and 2.0 km/sec are shown.

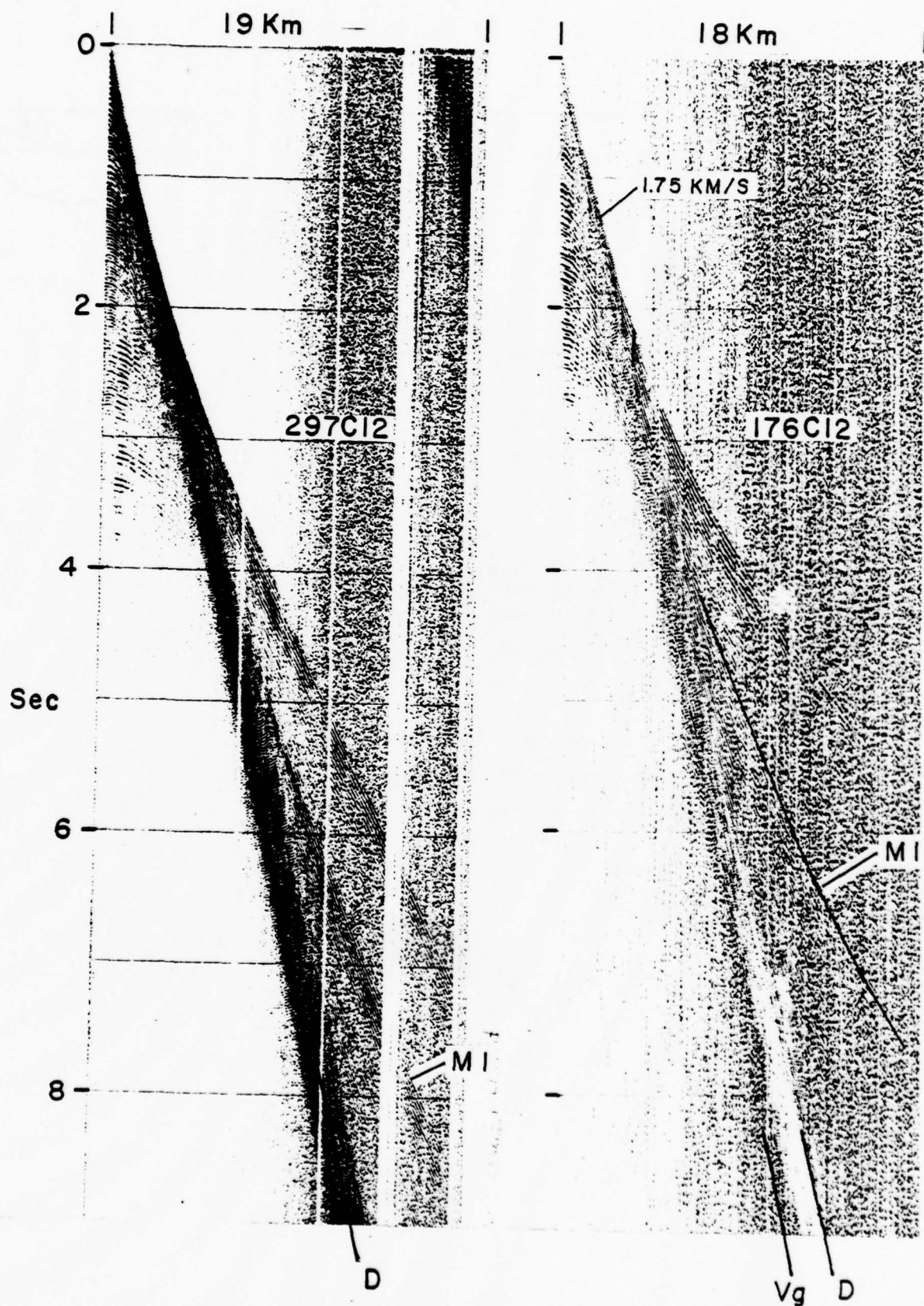
Fig. 8→ Range as a function of incident angle, computed from $v = 1.7 + 1.2 h$.

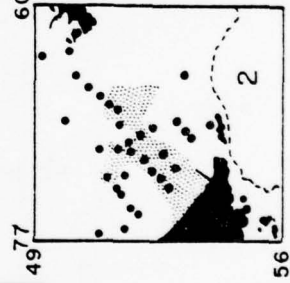
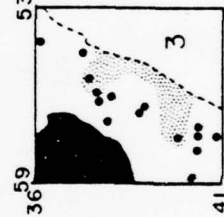
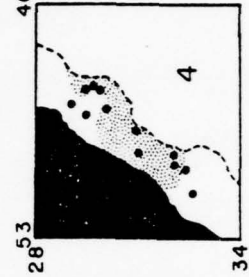
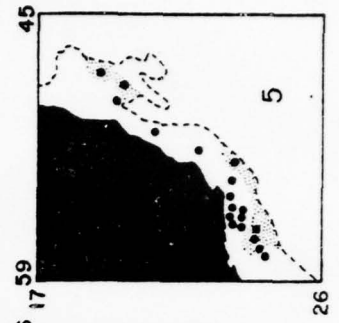
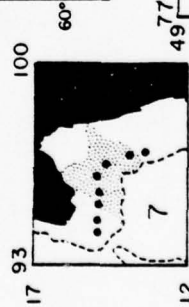
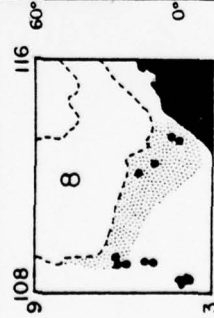
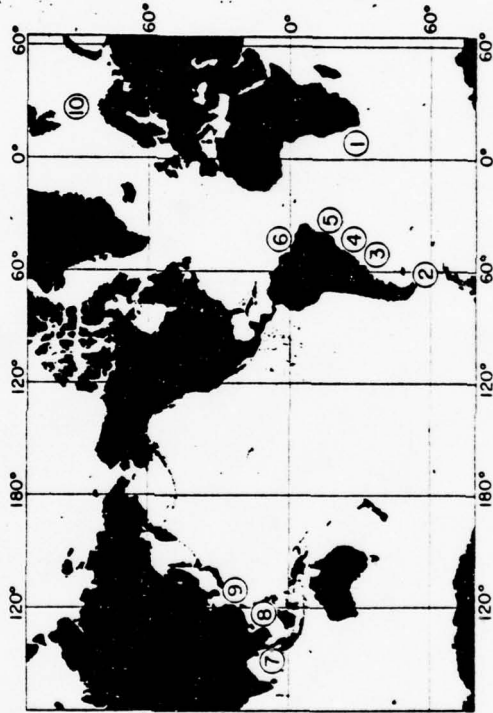
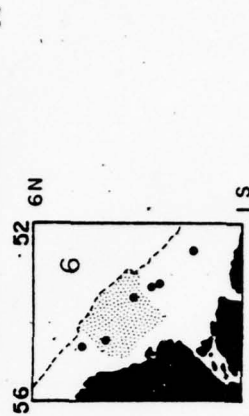
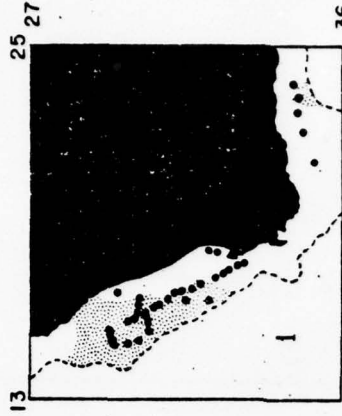
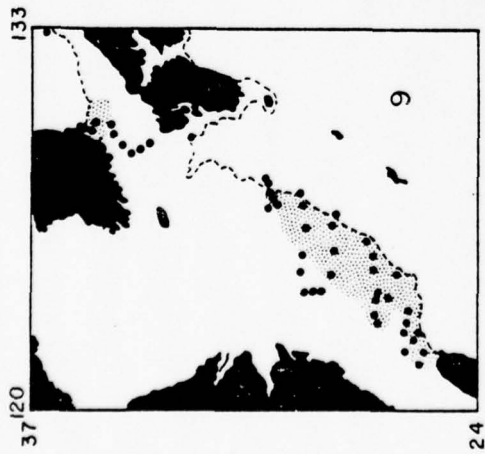
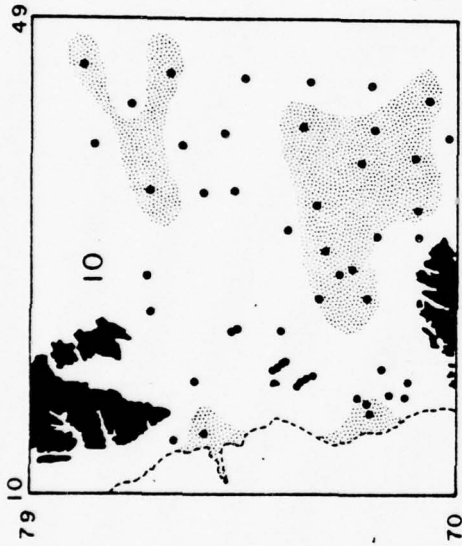


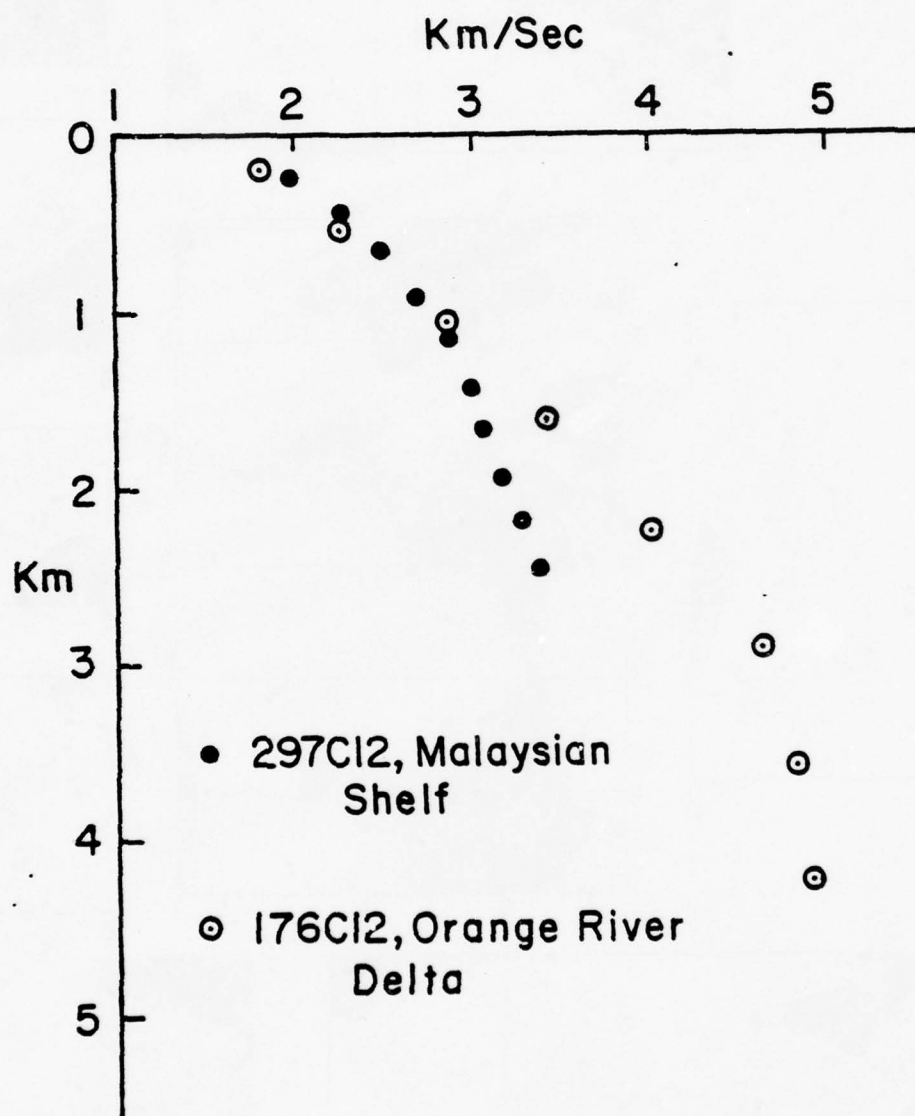
(c)

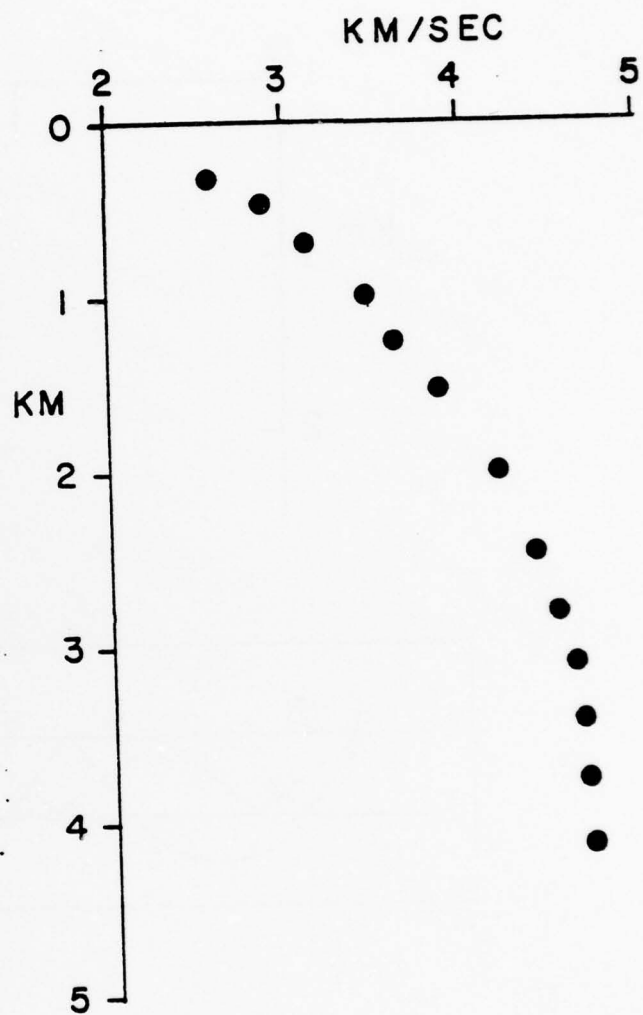
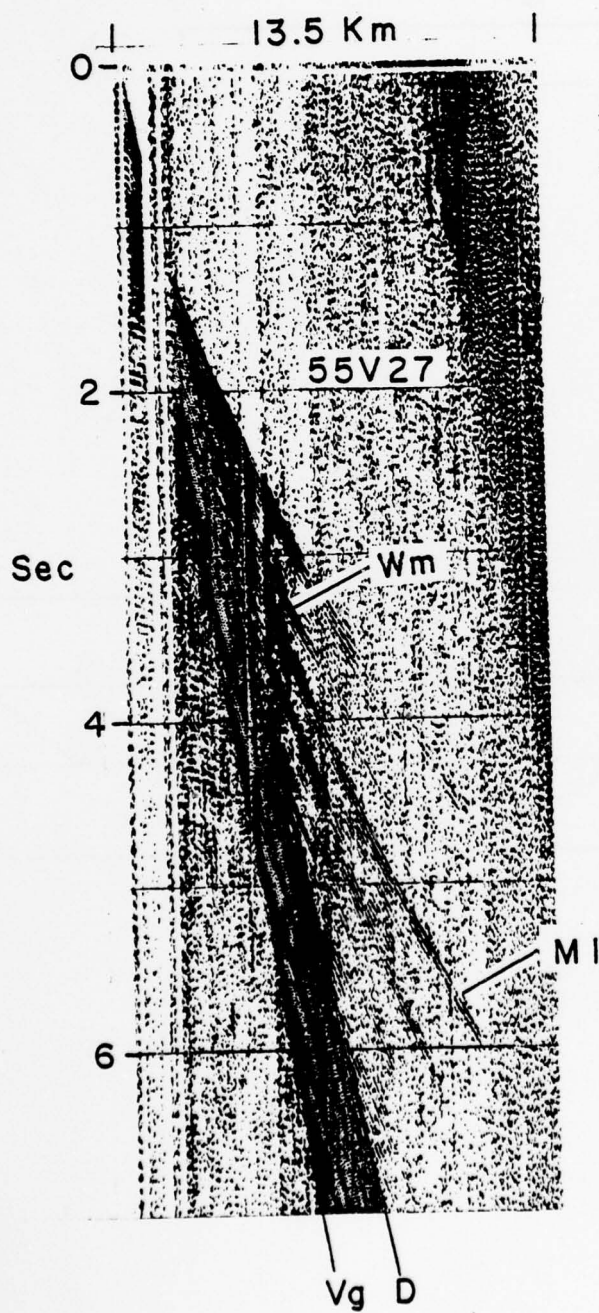
$$\tan \theta = D / a b n$$

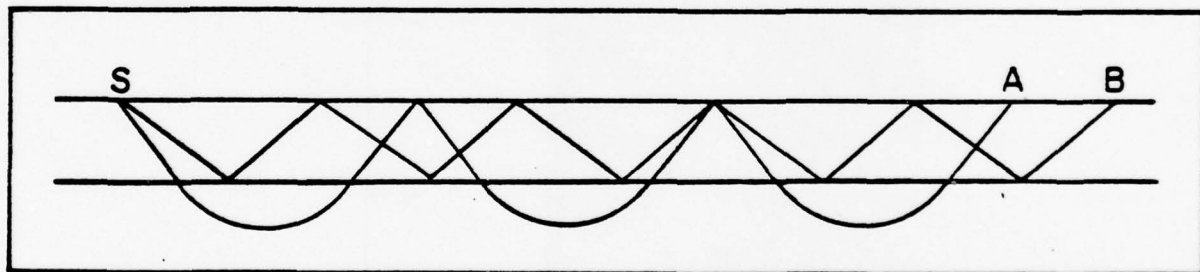
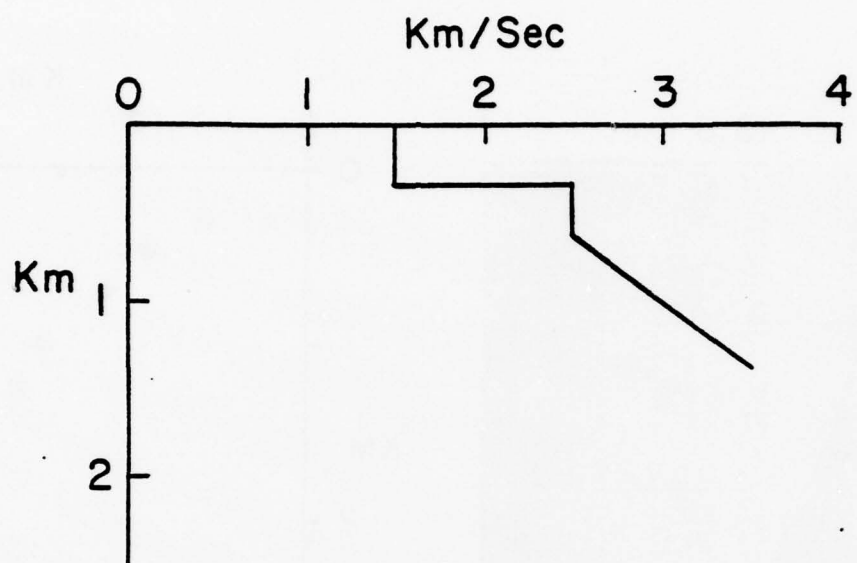


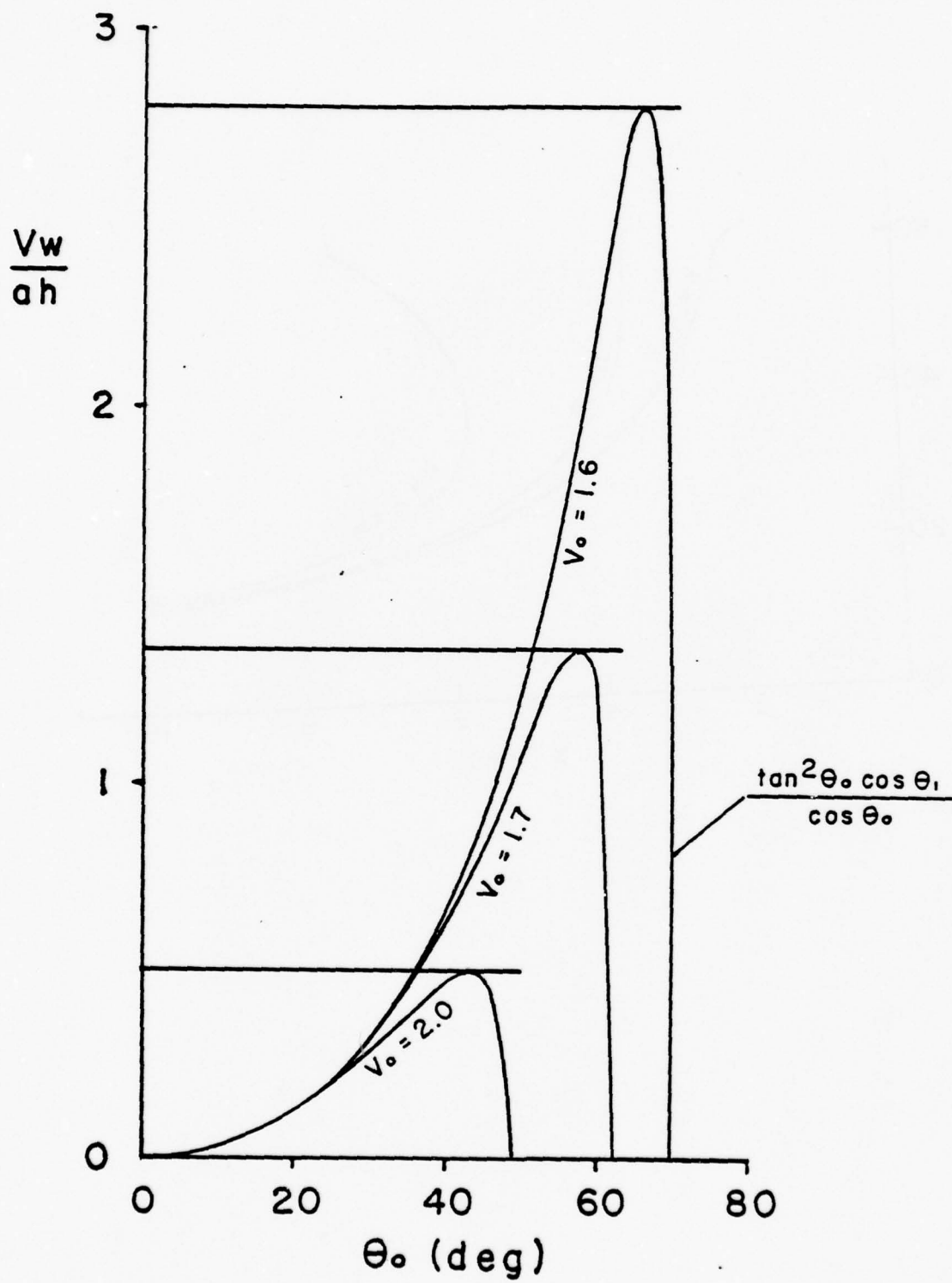


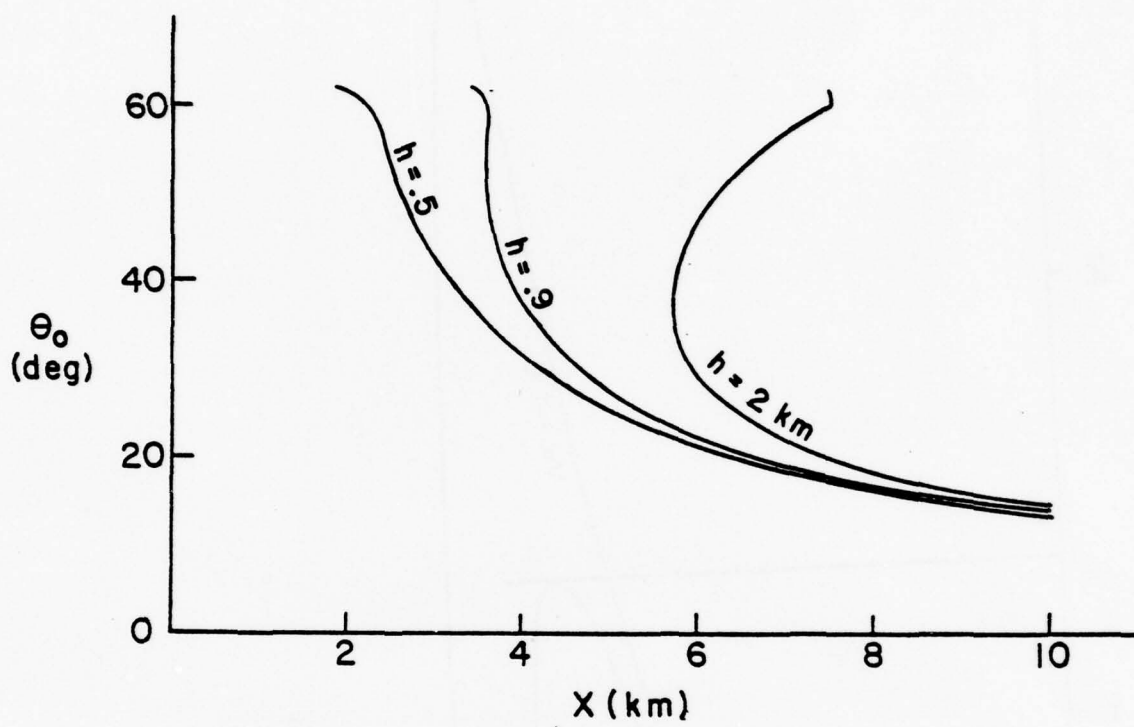












11 July 1978

Analysis Techniques for Seismic Signals
in an Underwater Acoustic Experimental Range

Presented at

ONR Workshop on Seismic Wave Propagation in Shallow Water
July 6-7, 1978

by

Don Fletcher
Institute for Acoustical Research
Miami Division of Palisades Geophysical Institute
615 SW 2 Avenue
Miami, Florida 33130

Table of Contents

<u>Section</u>	<u>Title</u>	<u>Page No.</u>
1	Introduction	1
2	Seismic Waves Observed on the Bottom Mounted Array	2
3	Seismic Artillery Location	9

Section 1

Introduction

During the last few years the Institute for Acoustical Research (IAR) has become involved in the analysis of seismic wave propagation. Presently there are two projects in this field underway at IAR:

- 1) An in-house study of some experimental results observed on IAR's ocean-bottom mounted hydrophone array;
- 2) An ONR-Marine Corps study of some experimental data generated by the recoil of various howitzers.

Both of these projects have yielded results of significant interest, and work is continuing on each of them.

The first of these topics is discussed in Section 2 below; the second topic is discussed in Section 3.

Section 2

Seismic Waves Observed on the Bottom Mounted Array

IAR has an underwater acoustic source installed off Eleuthera, Bahamas, capable of generating acoustic signals of great output power and stability. The source is capable of transmitting phase-encoded, pseudorandom signals with a 206 Hz carrier and a bandwidth of 20 Hz. It is also capable of transmitting transient signals. The source is mounted offshore at Eleuthera in 260 meters of water. The original purpose of this source was to study fluctuations in the transmission paths between Eleuthera and Bermuda and at intermediate points. The work is well-documented in the journals.

There are, as well, bottom mounted receivers (c.f. Figures 2.1 and 2.2) located at 8 km and 20 km from the Eleuthera source. These receivers are bottom mounted, and they are almost certainly covered with silt. The receivers have been in place over one year and were well surveyed. However, the geology of the bottom is not well known to us. Figures 2.1 and 2.2 show that the 8 and 20 km receivers are located at depths of 1400 and 4500 meters on slopes of 12° and 18° , respectively. This slope indicates that there is some hard material not too far beneath the interface, and this indication should be born in mind. No detailed bottom refraction study has been carried out.

Figures 2.1 and 2.2 indicate as well that the purely waterborne paths have travel times of about 6 and 15 seconds, respectively. IAR has observed, however, that acoustic signals (at 206 Hz) are getting to these phones in about 4 and 9 seconds, respectively. The top trace of Figure 2.3 a. shows the emitted transient signal, and the lower trace shows the received wave form at the 8 km phone. One large division represents one-second delay, and accordingly the transmission delay can be read to be about 4 seconds. Figure 2.3 b. shows a similar result at the 20 km phone. It can be seen in each of these traces that some later arrivals are coming in at the times indicated by the (waterborne) ray trace.

Figure 2.4 shows the temporal fluctuation of the waveform received at the 8 km phone. The emitted signal is a continuous 206 Hz carrier phase encoded, pseudorandom sequence. The fluctuations indicate that the wave is at least partially waterborne.

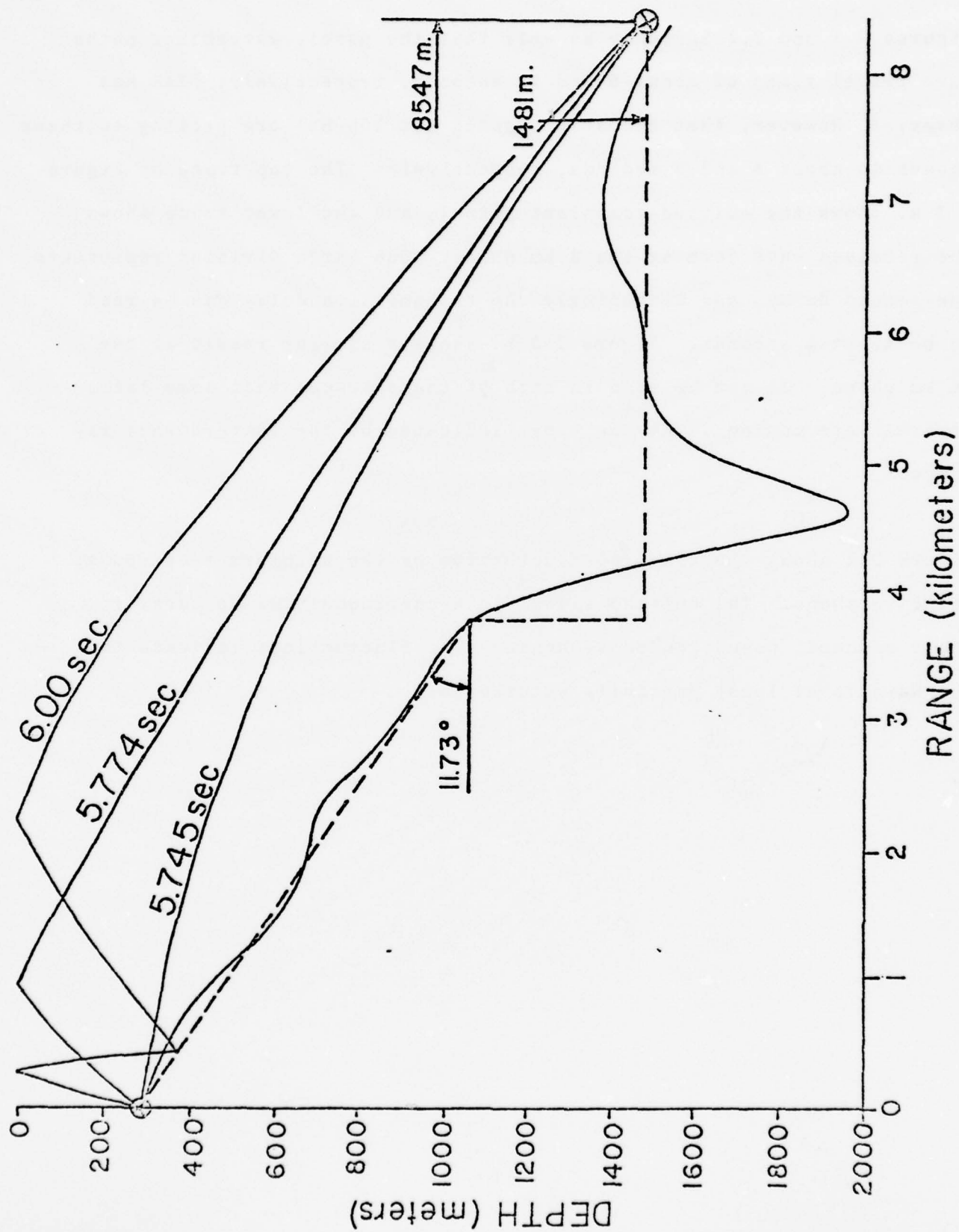


Fig. 2.1, Major Ray Paths; 8 km Phone.

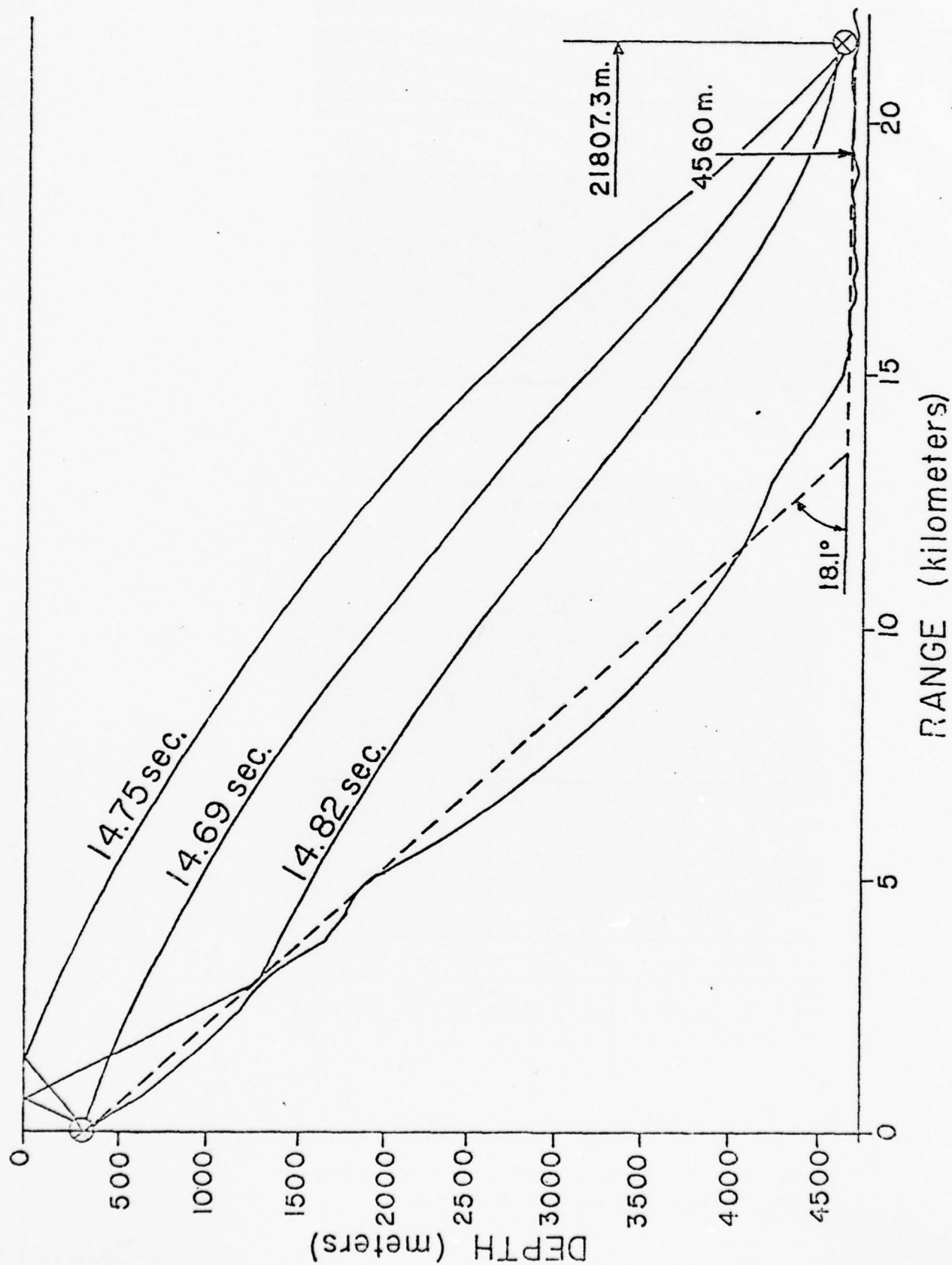


Fig. 2.2, Major Ray Paths; 20 km Phone

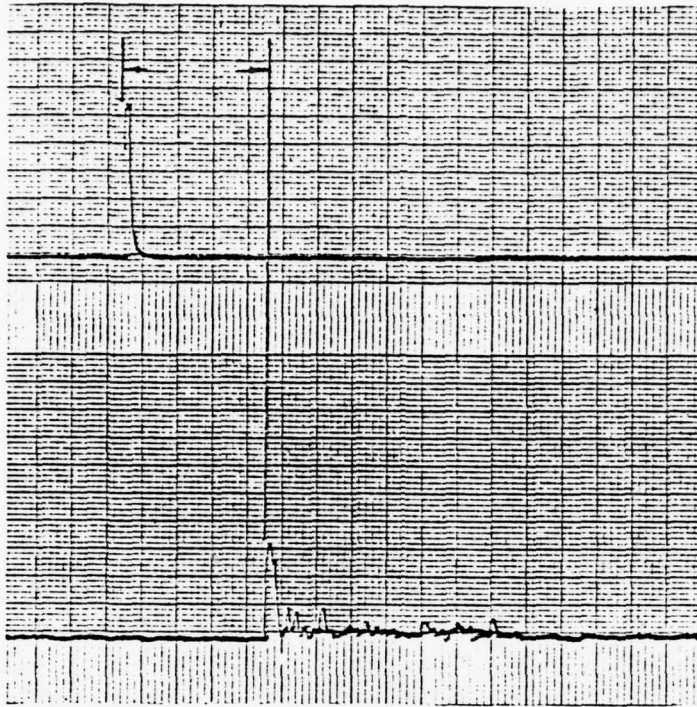


Fig. 2.3 a, Emitted and 8 km Received
Raw Traces (Transient Signal).

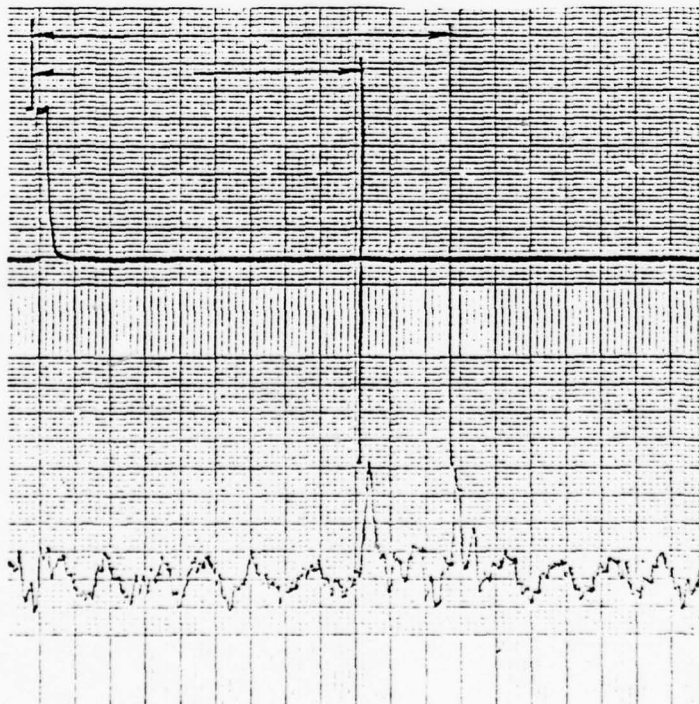


Fig. 2.3 b, Emitted and 20 km Received
Raw Traces (Transient Signal).

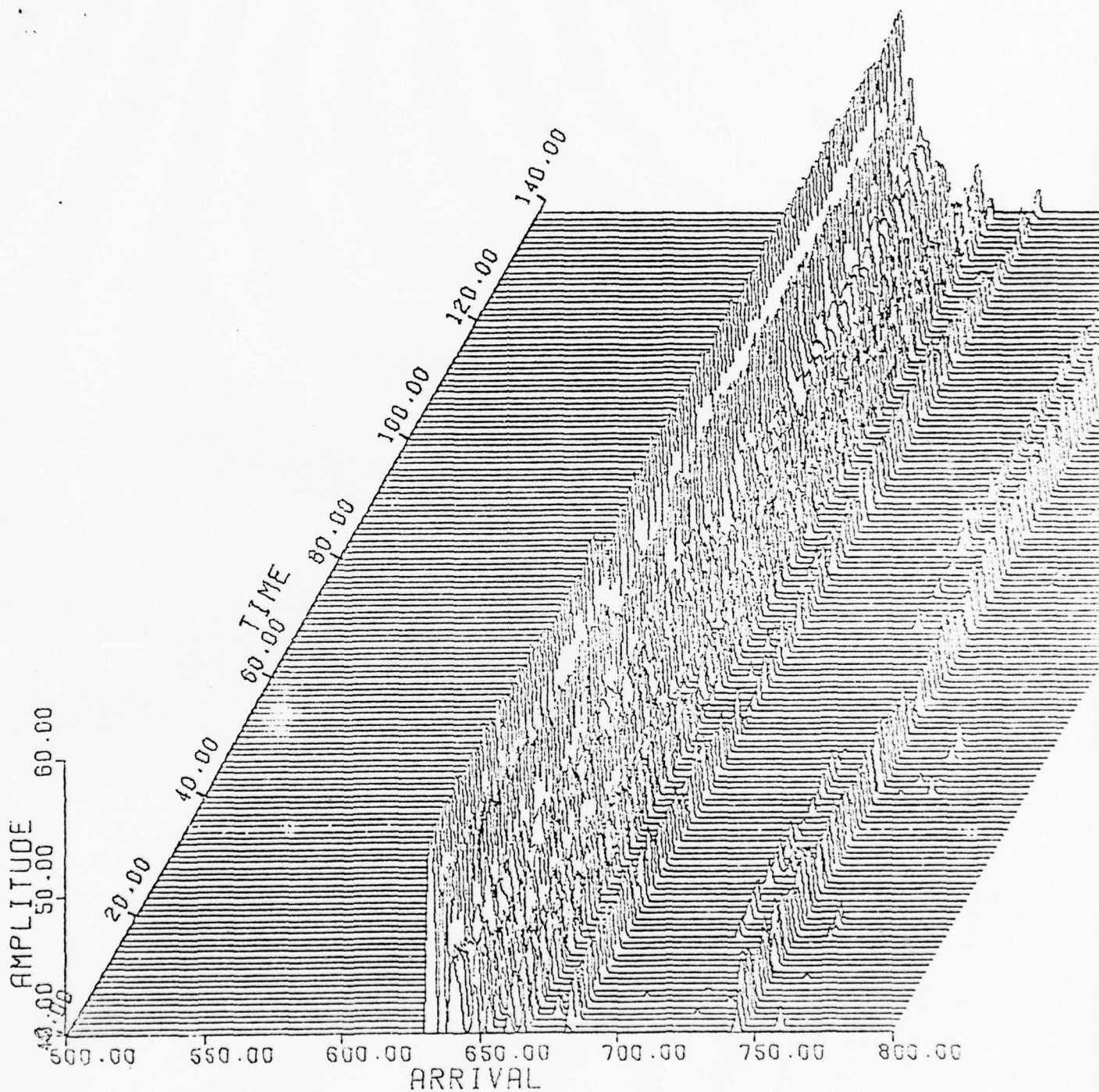


Fig. 2.4, Temporal Fluctuation of 3 km Received Continuous Signal.

Section 3

Seismic Artillery Location

This Section discusses briefly some work IAR has done for ONR and the U.S. Marine Corps on the seismic location of artillery units. A series of firings at the ranges of 5, 11, and 17 km were carried out by the Environmental Research Institute of Michigan (ERIM) and Honeywell, Inc. The experiment is described in Appendix A, and the geology of the site is given in Appendix C. The processing IAR employed on the 5 km events is described in detail in Appendix B.

This work is considered exploratory in nature, and is by no means theoretically complete. However, at 5 km the processing of Appendix B yields bearing estimates whose deviation from true bearing is only a few hundredths of a degree, and whose precision measure (standard deviation) is about 1.5 degrees. Considering the terrain and the naivete of the propagation model, these results must be considered very promising.

Figures 3.1 a. through 3.9 b. present some power spectra on the firings at 11 km. The figures subscripted "a" are N-S channels, and those subscripted "b" are vertical channels. The dashed curves denote ambient noise spectra before the howitzer firing. The solid curves denote spectra after the howitzer firing corresponding to a portion of the data record in which signal energy is present.

Pg. 7 is missing

A number of observations can be made from these spectra:

- 1) Signal is appearing on all phones and all channels in the frequency regions 3-5 Hz and 20-25 Hz.
- 2) The ambient is also strong in the region 3-5 Hz.
- 3) The ambient is weak in the region 20-25 Hz, therefore the signal-to-noise ratio is good in this region.
- 4) The vertical channels appear especially strong in the high-frequency region although the peak fluctuates in frequency somewhat more.

These observations lead to the following conclusions:

- 1) Rayleigh waves are probably being received at approximately 20-25 Hz.
- 2) Simple processing methods may be effective on these waves due to the good signal-to-noise ratio.
- 3) The region 3-5 Hz shows promise but will require sophisticated processing to extract the signal from the noise. These methods may be required to utilize jointly (rather than pair-wise) all array data; may require adaptive whitening; and possibly joint processing with the Rayleigh wave at 20-25 Hz.

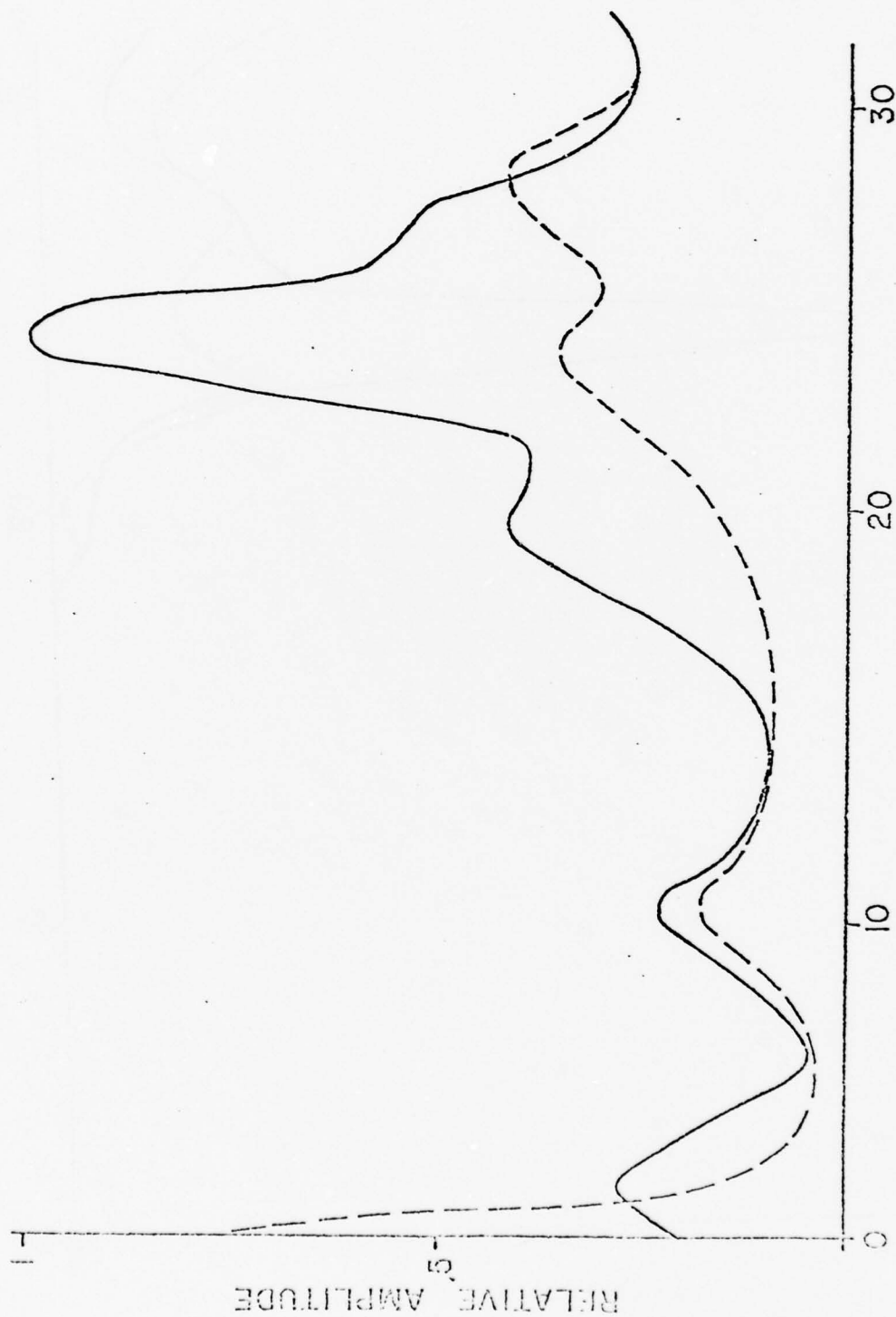


Fig. 3.1 a.

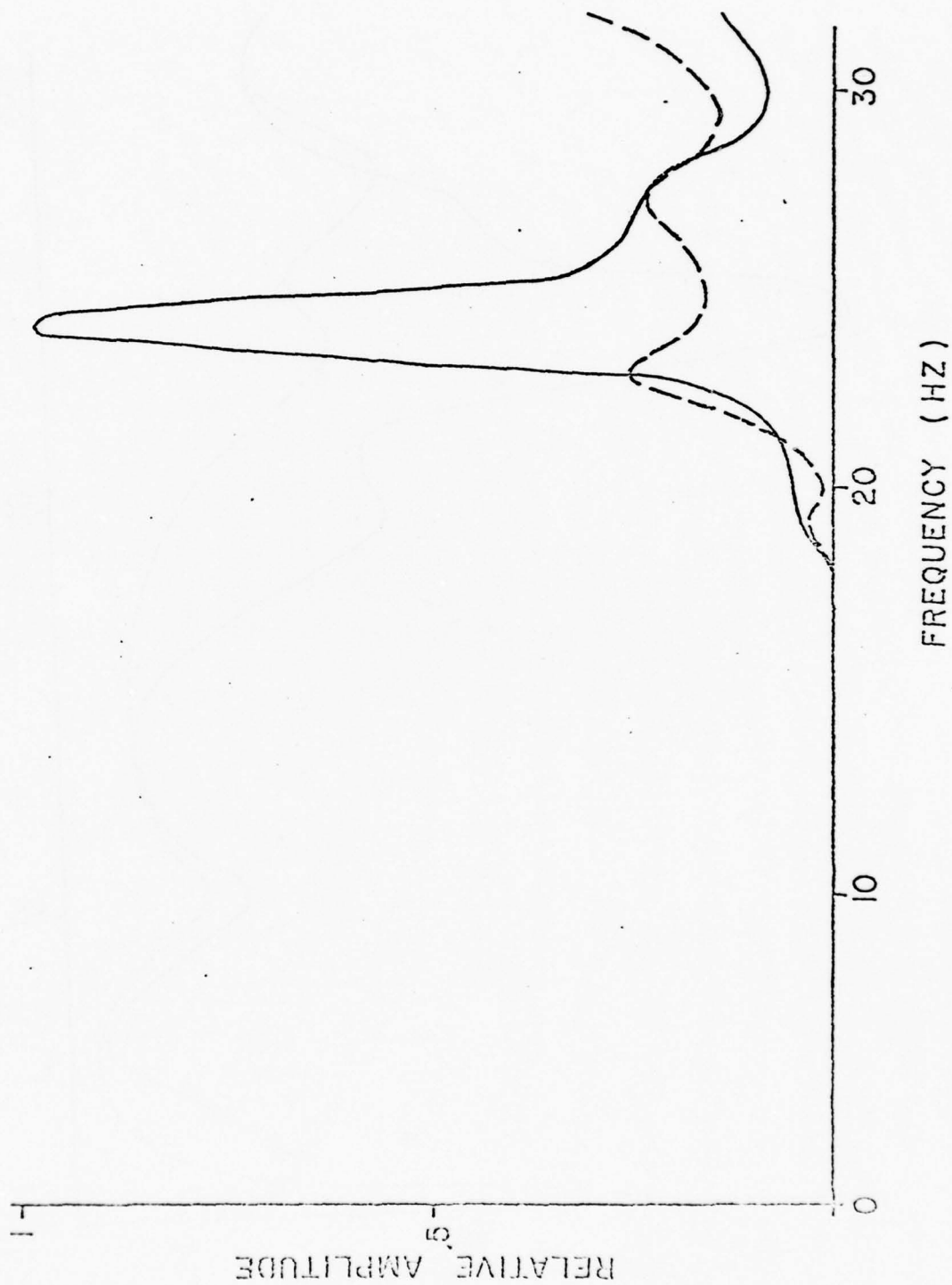


Fig. 3.1 b.

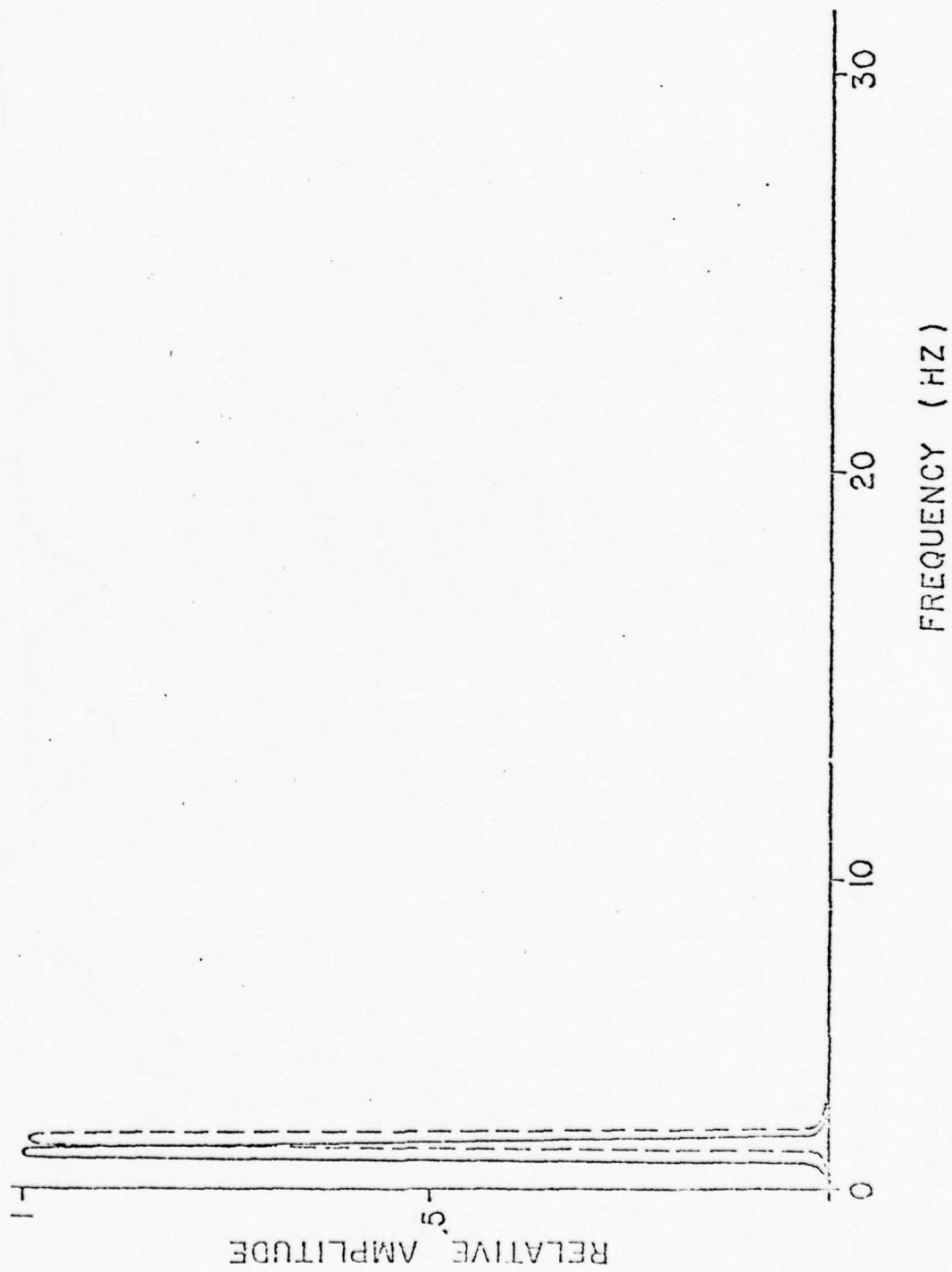


Fig. 3.2 a.

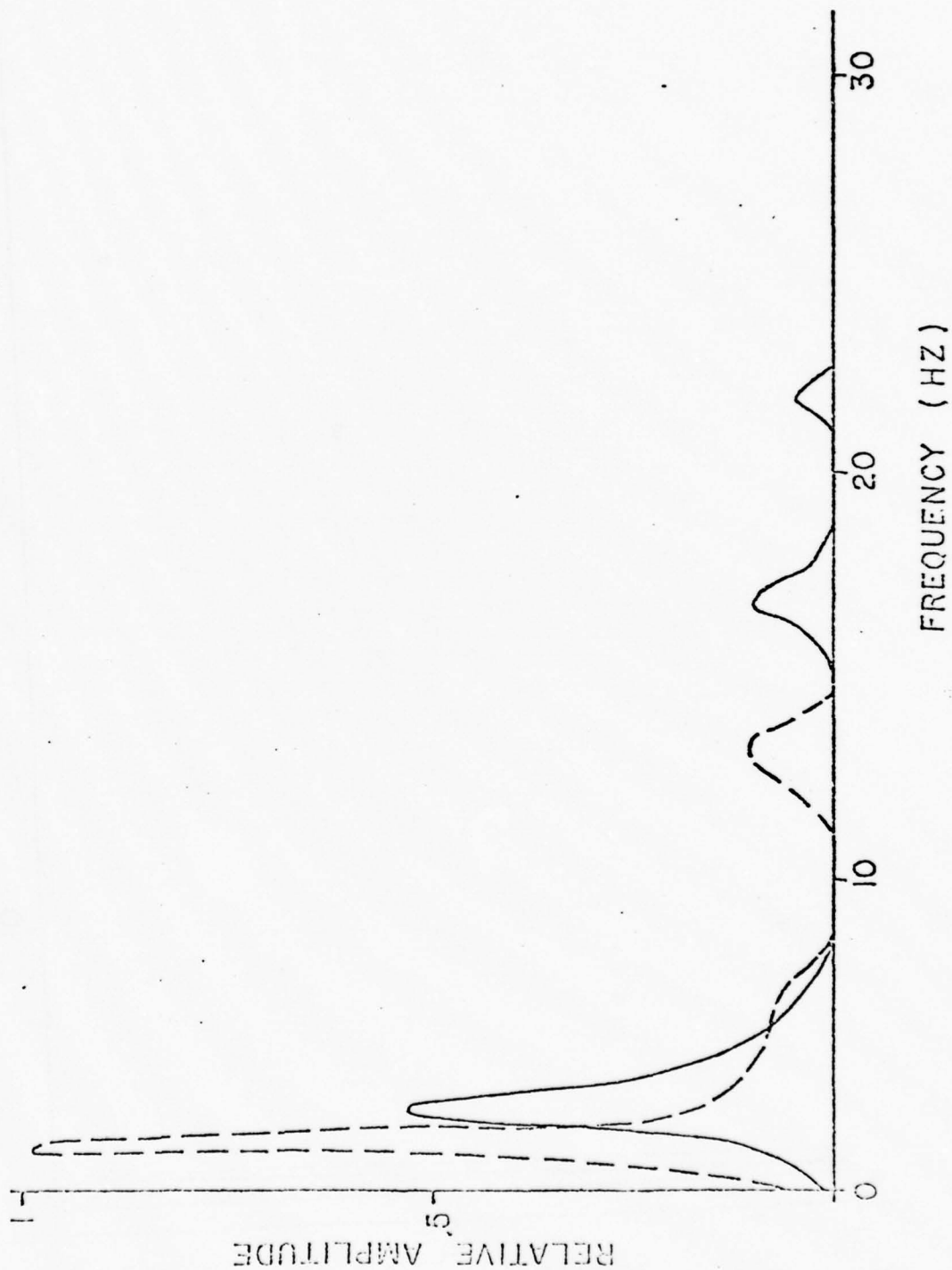


Fig. 3.2 b.

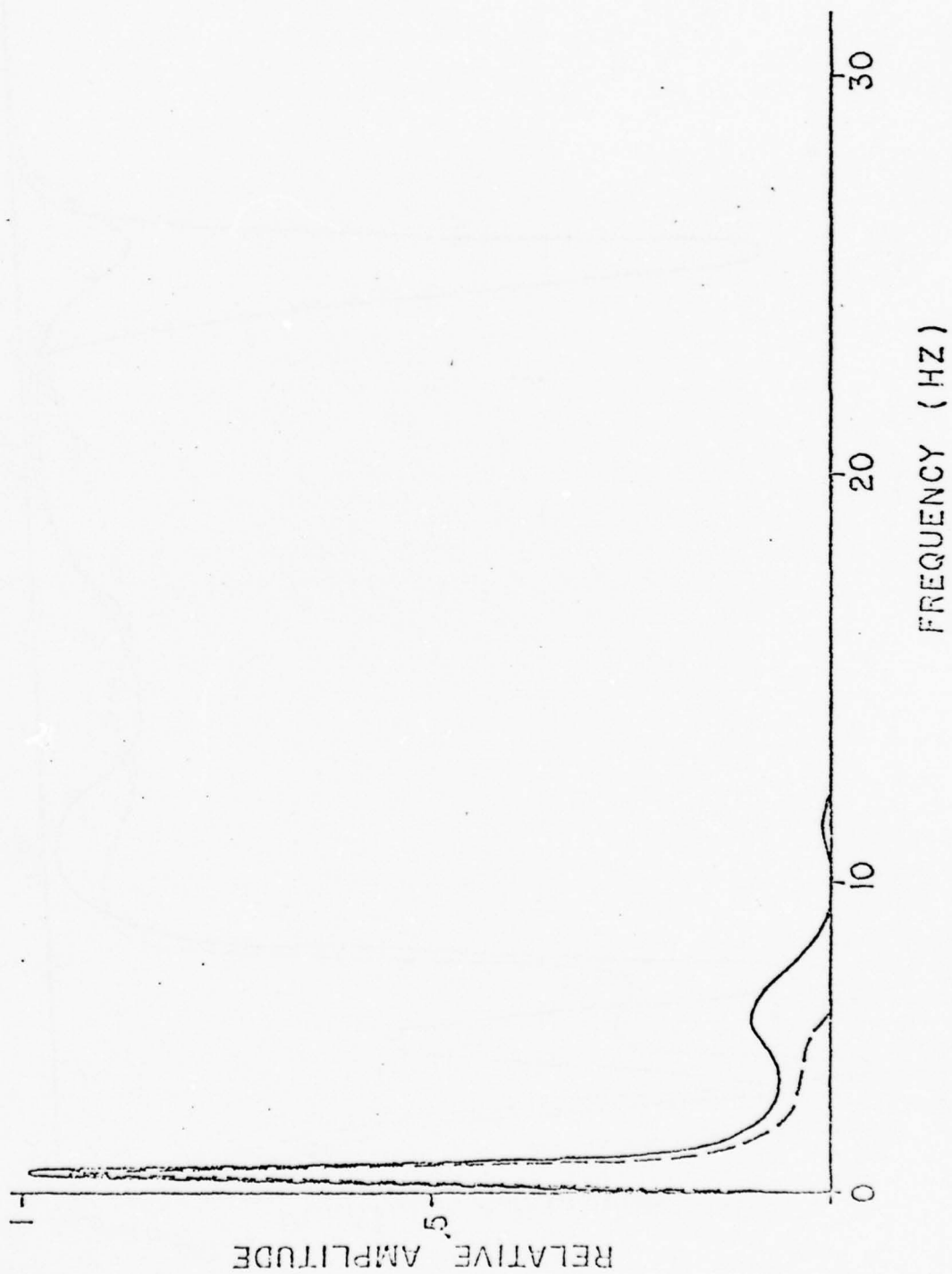


Fig. 3.3 a.

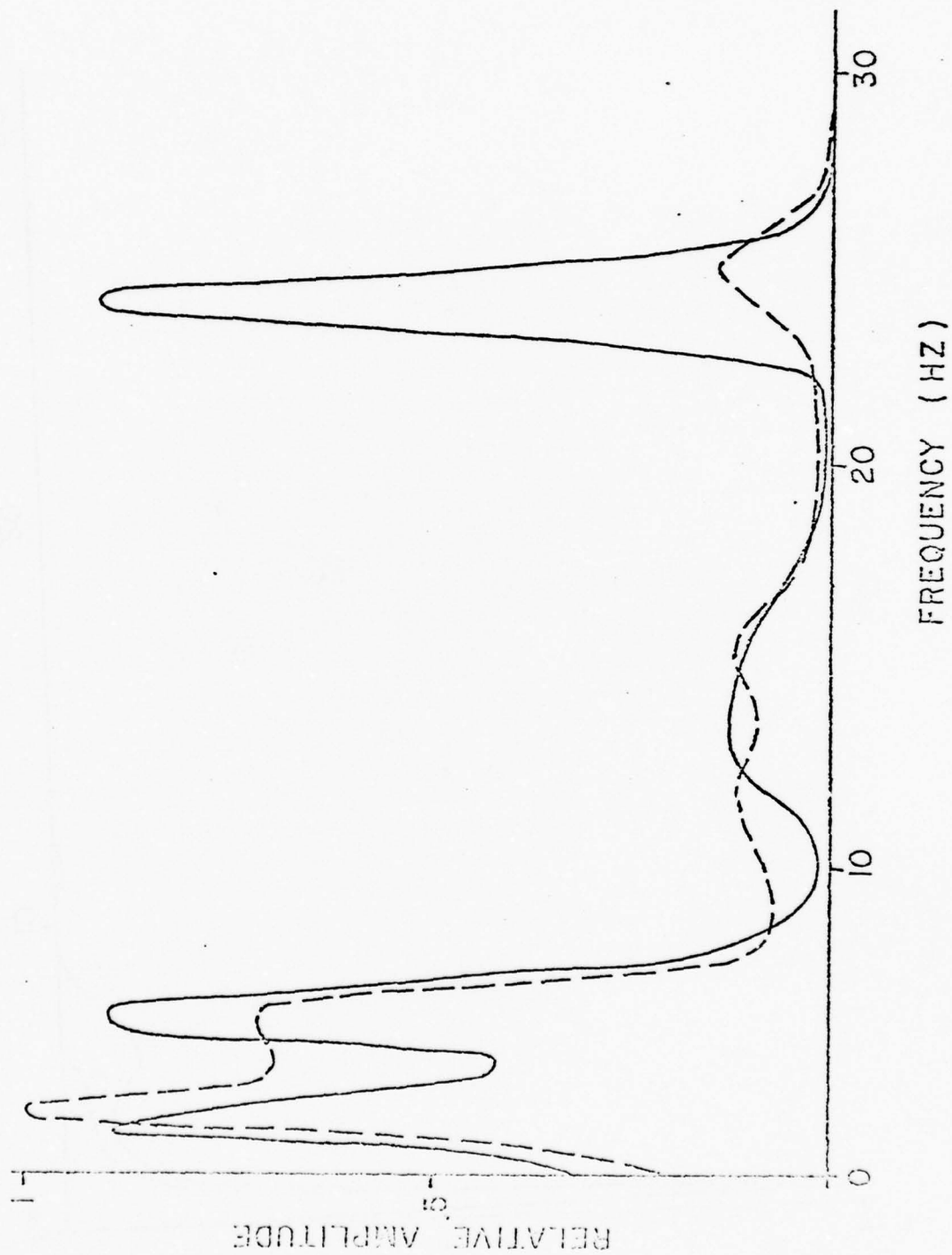


Fig. 3.3 b.

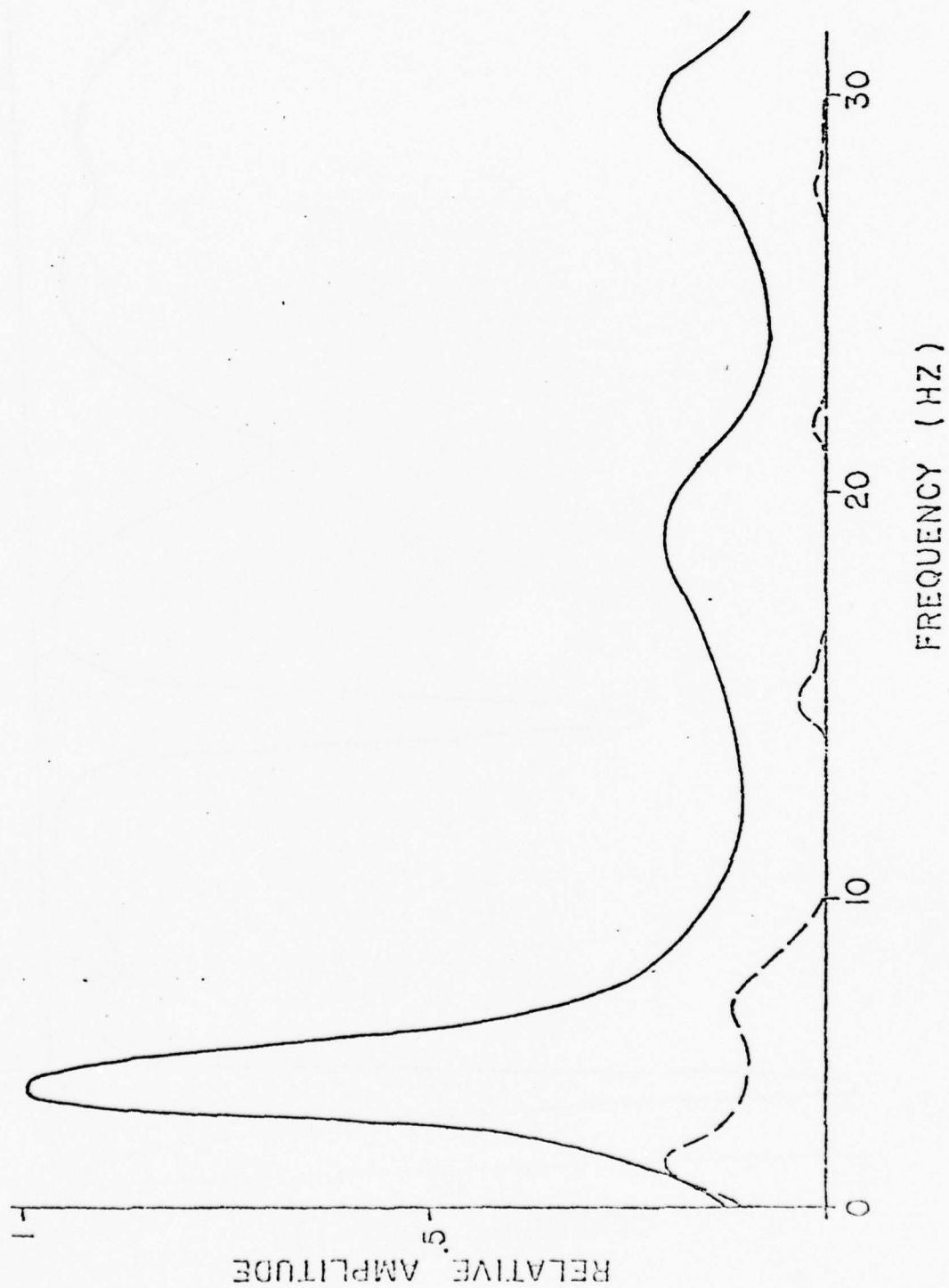
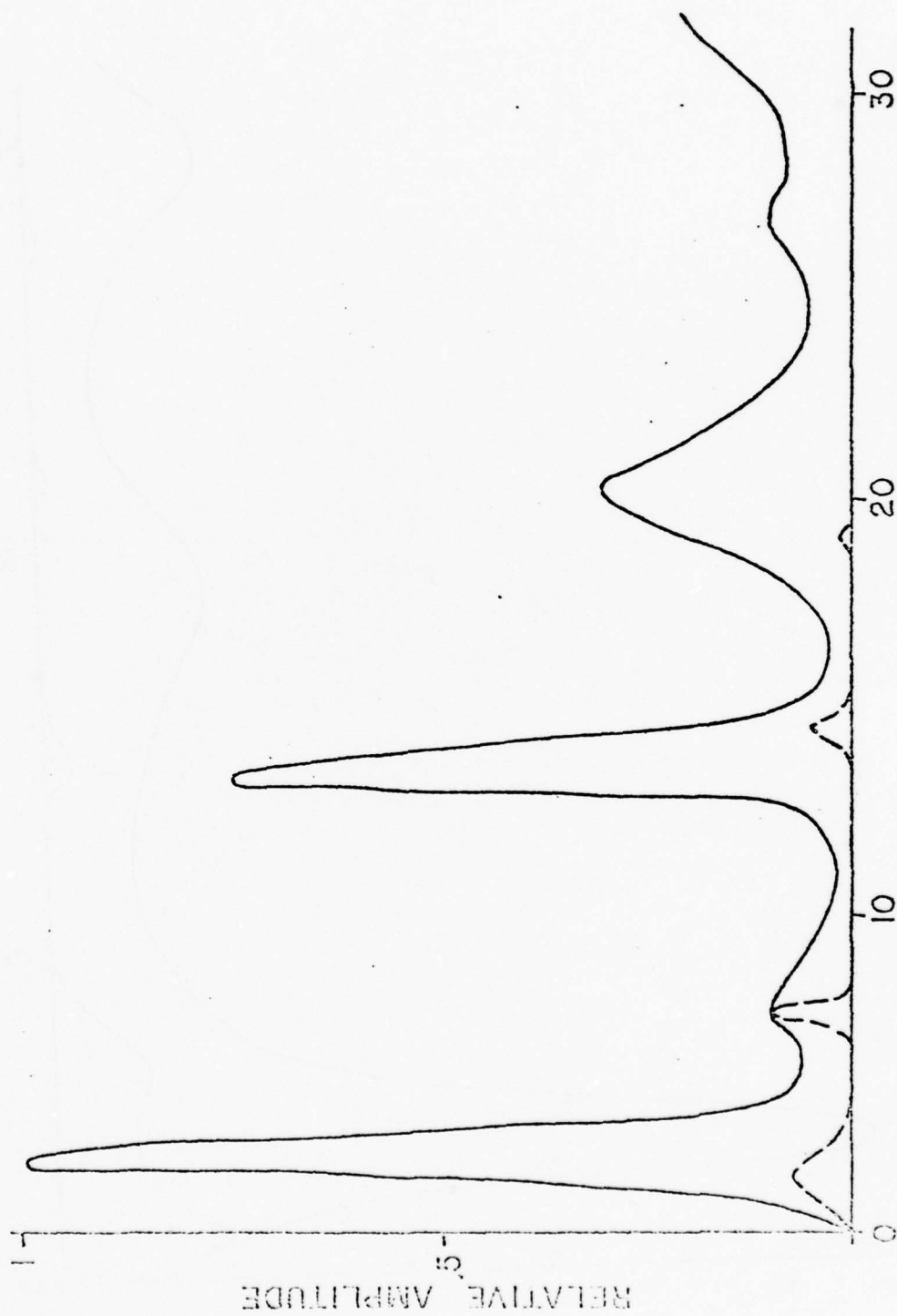


Fig. 3.4 a.



FREQUENCY (HZ)

Fig. 3.4 b.

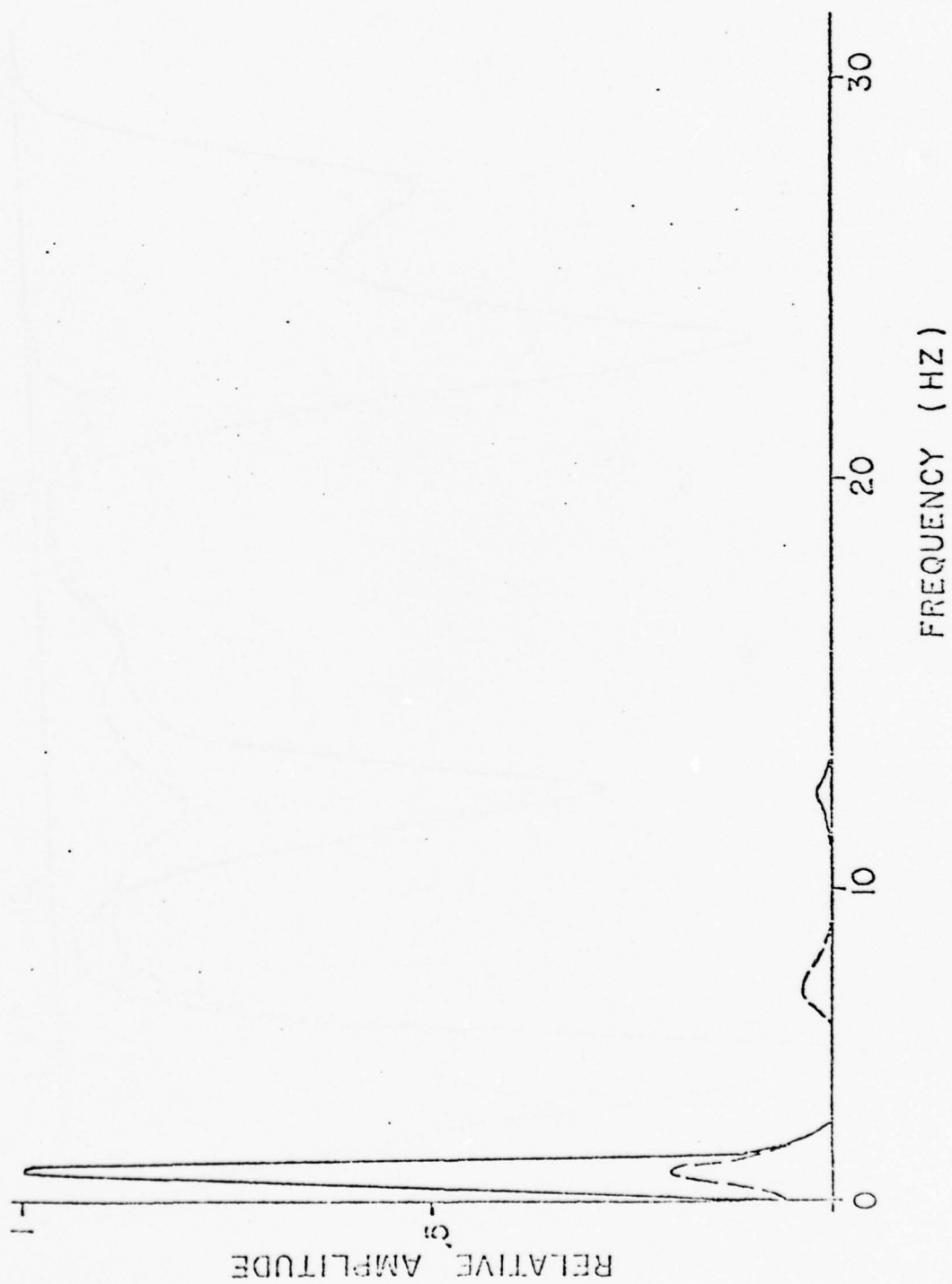


Fig. 3.5 a.

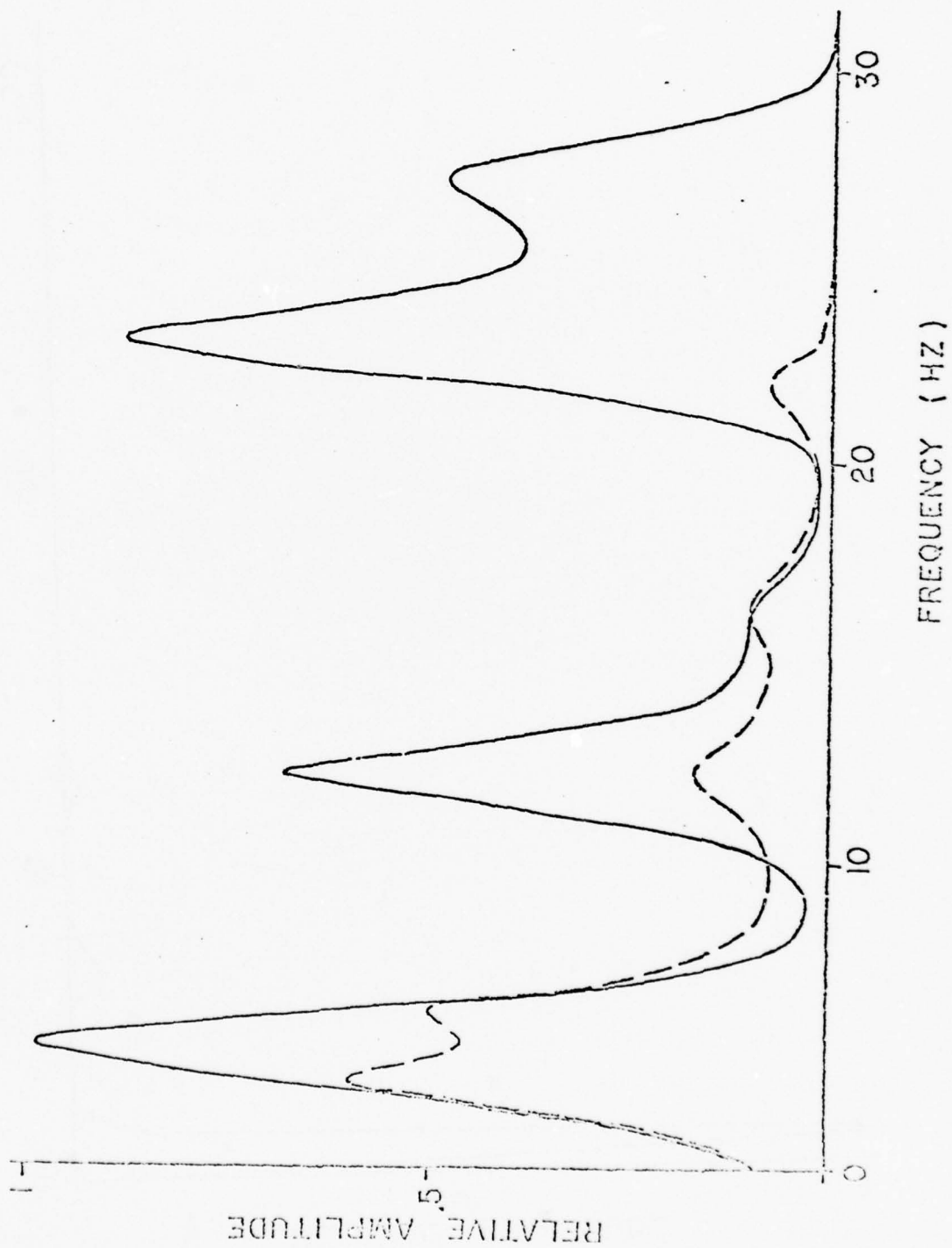


Fig. 3.5 b.

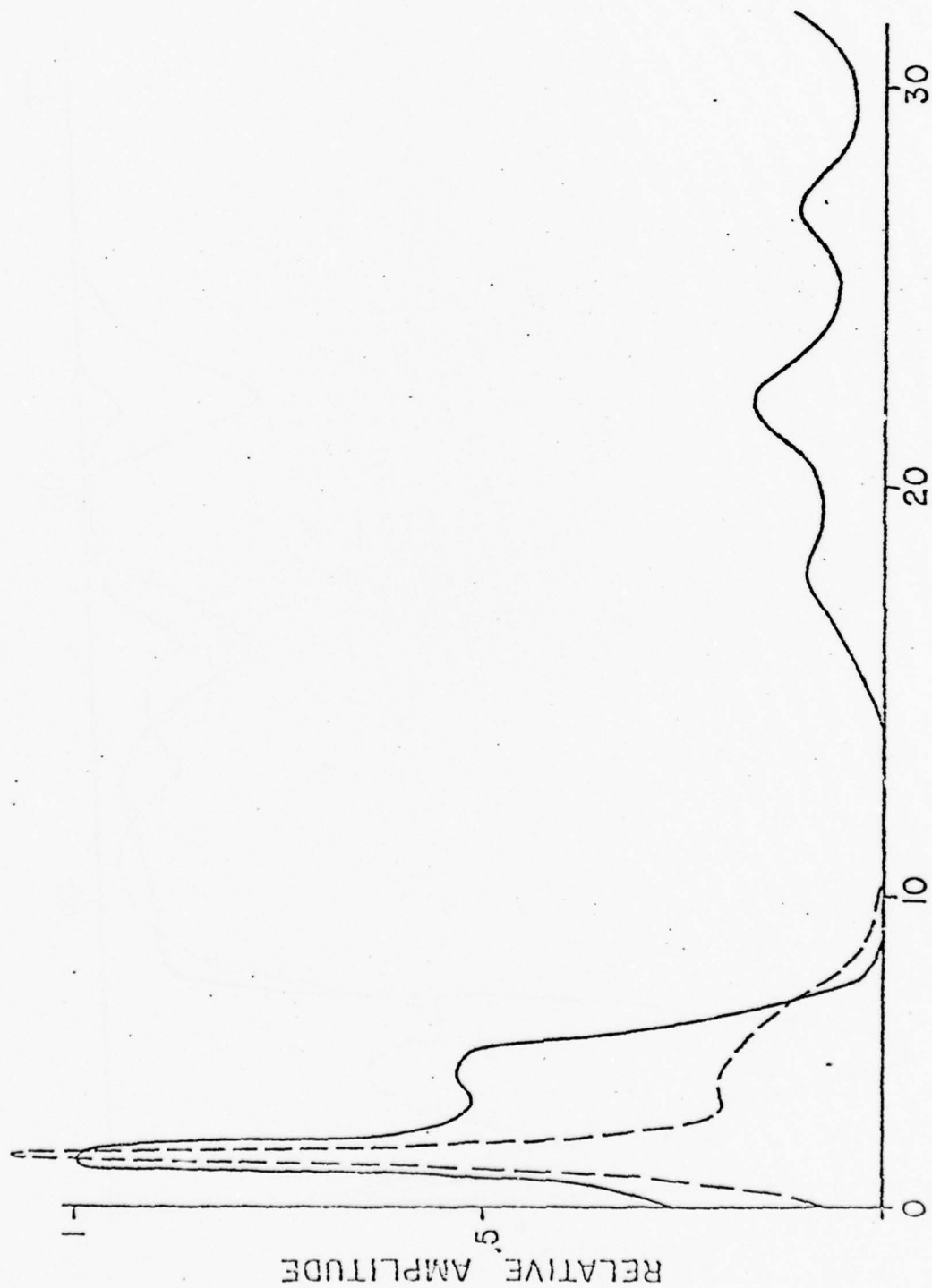


Fig. 3.6 a.

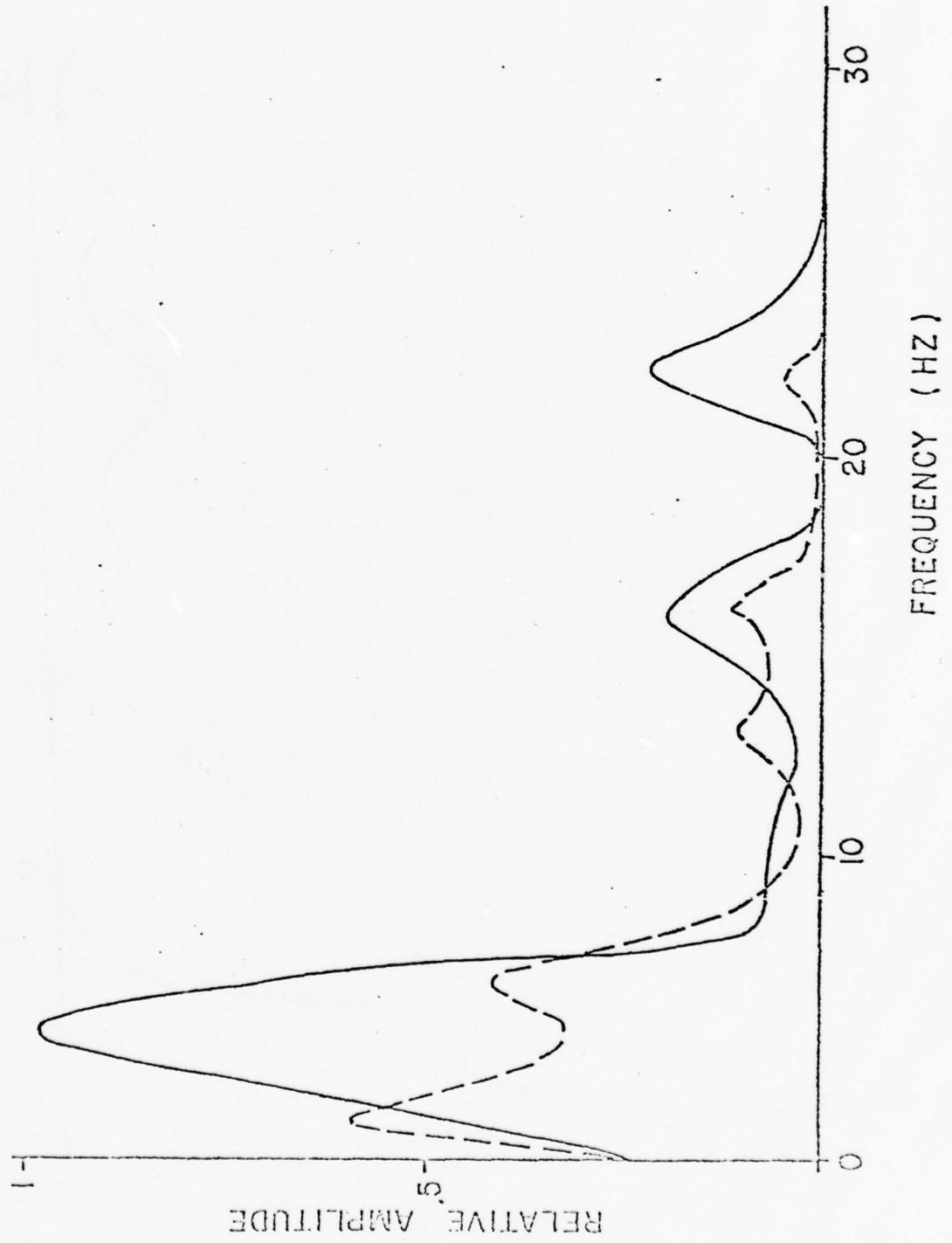


Fig. 3.6 b.

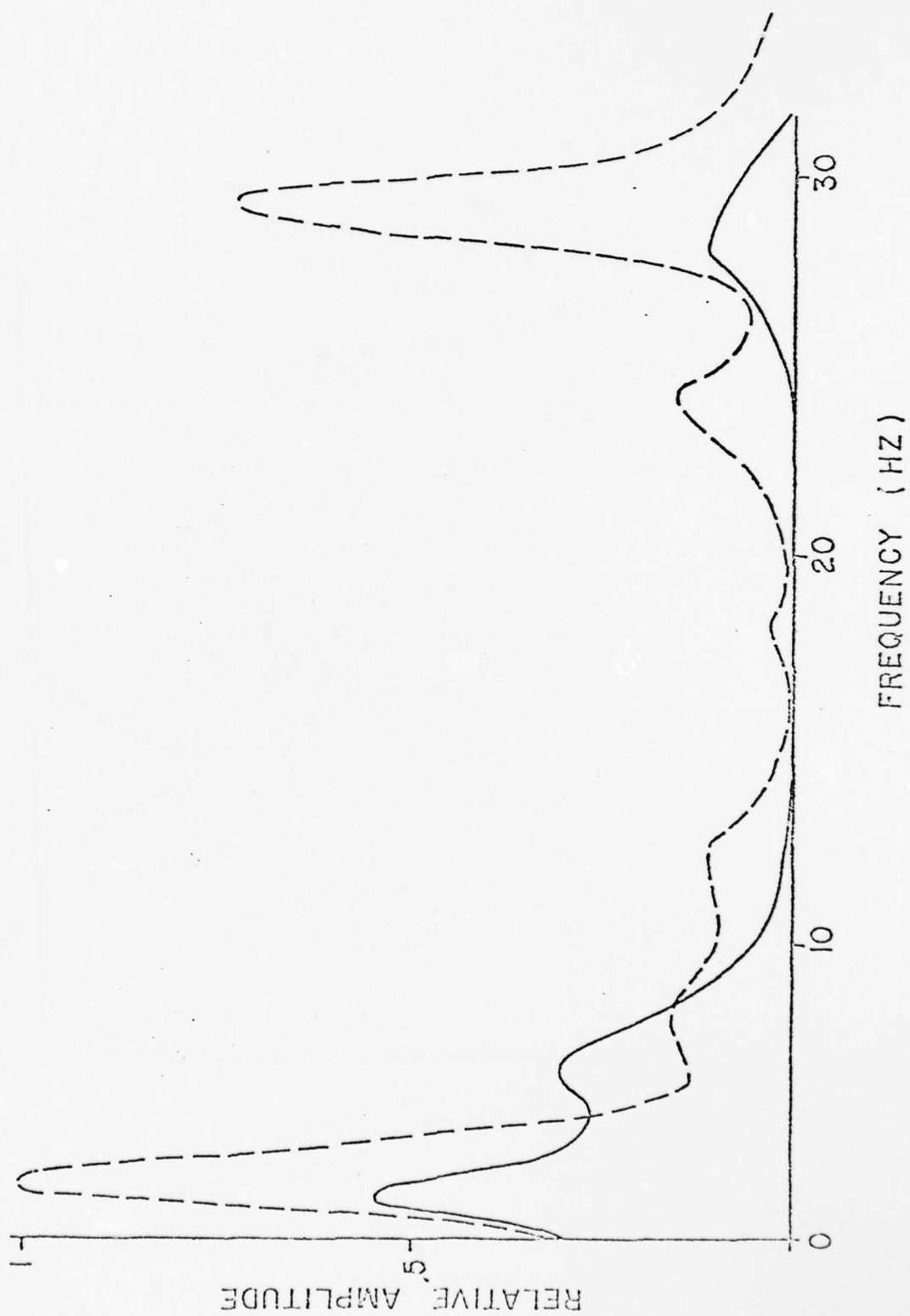


Fig. 3.7 a.

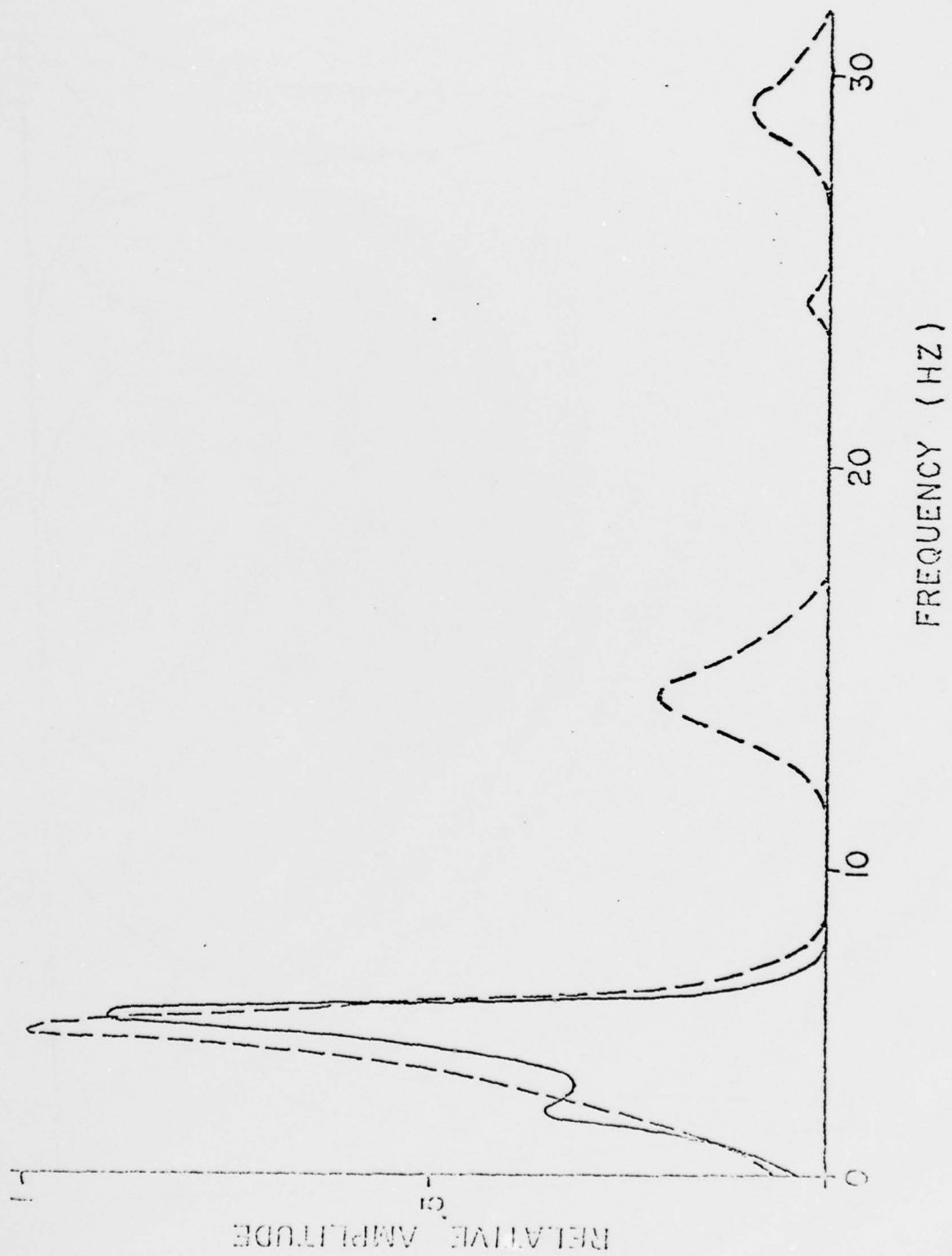


Fig. 3.7 b.

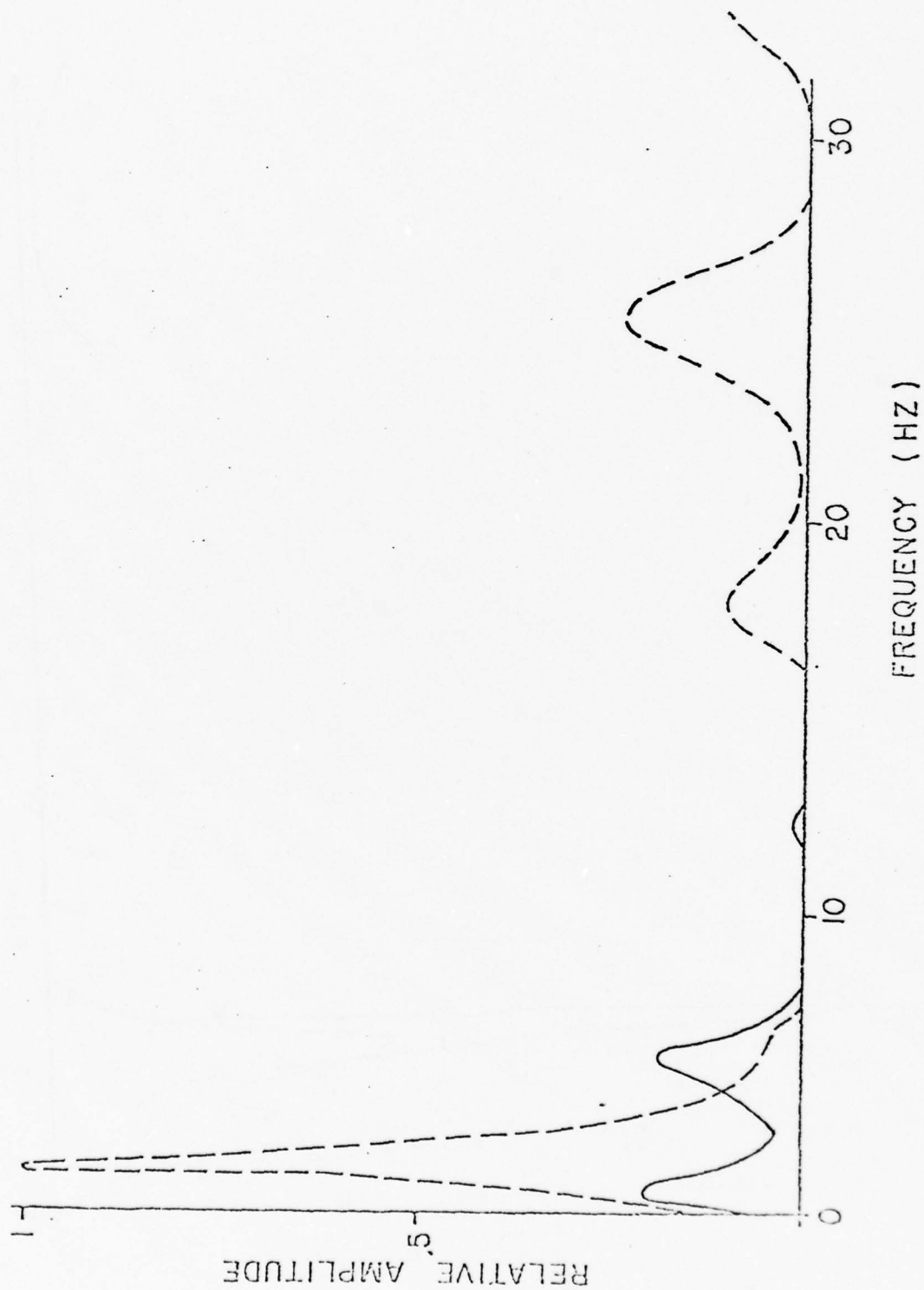


Fig. 3.8 a.

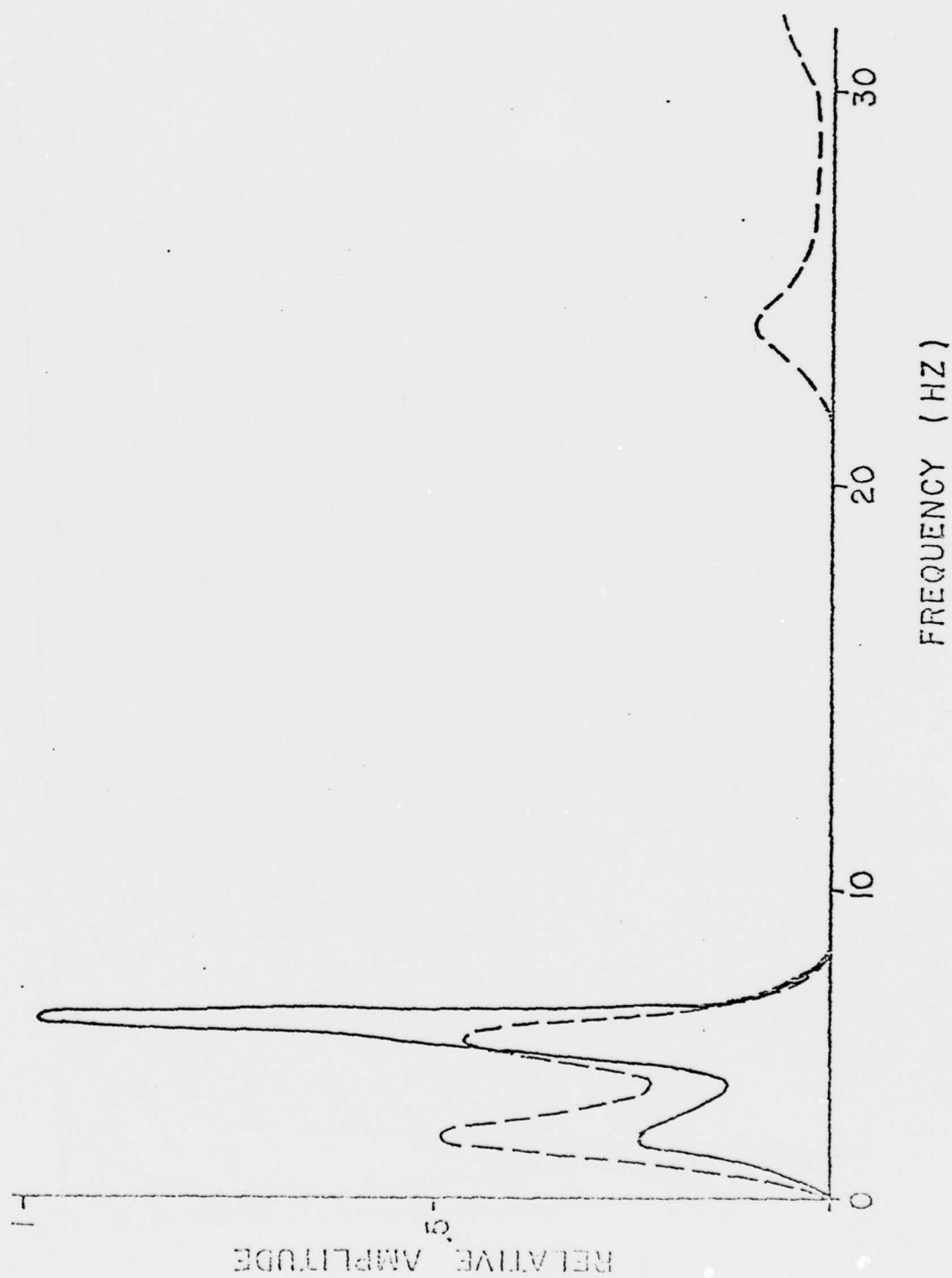


Fig. 3.8 b.

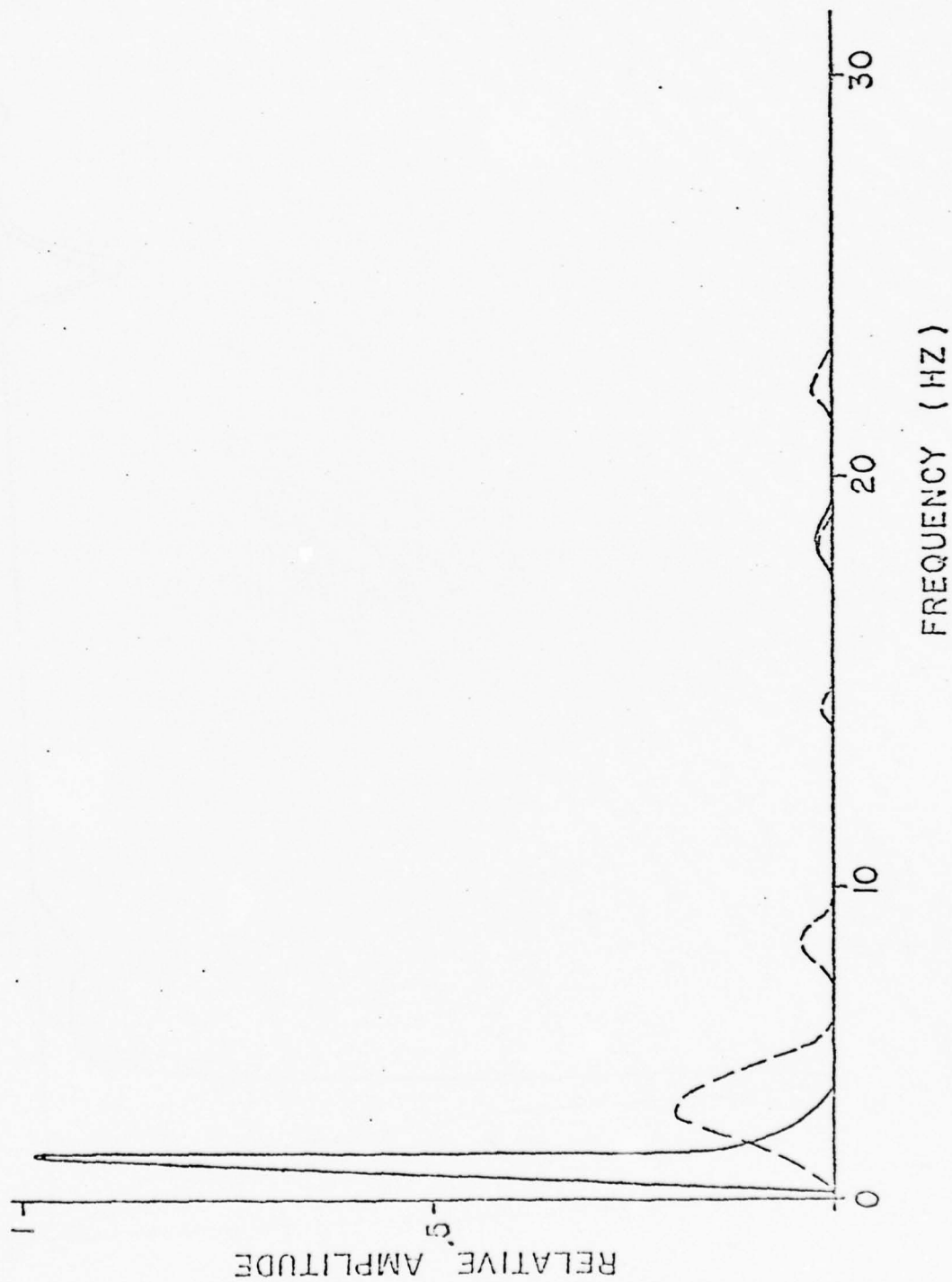


Fig. 3.9 a.

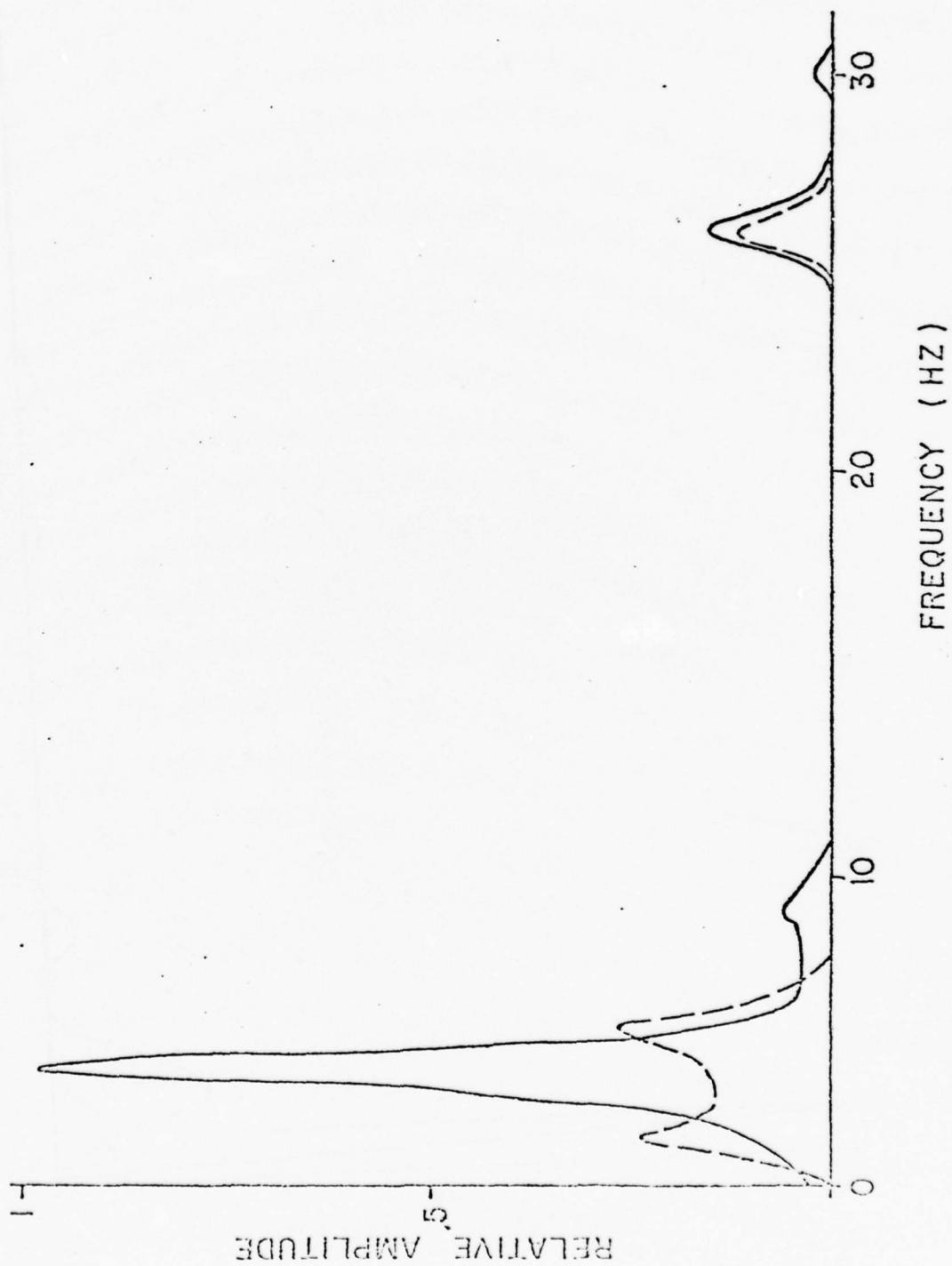


Fig. 3.9 b.

Appendix A
ERIM Experiment

This experiment was planned by Honeywell, Inc. and the Environmental Research Institute of Michigan (ERIM), and was carried out during December 1975. The weapon firings were done in the northwest corner of Anoka county, Minnesota, and the geophone arrays were located in Insanti and Sherbourne counties. The relative locations are depicted in Fig. A.1.

The geology of the test region is given in Appendix C, but it is worth noting here that there were a number of frozen lakes between the firing site and the geophone arrays. There was significant snow cover, but some care was taken to ensure geophone contact with the ground.

The recording array consisted of nine 3-axis geophones arranged in a cross, as shown in Fig. A.2. The geophone spacing along each leg of the cross was 75 meters. The legs were at right angles with the north-south leg aligned with true north. It is not known how precisely this configuration was surveyed.

The weapon was fired horizontally into a corrugated steel catcher backed by 20 feet of coarse sand between the steel and a 100 foot earth backstop. The azimuth relative to true north was 268.5° as shown in Fig. A.1. All weapon shots were a charge 7 with a sand load.

There were a total of 88 firings. IAR has examined all 5 km recorded weapon firings, of which three were free of significant hardware problems.

There remain 77 events consisting of forty 11 km events and thirty-seven 17 km events. Regarding these events, IAR has taken the point of view that it is best to concentrate heavily on a single event at a given range until it is thoroughly understood before attempting further events at that range. Moreover it is thought best to understand thoroughly the 11 km events rather than to prematurely examine the 17 km events.

There are very sound scientific and economic reasons for adopting this point of view. The scientific reasons are clear, and the economic reasons stem from the necessity to obtain computer generated plots of the raw data. This process is very time consuming, and consequently the IAR approach has been to generate these plots until an event is found which is free of hardware clipping and electronic noise. This event is then intensively studied as described above. Thereafter all other "hardware o.k." events at the same range are processed.

IAR has examined the raw data for the 17 km events 36, 37, and 38 and has selected event 38 for study. The progress to

date on this event has been good. This matter is further described in section 3. The plotting of raw data for the 17 km. events was chosen to begin at event 36 because it is the first event with a 109 m.m. howitzer. This weapon was chosen by virtue of the fact that of the three processable 5 km events (#8, 9, 10), two of them were with the 109. It should be stressed again that "processable" refers only to freedom of the recording from hardware problems. Whether the 109 m.m. howitzer produces a larger seismic signal than other weapons, has not yet been examined.

Table A-1 gives the correspondence between the data channel no. and the geophone - axis.

Table A-1. Recording Channels for Standard Geophone Positions

Standard Position	5 km Site Recording Channel (N, E, V)	11 km Site Recording Channel (N, E, V)	17 km Site Recording Channel (N, E, V)
1	13, 14, 15	1, 2, 3	1, 2, 3
2	16, 17, 18	4, 5, 6	4, 5, 6
3	19, 20, 21	7, 8, 9	19, 20, 21
4	22, 23, 24	10, 11, 12	22, 23, 24
5	7, 8, 9	13, 14, 15	13, 14, 15
6	10, 11, 12	16, 17, 18	16, 17, 18
7	1, 2, 3	19, 20, 21	7, 8, 9
8	4, 5, 6	22, 23, 24	10, 11, 12
9	25, 26, 27	25, 26, 27	25, 26, 27

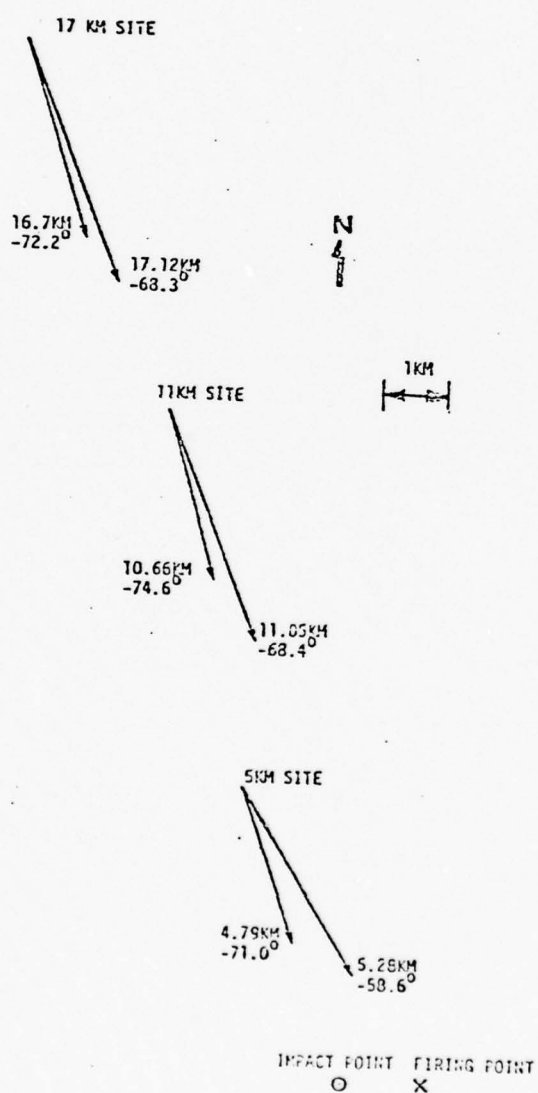


Fig. A.1 Relative Locations of Recording Sites and Firing Area (Bearing Angles are Measured from Due East)



Fig. A.2

Appendix B

This Appendix presents a brief though precise discussion of the mathematical procedure by which IAR has processed the Honeywell ERIM data. The mathematics is deliberately simple for this first approach to the problem and much has been learned to prepare the way for later studies. In particular, the approach to date has been to regard the Haar transform as a detector of local nonstationary behavior, and this seems valid. However, it has been noted as a result of these studies, that its success stems from its ability to whiten the background. The Haar transform is a fixed (in time) linear operator and thus works best on stationary or quasi stationary data. At great range, however, the S/N ratio is small enough that a detection system must contend as well with non stationary ambient noise; therefore, recently IAR has begun to focus on generalizations of the Haar transform which adapt to non stationarities in the background and still whiten them relative to the "signal". This broad class of operators are the adaptive autoregressive operators and they show great promise. As an example, the Haar transform detects a low frequency transient on 7 phones of event 39 at 11 km. This detection is sharpened by these operators.

The implemented IAR detection scheme is conceptually divided into two stages. Stage one obtains a set of arrival times of transients, and stage two processes these to determine whether they comprise a signal, and if so where did

it originate.

Explicitly the stages are as follows:

First Stage

At a particular geophone, a time series $x(t)$ is measured. It is then lowpass filtered (anti-alias) at some frequency F and sampled appropriately ($\Delta t \leq \frac{1}{2F}$)

Let the samples be denoted as:

$$X(n) = X_F(n \Delta t)$$

The discrete sequence $x(n)$ is organized into blocks of length N (a power of two, $N = 2^M$) samples each.

Let $x(n): n = 0, \dots, N-1$ denote such a block, and let $\hat{x}_m(k)$ denote its k^{th} Haar coefficient for some sequence group m :

$$\hat{x}_m(k) = \frac{1}{N} \sum_{n=0}^{N-1} x(n) H_m\left(n, \frac{k}{N}\right) \quad \begin{matrix} k=0, \dots, 2^m-1 \\ m=0, \dots, M-1 \end{matrix}$$

where

$$H_m(k, \xi) = \begin{cases} H_0(0, \xi) = 1 & 0 \leq \xi \leq 1 \\ H_m(k, \xi) = \frac{1}{\sqrt{2^m}} & \frac{k}{2^m} \leq \xi \leq \frac{k+1}{2^m} \end{cases}$$

The original sequence can be retrieved from the transform coefficients as

$$X_n = \sum_{m=0}^{N-1} \sum_{k=0}^{2^m-1} X_{mk}(R)$$

The Haar functions $H_m(k,t)$ form an orthogonal set of functions:

$$\int_0^1 H_m(k,t) H_n(l,t) dt = \delta_{mn} \delta_{kl}$$

It is seen that the Haar transform (for $n \neq 0$, $k \neq 0$) effectively forms the difference between the pair of two mean values computed over adjacent subregions of the data block. Each local mean is computed over $N/2^n$ samples. Consequently, each Haar coefficient (differenced local mean) is affiliated with a data sub-block whose center is located at time $t = n\Delta t = T \cdot \frac{R+1/2}{2^m}$. The index k is therefore, effectively, a decimated time index. For $m = 0$ the value of the single Haar coefficient is the mean value of the time series.

The Haar transform therefore provides a way to examine the change in the mean value of a time series. Note, as well, that if the time series is squared before being transformed, then the coefficients of the transform will represent changes in the second moment of the original series. These operations could be done by other means, but an advantage of the Haar transform is that there exists a fast computer algorithm for the computation of the coefficients, based

upon the factorability of the matrix $H_m(k,t)$. For sequences of length 1024 pts the Haar transform is roughly 35 times faster than the FFT. Even greater speed advantage is attained if the digital computer utilized does not have floating pt. hardware, or if the sequences are longer.

If the input sequence is a sample of a stationary time series which is independently normally distributed with known parameters $N(\mu, \sigma^2)$ then the Haar coefficients $x_m(k)$ will be independent, normally distributed as $N(0, \frac{2^{m+1}}{N} \sigma^2)$. If the variance is unknown the Haar coefficients, normalized by the sample standard deviation, will be t-distributed with degrees of freedom $\nu = \frac{2^{m+1}}{N} - 1$.

We assume that the ambient seismological noise series is stationary so that the mean is constant. The above described t-statistic will then fluctuate about zero. Significant departures from zero will then be correlated with local non stationarity in some sequency group. (Recall that there is a time dependent t-variable for each sequency group). We define such significant excursions of the t variable as designating the reception of a "transient" wave form within the data sub-block affiliated with the corresponding Haar coefficient. If the Haar coefficient is given by $x_m(k^*)$, then the sub-block is the one of length $2N/2^m$ centered at $t = \frac{k^*}{2^m}$. We refer to this data sub-block as a "contender segment".

Let us now suppose that the above procedure has been carried out on all geophone channels. (Note that if a rough bearing estimate is known, the data on the horizontal geophone channels should be rotated to this bearing. This procedure allows approximate separation of the data into components transverse, longitudinal, and vertical to the incoming wave front, and thereby facilitates separation into Love and Rayleigh wave components).

We further suppose that transients are detected on several phones within some time window. That is, let τ denote a maximum expected travel time across the array

$$\tau \approx A/c_{\min}$$

where A is the array aperture and c_{\min} is the minimum expected seismic wave group speed. And let T_i denote the center time of the contender segment on the i^{th} geophone. (These times should be drawn from channels of the same type).

We assume the times are within the window; that is:

$$\text{Let } T_{\max} = \max (T_i)$$

$$T_{\min} = \min (T_i)$$

$$\text{then } T_{\max} - T_{\min} < \tau$$

In this case, we further analyze this set of contender segments to determine whether a signal is present. Roughly speaking, a signal is present provided the relative times

between the transients allow the second stage (below) to obtain spatial positions whose covariance ellipse is small.

In order to obtain a more precise estimate of the relative times, cross correlation of the continuous Haar coefficients $\hat{x}_m(s)$ is carried out for fixed m (m being the sequency index whose t variable indicated a transient). The variable s here indicates that the center of the Haar sub-block is varied continuously across the contender segment. This process can be visualized as Haar filtration of the contender segment (and its adjacent neighbors). Briefly then, each contender segment within the window is Haar filtered and then cross correlated with a reference segment.

Let the reference segment be chosen as the center phone of the array (this is not essential), then cross correlation of each remaining segment with this reference segment will give correlation diagrams which have a maximum at some point. Let us choose the relative time between the i^{th} phone and the central phone to be the lag value at which this maximum occurs on the i^{th} correlation diagram:

$$\max_{\tau} R_i(\tau) = R_i(\tau_i^*)$$

We therefore obtain relative arrival times between all phones and the central one. This procedure yields sharp

time estimates provided the correlation peak falls off sharply. The precision of this estimate is given approximately by the formula

$$\sigma_{\Delta T} \approx \frac{1}{2.2w} (S/N)^{-1/2}$$

where S/N is the signal to noise peak power ratio and w is the bandwidth of the cross correlated signals. The bandwidth can be improved by carrying out the same procedure on higher frequency groups on the contender segment in the manner of a "protected t-test".

On the 5 km ERIM data, the S/N ratio is roughly 16 and the bandwidth $w \approx 4$ Hz. This formula indicates that $\sigma_{\Delta T} \approx .01$, which is consistent with the result $\Delta \theta \approx 2.5^\circ$ obtained from the second stage. If the relative arrival times are obtained by a procedure utilizing jointly all phones in the array (rather than pair wise as here) this precision can be expected to improve as the square root of the number of phones in array.

Second Stage

A set of relative arrival times has been obtained by the first stage, and these times are now processed by the second stage to determine if they jointly indicate that their respective transients all came from the same location in space. The criterion as to whether this is, in fact, the case is given by the area of the x,y confidence ellipse. The definition of the x,y confidence ellipse is that elliptic contour within which we can be 95% certain that the transient wave front originated.

The equations that follow explicitly state how the x,y position is obtained from the relative arrival times, and how the confidence ellipse is determined. Also presented is the statistical means by which the various geophone channels are combined to obtain estimates which are more precise. The times T_i below are those obtained by the cross correlation procedure of the first stage. Note that the time T_i to the reference phone is zero.

The fundamental physical model is extremely simple, but is successful on the 5 km events. The program is not in any way committed to these equations and they will be made more sophisticated including, for example, dispersion and inhomogeneity.

As depicted in Fig. B.1, suppose a source firing at time T is located at position x,y , and its seismic wave is received at times $T_i: i = 1, \dots, N$. Let the ranges to these sensors be denoted by $r_i: i = 1, \dots, N$. Then to first order (assuming straight line travel), we have the following equations:

$$T_i = T + \frac{1}{v} \left[(x_i - x)^2 + (y_i - y)^2 \right]^{1/2}$$

These comprise n equations in 4 unknowns (x, y, t, v) , and if $N = 4$ they can be solved exactly. However, the arrival times in fact contain random noise perturbations which will therefore introduce error into the solution. Consequently, many observations are made and the solution which maximizes the likelihood function is chosen.

The model thus becomes:

$$T_i = T + \frac{1}{v} \left[(x_i - x)^2 + (y_i - y)^2 \right]^{1/2} + \epsilon_i$$

where the Gaussian random process ϵ has zero mean and known covariance matrix Λ_{ϵ} .

We choose x, y, T, v to minimize the form

$$Q(x, y, T, v) = \sum_{i,j}^N (T_i - h_i) \left[\Lambda_{\epsilon}^{-1} \right]_{ij} (T_j - h_j)$$

where

$$h_i = T + \frac{1}{v} \left[(x_i - x)^2 + (y_i - y)^2 \right]^{1/2} \quad i = 1, \dots, N$$

Λ_{ϵ}^{-1} denotes the inverse of Λ_{ϵ}

We now let: $\underline{x} = (x, y, T, v)^T$

$$H_{ij}(\underline{x}) = \frac{\partial h_i}{\partial x_j} \bigg|_{\underline{x}}$$

The normal equations for this problem become

$$-\sum_{ij}^N H_{ik} \left[\Lambda_{\varepsilon}^{-1} \right]_{ij} (T_j - h_j) = 0 \quad k=1, \dots, 4$$

These non-linear equations are to be solved for the unknown vector $\hat{\underline{x}}$ estimating \underline{x} .

The solution is obtained as the convergent limit of the Gauss-Newton iteration scheme

$$\hat{\underline{x}}^{(n+1)} = \hat{\underline{x}}^{(n)} + \left[(H^T \Lambda_{\varepsilon}^{-1} H)^{-1} H^T \Lambda_{\varepsilon}^{-1} \right]_{\underline{x}^{(n)}} \underline{r}^{(n)}$$

where: $\underline{x}^{(n)}$ denotes the value of \underline{x} at the n^{th} iteration

$$\underline{r}^{(n)} = \underline{T} - h(\hat{\underline{x}}^{(n)})$$

$$\underline{T} = (T_1, T_2, \dots, T_N)^T$$

$\hat{\underline{x}}^{(0)}$ is an initial guess

The iterative scheme will converge for virtually any choice of $\hat{\underline{x}}^{(0)}$ to the same limit. In the program implemented the matrix Λ_{ε} is taken to be σ_{RMS}^2 times the identity matrix.

$$\sigma_{\text{RMS}}^2 = \frac{N}{\sum_i} \left[T_i - h_i (\hat{x}^{(n)}) \right]^2$$

The estimator \hat{x} has a covariance matrix given by

$$\Lambda_{\hat{x}} = (H^T \Lambda_{\epsilon}^{-1} H)^{-1}$$

The 1σ confidence ellipse about \hat{x} is derived from this matrix.

The above method estimates a velocity which should be taken to represent the mean horizontal group velocity from the source to the array. To a great extent the method succeeds on real data because this mean velocity is a very stable physical parameter, and its value is not assumed known by the program

The equations governing the combination of observations are as follows:

Let \hat{x} and \hat{y} independently estimate a parameter \underline{a} . Let $\Lambda_{\hat{x}}$ and $\Lambda_{\hat{y}}$ denote their covariance matrices. Then the minimum variance unbiased composite linear estimator \hat{z} is given by

$$\Lambda_{\hat{z}}^{-1} \cdot \hat{z} = \Lambda_{\hat{x}}^{-1} \cdot \hat{x} + \Lambda_{\hat{y}}^{-1} \cdot \hat{y}$$

$$\Lambda_{\hat{z}}^{-1} = \Lambda_{\hat{x}}^{-1} + \Lambda_{\hat{y}}^{-1}$$

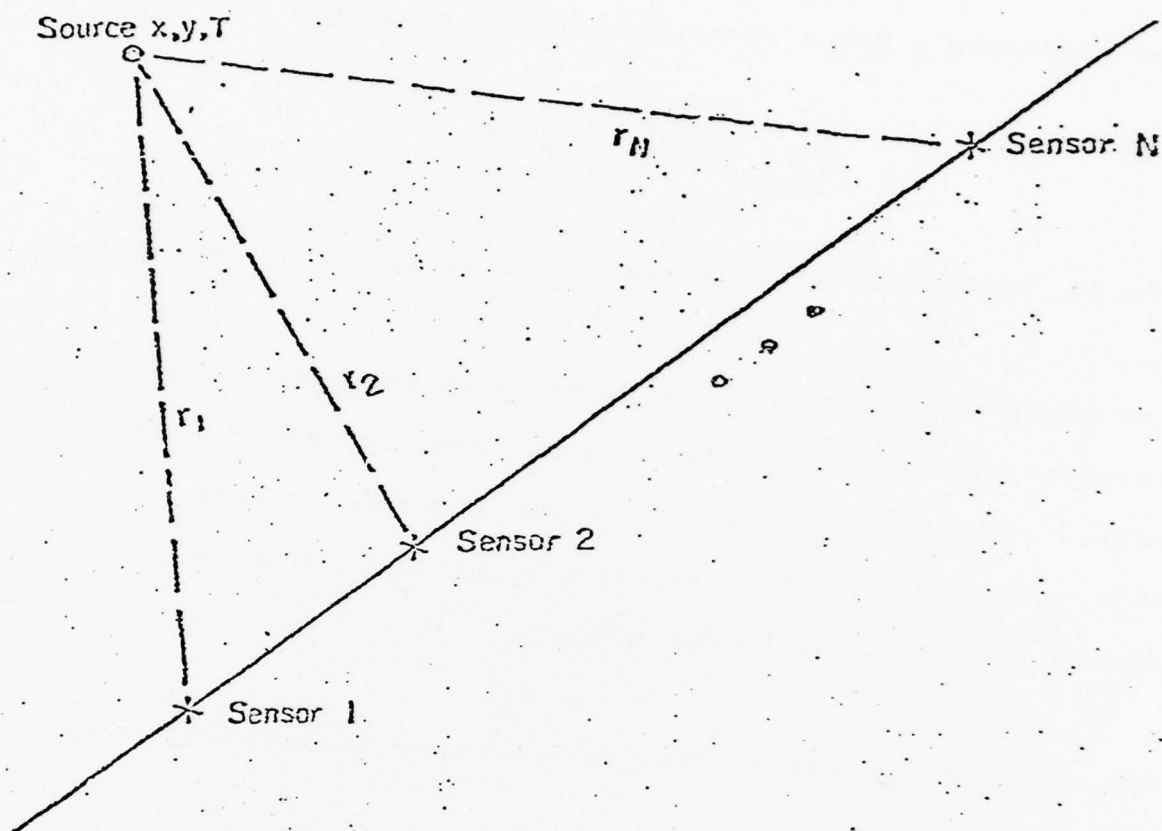


FIGURE B.1.

SYSTEM GEOMETRY

Appendix C.

MODEL OF SEISMIC WAVE PROPAGATION AT THE HONEYWELL TEST SITE

From seismic ray theory and wave theory applied to a model of seismic layering at the Honeywell Ordnance Proving Ground (HOPG), we can construct a graph of frequency vs. arrival time and phase velocity (apparent wave velocity) vs. arrival time for the various seismic phases that cross the geophone array: P waves, S waves, Love waves, Rayleigh waves and the sound (air) wave. This graph is a guide to identification of phases on seismograms from the HOPG test program.

We first define the model. The test program at the HOPG included shots fired to a moveable array set up alternately at three ranges: 5.28 km, 11.04 km, and 17.12 km. Short refraction profiles at several points served to establish the nature of shallow layering in the area (see Larson et al., 1976). From information in that document, a representative geologic and seismic velocity section for the area is:

	Layer Thickness	Compressional Velocity	Shear Velocity	Density
Post-glacial outwash	9.144 m (30 ft)	762 m/s (2500 ft/s)	440 m/s	1.9 g/cm ³
Ice-compacted glacial till	82.296 (270)	1825 (6000)	1056	2.3
Cambrian sandstone		3353 (11000)	1935	2.4

(See discussion in IAR Interim Report, January 1978).

In addition to simplifying the original refraction data, this table involves several assumptions: that shear velocity is related to the compressional velocity observed in the refraction profiles by Poisson's ratio = 0.25 or compressional velocity = $\sqrt{3}$ x shear velocity; representative densities for similar materials are taken from Clark (1966) in absence of values measured at HOPG; that layers are homogeneous and have plane, parallel upper and lower boundaries.

For this model we have calculated the arrival times for compressional and shear body waves (P and S waves) refracted through the third layer (at 3353 m/s or 1935 m/s). This represents the least time path for P and S waves at all three ranges, assuming that there is no material of higher velocity at depth beneath the sandstone. Actually, the presence of granite at a depth of about 1 km may cause the body waves to arrive substantially earlier, especially at 11 and 17 km, than predicted by the model of shallow layering that was used for calculation.

We also have calculated the group arrival time vs. frequency and the associated phase velocity for Love and Rayleigh waves, assuming shallow layering as in the above table. This calculation was done by the method of Haskell (1953). Results are shown in the figure below. These results are affected very little by the granite or deeper layering because Love and Rayleigh waves are guided waves, with motion confined mainly to the surface wave guide. In the lower part of the figure, group arrival time is shown as a function of frequency. These curves represent the frequency of the wave motion that is seen on the recording at various times measured from the time of the shot. There are separate curves for Love and Rayleigh waves at each of the three ranges of interest. The upper part of the diagram shows the phase or wave velocity associated with each frequency and arrival time represented in the lower part. This is the velocity of individual waves crossing the array as measured by correlation of peaks or wave fronts from one geophone to the next. Finally, the figure shows the arrival time of a direct air wave travelling at 343 m/s.

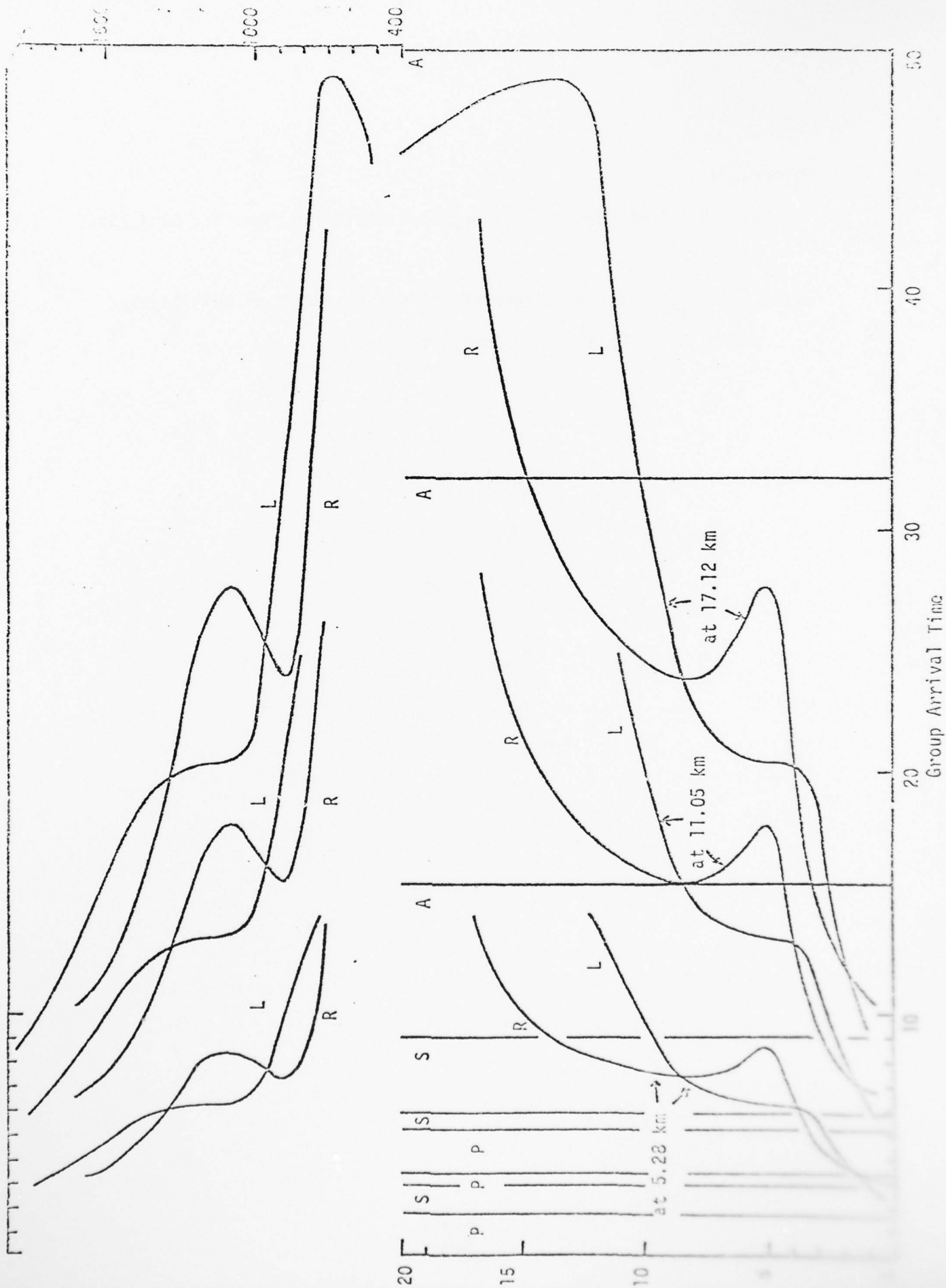
The air wave and the P and S waves are represented as undispersed, i.e., all frequencies arriving at the same time. On the other hand, the Love and Rayleigh waves are dispersed due to the velocity layering of the wave guide: lower frequencies or longer waves generally arrive earlier

than higher frequencies or shorter waves. There are also some bands of inverse dispersion where lower frequencies arrive after higher frequencies. These are due to the sharp velocity discontinuities between layers. If the boundaries are gradational, or if there are velocity gradients rather than discontinuities, then the dispersion curves are straighter than for this model, and may lack inverse portions.

In addition to the simplified approximations of layering, the model may also depart from actual conditions in the sense that there may be substantial local variations in the thickness of compacted till and unconsolidated glacial outwash which are not represented in the model. Due to these possible complications, the arrival times and frequencies represented in the figure are only approximate indications of the relationships which may exist in seismograms.

Also, the contents of seismograms depend on excitation and attenuation characteristics not represented in the figure. If a given frequency is generated at the source and propagates without strong attenuation then it will appear on the seismogram at a time shown approximately by the group arrival curves of the figures. Lower frequencies propagate farther with less attenuation than high frequencies in a given seismic medium; and surface (Love and Rayleigh) waves spread two-dimensionally rather than three-dimensionally as do body waves. Also, recoil sources are relatively rich in low frequencies by comparison with tamped explosions of similar energy. These factors suggest that low frequency Love and Rayleigh waves should be particularly useful for detection and identification of recoil sources at relatively large ranges.

Figure Caption. Group arrival time vs. frequency and corresponding phase velocity for seismic waves propagating on the layered seismic velocity model given in text. The lower portion of the figure gives group arrival time vs. frequency for compressional waves (P), shear waves (S), direct air waves (A), Love waves (L) and Rayleigh waves (R). $V_A = 344$ km/sec is used. P, S and A are undispersed; L and R are dispersed. Families of curves are given for each of three distances 5.28 km, 11.05 km and 17.12 km. The upper portion of the figure gives the phase velocity associated with the particular group arrival time and frequency given in the lower part. Phase velocity is the velocity with which individual waves cross the local array.



AD-A063 163

OFFICE OF NAVAL RESEARCH ARLINGTON VA
PROCEEDINGS OF THE WORKSHOP ON SEISMIC PROPAGATION IN SHALLOW W--ETC(U)
JUL 78

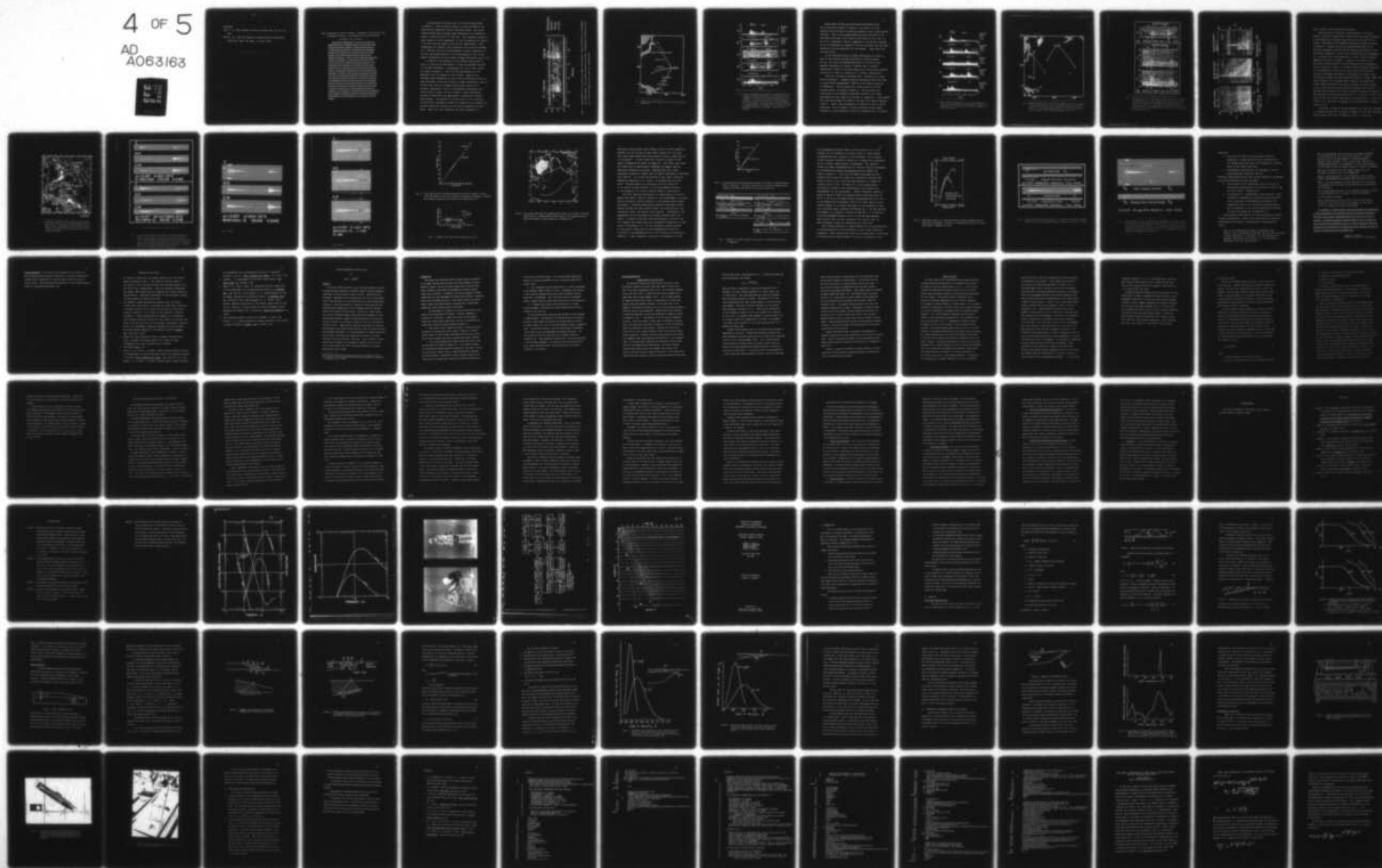
F/G 8/11

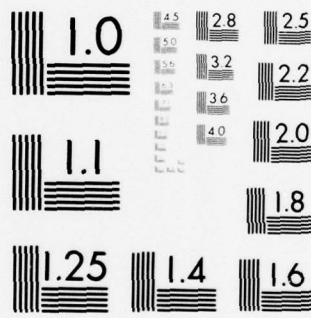
UNCLASSIFIED

NL

4 OF 5

AD
A063163





MICROCOPY RESOLUTION TEST CHART
NATIONAL BUREAU OF STANDARDS-1963-A

References

Clark, S. P., 1966, Handbook of physical constants, Mem. 97, Geol. Soc. Amer.

Haskell, N.A., 1953, The dispersion of surface waves on multilayered media, Bull. Seism. Soc. Amer., v. 43, pp. 17-34.

High Frequency Pn and Sn Phases: Frequency, Efficiency, and Propagation Paths in the Western and North Pacific

Dan Walker, Univ. of Hawaii

Aside from the SOFAR-channel of the world's oceans, the high-frequency Pn, Sn waveguide appears to be the earth's most efficient acoustical waveguide. Although high-frequency Pn, Sn phases have been observed on conventional 1Hz instruments for many years (especially Sn), the real character of these phases has only recently been revealed by special, high-frequency instruments. Some of the more spectacular observations include the following: (a) frequencies as high as 12 Hz for Pn and 15 Hz for Sn at distances in excess of 3000 km, (b) Sn efficiencies often exceeding Pn efficiencies, even at great distances, and (c) amplitudes for Pn and Sn phases recorded on special, high-frequency systems which are much larger than the amplitudes of identical phases recorded on standard 1Hz systems. These and other observations generate a wide range of questions with important implications--some of a very basic nature (Does the propagation take place in the lower crust or the uppermost mantle?) and others of a more applied nature (Could significant portions of the noise at the earth's surface, or at the bottom of oceans, be the result of acoustical energy from the high-frequency Pn, Sn waveguide?). The report which follows summarizes major findings of the Hawaii Institute of Geophysics concerning high-frequency Pn and Sn propagation in the western and north Pacific.

An appropriate starting point is the spectrogram shown in Figure 1. These Pn and Sn phases (1) were recorded on an ocean-bottom hydrophone located near Wake Island. The earthquake occurred near northern Japan (Hokkaido) at a distance in excess of 3000 km (28.34° or 3151 km). The frequency content of these phases is truly remarkable, in that frequencies as high as 12 Hz and 15 Hz are found for Pn and Sn, respectively. Such frequencies are normally only associated with local earthquakes (Δ 's $\lesssim 200$ km) and not with earthquakes at great distances (2). Another surprising feature of this spectrogram is that Sn has higher frequencies and more energy at higher frequencies than Pn (3).

In Figure 2 the epicenter of the Hokkaido earthquake is shown, as well as the epicenters of other earthquakes recorded on the Wake hydrophone. Spectrograms for all of these events are shown in Figure 3. Note that the spectrogram for the Hokkaido event is repeated in this figure. Again we see extremely high frequencies in the Pn and Sn wavetrains; and, in some instances, Sn has more energy at higher frequencies than Pn. We also note that the Solomon Island event, which is at a distance comparable to that of the Hokkaido earthquake, has a strong direct P phase, and no Sn phase. Three earthquakes recorded at Wake from the same general location had similar spectrograms. The absence of Sn may be due to Sn's inability to effectively propagate through the transition zone between the shallow Ontong Java Plateau and the deep Northwestern Pacific Basin. Bases for this contention are given elsewhere (4).

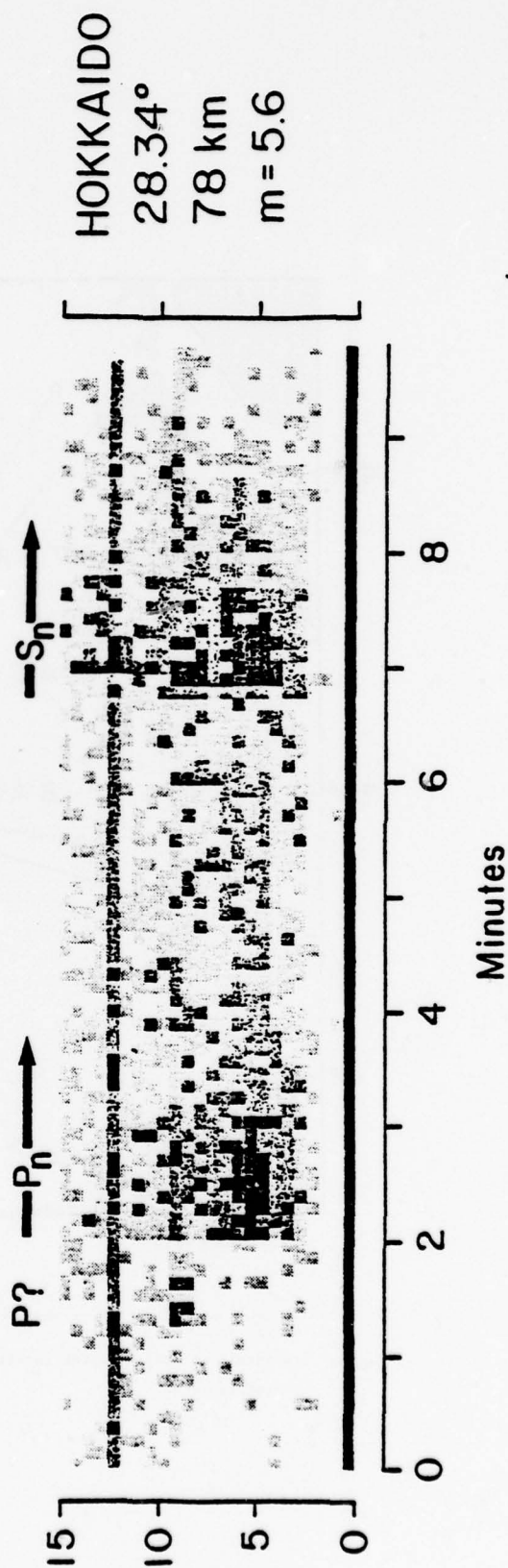


Fig. 1. Spectrogram of a P_n and an S_n phase from northern Japan recorded on a hydrophone near Wake Island. The contour interval is 10 dB. Frequencies as high as 12 Hz and 15 Hz are present for P_n and S_n , respectively.

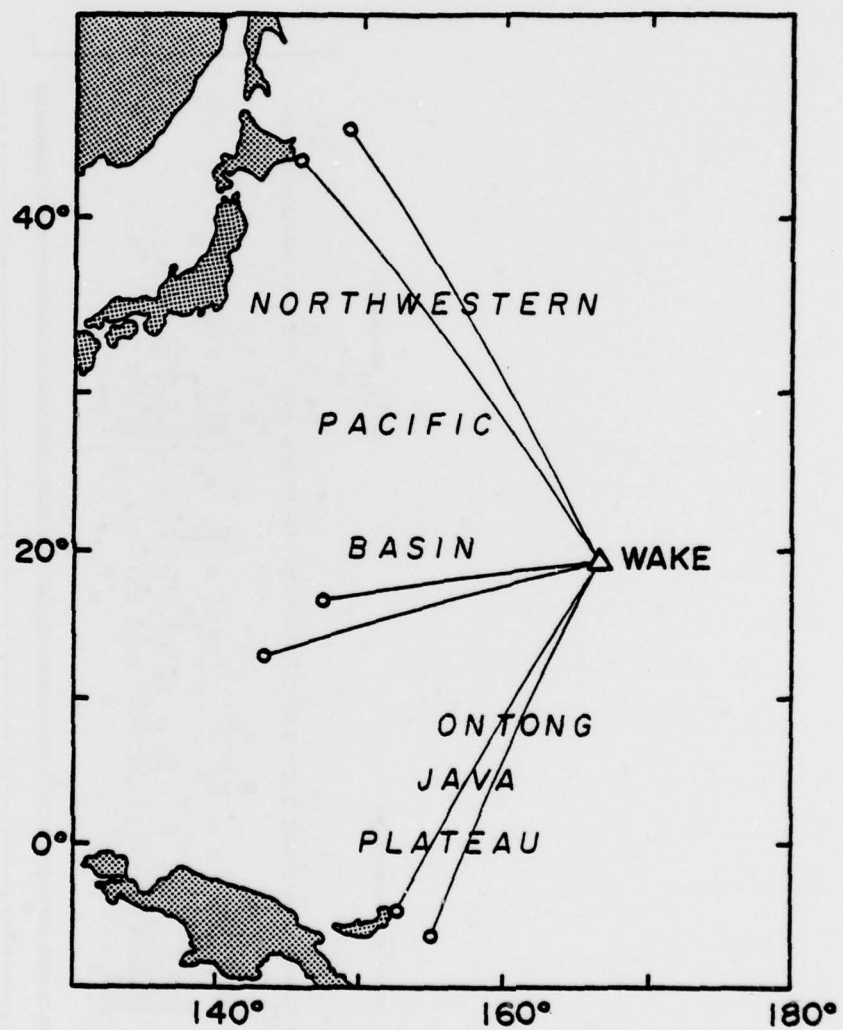


Fig. 2. Epicenters of six principal earthquakes recorded on the reactivated Wake Island hydrophone array.

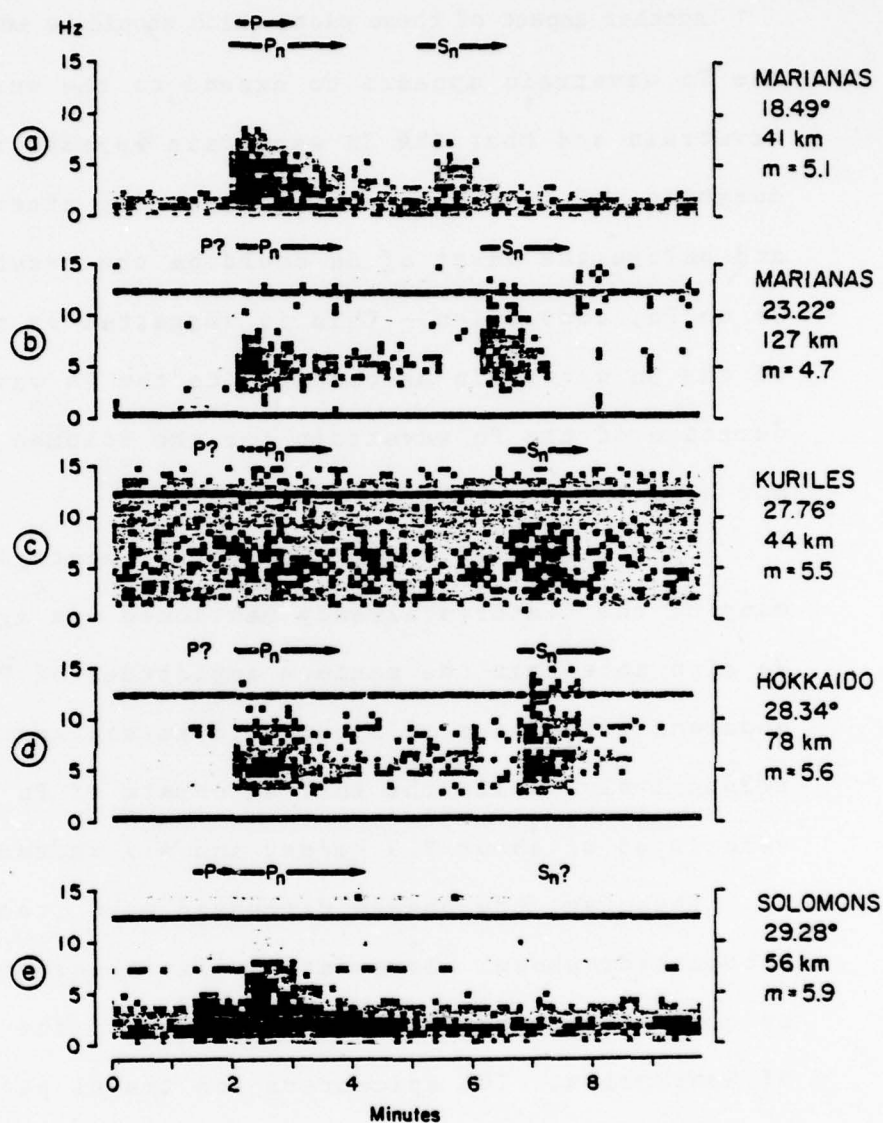


Fig. 3. Spectrograms of earthquakes having travel paths under the Northwestern Pacific Basin (a through d) and under the Ontong Java Plateau (e). The contour interval is 10 dB; m = magnitude. In (a) through (d), note (i) the increasing strength of the S_n phase with respect to the P_n phase as distance increases, (ii) energy at frequencies as high as 12 Hz for P_n and 15 Hz for S_n at 28.34°, and (iii) the apparent absence of P . For (e), which is comparable in its epicentral distance, focal depth, and magnitude to the Hokkaido earthquake (d), note the absence of S_n and the presence of P . Similar spectrograms have been found for other earthquakes in the Solomon Islands and in New Britain.

Another aspect of these plots which should be mentioned is that the Pn wavetrain appears to extend to the onset of the Sn wavetrain and that the Sn wavetrain appears to have a much shorter duration. Some of the energy appearing after the onset of Pn and before the onset of Sn could be the result of Pn to Sn, or Sn to Pn, conversion. This is suggested by the shorter duration of the Sn wavetrain as compared to the Pn wavetrain, and the short duration of the Pn wavetrain for the Solomon event which did not have an Sn.

In the rectified plots of these events, shown in Figure 4, many of the features already mentioned are again apparent. We also note that the maximum amplitudes of Pn and Sn have apparent velocities of around 7.6 km/sec and 4.5 km/sec, respectively, while the initial onsets of Pn and Sn have apparent velocities of about 8.3 km/sec and 4.7 km/sec, respectively.

Thus far, the phases discussed were recorded on an ocean bottom hydrophone. Somewhat similar observations have been made by ocean bottom seismographs (OBS's) of the Hawaii Institute of Geophysics. The epicenters and travel paths of the OBS recorded events are shown in Figure 5. The epicenter and travel path of the Hokkaido earthquake recorded on the Wake hydrophone are also shown for purposes of comparison. Spectrograms for these earthquakes are shown in the next two figures (Figures 6 and 7). Again, high frequencies are present in the Pn and Sn wavetrains, with Sn phases, in some instances, having signal strengths at high frequencies which are comparable to, or greater

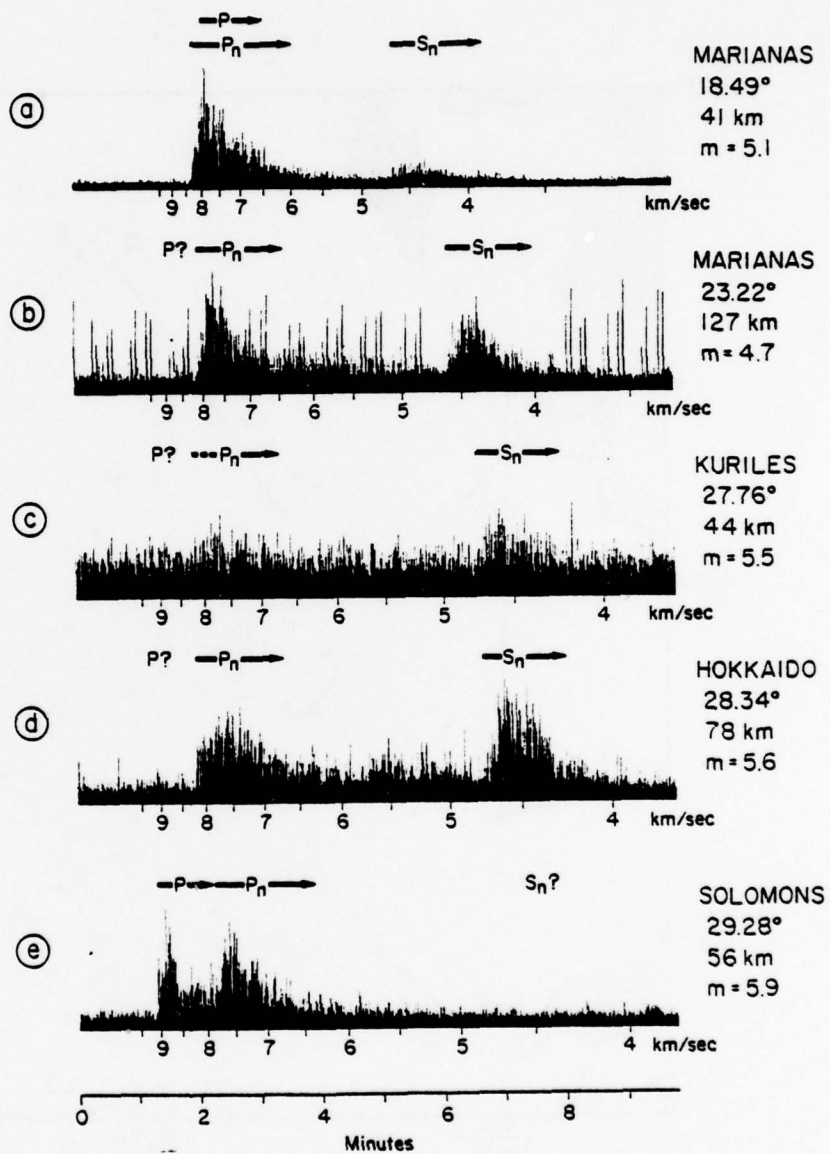


Fig. 4. Digitally rectified and compressed plots of P_n and S_n for the earthquakes shown in Fig. 1. The P_n and S_n arrivals have their maximum amplitudes at apparent velocities (approximately 7.6 and 4.5 km/sec for P_n and S_n , respectively) in agreement with values for the lower crust.

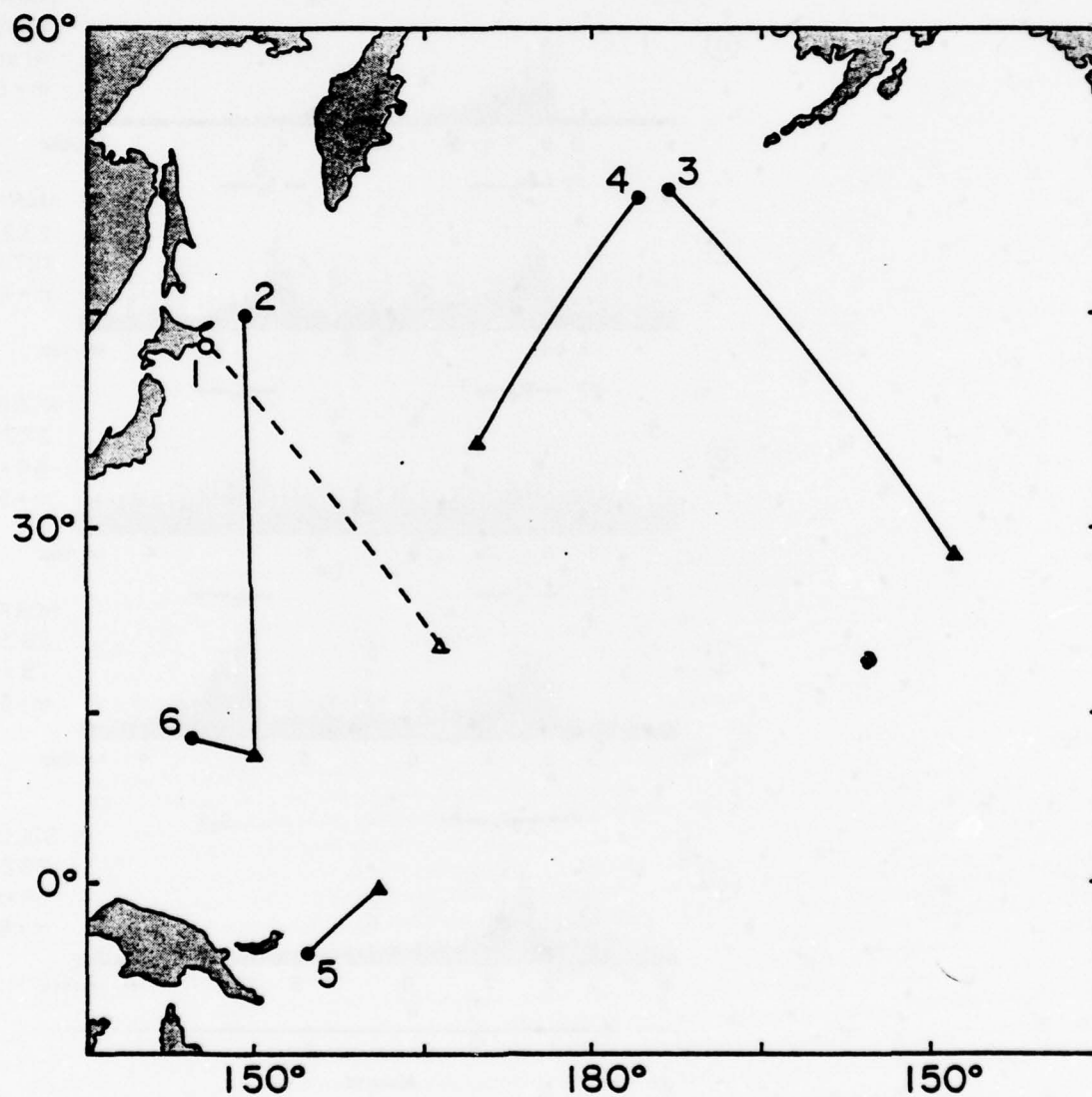


Fig. 5. Earthquake epicenters (circles), ocean bottom seismograph (OBS) locations (triangles), and great circle travel paths (lines). An earthquake epicenter and travel path (dashed line) for the Hokkaido earthquake recorded on a bottom hydrophone near Wake Island is also shown. Numbers identify events shown in Figs. 6 and 7.

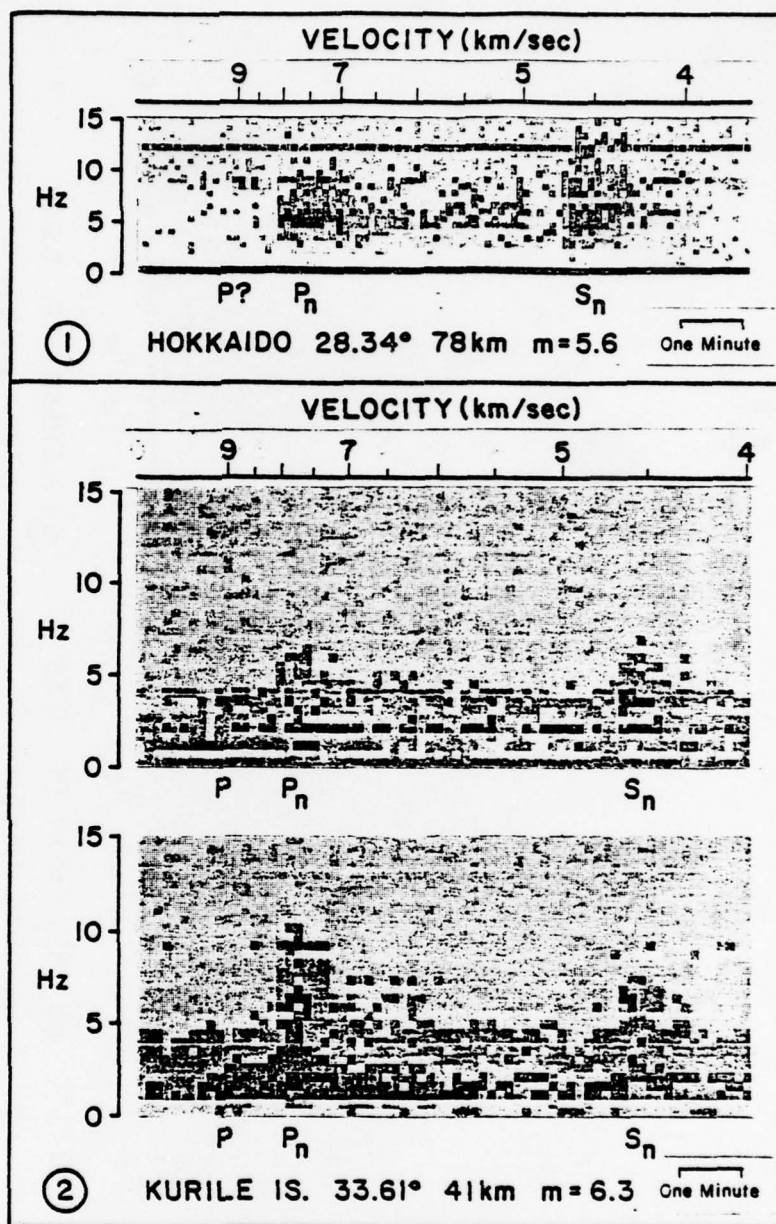


Fig. 6. Spectrograms of P_n and S_n for the Hokkaido earthquake (5 February 1976) recorded on the Wake hydrophone (no. 1), and an earthquake in the Kuriles (21 January 1976) recorded on two orthogonal horizontal components of an OBS east of Guam (no. 2). The contour interval is 10 dB; m = magnitude. The positions of the velocities (the numbers directly over the spectrograms) indicate the arrival times of (great circle) phases having those values.

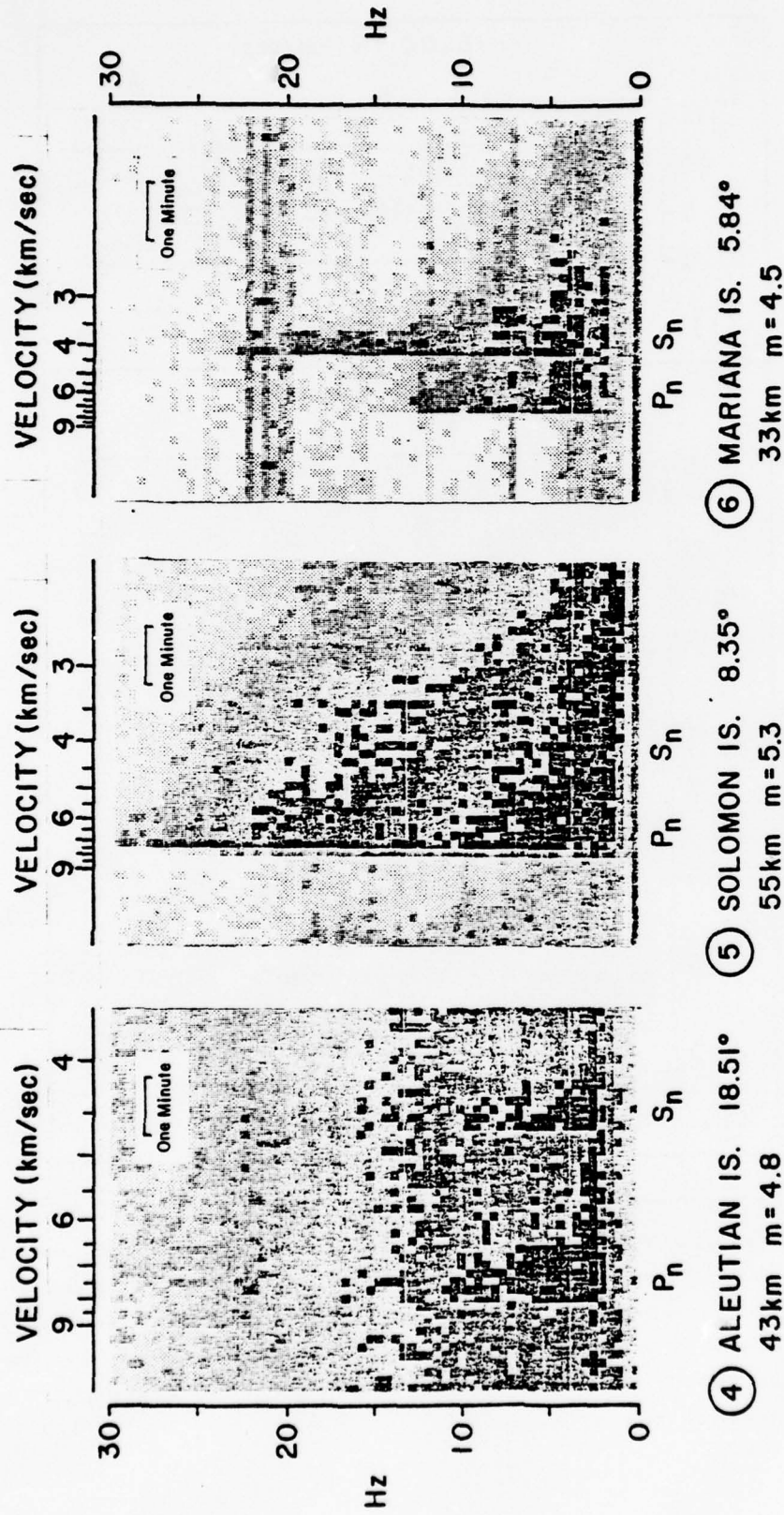


Fig. 7. Spectrograms of P_n and S_n phases recorded on horizontal components of OBS's from earthquakes in the Aleutians (22 September 1976) recorded along the eastern flank of the Emperor Seamount chain (no. 4), the Solomons (23 March 1976) recorded on the eastern edge of the Ontong Java Plateau (no. 5), and the Marianas (18 January 1976) recorded in the East Mariana Basin (no. 6). For additional explanations see the legend for Fig. 6.

than, those of their respective Pn phases.

Data acquired by a special, high-frequency, land-based seismic station at Ponape also indicate that the signal strengths of Sn phases may be greater than those of their respective Pn phases. Epicenters of earthquakes recorded at Ponape are shown in Figure 8. Usually Pn has its greatest amplitudes on the vertical component, while Sn has its greatest amplitudes on the horizontal components. Quite often Sn amplitudes are comparable to, or greater than, the amplitudes of their related Pn phases. Examples are given in Figure 9. Apparent velocities for Pn have been incorporated into earlier hydrophone and seismograph data in Figure 10. [Prior to the Wake Island experiment mentioned at the beginning of this report, data on Pn and Sn had been acquired from paper recordings of hydrophones at Midway, Wake, and Enewetak islands and from seismic stations at Midway, Wake, and Marcus islands; 5.] Although travel times for Pn phases with travel paths in excess of 30° are also shown, our main concern at this time will be with the data at distances less than 30° . A reduced travel time plot for all of the data is shown in Figure 11. The equation for the travel time of Pn is $T = X/(8.33 \pm 0.05) + 2.7$, while Sn data has travel times given by the equation: $T = X/(4.77 + 0.03) + 6.9$. The ratio of V_{Pn}/V_{Sn} is 1.75 indicating a Poisson's ratio of 0.26.

Epicenters of some of the earthquakes which have been observed at distances beyond 30° are shown in Figure 12. [The data discussed here includes that shown in Figures 10 and 11, as well as

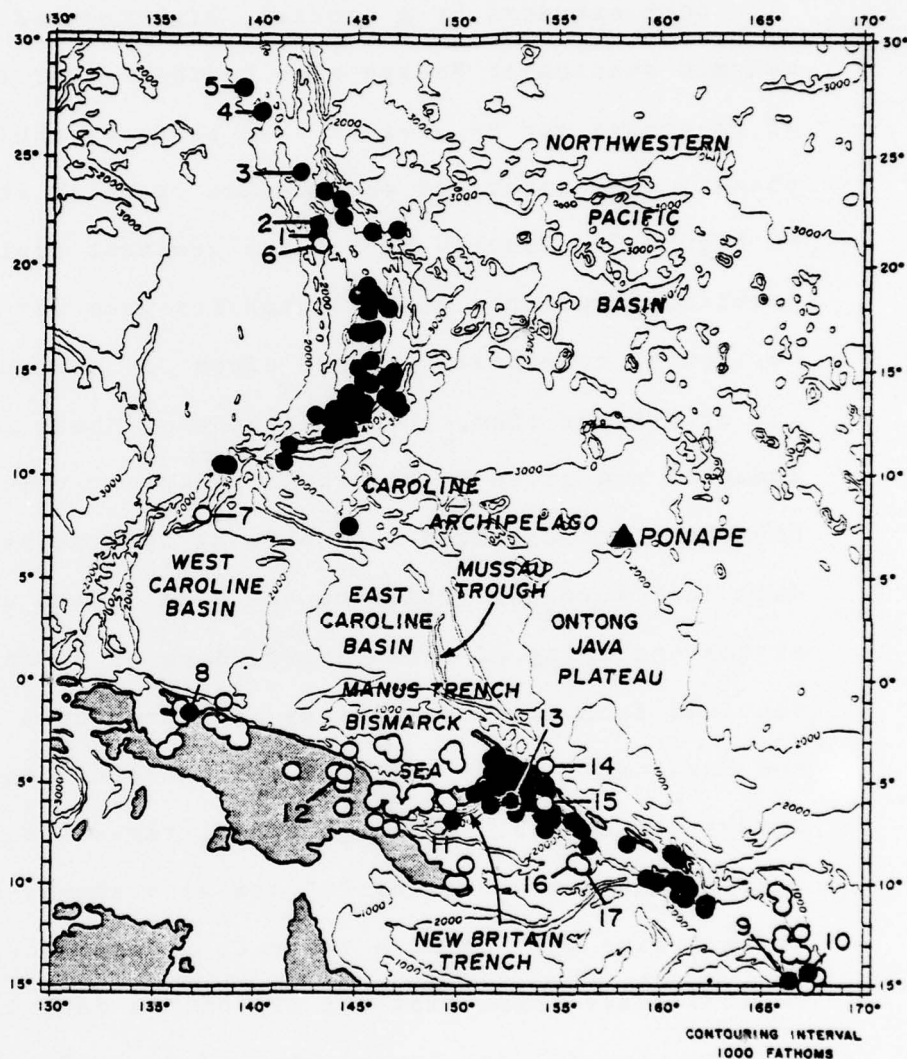


Fig. 8. Bathymetry map of the Northwestern Pacific area showing epicenters of earthquakes having P_2 phases at Ponape (solid circles) and epicenters of earthquakes at distances of less than 25° which generated a normal, mantle-refracted P but no P_2 at Ponape (open circles). In many instances, more than one epicenter is indicated by a single circle. Earthquakes of special interest are numbered and discussed in the original publication (Walker; 7).

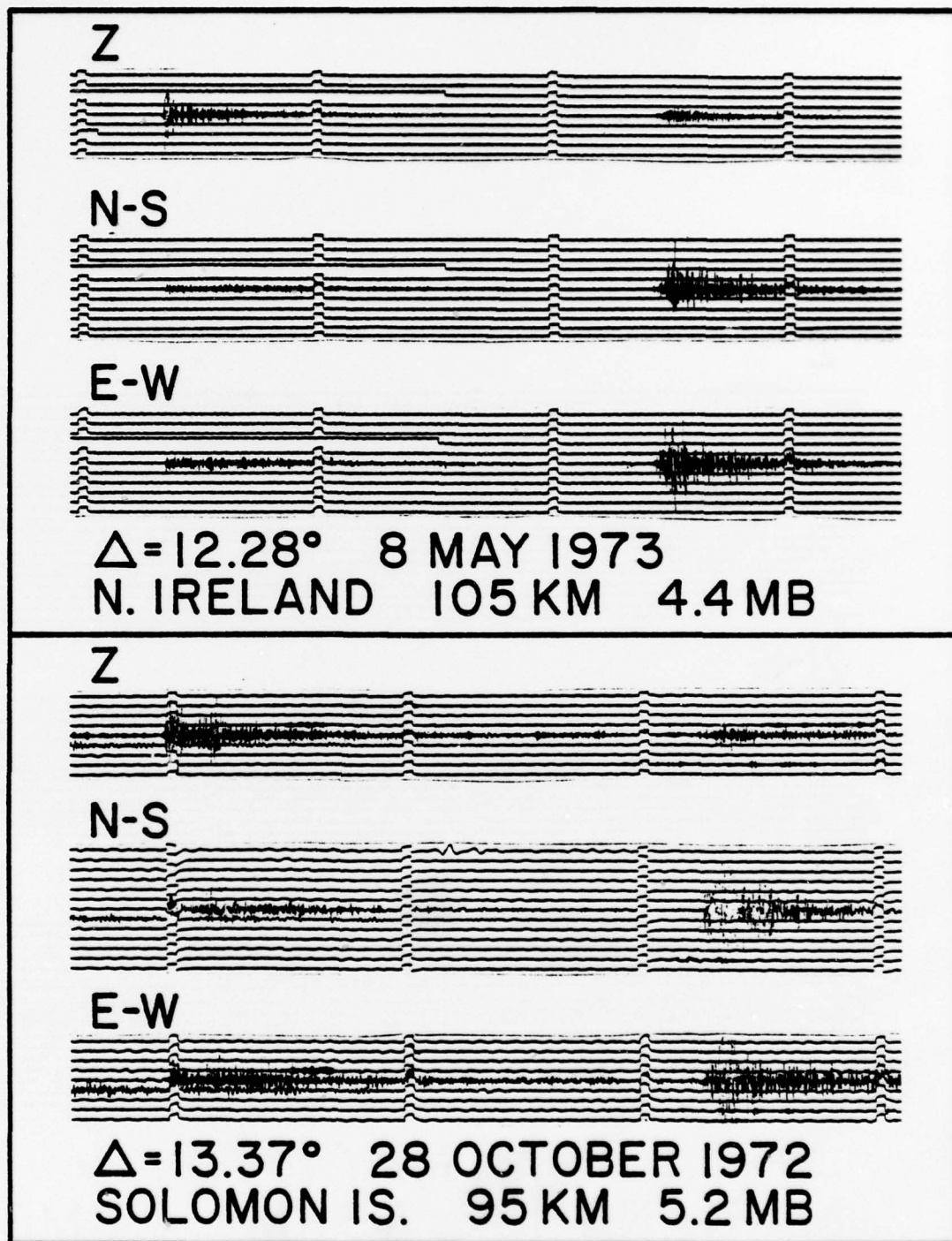
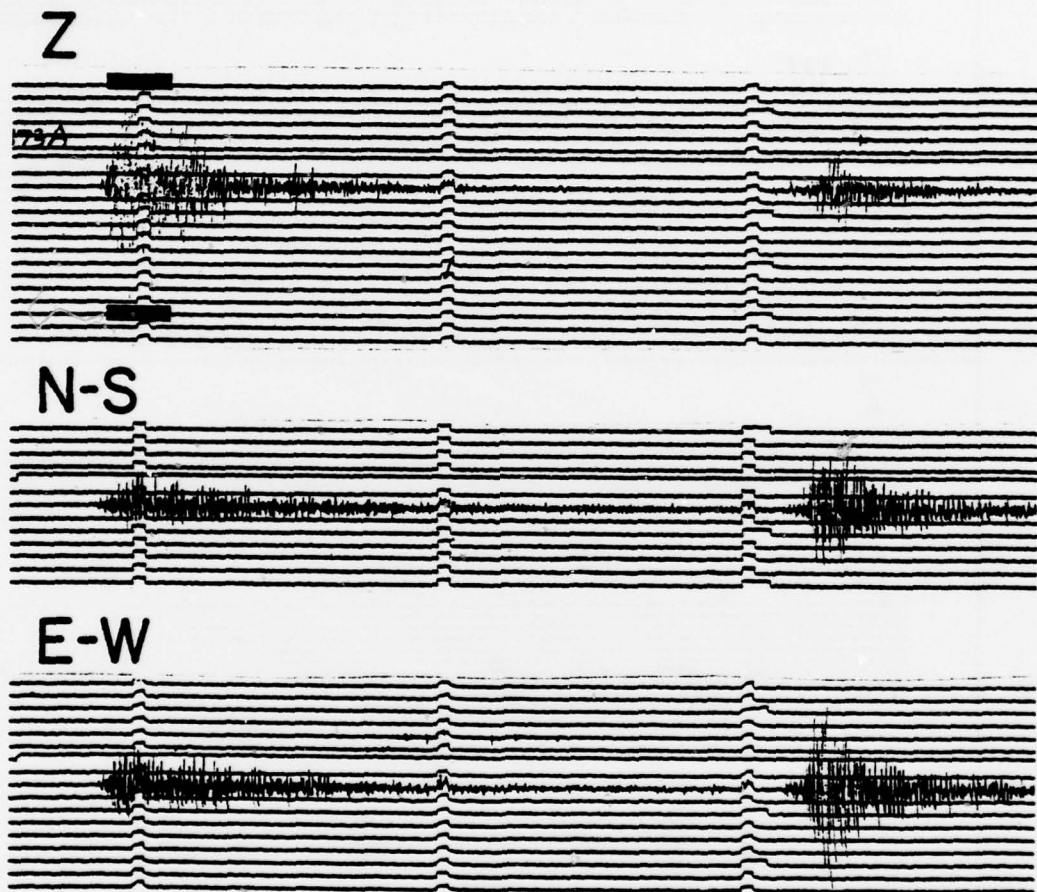


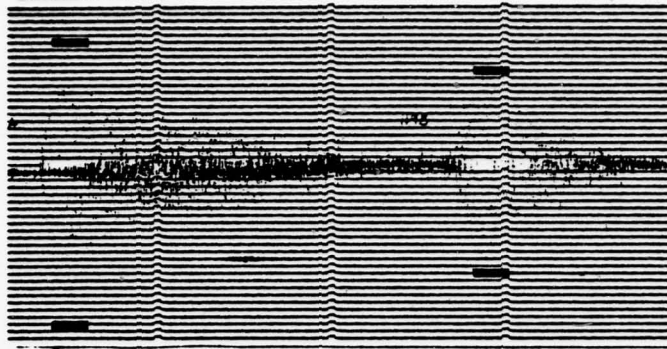
Fig. 9. P_n and S_n phases recorded on three orthogonal, high-frequency seismographs at Ponape. In some instances the trace is not visible on these reproductions. Solid bars indicate maximum peak-to-peak amplitudes based on the original recordings. For the E-W component of the earthquake at 14.46° (1609 KM), actual motion exceeded the limits ($\sqrt{140}$ mm peak-to-peak) of the instrumentation. It should be noted that this earthquake is not especially large (MB = 5.1).



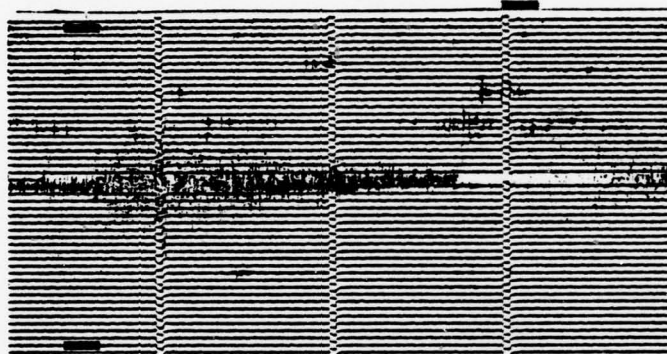
$\Delta = 13.83^\circ$ 12 MAY 1973
MARIANA IS. 56KM 4.8MB

Fig. 9. (cont'd).

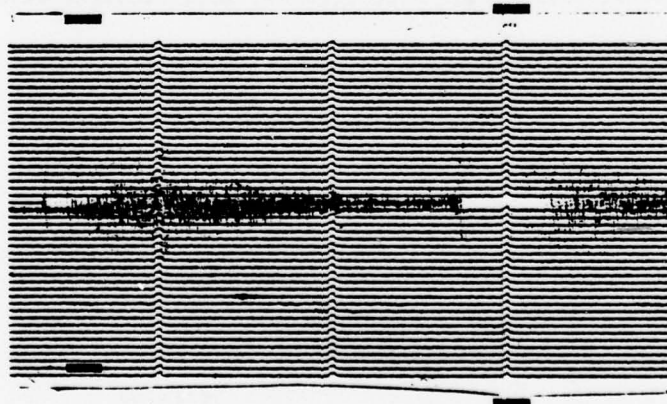
Z



N-S



E-W



$\Delta = 14.46^\circ$ 31 JULY 1972
MARIANA IS. 111 KM
5.1 MB

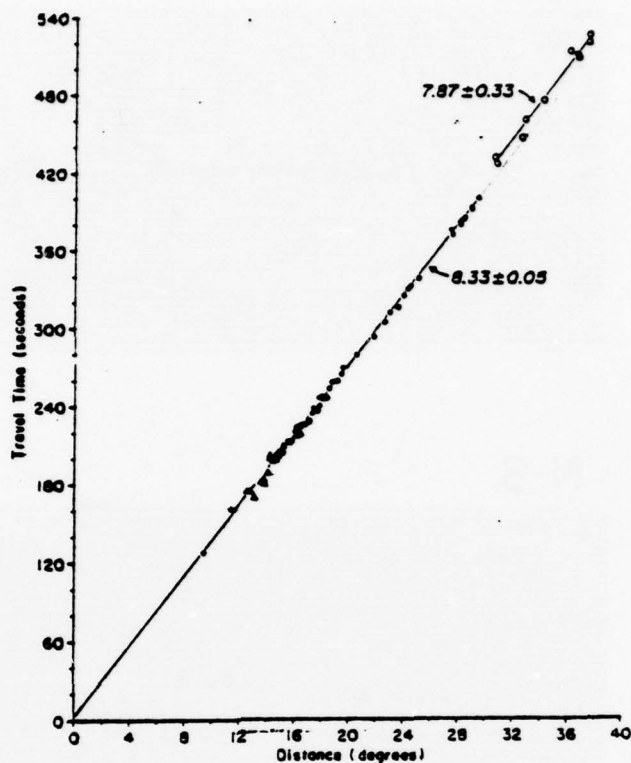


Fig. 10. Travel time plots for P_n arrivals from shallow focus events (depths of <100 km) in the North Pacific (solid circles indicate data recorded on hydrophones; triangles, data recorded at Ponape; and open circles, data recorded beyond 30°).

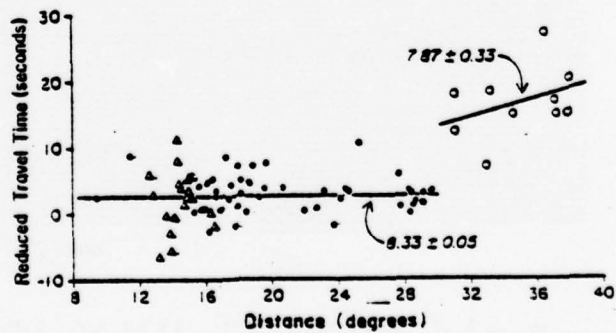


Fig. 11. Reduced travel time plot for data shown in Fig. 10.

additional data acquired since Figures 10 and 11 were originally drafted.] As can be seen in this figure (Figure 12), the area over which these phases have been observed covers a large portion of the Pacific. A travel time plot is given in Figure 13 and sample seismograms are shown in Figure 14. The travel time curve for these data is significantly different to suggest that an additional waveguide is present, implying that this slower waveguide is masked by phases from the faster waveguide at distances less than 30° . It is also interesting to note that a slower S_n waveguide comparable to the slower P_n waveguide has not been found. The main reason for mentioning the data beyond 30° is to provide further evidence of the extraordinary efficiency of the waveguide (s?) and its lateral extent in the Pacific.

The first reported observations of high-frequency P_n and S_n phases were made in 1940 by Linehan (6) for earthquakes in the West Indies recorded by seismic stations in the eastern United States and Canada. Differing geophysical provinces traversed by these phases included the deep Atlantic basin, the Blake Plateau, the continental shelf, and eastern North America. Subsequently, the phenomenon was not discussed in published journals until the 1960's. In spite of the fact that publications in the 60's and 70's suggest that these phases are propagated through most of the earth's lithosphere (i.e., in the lithosphere underlying most of the world's oceans and the more homogeneous portions of continents), the phenomenon has not yet received the attention it deserves. A major reason for this lack of recognition is that

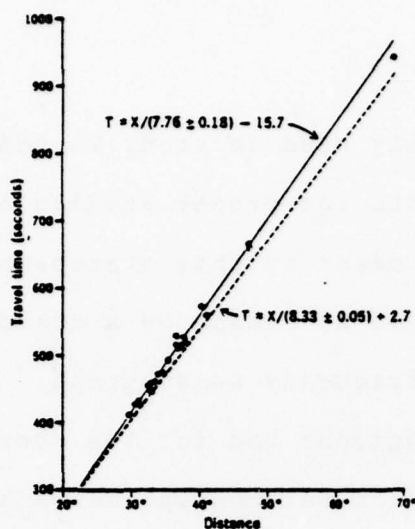


Fig. 13. Travel time curve for waveguide phases observed in the Pacific at distances greater than 30° (solid line). The travel time curve for the 8.3-km/sec waveguide phases observed at distances less than 30° is also plotted (dashed line).

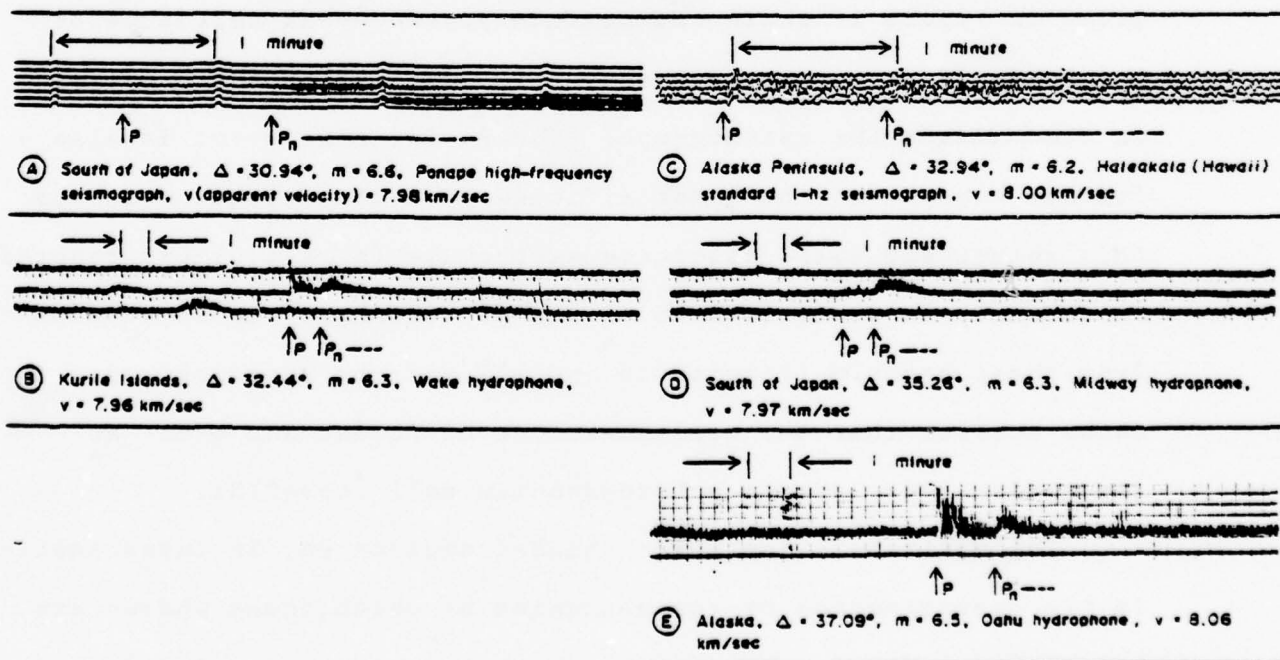


Fig. 14. Examples of P_n phases recorded in the Pacific at distances greater than 30° ; m = magnitude.

the seismographs normally used to study Pn and Sn (i.e., 1Hz systems) are not adequate for proper studies of these phases. To demonstrate what is meant by this statement, let us compare Pn and Sn phases recorded at Ponape on a standard 1Hz seismograph and on a special high-frequency seismograph. The response curves for these seismographs and for the short-period instruments of the World-Wide Standard Seismograph Network (WWSSN) are shown in Figure 15. Note that the WWSSN seismograph and the standard short-period at Ponape have comparable responses with peaks at about 1.5 Hz, while the high-frequency at Ponape has a peak at about 10 Hz. In Figure 16, we have simultaneous recordings at Ponape of the high-frequency and standard 1Hz seismographs for two earthquakes. Another remarkable example is given in Figure 17 where the maximum peak-to-peak amplitude of the Pn is 79 mm on the high-frequency seismograph and only 4 mm on the standard 1Hz seismograph. [The Pn for this event is also a further example of the great efficiency of the waveguide in that this relatively small magnitude earthquake ($m_b = 4.0$) was recorded so strongly at a distance in excess of 1600 km.] It is obvious from these examples (Figures 16 and 17) and the spectrograms shown earlier that the real character of Pn and Sn, even at great distances, exists at frequencies well above 1Hz.

The ultimate objective of high-frequency Pn, Sn investigations is the determination of the mechanism by which these phases are propagated. Major observations which any proposed model (consisting of velocities and elastic moduli) will have to explain are the

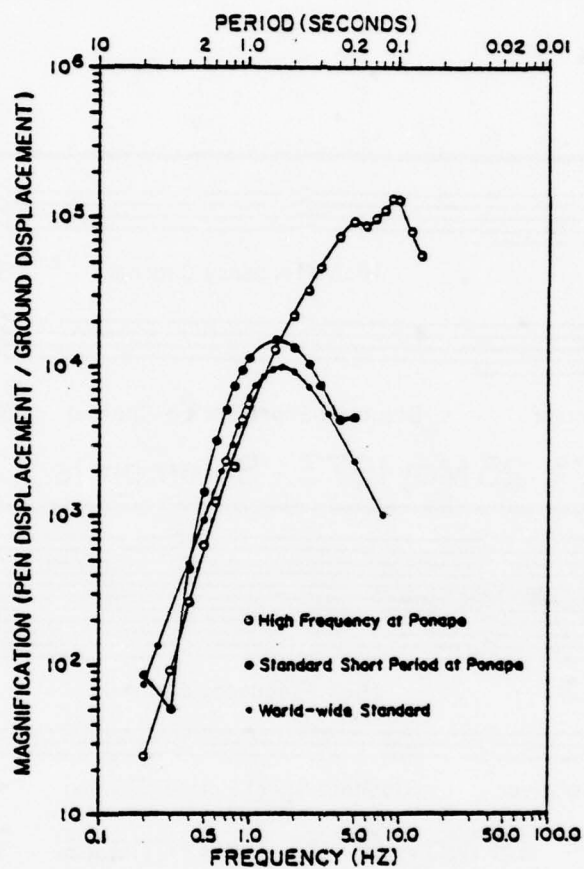


Fig. 15. Magnification curves of the Ponape and Word-Wide Standard Seismograph Network short-period seismographs. Also shown is the magnification curve for the special high-frequency seismograph at Ponape.

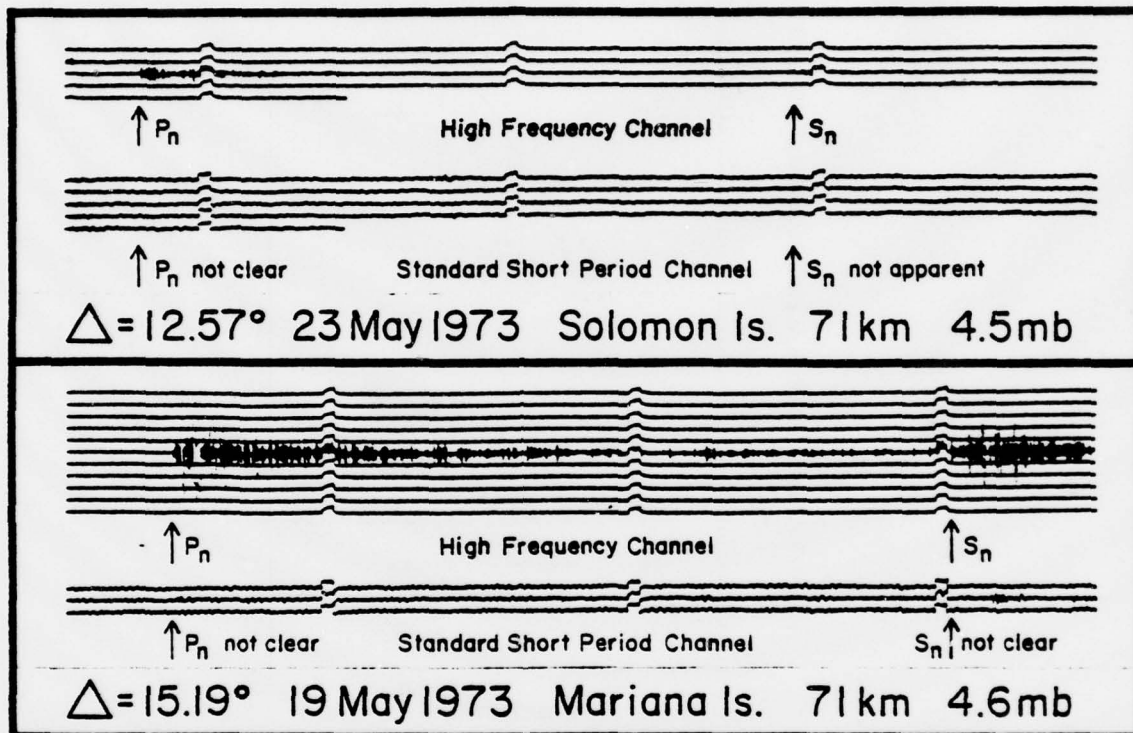
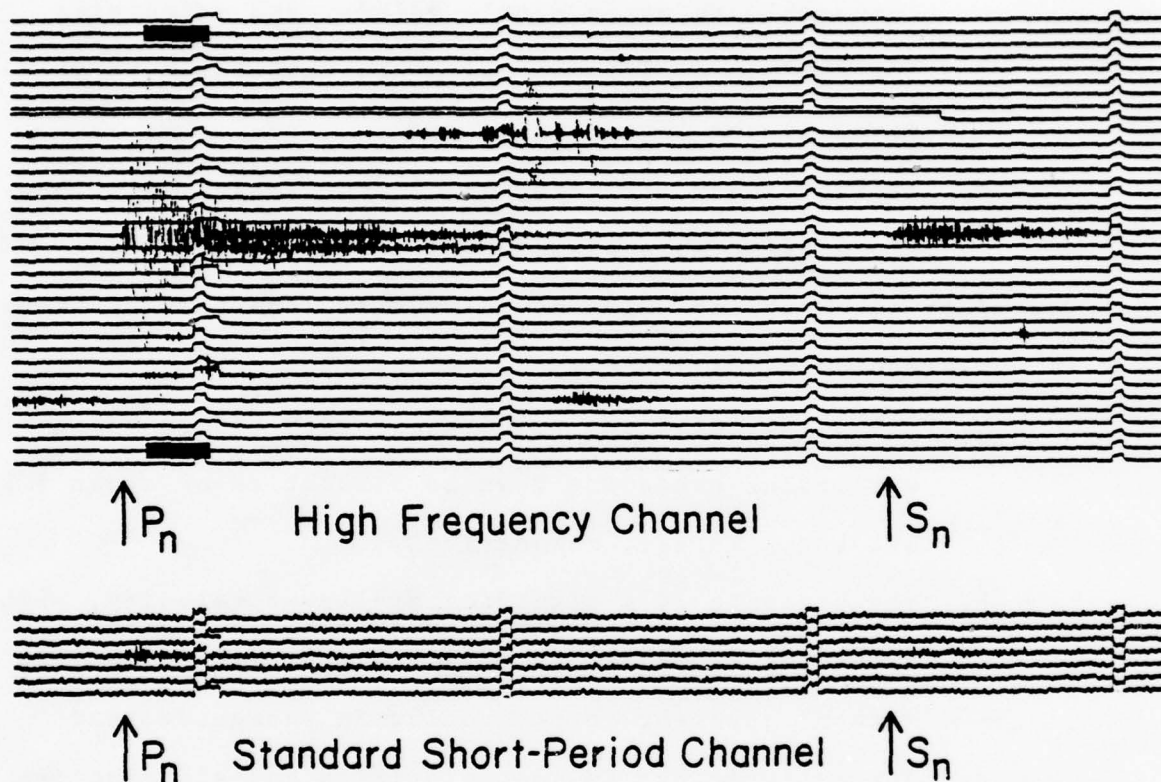


Fig. 16. Earthquake phases recorded simultaneously on the special high-frequency seismograph (upper trace) and on the standard short-period seismograph (lower trace) at Ponape.



$\Delta = 15.05^\circ$ 25 June 1973 Mariana Is. 114 km 4.0 mb

Fig. 17. Another example of P_n and S_n phases recorded simultaneously on the high-frequency and standard short-period seismographs. The amplitude of the P_n phase is 79 mm on the high-frequency component and only 4 mm on the standard short-period component. Although this earthquake had a magnitude of only 4.0, the extremely strong P_n was recorded at a distance of 15.05° (1674 KM).

following:

- a. velocities for first arriving phases which are comparable to upper mantle values, and velocities for maximum amplitudes which are comparable to values found in the lower crust, and
- b. extraordinary efficiencies of propagation, with Sn often being more efficient than Pn.

Secondary observations which could provide important refinements to any proposed model are the following:

- a. the duration of the wavetrains, with the Pn and Sn wavetrains extending down to velocities of about 5 km/sec and 4 km/sec, respectively,
- b. the presence of a significantly lower velocity, high-frequency Pn waveguide at distances beyond about 30° with no apparent corresponding Sn waveguide, and
- c. suggestions that Pn, Sn velocities and efficiencies may be dependent on the type of geophysical province in which the phases are transmitted (7).

Unfortunately, many aspects of these observations require further investigation. Some of the questions which should be investigated with special, high-frequency instrumentation follow.

What is the relationship between lithospheric age (and/or type of geophysical province) and (a) the velocities of first arriving Pn, Sn phases, (b) the velocities of maximum amplitudes of Pn and Sn, (c) the duration of wavetrains, and (d) efficiencies?

How do spectrograms for the slower Pn waveguide compare to spectrograms for the faster Pn waveguide? Quantitatively how do the efficiencies of these waveguides compare to one another? Is it certain that there is no corresponding slower Sn waveguide? Is the disappearance of the faster Pn and Sn phases beyond 20° abrupt or gradual?

What are the effects of focal depth, magnitude, and epicenter location on Pn, Sn propagation?

Could a zero focus event, or an explosion in the ocean, produce a teleseismically recordable high-frequency Pn or Sn?

What is the relationship of high-frequency Pn, Sn phases to classical Pn, Sn phases associated with the Mohorovicic discontinuity?

For a given magnitude what is the maximum distance at which a high-frequency Pn or Sn phase could be recorded?

Are the phases coherent?

Could significant portions of the noise at the earth's surface, or at the bottom of the oceans, be the result of Pn, Sn phases from small earthquakes?

At present, it seems certain that the phases are propagated in the lithosphere; but whether they are associated primarily with the lower crust, uppermost mantle, or both, is not yet certain. Although attempts should be made to find a model for the observations accumulated thus far, major emphasis should be placed on the acquisition of additional data through the use of special, high-frequency instrumentation.

Daniel A. Walker
Hawaii Institute of Geophysics

Acknowledgments. This report was prepared for an Office of Naval Research/Naval Research Laboratory sponsored workshop in Seismic Wave Propagation in Shallow Water which was held in July of 1978. More detailed descriptions of the concepts may be found in existing publications (8).

References and Notes

1. It should be noted that the phases shown are not the direct, mantle-refracted P and S. The expected arrival times of the direct P and S arrivals precede the observed phases by 36 sec and 42 sec, respectively. Also the observed frequencies far exceed those which would be expected from direct phases at this distance. Additional discussion of the frequency content of these phases is given in the text.
2. For example, rough calculations indicate that the direct S would lose about 60% of its energy at 15 Hz after traveling a distance of only 10 km, while the Sn would not lose this amount of energy at 15 Hz until it had traveled a distance of 1000 km. These computations are based on an estimated Q (the effective quality factor) for the direct S of 200 and the value of 20,000 for the Q of Sn as taken from Walker, McCreery, Sutton, and Duennebier (Spectral analyses of high-frequency Pn and Sn phases observed in the western Pacific, Science, 199, 1333-1335, 1978).
3. Unlike the high frequency Pn and Sn phases discussed here, direct P phases are always found to be richer in high frequencies than their related direct S phases.
4. See Walker et al. (2).
5. Sutton, G. H., and D. A. Walker, Oceanic mantle phases recorded on seismographs in the Northwestern Pacific at distances between 7° and 40°, Bull. Seismol. Soc. Amer., 62, 631-655, 1972; and Walker, D. A., and G. H. Sutton, Oceanic mantle phases recorded

- on hydrophones in the Northwestern Pacific at distances between 9° and 40° , Bull. Seismol. Soc. Amer., 61, 65-78, 1971.
6. Linehan, D., Earthquakes in the West Indian region, EOS Trans. AGU, 21, 229-232, 1940.
 7. Hart, R. S., and F. Press, Sn velocities and the composition of the lithosphere in the regionalized Atlantic, J. Geophys. Res., 78, 407-411, 1973; Walker, D. A., High-frequency Pn and Sn phases recorded in the Western Pacific, J. Geophys. Res., 82, 3350-3360, 1977; and Barazangi, M., J. Oliver, and B. Isacks, Relative excitation of the seismic shear waves Sn and Lg as a function of source depth and their propagation from Melanesia and Banda arcs to Australia, Annali di Geofisica, in press.
 8. See references given in notes (4) through (7) above, and Walker, D. A., High-frequency Pn phases observed in the Pacific at great distances, Science, 197, 257-259, 1977.

Seismic Measurements on the Sea Floor

by

Gary V. Latham⁽¹⁾

ABSTRACT

A low-cost, seismic station for use on the ocean bottom at virtually any depth has been developed by the Marine Science Institute (Geophysics Laboratory) of the University of Texas at Austin. Through the use of micropower, integrated circuits operating near the limits of the present state of the electronic art, and through the use of event-triggered data recording, it has proved possible to construct a system whose cost and operating power consumption are very low compared with what has been possible for systems of earlier design. In particular, these factors, low cost and low operating power, make possible the deployment of ocean-bottom seismic networks, capable of continuous operation for periods up to several months, at a cost that is quite low in terms of the potential scientific return. Twenty stations have been constructed, and they have been deployed at 106 locations during the past 2 years for both refraction and earthquake experiments. In these experiments water depths ranged from 60 m to 6400 m, and bottom time ranged from a few hours to 3 months. Successful recoveries were made in 100 cases. From the results of these and previous experiments, new information on ambient noise at the sea floor has been gained, and criteria have been developed for improved ocean-bottom seismic systems.

University of Texas, Marine Science Institute, Contribution No. 293.

(1) University of Texas, Marine Science Institute, Geophysics Laboratory, Galveston, Texas 77550.

INTRODUCTION

Many groups have constructed seismic systems capable of operation on the ocean floor and have used them with varying degrees of success. Generally, however, the costs of these systems were so high and their useful lifetimes so short that the deployment of extensive networks simply was not feasible. In addition, the sizes and weights of earlier systems were such that deployment and recovery were difficult, frequently requiring the equipment that only a large research vessel can provide. Several factors have made possible a new generation of ocean-bottom systems that greatly reduce previous shortcomings.

1. The development of integrated circuits has now evolved to the extent that the equivalent of thousands of discrete components is available in a single chip. Proper use of these circuits greatly reduces the volume, weight, power drain, and cost of electronics subsystems while expanding internal processing capability.

2. Application of the "triggering" concept, in which the recording device is activated only when a signal of interest is sensed, greatly reduces the data storage requirement permitting use of small, low-cost tape recorders and greatly increased operational lifetimes.

3. Use of high-strength glass spheres reduces the costs of the pressure vessel by a factor of about five. These spherical vessels can withstand the maximum pressures encountered in the ocean. The use of glass pressure vessels offers an important additional advantage. We have found that a piezoelectric crystal transducer bonded to the inner wall of the sphere both transmits and receives sound energy at

12 KHz with very high efficiency. This discovery makes feasible the design of a low-cost transponder for use in locating the OBS and for acoustic recall.

4. It is recognized that the ocean bottom is a "quiet" environment in the frequency range of about 5 to 20 Hz. Seismometers that operate in this range are inexpensive and do not require automatic leveling under normal circumstances. Also, the proper choice of seismometer natural frequency does not reduce useful sensitivity at low frequencies.

5. A release device, based on the electrolysis of a single restraining member, has proved to be highly reliable and can be constructed at very low cost.

An ocean-bottom seismic system has been designed to take advantage of these concepts. The objective of the design program was to produce a seismic system capable of operation at any ocean depth for periods of several months, at a cost of less than \$5,000 per system at commercial rates. An additional aim was to keep the system weight at deployment to less than 75 kg to ease deployment and recovery operations. The cost criterion limits the total parts cost to between \$2,000 and \$3,000 per unit. These objectives have been met in the system described in the following paragraphs. The system has been tested successfully and a second generation design, using microprocessors and digital recording, is in progress.

DESIGN CONSIDERATIONS

Ambient Noise at the Sea Floor

The continuous vibrations of the surface of the earth, called microseisms, generally have much larger amplitudes at the sea floor than on dry land at frequencies below 2-3 Hz. The horizontal component of this sea floor "noise" is larger than the vertical component by a factor that usually ranges between 2 and 5. This has been explained by Latham and Sutton⁵ to be a result of concentration of surface wave energy at the water-sediment interface. On the other hand, in the absence of wind noise and cultural activity, the deep-water environment is relatively quiet at high frequencies. Ambient noise spectra measured in deep-ocean experiments by Asada and Shimamura¹ and Latham and Sutton⁵ are compared in Fig. 1. Both spectra are for the vertical components of motion. Despite an offset of three orders of magnitude in absolute level, the microseismic noise level increases at a rate of 25 db/octave toward low frequencies in both spectra. Minimum noise level occurs at about 15 Hz, with a modest increase in level from this point toward higher frequencies. Obviously, the very rapid increase in noise toward low frequencies makes signal detection more difficult in this frequency range. On the other hand, absorption and scattering of seismic waves favor the low-frequency end of the spectrum. The signal frequency giving maximum signal-to-noise ratio depends upon distance, wave velocity, and the Q (quality factor) of the medium. We can bracket the range of practical interest by considering the short-range and long-range

limiting cases given in the caption of Fig. 1. We define the signal-to-noise (S/N) ratio by the function

$$S/N = e^{-\pi f D / QC} / A(f) \quad (1)$$

where the effect of absorption is given by the numerator³ with f = frequency, D = source receiver separation, Q = quality factor, and C = wave velocity. Unit source amplitude over the entire frequency band (flat source spectrum) is assumed. The quantity $A(f)$ is the value of background noise level at each frequency, as given by Asada and Shimamura. Variations of S/N with frequency, for the limiting cases considered, are shown in Fig. 1. These results indicate that a signal frequency of about 15 Hz will give maximum S/N at ranges up to 10 to 20 km. The optimum signal frequency is reduced to about 7 Hz at a range of 1000 km for a medium with a Q of 1000. The frequency of the peak value is reduced to 5 Hz for the long-range case if Q is reduced from 1000 to 500.

A special note on ambient noise in the shallow-water environment is appropriate at this point. Microseismic amplitudes measured on the outer continental shelf are usually found to be larger than at deep-water sites by a factor ranging between 2 and 4. This is simply because shallow sensors are located closer to the water surface, where the pressure field that generates the observed microseisms originates by interaction of water waves. It may also be that microseism generation is most intense near shore; although this point is not well established.

Aside from the increase in microseismic noise, four additional noise sources may be important at shallow depth: (1) biological activity, (2) direct wave action, (3) bottom currents, and (4) ship noise. A wide variety of signals of unexplained origin have been recorded during our shallow-water experiments. These signals generally disappear at depths greater than about 1 km. We attribute them to biological activity, i.e., direct physical contact between the OBS package and sea life attracted to the instrument, and/or acoustic signals of biological origin. The pressure field associated with a water wave decreases exponentially with depth. Nevertheless, at depths as great as 60 m with 5-m wave heights, we have recorded strong signals that we believe to be a result of direct wave action on the sea floor. Bottom currents as great as several knots are not uncommon at shallow depths. These produce turbulent flow over the OBS package and induced vibration. Owing to this effect, the drag coefficient of the system must be kept as low as possible.

Signals from passing ships, at frequencies corresponding to propeller rotation rates can be a significant source of noise in shallow water. Signals from passing freighters are easily detected by ocean bottom seismic stations at ranges of 20 km (usually at a frequency of about 8 Hz).

Finally, in regions of offshore oil and gas production, we have found that drilling platforms, production platforms and bottom pipe lines are significant noise sources.

Choice of Sensor

The ideal sensor for an ocean-bottom seismic station would have a response function (voltage output vs ground motion input) that is the inverse of the noise spectrum shown in Fig. 1. If this can be achieved, the spectrum of the sensor output will be flat, and the dynamic range requirements imposed on the amplifier/recording system will be minimized. The velocity sensitive transducers used in exploration seismology (geophones) serve this function adequately if the geophone resonant frequency is chosen properly. For a constant amplitude of ground motion, the output signal from a geophone decreases at a rate of 18 db/octave at frequencies below the geophone resonant frequency. This rolloff adequately compensates the 25 db/octave increase in the ocean-bottom background noise. By inspection of the noise spectrum shown in Fig. 1, a geophone with resonant frequency of between 10 and 15 Hz will optimally flatten the ambient noise spectrum. Using lower-frequency sensors does not result in a useful increase in low-frequency sensitivity of the system, unless the output of a higher-frequency sensor falls below the equivalent input noise of the amplifier for ambient ground motion at frequencies within the band of interest. With these considerations in mind, we have selected a geophone with a resonant frequency of 8 Hz for refraction experiments. This does increase the low-frequency noise component slightly above the minimum possible, but places less stringent requirements on the amplifier than would a higher-frequency geophone. We frequently use a geophone with a resonant frequency of 4.5 Hz for earthquake

monitoring stations, where we are attempting to match the response of complementary land stations. Typical magnification curves for the two cases, for deep-water experiments, are shown in Fig. 2. Instrument magnification is defined as the ratio of the playback trace amplitude to the input ground motion amplitude. The recorder sensitivity and geophone amplifier gain have been adjusted in both cases so that the amplitude of background noise on an analog record is about 1 mm peak-to-peak. As shown in Fig. 2, peak magnification typically obtained with the 8-Hz geophone is about 3 million at a frequency of 16 Hz. Peak magnification obtained with a 4.5-Hz geophone is about 475,000 at 8 Hz; a factor of 6.3 times lower than that obtained with the 8-Hz geophone. Of course, this difference is partly a consequence of the differing filter cutoff frequencies in the two cases. Use of the 15-Hz filter with the 4.5-Hz geophone would have resulted in a peak magnification of 1 million at 15 Hz. Both systems have about the same low-frequency sensitivity. The difference in peak magnifications is simply a consequence of the fact that the low-frequency sensitivity of the 8-Hz geophone is 5.6 times lower than that of the 4.5-Hz geophone. This difference is compensated by using higher amplifier gain with the 8-Hz geophone. These experimental results support our contention that previous OBS designs, using geophone resonant frequencies of from 1 to 4 Hz, have not yielded optimum S/N characteristics in the band of interest in typical refraction or micro-earthquake experiments. If we had chosen

a geophone frequency of 1 Hz, e.g., peak magnification would have been limited to about 50,000 at 15 Hz, a factor 60 times lower than the value achieved with the 8-Hz geophone. Magnification at 1 Hz is about 6,000 in all cases.

Recognition that high-frequency sensors are suitable for ocean-bottom seismic stations is important for several reasons. First, seismometers become less tilt sensitive as the resonant frequency increases. Vertical component geophones with resonant frequencies of 8 Hz can easily be made to operate over a tilt range of $\pm 20^\circ$. This eliminates the need for active or passive leveling systems that are necessary when using lower-frequency sensors. Second, the higher-frequency sensors are normally smaller, lighter, and less costly than their lower-frequency counterparts. These advantages are crucial to the design of a light-weight, low-cost system.

The Coupling Problem

Ideally, the instrument frame would exactly follow the motion of the sea floor. Departure from this goal introduces waveform distortion. The ideal case is approached with sensors of small size embedded in the sea floor, having an average density equal to that of the surrounding medium, i.e., the sensor properties are made to match those of a particle of the medium as closely as possible. Unfortunately, sensor imbedment is a difficult engineering problem where eventual retrieval is required.

One way to estimate ground coupling is to consider the sensor system as an inertial mass mounted on a spring, or springs, with elastic constant determined by the properties of the supporting material. At frequencies well below the free resonant frequencies of the system, the inertial mass (OBS) will faithfully follow the motion of the supporting material. The most important system resonance for vertical component seismometers is one in which simple vertical oscillation of the frame occurs. For this mode, Sutton et al. (1965) derive the following expression for a tripod frame and soft sediment ($V_p \gg V_s$):

$$f = V_s (3\rho/8M)^{1/2} \quad (1)$$

where

f = resonant frequency for vertical oscillation

V_p = velocity of compressional waves in the supporting material

V_s = velocity of shear waves in the supporting material

ρ = density of the supporting material

M = mass of the OBS

r = footpad radius

This equation applies strictly only if the footpad does not sink into the supporting material. If the footpads are actually embedded, buoyancy effects must be taken into account. This will increase the resonant frequency, but, in the present case, the magnitude of the effect is less than 1%.

Since a portion of the supporting material and surrounding water will move with the OBS, the total inertial mass will be larger than that of the OBS. A conservative estimate (lower limit) of the resonant frequency is given by (1), in which the total moving mass is assumed to be twice that of the instrument structure. From analysis of the propagation of Stonely waves recorded at the sea floor, Davies (1965) obtained a value of $V_s = 50$ m/sec for the top of the sediment column. From data given by Nafe and Drake (1957), we assume $\rho = 1.65$ gm/cc. The mass of the Texas OBS in its normal configuration, is 61 kg, and the footpad radius is 6.8 cm. From these values, (1) yields $f = 41.6$ Hz. For stiffer sediment or hard-rock cases, the resonant frequency would be higher. Thus, for the present system, waveform distortion for small motions, owing to decoupling, will be negligible at frequencies below about 20 Hz. From (1), it is evident that system mass should be made as small as possible, and the footpad radius as large as possible. Increasing footpad cross-section, of course, increases drag, and reduces the descent rate. Resonances at lower frequencies can be

expected from various torsional modes of oscillation. These would be of concern mainly in their effects on horizontal-component seismometers.

Signal amplitude is also a consideration in ground coupling. The treatment above assumes that sediments can be treated as linearly elastic materials. This assumption will obviously be invalid for strain levels above some threshold. Thus, better coupling methods will be needed for ocean-bottom seismic stations designed for strong-motion measurements. An obvious method to increase coupling is simply to add a spike or shear vane to the bottom of each footpad. However, if imbedment of such coupling devices is to be achieved by adding mass to the system, the effect on system resonant frequencies must be kept in mind.

Description and Operational History of the Texas OBS

The seismometer electronics subsystems, tape recorder, strobe light, and battery pack are contained in a single, spherical pressure vessel made of high-strength glass. The sphere is 43 cm in diameter and has a net positive buoyance of 25.5 Kg.

The bottom hemisphere of the glass pressure vessel fits snugly into a molded plastic cap. A small radio, used in recovery, is mounted to a flange on the plastic cap. The pressure vessel, with its plastic bottom cap and recovery radio, and internal components, are referred to as the return capsule (see figure 3).

The return capsule is firmly attached to a tripod frame by three elastic straps. These are joined at the top of the sphere by a triangular-shaped piece of stainless steel wire. Lead hemispheres are used as foot pads on the expendable frame to give a low drag-to-weight ratio. The complete system, ready for deployment, is shown in figure 3.

The OBS subsystems are shown schematically in figure 4. Signals from the seismometer (single, vertical component) are amplified, filtered, and fed in parallel into an analog section and digital (memory) section. The analog section performs the functions of event recognition and recorder activation. The signals are first rectified and smoothed (low-pass filtered) with two time constants: 100 sec and 1 sec. The 100 sec time constant produces a voltage level proportional to the average background (microseismic) level. This level is continuously

compared with the short-term variations (1 sec average). The comparator triggers when the short-term signal power exceeds the long-term power by a preset ratio (usually 6:1).

The digital section includes a 12-bit A/D converter, static random access memory, and D/A converter. The memory capacity is 160 sec. The tape recorder is activated 140 sec (nominal) after a trigger and the data in memory are clocked out through the D/A converter and voltage controlled oscillator (VCO) at four times real time. Thus, the total record length for each event is 160 sec, and the recorder operates for 40 sec per event. Timing signals from a crystal-controlled oscillator are multiplexed into the digital data stream by adding a 13th bit to each dataword. The first data recorded for each event were read into the memory 20 sec before the trigger instant. This ensures that the true signal onset is included in the record interval. The system idles at low power drain between triggers. Use of a VCO moves the seismic data from the sub-audio band to the audio band where it can be recorded by an inexpensive cassette tape recorder of the home entertainment variety. A steady reference frequency, used for compensation of tape recorder wow and flutter during playback, is also recorded.

A major advantage of this approach is that the tape recorder is not operating while data are being stored in memory. This eliminates the problem of data contamination by the mechanical vibration induced by the tape recorder. System dynamic range is limited by tape wow and flutter. With properly adjusted compensation, the overall dynamic range is presently 50 db.

For a record length of 160 sec per event (40 sec recording time), 90 events can be recorded on a standard C-120 cassette. Using a four-track head and reducing the tape speed from the standard 1-7/8 ips by a factor of two increases the total capacity to 720 events.

The total continuous power drain of the system is 7 ma at 15 volts. Thus, a battery pack of 20 D-size lithium cells, weighing 2 kg, will operate the system for about 60 days.

The seismometer used can accommodate a tilt of about 20°. This eliminates the need for internal leveling devices. The seismometer is bonded to the inner wall of the bottom hemisphere by a compliant epoxy.

All internal elements, except the seismometer, are mounted on a single, removable frame. The frame is inserted into the lower hemisphere after the seismometer is connected to the amplifier input and is held in place on compliant rubber blocks bonded to the inner surface of the glass. Rigid mounting to the inner wall of the sphere must be avoided because slight deformation of the sphere does take place under high pressure (about 1 mm decrease in diameter at 10,000 psi).

A small piezoelectric transducer, with a resonant frequency of 12 KHz, is bonded to the inner surface of the upper hemisphere. Tests of the transmitting and receiving efficiency of this system have been conducted at the acoustic test range of the Applied Research Laboratories of the University of Texas at Austin. These tests show that the system is nearly omnidirectional and quite efficient in both modes

of operation (transmitting and receiving). The system is used in the transponder mode for precise positioning following deployment, and in the receiver mode for acoustic recall.

A standard 12 kHz precision depth recorder (PDR) is used to locate the OBS after it reaches the bottom. The rate of transmission of 12 kHz pulses by the shipboard system, is adjusted according to water depth (usually 1 pulse every 8 seconds). The answering signal from the OBS transponder is recorded on each sweep of the shipboard, flatbed recorder, along with the usual bottom echo. Recordings from a series of passes past the OBS yields the bottom position to an accuracy usually determined by the uncertainty of the location of the ship. Uncertainties in the location on the bottom and the clock drift of an OBS can be reduced by recording a series of sound sources generated at known times and locations. This is a particularly useful calibration in multistation experiments.

For acoustic recall, the PDR is programmed to send 12 kHz pulses at a rate of 1 pulse every 10 seconds. Following receipt of an initial pulse at the OBS, command decode logic searches for 5 consecutive pulses at a 10 second repetition rate. Pulses must be received prescribed time to within 0.5 seconds. Any pulse received outside of this time window initializes the decoder, and the search begins again. The system is immune to premature release in the presence of high background noise, because the decoder will simply continue to reset at a rate equal to the time constant of the transponder (approximately every 3.5 seconds). Immunity to random noise depends

on the average rate of noise pulses assumed. For a completely random series of pulses, the worst case is for an average rate of 1 pulse every ten seconds. For this case, the probability of false release is about 0.1% in any 24 hour interval. The probability decreases rapidly for lower noise pulse rates. Greater code security can be gained, of course, by demanding a longer string of pulses for recall, at the cost of increased recall time.

At deployment, the complete system weighs 61 kg. The descent rate is about 60 m/min. An E-cell timer turns on system power, enabling the automatic gain adjustment sequence, at any pre-selected time after deployment. The amplifier gain then increases in 6 db steps until the voltage level of the long-term average reaches a prescribed minimum. Thereafter, the gain level is checked every 10 minutes and adjusted if necessary. Amplifier gain is recorded as a binary code in each 10-sec time code sequence. In multiple OBS experiments, initial activation of each OBS is normally timed to begin operation after the entire array is deployed.

The system is released by acoustic command, as described above. On command, a relay is closed, supplying 0.5 amps to the stainless steel restraining wire. The wire plates into solution at exposed points within 5 to 15 minutes, releasing the elastic containment bands and the return capsule. The return capsule ascends at a rate of 57 m/min (1-1/2 hours ascent time in 5 km water depth). The system clock and an E-cell timer are used as backups to the acoustic recall system. Experimental data are as yet inadequate to determine

the stability of the system clock.

A strobe light, flashing once per second, is activated by the release command. The interior of the upper hemisphere is coated with phosphorescent paint to increase illumination. Visual detection of the flashing light serves as the primary location method for night time recovery. An external radio beacon is activated when the antenna clears the water surface. A radio direction finder is used to locate the return capsule during daytime recovery.

The weight of the return capsule is 35 kg. In previous recoveries, the ship has been maneuvered alongside of the return capsule, and the capsule was then caught in a scoop net and lifted aboard manually.

Numerous drops have been made at dockside to test the reliability of the release device. In addition, 106 operational drops have been made at water depths ranging from 60 m to 6,400 m. Successful recoveries were made in 100 cases. Bottom time in these experiments has ranged from a few hours to over three months.

Refraction experiments have been conducted on the shelf zone of the Gulf of Mexico, the North Pacific, the Middle America trench, and in the New Hebrides. Networks of OBS stations have been operated off Central America and the New Hebrides to record local earthquakes. In each case, a complementary network of land stations was operated for the duration of the ocean bottom experiment. These used a simplified version of the OBS instrument. The land station version employs the triggering principle, but the tape recorder is activated at the trigger

instant, and record length is adjusted simply by setting the run time of the tape recorder. This permits the use of a much shorter memory, and is satisfactory in applications where the seismometer is remote from the recorder (as in land use), or where low-gain operation is desired (strong motion instruments).

A sample of data obtained in short refraction experiments is shown in figure 5. This line was obtained at a water depth of 0.8 km, on the New Hebrides ridge, using a single 300 cubic inch airgun fired at 1800 psi air pressure.

In some of the initial, long-term OBS experiments, data quality was poor or totally unreadable, even though thorough checks before and after use revealed no functional problem. We now believe that these problems were caused by condensation of water on critical circuit elements as the system cooled on the ocean floor. Low power devices are also high impedance devices. Thus, even a very small amount of current leakage can cause serious problems. The liberal use of dessicant inside of the pressure vessel has eliminated this type of malfunction.

Some of our colleagues were skeptical about the stability of glass pressure vessels in repeated use. It was felt that internal stresses might not be adequately relieved, and that failure would occur after a few round trips to the ocean floor. This concern seems unfounded. We have used the same sphere in as many as 20 deep sea experiments. Slight spalling has been observed on inner and outer surfaces, but there is no evidence that this sphere could not be used indefinitely.

New Directions for Ocean-Bottom Instrumentation Development

The success achieved with the Texas Ocean Bottom Seismograph described above encourages serious consideration of the feasibility of developing new ocean-bottom instrumentation systems having enhanced capabilities. Several possible new directions for the development of improved ocean-bottom systems are discussed below, including brief descriptions of several new systems currently under development at UT-MSI. In the examples given here, attention is confined primarily to enhancements of the present OBS system which maintain its ease of deployment and recovery and its capability for ocean-bottom operation over extended periods of time.

1. Digital Data Recording: One of the most serious drawbacks to the present system is its use of fm analog data recording, with the resulting loss of fidelity and dynamic range and inconvenience for data analysis. As mentioned in a previous section, it is now possible to achieve adequate data-storage capacity on the 3M-type tape cartridge. Although the cost of a digital recording system is substantially higher than that of the present analog fm system, the advantages of a possible 90-100 dB dynamic range and machine readability of the data outweigh the question of cost in many applications. A digital recording system is under development for incorporation into new systems and possible retrofitting into existing OBS systems.

2. Multiple Sensors: An obvious extension of the present system is expansion to include three-axis seismic detection and pressure-wave

detection in the water outside the package. A system currently under development makes use of two horizontal-axis and one vertical-axis geophones and an external hydrophone. The fourfold increase in data-acquisition rate can be accommodated with available electronic techniques with little difficulty, but the number of seismic events which can be recorded within a given tape budget is correspondingly reduced. For refraction applications this data-storage limitation is not serious, but for long-term earthquake-monitoring applications it presents serious problems. The system now under development which is microprocessor controlled, will permit some increase in data-storage efficiency through the use of better trigger-detection discriminants to eliminate false triggering, but more sophisticated methods of data compression and data-storage efficiency, along lines described below, will ultimately be necessary.

3. Strong-Motion Systems: The need for seismic-risk analysis in regions of offshore oil and gas production suggests the need for an ocean-bottom system for the measurement of strong-motion accelerations associated with earthquakes strong enough to cause structural damage to platforms, pipelines, etc. The capabilities of the present Texas OBS system can easily be expanded to permit such measurements. The use of properly filtered large-motion geophones as acceleration sensors instead of the more usual force-balance accelerometers permits the maintenance of long-term unattended operation by eliminating the steady power drain associated with the force-balance devices. A system with a three-axis sensor is currently under development at UT-MSI. This system will be capable of operation for periods up to one year. It will employ

digital data recording, and its cost will be comparable to that of the present OBS system. The low cost will permit the deployment of large numbers of sensors over regions of high seismic activity.

4. Systems of Added Functional Capability: In addition to seismic data acquisition, data on such physical quantities as temperature, pressure, and current (both magnitude and direction) can be recorded in a system such as the present Texas OBS. The added capability to measure these and other physical quantities could, of course, be achieved in a simpler package without the seismic data-acquisition capability, but even in such a case the present OBS packaging scheme could readily be employed to advantage because of the ease of deployment and recovery of this system.

5. On-Site Data Compression and Data Processing: In the present realization of the OBS described in this paper, the availability of semiconductor memory devices of ultra low power drain made possible the use of the triggering principle and incorporation of the tape recorder and geophone inside the same pressure vessel. Because of the desire to keep the cost of the present system as low as possible, no effort was made to make use of the very powerful techniques of signal processing now made possible by the existence of sophisticated microprocessors. In fact, as observed above, the treatment of the seismic data in the present system is one of the deficiencies of this system. Improvement of the quality of the data can be obtained through the use of digital recording, as mentioned above, but once a digital recording technique is employed, the

door is open to considerable further improvement in the treatment of the data. For example, digital filtering or digital spectral analysis would permit the use of much more reliable discriminant algorithms for event recognition. Sequence bandlimiting and data encoding, as proposed by Wood (1974), would permit a very high degree of data compression without loss of essential information, thereby allowing much greater ocean-bottom operating times. Digital signal analysis would also permit the implementation of pattern-recognition capabilities. A study is underway at UT-MSI to investigate the feasibility of employing the very powerful 16-bit microprocessors for the purpose of introducing sophisticated digital data-processing capabilities into the Texas OBS system.

6. Telemetry: In the present Texas OBS, an acoustic transponder provides a means for position determination after deployment and a facility for command recall of the OBS. No other communications functions are provided at this time. It would be very useful if an acoustic communications link could be provided to permit the transmission of data and/or instrument status signals, from the OBS while it is in place. Complete sets of slowly varying data, such as temperature, current, etc., could undoubtedly transmit all essential information to the surface. If satisfactory telemetry can be developed, the usefulness of OBS-type instrument packages will be greatly increased and the cost of repeated deployment and recovery in a given location will be substantially reduced.

ACKNOWLEDGEMENTS

This work was sponsored by the Office of Naval Research
(Contract N00014-77-C-0028 and -0606).

References

1. Asada, T., and H. Shimamura, Observation of earthquake and explosions at the bottom of the Western Pacific: structure of the lithosphere revealed by longshot experiment, The Geophysics of the Pacific Ocean Basin and its Margin, Geophysical Monograph 19, American Geophysical Union Monograph Series, 135-153, 1975.
2. Davies, D., Dispersed Stoneley waves on the ocean bottom, Bull. Seismol. Soc. Am., 55, 903-918, 1965.
3. Futterman, W. I., Dispersive body waves, J. Geophys. Res., 67, 5279-5291, 1962.
4. Ibrahim, A., and G. Latham, A comparison between sonobuoy and ocean bottom seismograph data and crustal structure of the Texas shelf zone, Geophysics, 43, April, 1978 (in press).
5. Latham, G. and G. Sutton, Seismic measurements on the ocean floor, 1. Bermuda area, J. Geophys. Res., 71, 2545-2573, 1966.
6. Nafe, J., and C. Drake, Variation with depth in shallow and deep water marine sediments of porosity, density, and the velocities of compressional and shear waves, Geophysics, 22, 523-552, 1957.
7. Sutton, G., W. McDonald, D. Prentiss, and S. Thanos, Ocean-bottom seismic observatories, Proc. IEEE, 53, 1909-1921, 1965.
8. Wood, L., Seismic data compression methods, Geophysics, 39, 499-525, 1974.

Figure Captions

- Figure 1. Amplitude spectra for the vertical component of ocean bottom ambient noise as given by Latham and Sutton (1966) and Asada and Shimamura (1976). Using these data, signal-to-noise ratios (S/N) are calculated for short-range and long-range refraction experiments. Parameter values used in the calculation are as follows: (1) short range case, $D = 10$ km, $C = 4$ km/sec, $Q = 100$; (2) long range case, $D = 1,000$ km, $C = 8$ km/sec, $Q = 1,000$. Symbols are defined in the text.
- Figure 2. Typical magnification curves for the Texas ocean bottom seismic station for geophone natural frequencies of 4.5 Hz and 8.0 Hz. The corner frequency of the high-cut filter is 7.5 Hz for the 4.5 Hz geophone, and 15 Hz for the 8.0 Hz geophone. The rolloff is 12 db/octave in both cases. These curves apply for ambient noise conditions typically found in deep-sea experiments.
- Figure 3. Photographs of the Texas OBS showing (a) the complete system ready for deployment, and (b) the return capsule.
- Figure 4. Functional block diagram of the Texas OBS system. Signal paths are coded as follows: A = analog data signal, D = digital data or time code signals, C = digital control signal, and F = FM analog signal.

Figure 5. Data obtained by the Texas OBS during a short-range refraction experiment in the New Hebrides, using a small air-gun source (300 cubic inches). Water depth along the profile was 800 meters. Spacing between shots is about 500 meters. An 8 Hz geophone was used in this case. Identified arrivals are indicated by numbered lines. Arrivals along line 1 are pressure waves transmitted through the water. The remaining lines mark the onsets of ground arrivals.

Fig. 1

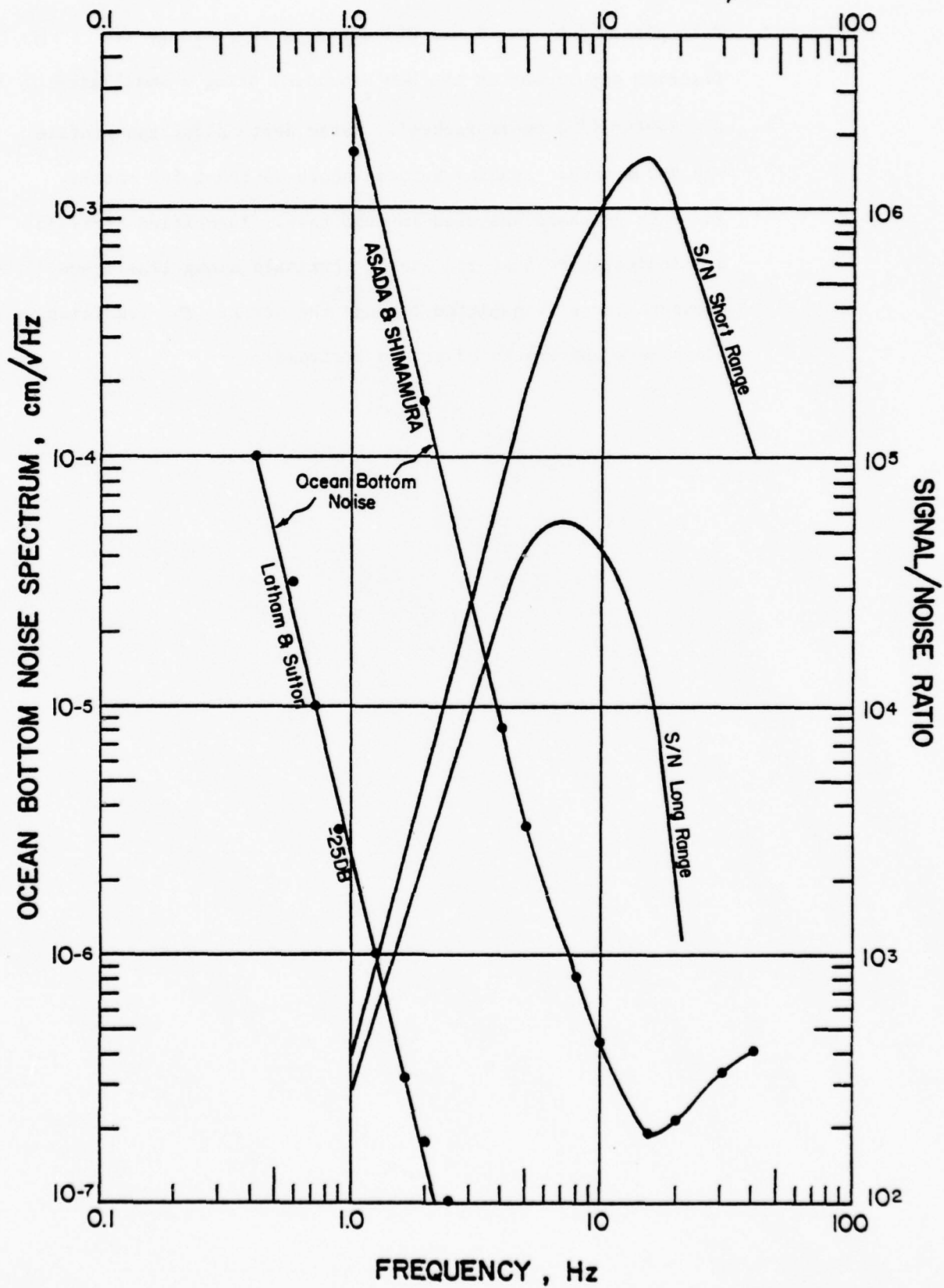


Fig. 2

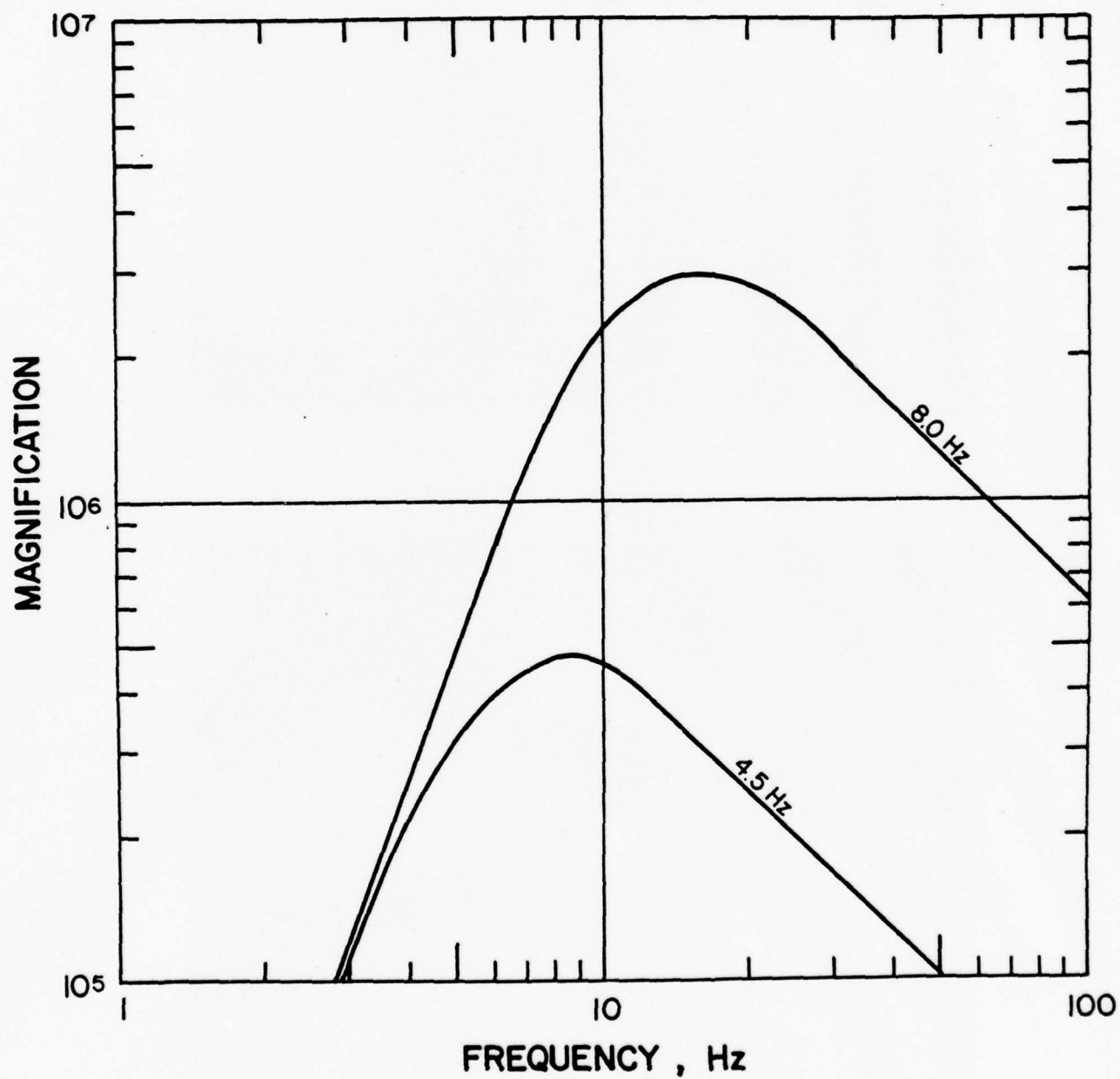


Fig. 3

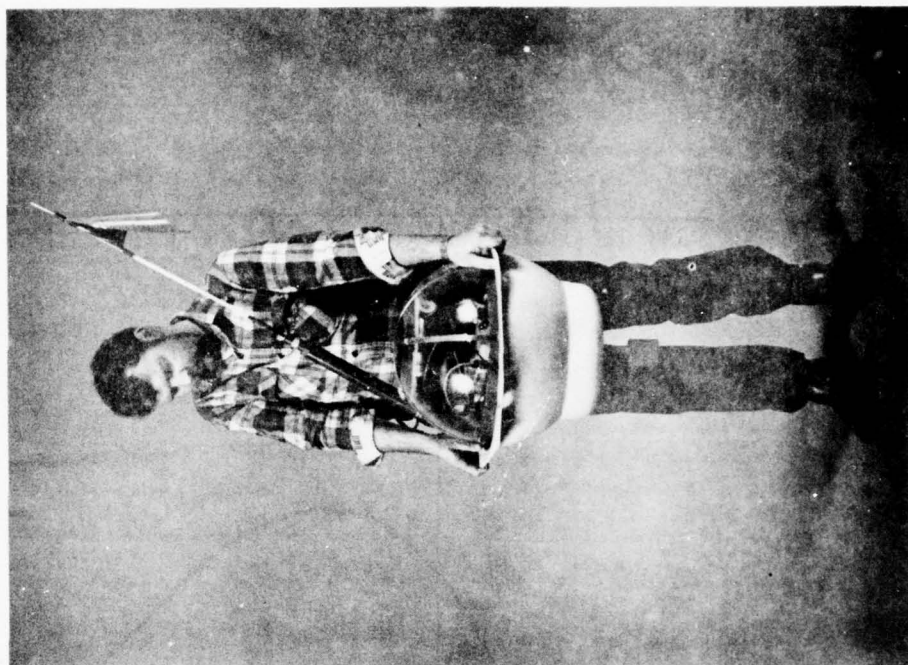


Fig. 4

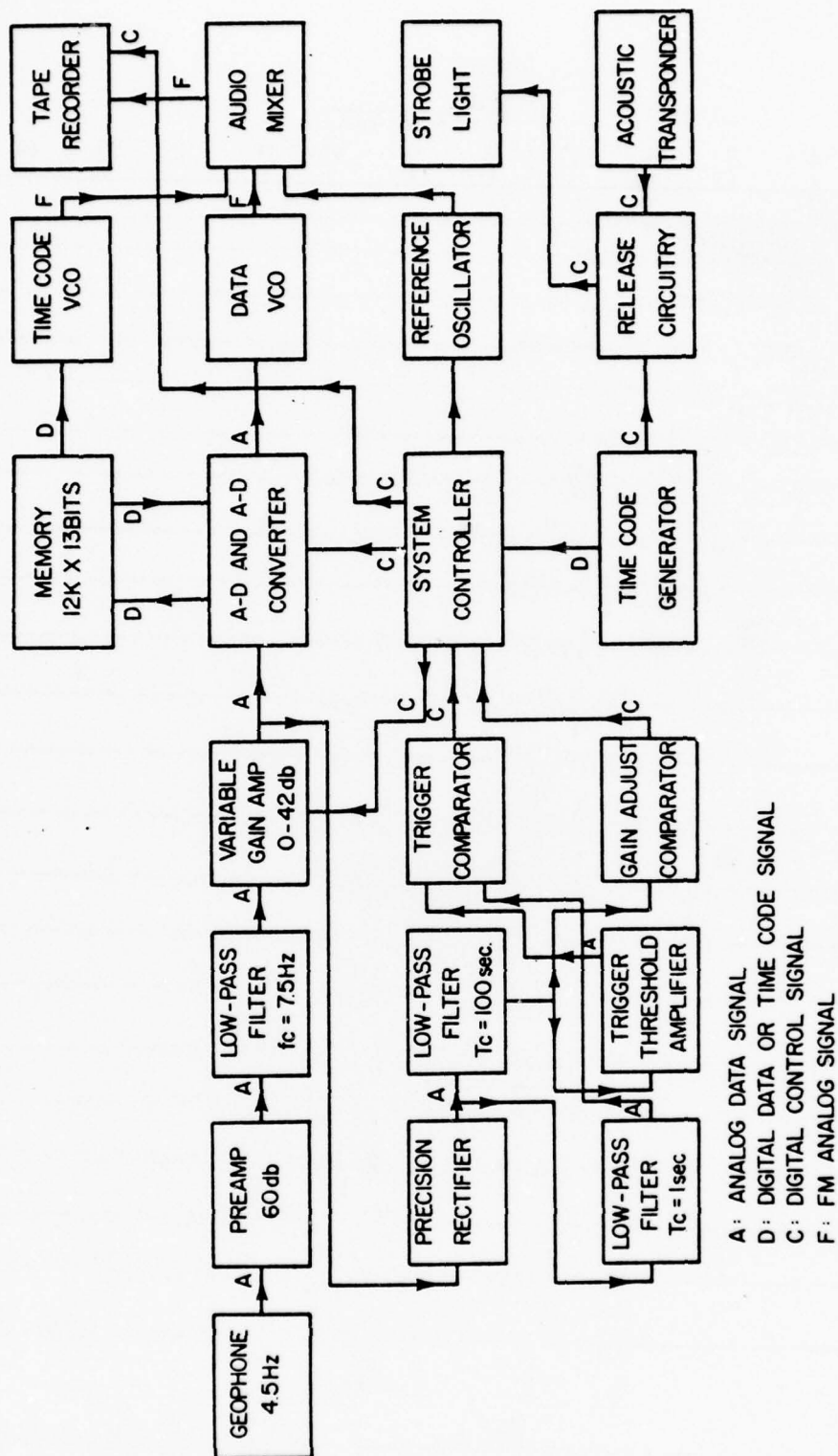
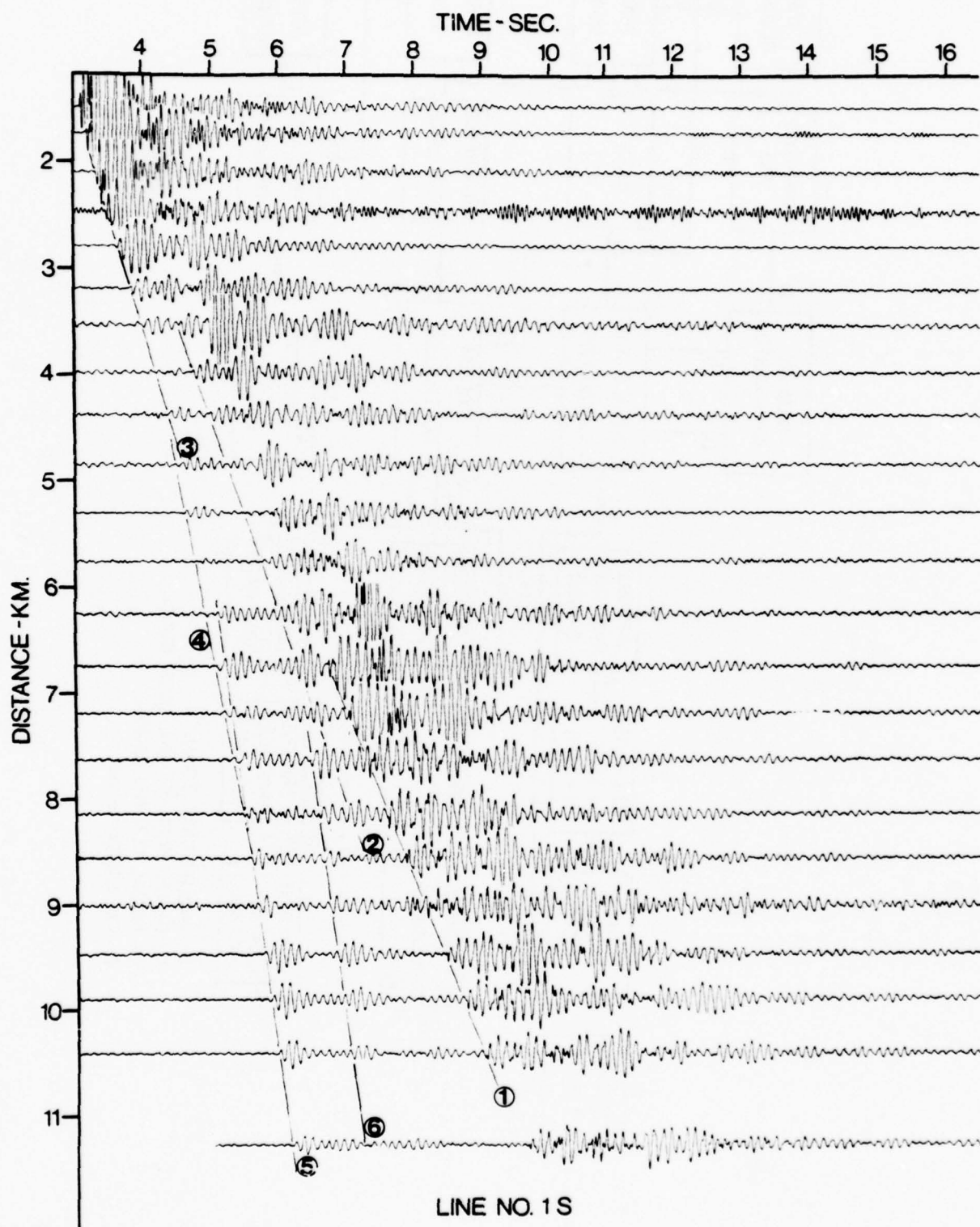


Fig. 5



UNIVERSITY OF WASHINGTON
COLLEGE OF ENGINEERING
DEPARTMENT OF ELECTRICAL ENGINEERING

OCEAN-EARTH ACOUSTIC COUPLING
Contract N66001-77-C-0264

Robert I. Odom, Jr.
Rubens A. Sigelmann -
Gordon Mitchell
Donald K. Reynolds

Technical Report #209
May 1978

Principal Investigator
Rubens A. Sigelmann

Prepared for
Naval Ocean Systems Center
San Diego, California 92152

I. INTRODUCTION

This is a progress report on the continuation of the investigation of acoustic propagation in a tapered water layer over a solid elastic half-space. The geometry approximates that of a shoreline. The research developed from encouraging preliminary results by Reynolds et al. [1].

Using ultrasonic waves and an aluminum slab in water as a model, they found:

1. Acoustic energy coupling from the water to the aluminum was localized in a small region.
2. The energy coupled out from the solid into the water below the slab, and hence the energy within the solid, was in the form a well-defined beam.
3. The efficiency of the coupling was high.

These results indicated a direction for further work which included upgrading the experimental facility by adding automatic data logging capabilities and a detailed theoretical investigation to be used in the interpretation of experiments and as a guide for future experiments.

The status of the work at this time may be summarized as follows:

1. A computer program has been written to calculate dispersion curves for the propagating acoustic modes in a planar liquid layer over a solid elastic half-space. Dispersion curves have been calculated using the

physical parameters appropriate for our laboratory model of fresh water and aluminum and for a system involving seawater and the continental crust.

2. An approximate mathematical model has been used to examine the acoustic coupling from a tapered water layer to solid elastic half-space. This model has been applied to two systems, one involving fresh water and aluminum and one involving seawater and continental crust.
3. A motorized probe carriage has been constructed, facilitating automation of data logging.

The results so far have been promising as even the approximate mathematical model predicts the gross features of the experimental results.

The ongoing efforts are being directed toward making careful measurements of the reflected energy which propagates from the beach to deeper water, measurement of the acoustic fields along the bottom of the liquid waveguide and development of an accurate theoretical model. The results of the laboratory experiments and theoretical modeling will be integrated and used to make recommendations for further study.

II. ANALYSIS

Plane Layer Mode Dispersion

The case of a plane liquid layer over a solid elastic half-space has been studied by a number of people [2,3]. It is found

that the propagation of sound in such a structure may be described by a set of discrete guided modes propagating in the water layer. The dispersion equation for the waveguide as given by Tolstoy [3] is:

$$\tan(qh) = \frac{\rho_2}{\rho_1} \left(\frac{\beta_2}{\omega}\right)^4 \frac{q}{r} [4rsk^2 - (k^2 + s^2)^2] \quad (1)$$

where

h = thickness of liquid layer

ρ_1 = density of the liquid

ρ_2 = density of the solid

$\omega = c_1 k_1$ = angular frequency of the radiation

c_1 = speed of sound in the liquid

$k_1 = 2\pi/\lambda$ = wavenumber

$q = k(c^2/c_1^2 - 1)^{1/2}$

$k = k_1 \sin \theta$

θ = angle of incidence of a ray at the liquid-solid boundary

$c = c_1 \csc \theta$ = phase velocity of mode in general

$r = k(1 - c^2/\alpha_2^2)^{1/2}$

$s = k(1 - c^2/\beta_2^2)^{1/2}$

α_2 = compressional wave velocity in the solid

β_2 = shear wave velocity in the solid

The geometry is shown in figure 1.

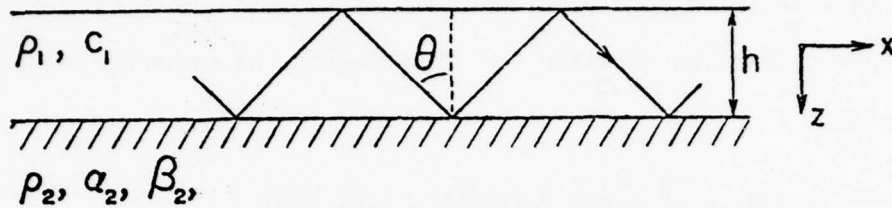


Figure 1. Plane liquid layer over a solid elastic half-space.

Equation (1) may be rewritten so the phase velocity c is a parameter

$$kh = \left(\frac{c^2}{c_1^2} - 1\right)^{-\frac{1}{2}} \left\{ m\pi + \arctan \left[\frac{\rho_2}{\rho_1} \left(\frac{\beta_2}{c}\right)^4 \frac{\left(\frac{c^2}{c_1^2} - 1\right)^{\frac{1}{2}}}{\left(1 - \frac{c^2}{\alpha_2^2}\right)^{\frac{1}{2}}} G \right] \right\} \quad (2)$$

where

$$G = \left[4 \left(1 - \frac{c^2}{\alpha_2^2}\right)^{\frac{1}{2}} \left(1 - \frac{c^2}{\beta_2^2}\right)^{\frac{1}{2}} - \left(2 - \frac{c^2}{\beta_2^2}\right)^2 \right] \quad (3)$$

and $m = 0, 1, 2, \dots$ is the mode number. Solutions also exist for m negative. These are redundant and may be interpreted as propagation in the negative x -direction. Cutoff for some mode $m > 0$ occurs when the phase velocity c becomes equal to the shear wave velocity β_2 of the elastic substrate. The cutoff frequencies are found by setting $c = \beta_2$ in (2) and are given by

$$(k_c h)_m = \left(\frac{\beta_2^2}{c_1^2} - 1\right)^{-\frac{1}{2}} \left\{ m\pi - \arctan \left[\frac{\rho_2 \alpha_2}{\rho_1 c_1} \left(\frac{\beta_2^2 - c_1^2}{\alpha_2^2 - \beta_2^2}\right)^{\frac{1}{2}} \right] \right\} \quad (4)$$

for $m > 0$

The $m = 0$ mode does not have cutoff. Instead, it converts to a surface Rayleigh wave either as the thickness h of the liquid layer or the wavenumber k goes to zero.

Examples of dispersion curves for two different sets of material parameters are shown in figure 2. These were calculated from (2) using the computer program listed in appendix 1. The values used for the density and compressional and shear wave velocities for the seawater-continental crust model are typical values taken from Stacey [4].

For the case of a tapered liquid layer over a solid elastic half-space (figure 3), if the taper is very gradual, that is, the change in depth h is very small over distances on the order of a wavelength, it may be useful to describe the propagation in terms of local normal modes. As the acoustic radiation propagates towards the apex of the taper, a particular mode may couple to the next lower order mode or radiate into the elastic substrate as a shear wave as it reaches cutoff depth. Ultimately

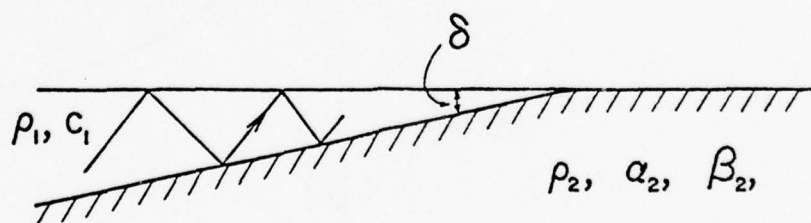


Figure 3. Tapered liquid layer over a solid elastic half-space.

the energy is partitioned between the $m = 0$ surface wave, a radiated shear wave and a reflected wave. It can be inferred

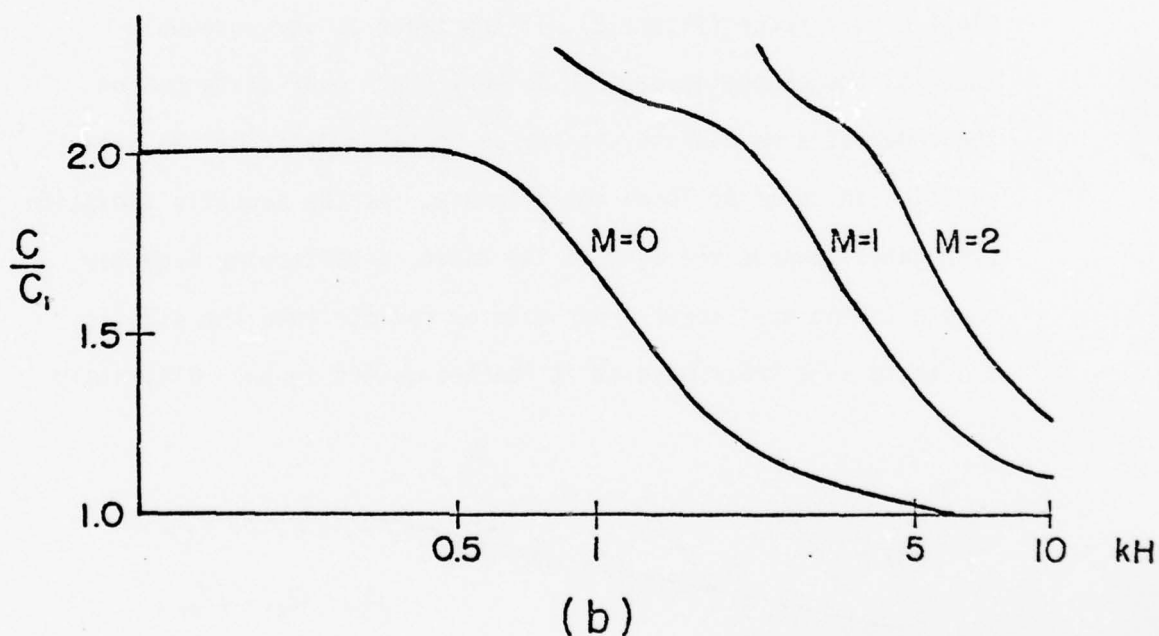
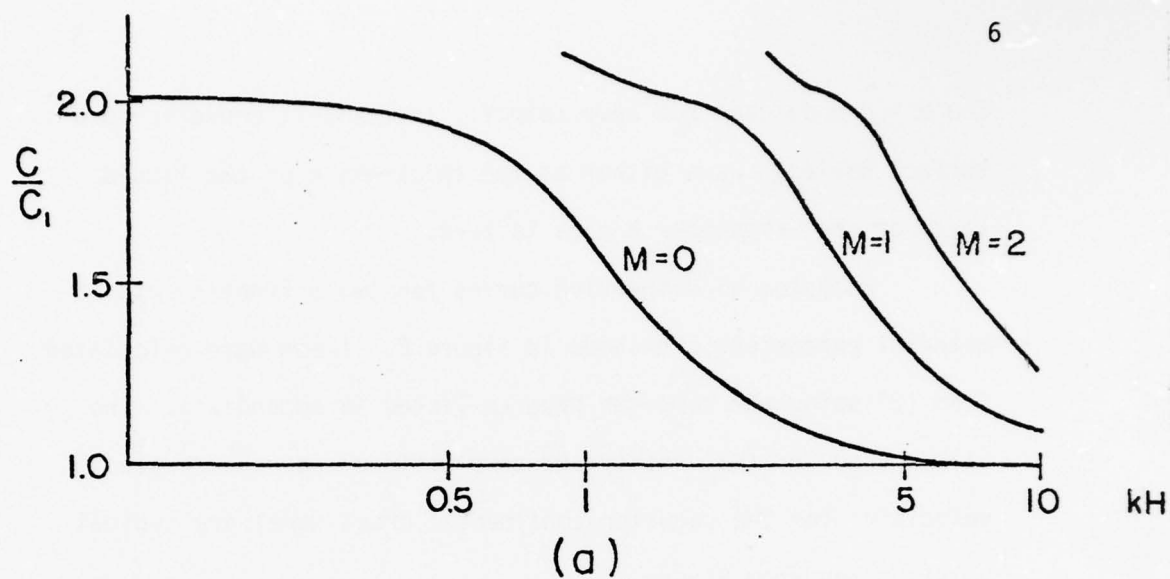


Figure 2. Dispersion curves for acoustic normal modes propagating in a plane liquid layer of depth h over a solid elastic half-space.

- a. Water-Aluminum, where $\rho_1 = 1.0 \cdot 10^3 \text{ Kg/m}^3$, $c_1 = 1430 \text{ m/s}$, $\rho_2 = 2.7 \cdot 10^3 \text{ Kg/m}^3$, $\alpha = 6260 \text{ m/s}$ and $\beta = 3080 \text{ m/s}$.
- b. Seawater-Continental Crust, where $\rho_1 = 1.03 \cdot 10^3 \text{ Kg/m}^3$, $c_1 = 1500 \text{ m/s}$, $\rho_2 = 2.72 \cdot 10^3 \text{ Kg/m}^3$, $\alpha = 5800 \text{ m/s}$ and $\beta = 3450 \text{ m/s}$.

from a ray optic argument that the reflected wave should be almost nonexistent. If the taper is very shallow, a particular ray will suffer many reflections at angles of incidence less than the critical angle. By the time the angle of incidence reaches 0° and the ray turns around, most of the energy will have radiated into the substrate.

Tapered Waveguide

It has been demonstrated by Tien and Martin [5] that guided optical radiation in a tapered optical waveguide is radiated into a well-defined beam which propagates in the substrate (figure 4). Guided by further optical work by Tien et al. [6], an approximate mathematical model for acoustic coupling from a

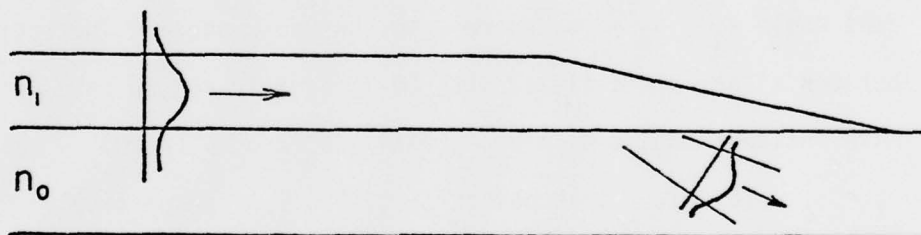


Figure 4. Optical tapered coupler.

liquid layer to a solid elastic layer has been developed. A computer program, which is listed in appendix 2, has been written to calculate the power in the shear wave radiated into the elastic layer and in the acoustic wave transmitted into the water from the back side of the aluminum slab model (figure 11). The inputs

required by the model are the initial power in the liquid taper, the material parameters of the system and the beach or taper angle.

The analysis done is exactly analogous to that done by Tien et al. [6] for the structure shown in figure 3.

As some mode propagates into the tapered region, the thickness of the layer decreases to the point at which the mode cuts off. This corresponds to a ray whose angle of incidence is just equal to the critical angle, $\theta_c = \sin^{-1}(n_0/n_1)$, for the optical case. n_0 and n_1 are the indices of refraction of the substrate and tapered layer, respectively.

In figure 5, taken from Tien et al. [6], a' is the point at which a mode reaches cutoff. At this point there is a ray, $a - a'$, which is incident at just the critical angle, $\theta_i = \theta_c$. After one more bounce, the ray reaches the point b' and has incident angle $\theta_i = \theta_c - 2\delta$, where δ is the taper angle. The region between a' and b' is filled with $(N-1)$ equally spaced rays which have incident angles $\theta_i = \theta_c - (2\delta/N)$, $\theta_i = \theta_c - (4\delta/N)$, $\theta_i = \theta_c - (6\delta/N)$, ... at points 1, 2, 3, ... , respectively. The angle of refraction at each point can be computed from Snell's Law. N is arbitrary and depends on how finely one desires to divide the region between a' and b' .

The geometry used for the calculations for the case of a tapered liquid layer over a solid elastic half-space is shown in figure 6.

The calculations performed paralleled exactly those done by Tien et al. [6] except for the appropriate modifications for

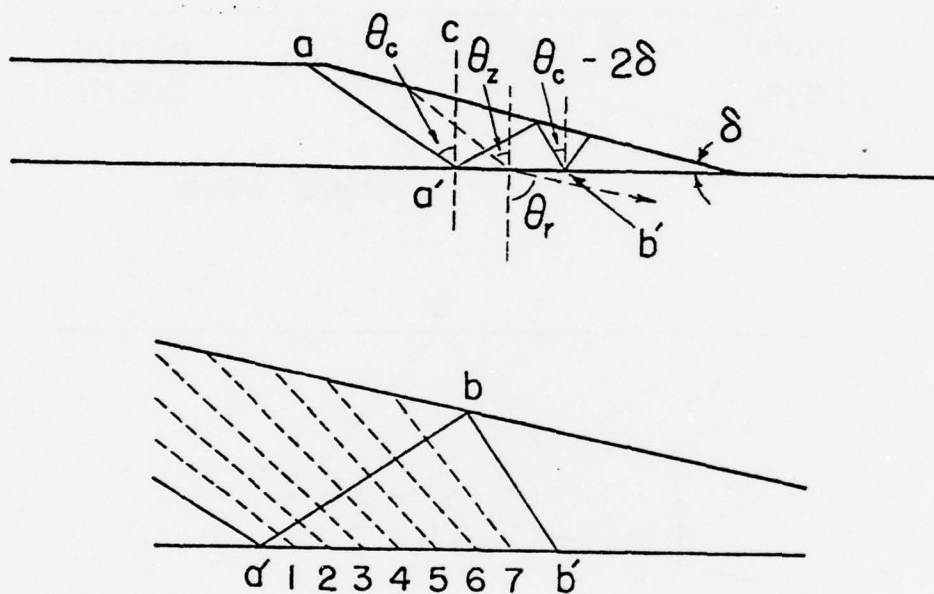


Figure 5. Schematic representation of a light wave propagating in a tapered optical coupler.

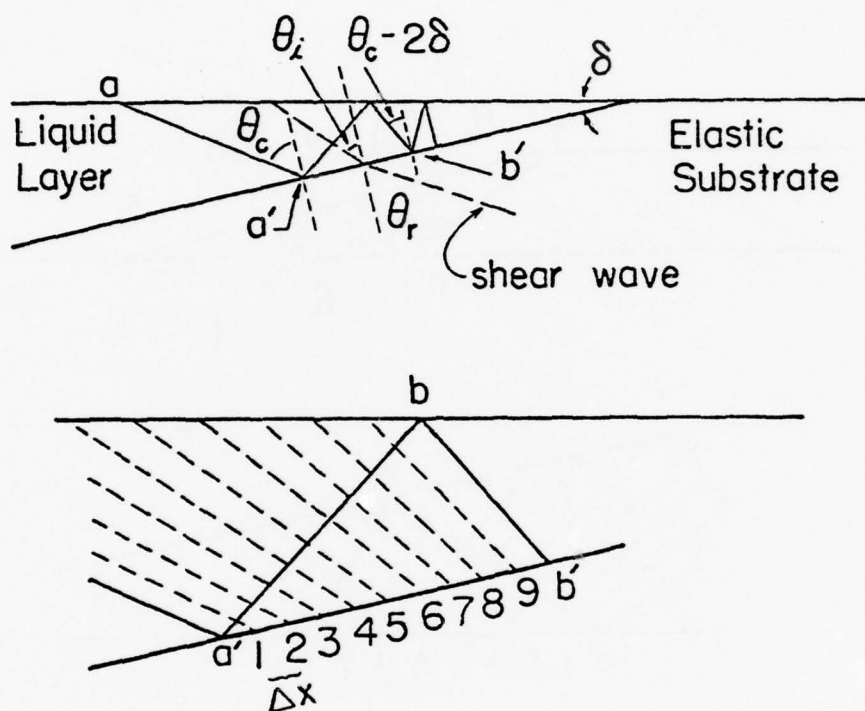


Figure 6. Schematic representation of an acoustic wave propagating in a tapered liquid layer and coupling to a radiated shear wave in the elastic substrate.

our acoustic case. The critical angle is $\theta_c = \sin^{-1}(c/\beta_2)$, where c and β_2 are as previously defined. The depth h at which a particular mode ($m > 0$) cuts off is determined from (4). The time averaged power $\langle P \rangle$ propagating in the liquid layer in the x -direction and integrated over the depth h of the layer is given by

$$\langle P \rangle = \frac{1}{2} \int_0^h \operatorname{Re} (\tau_{xx}^* \dot{u}_x) dz \quad (5)$$

where

$u_x = A_1 \sin qz e^{i(kx - \omega t)}$ is the particle displacement in the x -direction

$$\tau_{xx} = \lambda \frac{\partial u_x}{\partial x}$$

λ = Lamé's constant

The result, which gives a relationship between the time averaged power in the liquid layer incident on the liquid-solid boundary and the amplitude of the particle displacement A_1 , is

$$\langle P \rangle_i = \frac{1}{4} h \rho_1 c_1^3 k_1^2 \sin \theta_i A_1^2 \quad (6)$$

Similarly, the time averaged power in the shear wave in the elastic substrate to which the acoustic wave couples along the interface at distances Δx between any two adjacent points is related to the radiated shear wave amplitude β_2 by

$$\langle P \rangle_{rs} = \frac{1}{2} \rho_2 \beta_2 c_1^2 k_1^2 \Delta x \cos \theta_r \beta_2^2 \quad (7)$$

β_2 at successive points along the liquid-solid interface may be computed from A_1 at that point from the formula for the appropriate transmission coefficient ([7], p. 79).

The calculation proceeds as follows:

1. The power $\langle P \rangle_i$ in the liquid taper is set to 1.0 at point 1.
2. The amplitude of the incident wave is calculated from (5).
3. The amplitude of the transmitted shear wave is computed from the formula for the appropriate transmission coefficient.
4. The power refracted into the substrate through the space 1-2 is computed from (6).
5. The power in the taper at point 2 is now

$$\langle P \rangle_{i2} = \langle P \rangle_{i1} - \langle P \rangle_{rs1} .$$
6. The same set of computations are performed for point 2, and so on.

The reason for pursuing this simplified analysis was that Tien et al. [6] got remarkably good qualitative agreement between their calculations and experiment for the tapered optical waveguide. Our analysis was applied to two different cases illustrated in figures 7 and 8. The first case was for the water and aluminum system of our experimental model. As indicated in figure 7, the calculation was done for the acoustic field in the water behind the slab since that is where our pickup transducer is located. Multiple reflections in the aluminum slab were not considered.

Figures 7 and 8 are plots of power per unit angle I_θ as a functions of refraction angle θ_r and include curves for beach angles of 0.25° and 1.3° , values which have been used in the experiments. I_θ at point 2 on figure 6, for example, is $P_{r2}/(\theta_{r3} - \theta_{r2})$. P_{r2} is the refracted power at point 2 and θ_{r2}

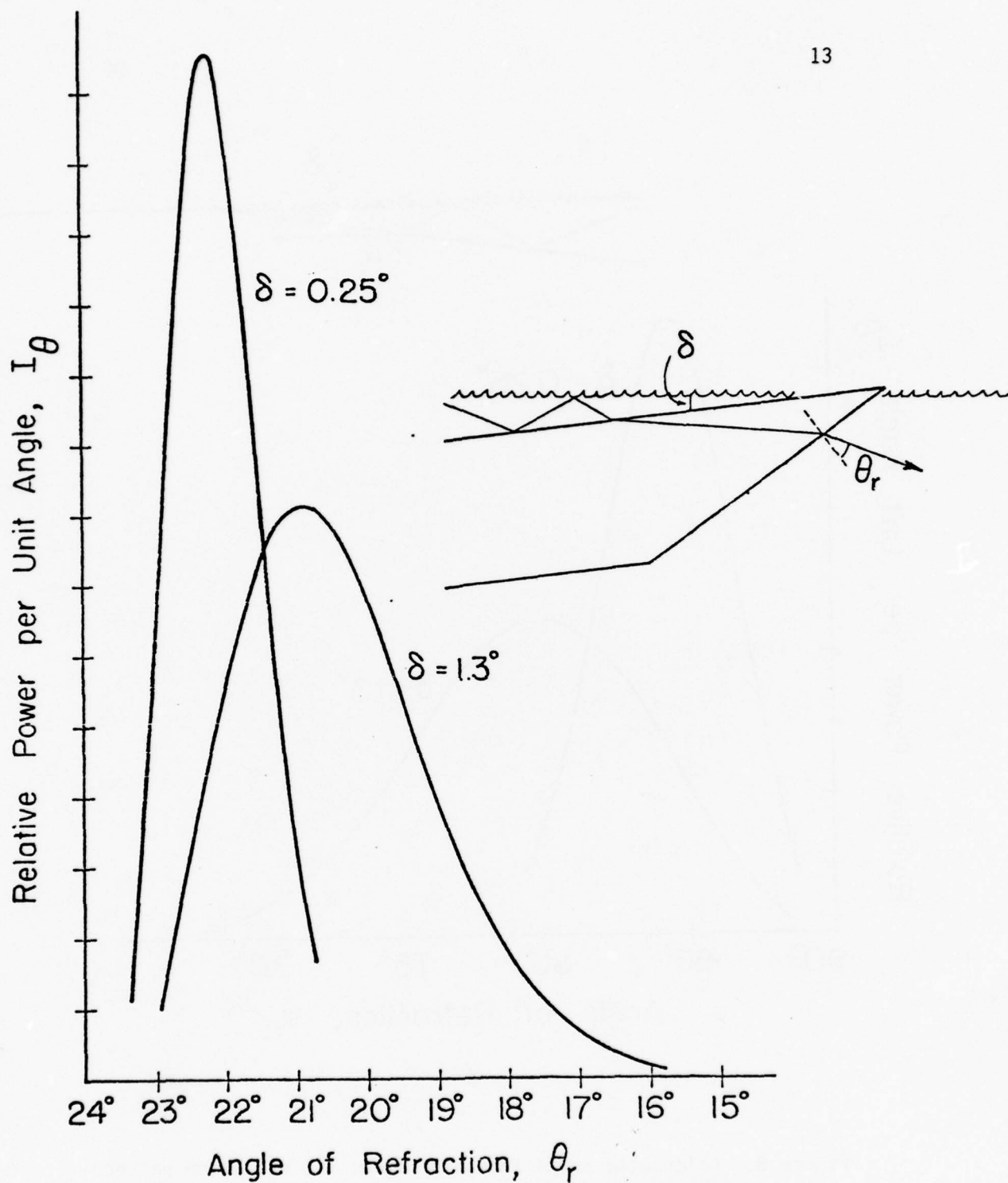


Figure 7. Calculated sound intensity I_θ of the radiation pattern for an $m=1$ mode wave as a function of the angle of refraction θ_r . This is the sound intensity distribution in the water behind the aluminum slab.

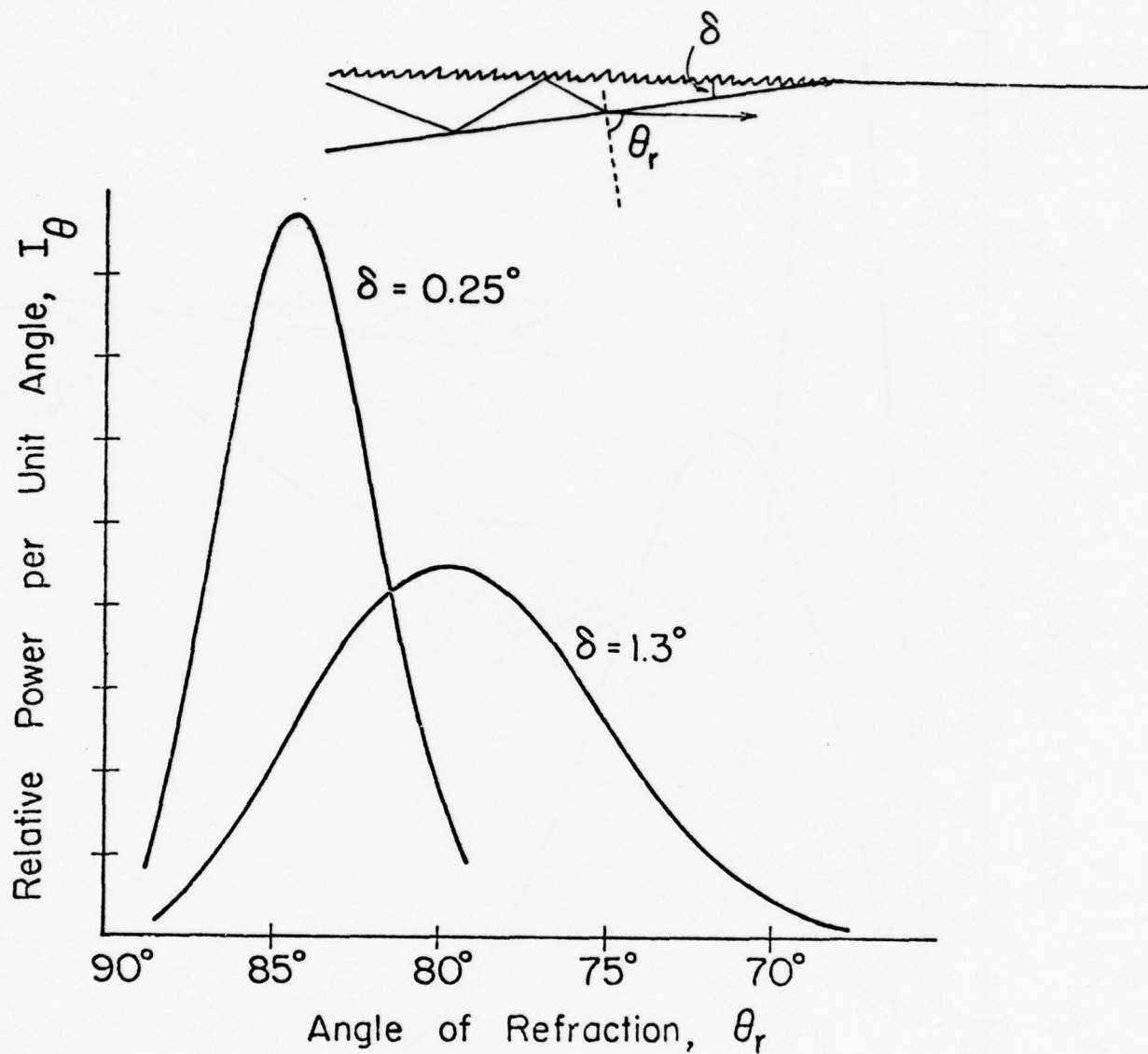


Figure 8. Calculated sound intensity I_θ of the radiation pattern for an $m=1$ mode wave as a function of the angle of refraction θ_r for seawater over a model continental crust.

θ_{r3} are the angles of refraction at points 2 and 3, respectively. In figure 7 these points are referred to the back surface of the aluminum slab. At the cutoff point in the liquid taper, I_θ is zero because the liquid-solid interface is still totally reflecting. As the wave propagates beyond this point, both θ_i and the refraction angle at the liquid-solid interface decrease. I_θ first increases because as θ_i decreases, transmission into the solid substrate increases. I_θ increases, reaching a maximum, then falls to zero as the power available in the liquid taper is depleted. It can be seen that a small beach angle produces a narrower radiation pattern, consistent with Tien et al.'s [6] optical results.

Typical values for the compressional and shear wave velocities ($\alpha_2 = 5800$ m/s, $\beta_2 = 3450$ m/s from [4], p. 338) in the continental crust were used to generate the plots in figure 8. Also, the second interface was not included. It can be seen that the radiation intensity peaks at an angle a few degrees below the grazing angle, $\theta_r = 90^\circ$, and that for a steeper beach angle the intensity pattern broadens and shifts more towards the normal.

In doing these calculations, the cutoff point for the $m = 1$ mode was used. The $m = 0$ mode does not, as has been previously mentioned, cutoff to a radiated shear wave but becomes a surface Rayleigh wave as the depth h goes to zero. Also in the course of these calculations, it was found that for this mathematical model conversion from the acoustic wave in the liquid to a compressional wave in the solid did not have to be considered. In

general, the compressional wave velocity, α_2 , is greater than the shear velocity, β_2 . Consequently, the critical angle for compressional waves is less than that for shear waves. For pure water and aluminum the critical angle of incidence for shear waves is 27.7° and for compressional waves is 13.2° . For seawater and a model continental crust, the critical angles are 15° and 25.8° for compressional and shear waves, respectively. It was found that as the angle of incidence decreased, the power in the tapered layer was depleted to zero long before θ_i approached the critical angle for compressional waves.

Work is continuing on developing a more complete mathematical model of the coupling of acoustic radiation from a tapered liquid layer to a solid elastic half-space. The results should lead to an increased understanding of the acoustic propagation and radiation mechanisms in such a structure. The development of a computer program which can be applied to general problems of this type is a goal of the ongoing research.

III. COMPARISON OF THEORETICAL MODEL WITH EXPERIMENT

Besides sound intensity I_θ as a function of the angle of refraction θ_r , the acoustic power P_r as a function of the probe displacement D was calculated using the previously defined model. The geometry, which is that of our experimental system is illustrated in figure 9.

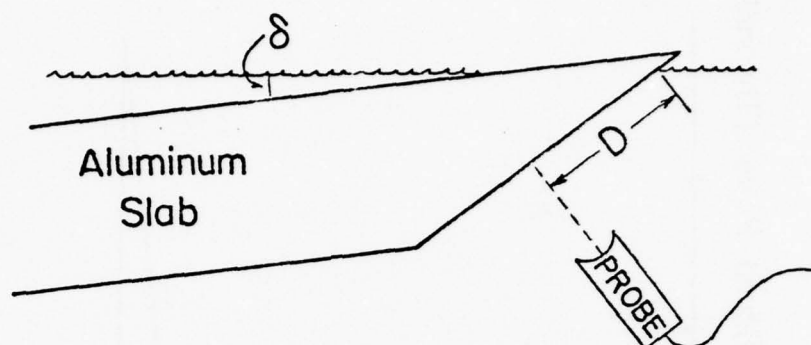


Figure 9. Geometry of experimental system.

The bottom curve of figure 10 is the result of an experiment with beach angle of $\delta = 1.3^\circ$. The upper curve is the result of a calculation using the same parameters present in the experiment as inputs for the computer program. The shear and compressional wave velocities for aluminum are 3080 m/s and 6260 m/s, respectively.

Three different transducers are available for use in the experiment. The source for the acoustic radiation is a 1 MHz transducer which produces 30 μ s bursts of 1 MHz radiation in a beam with 3° divergence. Two additional transducers are available for use to probe the sound field behind the aluminum model. One, a 7 cm focal length, 1 MHz probe, was used to obtain the bottom curve in figure 10. The other transducer is a 1 MHz point probe.

The experiment indicated a strong peak in the sound pressure at a probe displacement of about 35 mm. The calculated sound power peaks at about 37 mm and is much narrower than the

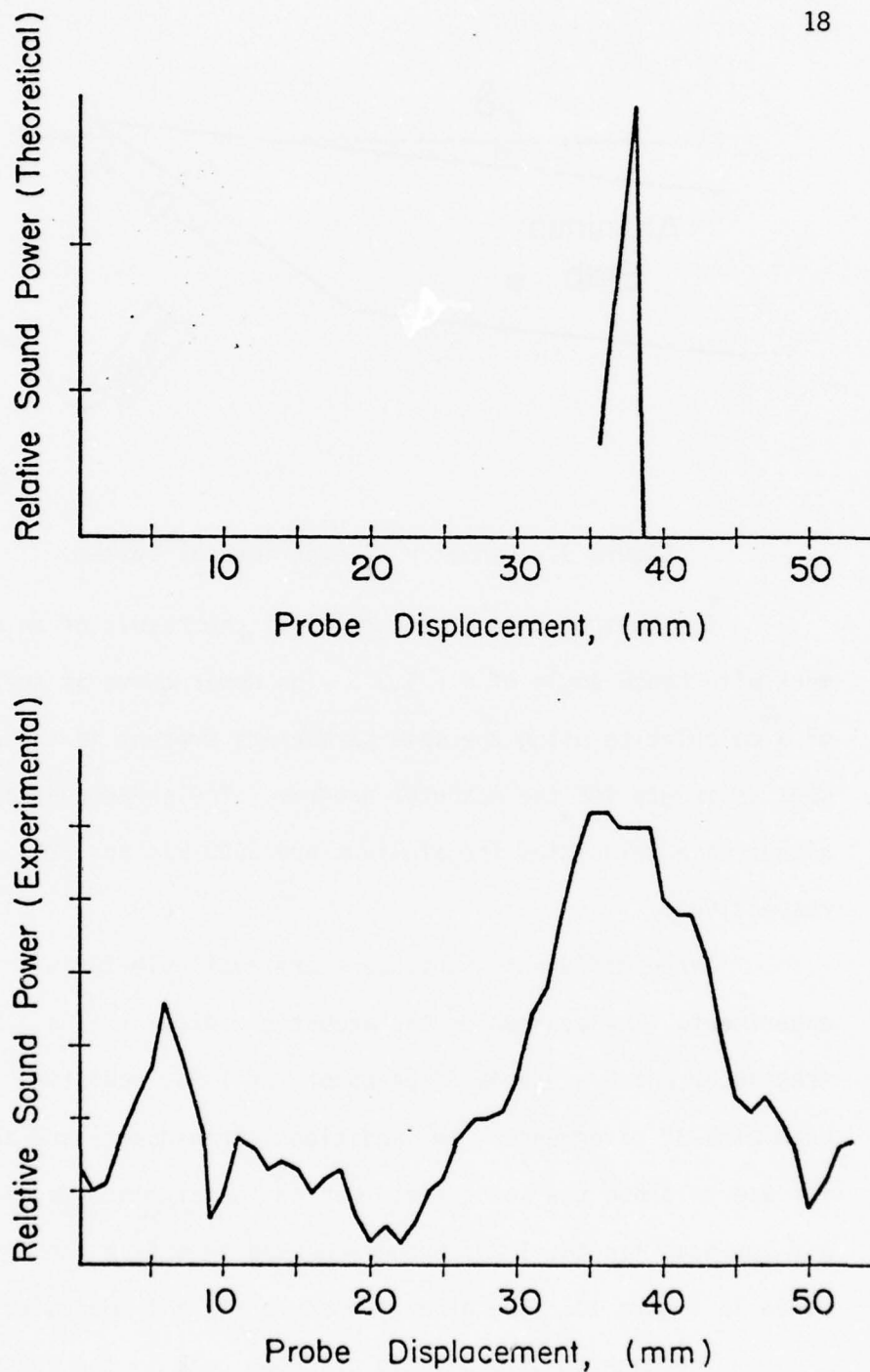


Figure 10. Experimental and theoretical radiated acoustic fields. Both curves are for the geometry represented in figure 9, with $\delta = 1.3^\circ$. Although the theoretical curve is much narrower, the positions of the maxima are almost identical.

measured curve. The difference in the widths is not too surprising because of the simplicity of the theoretical model. The theoretical model was derived using a plane wave assumption, while the acoustic radiation source for the experiments produces a beam of 3° divergence. The agreement on the location of the maximum in the signal is quite good.

Also as was reported by Reynolds et al. [1], almost all the coupling of sound energy from the liquid layer to the substrate occurs in a region where the water depth is less than the wavelength of 1 MHz sound ($\lambda = 1.5$ mm) and before the depth has decreased to zero. This indicates two things: first, that the sound field does exhibit a mode structure in the liquid layer since the point at which a particular mode cuts off does depend on the depth of the liquid layer; and second, that diffraction effects due to the corner of the taper in the liquid layer are negligible. These preliminary results are very encouraging and indicate the tractability of the problem and provide the impetus for development of a more sophisticated theoretical model.

Improvements to Experiment.

Figure 11 is a schematic of the tank and probe arrangement for the experiments. This system has been upgraded as illustrated by figures 12 and 13. An automatic probe carriage assembly has been constructed allowing the probe to be translated automatically by means of a variable speed dc motor.

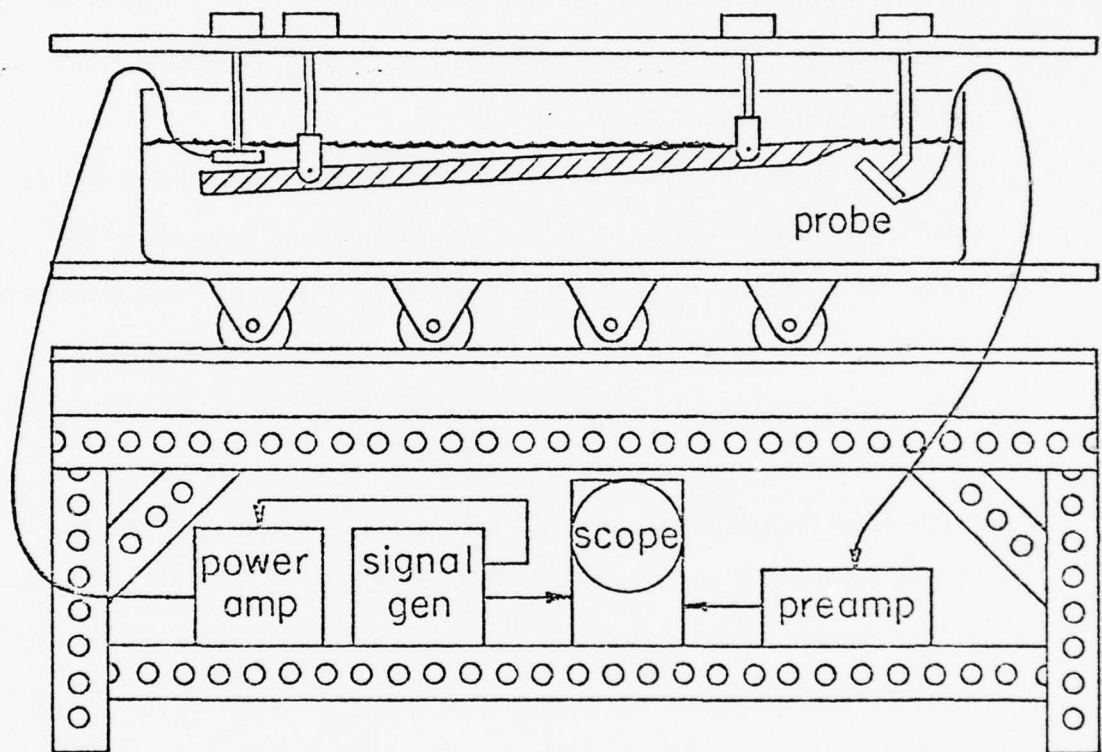


Figure 11. Schematic of tank and probe arrangements for measuring acoustic coupling from a tapered liquid layer to an elastic substrate.

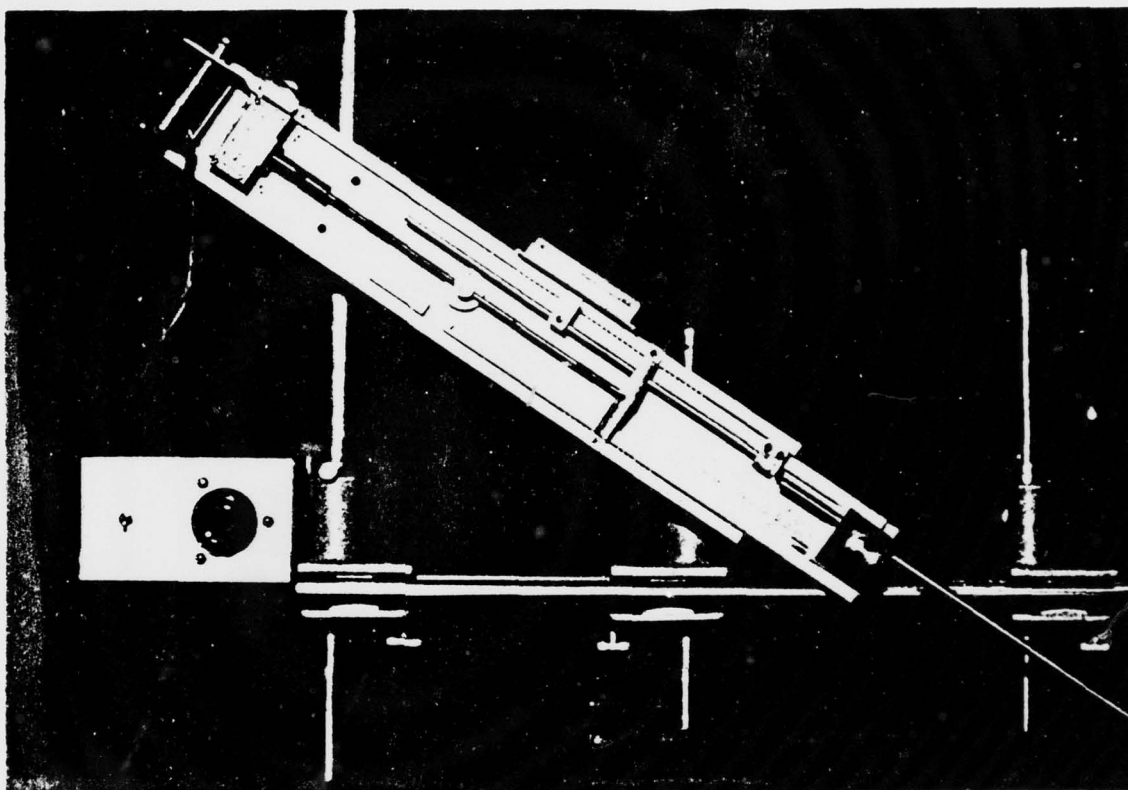


Figure 12. Photograph of the motorized probe carriage. The carriage is driven by a variable speed dc motor. The position of the probe may be determined from a linear 10 k Ω slide potentiometer attached to the carriage.

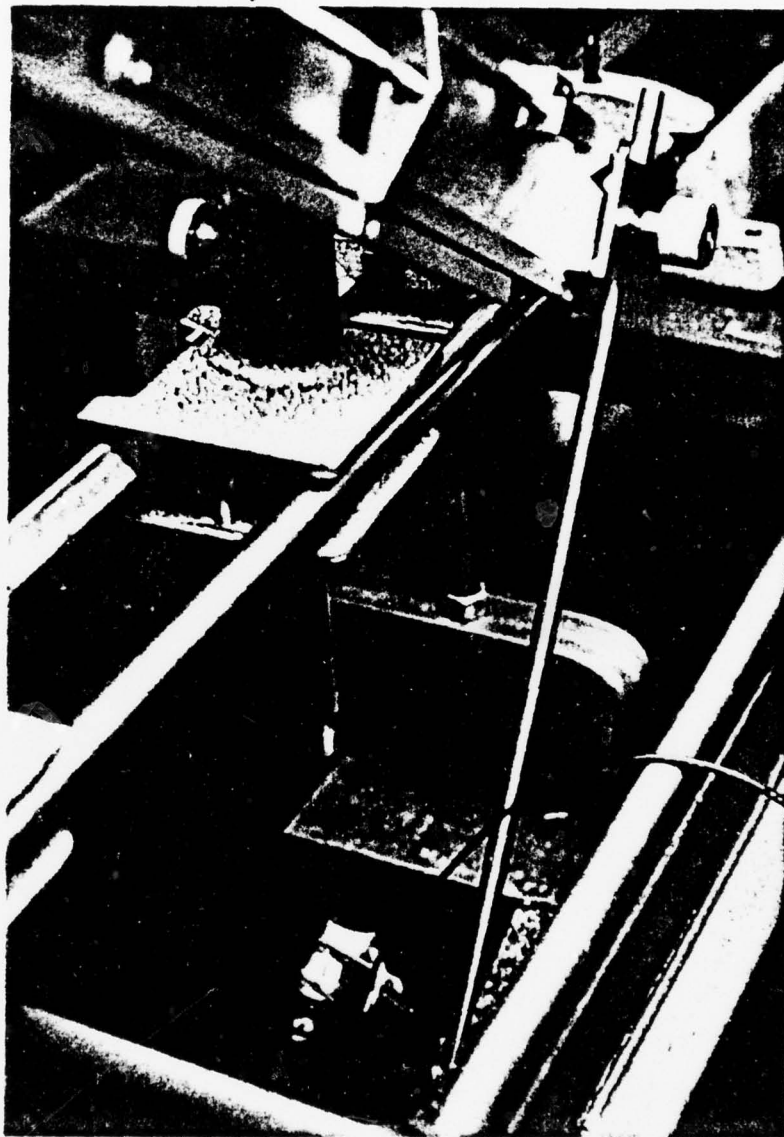


Figure 13. Another view of the motorized probe carriage showing the focused probe in position.

A 10 k Ω linear slide potentiometer is attached to the probe carriage which permits the position to be recorded on one axis of an X-Y plotter. The other input to the plotter may be provided by the level of the probe signal, allowing automatic acquisition of sound pressure versus probe displacement data.

IV. CONCLUSIONS AND PROJECTED WORK

The results to this point may be summarized as follows:

- A. A computer program, listed in appendix 1, has been written, allowing us to calculate the mode dispersion curves for sound propagation in a plane liquid layer over a solid elastic half-space. This has been applied to a system with pure water over an aluminum substrate, conforming to the parameters of our experiment and to a system with seawater over a model continental crust ($\alpha_2 = 5800$ m/s, $\beta_2 = 3450$ m/s).
- B. A simple theoretical model paralleling optical work done by Tien et al. [6] has been developed for the coupling of acoustic radiation from a tapered liquid layer to a solid elastic half-space. A computer program, listed in appendix 2, has been written which allows specialization of the calculation to the system of interest. The results indicate that the energy propagates in a shear wave beam whose width depends on the beach angle. A narrower beam is produced by a small beach angle. When compared with experimental results, the simple model accurately predicts the position of the maximum in the sound pressure.

- C. A motorized probe carriage has been constructed which allows automatic probing of the sound pressure field and recording of sound pressure versus probe displacement on an X-Y plotter.

As previously stated, work is continuing on the development of a more sophisticated theoretical model and accompanying computer programs.

Measurements of reflected energy and the sound field at the bottom of the liquid waveguide are in preparation.

The results so far are very encouraging at both the theoretical and experimental levels. The end results should provide a complete understanding of the propagation of sound in a tapered liquid layer over a solid elastic half-space and should point the direction to be taken for full-scale experiments.

REFERENCES

1. D. K. Reynolds, G. L. Mitchell, R. A. Sigelmann, "Ocean-Earth Acoustic Coupling," Final Report: Navy Contract N66001-76-C-0135, 1976.
2. C. L. Pekeris, "Theory of Propagation of Explosive Sound in Shallow Water," Mem. Geol. Soc. Am., 27, 1948.
3. I. Tolstoy, "Dispersive Properties of a Fluid Layer Overlying a Semi-Infinite Elastic Solid," Bull. Seism. Soc. Am., 44, 1954.
4. J. D. Stacey. Physics of the Earth. New York: John Wiley and Sons, 2nd edition, 1977.
5. P. K. Tien, R. J. Martin, "Experiments on Light Waves in a Thin Tapered Film and a New Light Wave Coupler," Applied Physics Letters, 18, 1971.
6. P. K. Tien, G. Smolinsky, R. J. Martin, "Radionation Fields of a Tapered Film and a Novel Film-to-Fiber Coupler," IEEE Trans. Microwave Theory and Techniques, MTT-23:1, 1975.
7. W. M. Ewing, W. S. Jardetsky, F. Press. Elastic Waves in Layered Media. New York: McGraw-Hill, 1957.

APPENDIX 1

```

PROGRAM DISPER(INPUT,OUTPUT,TAPES=INPUT,TAPE6=OUTPUT)
3  DIMENSION CNORM(100),WAVH(100),WAVIH(100)
3  COMMON RH01,RH02,ALPHA2,BETA2,C1,H,PI,MODE
C   THIS PROGRAM CALCULATES DISPERSION RELATIONS FOR A PLANE LIQUID
C   LAYER OVER A SOLID ELASTIC HALF SPACE
C   THE FOLLOWING PARAMETERS MUST BE SUPPLIED
C   RH01=DENSITY OF LIQUID
C   RH02=DENSITY OF SOLID
C   C1=ACOUSTIC VELOCITY IN LIQUID
C   ALPHA2=P WAVE VELOCITY IN SOLID
C   BETA2=SHEAR WAVE VELOCITY IN SOLID
C   CR=RAYLEIGH WAVE VELOCITY IN SOLID
C   H=THICKNESS OF LIQUID LAYER
C   MAX=MAXIMUM NUMBER OF MODES TO BE CALCULATED
C   THE FOLLOWING ARE OUTPUTS
C   WAVIH(I)=(INTRINSIC WAVENUMBER IN LIQUID)*H
C   WAVH(I)=(MODE WAVENUMBER)*H
C   CNORM(I)=(PHASE VELOCITY OF MODE)/C1
C
3  RH01=1.03
5  RH02=2.72
6  C1=1.5E5
10 ALPHA2=5.8E5
11 BETA2=3.45E5
13 CR=3.009E5
14 H=3.0E-1
16 MAX=5
C
17 PI=ACOS(-1.)
23 DO 10 M=1,MAX
24 MODE=M-1
26 WRITE(6,90)
31 WRITE(6,100)MODE
37 IF(MODE.NE.0)GO TO 1
41 C=CR
43 GO TO 2
43 1 C=BETA2
45 2 DELTA=(C-C1)/100.
51 DO 20 KK=1,100
52 CALL WAVNO(WAVH,C,KK)
54 CNORM(KK)=C/C1
60 WAVIH(KK)=C*WAVH(KK)/C1
66 C=C-DELTA
70 IF(C.LT.C1)GO TO 15

```

```

73      20 CONTINUE
75      15 WRITE(6,200) (WAVH(I),CNORM(I),WAV1H(I),I=1,100,2)
116     10 CONTINUE
121     90 FORMAT(1H1)
121     100 FORMAT(1H ,/1X,5HMODE=,I2,8X,2HKH,12X,4HC/C1,12X,3HK1H)
121     200 FORMAT(1H ,10X,F10.6,5X,F10.6,5X,F10.6)
121     STOP
DISPER

123     END
DISPER

SUBROUTINE WAVNO(WAVH,C,KK)
6      DIMENSION WAVH(100)
6      COMMON RH01,RH02,ALPHA2,BETA2,C1,H,PI,MODE
C      THIS SUBROUTINE EVALUATES THE DISPERSION RELATION WITH THE
C      PHASE VELOCITY C AS A PARAMETER
6      Q=SQRT((C/C1)**2-1.)
22      R=SQRT(1.-(C/ALPHA2)**2)
36      S=SQRT(1.-(C/BETA2)**2)
52      G=4.*R*S-(2.-(C/BETA2)**2)**2
67      WAVH(KK)=(MODE*PI*ATAN((RH02/RH01)*((BETA2/C)**4)*(Q/R)*G))/Q
116     RETURN
117     END
WAVNO

```

APPENDIX 2

```

3      PROGRAM INTEN(INPUT,OUTPUT,TAPES=INPUT,TAPE6=OUTPUT)
3      DIMENSION THETI(100),THETR(100),PWRR(100),PWR(100),THETI1(100)
3      DIMENSION THETR1(100),THETRP(100)
      COMMON RH01,RH02,ALPHA,BETA,C1,H,PI
      C      THIS PROGRAM CALCULATES ACOUSTIC POWER AS A FUNCTION OF
      C      REFRACTION ANGLE FOR THE RADIATED SHEAR WAVE FOR A TAPERED
      C      LIQUID LAYER OVER A SOLID ELASTIC HALF-SPACE. A SECOND SOLID
      C      LIQUID INTERFACE INCLINED AT SOME ANGLE ANG2 TO THE FIRST
      C      LIQUID-SOLID INTERFACE MAY BE INCLUDED BY SETTING THE PARAMETER
      C      IFACE=2.
      C
      C      THE FOLLOWING PARAMETERS MUST BE SUPPLIED
      C
      C      RH01=DENSITY OF LIQUID
      C      RH02=DENSITY OF SOLID
      C      C1=ACOUSTIC VELOCITY IN LIQUID
      C      ALPHA=P WAVE VELOCITY IN SOLID
      C      BETA=SHEAR WAVE VELOCITY IN SOLID
      C      WAV1=WAVE NUMBER IN LIQUID
      C      H=DEPTH OF LIQUID AT CUTOFF FOR MODE OF INTEREST
      C      ANG=ANGLE OF LIQUID TAPER IN DEGREES
      C      ANG2=ANGLE OF INCLINATION OF SECOND INTERFACE TO FIRST
      C      INTERFACE IN DEGREES
      C      IFACE=NUMBER OF INTERFACES---EITHER IFACE=1 OR IFACE=2
      C      N=NUMBER OF ITERATIONS IN CALCULATION
      C      MAX=MAXIMUM NUMBER OF RAY BOUNCES
      C      MAX SHOULD BE AT LEAST 1 BUT NOT GREATER THAN
      C      IFIX((THEIC-THETCA)/2.*ANG)
      C      S=LENGTH OF BEACH ON INPUT SIDE FOR CASE IFACE=2 IN CENTIMETER
      C      PWRI=INITIAL ACOUSTIC POWER IN LIQUID LAYER----NORMALLY=1.0
      C
      C      VARIABLE LIST
      C
      C      THETI(I)=ANGLE OF INCIDENCE OF RAY IN THE LIQUID LAYER
      C      THETR(I)=ANGLE OF REFRACTED SHEAR WAVE
      C      PWRR(I)=POWER IN REFRACTED SHEAR WAVE
      C      PWR(I)=POWER IN REFRACTED ACOUSTIC WAVE AT SECOND INTERFACE
      C      THETI1(I)=ANGLE OF INCIDENCE OF SHEAR WAVE AT SECOND INTERFACE
      C      THETR1(I)=ANGLE OF INCIDENCE
      C      THETR1(I)=ANGLE OF REFRACTED ACOUSTIC WAVE AT SECOND INTERFACE
      C      THETRP(I)=ANGLE OF REFLECTED P WAVE AT SECOND INTERFACE
      C
      C      THE FOLLOWING VARIABLES ARE OUTPUTTED
      C
      C      AVANG=AVERAGE ANGLE OF REFRACTION
      C      BRIGHT=INTENSITY PER UNIT ANGLE
      C      AP=DISTANCE FROM CRITICAL RAY TO ENTRY POINT OF LAST RAY
      C      TOTAP=DISTANCE FROM CRITICAL RAY TO POINT WHERE POWER IN
      C      LIQUID LAYER GOES TO ZERO

```



```

C      D=PROBE DISPLACEMENT IN CENTIMETERS
C      PWRI=RESIDUAL POWER IN LIQUID TAPER
C
3      RH01=1.0
5      RH02=2.7
6      ALPHA=6.260E5
INTEN
10     BETA=3.080E5
11     C1=1.430E5
13     WAV1=98.86
14     H=0.02
16     ANG=1.3
17     ANG2=30.0
21     IFACE=2
22     N=100
24     MAX=1
25     C=4.
27     PWRI=1.0
C
30     PI=ACOS(-1.)
34     RAD=PI/180.
36     ANG=ANG*RAD
37     ANG2=ANG2*RAD
41     THETC=ASIN(C1/BETA)
46     THETCA=ASIN(C1/ALPHA)
53     AP1=0.
54     AP=0.
55     M=0
56     DO 10 L=1,MAX
57     CALL APTURE(ANG,THETC,M,AP,AP1)
62     10 CONTINUE
65     OUTPUT,AP
74     DELX=AP/FLOAT(N)
100    DO 20 I=1,N
102    VV=I
103    THETI(I)=THETC-(2.*MAX*I*ANG)/FLOAT(N)
117    IF(THETI(I).LT.THETCA.AND.IFACE.EQ.1)GO TO 30
135    IF(THETI(I).LT.THETCA.AND.IFACE.EQ.2)GO TO 45
153    SINE=SIN(THETI(I))
160    C=C1/SINE
161    THETR(I)=ASIN(BETA/C)
170    ASQU=(PWRI*4.)/(RH01*H*SINE*(WAV1**2)*(C1**3))
206    CALL STRAN(THETI,WAV1,ASQU,BSQU,I)
211    PWRR(I)=0.5*RHO2*BETA*C1*C1*WAV1*WAV1*BSQU*COS(THETR(I))*DELX
226    PWRI=PWRI-PWRR(I)
232    IF(PWRI.LT.0..AND.IFACE.EQ.1)GO TO 30
245    IF(PWRI.LT.0..AND.IFACE.EQ.2)GO TO 45
260    IF(IFACE.EQ.1)GO TO 20
263    IF(IFACE.EQ.2)GO TO 15

```

```

266      15 CONTINUE
266          THETI1(I)=THETR(I)-ANG2
274          THETRI(I)=ASIN((C1*SIN(THETI1(I)))/BETA)
310          CALL PTRANS(THETI1,THETRI,BSQU,ASQU,I)
313          PWR(I)=0.5*RHO1*C1*C1*WAV1*WAV1*ASQU*DELX*COS(THETR(I))
          $*COS(THETI1(I))*COS(THETRI(I))
342      20 CONTINUE
345          IF(IFACE.EQ.1)GO TO 25
347          IF(IFACE.EQ.2)GO TO 45
352      25 CONTINUE
352      30 DO 35 K=1,NN
354          THETR(K)=THETR(K)/RAD
361      35 CONTINUE
363          J=NN-1
INTEN
365          DO 40 KK=1,J
366              J=KK+1
370          BRIGHT=ABS(PWRR(KK)/(THETR(KJ)-THETR(KK)))
405          AVANG=(THETR(KJ)+THETR(KK))/2.
414          OUTPUT,AVANG,BRIGHT,PWRR(KK)
432      40 CONTINUE
435          GO TO 60
435      45 DO 50 K=1,NN
437          THETRI(K)=THETRI(K)/RAD
444      50 CONTINUE
446          J=NN-1
450          XAV=H-TAN(ANG)-DELX/2.
455          DO 55 KK=1,J
457              KJ=KK+1
461          BRIGHT=ABS(PWR(KK)/(THETRI(KJ)-THETRI(KK)))
476          AVANG=(THETRI(KJ)+THETRI(KK))/2.
505          D=(SIN(PI/2.-AVANG*RAD)/(SIN(PI/2.+AVANG*RAD-ANG2)))*(XAV+S)-
          $ (S*ANG)/SIN(PI-ANG-ANG2)
540          XAV=XAV-DELX
542          OUTPUT,AVANG,BRIGHT,D,PWR(KK)
564      55 CONTINUE
567      60 TOTAP=DELX*NN
572          OUTPUT,PWRI,TOTAP
604          STOP
606          END
INTEN
      SUBROUTINE APTURE(ANG,THETC,M,AP,API)
      COMMON RHO1,RHO2,ALPHA,BETA,C1,H,PI
      C THIS ROUTINE CALCULATES THE APERTURE
      A=H
      A=A-API*TAN(ANG)
      API=(A*SIN(PI/2.-ANG)*(SIN(THETC-M*2.*ANG)+COS(THETC-M*2.*ANG)*
      $ TAN(THETC-M*2.*ANG-2.*ANG)))/SIN(PI/2.+ANG-THETC-M*2.*ANG)
      M=M+1
      AP=AP+API
      RETURN
      END
APTURE

```

```

11      SUBROUTINE STRAN(THETI,WAVI,ASQU,BSQU,I)
11      DIMENSION THETI(100)
11      COMMON RHO1,RHO2,ALPHA,BETA,C1,H,PI
C      THIS ROUTINE CALCULATES THE SQUARE OF THE S WAVE TRANSMISSION
C      COEFFICIENT FOR A P WAVE INCIDENT ON LIQUID-SOLID BOUNDARY
11      SHEAR=RHO2*BETA*BETA
13      SINE=SIN(THETI(I))
23      C=C1/SINE
24      A=COS(THETI(I))/SINE
35      AI=SQRT(1.-(C/ALPHA)**2)
47      B=SQRT((C/BETA)**2-1.)
61      F1=SHEAR*A*((C/BETA)**2-2. )**2
75      F3=4.*RHO1*A*AI*C*C
102     G2=(RHO1*AI*(C**4))/(BETA**2)+4.*SHEAR*A*AI*B
120     BSQU=((F3*G2)/(F1*F1+G2*G2))**2+((F1*F3)/(F1*F1+G2*G2))**2)*ASQU
151     RETURN
151     END
STRAN

11      SUBROUTINE PTRANS(THETI1,THETR1,BSQU,ASQU1,I)
11      DIMENSION THETI1(100),THETR1(100),THETRP(100)
11      COMMON RHO1,RHO2,ALPHA,BETA,C1,H,PI
C      THIS ROUTINE CALCULATES THE SQUARE OF THE P WAVE TRANSMISSION
C      COEFFICIENT FOR AN INCIDENT S WAVE ON A SOLID LIQUID BOUNDARY
11      SINH(Z)=(EXP(Z)-EXP(-Z))/2.
31      SHEAR=RHO2*BETA*BETA
34      SINE1=SIN(THETI1(I))
44      C2=BETA/ABS(SINE1)
50      IF(C2.LT.ALPHA)GO TO 1
56      IF(C2.GT.ALPHA)GO TO 2
61      1 FF=2.*SQRT(RHO2*ABS(SIN(2.*THETI1(I))*SIN(2.*THETR1(I))))
123     GG=(ALPHA/BETA)*COS(THETR1(I))*(COS(2.*THETI1(I)))**2
152     HH=COS(THETR1(I))/((ALPHA/BETA)*SIN(2.*THETI1(I)))
200     AA=SQRT(1.-(C2/ALPHA)**2)
212     COMP=ALOG((1.-AA)/(1.+AA))
222     FTIL=SINH(0.5*COMP)
231     HTIL=(HH/SINH(COMP))-RHO2*(C1/BETA)*SINH(0.5*COMP)
246     ASQU1=BSQU*((FF*FTIL*HTIL)**2+(GG*HH*FTIL)**2)
302     $/((GG**2+HTIL**2)**2)
302     GO TO 3
344     2 FF=2.*SQRT(RHO2*ABS(SIN(2.*THETI1(I))*SIN(2.*THETR1(I))))
373     GG=(ALPHA/BETA)*COS(THETR1(I))*(COS(2.*THETI1(I)))**2
421     HH=COS(THETR1(I))/((ALPHA/BETA)*SIN(2.*THETI1(I)))
433     AA=SQRT((C2/ALPHA)**2-1.)
447     THETRP(I)=PI/2.-ATAN(AA)
     ASQU1=BSQU*((FF*COS(THETRP(I)))/(GG+HH/SIN(2.*THETRP(I)))
     $+(C1/BETA)*RHO2*COS(THETRP(I)))
511     3 RETURN
512     END
PTRANS

```

THE MODEL: TRANSMISSION OF SOUND INTO A FAST FLUID BOTTOM
FROM AN OVERLYING FLUID WEDGE

Alan Coppens
Naval Postgraduate School

In the short amount of time available, we shall present the concepts underlying a relatively simple model of the transmission of sound from a fluid wedge into an underlying fast fluid bottom, and present some results for a simple limiting case. Refer to Fig. 1. As a sound wave of frequency ω propagates toward the apex of the wedge, there is complete internal reflection until the angle of incidence on the bottom exceeds the critical (grazing) angle θ_c . Subsequently, there will be sound transmitted into the bottom until the original sound wave in the wedge is attenuated or reverses its direction of propagation and propagates away from the apex. We assume here that the sound wave is essentially completely transmitted into the bottom before this reversal occurs. From a normal mode point of view, the exponential tail of the pressure amplitude assumes greater importance and extends further into the bottom, Fig. 2, until at the position corresponding to the equivalent rays attaining grazing angle θ_c the tail extends infinitely deep into the bottom. If the slope β of the wedge is sufficiently small, we can assume that the normal mode retains its identity - the adiabatic approximation.

Under these assumptions, the pressure field in the wedge can be written as

$$p_1(x', z') = A(x') \cos K_z z' e^{i(\omega t - K_x x')}$$

where

$$K_x = \frac{\omega}{c_1} \sqrt{1 - \left(\frac{\sin \theta_c}{1 - x'/X} \right)^2}$$

and

$$K_z = \frac{\omega}{c_1} \frac{\sin \theta_c}{1 - x'/X}$$

These expressions are valid within the wedge for positive x' . The amplitude $A(x')$ is estimated by assuming that the reflection of the equivalent rays from the interface between the wedge and the bottom is governed by the plane-wave reflection coefficient. We have obtained an exact expression for $A(x')$, but its form is too complicated for easy discussion. In the limit of small β , however, $A(x')$ assumes the relatively simple form

$$\frac{A(x')}{A_0} = e^{-\frac{\rho_1}{\rho_2} \frac{\tan \theta_c}{\beta} \frac{2\sqrt{2}}{3} \left(\frac{x'}{X} \right)^{3/2}}$$

where A_0 is the value of $A(x')$ where the rays attain grazing angle θ_c . This expression is valid for $x'/X \ll \frac{1}{2} \cos^2 \theta_c$ which is equivalent to the fluids in the wedge and bottom being acoustically well-matched.

The above arguments allow us to write an expression for the pressure amplitude and phase of the sound field in the wedge for positive x' . Evaluation at the interface ($z'=0$) gives us the amplitude and phase characteristics of an equivalent pressure source radiating sound into the bottom. Now, standard Green's function techniques applied to a pressure distribution on the interface results in the integral shown in Fig. 3. (The denominator of the integrand is a correction for the cylindrical convergence of the sound field as it travels toward the apex of the wedge.)

In the limit of small β , evaluation of the Green's function integral by the method of stationary phase results in a simple expression

$$|P(x, z, t)| \doteq \sqrt{\frac{X}{r}} \frac{A_0}{2\sqrt{2}} r e^{-\frac{\rho_1 \tan \theta_c}{\rho_2 \beta} \frac{1}{6\sqrt{2}} r^3}$$

AD-A063 163

OFFICE OF NAVAL RESEARCH ARLINGTON VA
PROCEEDINGS OF THE WORKSHOP ON SEISMIC PROPAGATION IN SHALLOW W--ETC(U)
JUL 78

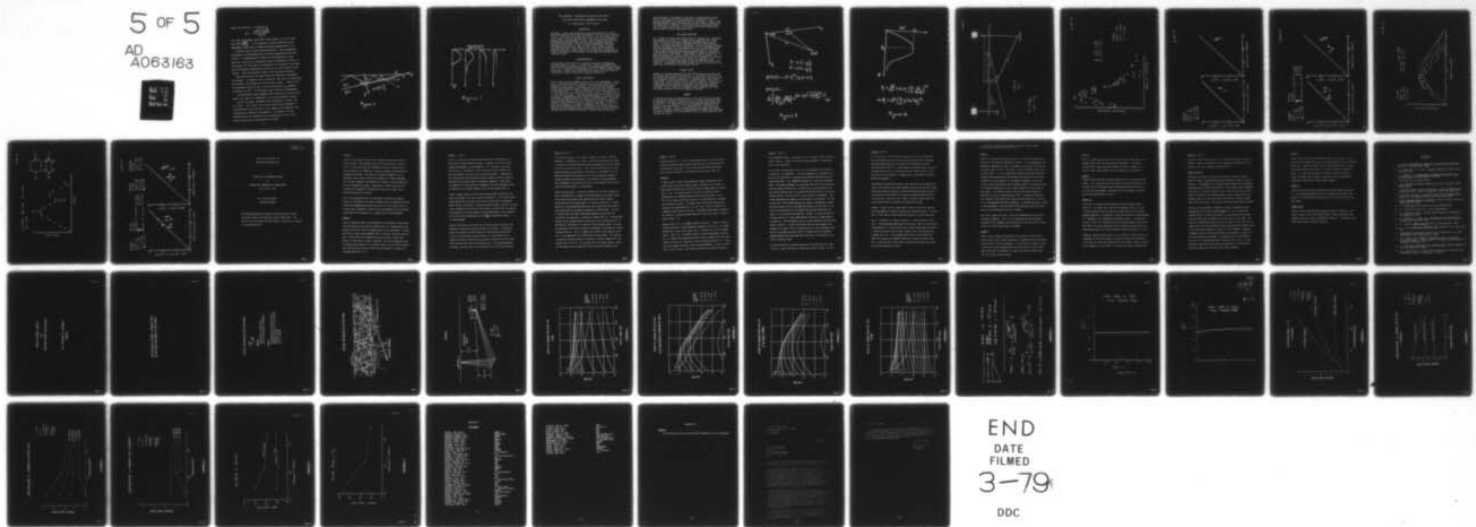
F/G 8/11

UNCLASSIFIED

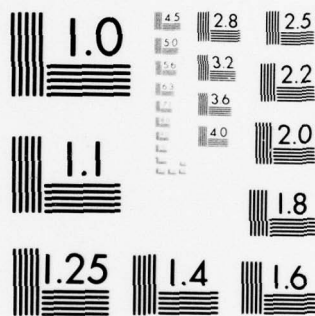
NL

5 OF 5

AD
A063163



END
DATE
FILMED
3-79
DDC



MICROCOPY RESOLUTION TEST CHART
NATIONAL BUREAU OF STANDARDS-1963-A

where the quantity v is defined by

$$v = \frac{\sqrt{2(1 - \cos \theta)}}{\tan \theta_c}$$

For small depression angle θ in the bottom, it can be seen that $v \approx \frac{\sin \theta}{\tan \theta_c}$; v is therefore a direct measure of the depression angle and is almost directly proportional to it.

Analysis now is quite straightforward. This expression describes a well-defined beam of sound propagating into the bottom. A representative sketch of the amplitude of the beam as a function of depression angle is presented in Fig. 4, and values for the angle of depression of the axis of the beam and the pressure amplitude on the axis are also given in that figure. These expressions reveal some important effects:

The amplitude of the beam shows the required cylindrical divergence. It depends only slightly on the ratio of densities, the angle of the wedge, and the critical angle. (Since X can be expressed as $H_0 / \tan \beta$, it can be seen that P_{ax} depends inversely on $\beta^{1/6}$, an extremely weak functional dependence.

The depression angle depends most strongly on the critical angle, but again the dependence is not particularly strong.

As will be seen, agreement with experiment is fair, but not exact. Our current and future efforts are focussed on investigating the validity of the underlying assumptions and searching for possible refinements. At present, we are investigating the adequacy of our prediction of $A(x')$ by a direct calculation using method of images.

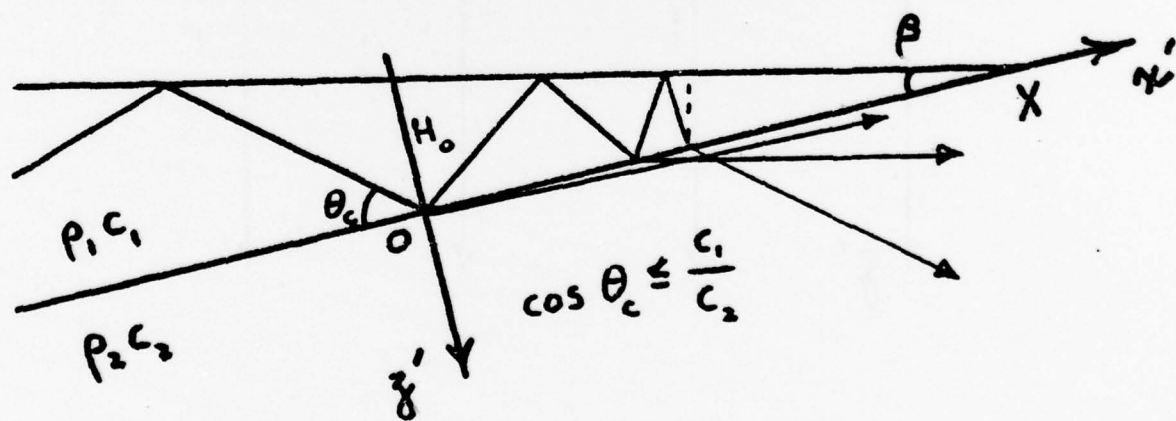


Figure 1

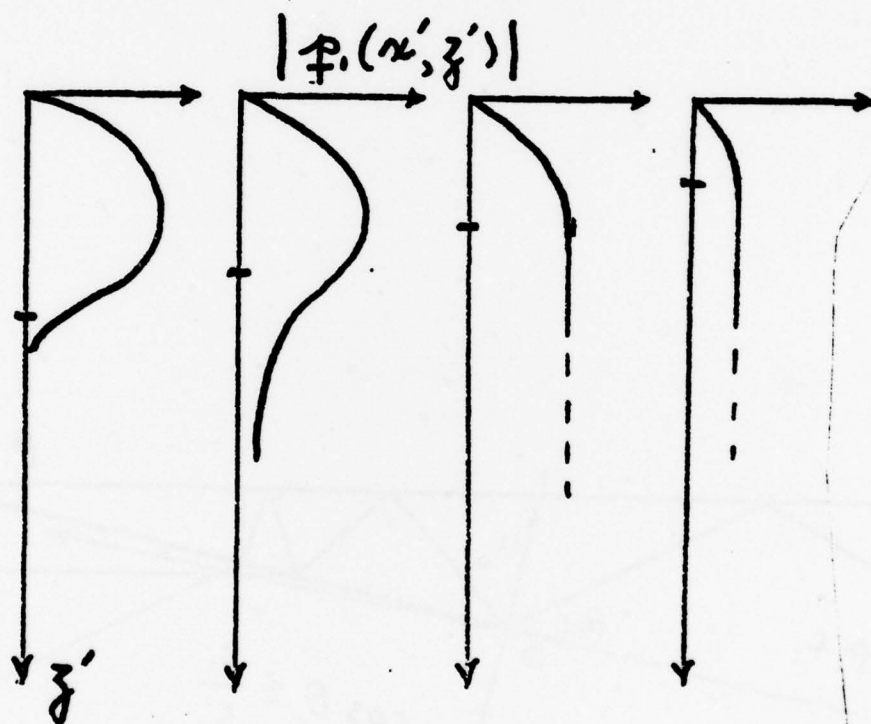


Figure 2

THE EXPERIMENT: TRANSMISSION OF ACOUSTIC WAVES INTO A FAST FLUID BOTTOM FROM A CONVERGING FLUID WEDGE

Dr. James Sanders, NPS, Monterey

INTRODUCTION

Gentlemen, I would like to describe to you some experimental results that quantitatively confirm the predictions of the model just presented to you. I would like to present such results, but I am unable to do so at this time. While we have been able to show qualitative agreement between theory and experiment in that a beam of energy does enter into the bottom and that this beam does have the approximate properties predicted by the model, curious and possibly significant deviations from predictions do exist. What is worse, every attempt to bring experiment and theory closer together has served only to emphasize these discrepancies. Today I would like to share with you some of our triumphs and some of our frustrations in the hope that we might benefit from your council.

ACKNOWLEDGEMENTS

The experiments described cover a period of two years encompassing three generations of setups. I would like to begin by acknowledging the people who actually performed most of the measurements to be reported here: Lts. Jim Edwards & Greg Netzog, USN and Lt. Masami Kawamura, JMSDF. In addition, I would like to thank NOSC, San Diego, for their financial assistance and ONR for making this presentation possible.

INITIAL EXPERIMENTS

Slide 1 shows the basic geometry used in all of our experiments. A long burst of sinusoidal energy is introduced into the thick end of a fluid wedge overlying a fast, fluid bottom. The amplitudes of the pulses received by a hydrophone in the bottom are read on an oscilloscope thereby determining the spatial distribution of the sound field existing in the bottom fluid. Lt. Edwards carried out initial investigations in a large tank filled with brine solution over which a thin layer of olive oil was carefully added. Since the interface between the two fluids was horizontal, a wedged-shaped upper layer was created by inserting a board of pressure-release material at an angle to the horizontal. The sound field was then probed in vertical transverses at various horizontal distances from the predicted point of entry of the beam. If the sound field, in the bottom, is a beam as predicted, then a plot of the amplitude of the received signal, normalized for cylindrical spreading, against the angle measured about the predicted point of entry should be the same for all horizontal distances. Slide 2 shows the results at

three distances. The tendency of the data to cluster about a single curve is consistent with the existence of a narrow beam of sound entering the bottom at a relatively shallow inclination. Slide 3 shows the experimentally measured beam angles and beam widths as compared to the predictions of the model. While these initial experiments showed that the general predictions of the model were correct, there was an obvious need for better experimental data.

THE SECOND EXPERIMENT

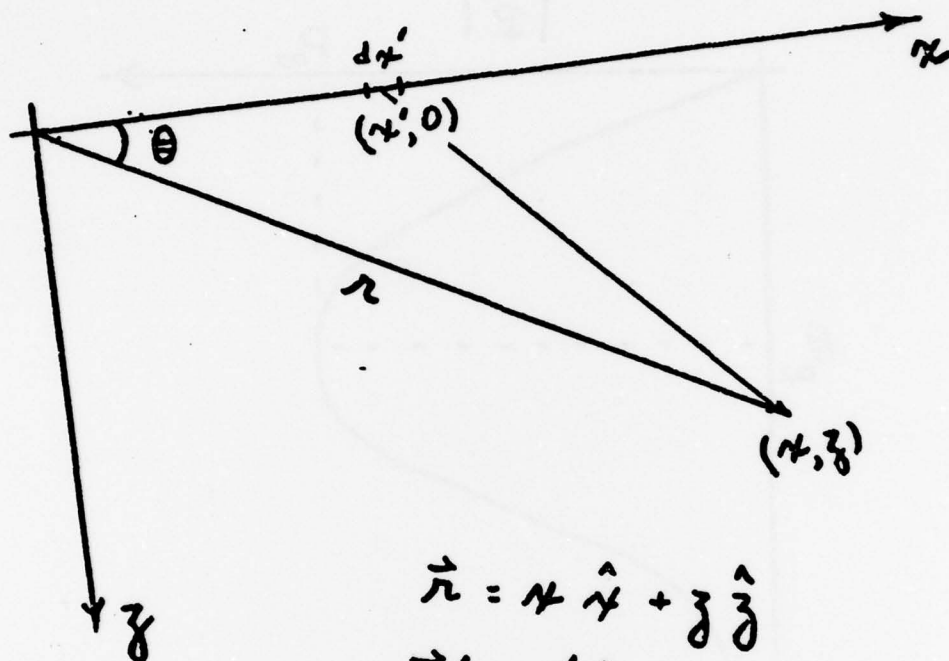
In an attempt to obtain more precise data, Lt. Netzorg and I redesigned the apparatus to consist of a wedge of water separated from a small tank of brine by a 1-mil mylar diaphragm stretched tightly within a frame. The bottom and sides of the tank were lined with absorbing material to reduce interfering reflections. Since we now were confident that the beam entered at the predicted position, all measurements were in polar coordinates with the origin at the predicted point of entry. Slide 4 shows the measured beam angles and beam widths as compared to the predictions of the model. The agreement is better but still not as good as we would like. Slide 5 shows for two radial distances the received amplitudes, normalized for cylindrical spreading, as a function of the angle of inclination. These results are compared to the predictions of the model normalized to have the same peak value at one distance. A significant difference between theory and experiment on the lower side of the beam is now painfully obvious.

PRESENT STATUS

Because of a growing awareness that the difficulties on the lower side of the beam were caused by interference, it was decided to move into a much larger system using silicon oil in the wedge and a large water tank for the bottom. We also regressed to a cartesian-type survey of the sound field. Slide 6 shows a typical vertical traverse. The distortion on the lower side of the beam is now seen to be definitely caused by interference as indicated by the sketches of the observed waveform envelopes. Slide 7 shows the agreement between experiment and theory for some preliminary runs by Lt. Kawamura and myself.

SUMMARY

It is now clear that the beam pattern is being significantly disturbed by destructive interference whose effect is to move the apparent angle of the beam to shallower angles and to make the beam seem narrower than it really is. Our studies have not yet succeeded in identifying the source of this interference. It is definitely not from the walls or bottom of the tank. It may be associated with the wedge, but whether this is an inherent property of wedge propagation omitted from the theory or merely an artifact of the experimental set up is the question we will now seek to answer.



$$\vec{r} = x \hat{x} + z \hat{z}$$

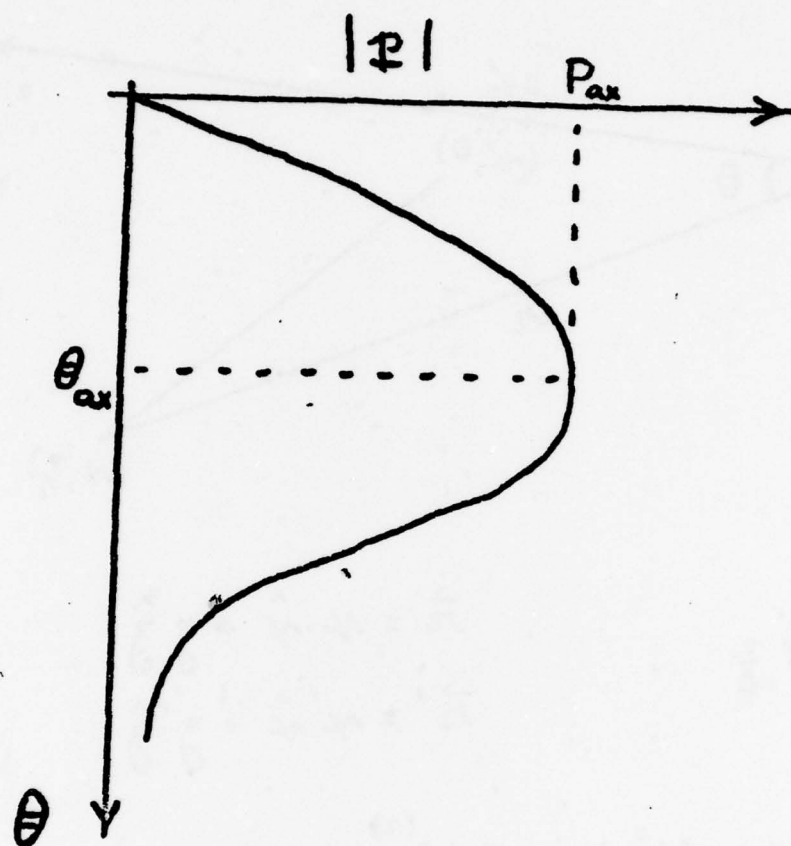
$$\vec{r}' = x' \hat{x} + z' \hat{z}$$

$$G(\vec{r}, \vec{r}') = i\pi H_0^{(2)}\left(\frac{\omega}{c_1} |\vec{r} - \vec{r}'|\right)$$

$$p(x, z, t) =$$

$$\frac{1}{4\pi} \int \left. \frac{\partial G}{\partial z'} \right|_{z'=0} \frac{A(x')}{\sqrt{1-x'/x}} e^{i\left(\omega t - \frac{\omega}{c_1} \sqrt{1 - \left(\frac{\sin \theta_c}{1-x'/x}\right)^2} x'\right)} dx'$$

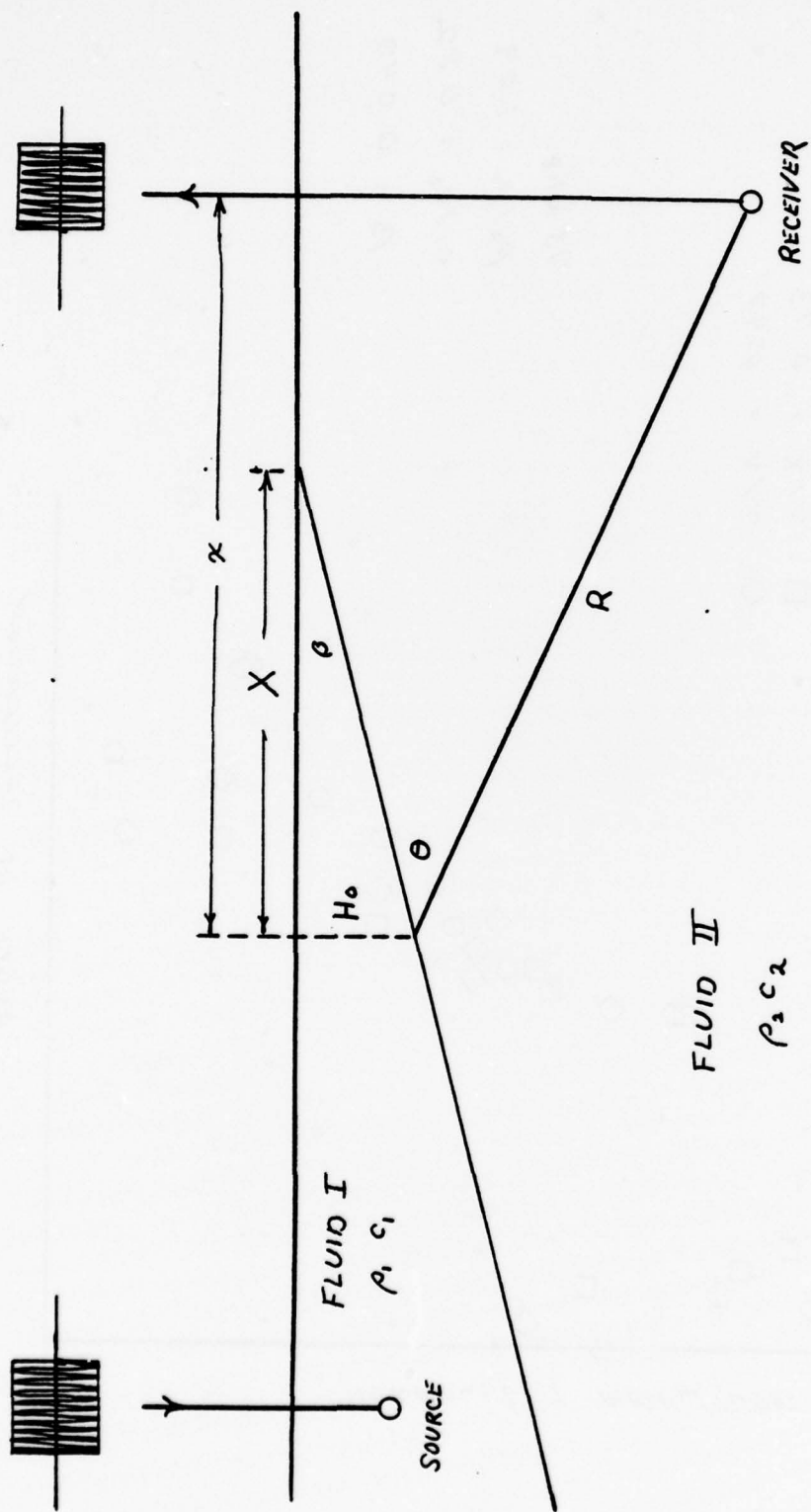
Figure 3



$$P_{\max} \doteq \sqrt{\frac{X}{Z}} 0.36 A_0 \left(\frac{P_2}{P_1} \frac{\beta}{\tan \theta_c} \right)^{1/3}$$

$$\sin \theta_{\max} \doteq \sqrt{2} \left(\frac{P_2}{P_1} \beta \tan^2 \theta_c \right)^{1/3}$$

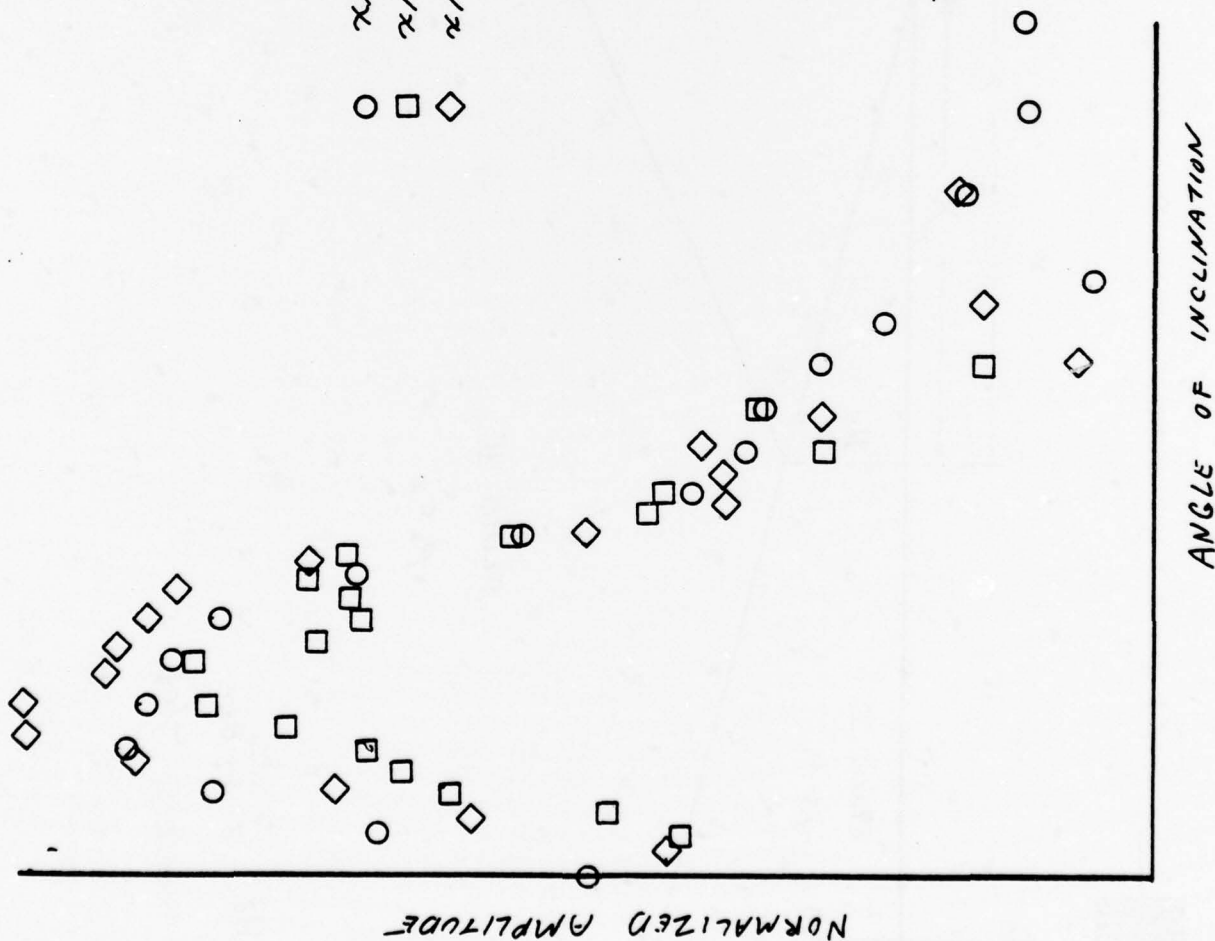
Figure 4



$$H_0 = \frac{1}{4} \frac{\lambda_1}{\sin \theta_c}$$

$$\cos \theta_c = c_1/c_2$$

SLIDE 2



75 kHz

$\rho_2/\rho_1 = 1.29$

$c_1/c_2 = 0.82$

$\beta = 0.040$

SLIDE 3

EDWARDS

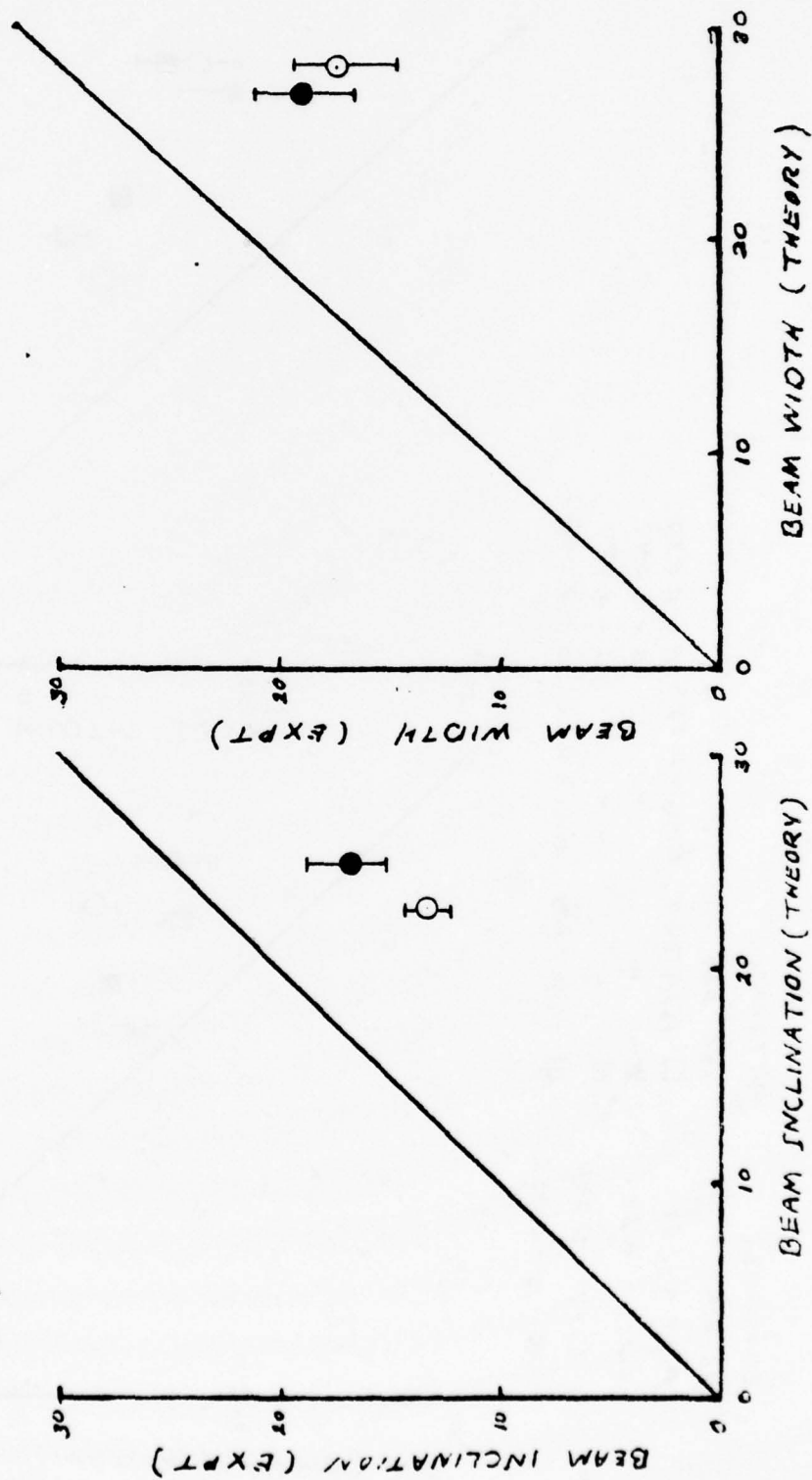
76 KHZ

$\rho_2/\rho_1 = 1.29$

$c_1/c_2 = 0.82$

○ $\beta = 0.040$

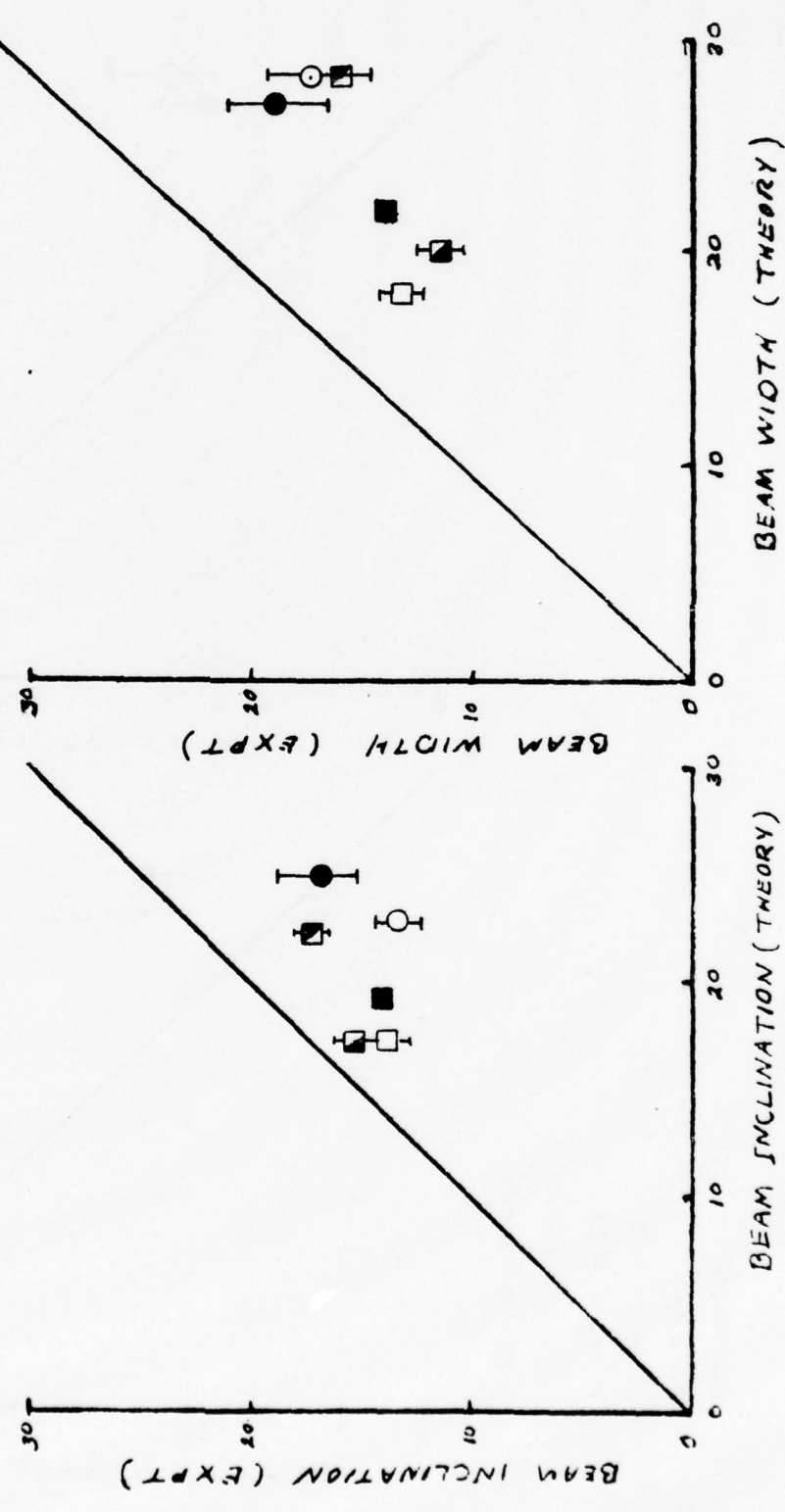
● $\beta = 0.052$



SLIDE 4

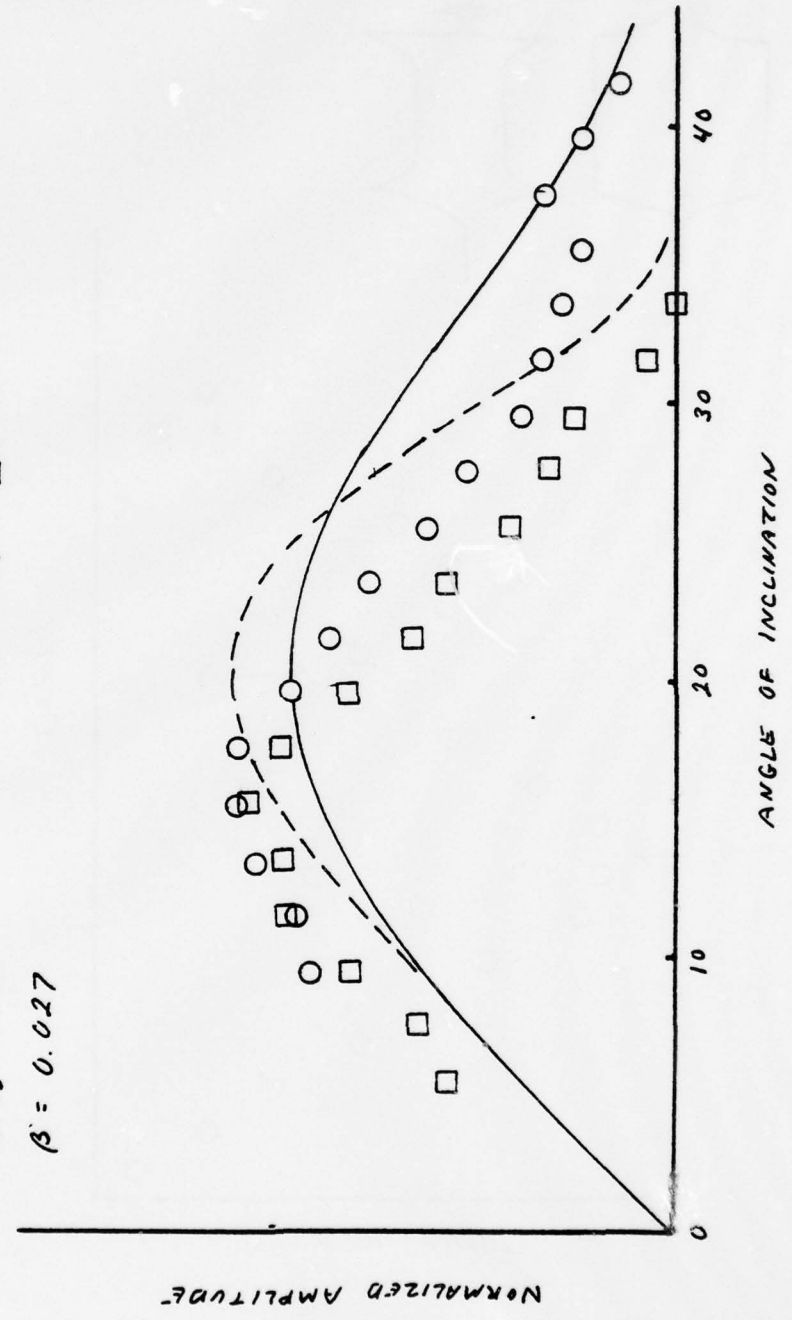
EDWARDS
76 kHz
 $\rho_2/\rho_1 = 1.29$
 $c_1/c_2 = 0.82$
 $\beta = 0.040$
 $\beta = 0.052$

NETZORG
150 kHz
 $\rho_2/\rho_1 = 1.15$
" " " " " "
 $\rho_2/\rho_1 = 1.08$
 $c_1/c_2 = 0.88$
" " " " " "
 $c_1/c_2 = 0.92$
 $\beta = 0.027$
 $\beta = 0.044$
 $\beta = 0.077$
 $\beta = 0.046$



150 kHz
 $\rho_2/\rho_1 = 1.15$
 $c_1/c_2 = 0.88$
 $\beta = 0.027$

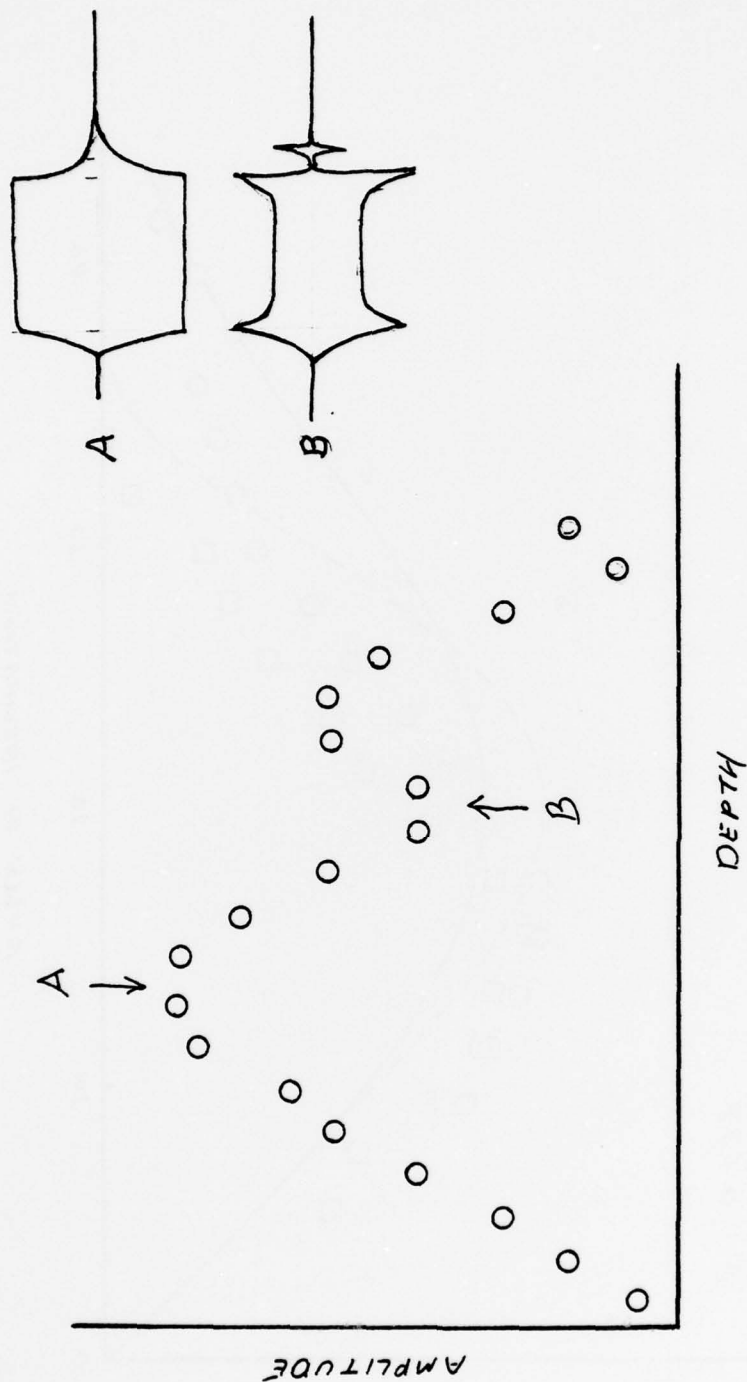
EXPT. THEORY
 $R/X = 0.83$ ○ ---
 $R/X = 2.37$ □ —



SLIDE 6

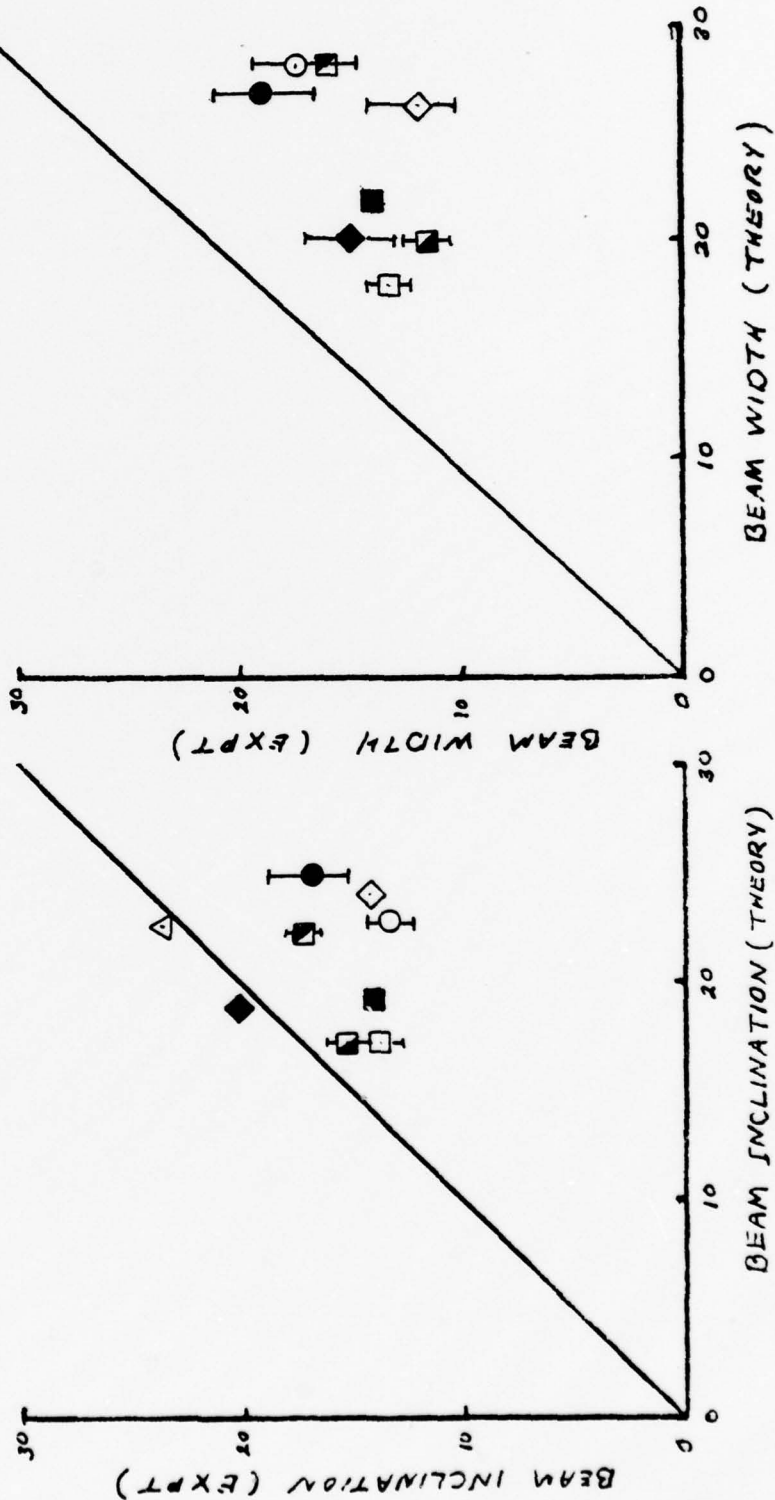
$f = 100 \text{ kHz}$ $\rho_2/\rho_1 = 0.88$ $c_1/c_2 = 0.78$

$\beta = 0.038$



SLIDE 7

EDWARDS	NETZORG	SANDERS	HAWAMURA
76 kHz	150 kHz	100 kHz	100 kHz
$\rho_2/\rho_1 = 1.29$	$\rho_2/\rho_1 = 1.15$	$\rho_2/\rho_1 = 0.98$	$\rho_2/\rho_1 = 0.98$
$c_1/c_2 = 0.82$	"	$c_1/c_2 = 0.78$	$c_1/c_2 = 0.78$
$\beta = 0.040$	"	$\beta = 0.038$	$\beta = 0.29$
$\beta = 0.052$	$\rho_2/\rho_1 = 1.08$	$\beta = 0.020$	Δ
	$c_1/c_2 = 0.92$		



BURIED SEISMIC ARRAYS FOR
SHALLOW WATER SURVEILLANCE

Presented at the ONR/NRL Workshop
on
SEISMIC WAVE PROPAGATION IN SHALLOW WATER
July 6 and 7, 1978

Dr. Richard Edsinger
The Boeing Company

The attached presentation addresses the implication of seismic and oceanic noise on the detection range of deep arrays. The depth of the arrays below the ocean bottom is taken to be a maximum of a few thousand feet.

FIGURE 3

Figure 3 lists several factors that influence the detection range of a seismic system. Site dependent factors include the quality factor Q (Ref. 1), which describes the attenuation of seismic signals due to viscous damping (via., $\frac{27.3}{Q}$ dB of viscous attenuation per wavelength of propagation distance). The velocity of signal propagation is also important since a higher velocity corresponds to a longer wavelength (for a given frequency) and therefore to a smaller viscous attenuation per unit propagation distance. Additionally, velocity gradients can strongly affect geometrical spreading and thus play a major role in determining detection distances.

Use of buried geophones have the advantage of reducing the negative effects of multipath but the ocean's bottom has the disadvantage of being a much less homogeneous medium and one that has a much higher level of viscous signal attenuation. Much of this disadvantage can be eliminated using deeply buried sensors (i.e., greater than a few wavelengths).

FIGURE 4

Figure 4 summarizes some of the advantages of using deeply buried arrays. By burying deep one can avoid the surface waves (or interface waves) and instead utilize the P wave (or compressional or pressure waves). Surface waves have a large S wave component (Ref. 2) and the literature indicates (Ref. 3) that the S wave attenuations can be as much as eight times greater (in dB) than for P waves. Moreover, the P wave propagation path for deeply buried sensors will in general result in less viscous attenuation since both the Q factor and the velocity generally increase with increased depth (Ref. 4, 5).

FIGURE 4 (Cont'd.)

Figure 4 also points out that the directionality of geophones can be exploited to increase detection range. In general, far field noise is strongly attenuated by viscous damping. It is the nearer noise that hurts the most. The effect of near field noise can be lessened with polarized sensors since near noise is above the sensor. Theoretically, the closest noise, which would be directly overhead, would be cancelled completely by using the sensor's horizontal components. Shear waves (or S-waves) will have horizontal components, but their magnitude should be relatively low at depths greater than a few wavelengths (Ref. 2).

Further, Figure 4 points out that burying deep tends to neutralize the effect the bottom's low Q has on signal attenuation. This neutralization stems from the fact that due to the low Q of the bottom of predominant oceanic noise is from above. Burying the sensor subjects the noise to additional attenuation while having little effect on signals when the range is long compared to the sensor depth (a purely experimental viscous damping will give a 4.34 dB attenuation for each $\frac{Q\lambda}{2\pi}$ of penetration where λ is the wavelength).

Figure 4 also points out that the use of buried seismic arrays has the advantage of reducing the negative effect of multipath. An important reason for looking to seismic sensors for shallow water surveillance is that in shallow water multipath results in a significant loss in temporal and spacial coherency for acoustical signals while at the same time increasing the level of the ambient noise. For buried geophones, in general, only two rays of any significance reach the array from any

FIGURE 4 (Cont'd.)

given acoustic source. This greatly increases the signal's temporal coherency. Furthermore, as a result of multipath the acoustical energy in the water is polarized with more energy propagating in the horizontal direction than in the vertical. Thus a smaller proportion of the rays passing through any given point in the water will be coupled into the bottom than would be accounted for by a critical angle-ray theoretic argument assuming no polarization. Thus the use of buried geophones takes advantage of the bottom to filter out the increase in noise level resulting from multipath in shallow water.

Before leaving Figure 4 it should be pointed out that even without the above considerations, it appears to be advantageous to use deep P-waves for surveillance purposes since they should give simpler signals. Surface waves are very complicated in a realistic situation. In homogeneities in the propagating medium can cause scatterings which greatly reduce both spacial and temporal coherence in surface waves. The coda of seismic waves from small earthquakes appears to arise from such scatterings, and coherence is drastically reduced (Ref. 6). Correlational studies of near earthquake waves confirm this lack of coherence (Ref. 7). Additionally, the effect of a spacially varying surface layer is to make the waveform of an arriving surface wave dependent in the specific terrain traversed (Ref. 8). Thus, it appears that seismic arrays would be difficult, if not impossible, to calibrate using surface waves. This opinion is apparently shared by experts in the area of seismic detection of land targets (Ref. 9, 10, 11). On the other hand, the simpler signals resulting from deeply buried sensors and P waves could make coherent array

FIGURE 4 (Cont'd.)

processing possible. It should further be pointed out that land based seismic exploration studies using arrays rely not on surface waves but on reflected P waves (Ref. 11) and even then nontrivial corrections must be made to account for the weathered surface layer (Ref. 10).

FIGURE 5

In order to get an idea of what detection ranges are possible using buried seismic arrays the scenario shown in Figure 5 will be used. A water depth of 300 feet was selected to be an average depth of interest (Ref. 4, 13). The nominal ocean noise level of 90 dB at 60 Hz is representative of moderately heavy traffic conditions (Ref. 14, 15). (All of the numbers given here assume a 1 Hz band width and a reference level relative to $1 \mu\text{Pa}$). The signal level of 150 dB at one yard was selected to be representative of a line in the vicinity of 60 Hertz for a moderate signal level of interest. The maximum sensor depth of 2000 ft. was chosen as a sensible maximum depth well within the limits of current practice (Ref. 5, 1).

Nominal values of Q , V , and $\frac{dV}{dZ}$ are shown in Figure 5. Actually, there is enormous variation in these parameters depending on the site. For common surface soils (clay, sand, gravel, etc.), Q ranges from 5 to 50, approximately. (Ref. 16). For bedrock (basalt, crystalline basement, granite, etc.), Q ranges from approximately one to several hundred, while for deep bedrock, Q -values of a thousand or more are encountered (Ref. 17). P-wave velocities beneath the water, range from approximately 1.5 km/s to 6 km/s (Ref. 12, 13) or more. The velocity gradient also cannot be assigned a

FIGURE 5 (Cont'd.)

site independent number. The numbers shown in Figure 5 simply represent nominal values. A range of values for these parameters is considered later in the discussion.

For the sake of modeling, the noise on a buried geophone was assumed to be made up of two components. The first component, N_0 , represents that part of the noise which is coupled into the bottom from the acoustical ocean noise above. This component decreases as a function of geophone depth. The second component, N_s , represents that part of the noise that does not emanate from the sea. The level of N_0 can be estimated from the level of ambient noise in the ocean and the efficiency of the sea to bottom coupling. The level of N_s is more difficult to estimate. Very little documented data appears to be available on the subject. For the nominal case it was assumed that N_s was constant, independent of depth and that an upper limit on its magnitude should be on the order of the level of noise coupled into the bottom from the ocean above when the ocean is in a sea state zero condition (35 dB). It turns out that for a bottom velocity of 3 km/s approximately 10 dB loss is experienced in the coupling. Thus the nominal value of N_s was selected to be the 25 dB shown in Figure 5. In spite of the fact that this was assumed to be somewhat of an upper limit, it turned out (as will be illustrated later) that for the higher sea noise levels of interest and for reasonable geophone depths (less than 2000 feet) that N_0 has little effect on the overall detection range.

The justification for using the coupling of sea state zero as an upper limit on N_s stems from data on seismic noise levels on land. On land

FIGURE 5 (Cont'd.)

it is found that, in the frequency range of interest, wind noise and other environmental noises on the surface form the dominant component (assuming measurements are not taken during earthquakes or other transient events) (Ref. 4). There appears no apparent reason to believe the same should not be true when the surface is under water, in fact, the water to rock interface is supposed to be a good means of coupling energy into hardrock.

The approach of setting the seismic level relative to the ambient noise level in the ocean has the added advantage that one need not worry about converting acoustical pressure to seismic amplitude or need not worry if the reflection coefficient for the ocean to bottom interface contains scaling errors. Such errors will result in errors in both signal and noise levels and thus not effect the resulting S/N ratio.

However, in order to get a rough idea of how the value of N_s compares with measurements of seismic noise taken on land the formula $P = 2\pi f p c a$ (Ref. 14) was used to relate acoustical pressure to seismic amplitude.

Here f = frequency, p = density of water, c = sound velocity in water and a = the displacement amplitude of the bottom. When p is the pressure corresponding to a 25 dB acoustic noise level the amplitude at 60 Hertz is about 15 dB lower than the total seismic noise level outside Rifle, Colorado (Ref. 18). If one assumes that 15 dB of the Colorado noise comes from surface environmental conditions as might be implied from Ref. 4, then the noise levels used in the model make sense with regard to seismic measurements on land.

ALL SUBSEQUENT DISCUSSION AND FIGURES ARE BASED ON SINGLE SENSOR CALCULATIONS AND ISENTROPIC NOISE FIELDS.

FIGURE 6

Figure 6 illustrates the signal-to-noise as a function of depth which is obtained for the scenario depicted in Figure 5. It is assumed that only horizontal components are used. The numbers by the curves indicate the horizontal range in miles. The signal to noise ratios given here are for a single sensor. If it is assumed that through calibration, perfectly coherent array processing can be obtained then these S/N ratios can be increased by $10 \log N$ where N is the number of elements in the array. It can be seen from Figure 6 that in general there is an increase in S/N as the depth increases due to the viscous reduction of noise from the ocean above. For ranges of greater than one mile and at depths of 2000 feet, this gain is approximately 10 dB. It should be noted that this increase in S/N results only from the neutralization of Q and the use of the geophone's horizontal components. No attempt was made to factor in the improvement in S/N resulting from getting away from the surface wave (such an improvement should be sizeable).

The S/N for ranges less than .2 miles are depressed due to the use of horizontal components. This is to be expected using the horizontal components of the geophone since theoretically there would be no P wave signal for a noise source directly overhead.

FIGURE 7

Figure 7 gives a better illustration of the effect of neutralizing Q . Here a lower Q (more viscous attenuation) is assumed and thus the neutralization effect is more pronounced. A significant S/N increase (20 dB) is seen with increasing depth after which the S/N falls as the signal level drops (due to attenuation) to where the internal seismic noise level (N_s) starts being important.

FIGURE 8

Figure 8 illustrates the effect of using the total signal power at the geophone rather than just the horizontal components. As would be expected short range performance improves but there is about a 7 dB loss for longer range targets (when the geophone is at 2000 feet).

FIGURE 9

Figure 9 shows the effect of sensor depth on S/N for a relatively high Q (200). It is seen that for this Q the S/N is much better but to get the same kind of improvement due to neutralization one would have to bury the array much deeper. Here 2000 feet only produces a 6 dB gain due to the neutralization of the Q:

FIGURE 10

The curves in Figures 6-9 were obtained by using the model shown in Figure 10. The signal level involves the reference level at 1 yard, a "cosine-squared" factor to take into account the use of horizontal geophone components, an exponential factor describing the viscous damping (f = frequency), and a geometrical attenuation factor. The remaining factor of $1/10$ in this expression arises as an approximate expression for the effect of ray path bending due to the velocity contrast across the interface and due to the velocity gradient which was assumed (1.0 sec^{-1}).

Although a constant factor such as $1/10$ is clearly not exact since it is independent of the entry angle it was used to simplify the computation of the S/N ratio (with the constant factor the integral shown in Figure 9 can be computed in closed form). Ray theory was used to determine that

FIGURE 10 (Cont'd.)

the actual factor varied by only 3 or 4 dB for the ranges and depths of interest. That is, the factor of 1/10 represents an average value and deviation from this average is relatively small.

FIGURE 11 and 12

The actual variation as a function of depth at a range of 3 miles is shown in Figure 11 and the variation as a function of angle is given in Figure 12. The assumption of a constant factor appears to be reasonable considering the variation with regard to site and other model parameters. Intuitively, a relatively constant factor stems from the fact that the velocity contrast at the interface tends to cause a depletion of rays entering near the critical angle while the positive velocity gradient tends to do the reverse. The rays are thus distributed rather uniformly.

The noise at the geophone is modeled as a depth independent seismic component N_s and an ocean induced component N_o . N_o is obtained by integrating over a surface distribution of non-coherent noise sources using the same type of propagation function used for the signal. The term N_o is normalized by requiring that the seismic noise level due to ocean noise at one yard below the surface should equal the acoustic noise of the ocean above reduced by a factor of 10 for geometric spreading (argument similar to the one given above) and reduced by a factor of 8 due to elimination of multipath. The reduction due to multipath has the effect of increasing the overall signal to noise ratio. In the discussion that follows this effect of multipath can be eliminated if desired by assuming a 9 dB lower input signal strength.

FIGURE 13

Figure 13 shows the predicted detection range for a 60 Hertz line as a function of the product of Q and v , for three different levels of ambient ocean noise. Detection ranges are for a single sensor (not an array), an assumed processor resolution of .1 Hz and a detection threshold of 6 dB. It is seen that for higher Qv products much more increase in range is obtained with increase in signal to noise (or equivalently a decrease in noise holding signal level constant).

FIGURE 14

Figure 14 shows the effect of varying the internal seismic noise level N_s . As was stated previously only for low ambient noise levels (sea state 0) is the detection range sensitive to N_s (for levels of N_s less than 30 dB).

FIGURES 15-18

Figures 15 and 16 show detection ranges for several frequencies. The signal strength varies from 120 dB to 150 dB. Ocean noise levels were obtained from Ref. 14 and are displayed in Figure 17. The seismic noise levels were chosen as shown in Figure 18.

REFERENCES

1. J. E. White, Seismic Waves: Radiation, Transmission and Attenuation, McGraw-Hill, Inc. (New York), 1965.
2. L. D. Landau and E. M. Lifshitz, Theory of Elasticity, Pergamon Press (New York), 1970.
3. F. J. McDonal, et al, "Attenuation of Shear and Compressional Waves in Pierre Shale," Geophysics XXIII, 421 (1958).
4. K. Aki, MIT, private communications.
5. R. M. Turpening, Environmental Research Institute of Michigan, private communications.
6. K. Aki and B. Chouet, "Origin of Coda Waves: Source, Attenuation, and Scattering Effects," Journal of Geophysical Research 80, 3322 (1975).
7. K. Aki and M. Tsujiura, "Correlational Study of Near Earthquake Waves," Bulletin of the Earthquake Research Institute 37, 207 (1959).
8. M. Bath, Spectral Analysis in Geophysics, Elsevier Scientific Publishing Company (New York), 1974.
9. C. L. Woodbridge, MITRE Corporation, private communications.
10. R. L. Lacoss, MIT Lincoln Lab., private communications.
11. L. C. Wood and S. Treitel, "Seismic Signal Processing," Proceedings of the IEEE 63, 649 (1975).
12. C. A. Burk and C. L. Drake, eds., The Geology of Continental Margins, Springer-Verlag (New York), 1974.
13. F. P. Shepard, Submarine Geology, Harper and Row (New York), 1963.
14. R. J. Urick, Principles of Underwater Sound, McGraw-Hill, Inc. (New York), 1975.
15. "Oceanography and Underwater Sound for Naval Applications," U.S. Naval Oceanographic Office, Washington, DC, 1965.
16. J. R. Lundien and H. Nikodem, "A Mathematical Model for Predicting Microseismic Signals in Terrain Materials," Waterways Experiment Station, Vicksburg, Mississippi, 1973.
17. P. J. Hart, ed., The Earth's Crust and Upper Mantle, American Geophysical Union (Washington, DC), 1969.
18. G. E. Frantti, et al, "The Spectrum of Seismic Noise," Bulletin of the Seismological Society of America 52, 113 (1962).

BURIED SEISMIC ARRAYS
for
SHALLOW WATER SURVEILLANCE

DR. RICHARD W. EDSINGER
BOEING

FIGURE 1

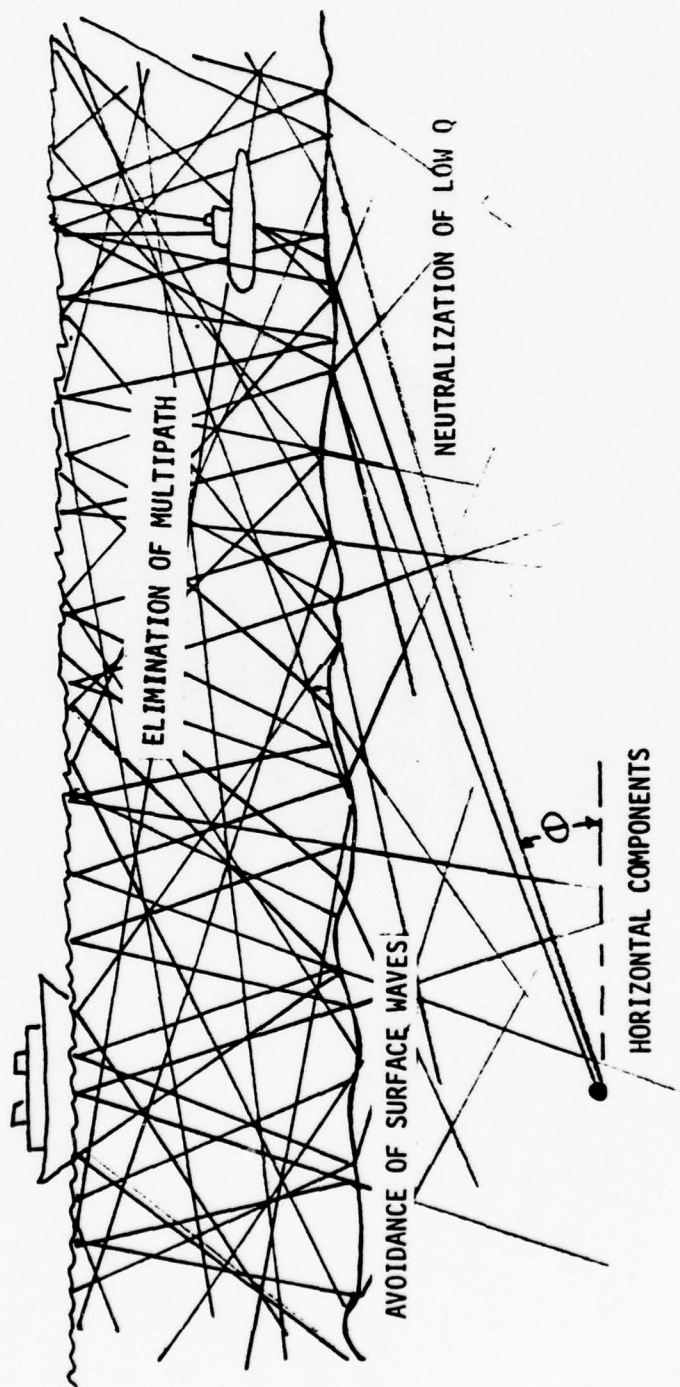
FIGURE 2

IMPLICATION OF SEISMIC & OCEANIC NOISE
ON THE DETECTION RANGE OF DEEP ARRAYS

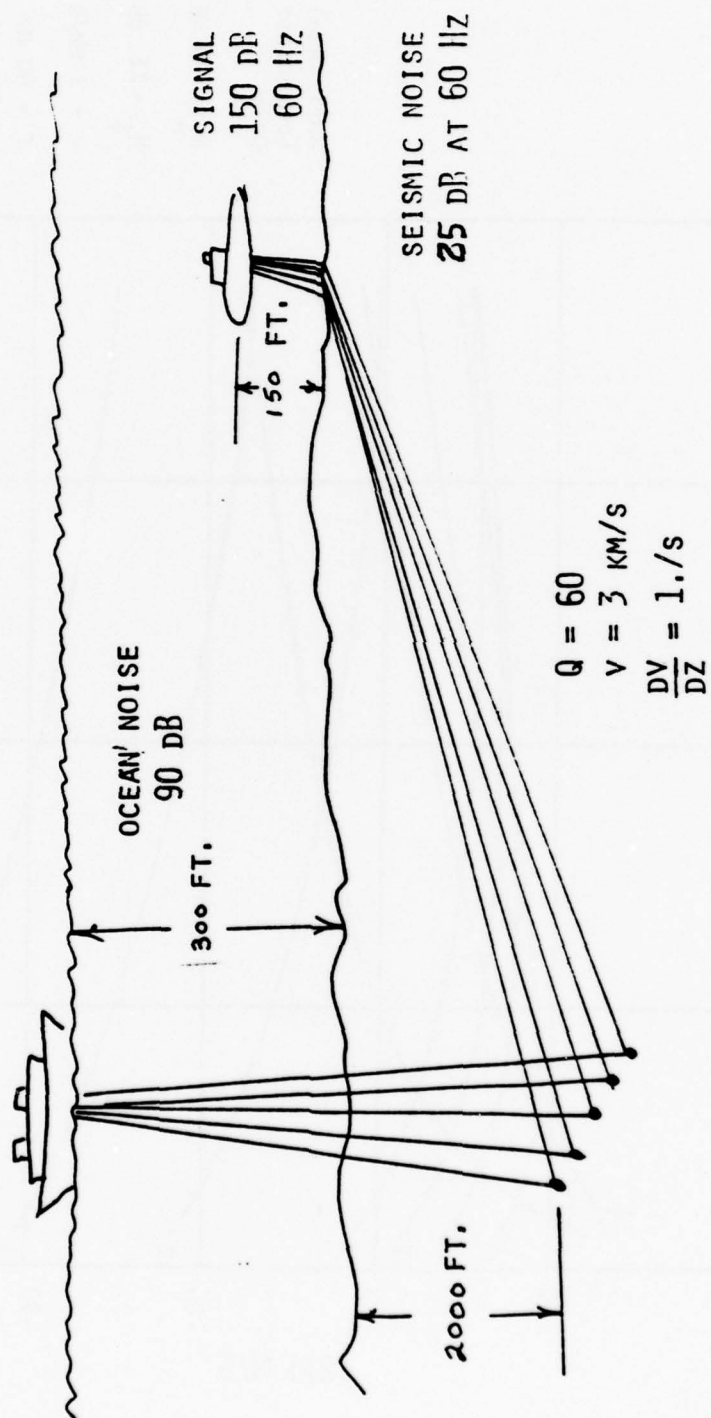
FACTORS INFLUENCING DETECTION RANGE

- SITE
 $Q, v, \frac{\partial v}{\partial z}$
- BURIED
REDUCTION OF MULTIPATH
USE OF HORIZONTAL COMPONENT
- DEPTH
ELIMINATION OF SURFACE WAVES
NEUTRALIZATION OF LOW Q EFFECT
SIMPLER SIGNAL
USE OF ARRAYS

FACTORS INFLUENCING DETECTION RANGE



SCENARIO



EFFECT OF SENSOR DEPTH ON S/N

Q = 60

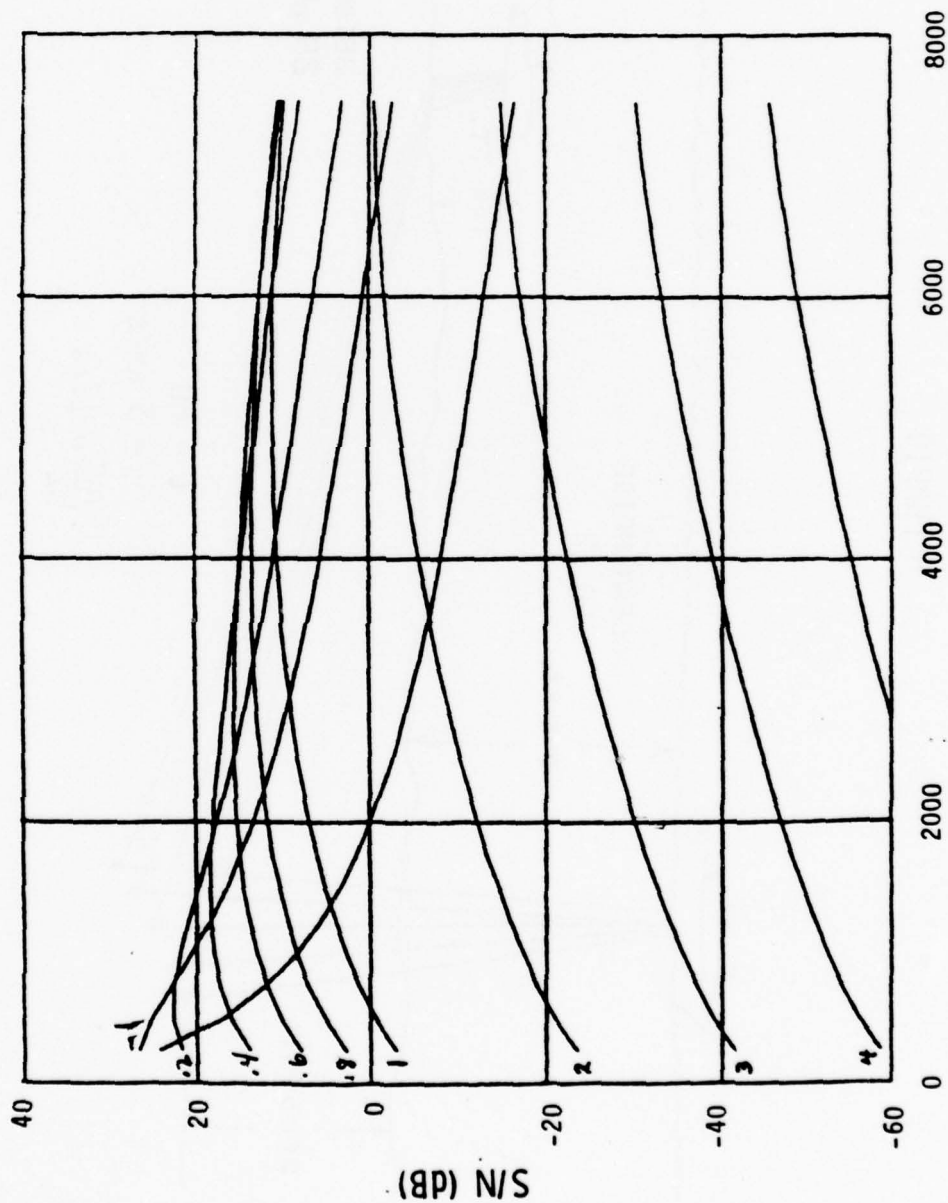


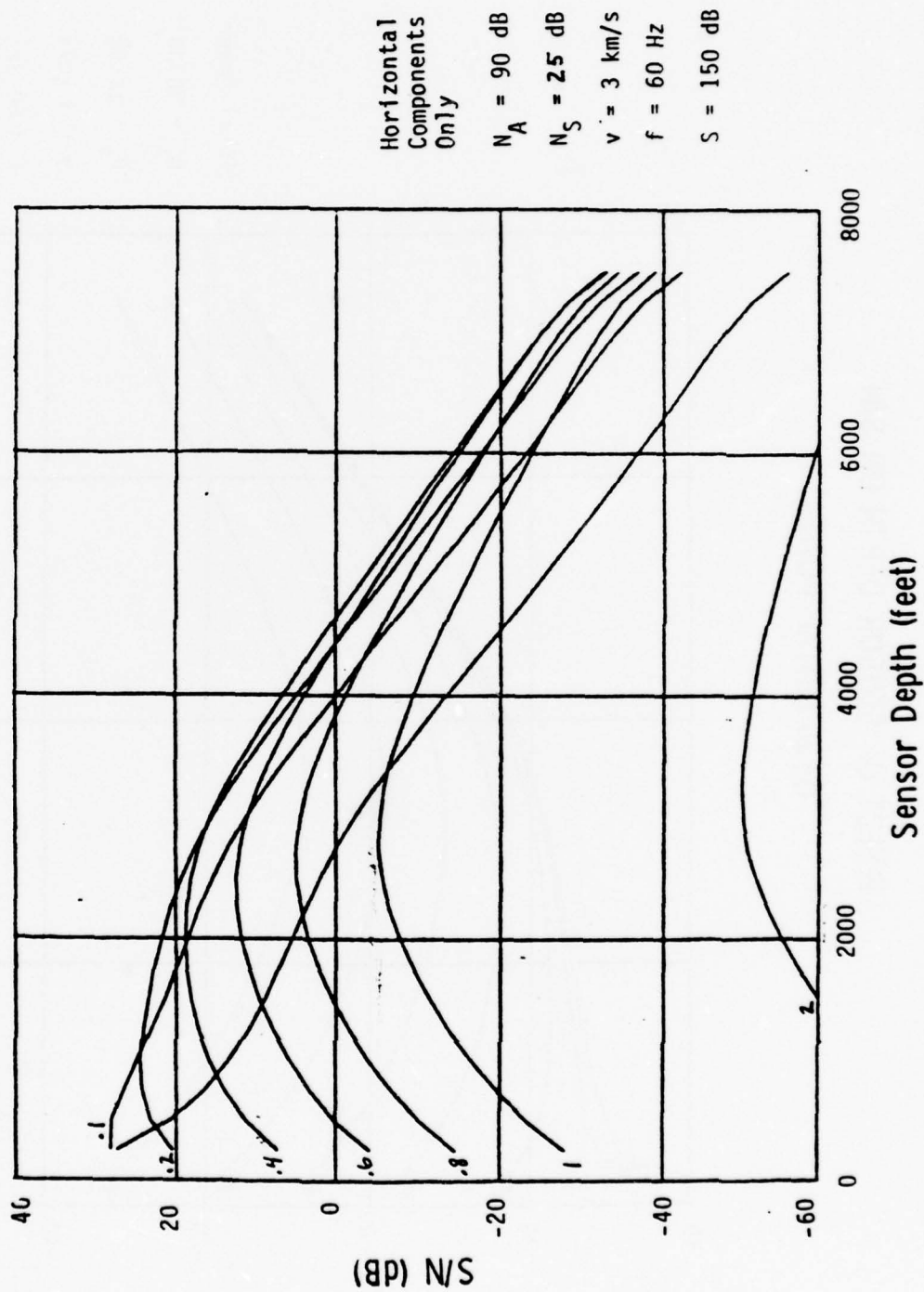
FIGURE 6

Sensor Depth (feet)

THE BOEING COMPANY
SEATTLE, WASHINGTON

FIGURE 7

EFFECT OF SENSOR DEPTH ON S/N
Q = 20 (HORIZONTAL COMPONENTS ONLY)



EFFECT OF SENSOR DEPTH ON S/N Q-20 (TOTAL POWER)

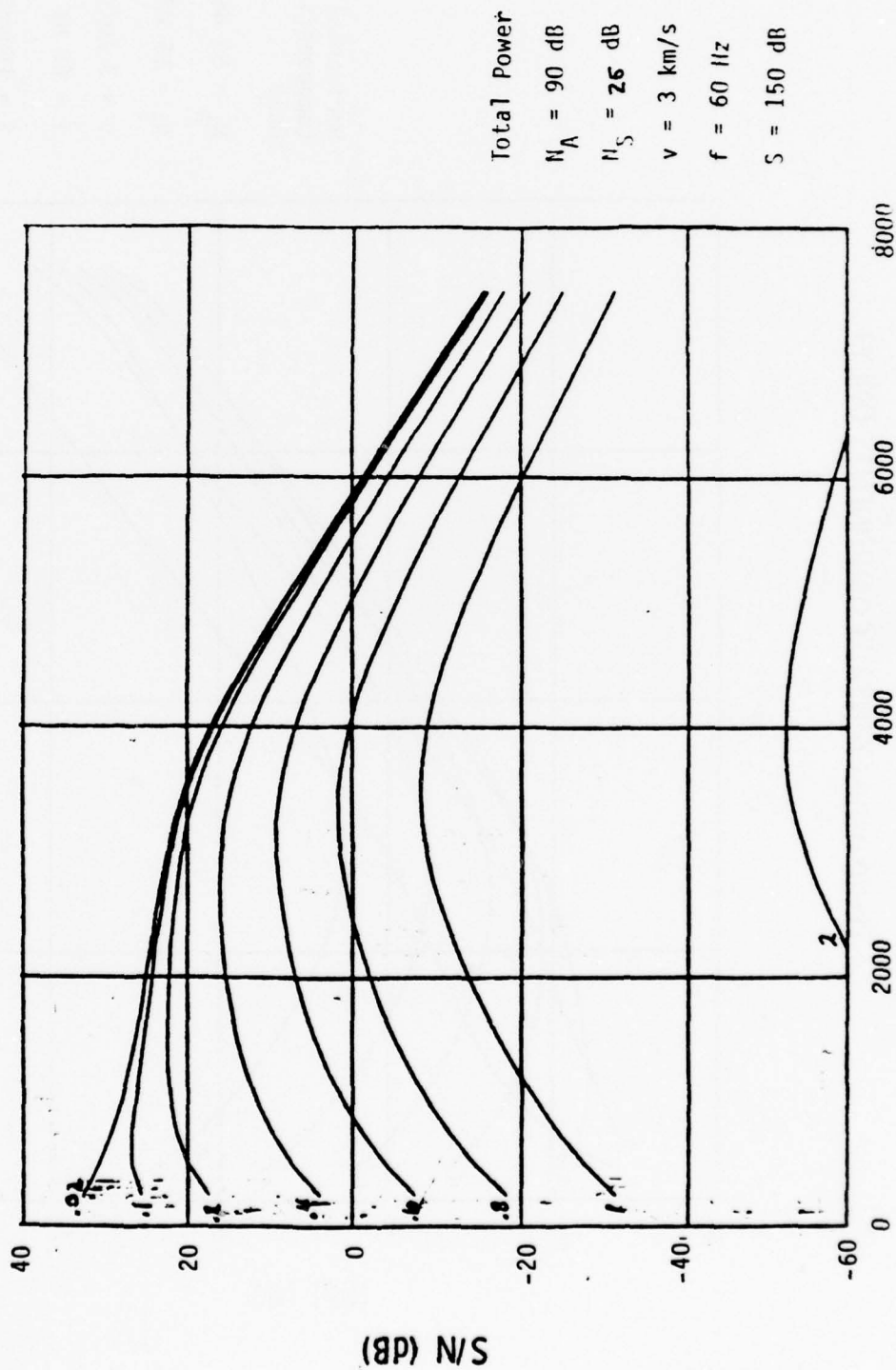
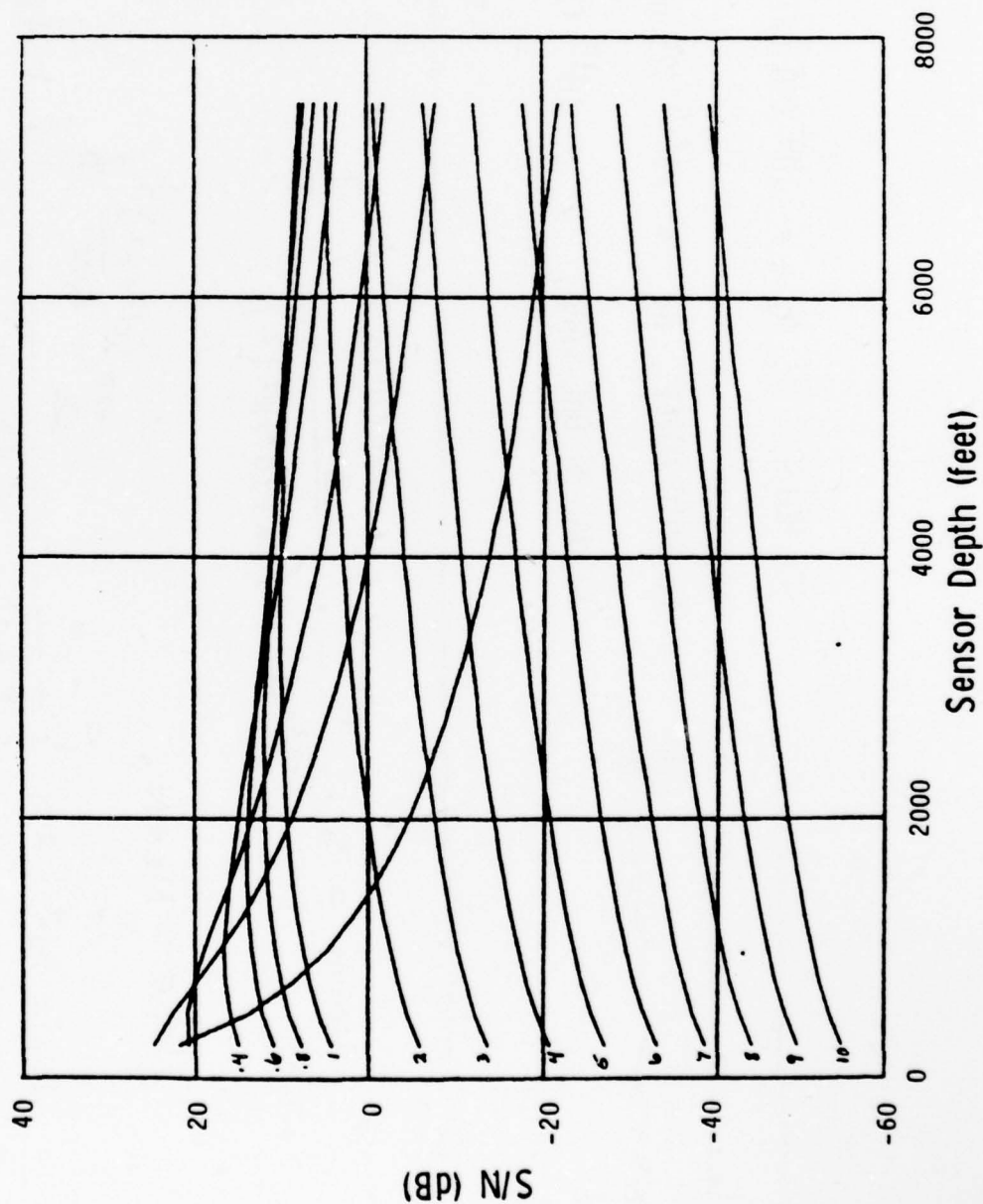


FIGURE 8

Sensor Depth (feet)

EFFECT OF SENSOR DEPTH ON S/N

Q = 200



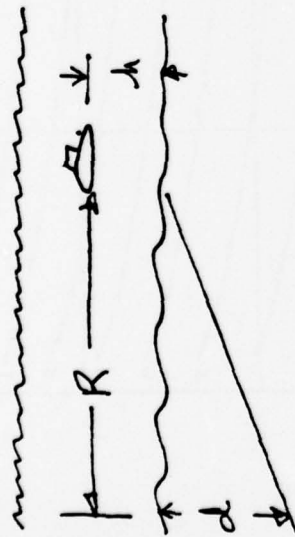
Horizontal
Components
Only
 $N_A = 90 \text{ dB}$
 $N_S = 25 \text{ dB}$
 $v = 3 \text{ km/s}$
 $f = 60 \text{ Hz}$
 $S = 150 \text{ dB}$

FIGURE 9

SEA NOISE , $N_A = 10^9$ (90 dB)

INTERNAL
SEISMIC NOISE, $N_S = 10^{2.5}$ (25 dB)

SIGNAL AT ONE YARD, $S = 10^{15}$ (150 dB)



$$\text{Signal} = S \cdot \frac{R^2}{R^2 + d^2} \cdot \frac{e^{-2\pi \frac{(d^2 + R^2)}{QV}}}{(1 + (d^2 + R^2)^2)^2} \cdot \frac{1}{10}$$

$$\text{Noise} = N_S + N_0$$

$$N_0 = N_A \cdot 2\pi \int_0^\infty \frac{r^2}{r^2 + d^2} \cdot \frac{e^{-2\pi \frac{(d^2 + r^2)}{QV}}}{(d^2 + r^2)^2} \cdot r dr$$

where N_A is selected so that N_0 (at $d=1$ yard) = $N_A / (8.10)$

FIGURE 10

FIGURE 11

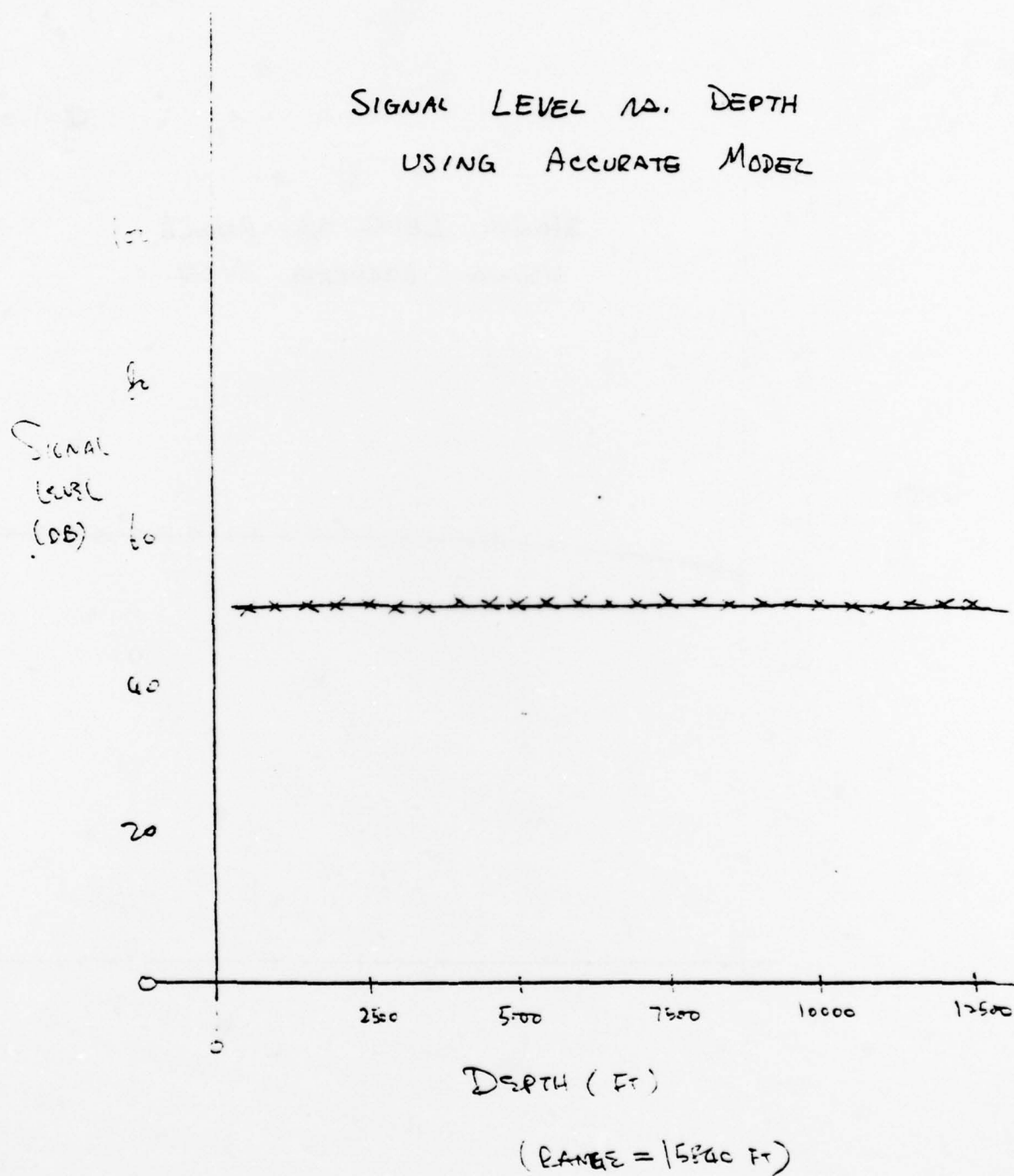
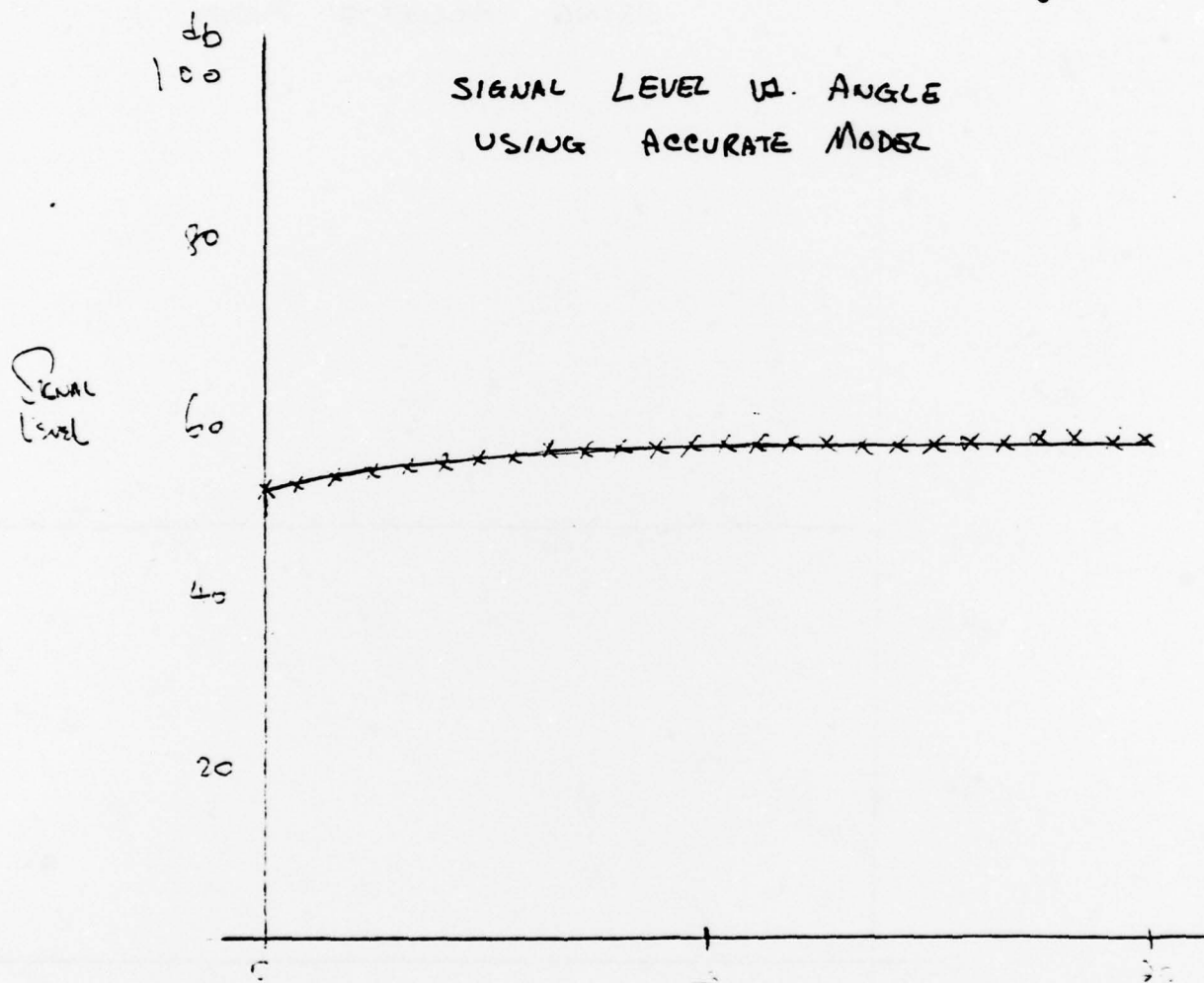
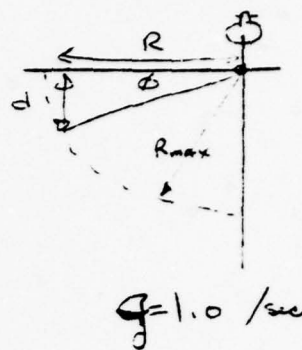


FIGURE 12



DETECTION RANGE VS Qv

(f = 60 Hertz)

S = 150 dB
 $N_S = 25$ dB
 d = 2000 feet
 Resolution
 = 0.1 Hz
 Detection
 Threshold
 = 6 dB

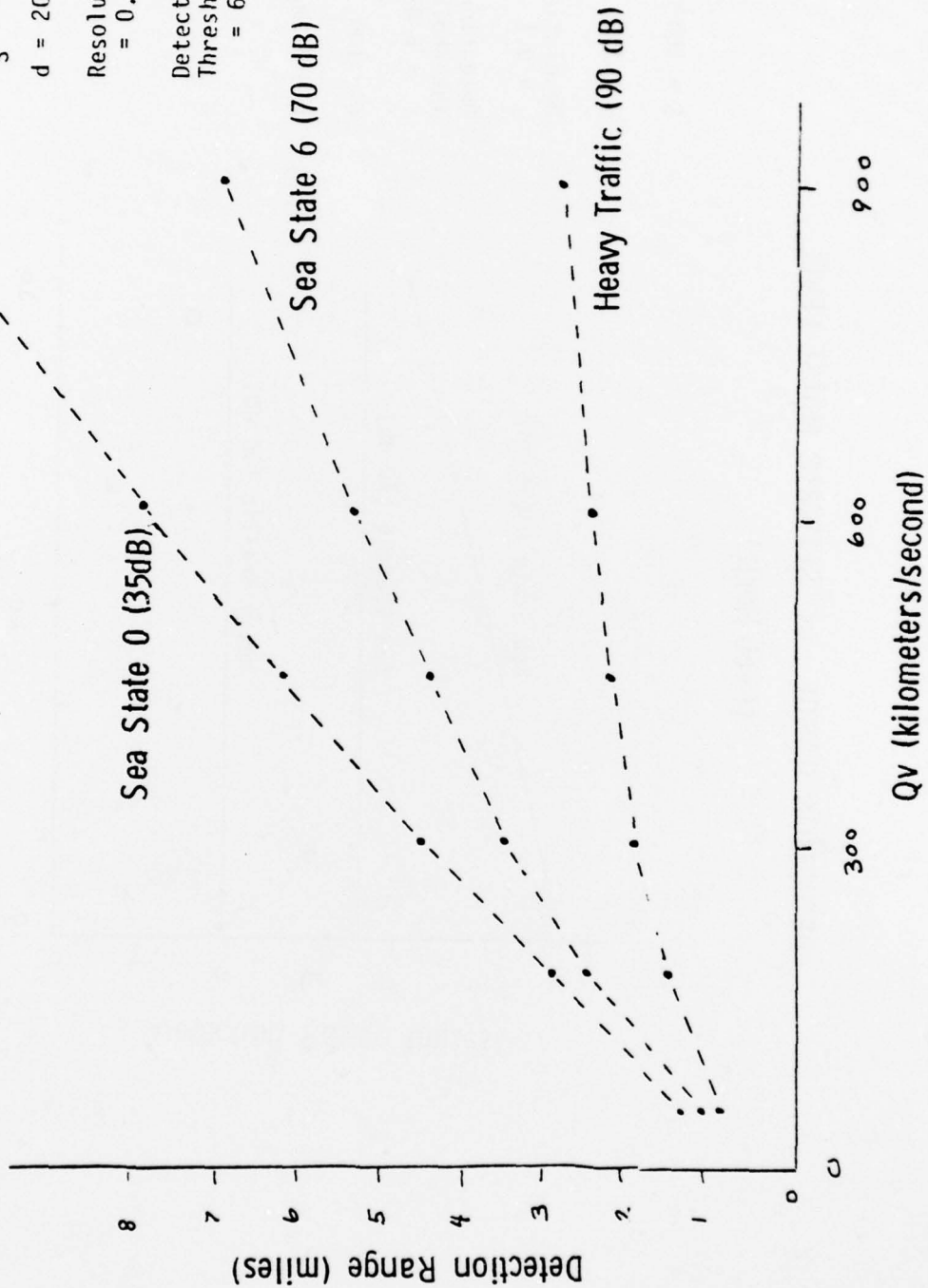


FIGURE 13

DETECTION RANGE VS SEISMIC NOISE LEVEL (f = 60 Hertz)

S = 150 dB
d = 2000 feet
Resolution
= 0.1 Hz
Detection
Threshold
= 6 dB
Q = 100
v = 3 km/s

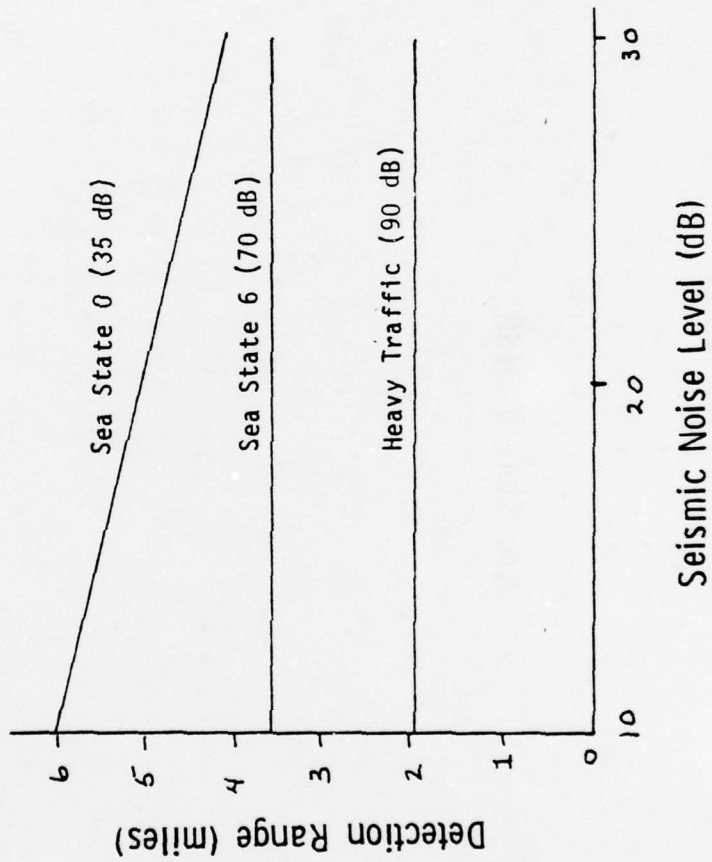


FIGURE 14

DETECTION RANGE VS FREQUENCY (SCOTIAN SHELF)

$v = 3 \text{ km/s}$
 $Q = 60$
 $d = 2000 \text{ feet}$
 Resolution
 $= 0.1 \text{ Hz}$
 Detection
 Threshold
 $= 6 \text{ dB}$

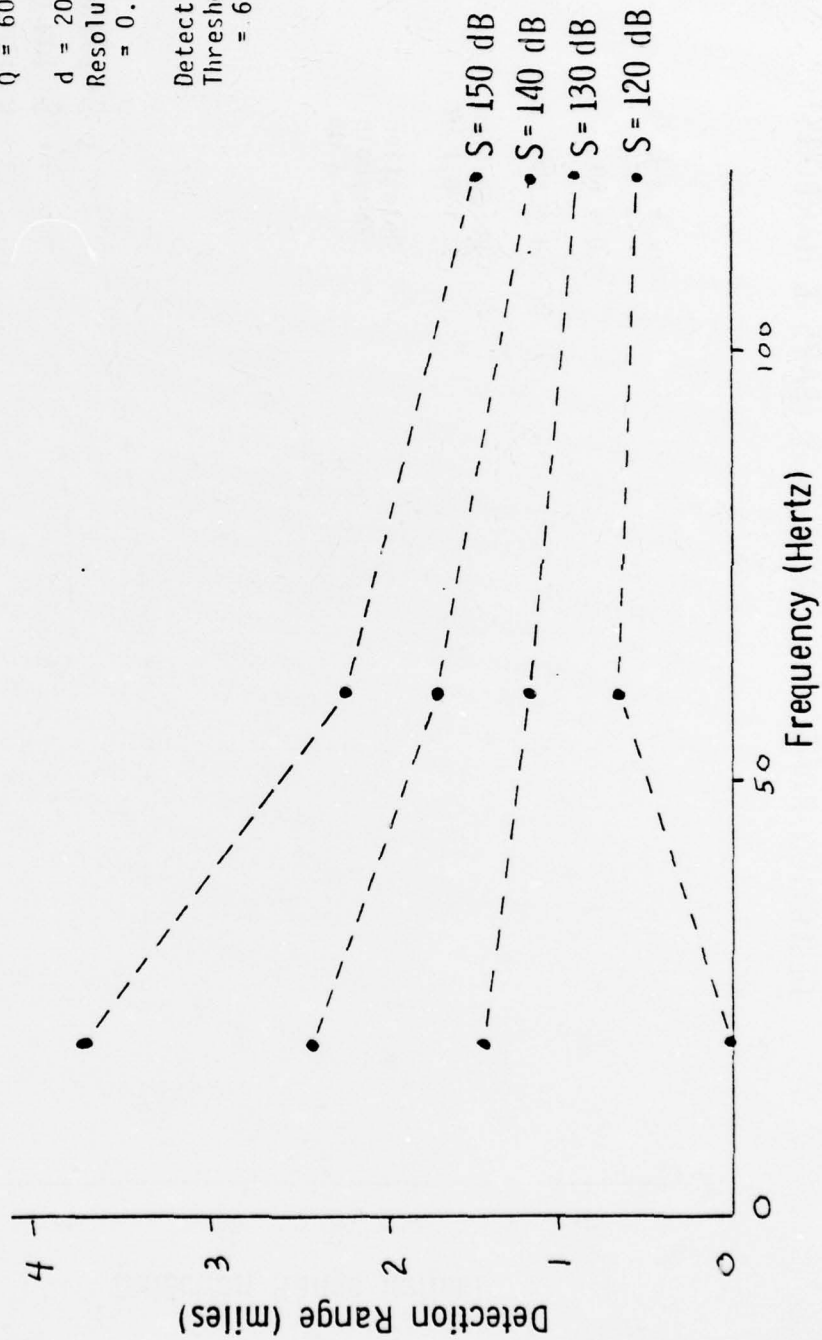


FIGURE 15

DETECTION RANGE vs FREQUENCY (BAYS & HARBORS)

$v = 3 \text{ km/s}$
 $Q = 60$
 $d = 2000 \text{ feet}$
 Resolution
 $= 0.1 \text{ Hz}$
 Detection
 Threshold
 $= 6 \text{ dB}$

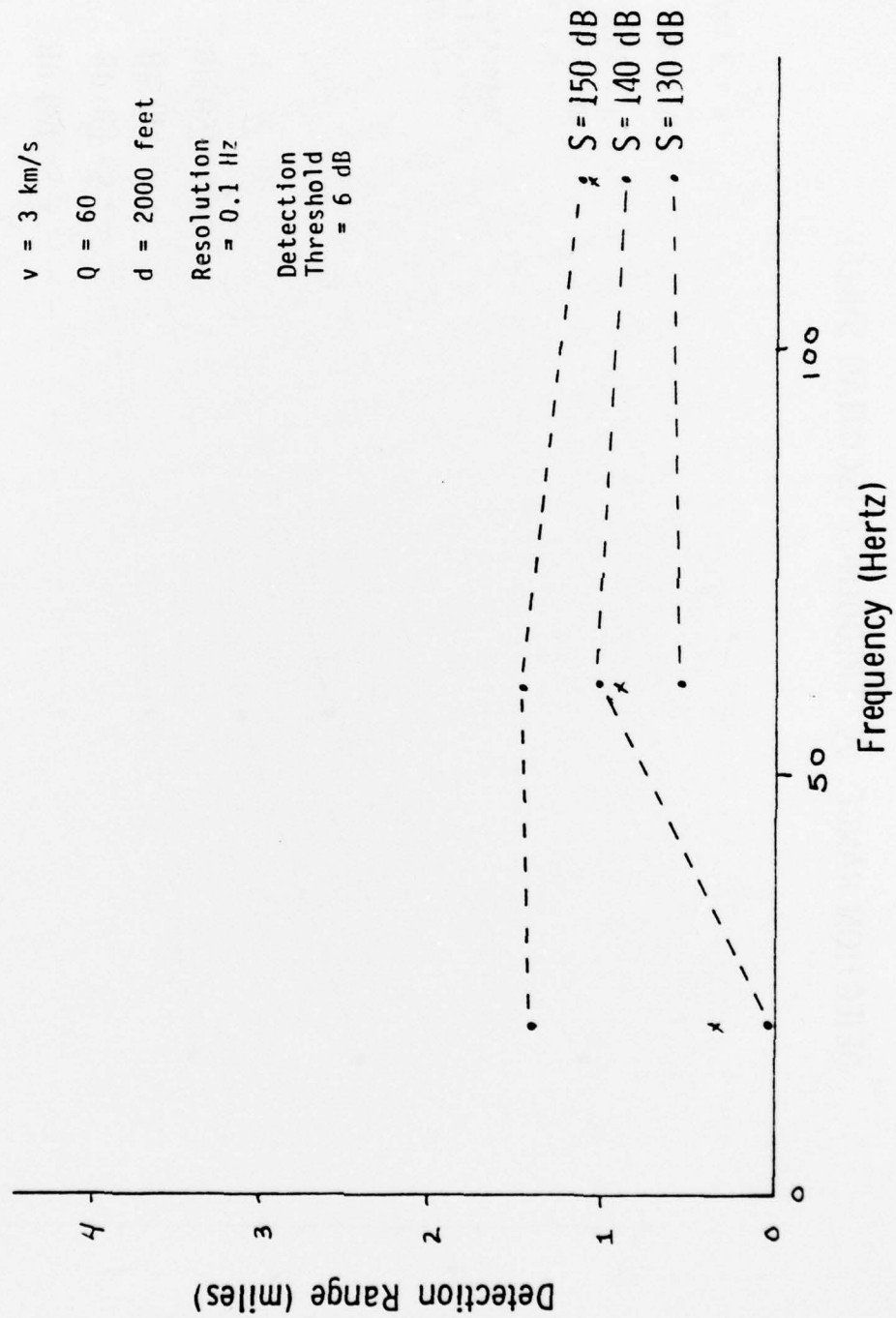
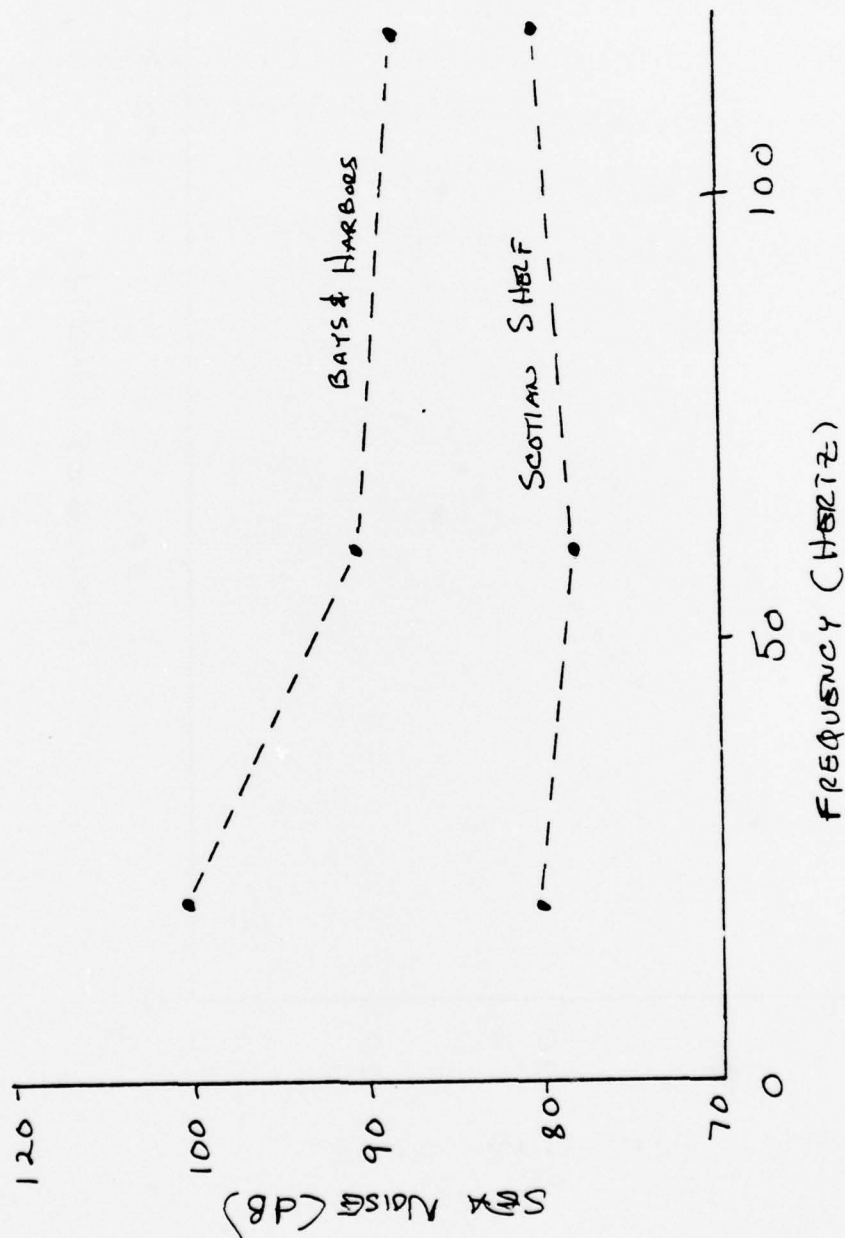


FIGURE 16

FIGURE 17

SEA NOISE vs. FREQUENCY



SEISMIC NOISE vs. Freq.

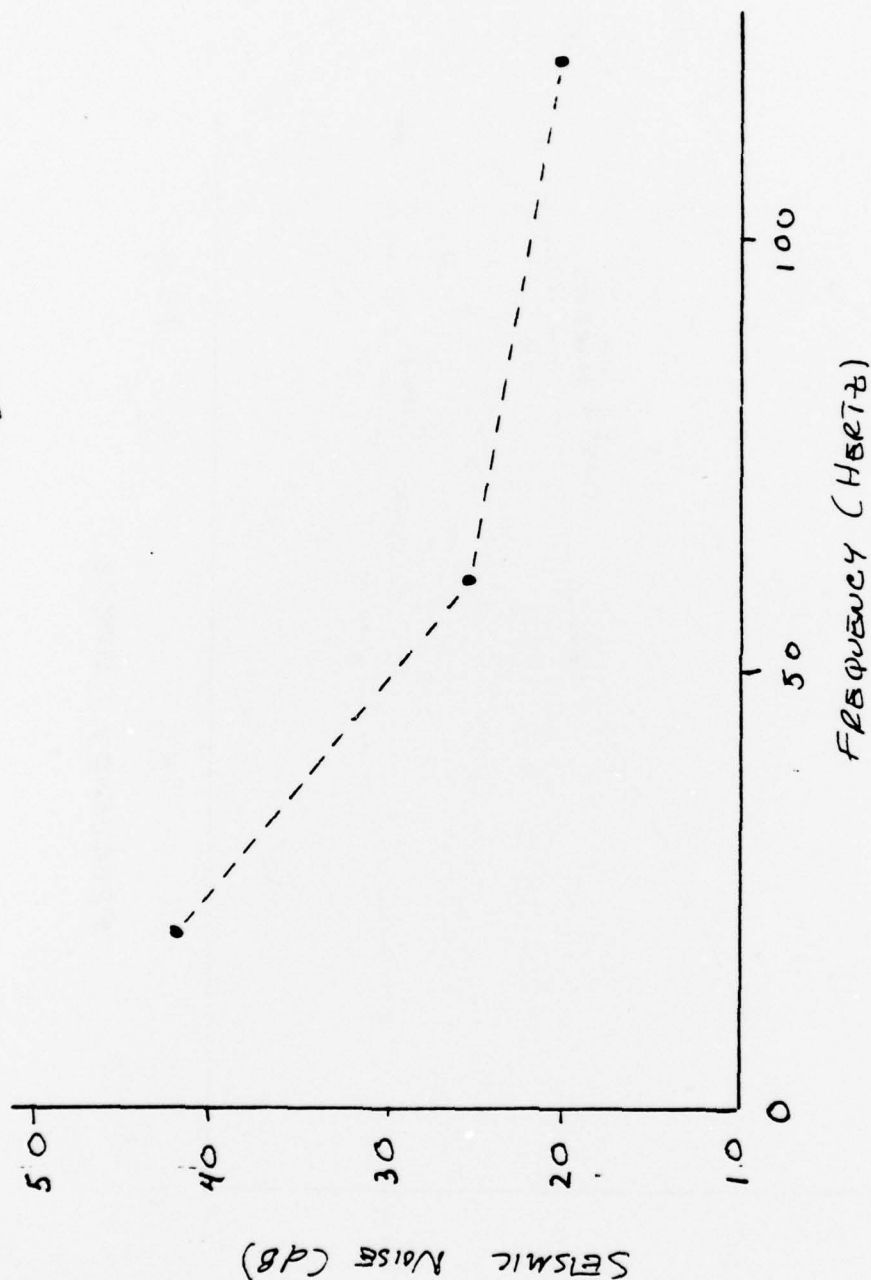


FIGURE 18

THE **BOEING** COMPANY
SEATTLE, WASHINGTON

Appendix A

Attendees

Ackler, Lynn (Mr.)	ENSCO
Alewine, Ralph (Dr.)	DARPA NMRO
Anderson, Rockne (Dr.)	NORDA
Andrews, Robert (Dr.)	ONR
Arnold, Robert (Mr.)	BOEING
Bailey, James (Dr.)	ONR
Ballard, J. A. (Mr.)	NORDA
Boosman, Jaap (Dr.)	OPNAV
Brodsky, S.L. (Dr.)	ONR
Chin Bing, Stanley (Dr.)	NORDA
Cybulski, John (Mr.)	NAVLEX
Cohen, John (Mr.)	U. of Denver
Diemer, Ferdinand (Mr.)	ONR
Dorman, H. James (Dr.)	U. Texas/Galveston
Diachok, Orest (Mr.)	NRL
Edsinger, Richard (Dr.)	BOEING
Eller, Anthony (Dr.)	NRL
Ferris, Raymond H. (Mr.)	NRL
Fletcher, Don (Dr.)	IAR
Fugimoto, Dwight (Dr.)	BOEING
Green, John (Mr.)	ENSCO
Hanish, Sam (Dr.)	NRL
Hawker, Kenneth (Dr.)	U. Texas/Austin
Hays, Earl (Mr.)	WHOI
Hecht, Richard (Mr.)	USI
Hersey, J. B. (Dr.)	ONR
Houston, Mark (Dr.)	U. Texas/Galveston
Houtz, Robert (Mr.)	L-DGO
Joiner, Gracen (Mr.)	ONR
Kronengold, Morton (Dr.)	IAR
Landers, Thomas (Dr.)	Lincoln Labs
Latham, Gary (Dr.)	U. Texas/Galveston
Matthews, James (Mr.)	NORDA
Mercer, James A. (Dr.)	APL (Washington)
Minard, CDR Julian (USN)	ONR
Moose, Paul (Dr.)	NPS-Monterey
Murphy, H.F. (Mr.)	NAVSEA
McLeroy, E. Glenn (Dr.)	NCSC
Narsworthy, Keith (Dr.)	BOEING
Nelson, Donald (Dr.)	BOEING
Northrop, John (Dr.)	NOSC

O'Brien, CDR E. (USN)
Oliver, Jack (Dr.)
Palmer, David (Dr.)
Pyle, Thomas (Dr.)
Rollins, Carl R. (Mr.)
Rothman, Robert (Dr.)
Sanders, James V. (Dr.)
Shore, CAPT Michael (USAF)
Sigelmann, R.A. (Dr.)
Spalding, G.R. (Mr.)
Stoll, Robert (Dr.)
Sykes, Alan (Dr.)
Tomei, Joji (Mr.)
Urlick, Robert J. (Mr.)
Walker, Dan (Dr.)
Young, Greg (Mr.)

ONR
Cornell U.
NRL
ONR
NRL
VELA Seismo Ctr.
NPS-Monterey
VELA-Seismo Ctr.
U. of Washington
NAVMAT
ONR
ONR
NAVOCEANO
TRACOR
U. of Hawaii
CIA

Appendix B

Letters

The following letter was received commenting on the workshop.

Department of Geological Sciences
110 Kimball Hall
(607) 256-2377

11 July 1970

Dr. Robert S. Andrews
Earth Physics Program
Code 402
Office of Naval Research
Arlington, Virginia 22217

Dear Bob:

You asked that those of us who attended the meeting at NRL in early July write to you with any comments we might have concerning the Navy's problems of seismic-wave detection in shallow water areas.

Let me begin with one general comment which you and all of us have heard over and over, but it seems of such importance that I cannot resist the opportunity to make it again. There is a real problem of communication that covers the entire range of parties from those who on one extreme view the Navy's immediate practical problems on a day-to-day basis through the spectrum of workers to, at the other extreme, those academic scientists who are studying features of the earth that have some relevance to the Navy's problems. The fact that you held the seminar at NRL is an indication that you and others in the Navy are aware of this communication problem. That such a meeting of this sort not only is a step toward alleviation of the problem, but also serves to emphasize it.

Of course there is no single factor one can point to as the cause of the problem, and there is no simple solution. One might single out many factors: the relative decline of ONR in support of basic scientific research, the growth, the recent tendency of scientists in academia to shy away from problems of military significance, the lure of the ivory tower, an increasing portion of funds for research, etc., etc. It is not possible to eliminate one, let alone all of these, and so the only solution is to work constantly to offset the effects insofar as possible. I therefore encourage you to continue to hold such meetings and also to look toward other methods of enhancing communication.

I would like to draw attention again to a point I made in closed session at the meeting due to the "wedge" of water in shallow areas on seismic waves. This would very likely have a related and more easily observable effect in the water. Although this comment is not strictly like reinventing the wheel, it is almost like reinventing the car trumpet.

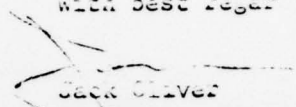
Dr. Robert S. Andrews

-2-

11 July 1970

The time is ripe for some experiments in shallow water in which shallow-buried seismometers are used to monitor ships (or whatever else the Navy wants to listen to). The experiments should be simple, as inexpensive as possible, and should take place at several sites. Perhaps droppable packages can be used. Existing models of bottom seismographs may be adequate. In any case, it is time to get some empirical data.

With best regards,


Jack Oliver
Chairman